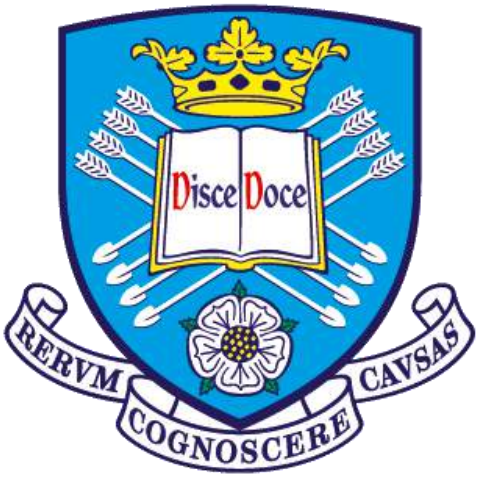

The University Of Sheffield.

Understanding the Effectiveness of Plutonium Surrogates for Waste and Stockpile Immobilisation

Lewis R. Blackburn

A thesis submitted in partial fulfilment of the requirement for the degree of Doctor of Philosophy

NucleUS Immobilisation Science Laboratory
Department of Materials Science and Engineering
The University of Sheffield

May 2021

ABSTRACT

Continued reprocessing of spent nuclear fuel inventories in the United Kingdom has afforded a significant stockpile of separated PuO_2, presenting a unique decommissioning prospect and a challenge of materials degradation. Indefinite storage is not considered to be a viable long-term management strategy, hence the UK Government are considering alternative strategies favouring a combination of reuse and/or disposal to place the material beyond reach. Zirconolite ceramic wasteforms are the favoured immobilisation matrix for Pu oxides and residues, on the basis of high aqueous durability, moderate wasteloading potential, and successful deployment as the actinide-bearing phase in the multiphase SYNROC wasteform, specifically developed for as an alternative to borosilicate glass for high level waste conditioning. In order to underpin the safety case for geological disposal of Pu-loaded zirconolite matrices, it is necessary to systematically establish the preferred solid solution regime, promoting maximum wasteloading and chemical durability whilst suppressing the formation of secondary actinide-bearing phases. To this effect, a systematic analysis of Ce, U and Th incorporation within zirconolite was performed, under a variety of synthesis conditions, in order to correlate the effect of surrogate choice and oxidation state on zirconolite phase evolution.

In Chapter 5, the isovalent solid solution $CaZr_{1-x}M_xTi_2O_7$ (where M = Ce, U and Th) was targeted, with the effect of surrogate oxidation state controlled through varying the sintering environment. Incorporation of Ce, *i.e.* $CaZr_{1-x}Ce_xTi_2O_7$, was most effective under oxidising conditions, whereby a transformation to the zirconolite-4M polytype was observed in the compositional interval $0.10 \leq x \leq 0.20$, occupying ~ 68 wt. % of the overall phase assemblage when targeting a Ce concentration equivalent to x = 0.40. Imposing reducing conditions (5% H_2/N_2 mixture) during synthesis favoured the formation of a significant perovskite fraction, occupying ~ 48 wt. % of the phase assemblage at x = 0.40. The formation of the perovskite phase was attributed to complete reduction of the available Ce^{4+} inventory to Ce^{3+}, determined by Ce L_3 XANES. Phase formation in the $CaZr_{1-x}U_xTi_2O_7$ solid solution was also controlled by U oxidation state. Synthesis in inert Ar gas was sufficient to maintain the U inventory as U^{4+}, promoting the formation of the zirconolite-4M polytype, confirmed by selected area electron diffraction. Synthesis under reducing 5% H_2/N_2 stabilised a U-bearing accessory perovskite phase at all levels of U concentration, alongside a pyrochlore-structured phase with elevated U content relative to zirconolite, accounting for 30 wt. % of the overall phase assemblage when targeting the nominal composition x = 0.40. Synthesis in air promoted the formation of higher U oxidation states, determined to be > U^{5+} by U L_3 XANES analysis, resulting in U partitioning in a defect fluorite structured phase beyond x = 0.20. Synthesis of the novel $CaZr_{1-x}Th_xTi_2O_7$ solid solution established that the zirconolite-4M intermediate phase was not stabilised at the expected compositional interval, rather, the Th inventory was concentrated in a secondary pyrochlore phase in the range $0.10 \leq x \leq 0.50$. A single phase product with the nominal formulation $CaZr_{0.40}Th_{0.60}Ti_2O_7$ was produced when targeting x = 0.60, presenting a potential route for immobilisation of Th-rich wastes.

The suitability of Cr^{3+} as a charge balancing species for non-isovalent zirconolite solid solutions was investigated in detail in Chapters 6 and 7, with the $Ca_{1-x}Ce_xZrTi_{2-2x}Cr_{2x}O_7$ solid solution synthesised by conventional sintering, reactive spark plasma sintering and hot isostatic pressing. Single phase

zirconolite-2M was stabilised in the compositional range $0 \leq x \leq 0.15$ when sintering in air, with secondary Ce-perovskite, CeO_2, Cr_2O_3 and ZrO_2 phases stabilised when targeting higher Ce concentrations. Poor densification was achieved throughout the solid solution; hence reactive spark plasma sintering was deployed to achieve greater consolidation. Despite a marked improvement to near theoretical density, the reducing conditions imposed by the graphite die were sufficient to entirely reduce the available Ce^{4+} inventory to Ce^{3+}, destabilising the phase assemblage through preferential formation of Ce-perovskite, accounting for ~ 19 wt. %. A subset of this material was also processed *via* HIP, as this is the preferred thermal treatment route for UK Pu inventories. Processing at 1320 °C with a dwell pressure of 100 MPa failed to yield a single phase product, with unincorporated CeO_2, Cr_2O_3 and ZrO_2 present in the bulk microstructure. Observations of the canister-ceramic interface were consistent with those previously detailed for similar HIPed microstructures, dominated by a 10 μm thick Cr-rich oxide interface. Elevated quantities of Ce-perovskite were observed at the interface, indicative of slightly reducing conditions at the periphery.

The influence of surrogate choice, and in turn the effect of secondary phase formation, on the chemical durability of zirconolite compositions under aggressive leaching conditions was resolved in Chapter 8. Using a unique dissolution methodology, whereby three distinct zirconolite compositions were exposed to a variety aggressive leaching environments (including 8M HNO_3 and 1M H_2SO_4), it was possible to quantify the extent to which the fissile surrogate fraction was extracted from the wasteform into solution. We report that the extent of dissolution was controlled by both the presence of detrimental secondary phases present in the microstructure, and choice of surrogate used. Through careful optimisation of the zirconolite composition, by which the wasteform was buffered with excess Zr/Ti to preclude secondary phase formation, the quantity of the original surrogate fissile inventory dissolved from the ceramic material significantly reduced.

ACKNOWLEDGEMENTS

First and foremost, my profound gratitude is given to my supervisors Prof. Neil Hyatt, Dr. Martin Stennett, Dr. Claire Corkhill and Dr. Ewan Maddrell. You have all displayed a touching confidence in my abilities, providing me with the freedom to pursue independent scientific thought, and for that I am extremely grateful. The completion of this thesis a testament to your knowledge, patience and demeanour, I hope that my appreciation is reflected by the quality of the work contained within.

Without the support of Prof. Shi-Kuan Sun, Dr. Laura Gardner, Dr. Daniel Bailey and Dr. Sebastian Lawson, large portions of this thesis could not have been completed. You have all provided a wealth of technical and moral support, alongside some of the most insightful scientific conversations I've ever had (often after few too many beers, admittedly). I am indebted to you all, and I am grateful for your continued friendship. I extend my highest praise to Dr. Sam Walling, Dr. Amber Mason, Dr. Clémence Gausse, Dr. Colleen Mann, Max Cole, Merve Kuman and Rachel Crawford for enabling various stages of this work, through the provision of invaluable technical insight and proficiency. Moreover, I give my thanks to Dr. Peter Apps at NNL, for collaboration with TEM data collection and analysis of uranium zirconolite samples at the NNL Central Laboratory.

The completion of a PhD can be, at often times, a difficult and testing experience, especially amidst a global pandemic. However, I have been fortunate enough to spend it in an incredible research group, surrounded by some of the most talented and inspiring individuals that one could hope to meet. I cannot take the time to thank all of you individually, but I have to give my warmest thanks to my good friends Chris, Dan A, Max and Lucas, for many a pleasant evening and for all the school-night beers. I also extend my appreciation to my friends Sam, Shem, Jonny, Ryan, Gravey, Jack and Pinch for putting up with me moping on about ceramics and plutonium for the last few years.

I extend my gratitude to EPSRC, Nuclear Decommissioning Authority, and National Nuclear Laboratory for funding and technical collaboration.

I give my warmest thanks to my mum, dad, brother and sister for supporting me morally, and at times financially, for the past 8 years of my higher education. Without you none of this work would have been possible.

Last of all, to Molly, for your many years of unwavering companionship. Loving you comes as naturally as breathing, and every hour spent in your presence is a gift that I surely do not deserve. You forever provide me with motivation to become a better person, and with this in mind, I dedicate this thesis to you.

PUBLICATIONS

During the course of this thesis, the author has contributed to the following publications:

L. R. Blackburn *et al.*, “Hot Isostatically Pressed Zirconolite Wasteforms for Actinide Immobilisation,” in *IOP Conf. Series: Materials Science and Engineering*, 2020.

L. R. Blackburn and N. C. Hyatt, “Actinide Immobilization in Dedicated Wasteforms: An Alternative Pathway for the Long-Term Management of Existing Actinide Stockpiles” *Encyclopedia of Nuclear Energy*, Elsevier, 2021.

L. R. Blackburn *et al.*, “Synthesis and Characterisation of $Ca_{1-x}Ce_xZrTi_{2-2x}Cr_{2x}O_7$: Analogue Zirconolite Wasteform for the Immobilisation of Stockpiled UK Plutonium,” *J. Eur. Ceram. Soc.*, vol. 40, no. 15, pp. 5909–5919, 2020.

L. R. Blackburn *et al.*, “A systematic investigation of the phase assemblage and microstructure of the zirconolite $CaZr_{1-x}Ce_xTi_2O_7$ system,” *J. Nucl. Mater.*, vol. 535, p. 152137, 2020.

L. R. Blackburn *et al.*, “Influence of Transition Metal Charge Compensation Species on Phase Assemblage in Zirconolite Ceramics for Pu Immobilisation,” *MRS Adv.*, Feb. 2020.

L. R. Blackburn *et al.*, “Synthesis, Structure and Characterisation of the Thorium Zirconolite $CaZr_{1-x}Th_xTi_2O_7$ System” *J. Am. Ceram. Soc.*, vol 104, no. 7, pp. 2937-2915; 2021.

L. R. Blackburn *et al.*, “Review of Zirconolite Crystal Chemistry and Aqueous Durability” *Advances in Applied Ceramics,* Taylor & Francis, 2020.

L. R. Blackburn *et al.*, “Accelerated Leaching of Ce- and U-Zirconolite Wasteforms for Pu Immobilisation: Influence of Accessory Phases and Surrogate Type” *npj Materials Degradation*, 2021.

L. R. Blackburn *et al.* “Synthesis and Characterisation of the $CaZr_{1-x}U_xTi_2O_7$ Zirconolite Solid Solution” (IN DRAFT)

L. R. Blackburn *et al*., “Synthesis and Characterisation of HIP $Ca_{0.80}Ce_{0.20}ZrTi_{1.60}Cr_{0.40}O_7$ Zirconolite and Observations of the Ceramic-Canister Interface” *MRS Adv.* no. 6, pp. 112-118, 2021.

L. R. Blackburn *et al.*, “Solid Solution Limits of Plutonium and Neutron Poisons in Zirconolite Ceramics – A Literature Review and Gap Analysis for Immobilisation of UK Inventory” (IN DRAFT)

Z. Wei *et al.*, “Rapid synthesis of zirconolite ceramic wasteform by microwave sintering for disposition of plutonium,” *J. Nucl. Mater.*, vol. 539, p. 152332, 2020.

L. M. Mottram *et al.*, “A Feasibility Investigation of Laboratory Based X-ray Absorption Spectroscopy in Support of Nuclear Waste Management,” *MRS Adv.*, Jan. 2020.

Z. J. Wei *et al.*, “Synthesis of zirconolite-2M ceramics for immobilisation of neptunium,” *Ceram. Int.*, no. August, pp. 1–6, 2020.

S. M. Lawson *et al*., "Synthesis and in situ ion irradiation of A-site deficient zirconate perovskite ceramics," J. Mater. Chem. A, 2020.

Barlow ***et al.*** *"*Thermal treatment of nuclear fuel-containing Magnox sludge radioactive waste in Mg-based glass compositions" *J. Nuc. Mat*., vol. 552, 152956, 2021.

Yuan *et al*. "Effect of ZrB_2 Powders on Densification, Microstructure, Mechanical Properties and Thermal Conductivity of ZrB_2 – SiC Ceramics" *Ceram. Int.* vol. 47, no. 11, pp. 15843-15848, 2021.

ORAL AND POSTER PRESENTATIONS

This work has also been disseminated, wholly or in part, at a number of conferences, as listed below:

6th Nuclear Decommissioning Authority (NDA) PhD Seminar, 17th Jan 2018, Manchester, UK.

ANNETTE Summer School on Nuclear Technology, Nuclear Waste Management and Radiation Protection, 24 – 30th June 2018, Turku, Finland.

Uranium Science, 21 – 22nd Jan 2019, Bristol, UK.

7th Nuclear Decommissioning Authority (NDA) PhD Seminar, 23th Jan 2019, Manchester, UK.

THERAMIN Technical Training Workshop, 12 – 14th June 2019, Avignon, France.

43rd Symposium of the Scientific Basis for Nuclear Waste Management, 21 – 24th Oct 2019, Vienna, Austria.

PACRIM 13, 27th Oct – 1st Nov 2019, Okinawa, Japan.

8th Nuclear Decommissioning Authority (NDA) PhD Seminar, 29th Jan 2020, Manchester, UK.

THERAMIN2020 Conference, 4 – 5th Feb 2020, Manchester, UK.

AWARDS AND PRIZES

ENEN+ Mobility Fund 2018 – Award: €750

Learned Society Fund (University of Sheffield) 2018 – Award: £450

Doctoral Researcher Award 2020 – Honourable Mention

Davidge Award 2020 – Award: £500 & publication in Advances in Applied Ceramics

EPSRC Doctoral Prize Fellowship 2020

NOTES ON THESIS STRUCTURE

The format of this thesis is such that it deviates from a conventional structure, insofar as the majority of the work has already been published, or is in the process of being reviewed for journal publication. Chapters 1, 2 and 4 conform to a regular structure, however Chapter 3, 5, 6, 7 and 8 have been largely replaced by peer-reviewed journal articles. It is hoped that this will aid the reader's comprehension of the work.

Contents

1. INTRODUCTION

The United Kingdom is currently in possession of the largest stockpile of separated plutonium under civil safeguards worldwide [1]. The 2019 Radioactive Waste Inventory reported that approximately 112 tHM (tonnes, heavy metal equivalent) of PuO_2 is consolidated at the Sellafield site, and this is forecast to increase to around 140 tHM upon completion of scheduled reprocessing operations [2]. This material was derived from aqueous reprocessing of spent nuclear fuel (SNF) from the Magnox and advanced gas cooled (AGR) fleet of reactors, at the Magnox and ThORP (thermal oxide reprocessing plant) facilities, respectively. The separated PuO_2 in its current form poses significant security risk, and a long term management strategy must be implemented in order to reduce the risk imposed to the public and wider environment, and reduce the burden for future generations [3]. The corporate body liable for the storage, transport, decommissioning and eventual disposal of all radioactive material, produced as a consequence of the civil nuclear fuel cycle, is the Nuclear Decommissioning Authority (NDA), established through the 2004 Energy Act [4]. Accordingly, the NDA are wholly responsible for the disposition of the plutonium stockpile, whether through reuse, disposal or otherwise. The NDA has outlined several credible options for the plutonium stockpile, with emphasis on deliverability, technological feasibility, socioeconomic viability and benefit, safety, and environmental compatibility [5]. The two high-level options that are currently being considered are: reuse as mixed oxide (MOX) fuels, followed by disposal in a geological disposal facility (GDF) or prompt immobilisation and disposal.

At a broad level, immobilisation of radioactive or otherwise hazardous material typically involves the conversion, either by vitrification, cementation, incineration, or ceramic processing of waste into a passively safe wasteform, thereby reducing the risk associated with storage, transport and ultimate disposal [6]. The choice of immobilisation matrix and compositional specifications of a radioactive wasteform are tailored, with considerations given to the physical state of the feedstock, radionuclide inventory, required lifetime, chemical durability, thermal footprint, volume, cost and technical maturity of available technology. Considering waste streams with a high actinide fraction, such as calcined PuO_2 powder, crystalline ceramic materials offer a suite of desirable properties and natural mineral analogues, and are therefore considered to be superior immobilisation matrices to cementitious or vitrified materials [7]. Fundamentally, radionuclides may be accepted in solid solution within specific lattice sites in the ceramic structure, allowing the radioactive species to adopt the properties of the parent structure. Therefore, candidate ceramics for immobilisation of high activity wastes are typically derived from naturally occurring mineral structures that have demonstrated exceptional longevity, and resistance to natural weathering processes. As a result, there have been several international research programmes aiming to identify crystalline systems that may offer a suitable combination of properties for the immobilisation of plutonium. The most successful of these programmes was undertaken the Australian Nuclear Science and Technology Organisation (ANSTO), with the development of the SYNROC (SYNthetic-ROCk) concept. SYNROC was developed as a multiphase ceramic consisting of synthetic titanate phases, designed with analogy to naturally occurring mineral specimens, with a demonstrated capacity to host most elements that are present in generic high level waste streams [8]. The SYNROC wasteform is generally comprised of three phases: hollandite ($BaAl_2Ti_6O_{16}$ – capable of

accommodating Cs^{+}, Rb^{+}, K^{+}, Ba^{2+}, Fe^{2+}, Cr^{3+} *etc.*), zirconolite ($CaZrTi_2O_7$ – capable of accommodating U^{4+}, Pu^{4+}, Th^{4+}, Cm^{4+}, Am^{4+}, Np^{4+} *etc*.) and perovskite ($CaTiO_3$ – capable of accommodating Na^{+}, Sr^{2+}, Am^{3+}, Cm^{3+}, Np^{3+} *etc*.). The SYNROC design philosophy is such that liquid high level waste derived from aqueous reprocessing may be calcined and intimately mixed with mineral forming precursors, and hot pressed to form a synthetic rock-like material, with chemical durability superior of that to conventional borosilicate glass matrices [9], [10]. Furthermore, the relative fraction of each mineral may be tailored to provide greater compatibility with the feedstock chemistry, *e.g.* SYNROC-D was developed for the immobilisation of U.S. defence wastes containing considerable processing contaminants Mn, Ni, Si [11]. The success of the SYNROC programme has promoted considerable research into the development of single phase ceramic wasteforms for the immobilisation of high-purity actinide waste streams, such as surplus plutonium. In particular, zirconolite has been considered as a suitable host for $Pu^{3+/4+}$, and has been the subject of considerable study [12]–[20]. The parent structure is comprised of alternating layers of CaO_8/ZrO_7 polyhedra and planes of TiO_6/TiO_5 polyhedra arranged in hexagonal tungsten bronze-type motifs. Pu may be accommodated in solid solution *via* substitution within Ca^{2+} and Zr^{4+} sites [12], [21], [22]. The Ti^{4+} site has also demonstrated extensive solubility of lower valence cation species (Fe^{3+}, Mg^{2+}, Al^{3+}) to provide charge compensation. Natural specimens of zirconolite have demonstrated exceptional resistance to chemical alteration over geological timescales, with some specimens retaining significant (~ 20 wt. %) fractions of their original radionuclide inventory, typically U/Th [23]–[25]. Synthetic specimens have exhibited normalised leach rates of the order 10^{-6} g m^{-2} d^{-1} in some instances [26] providing a considerable safety margin as a host of Pu, for which the ^{239}Pu isotope has the longest half-life of approximately 24,100 y.

Although the zirconolite system has been the subject of considerable research, inactive chemical surrogates are typically utilised *in lieu* of isotopes of Pu, due to the stringent safety requirements necessary for laboratory scale manipulation of Pu. Specifically, Ce^{4+}, Ce^{3+}, Gd^{3+}, Hf^{4+}, Sm^{3+}, U^{4+}, Th^{4+} are commonly used as surrogates for Pu^{4+} and Pu^{3+}. These surrogates have comparable electronegativity, ionic radii, oxide melting temperature, valence, and redox behaviour (amongst other physicochemical properties), and can therefore, under suitable conditions, provide reasonable simulant behaviour. Although none of the elements above can perfectly replicate Pu in all chemical environments, surrogates have proven to be very useful with regards to scoping the incorporation of Pu in glass and ceramic wasteforms. Nevertheless, there is considerable inconsistency and non-compatibility within the literature regarding synthesis routes, sintering regimes and surrogate use, making a useful comparison of surrogate retention within the zirconolite phase difficult to systematically catalogue. The provision of a useful safety case for the deployment of zirconolite wasteforms for Pu in the context of geological disposal is therefore contingent on the success of careful systematic trials investigating the efficacy of Pu surrogates.

The primary objective of this thesis was to systematically characterise the solid solution behaviour of Pu surrogates within the zirconolite phase, allowing expedient optimisation of potential wasteform formulations, therefore further underpinning the safety case for immobilisation as a disposal route. Specifically, this work herein utilised Ce, U and Th as surrogates, on the basis of the aforementioned

criteria. Furthermore, the impact of surrogate valence on zirconolite phase formation, microstructure properties and chemical durability was to be assessed through careful and systematic control of processing environment and synthesis route. The expectation, in this case, was that the production of an extensive catalogue of zirconolite solid solutions, fabricated with Ce, U and Th, with formal valence states explicitly determined, would serve as a useful screening tool to easily down-select undesirable compositions, and identify potential candidates to promote to Pu validation trials. It was also the expectation that this could be achieved during the course of this study, however due to the COVID-19 pandemic, Pu validation trials did not materialise. On the basis of expediency and ease of processing, a conventional mixed oxide cold-press and sintering (CPS) ceramic processing route was used, however, this thesis also aimed to develop the use of novel thermal processing treatments, for example Hot Isostatic Pressing (HIP) and Reactive Spark Plasma Sintering (RSPS).

2. NUCLEAR PROCESSES, POWER AND WASTE

2.1 Atomic Structure and Radioactive Decay

Atoms are the building blocks of the elements, consisting of a nucleus of protons and neutrons (baryons) with electrons (leptons) orbiting the nucleus in quantized orbitals. Elements are charge stabilised by inclusion of an equal number of protons and electrons, and arranged in the periodic table according to the increasing number of protons Z, with the number of neutrons given by N. Hence, the mass of an atomic nucleus (disregarding the negligible ~ 10^{-31} kg electron mass) can be given by Z + N = A, where the unit of A is the atomic mass unit (u) = 1.66 × 10^{-27} kg [27]. Electrons are bound to protons in the nucleus *via* the electromagnetic force, as protons and electrons have opposing charge +e and -e respectively where e = 1.6 × 10^{-19} C. The presence of neutrons in the nucleus permits stability *via* the strong nuclear force, which acts over a range of approximately 10^{-15} m. All protons experience mutual electrostatic repulsion and accordingly must overcome the Coulomb barrier that prevents nuclear stability. Therefore, as the number of protons increases so must the proportion of neutrons necessary to ensure the stability of the nucleus. This is illustrated in **Fig. 1**. Nuclei with differing numbers of neutrons (isotopes) may be unstable and will subsequently decay by one of several radioactive decay modes, accompanied by the emission of ionising radiation: alpha, beta, or gamma. Each decay mode is characterised by varying ionisation potential and penetration depth. The relationship between Z and decay mode is shown in **Fig. 1**, demonstrating α-decay is favoured by heavier species, whilst lighter elements are more susceptible to β-decay. The mass of a nucleus is always slightly lower than the mass of the constituent nucleons, this is called the mass defect (Δm). According to the Einstein mass-energy equivalence ($E = mc^2$) the total energy of the nucleus is less than the combined energy of the individual nucleons. The energy released in the formation of a nucleus is therefore described as the *binding energy,* and is considered a measure of nuclear stability. The energy liberated (or absorbed) in a nuclear process is therefore dependent on the binding energy, and is defined as the *Q-value*. This is described by **Eq. 1**, where 931.5 MeV/c^2 = 1 amu.

$$Q\,(MeV) \;=\; -931.5 \cdot \Delta m \qquad \text{Equation (1)}$$

Isotopes may achieve stability by a number of radioactive decay processes until a stable isotope is reached (at a broad level, these are alpha (α), beta (β) and gamma (γ) decay). A symbolic representation of the dominant radioactive decay processes is summarised in **Table 1**. It should be noted that there are several quantities that are conserved during these decay processes: the total energy of the system; linear momentum; total charge; number of nucleons (mass number); total angular momentum.

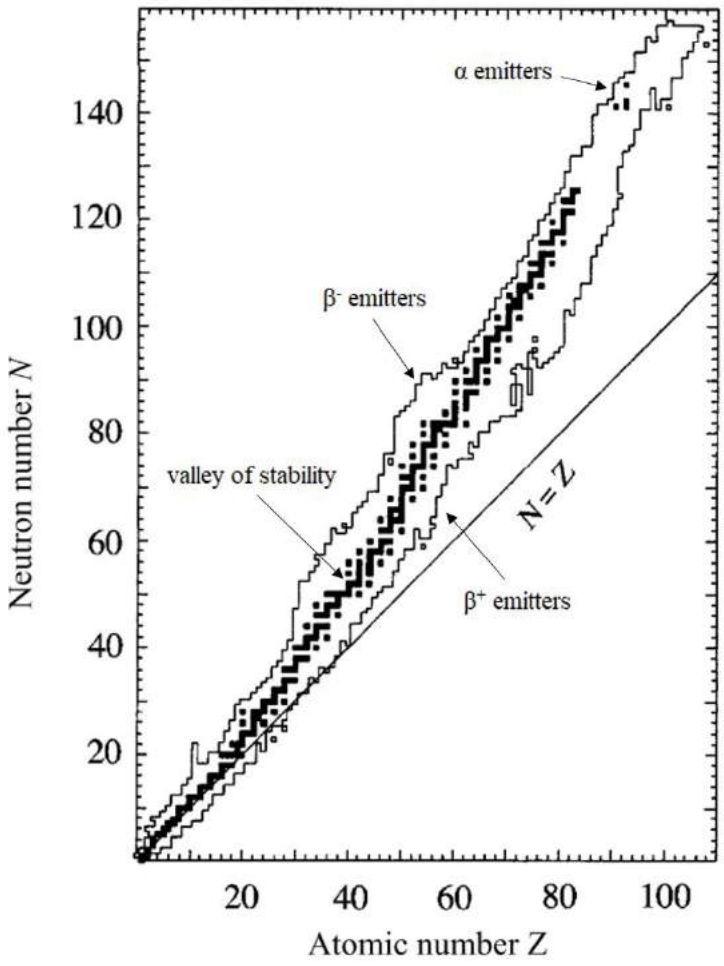

Fig. 1) Relationship between number of protons and neutrons held within the atomic nucleus, with major nuclear decay modes indicated (adapted from [28])

2.1.1 Alpha Decay

Alpha (α) radiation is typical of neutron deficient isotopes (such as those in the actinide region of the periodic table) and is the most ionising natural form of radiation. Alpha decay is characterised by the ejection of a ^{4}He nucleus (α-particle), producing a daughter nucleus. The daughter nucleus may exist briefly in an excited state, and may be accompanied by emission of a γ-ray. A specific example of α-decay is given in **Eq. 2**. The atomic number Z is decreased by 2 and the mass number A is decreased by 4 in all alpha ejections. Following the conservation of momentum, the decay energy is transferred overwhelmingly to the α-particle.

$$^{238}_{92}\mathrm{U} \rightarrow {}^{234}_{90}\mathrm{Th} + {}^{4}_{2}\mathrm{He} + \gamma \qquad \text{Equation (2)}$$

As the ejected ^{4}He nucleus is positively charged it must overcome the repulsion provided by the parent nucleus (~ 25 MeV) [29]. Alpha decay is a particularly important process in the development of immobilisation matrices for actinides such as ^{238}U, as at low energy the ^{4}He nucleus will acquire electrons to form He-gas, the accumulation of which causes swelling, ultimately degrading the mechanical integrity of the wasteform [30]. The positive charge of α-particles means have a high rate of

energy loss in matter. Shielding requirements for α-particles are often minimal, for example the range of an α-particle in air (approximate density 1.2 mg/cm^3) is around 3.7 cm.

2.1.2 Beta Decay

Beta decay is the most common mode of radioactive decay. There are three types of β-decay: electron emission (β^- decay), positron emission (β^+ decay), and electron capture (EC). In order to satisfy the conservation of angular momentum, beta-decay is accompanied by emission of a neutrino. β^- decay is observed when a high velocity electron is emitted from the core of an unstable nucleus *via* neutron decay. As indicated by **Fig. 1** this occurs when there is an abundance of neutrons relative to the N-Z stability curve. The Z number increases by 1 and there is negligible change in mass A. An example of β^- decay is given by **Eq. 3**.

$$^{234}_{90}\mathrm{Th} \rightarrow {}^{234}_{91}\mathrm{Pa} + e^- + \bar{\nu}_e \qquad \text{Equation (3)}$$

β^- decay is accompanied by the emission of an electron antineutrino in accordance with energy conservation. Here, a neutron is decaying into a proton (demonstrating the increase in Z value) alongside an electron and an antineutrino.

β^+ decay is characterised by the ejection of an antielectron (positron) and a neutrino from an unstable atomic nucleus. This is typical of isotopes with a low ratio of N-Z. Akin to β^- there is negligible change in A, however, there is a decrease in Z as β^+ involves proton decay into a neutron accompanied by emission of a positron and electron neutrino. A specific example of β^+ decay is given in **Eq. 4**. As the positron is the antiparticle of the electron, the ionising potential is identical and the necessary shielding is the same (*e.g.* Al foil).

$$^{17}_{9}\mathrm{F} \rightarrow {}^{17}_{8}\mathrm{O} + e^+ + \nu_e \qquad \text{Equation (4)}$$

Elements may also achieve stability *via* electron capture, during which an electron from the inner shell combines with a proton in the nucleus to form a neutron and a neutrino (this process is sometimes referred to as K-capture, as the electron is captured from the K shell). **Eq. 5** provides an example of EC. In this example, the neutrino is discharged with the entirety of the decay energy. The EC process is also accompanied by the emission of a γ-ray, resulting from electron transitions to fill the lower-shell vacancy produced.

$$^{67}_{31}\mathrm{Ga} + e^- \rightarrow {}^{67}_{30}\mathrm{Zn} + \nu_e \qquad \text{Equation (5)}$$

2.1.3 Gamma Decay

Gamma emission (γ-emission) is not typically a primary decay mode and often accompanies α and β decay, when the daughter product from the decay exists in a metastable state (often referred to as the *excited* state). The exited state decays rapidly to the relaxed state over timescales of 10^{-12} s by emission of high frequency quantised electromagnetic radiation, termed γ-emission. Gamma rays are highly penetrating and therefore require a substantial degree of shielding relative to α and β-decay. As the

attenuation of electromagnetic radiation is generally proportional to *Z*, heavy metals such as lead are used in combination with concrete and even water. The process by which γ-emission accompanies the β^- decay of ^{60}Co is illustrated in **Fig. 2**.

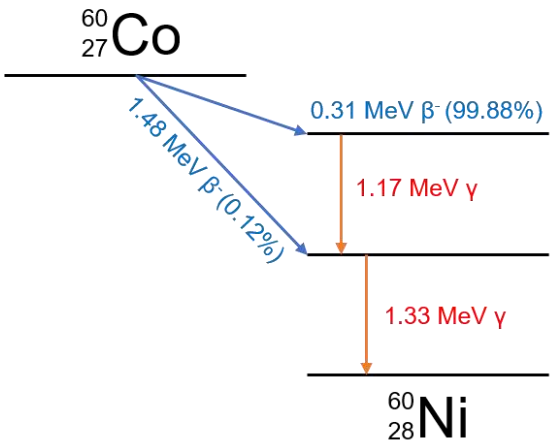

Fig. 2) Illustration of β^- and γ-decay processes for ^{60}Co

Table 1) Summary of radioactive decay modes [31]

Decay Mode	Symbolic Representation	Decay Energy (MeV)
α	${}^{A}_{Z}X \rightarrow {}^{A-4}_{Z-2}X + {}^{4}_{2}He$	$Q\,(MeV) = -931.5\,(M_{Z-2} + M_{He} - M_Z)$
β^-	${}^{A}_{Z}X \rightarrow {}^{A}_{Z+1}X + e^- + \bar{\nu}_e$	$Q\,(MeV) = -931.5\,(M_{Z+1} - M_Z)$
β^+	${}^{A}_{Z}X \rightarrow {}^{A}_{Z-1}X + e^+ + \nu_e$	$Q\,(MeV) = -931.5\,(M_{Z+1} + 2M_e - M_Z)$
EC	${}^{A}_{Z}X + e^- \rightarrow {}^{A}_{Z-1}X + \nu_e$	$Q\,(MeV) = -931.5\,(M_{Z-1} - M_Z)$
γ	${}^{A}_{Z}X^* \rightarrow {}^{A}_{Z}X + \gamma$	-

2.2 Nuclear Fission and the Chain Reaction

The interaction of neutrons with fissile elements contained within nuclear fuel is the fundamental basis of nuclear power generation. There are two fundamental interactions that an incident neutron can have with matter: scattering or absorption. The statistical probability of an interaction occurring between a target element and an incident neutron is the 'cross section', measured in barns (1 barn = 10^{-28} m^2). Neutron scattering can be elastic or inelastic and can be treated similar to macroscopic scattering. Considering a neutron incident on a stationary nucleus, an elastic collision would result in a change in the kinetic energy of the neutron resulting in a change in speed and direction, due to the conservation of momentum. This energy is transferred to the nucleus *via* the collision yet the properties of the nucleus are not altered. The process of inelastic scattering however results in the excitation and subsequent decay of the target nucleus. An example of this principle is given in **Eq. 6**.

$$ {}^{1}_{0}n + {}^{238}_{92}U \rightarrow {}^{1}_{0}n + {}^{238}_{92}U^* \rightarrow {}^{1}_{0}n + {}^{238}_{92}U + \gamma \qquad \textbf{Equation (6)} $$

Here, the intermediate product is a $^{238}U^*$ nucleus in an excited state (denoted by an asterisk). This excited nuclear state decays with the emission of a γ-ray photon. The kinetic energy of the incident neutron determines whether the collision is elastic or inelastic: the latter occurs when this energy is greater than the energy necessary to excite the nucleus from its ground state to the lowest possible excited state. This process is referred to as inelastic scattering as, whilst energy is conserved, the kinetic energy is different due to the emission of radiation.

Neutrons can be also absorbed (radiative capture) propagating two fundamental processes: fission, and transmutation. A simplified illustration of the fission process is given in **Fig. 3**. If the binding energy per nucleon is sufficiently lower for a metastable compound nucleus subsequent to the absorption of a neutron, the nucleus will split (fission) into two roughly equal fragments, releasing energy and neutrons. Considering the specific case illustrated in **Fig. 3**: a slow moving neutron is absorbed by the nucleus of ^{235}U; the $^{236}U^*$ nucleus formed is highly unstable and begins to deform into two fragments of roughly equal size; the nucleus splits into ^{92}Kr and ^{141}Ba, producing three neutrons (this varies for each individual fission event) and a release of around 200 MeV per fission **[32]**. The fission fragment yield is different for the fission spectrum (*e.g.* thermal fission or fast fission) and the fissile species. Thermal neutrons have an energy of approximately 0.025 eV, whereas fast neutrons have energies < 1 MeV. The general fission yield is a bimodal distribution centred around two maxima as displayed in **Fig. 4**. The liberated neutrons can then initiate further fission, creating a chain reaction. The probability of fission (*i.e.* the fission cross section) is dependent on the energy of the incident neutron. As can be seen from **Fig. 5**, the fission cross section of ^{235}U is greater for neutrons with lower energy (eV), hence neutrons must be moderated in the reactor core, to reduce their speed such that they are thermal neutrons. The balance of neutrons in the reactor is often referred to as the neutron population, or neutron economy; the ratio of neutrons generated from a reaction to absorption and leakage in the preceding reaction is called the multiplication factor (**Eq. 7**).

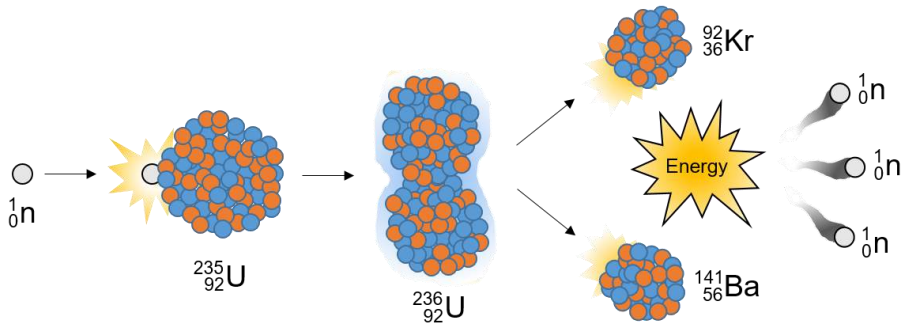

Fig. 3) Schematic of the neutron induced fission of ^{235}U

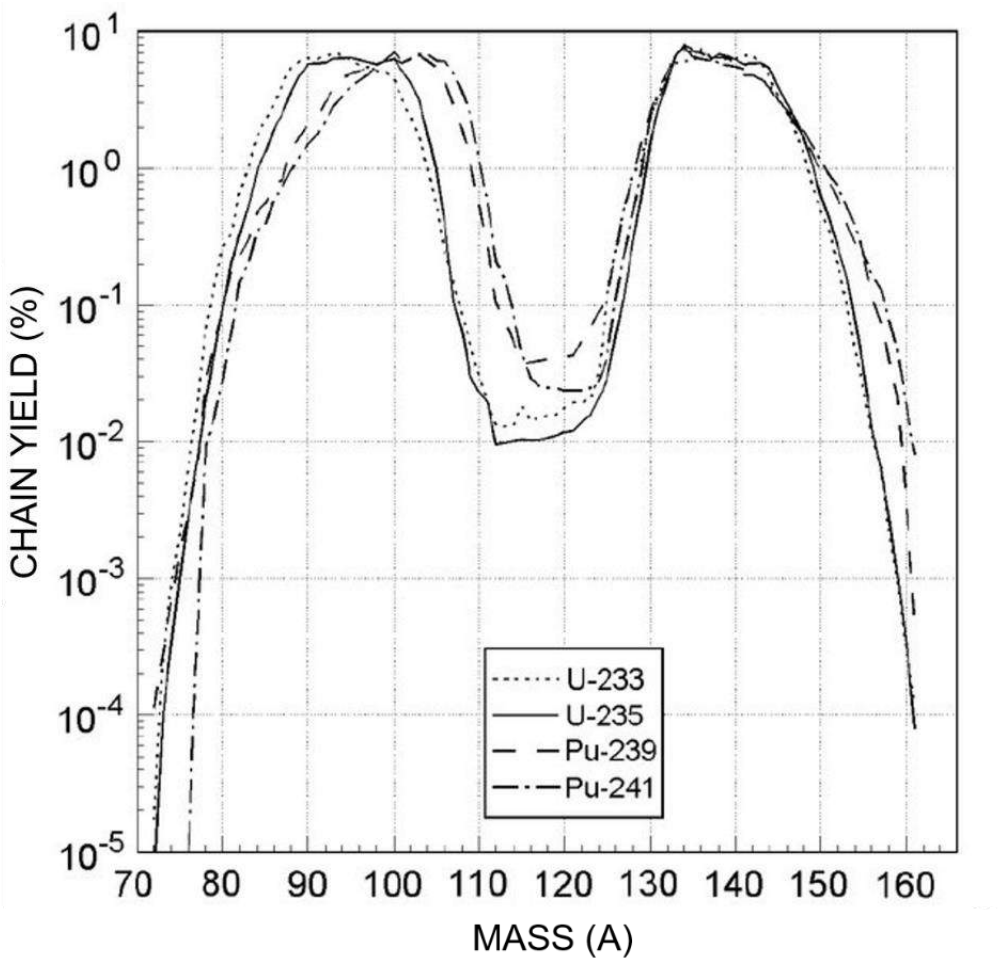

Fig. 4) Thermal fission yield for ^{233}U, ^{235}U, ^{239}Pu and ^{241}Pu as a function of A [31]

$$k = \eta \cdot f \cdot p \cdot \varepsilon \cdot P_{NL} \qquad \text{Equation (7)}$$

From **Eq. 7** the effective multiplication constant is calculated, which describes the criticality conditions within the core of a reactor:

- η – number of neutrons liberated from fission reaction within the fuel
- f – fraction of neutrons absorbed in fissile nuclides
- p – probability that a neutron does not undergo resonance capture
- ε – fast fission factor
- P_{LN} – probability that fast and thermal neutrons do not leak from the system

Using **Eq. 7**, it is possible to describe the *criticality* of a nuclear system in regards to neutron economy; if $k = 1$, the system is said to be in a condition of criticality, in which on average one neutron survives to cause another fission; if $k > 1$, the system is supercritical and more neutrons are generated than absorbed, and must be removed; if $k < 1$, the condition is subcritical, and the fission reaction is not self-sustaining. The objective of a nuclear reactor is to maintain a self-sustaining chain reaction *i.e.* $k = 1$.

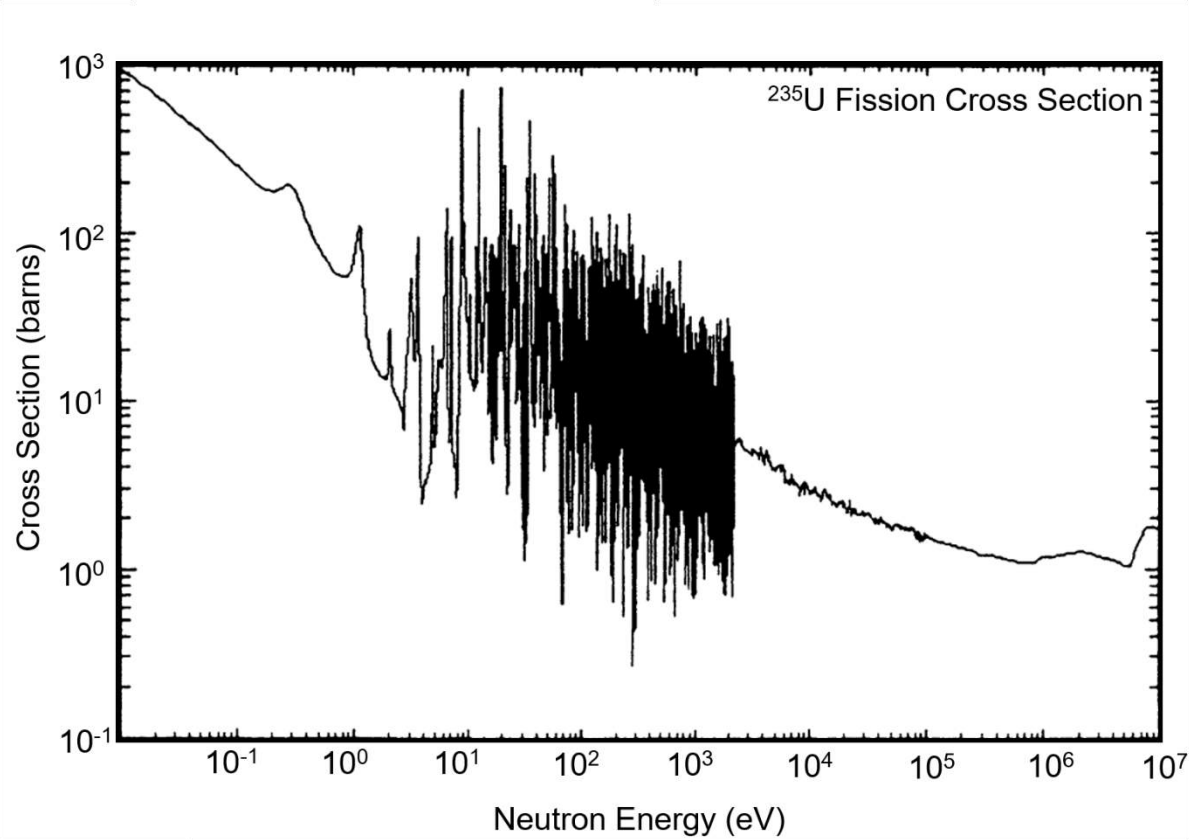

Fig. 5) Fission cross section for ^{235}U [33]

2.3 Nuclear Power

Nuclear power constitutes a significant portion of the U.K. energy portfolio, and in some nations (*e.g.* France) is the principle contributor towards civil power generation. Nuclear energy exploits the controlled fission of ^{235}U nuclei into lighter fragments, allowing the transfer of energy to a useful medium to generate electrical energy. This energy can be harnessed in a number of ways depending on the type of reactor and the fuel that is utilised, however, the fundamental basis of power generation is the same, in which the heat released from the fission reaction is used to generate steam, which can then drive a turbine and produce an electrical output. The U.K. was the first nation to implement a civil nuclear power programme following the Second World War. As of 2019 the U.K. maintains seven advanced gas cooled power stations and a pressurised water reactor (PWR), producing a net capacity of 8918 MW(e), and contributing around 20% of total national electricity output, with two more reactors now under construction at Hinkley Point C [34]. Nuclear facilities in the U.K., including medical and industrial, are illustrated in **Fig. 6**.

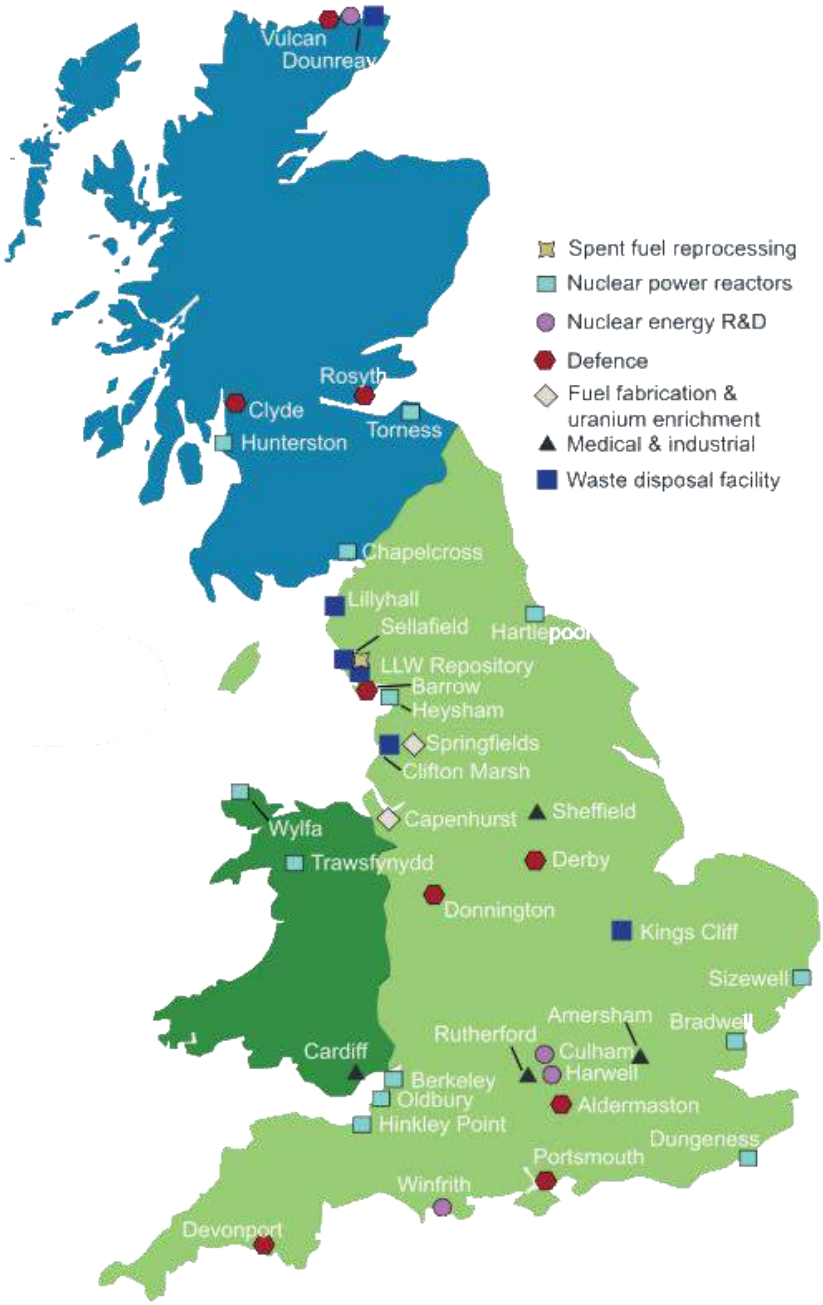

Fig. 6) Nuclear facilities in the UK [35]

2.3.1 Nuclear Fuel Fabrication and Enrichment

The type of nuclear fuel, and operational parameters of the reactor, are ultimately responsible for the characteristics of the waste output. Nuclear fuel is comprised of a fissile element, typically uranium metal bars or oxide formed as pellets. The fuel assembly consists of two primary features: the fuel itself and cladding. A cladding surrounds the arrangements of fuel and is responsible for isolating the fuel from its immediate environment and providing containment for fission gasses produced during the course of the fuel lifetime. Collections of fuel rods (assemblies) must adhere a host of requirements to enable maximum reactor efficiency and safety. An example of a PWR fuel assembly is displayed in **Fig. 7**. Imperatively, the fuel assemblies must be able to withstand the strain imposed by pellet-clad

mechanical interactions, maintain resistance against corrosion of cladding, have sufficient internal volume to contain evolved gasses, and be robust against the possibility of loss-of-coolant (LOC) events.

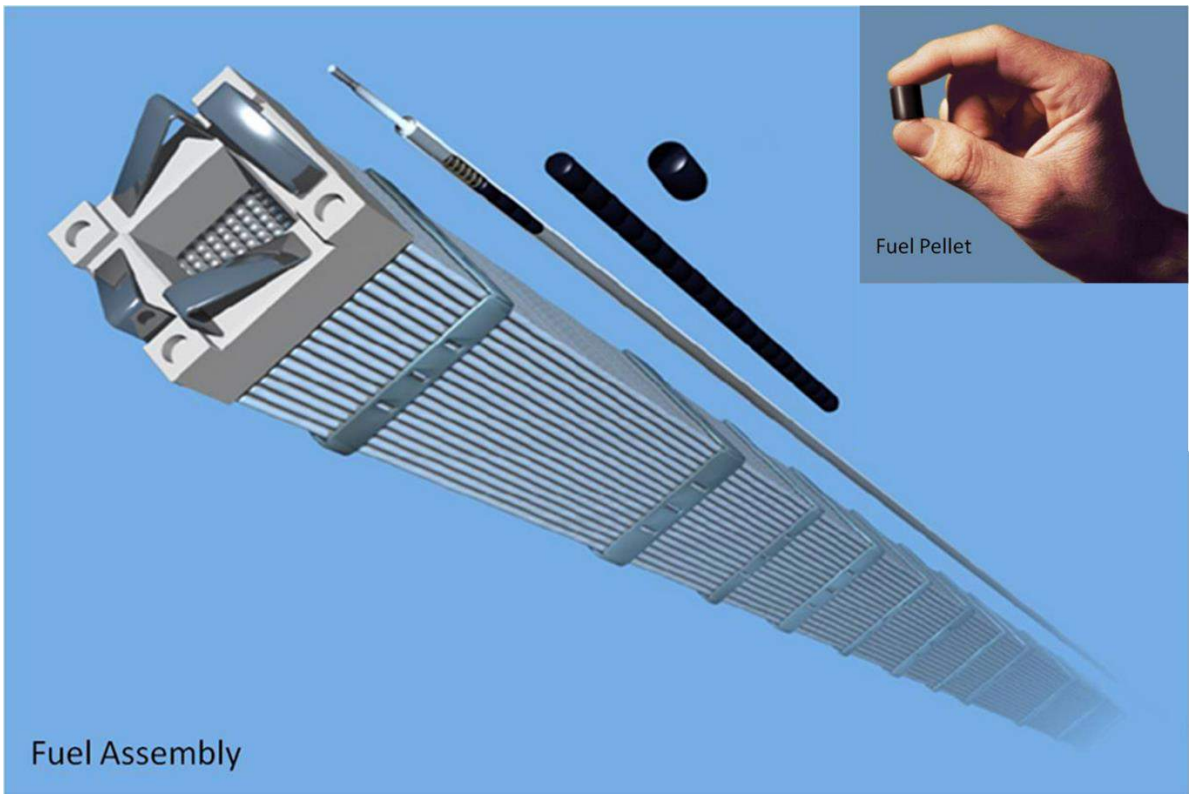

Fig. 7) Illustration of PWR fuel assembly (adapted from [36])

The uranium resource is mined from a variety of ores worldwide (this will not be discussed here, although it is important to note that U is leached and extracted from ore, and subsequently converted to U_3O_8 yellowcake). The natural isotopic content of uranium is ~ 99.3% ^{238}U, alongside ~ 0.7% ^{235}U, and a very small amount (0.0053%) of ^{234}U [37]. Of these isotopes, only ^{235}U is capable of undergoing fission to produce a self-sustaining chain reaction, hence the decision may be taken to isotopically enrich the uranium precursor prior to fuel fabrication, allowing greater efficiency for large-scale water moderated reactors, such as the Boiling Water Reactor (BWR). In such a process, the relative quantity of the fissionable ^{235}U isotope is increased. As the chemical and physical properties of nuclear isotopes are practically identical, any manner of separation technique will likely be highly inefficient and energy intensive. The U enrichment process takes advantage of the small mass difference between ^{235}U and ^{238}U by combining with fluorine, which has one naturally occurring isotope with amu = 19.00. The UO_2 is fluorinated to form UF_6, and fed into a gas-centrifuge or gaseous-diffuser, exploiting the small mass difference between $^{235}UF_6$ and $^{238}UF_6$, resulting in the lighter $^{235}UF_6$ molecules travelling slightly faster. In the case of enrichment by gas-centrifuge, the gaseous UF_6 is introduced into the gas cylinder rotating at high speed; the $^{238}UF_6$ migrates towards the outer volume of the gas column, whilst the lighter $^{235}UF_6$ accumulates in the centre of the centrifuge [38]. This process must be repeated hundreds of times to achieve the desired enrichment, hence centrifuges are connected in series called a *cascade*. Enrichment *via* gaseous diffusion also exploits the mass difference of U isotopes in UF_6 by using a

compressor to force the material through a semi-permeable diffusion barrier; as $^{235}UF_6$ will travel faster through the barrier, separation may be achieved (although akin to enrichment by gas-centrifuge, this process must be repeated hundreds of times to achieve a desirable separation factor) [38]. A simplified schematic of both enrichment techniques is presented in **Fig. 8**. In order to convert the enriched UF_6 to enriched UO_2, the UF_6 is hydrolysed to form UO_2F_2 and subsequently precipitated with ammonium hydroxide ($NH_4(OH)$) to form ammonium diuranate ($(NH_4)U_2O_7$ [39]. This is then reduced by heating in H_2, allowing conversion to UO_2 for fuel fabrication. These pellets may be machined to suit the desired dimensions and arranged into fuel rods and assemblies.

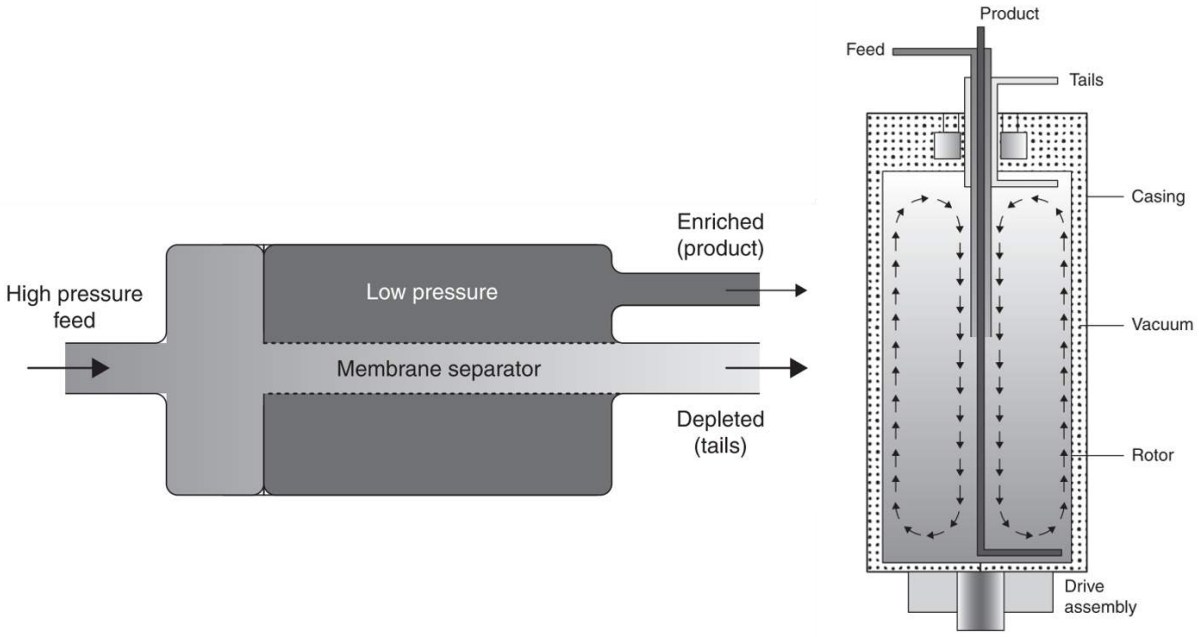

Fig. 8) Schematic of gaseous diffusion unit (left) and gas centrifuge unit (right) (reproduced from [37])

2.3.2 Nuclear Reactors

All commercial nuclear reactors utilise the heat produced from the fission reaction to generate an electrical output. Historically the U.K. has operated three types of commercial reactor: Magnox (the name derived from the magnesium alloy used for fuel cladding), AGR and PWR. The U.K. also operated a prototype fast breeder reactor at Dounreay. A host of research-scale reactors are also operated nationwide, yet they shall not be discussed here. Whilst the aim of this section is not to discuss in detail the physical parameters governing the operation of a nuclear reactor, it is necessary to discuss the key features of a commercial nuclear power plant:

- **Fuel** – The fuel component contains the fissile element (typically ^{235}U) in the form of metallic uranium (natural isotopic content – Magnox) or UO_2 (isotopically enriched – AGR) ceramic pellets. Advanced fuels may also incorporate additives such as Al_2O_3 and Cr_2O_3 to improve grain properties.
- **Cladding** – The purpose of cladding is to provide a physical (yet not thermal) barrier between the fuel material and the coolant medium, to prevent exposure of coolant to highly radioactive

fission products. The cladding is ideally fabricated from material with high corrosion resistance and a low neutron absorption cross section.

- **Moderator** – The purpose of a moderator is to reduce the speed of neutrons, to increase the fission yield within the reactor core. The choice of moderator is typically water (PWR, BWR – heavy water for PHWR) or graphite (AGR, LWGR).
- **Coolant** – The coolant medium is passed through the core and heated. This is then pumped to the heat exchanger to a secondary steam generating loop (with the exception of the BWR reactor type, in which the steam cycle is integrated with the core). The flow of coolant is paramount in the operation of a reactor, as a LOCA (loss of coolant accident) can lead to partial core melting, due to residual heat output.
- **Control Rods** – Control rods are inserted or removed from the core to control the reactor. These are produced from materials with a high neutron absorption cross section in order to effectively remove neutrons from the flux and reduce the rate of fission.
- **Reactor Pressure Vessel** – The reactor pressure vessel (RPV) contains the nuclear reactor core and fuel assembly. It is typically fabricated from stainless steel to mitigate corrosion. The interior of the RPV is also lined with a neutron reflecting material such as beryllium.

2.3.2.1 Magnox Reactor

Although the design of the Magnox reactor was utilised for the production of weapons grade Pu for military purposes, it was considered that the thermal output could also be utilised to generate power for civilian applications. Thus, the Calder Hall reactor, opened in 1956, was the first commercial nuclear reactor to be integrated into the power grid. A large fleet of Magnox reactors were subsequently constructed following the generic reactor design, although each reactor inevitably had individual design features. Each iteration of the Magnox design was refined, such that the average efficiency and fuel rating was increased over time. All U.K. Magnox reactors were based on the design of the experimental Calder Hall and Chapelcross reactors. There are no longer any operational Magnox reactors in the U.K., with the closure of the Wylfa reactor in 2015, although decommissioning is still progress. A list of all retired Magnox power stations, and associated output efficiency, is presented in **Table 2**.

Table 2) List of retired Magnox reactors and output (data from [40], [41])

Power Station	Net Output (MWe)	Commercial Operation	Efficiency (%)	Average Fuel Rating (MWt/tU)
Calder Hall	200	1959 – 2003	23	1.53
Chapelcross	240	1960 – 2004	23	1.53
Berkeley	276	1962 – 1989	25	2.42
Bradwell	246	1962 – 2002	28	2.52
Hunterston A	300	1964 – 1990	30	2.11
Hinkley Point A	470	1965 – 2000	26	2.65
Trawsfynydd	390	1965 – 1991	29	3.10
Dungeness A	450	1965 – 2006	33	2.80
Sizewell A	420	1966 – 2006	31	2.95
Oldbury	434	1968 – 2012	34	2.85
Wylfa	980	1972 – 2015	33	3.15

A schematic overview of the generic Magnox reactor design is given in **Fig. 9**. The Magnox design had several distinct design features. The design used CO_2 gas as a coolant, typically with additions of 1 – 1.5% CO, H_2 (10 ppm vol.), CH_4 (10 ppm vol.) and H_2O (1 ppm vol.) [37]. The CO_2 was introduced to the manifold under the reactor at around 100 psi at a mass flow rate of 891 kg/sec; the temperature at the core inlet was 140 °C, as the CO_2 was circulated through the core heat transfer from the fission reaction occurs, raising the outlet temperature to 336 °C [41]. The coolant was circulated to the heat exchanger, where it was passed over an isolated water circuit to enable efficient heat transfer. The water was converted to steam which was then passed to the turbine stop valve, at a temperature and pressure of 310 ˚C and 14 kg/cm^2, respectively. The temperature of the CO_2 decreased and passed back into the manifold and recirculated into the reactor core. The Magnox design utilised uranium metal fuel of natural isotopic content, encased in cladding. The use of uranium metal fuel and Magnox cladding resulted in an operational temperature limit < 450 °C, to prevent excessive oxidation and creep of the cladding material [42]. Furthermore, uranium metal undergoes an α-β phase change at 662 °C, leading to a considerable volume expansion, and subsequently placing undesirable stress on cladding elements if exceeded [43]. The magnesium rich cladding (from which the name Magnox is derived) refers to two specific alloys, named AL80 (Mg + 0.7 – 0.9% Al) and Zr55 (Mg + 0.45 – 0.65% Zr) [44]. Both alloys were utilised in the Magnox fleet although the AL80 was more common. Metallic uranium fuel was machined and placed into fuel pins, with approximate dimensions 100 cm by 2.8 cm, with a cladding thickness of 2.0 mm [45]. An example of a Magnox fuel rod is displayed in **Fig. 10**, exhibiting the helically finned surface applied to increase heat transfer with the CO_2 coolant. Neutron moderation in the Magnox reactor design was facilitated by the installation of graphite blocks surrounding the fuel elements. The radiolytic oxidation of graphite moderator was considered to be a determining factor in the lifetime commissioning of Magnox reactor, leading to reduction in strength and moderating capacity [46]. The accumulation of ^{14}C in reactor graphite can be up to 1 wt. %, and is a considerable decommissioning concern due to the presented internal hazard to humans [6]. It is estimated that 36,000 m^3 of graphite was utilised in the U.K. Magnox fleet [47].

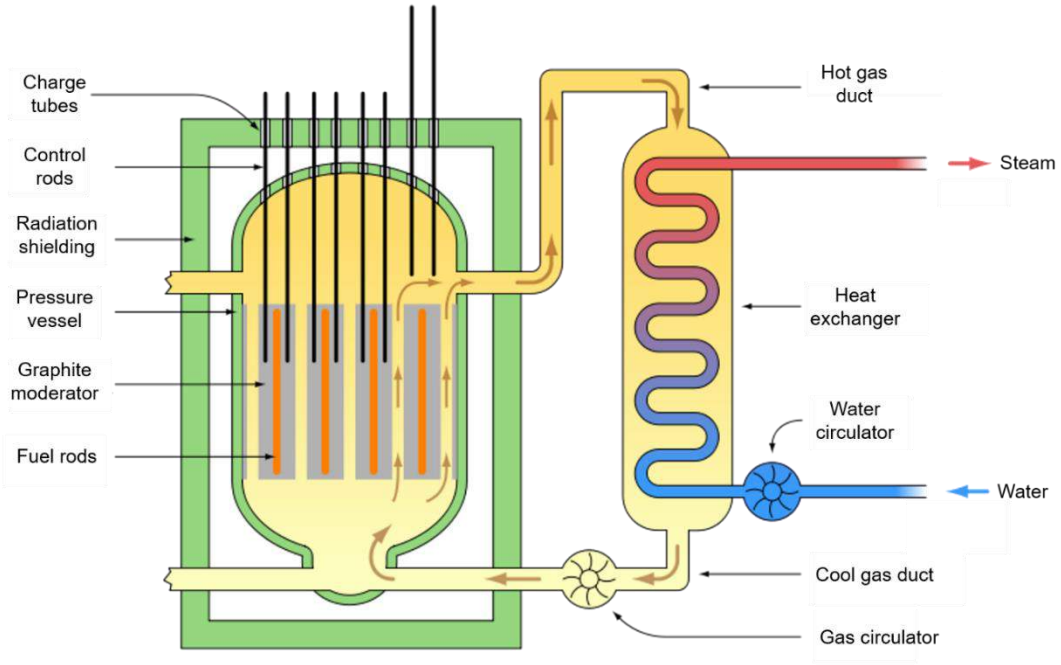

Fig. 9) Schematic overview of the Magnox design (adapted from [48])

Fig. 10) Magnox fuel rod can used at Sizewell-A Reactor 1 [49]

Subsequent to irradiation, Magnox fuel was unloaded from the reactor and placed into a cooling pond for around 180 d prior to transport to Sellafield for further cooling and reprocessing. The corrosion of the Mg-rich cladding in sub optimal wet storage has resulted in a significant accumulation of some 1500 m^3 sludge (estimated quantity in 2013); the sludge is rich in $Mg(OH)_2$, $Mg_6Al_2(CO_3)(OH)_{16}{\cdot}4H_2O$ and $Mg_2CO_3(OH)_2{\cdot}3H_2O$, alongside corroded uranium, fission products ^{90}Sr, ^{137}Cs and minor Pu [50]. Under current U.K. guidelines, these waste streams are classified as intermediate level wastes (ILW). Potential

immobilisation and disposal routes for Magnox sludge have recently been demonstrated, including vitrification and hot isostatic pressing into a glass-ceramic matrix [51], [52].

2.3.2.2 Advanced Gas Cooled Reactor (AGR)

The AGR reactor type constitutes 14 of the 15 power plants currently operated in the U.K., and is a technical improvement upon the indigenous Magnox reactor fleet, allowing greater efficiency and fuel burn-up by use of 2.5 – 3.5% enriched ceramic UO_2 fuel pellets, in place of metallic uranium fuel. The prototype Windscale Advanced Gas Cooled Reactor (WAGR) was opened in 1963; the Hinkley Point B site was the first commercially operated AGR, opening in 1976, consisting of two reactors with a combined net output of 1220 MWe. A fleet of AGR reactors have since been constructed, all of which remain in operation (**Table 3**). Unlike the Magnox fleet, for which the fundamental design criteria was Pu breeding and electricity co-generation, the AGR was optimised for power generation, and as such allowed greater temperature of the gas-coolant cycle, increasing the thermal efficiency.

Table 3) List of operational AGR reactors and output (data from [40], [53])

Power Station	Net Output (MWe)	Anticipated Operational Period	Efficiency (%)	Average Fuel Rating (MWt/tU)
Dungeness B	1100	1985 – 2028	41.6	9.5
Hartlepool A	1210	1989 – 2024	41.1	12.5
Heysham 1	1150	1989 – 2024	41.1	12.5
Heysham 2	1250	1989 – 2030	40.7	13.65
Hinkley Point B	1220	1976 – 2023	41.1	13.2
Hunterston B	1190	1976 – 2023	41.1	13.2
Torness	1250	1988 – 2030	40.7	13.65

A schematic overview of the AGR reactor design is shown in **Fig. 11**. Many of the design features are inherited from the Magnox predecessor; the AGR utilises a CO_2-rich gas coolant, with graphite moderator. The coolant chemistry of the AGR reactor is more complex than the Magnox design, due to the greater operating temperature. Excessive graphite oxidation under elevated reactor temperatures produces CO; the radiolytic breakdown of CO results in the formation of carbonaceous species which may deposit on the fuel pins, significantly reducing heat transfer [37]. Accordingly, the CO_2 gas stream is seeded with 1 vol. % CO, CH_4 (230 ppm vol.) and H_2O (300 ppm vol.); the option to inject carbonyl sulphide into the coolant stream to control carbonaceous deposition is also recognised [37]. The coolant is introduced into the gas manifold in the reactor core with a total gas flow rate of 4076 kg/s, with an average inlet temperature of 339 ˚C; in much a similar manner to the Magnox design, the CO_2 rises through the core, absorbing heat from the fission reaction; the mean outlet gas temperature is increased to 639 ˚C [53]. The gas is circulated to the heat exchanger, where the heated feedwater temperature is introduced at 158 ˚C. A superheater channel is placed above the boiler section producing steam at a pressure of 167 bar and 538 ˚C to the high pressure turbine. Although the original AGR design utilised Be as a cladding material, it was realised that high neutron flux led to a significant decrease in density

of Be cladding specimens, and accordingly the material was considered too brittle [54]. Accordingly, austenitic stainless steel alloy (20Cr/25Ni steel) was used as a cladding material, allowing the operating temperature to be elevated to 600 ˚C, providing improved thermal efficiency [42]. However, due to the elevated neutron capture cross section of the austenitic stainless steel cladding, it was necessary for greater fuel enrichment levels. Accordingly, AGR fuel is comprised of sintered UO_2 cylindrical pellets (14.5 mm diameter) with enrichment levels varying between 2.8 – 3.8%; pellets are stacked into fuel pins, which are arranged into elements of 1036 mm length and 264 mm diameter [37], [53]. An AGR fuel assembly is shown in **Fig. 12**. Neutron moderation in AGR reactors is achieved similar to Magnox, in which a graphite sleeve is placed around the fuel assembly. Following discharge of spent fuel from the reactor, AGR fuel is stored on site for around 180 d, prior to transport to Sellafield for storage at ThORP [55].

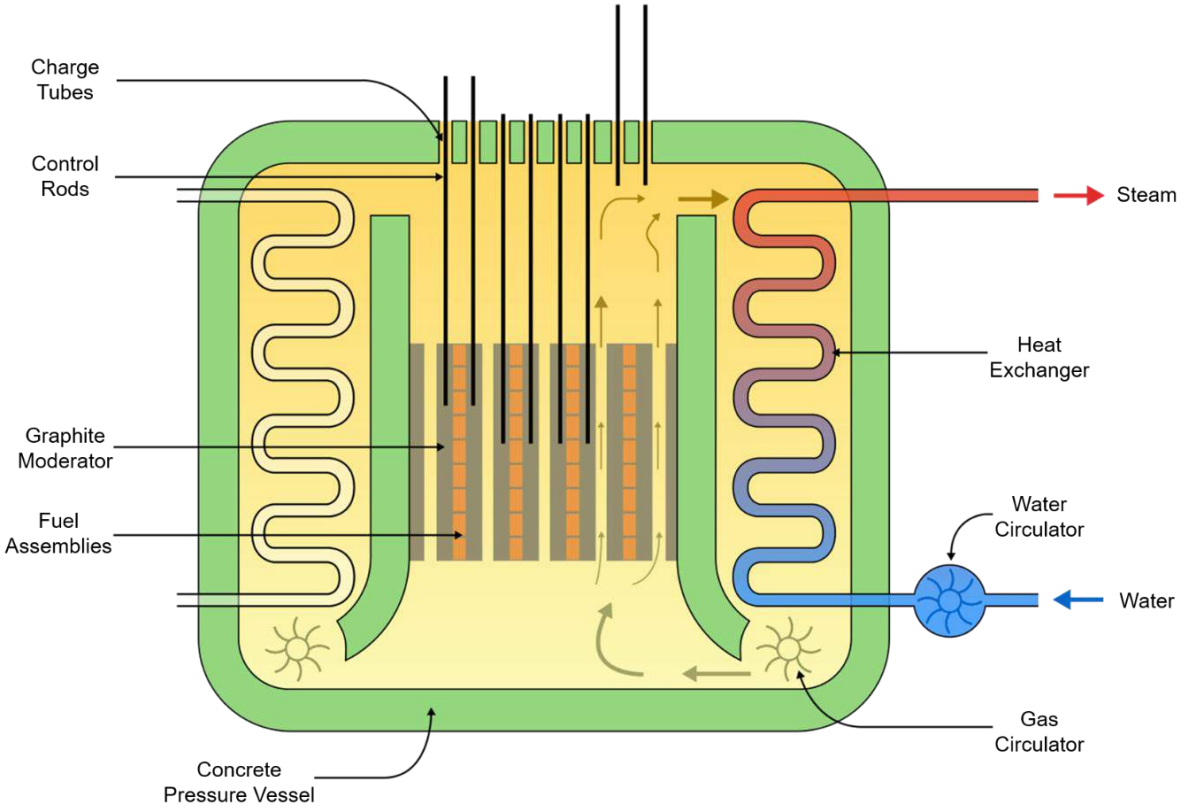

Fig. 11) Schematic overview of the AGR reactor design (adapted from [56])

Fig. 12) AGR fuel assembly [57]

2.3.3 Nuclear Waste

Nuclear wastes are produced at each step of the fuel cycle, from uranium ore purification through to fuel enrichment and spent fuel reprocessing. 'Wastes' are defined as materials contaminated with levels of radionuclides higher than clearance levels (depending on the country of origin) and for which there is no foreseen future use. Attitudes towards the safe and responsible management of nuclear wastes changed dramatically over the latter half of the twentieth century. The lack of strategic and defined management strategies for high level waste has resulted in many nations, including the U.K. and U.S., maintaining a legacy of damaged fuels and reprocessing wastes that have been left to degrade considerably over time, resulting in extreme challenges in terms of site decommissioning. The separation and accumulation of plutonium is also considered a significant threat with regards to proliferation. Whilst a large proportion of domestic nuclear wastes produced contain low levels of radioactivity and can be disposed of safely at near-surface storage facilities, high activity wastes (such as those containing minor actinides and transuranic elements) must be conditioned in a suitable, chemically durable wasteform such as cement, glass, or ceramic, such that the waste is isolated from the biosphere and robust with regards to proliferation. This process of nuclear waste conditioning is defined as waste *immobilisation*, in such that the waste is immobilised, mitigating the potential for radionuclide migration.

2.3.3.1 Generic Waste Classifications

Waste classifications vary in accordance with the stipulations of individual nations. For example, some nations operate an open fuel cycle in which spent nuclear fuel is designated as waste and conditioned for disposal. In the U.K. spent fuel is reprocessed in order to recycle useful components U and Pu, and the reprocessing raffinate is designated as high level waste. Nevertheless, the axioms governing general classification strategies are typically similar and are contingent on the activity and half-life of the waste [58]. This concept is highlighted in **Fig 13**. Activity specific classifications are as such:

VLLW: This material is of such low level of radioactivity that it may be disposed of in municipal landfill subsequent to incineration. This material is predominantly derived from university and hospital wastes

LLW: Low level waste refers to material that has an activity level < 4 GBq/t of alpha activity and < 12 GBq/t beta/gamma. Although LLW and VLLW constitute approximately 90% of total nuclear waste volume, compaction and subsequent incineration into landfill is often the preferred route of disposal.

ILW: Generally composed of lesser contaminated materials than HLW, such as cladding and sludge, the heat generated by ILW does not have to be factored into the design of a final repository. There are thus fewer constraints on the handling and disposal mechanism, yet it still accounts for around 4% of total radioactivity of all wastes. Immobilisation by cementitious wasteform is typically employed for materials meeting these criteria.

HLW: The activity of this waste can lead to considerable rises in temperature (power output > 2 kW/m^3). This must be considered when designing a suitable facility to permanently store the material, which typically comprises of SNF and waste arising from reprocessing activities. The target wasteform for materials of this classification is typically glass and ceramic matrices, as the high activity and heat generation is often unsuited for cementitious containment.

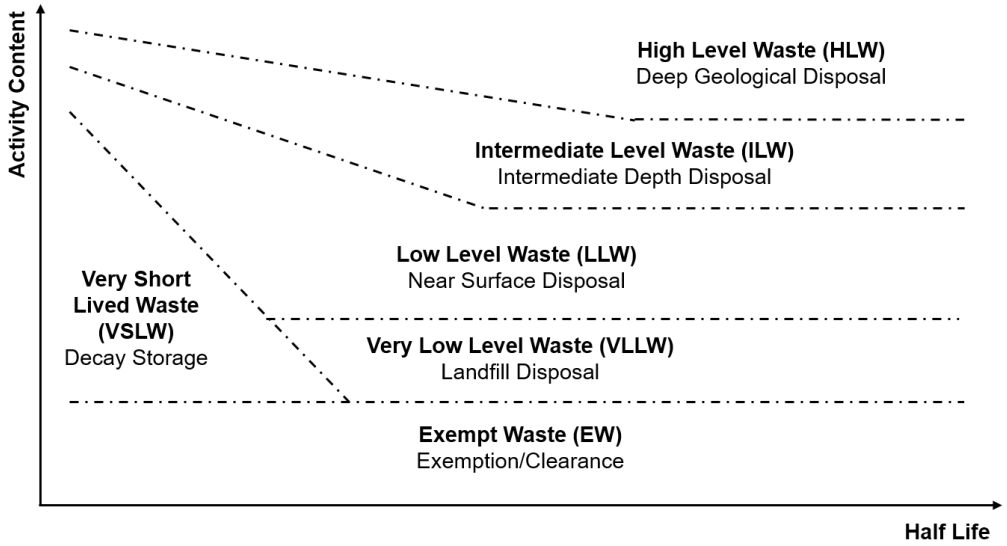

Fig. 13) Conceptual approach to nuclear waste classification, as outlined by the International Atomic Energy Agency (IAEA), with general disposal routes indicated

2.3.3.2 Spent Nuclear Fuel

Over time, the composition of nuclear fuel under irradiation changes, due to accumulation of high yield fission products, activation products and minor actinides. The burn-up properties of the fuel are altered such that it becomes more economical to remove and replace the fuel assembly. At this point, the spent fuel matrix is highly radioactive and produces a significant thermal heat output, so much so that removal operations must be handled remotely. The SNF assemblies must be cooled such that the radiogenic heat can be dissipated, and the radioactivity can decrease with time. Estimates place the dose rate emitted from a BWR fuel assembly irradiated with a burn-up of 30,000 MWd/MT, at a distance of 1 m from the fuel edge, at ~ 105 Sv/h [59]. Even after a cooling period of 15 y, a lethal dose of would be received after several minutes of exposure, at a distance of 1 m. Accordingly, SNF is handled remotely and stored in cooling ponds for between 5 – 10 y, at which point the decision may be taken to operate an open or closed fuel cycle:

Open – The SNF matrix is considered the final wasteform and no attempt is made to recover uranium/plutonium for further use. This approach is favoured in nations such as Sweden and the U.S. [60]. After a suitable cooling period, the spent fuel assemblies would be inserted into large copper casks to provide an additional barrier. The metallic fuel cladding would also be considered to provide further protection [6].

Closed – The closed fuel cycle approach exploits the fact that much of the indigenous U content of the fuel remains present (~ 95%) alongside an ingrowth of ~ 1% Pu. Accordingly, in a closed cycle, SNF is cooled for a sufficient period prior to aqueous reprocessing, in order to co-extract and purify U/Pu for fabrication of fresh fuel. This is the approach adopted in the U.K.; a simplified flowsheet for the receipt and treatment of SNF at the Sellafield site is outlined in **Fig. 14**.

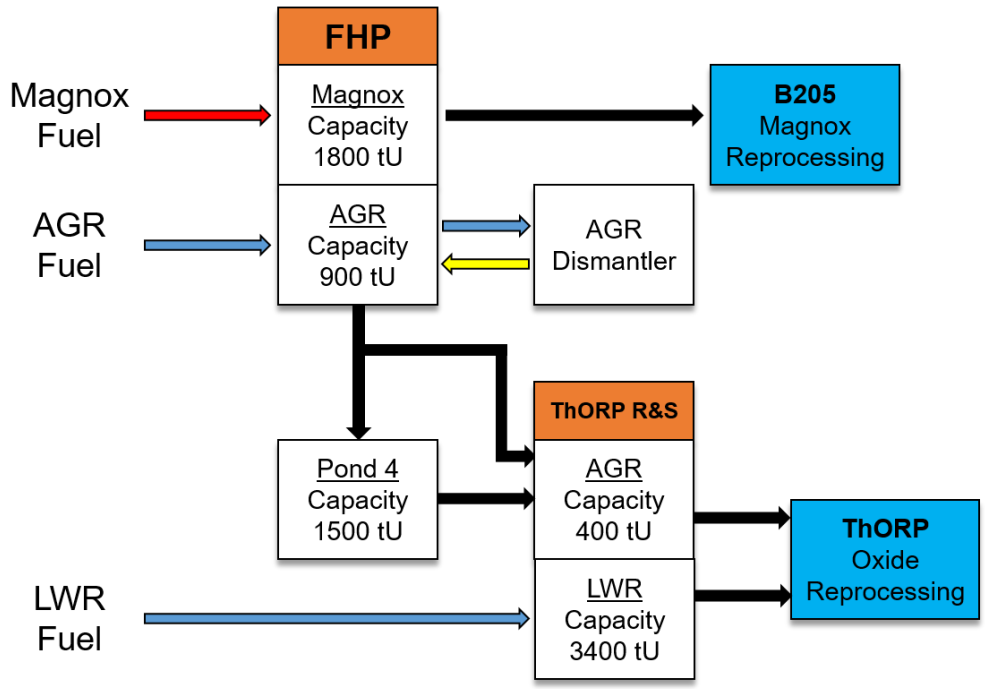

Fig. 14) Flowsheet of fuel receipt, storage and treatment at Sellafield (reproduced from [61])

The spent fuel matrix contains a wide distribution of elements, a large portion of which arise as a by-product of the fission reaction, and neutron activation of material that does not undergo fission. Most importantly, a significant fraction of the bulk uranium fuel remains present that may be purified, re-enriched and reintegrated into the civil fuel cycle. At this point, the option to recover Pu for the fabrication of weapons is also available. The exact composition of the SNF matrix is determined by the type of fuel, operational parameters of the reactor *i.e.* burn-up and time elapsed between discharge and recovery, although, it is accepted that the general composition of SNF is 94% U, 4 – 5% fission products (FP), 1% Pu and ~ 0.1% minor actinides (MA) [62]. FP are produced arise from the fissioning of the fissile portion of the fuel matrix, namely ^{235}U and ^{239}Pu/^{241}Pu, and encompass a large range of elements from various families of the period table [63]. The FP components of the SNF matrix contribute significantly to the overall radioactivity and radiotoxicity output. Examples of short-lived FP isotopes include ^{137}Cs ($t_{1/2}$ ≈ 30.2 y), ^{90}Sr ($t_{1/2}$ ≈ 28.8 y), ^{85}Kr ($t_{1/2}$ ≈ 10.8 y), ^{154}Eu ($t_{1/2}$ ≈ 8.6 y), ^{147}Pm ($t_{1/2}$ ≈ 2.6 y), whilst long-lived radionuclides include ^{135}Cs ($t_{1/2}$ ≈ 2.6 My), ^{129}I ($t_{1/2}$ ≈ 15.7 My), ^{107}Pd ($t_{1/2}$ ≈ 6.5 My) and ^{99}Tc ($t_{1/2}$ ≈ 0.21 My) [64]. The presence of MA species in the spent fuel matrix is mainly attributed to neutron capture of ^{238}U and are typically α-emitters: ^{239}Pu ($t_{1/2}$ ≈ 21,400 y), ^{240}Pu ($t_{1/2}$ ≈ 6580 y), ^{237}Np ($t_{1/2}$ ≈ 1.2 My), ^{237}Cm ($t_{1/2}$ ≈ 1.56 My) although some MA species such as ^{241}Am ($t_{1/2}$ ≈ 433 y) are also γ-emitters [37]. The SNF matrix may also contain dilute quantities of activation products such as ^{55}Fe, ^{60}Co, ^{14}C, ^{93}Zr arising from the transmutation of non-active species present in the fuel cladding and structural assembly materials [63].

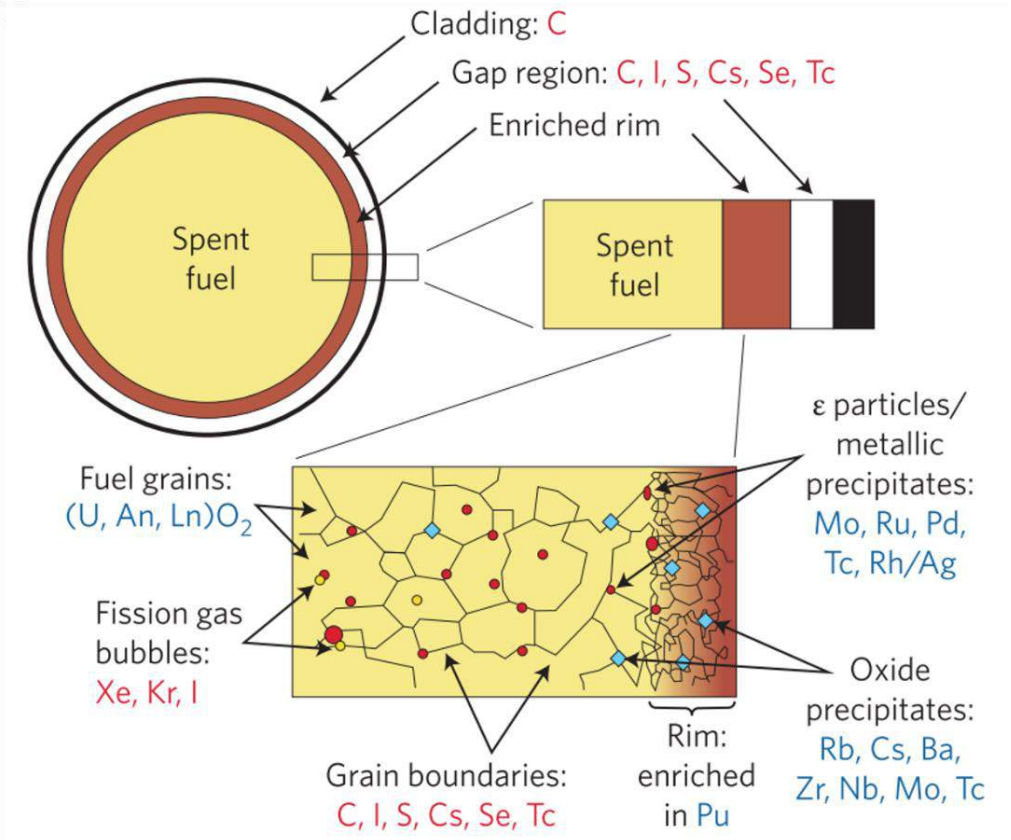

Fig. 15) Microstructure of spent nuclear fuel [65]

As mentioned, the spent fuel matrix may act as the final wasteform for disposal, after a suitable time has elapsed for cooling, and allowing for a decrease in radiogenic heat output. During the operational period, the microstructure of the fuel matrix is altered due to several processes: the steep thermal gradient leading to cracking of fuel pellets; migration of fission products; grain growth; gas bubble formation; the formation of metallic and oxide precipitates. These processes result in a heterogeneous microstructure, a generic example of which is illustrated in **Fig. 15** [65]. A significant contribution to the dispersion of fission products within the fuel matrix is the thermal gradient across the fuel pellets, which may be as high as 1700 °C at the centre, and just ~ 400 °C at the rim. The migration of fission products within the fuel matrix is largely controlled by temperature; at low operating temperature *e.g.* < 1000 °C, the majority of fission products can be expected to remain in close vicinity of the recoil position, as the diffusivity of these species through the UO_2 matrix is low at these temperatures (~ 10^{-21} m^2/s) [66]. Nevertheless, as the peak operating temperature is elevated in the temperature range 1000 °C – 1800 °C, the migration of FP is increased, resulting in accumulation in inter-granular pores and grain boundaries. The distribution of fission products either as gas, oxide or metallic precipitates is determined by the oxygen potential and fuel stoichiometry, whereby precipitates such as Rb and Nb are present as oxides, whereas other species will be present as metallic precipitates (*e.g.* Pd, Ru) due to greater oxygen potential than UO_2 [67]. These metallic precipitates are referred to as ε-particles and are typically < 1 μm in diameter. Coarsening of grain size and cracking of the fuel matrix is also common, occurring as a result of the steep thermal gradient across the pellet surface, and low mechanical strength of ceramic UO_2. Cracking is deleterious for the disposability of the SNF wasteform, as it induces radical migration of volatile fission products, resulting in accumulation at the fuel-cladding gap, significantly elevating the available surface area of fission products that may be potentially exposed to groundwater in the disposal environment [66], [67].

2.3.3.3 Aqueous Reprocessing

There is arguably an economic incentive to chemically separate and recycle the energy-rich constituents of spent nuclear fuel, by further exploitation of the fissile component, thus reducing the volume footprint for geological disposal, increasing the overall efficiency of the fuel cycle. The fundamental objective of fuel reprocessing is to reclaim unused ^{235}U for the fabrication of fresh ceramic UO_2 fuel, separate useful ^{239}Pu, and condition highly radiotoxic fission products within a stable matrix prior to eventual disposal. At a broad level, reprocessing is achieved either through aqueous reprocessing or pyroprocessing, though the latter will not be discussed here. Aqueous reprocessing is achieved through a series of solvent extraction processes, by which a steam of concentrated U and Pu is removed from the bulk matrix by dissolution, leaving a highly acidic solution, host to transuranic species (TRU), fission products, processing impurities, entrained cladding elements and potentially residual U/Pu [68]. This solution, referred to as High Level Liquid Waste (HLLW) or Highly Active Liquor (HAL), is then concentrated by evaporation and stored prior to immobilisation into a stable wasteform *via* vitrification.

2.3.3.4 PUREX

The PUREX process is the most mature separations technology currently applied to the fuel cycle. The general flow scheme for PUREX-based reprocessing involves the dismantling of fuel assemblies and removal of cladding material; dissolution of fuel material in concentrated nitric acid solution; solvent extraction, and subsequent purification, of U and Pu; conversion of U and Pu to oxides. The dismantling of the fuel assembly, shearing of cladding material, size reduction (or 'chopping') of fuel pellets, dissolution and feed preparation are referred to as the 'head-end' steps, and occur before the solvent extraction process. The removal of the cladding material is necessary to expose the ceramic fuel to the aqueous solvent, and the sheared material is separated as solid waste, to ensure the minimisation of the produced HLLW. The chopped fuel pieces must be separated from cladding swarf, alongside other structural artefacts such as pins and spacers, this is typically achieved through placing the hardware in perforated baskets (this arrangement is employed at the ThORP plant) whilst the UP2 and UP3 facilities at La Hague utilise a continuous wheel-dissolver that rotates through the nitric acid solution [69]. Once isolated, the fuel matrix is dissolved by extended contact with a hot solution of 3 – 6M HNO_3 (at this point, this solution is referred to as the *aqueous* phase). During the dissolution stage, a gaseous effluent is produced, with isotopes of concern ^{3}H and ^{85}Kr, alongside other noble gases. Currently, treatments for ^{3}H involve percolation through water to produce tritiated water, allowing the remainder to exit as tritiated steam; ^{129}I is captured through the use of zeolites and $AgNO_3$ salt; high efficiency filters successfully retain > 99.9% airborne particulate matter; the remainder of the off-gas stream is sufficiently diluted such that the radiological impact on the environment is negligible, whilst continuously monitored [37]. Oxygen may also be introduced to the dissolver to allow recovery of nitrogen oxides that are liberated [31]. At this point, the feed solution may be adjusted prior to the solvent extraction process, for example the feed may be clarified to avoid plugging and emulsification in the subsequent extraction operations [68]. In the aqueous phase, the plutonium and uranium oxidation states are maintained as Pu^{4+} and U^{6+}, as these are their respective extractable valence configurations. Pu^{3+} does not co-extract to the organic phase, hence to ensure it is mainly present as Pu^{4+}, $NaNO_2$ may be added. The choice of extractant and diluent molecules comprising the organic phase in all reprocessing operations is contingent on chemical, thermal and radiation stability; for commercial PUREX operations the organic phase is comprised of a 20 – 40% vol. tributyl-phosphate diluted in inert kerosene [70]. The organic phase is introduced into the extraction column and the two phases are contacted and mechanically agitated to form an emulsion; U^{6+} and Pu^{4+} are extracted to the organic phase *via* formation of covalent bonds to TBP to form complexes (these reactions at equilibrium are given in **Eq. 8** and **Eq. 9**) leaving the majority (> 99%) remaining FP and MA in the aqueous nitrate solution referred to as the *raffinate*. The raffinate is separated from the solvent extraction column and evaporated prior to storage and vitrification.

$$UO_2^{2+} + 2NO_3^- + 2TBP \rightarrow UO_2(NO_3)_2 \cdot 2TBP \qquad \text{Equation (8)}$$

$$Pu^{4+} + 4NO_3^- + 2TBP \Leftrightarrow Pu_2(NO_3)_4 \cdot 2TBP \qquad \text{Equation (9)}$$

The U/Pu extracted in the first cycle is then washed in another nitric acid scrub (2M HNO_3) in order to remove entrained FP that may have been co-extracted into the loaded U/Pu phase; this solution is then fed back into the solvent extraction column [69]. The organic solution then enters the *partitioning* stage in which U and Pu are separated and purified. The separation of Pu^{4+} is achieved by backwashing the solution in a reductant species to promote reduction to Pu^{3+}, typically U^{4+} nitrate or Fe^{2+} sulfamate, leaving U^{6+} and some U^{4+} left in the solution [31]. The U solvent is the contacted with dilute HNO_3 and purified. The plutonium nitrate and uranyl nitrate solutions are stored, prior to conversion to oxides [68].

2.3.3.5 Vitrification of HLW

The conditioning of HLW raffinate in a vitrified product is the international standard treatment, with large scale vitrification plants operated in countries such as France, Germany, Japan, Russia, U.S. and U.K.; the choice of base glass used in each instance is compositionally varied to suit the feed characteristics of the respective waste streams, which in turn is determined by the operational parameters of the reactor fleet and separation conditions [71]. Glass is an attractive wasteform for complex wastes, such as HLW, due to the ability of the glass network to immobilise a wide variety of radionuclide species, with relatively little overall change to the durability or mechanical properties, thus allowing for considerable variations in feedstock chemistry [72]. In the U.K., three vitrification lines are in operation at the Sellafield Waste Vitrification Plant (WVP); Sellafield also operates the Vitrification Test Rig (VTR), an inactive full-scale replica of the WVP, constructed for the improvement of the vitrification campaign, with the specific aim to optimise glass composition, improve chemical durability and maximise wasteloading [73]. The formulated glass precursor used at the WVP is referred to as the 'MW' (Mixture-Windscale) glass, the approximate composition of which is listed in **Table 4**. There exists variations of the MW composition, such as the 'MW-1/2Li' glass, in which approximately half of the lithia is removed from the base glass and added to the HLW stream, in order to improve the reactivity of the calcine [74]. Other glass formulations such as the CaZn MW28 glass are also utilised at the WVP with additions of CaO/ZnO, promoting enhanced aqueous durability during initial stage dissolution [75], [76].

Table 4) Specification of MW and MW-1/2Li base glass (data from [74])

Composition	Quantity (wt. %)	
	MW	**MW-1/2Li**
SiO_2	61.75	63.42
B_2O_3	21.88	22.50
Na_2O	11.05	11.35
Li_2O	5.33	2.74

The WVP design is largely based on the two stage AVH (Atelier de Vitrification Le Hague, France) design. A schematic illustration of the vitrification of HLW is provided in **Fig. 16**. During the feed control step, the highly active reprocessing liquor (*e.g.* Magnox raffinate) containing fission products, minor actinides and entrained U/Pu, fuel additives *etc.* is combined with calcination additives. As mentioned, lithium nitrate is added to improve the reactivity of the calcine and suppress the formation of refractory

oxides. A sucrose solution may also be added to the calciner to act as a reducing agent, suppressing Ru volatilisation [77]. The feed is discharged into the rotary calciner (4 m x 300 mm) inclined 2% to the horizontal, rotating between 20 – 30 rpm, inside an electrically heated furnace, set between 600 and 840 °C [74]. This process acts to dry and de-nitrate the HAL waste to an oxide calcine, prior to addition of glass forming additives. There are three distinct products that may be produced by this process, determined by the composition of the HAL feed: Magnox reprocessing waste; AGR/LWR reprocessing waste; blended Magnox and AGR/LWR waste, in the ratio 25:75 [78]. It should be noted that the AGR/LWR oxide calcine may necessitate the addition of Al to provide a durability comparable to that of Magnox and blend product. The mixed calcine and frit are melted to a temperature of ~ 1050 °C, and poured through an induction heated freeze valve to 309 stainless steel vessel, with a volume of 169 L capable of accommodating ~ 400 kg of vitrified product [74]. An image of the WVP waste container is displayed in **Fig. 17**.

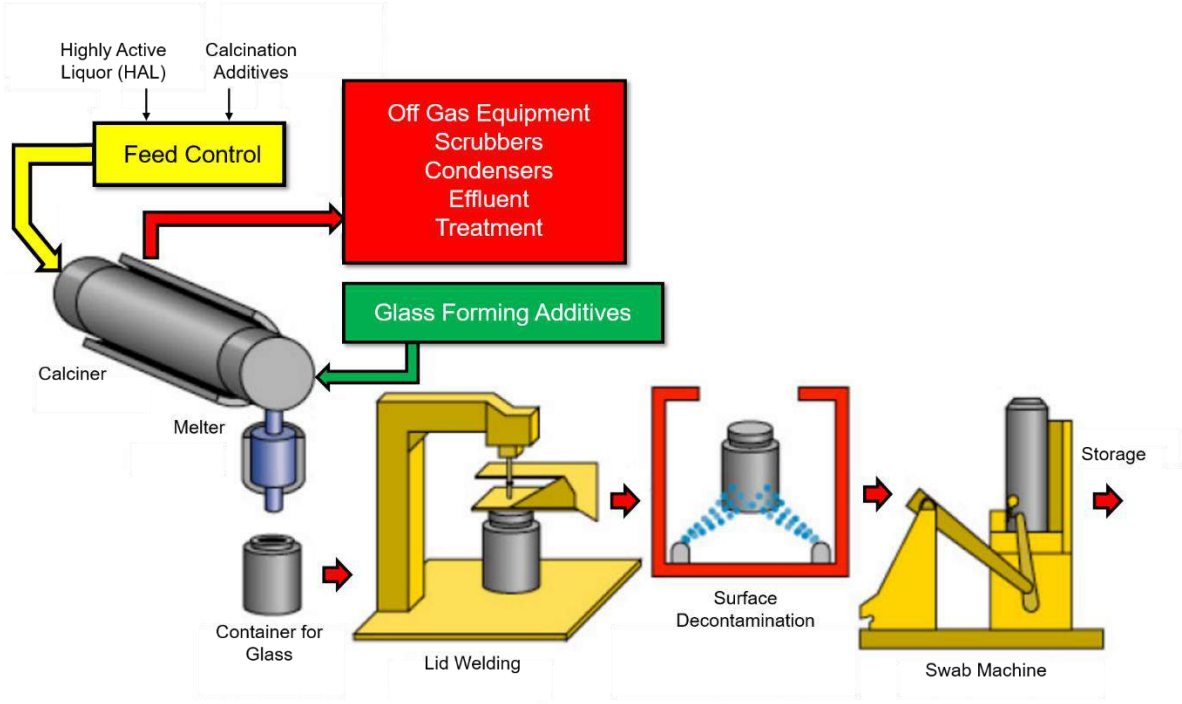

Fig. 16) Overview of the vitrification process for HLW (adapted from [74])

Fig. 17) Vitrified product container [79]

2.4 U.K. Radioactive Waste Inventory

2.4.1 Waste Volume

The 2019 Radioactive Waste Inventory, prepared for the Department for Business, Energy and Industrial Strategy (BEIS) by NDA, collates a detailed report of radioactive waste volumes, activity, compositions, treatment and packaging, planned disposal routes and forecasts of future arisings. The total reported volume of U.K. radioactive waste as of 2019 is summarised in **Fig. 18**. VLLW waste contributes to the vast majority of waste volume. The volume of HLW is significantly lower than ILW and LLW (1,390 m^3, compared to 247,000 m^3 and 1,480,000 m^3, respectively), with a total mass of 3,200 kg.

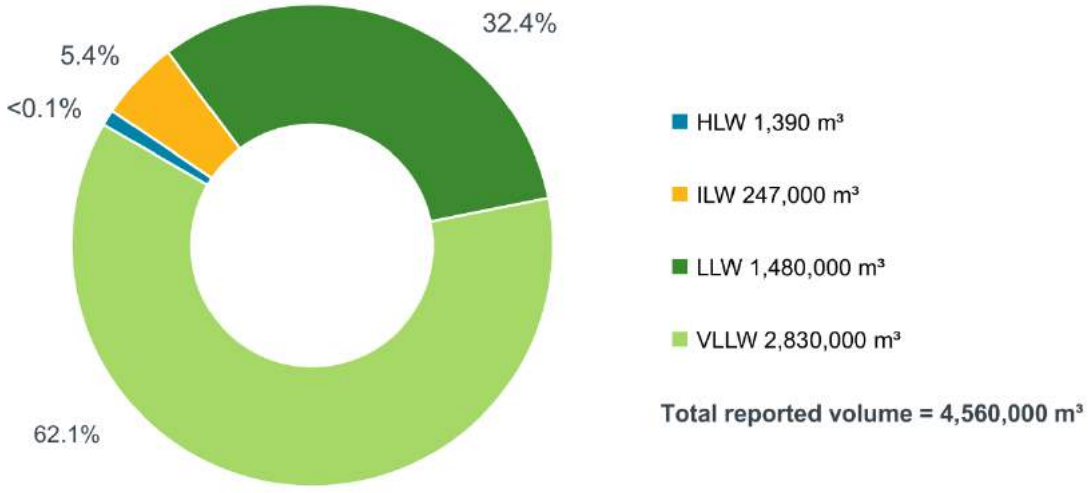

Fig. 18) Total reported volume of U.K. radioactive wastes (as of 01/04/2019) [2]

2.4.2 Waste Activity

The radioactive output associated with LLW and VLLW is drastically lower than HLW and ILW. The activity distribution as of 2019 between waste categories is summarised in **Fig. 19**. The estimated activity of HLW and ILW stocks are 80,000,000 TBq and 4,100,000 TBq, respectively. This is dramatically higher than LLW and VLLW, which contribute 32 TBq and 0.09 TBq, respectively. As such, LLW and VLLW may be super-compacted and disposed at near surface disposal facilities such as the Dounreay LLW facility. Currently, there is no existing facility that may accept higher activity wastes for disposal. In the U.K. it is envisaged that HLW and ILW will be permanently placed in geological disposal, after a sufficient cooling period. Including estimates for material arising due to new nuclear power stations in the U.K., it is predicted that the total radioactivity of all U.K. radioactive waste will decrease from 84,000,000 TBq to 1,900,000 TBq by the year 2200.

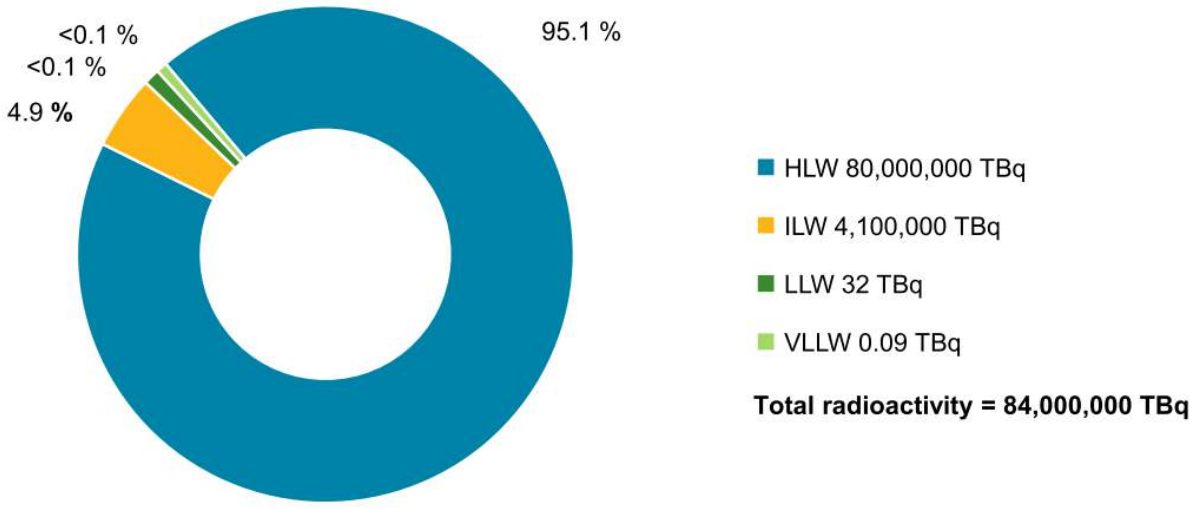

Fig. 19) Radioactivity contributions of individual U.K. waste categories (as of 01/04/2019) [2]

2.5 Geological Disposal Concept

The most robust concept for the permanent disposition of high level nuclear waste (either conditioned in glass/ceramic matrices, or with the spent fuel itself acting as the host matrix) is deep geological disposal [80]. This method is widely considered the only option with sufficient technical maturity for implementation. The placement of waste deep underground in an engineered facility will ensure isolation from the biosphere, such that radionuclide release to the near field environment, and subsequent migration to the surface, will occur over geological timescales. Moreover, the expected lifetime of the facility would be engineered such that the activity of the radionuclides that reach the surface is comparable to the natural background radiation levels emitted by natural uranium ores, this concept is illustrated in **Fig. 20**.

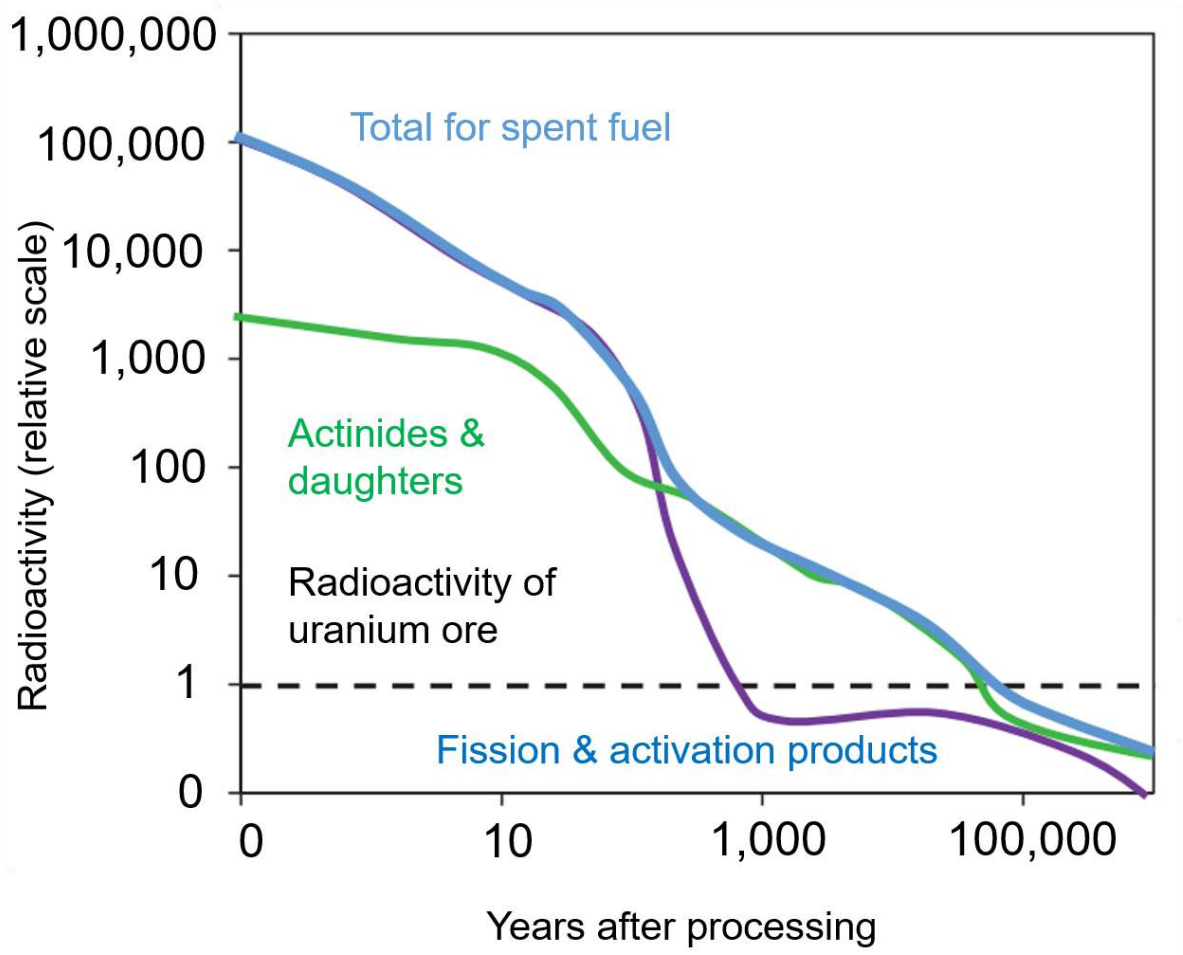

Fig. 20) Illustration of timescales necessary for geological disposal (adapted from [81])

It should be noted that there does not exist a standardised method of geological disposal or generic repository design, as this is fundamentally controlled by host geology; all nations aiming to construct a GDF play host to a rich variety of geological landscapes, hence each GDF design will be indigenous to the nation. Over the timescales necessary for the activity to decrease to the background level the nuclear wasteform itself will inevitably undergo degradation due to the heat output and self-irradiation from the radioactive inventory, hence a secondary barrier may be present to retard the migration of radionuclides. This may be further supported by a series of subsequent material barriers, with the view to ensure the release of radioactive material is achieved in a slow manner. This is referred to as the engineered barrier system (EBS), or colloquially as the 'Russian doll' approach (**Fig. 21**).

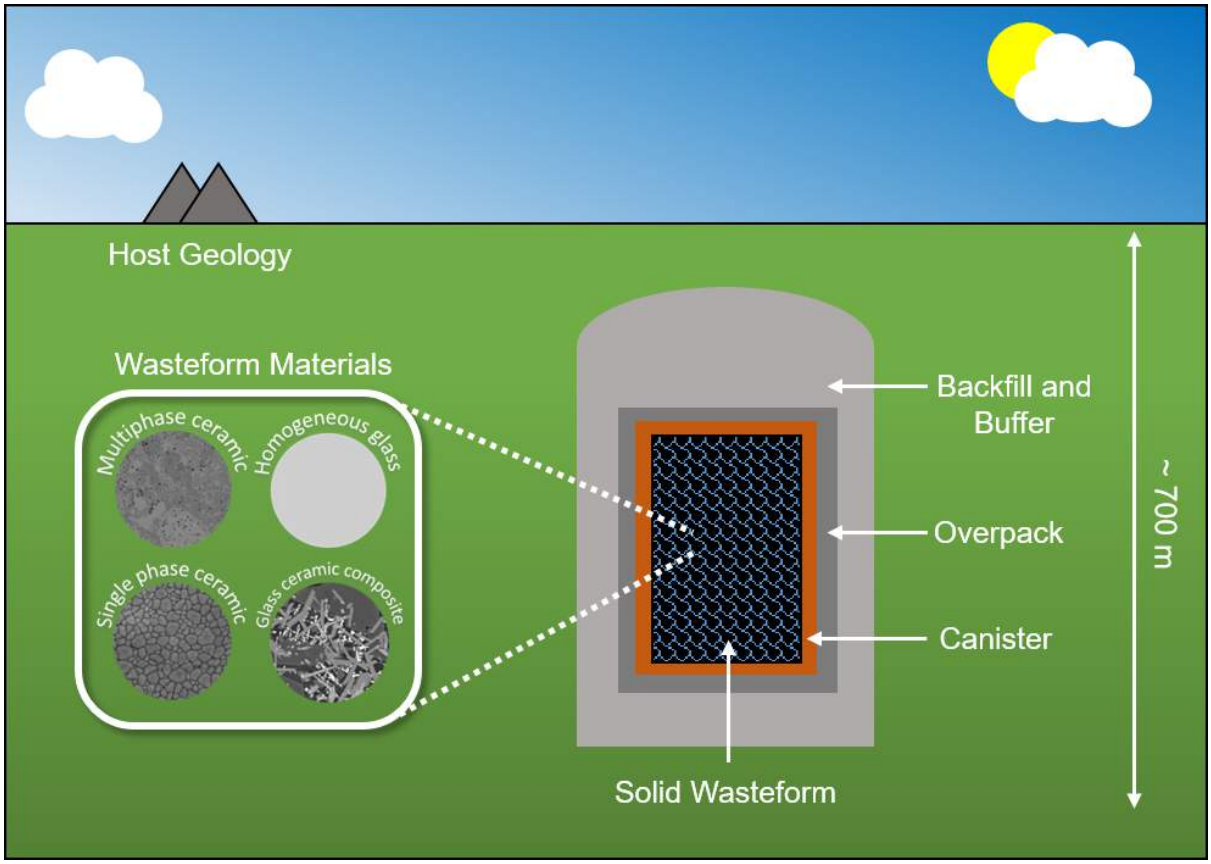

Fig. 21) Engineered multibarrier system for geological disposal of nuclear wastes

Wasteform: The wasteform itself acts as the primary containment matrix for the radioactive waste stream. Wasteform selection is contingent on the physical and chemical properties of the waste stream and is tailored accordingly. However, the wasteform will likely be comprised of a vitreous material (for HLLW waste stream from reprocessing operations) or a ceramic/glass-ceramic material for inventories with a high actinide fraction, such as plutonium contaminated material (PCM). At a broad level, the wasteform will incorporate the constituents of the waste at the atomic level within a highly durable matrix, providing a leach resistant barrier to the near field. This does not, however, apply to cementitious wasteforms, for which the waste is encapsulated in the cement matrix at the macroscopic scale. The wasteform must also be able to co-immobilise a sufficient concentration of a suitable additive (*e.g.* Gd, Hf) to act as a neutron poison, and thus mitigate the possibility of a criticality event in the near-field environment, post closure.

Container/overpack: The packaged wasteform itself will be placed within a container, in order to facilitate transport, handling and manipulation, and eventual emplacement within the GDF. The container will also further isolate the wasteform from groundwater and increase the impact protection of the waste package. The choice of container material is dependent on the long-term mechanical stability, corrosion resistance and susceptibility to enhanced corrosion *via* radiation. The choices for waste container materials are typically metallic, with candidates such as copper, carbon steel and stainless steel under consideration.

Backfill: Subsequent to the placement of waste packages within a GDF, the operational performance may be greater improved by the addition of a backfill, to act as a radionuclide buffer phase post-failure. The backfill will also prevent groundwater ingress, improve long term criticality control, and facilitate gas transfer. Candidate materials include cementitious grout and bentonite.

Host geology: The design and site placement for a GDF is contingent on the availability of desirable host geology. In the context of geological disposal in the U.K., this is further complicated by the adoption of the volunteer approach, by which a community may express interest to host the GDF facility. A technical assessment will then be performed in order to determine whether the host geology is suitable. There are many criteria that must be satisfied with regards to siting, however fundamental considerations include tectonic activity, seismicity, climate projections, sea level change and glacial advances [82]. There are three broad geological classes that are considered for a GDF: high strength rocks (typically igneous or metamorphic) in which water flow is typically through rock fractures and divisions; low strength sedimentary rocks in which water migration occurs through the rock mass; evaporites such as halites or anhydrites, which occur as a result of water evaporation from large deposits of dissolved salts [83].

2.6 Management Options for U.K. Plutonium Inventories

2.6.1 Plutonium Production

Pu isotopes are produced in the core of nuclear reactors. Nuclei of ^{238}U undergo capture neutrons to form the metastable ^{239}U which quickly undergoes two β^- decays to form ^{239}Np and ^{239}Pu**.** Plutonium isotopes ^{240}Pu, ^{241}Pu, ^{242}Pu, and ^{243}Pu form through further neutron capture, yet the accumulation yield is limited by the different half-life of each isotope. The nuclear speciation chain for plutonium isotopes is shown in **Fig. 22**.

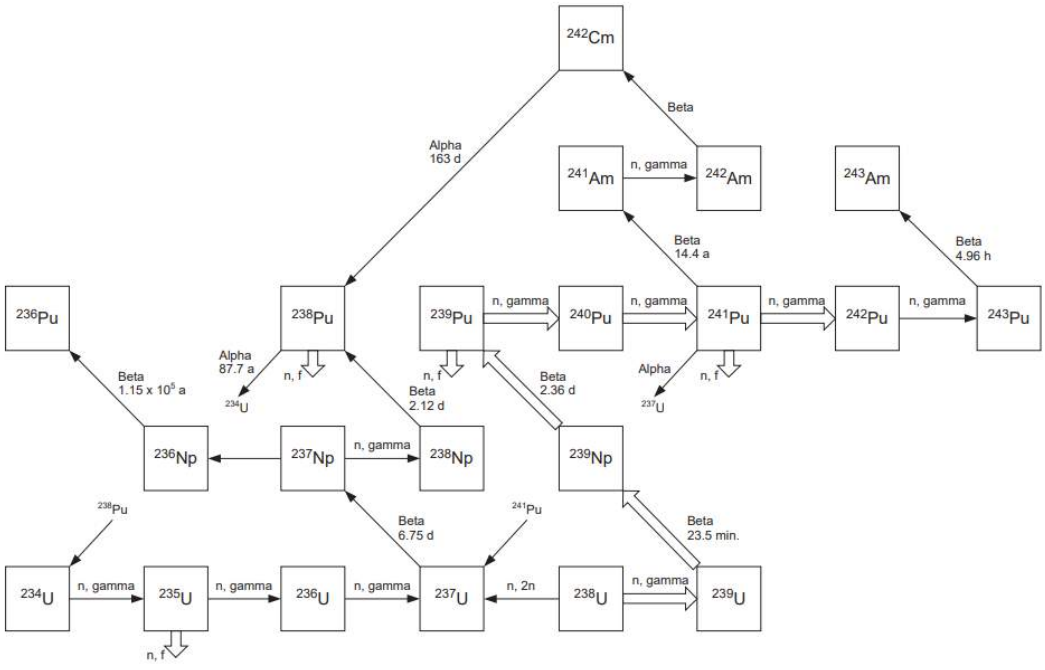

Fig. 22) Plutonium speciation chains indicating decay modes [84]

Ingrowth of residual species and daughter products, such as uranium and americium, must be considered in the management of accumulated Pu, as the impurities in feedstock that may be carried through for immobilisation and disposal may affect the long term performance of waste packages. In particular, the production of ^{241}Am (as a result of β-decay of ^{241}Pu) is a particular concern, as it (alongside other impurities residual from the chemical reprocessing stages) could be detrimental to the performance of MOX fuel fabricated from separated UK PuO_2 [85]. However, it is anticipated that sufficient blending and dilution of americium within PuO_2 stocks will ensure that Am-ingrowth does not present a substantial product quality issue [86]. Moreover, ^{241}Am is a γ-emitter, and therefore poses an increase dose uptake to workers, requiring additional shielding.

2.6.2 U.K. Plutonium Compositions and Stocks

The isotopic composition of separated plutonium is contingent on reactor and fuel types. The relationship between average reactor burnup and isotopic composition at discharge is given in **Table 5**. The breeding of plutonium for defence purposes necessitates very low burn up, as it is desirable for a high ratio of ^{239}Pu/^{240}Pu, as ^{240}Pu can undergo spontaneous fission, and decrease explosive yield. Yet plutonium reprocessed from the civil fuel cycle consists mainly of ^{239}Pu, ^{240}Pu, and ^{241}Pu.

Table 5) Isotopic composition of UK plutonium at discharge (data from [85])

Source	Mean fuel burn up (GWd/tHM)	Approximate Composition at Discharge (wt. %)				
		^{238}Pu	^{239}Pu	^{240}Pu	^{241}Pu	^{242}Pu
Magnox reprocessing	5	0	68.5	25.0	5.3	1.2
AGR reprocessing	18	0.6	53.7	30.8	9.9	5.0
Defence programmes	0.4	0	93.0	6.5	0.5	0
PFR reprocessing	95	0.9	58.1	35.9	2.7	2.4
PWR reprocessing	33	2.0	52.5	24.1	14.7	6.2

The activity and half-life of these isotopes vary, and as such, full accountancy and characterisation of these waste streams is imperative in the design and assured functionality of wasteforms; these are outlined in **Table 6**.

Table 6) Nuclear properties of plutonium isotopes (* 0.002% of ^{241}Pu undergoes α-decay) (data from [84])

Isotope	Half-life (a)	Decay mode	Specific activity (10^9Bq/g)	Spontaneous neutron rate (n/g per second)	Heat generation (W/kg)	He gas production rate (mmol/kg per year)	Product isotope
^{236}Pu	2.85	α	18600	3.7×10^4	17900	1000	^{232}U
^{238}Pu	87.7	α	600	2.62×10^3	560	32.6	^{234}U
^{239}Pu	2.41×10^4	α	2	0.03	1.9	0.12	^{235}U
^{240}Pu	6.54×10^3	α	8	1.02×10^3	6.8	0.44	^{236}U
^{241}Pu	14.4	β*	3700	-	4.2	-	^{241}Am
^{241}Pu	7.2×10^5	α*	0.07	8.8×10^2	0.06	0.004	^{237}U
^{242}Pu	3.76×10^5	α	0.1	1.7×10^3	0.1	0.01	^{238}U
^{241}Am	4.32×10^2	γ	120	1.1	114	6.8	^{237}Np

These characteristics must be accounted for when considering wasteform fabrication. Particularly, the specific activity (and subsequent heat generation) of ^{238}Pu, the half-lives of ^{239}Pu and ^{241}Pu are problematic and in turn result in difficulties regarding interim storage and eventual disposal.

The United Kingdom holds the largest stockpile of PuO_2 under civil safeguards worldwide, alongside a considerable quantity of reprocessed UO_2 and a small quantity of ThO_2. These data are collated in **Table 7**. There is currently 112 tHM of PuO_2 consolidated at the Sellafield site, although, this is predicted to rise to 114 tHM subsequent to the completion of Magnox reprocessing operations. Approximately 24 tHM of Japanese owned PuO_2 also resides in the U.K., produced as the result of contractual reprocessing. Alongside Pu production, the motive for spent fuel reprocessing concerns the recovery of U for fabrication of fresh fuel. These materials are stored at Capenhurst, Springfields, Sellafield and Dounreay. A small stock of ThO_2 is also held at Springfields, for which there is no foreseen use.

Table 7) Total mass of U.K. separated actinide stocks

Composition	Stock (tHM) as of 01/04/2019	Comments
PuO_2	112	Forecast to reach 114 tHM. Existing 24 tHM of foreign owned material.
UO_2	99,000	Future arisings estimated to be 85,000 tHM. Does not include > 1 tHM highly enriched material.
ThO_2	0.2	No reported future arisings.

2.6.3 Stockpile Risks and Motives for Conditioning and Disposal

Through a combination of biological, radiotoxic, radioactive and proliferation considerations, the storage of large Pu inventories at above ground facilities clearly presents a significant risk to human life and the wider environment. The predominant risk associated with storing large quantities of separated Pu at surface level facilities is that of a terrorist incident and/or theft. As Pu is capable of sustaining a fission chain reaction, the risk associated with theft, and subsequent manufacture of an improvised nuclear device is significant, as although the approximate isotopic discharge associated with reprocessed Magnox and AGR fuel has a relatively high yield of ^{241}Pu, it is still considered that a sophisticated operation would be able to produce a viable weapon from material contained within the civil stockpile [87]. Another credible threat pertains to widespread dispersion, either through accidental fire, or through a targeted explosion or attack at the Sellafield Products and Residues Store (SPRS) where the inventory is currently stored. Despite the low probability of such an event, the radiological and toxicological hazard posed by such an event would be catastrophic. Pu inventories further pose a substantial health risk to humans and animal life, and hence release into the wider environment is a notable risk. Oxides of Pu in the powder form are considered to pose an increased hazard, with further potential for dispersion and inhalation during handling and repackaging. Pu uptake can also occur through skin contact, exposure to open wounds and ingestion, yet the dose received through uptake is fundamentally dependent on the route of exposure, and the properties of the plutonium compound, as biological half-life within the body is determined by the isotope. Ionising radiation from α-decay inside

the body is known to induce DNA damage. Inhalation is considered the most detrimental vector for ingestion, due to the large alveolar surface area of the lungs (estimated to be around 140 m^2), resulting in an increased risk of cancer in soft tissues, alongside other health issues [88], [89]. An example of plutonium-induced lung fibrosis is shown in **Fig. 23**. Detailed reviews of the health risks of Pu ingestion are given here [84], [90], [91], [92].

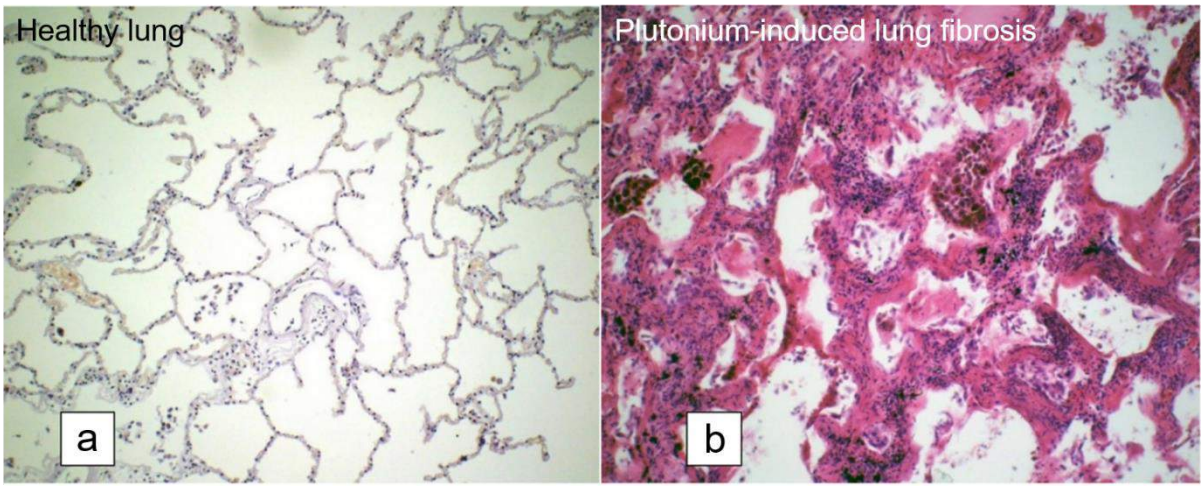

Fig. 23) Morphology comparison of healthy lung, and plutonium-induced lung fibrosis (edited and reproduced from [89])

2.6.4 Credible Options for Management of the U.K. Plutonium Inventory

As NDA is liable for the ultimate disposal of all legacy and forecast radioactive waste inventories in the U.K. on behalf of Government, a life cycle cost estimate (including separated civil Pu) has been undertaken. The potential management strategies have been outlined through in the NDA 'credible options' analysis, that have been periodically updated since 2008. The credible options framework outlines potential pathways that would minimise the risks that the stockpile poses in its current form, such as proliferation and/or diversion, accidental dispersion and theft. Options are evaluated on the basis of public and worker safety, technological readiness level of deliverable options, socioeconomic viability and compliance with existing disposal options. There are three options that are broadly compatible with the aforementioned criteria. These are indefinite storage, MOX fuel fabrication, and prompt immobilisation followed by permanent disposal.

2.6.4.1 Consolidation and Storage at Sellafield

The default management strategy regarding stockpiled U.K. owned plutonium is consolidation and indefinite storage at the Sellafield site, until such a time a decision regarding permanent disposal is reached, or the site-license of the facility is reached. A recent campaign of consolidation and storage began in 2019, with the aim to collate the entire civil stockpile at SPRS [3]. It is expected that any strategy of reuse or disposal will take several decades to implement, hence in the interim, consolidation and storage in this manner is an acceptable strategy. A programme of work has also been undertaken to address issues of packaging degradation that are prominent on some of the older portions of the inventory. The degradation of these packages, primarily due to the radiolysis-induced breakdown of the

poly-vinyl chloride (PVC) inner containment, has contaminated some fraction of the PuO_2 inventory, with upper limits of 2 wt. % Cl contamination, although there is considered to be some uncertainty and variation between each package [93]. As such, urgent action is necessary to repackage some of the older PuO_2 containers, to ensure their condition is such that they can withstand extended storage.

2.6.4.2 Reuse as Mixed Oxide Fuel

Though the primary driver for reprocessing SNF in the U.K. was fuelling of a fleet of fast reactors, this programme was halted and subsequently cancelled in 1994. Nevertheless, in principle it is possible that the existing Pu inventory could be used to fuel a fleet of three 1100 MWe PWR or 1600 MWe EPR reactors over a period of 60 y, as MOX fuel [94]. At present, this strategy is considered by U.K. Government as the preferred long-term management option, on the basis of perceived maturity of the available technology compared to existing disposal options. Whilst it is expected that such an option could reduce the stockpile by as much as 95%, there remain significant uncertainties, both technical and legislative, that may oppose Pu reuse in the domestic U.K. market. Primarily, there does not exist, at present, a facility in the U.K. that is capable of producing MOX fuels at the required industrial scale. Trials are currently underway in collaboration with Orano (formerly Areva) who have constructed and operated a MOX fabrication facility, in France to ascertain what portion of ThORP and Magnox-derived Pu could be feasibly converted into MOX fuels. However, implementation of such a strategy at large scale would present a monumental challenge to existing U.K. nuclear infrastructure, notwithstanding the commitments that would be required (and that are not currently favoured) by site licensed reactors to burn MOX fuels. Moreover, it must be recognised that a strategy favouring MOX fabrication would still incur MOX wastes and residues that would require treatment prior to disposal, and that some portion of the Pu stockpile is, at present, unsuitable for conversion to MOX. Therefore, regardless of the long-term strategy chosen, it remains necessary to develop a dual-track strategy whereby immobilisation options are developed in parallel to conditions any Pu whose conditions is such that it cannot be converted to MOX [86].

2.6.4.3 Prompt Immobilisation and Geological Disposal

A promising route towards the ultimate disposition of Pu inventories and residues is conversion into a solid wasteform matrix *via* an immobilisation process. A management campaign favouring immobilisation would essentially see the Pu stockpile designated as waste product for disposal, and as such would undergo processing *via* thermal treatment or otherwise to produce solid monolith wasteforms that are compatible with geological disposal, and would be placed alongside conditioned HLW packages in the U.K. GDF. As of 2019, NDA has identified three distinct immobilisation techniques that are considered viable:

- Consolidation *via* hot isostatic pressing to produce a monolith ceramic wasteform of near theoretical density
- Production of heterogeneous, low specification MOX pellets by conventional sintering
- Encapsulation in a cementitious grout, similar in composition for those used for U.K. ILW waste

Each of these approaches offers an advantage for at least some sub-portion of the overall inventory, however, it is widely accepted that for immobilisation of the bulk oxide powder stockpile, immobilisation in a dense ceramic matrix, either by HIP or conventional sintering, is considered the most reliable and technically feasible approach. The development of ceramic matrices for actinide immobilisation has gained notable traction in the preceding decades, on the basis of superior chemical durability and radiation stability relative to conventional borosilicate glasses used for HLW [7], [15], [20], [67], [95]–[98]. Moreover, the existence of natural analogue specimens provide a useful basis on which to evaluate the long-term performance behaviour of chosen wasteforms [24], [99], [100]. A selection of crystalline phases that have been previously identified as potential host materials for Pu, and other actinides, is provided in **Table 8**. An expansive discussion of wasteform design requirements and crystal chemistry of ceramic wasteform materials is provided in the ensuing chapter of this thesis.

Table 8) Candidate ceramic wasteforms for actinide immobilisation

Ceramic Phase	Ideal Formula	Space Group	Unit Cell Parameters (Å, °)	Calculated Density ($g \cdot cm^{-3}$)
Zirconolite	$CaZrTi_2O_7$	C2/c	a = 12.44; b = 7.27; c = 11.38; $\alpha = \gamma = 90$; β = 100.56	**4.44**
Pyrochlore (Zr)	$Gd_2Zr_2O_7$	$Fm\bar{3}m$	$a = b = c$ = 5.27; $\alpha = \beta = \gamma = 90$	**6.91**
Pyrochlore (Ti)	$Gd_2Ti_2O_7$	$Fd\bar{3}m$	$a = b = c$ = 10.18; $\alpha = \beta = \gamma = 90$	**6.57**
Zirconia	ZrO_2	$P2_1/c$	a = 4.15; b = 5.21, c = 5.32, $\alpha = \gamma = 90$; β = 99.21	**5.82**
Zircon	$ZrSiO_4$	$I4_1/amd$	$a = b$ = 6.60; c = 5.98; $\alpha = \beta = \gamma = 90$	**4.66**
Monazite	$CePO_4$	$P2_1/c$	A = 6.77; b = 7.00; c = 6.44; $\alpha = \gamma = 90$; β = 103.42	**5.26**
Xenotime	YPO_4	$I4_1/amd$	$a = b$ = 6.89; c = 6.03; $\alpha = \beta = \gamma = 90$	**4.26**
Brannerite	UTi_2O_6	C2/m	a = 9.81; b = 3.77; c = 6.93; $\alpha = \gamma = 90$; β = 118.96	**6.36**
Kosnarite	$KZr_2(PO_4)_3$	$R\bar{3}c$	$a = b$ = 8.73; c = 23.20; $\alpha = \beta = 90$; γ = 120	**4.38**
Perovskite	$CaTiO_3$	Pbnm	a = 5.38; b = 5.44; c = 7.64; $\alpha = \beta = \gamma = 90$	**4.04**

2.6.4.4 The Use of Chemical Surrogates in Wasteform Development

In the development of waste conditioning processes and immobilisation matrices, the use of chemical surrogates as a scoping mechanism towards understanding wasteform evolution and durability is both essential and invaluable. Some elements and compounds are highly radiotoxic and necessitate handling precautions such as shielding and high-efficiency extraction systems. This is exacerbated by the accountability and criticality requirements associated with the handling of fissile isotopes such as ^{239}Pu. Sample preparation and manipulation on the laboratory scale for wasteform development and scoping studies is therefore often expensive; labour intensive; and in the case of Pu, subject to stringent security requirements. It should be noted, however, that surrogates are often utilised simply on an economic basis; elements that typically require the use of chemical surrogates are illustrated in **Fig. 24**. The difficulty associated with the use radiotoxic and/or expensive species such as Pu may be alleviated through the use of lanthanide and actinide surrogates [43], [101], [102]. The use of a chemical surrogate pertains to the use another element in place, with the aim of simulating chemical and physical characteristics. The surrogate of choice must possess a suite of characteristics such that insight into the potential behaviour of plutonium may be acquired, ensuring any potential behaviours, whilst not entirely replicated, may be extrapolated to a meaningful extent. Whilst fundamentally it must be

recognised that no surrogate can replicate the behaviour of another element in all chemical environments, the use of several surrogates in conjunction, under identical processing conditions, may allow valid elucidation. There are numerous physical and chemical properties that surrogate elements must, to a certain extent, be able to replicate. These include (but are not limited to): accessible valence states, ionic radii, density, oxide melting temperature, electronic configuration and redox potential. Whilst factors like density may influence settling behaviours in vitrified glass melts, this would not be expected to cause issues for the formation of ceramic materials. Numerous surrogates have been previously used for $Pu^{3+/4+}$, including Eu, Gd, Hf, Nd, however the most commonly employed simulants are Ce, U and Th, hence will be the focus of this work. The relevant physical and chemical properties of these oxides, alongside plutonium, are listed in **Table 9**. Ce is the most commonly utilised surrogate for both Pu^{3+} and Pu^{4+}, as it is relatively inexpensive, non-toxic, and has similar solubility with Pu in borosilicate glass [103]–[107]. Ce exhibits Ce^{3+} and Ce^{4+} valence states, and has comparable ionic radii corresponding to relevant coordination environment. Studies by Cachia *et al*. and Lopez *et al*. formulated a series of borosilicate glass melts, utilising Ce as a Pu surrogate; it was determined that the propensity of Ce to reduce to the Ce^{3+} species improved the solubility within the glass matrix [108], [109]. The solubility of Pu was subsequently improved by addition of a reducing agent, allowing the formation of Pu^{3+}. It was also determined that the propensity of Ce^{4+} to reduce to Ce^{3+} was high relative to Pu^{4+}, and was sensitive to both processing temperature and redox potential of the melt, with a greater proportion of Ce^{3+} speciation at elevated temperature. As Ce has a more positive reduction potential than Pu, it is considered a limiting factor as a surrogate. Similar effects have been observed when using Ce as a surrogate in calcium phosphate ceramics, with Ce becoming increasingly trivalent at higher processing temperatures, when reacting in air [102]. The density of Ce is not comparable to that of Pu, although this is only considered a limiting factor for glass wasteforms, in which the viscosity of the melt may influence Ce settling and accumulation. Overall, it is widely accepted that Ce is a reasonable surrogate for Pu, with accountancy for redox behaviour [110]. U^{4+} may be utilised as a surrogate for Pu^{4+} however, as U is not stabilised as U^{3+} in the solid state under the conditions relevant to Pu immobilisation, surrogacy for Pu^{3+} is limited. Similar to U, Pu exists in Pu^{5+} and Pu^{6+} oxidation states, yet these are typically stabilised in highly oxidising conditions, that are typically irrelevant for wasteform development. Hence, the U^{4+} surrogate is typically achieved by synthesis under reducing or non-oxidising conditions to maintain the required valence. The density and oxide melting temperature of tetravalent U and Pu species are comparable, negating the differences in settling behaviour in vitrified wasteforms. Although the efficacy of U as a Pu surrogate has not been directly compared with Ce in any known studies, there are some studies allowing comparative behaviour with Pu. Phase fields in the $CaZr_{1-x}U_xTi_2O_7$ and $CaZr_{1-x}Pu_xTi_2O_7$ systems reported by Vance *et al*. and Begg *et al*. respectively were near identical, with a polytypical transformation from zirconolite-2M to zirconolite-4M observed in the same solid solution range (approximately x = 0.15) and a further transition to the pyrochlore structure around x = 0.60 [111], [112]. Th is scarcely used as a surrogate for Pu in any systematic manner, despite displaying comparable characteristics for Pu^{4+} with respect to ionic radius and density, with Th also being accessory to many natural zirconolite specimens. The incorporation of Th within the Zr^{4+} site in zirconolite was reported by Kesson *et al*. with $CaZr_{0.9}Th_{0.1}Ti_2O_7$ fabricated by hot pressing at 1400 ˚C

and 0.5 GPa yielding single phase zirconolite with stoichiometry $Ca_{0.99}Zr_{0.96}Th_{0.09}Ti_{1.96}O_7$ determined by EPMA analysis [113]. A two phase assemblage of "*zirconolite plus a fine-grained centred cubic phase*" was produced when targeting $CaZr_{0.8}Th_{0.2}Ti_2O_7$. Substitution of Th^{4+} was reported to be greater targeting Ca^{2+} site substitution (20 wt. %) with Mg^{2+} accommodated on the Ti^{4+} site (2.5 wt. %), however no diffraction or microstructural data were presented. Th was included by Zhang *et al*. as a surrogate for Pu targeting a zirconolite-rich phase assemblage (90 % zirconolite, 10% Ba-hollandite) fabricated by HIP at 1280 ˚C and 100 MPa [114]. It was confirmed that Th was fully incorporated within the zirconolite phase and an accessory $ThTi_2O_6$ phase. The high oxide melting temperature of ThO_2 with respect to PuO_2 may be a limiting factor for deployment as a surrogate (3390 ˚C and 2240 ˚C, respectively). Metcalfe *et al*. formulated a series of $Ca_{3-x}Th_{x/2}(PO_3)_4$ ceramics with Th^{4+} acting as a surrogate for Pu^{4+} [102]. Although some reaction occurred after calcination at 950 ˚C it was confirmed that unreacted ThO_2 was distributed throughout the microstructure, although it should be noted that this was also true for CeO_2. ThO_2 has also been used as a PuO_2 surrogate in vitrified wasteforms. The incorporation of ThO_2 and PuO_2 in the R7T7 borosilicate was investigated by Lopez *et al* [115]. Similar solubility was reported at 1200 ˚C, with 0.134 ± 0.06 and 0.26 ± 0.04 mol. % for Pu and Th, respectively.

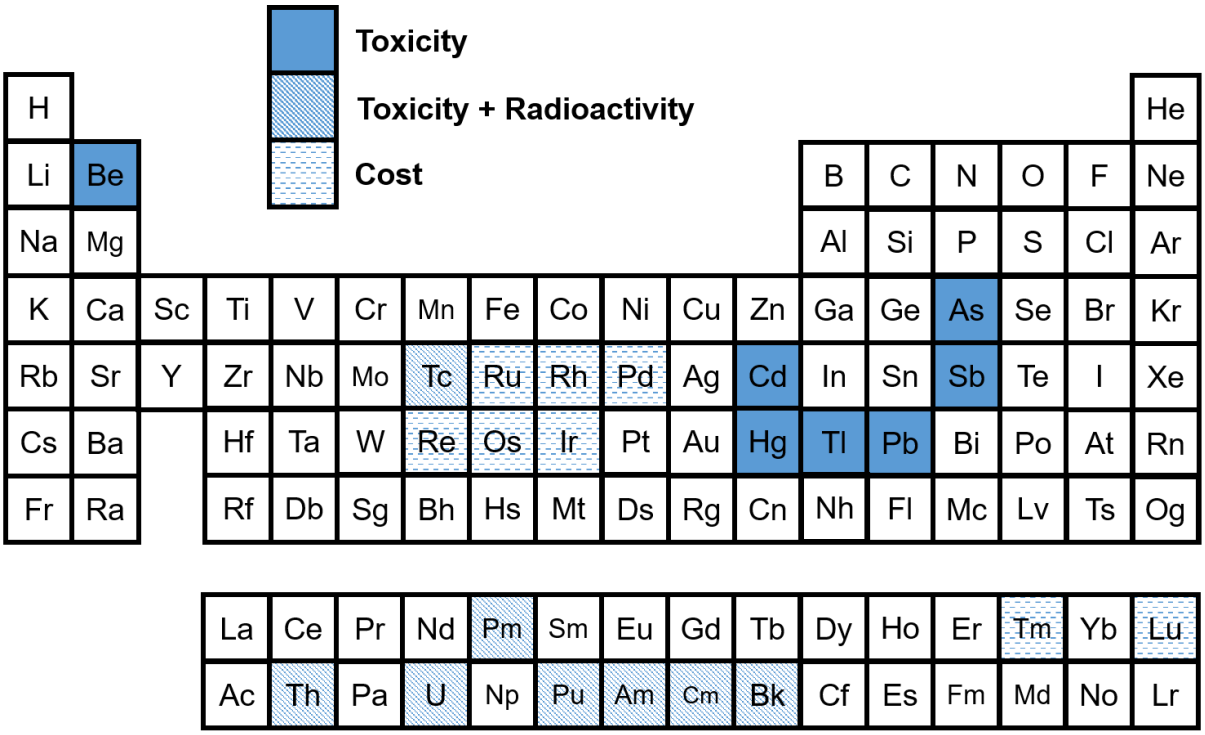

Fig. 24) Periodic table highlighted to show elements for which surrogates are typically used, on the basis of toxicity, radiotoxicity and cost (redrawn from [101])

Table 9) Physicochemical data for oxides of Ce, U, Th and Pu (data from [101], [116])

Element	Valence	Electronic Configuration	Ionic Radius	Oxide Density	Oxide Melting Temperature
Ce	(III)	[Xe]$4f^1$	[CN6]: 1.01 Å [CN7]: 1.07 Å [CN8]: 1.14 Å	6.20 g/cm^2	2230 ˚C
	(IV)	[Xe]	[CN6] 0.87 Å [CN7]: 0.92 Å [CN8]: 0.97 Å	7.65 g/cm^2	2400 ˚C
U	(IV)	[Rn]$5f^2$	[CN6]: 0.89 Å [CN7]: 0.95 Å [CN8]: 1.00 Å	10.97 g/cm^2	2827 ˚C
	(V)	[Rn]$5f^1$	[CN6]: 0.76 Å [CN7]: 0.84 Å [CN8]: N.A. Å	8.38 g/cm^2	1150 – 1300 ˚C → UO_2
	(VI)	[Rn]	[CN6]: 0.73 Å [CN7]: 0.81 Å [CN8]: 0.86 Å	7.30 g/cm^2	1150 – 1300 ˚C → U_3O_8
Th	(IV)	[Rn]	[CN6]: 0.94 Å [CN7]: N.A. Å [CN8]: 1.05 Å	10.00 g/cm^2	3390 ˚C
Pu	(III)	[Rn]$5f^5$	[CN6]: 1.00 Å [CN7]: N.A. Å [CN8]: N.A. Å	10.50 g/cm^2	2240 ˚C
Pu	(IV)	[Rn]$5f^4$	[CN6]: 0.86 Å [CN7]: 0.91 Å [CN8]: 0.96 Å	11.50 g/cm^2	2400 ˚C

References

[1] Parliament office of science and technology, “Managing the UK Plutonium Stockpile,” 2016.

[2] Nuclear Decommissioning Authority (NDA), “2019 UK Radioactive Material Inventory,” 2019.

[3] Nuclear Decommissioning Authority (NDA), “Progress on Plutonium Consolidation, Storage and Disposition,” 2019.

[4] *Energy Act 2004*. 2004.

[5] Nuclear Decommissioning Authority (NDA), “NDA Plutonium Options,” 2008.

[6] M. I. Ojovan and W. E. Lee, *An Introduction to Nuclear Waste Immobilisation*, 1st ed. Oxford: Elsevier, 2005.

[7] R. C. Ewing, “Ceramic matrices for plutonium disposition,” *Prog. Nucl. Energy*, vol. 49, pp. 635–643, 2007.

[8] A. E. Ringwood *et al.*, “Immobilization of High-Level Nuclear Reactor Wastes in Synroc: A Current Appraisal,” *Nucl. Waste Manag.*, vol. 2, pp. 287–305, 1981.

[9] K. L. Smith, G. R. Lumpkin, M. G. Blackford, R. A. Day, and K. P. Hart, “The durability of Synroc,” *J. Nucl. Mater.*, vol. 190, pp. 287–294, 1992.

[10] E. R. Vance, A. Jostsons, R. A. Day, C. J. Ball, B. D. Begg, and P. J. Angel, “Excess Pu Disposition in Zirconolite-Rich Synroc,” in *Mat. Res. Soc. Symp. Proc.*, 1996, vol. 412, pp. 41–47.

[11] J. Campbell *et al.*, “Properties of SYNROC-D Nuclear Wasteform: A State-of-the Art Review,” 1982.

[12] E. R. Vance *et al.*, “Actinide and rare earth incorporation into zirconolite,” *J. Alloys Compd.*, vol. 213/214, pp. 406–409, 1994.

[13] R. B. Greegor, F. W. Lytle, R. J. Livak, and F. W. Clinard, “X-ray spectroscopic investigation of Pu-substituted zirconolite,” *J. Nucl. Mater.*, vol. 152, no. 2–3, pp. 270–277, 1988.

[14] S. McCaugherty and A. P. Grosvenor, “Low-temperature synthesis of $CaZrTi_2O_7$ zirconolite-type materials using ceramic, coprecipitation, and sol-gel methods,” *J. Mater. Chem. C*, pp. 23–25, 2019.

[15] N. C. Hyatt, M. C. Stennett, E. R. Maddrell, and W. E. Lee, “Single Phase Ceramic Wasteforms for Plutonium Disposition,” *Adv. Sci. Technol.*, vol. 45, no. 2006, pp. 2004–2011, 2006.

[16] R. W. Cheary and A. A. Coelho, “A site occupancy analysis of zirconolite $CaZr_xTi_{3-x}O_7$,” *Phys Chem Miner.*, vol. 24, pp. 447–454, 1997.

[17] E. R. Vance, C. J. Ball, M. G. Blackford, D. J. Cassidy, and K. L. Smith, “Crystallisation of

zirconolite from an alkoxide precursor," *J. Nucl. Mater.*, vol. 175, pp. 58–66, 1990.

[18] A. A. Coelho, R. W. Cheary, and K. L. Smith, "Analysis and Structural Determination of Nd-Substituted Zirconolite-4M," *J. Solid State Chem.*, vol. 129, pp. 346–359, 1997.

[19] M. Gupta, P. K. Kulriya, R. C. Meena, S. Neumeier, and S. S. Ghumman, "Probing swift heavy ion irradiation damage in Nd-doped zirconolite," *Nucl. Instruments Methods Phys. Res. Sect. B Beam Interact. with Mater. Atoms*, vol. 453, no. April, pp. 22–27, 2019.

[20] E. R. Vance, B. D. Begg, R. A. Day, and C. J. Ball, "Zirconolite-rich Ceramics for Actinide Wastes," in *Mat. Res. Soc. Symp. Proc.*, 1995, vol. 353, pp. 767–774.

[21] E. R. Vance, P. J. Angel, B. D. Begg, and R. A. Day, "Zirconolite-Rich Titanate Ceramics for High-Level Actinide Wastes," in *Mat. Res. Soc. Symp. Proc.*, 1994, vol. 333, pp. 293–298.

[22] L. R. Blackburn *et al.*, "Synthesis and Characterisation of $Ca_{1-x}Ce_xZrTi_{2-2x}Cr_{2x}O_7$: Analogue Zirconolite Wasteform for the Immobilisation of Stockpiled UK Plutonium," *J. Eur. Ceram. Soc.*, vol. 40, no. 15, pp. 5909–5919, 2020.

[23] G. R. Lumpkin, Y. Gao, R. Gieré, C. T. Williams, A. N. Mariano, and T. Geisler, "The role of Th-U minerals in assessing the performance of nuclear waste forms," *Mineral. Mag.*, vol. 78, no. 5, pp. 1071–1095, 2014.

[24] G. R. Lumpkin, K. P. Hart, P. J. McGlinn, T. E. Payne, R. Gieré, and C. T. Williams, "Retention of actinides in natural pyrochlores and zirconolites," *Radiochim. Acta*, vol. 66/67, pp. 469–474, 1994.

[25] C. T. Williams and R. Gieré, "Zirconolite: A Review of Localities Worldwide, and a Compilation of its Chemical Compositions" *Bull. Nat. Hist. Museum London*, vol. 52, pp. 1–24, 1996.

[26] C. Meng, X. Ding, W. Li, J. Zhao, and H. Yang, "Phase structure evolution and chemical durability studies of Ce-doped zirconolite–pyrochlore synroc for radioactive waste storage," *J. Mater. Sci.*, vol. 51, pp. 5207–5215, 2016.

[27] W. N. Cottingham and D. a Greenwood, *An Introduction to Nuclear Physics*, 2nd ed. Cambridge University Press, 1986.

[28] B. R. Martin, *Nuclear and Particle Physics: An Introduction*, vol. 53, no. 9. Chichester: John Wiley & Sons Ltd, 2006.

[29] A. Vértes, S. Nagy, Z. Klencsár, R. G. Lovas, and F. Rösch, *Handbook of Nuclear Chemistry*, vol. 67, no. 6. Springer, 2007.

[30] R. C. Ewing, W. J. Weber, and F. W. Clinard, "Radiation effects in nuclear waste forms for high-level radioactive waste," *Prog. Nucl. Energy*, vol. 29, no. 2, pp. 63–127, 1995.

[31] G. Choppin, J.-O. Liljenzin, and J. Rydberg, *Radiochemistry and Nuclear Chemistry*, 3rd ed. Butterworth-Heinemann, 2002.

[32] S. Marguet, *The Physics of Nuclear Reactors*. Springer, 2017.

[33] S. M. Weston, *Nuclear reactor physics*, 3rd ed. Wiley-VCH, 2018.

[34] National Audit Office, “The nuclear energy landscape in Great Britain,” 2012.

[35] Nuclear Decommissioning Authority and Department for Business Energy & Industrial Strategy, “Radioactive Wastes in the UK: A Summary of the 2016 Report,” 2016.

[36] K. Whittle, *Nuclear materials science*. IOP Publishing, 2016.

[37] I. Crossland, *Nuclear Fuel Cycle Science and Engineering*. Woodhead Publishing, 2012.

[38] I. Hore-Lacy, *Uranium for Nuclear Power: Resources, Mining and Transformation to Fuel*, 1st ed. Woo, 2016.

[39] K. L. Nash and G. J. Lumetta, *Advanced Separation Techniques for Nuclear Fuel Reprocessing and Radioactive Waste Treatment*, 1st ed. Woodhead Publishing, 2011.

[40] C. R. Bayliss and K. F. Langley, *Nuclear Decommissioning, Waste Management, and Environmental Site Remediation*. 2003.

[41] S. E. Jensen and E. Nonbol, “Description of the Magnox Type of Gas Cooled Reactor (MAGNOX),” 1998.

[42] C. R. F. Azevedo, “Selection of fuel cladding material for nuclear fission reactors,” *Eng. Fail. Anal.*, vol. 18, no. 8, pp. 1943–1962, 2011.

[43] I. W. Donald, *Waste Immobilization in Glass and Ceramic Based Hosts*. Chichester: John Wiley & Sons Ltd, 2010.

[44] P. Greenfield, “A comparison of magnox A 12 and ZA alloys as canning materials for nuclear reactors,” *J. Nucl. Mater.*, vol. 11, no. 2, pp. 121–134, 1964.

[45] G. B. Gibbs, “The diffusion of plutonium and fission products in magnox fuel cans,” *J. Nucl. Energy*, vol. 21, no. 2, pp. 171–181, 1967.

[46] M. W. Davies, “Graphite core design in UK reactors,” 1996.

[47] G. Holt, “Radioactive Graphite Management at UK Magnox Nuclear Power Stations,” 1999.

[48] “Magnox reactor schematic.” [Online]. Available: https://upload.wikimedia.org/wikipedia/commons/thumb/1/10/Magnox_reactor_schematic.svg/1280px-Magnox_reactor_schematic.svg.png. [Accessed: 16-Dec-2020].

[49] Science Museum Group Collection, “Magnox fuel cans from Sizewell-A Nuclear Power Station.” [Online]. Available: https://collection.sciencemuseumgroup.org.uk/objects/co8233887/magnox-fuel-cans-from-sizewell-a-nuclear-power-station-1968-nuclear-fuel-cans%0Ahttps://creativecommons.org/licenses/by-nc-sa/4.0. [Accessed: 16-Dec-2020].

[50] S. A. Walling, H. Kinoshita, S. A. Bernal, N. C. Collier, and J. L. Provis, “Structure and properties of binder gels formed in the system $Mg(OH)_2$-SiO_2-H_2O for immobilisation of Magnox sludge,” *Dalt. Trans.*, vol. 44, no. 17, pp. 8126–8137, 2015.

[51] S. Tan, N. Kirk, M. Marshall, O. McGann, and R. J. Hand, “Vitrification of an intermediate level Magnox sludge waste,” *J. Nucl. Mater.*, vol. 515, pp. 392–400, 2019.

[52] P. G. Heath, M. W. A. Stewart, S. Moricca, and N. C. Hyatt, “Hot-isostatically pressed wasteforms for Magnox sludge immobilisation,” *J. Nucl. Mater.*, vol. 499, pp. 233–241, 2018.

[53] E. Nonbel, “Description of the Advanced Gas Cooled Type of Reactor (AGR),” 1996.

[54] C. E. Ells and E. C. W. Perryman, “Effects of Neutron Induced Gas Formation on Beryllium,” *J. Nucl. Mater.*, vol. 1, pp. 73–84, 1959.

[55] Nuclear Decommissioning Authority (NDA), “Packaging of Spent AGR Fuel,” 2012.

[56] “AGR reactor schematic.” [Online]. Available: https://commons.wikimedia.org/wiki/File:AGR_reactor_schematic.svg. [Accessed: 16-Dec-2020].

[57] “AGR Fuel Element.” [Online]. Available: https://collection.sciencemuseumgroup.org.uk/objects/co5473/agr-fuel-element-c-1982-nuclear-fuel-fuel-rods%0A. [Accessed: 16-Dec-2020].

[58] W. E. Lee, M. I. Ojovan, and C. M. Jantzen, *Radioactive Waste Management and Contaminated Site Clean-Up*. Woodhead Publishing, 2013.

[59] W. G. Sutcliffe, “Dose Irradiated Fuel Rate Estimates from Assemblies in Air,” 1994.

[60] IAEA, “Country Nuclear Fuel Cycle Profiles,” 2005.

[61] IAEA, *Storage of Spent Fuel from Power Reactors*, no. November. 1998.

[62] J. Veliscek-Carolan, “Separation of actinides from spent nuclear fuel: A review,” *J. Hazard. Mater.*, vol. 318, pp. 266–281, 2016.

[63] D. Caurant, P. Loiseau, O. Majerus, V. Aubin-Chevaldonnet, I. Bardez, and A. Quintas, *Glassses, Glass-Ceramics and Ceramics for Immobilization of Highly Radioactive Nuclear Wastes*. Nova Science, 2009.

[64] M. I. Ojovan and W. E. Lee, *Introduction to Nuclear Waste Immobilisation*. 2005.

[65] R. C. Ewing, “Long-term storage of spent nuclear fuel,” *Nat. Mater.*, vol. 14, no. 3, pp. 252–257, 2015.

[66] Center for Nuclear Waste Regulatory Analyses, “Characteristics of Spent Nuclear Fuel and Cladding Relevant to High-Level Waste Source Term,” 1993.

[67] W. Lutze and R. C. Ewing, *Radioactive Wasteforms for the Future*. Amsterdam: North Holland Physics Publishing, 1988.

[68] K. L. Nash and M. Nilsson, *Reprocessing and Recycling of Spent Nuclear Fuel*, vol. 2. 2015.

[69] M. F. Simpson and J. D. Law, “Nuclear Fuel Reprocessing,” 2010.

[70] A. Ramanujan, “An Introduction to the Purex Process,” *Iancas*, vol. 14, no. 2, pp. 11–20, 1998.

[71] S. Gin *et al.*, “An international initiative on long-term behavior of high-level nuclear waste glass,” *Mater. Today*, vol. 16, no. 6, pp. 243–248, 2013.

[72] S. Gin, P. Jollivet, M. Tribet, S. Peuget, and S. Schuller, “Radionuclides containment in nuclear glasses: An overview,” *Radiochim. Acta*, vol. 105, no. 11, pp. 927–959, 2017.

[73] K. Bradshaw, N. R. Gribble, D. O. Hughes, and A. D. Riley, “UK Full-Scale Non-Active Vitrification Development and Implementation of Research Findings onto the Waste Vitrification Plant,” in *Waste Management ’07 Conference, Tucson, Arizona*, 2007, no. March.

[74] M. T. Harrison, “Vitrification of High Level Waste in the UK,” *Procedia Mater. Sci.*, vol. 7, pp. 10–15, 2014.

[75] A. J. Fisher, M. T. Harrison, N. C. Hyatt, R. J. Hand, and C. L. Corkhill, “The dissolution of simulant UK Ca/Zn-modified nuclear waste glass: Insight into Stage III behavior,” *MRS Adv.*, vol. 5, no. 3–4, pp. 103–109, 2020.

[76] N. J. Cassingham, C. L. Corkhill, M. C. Stennett, R. J. Hand, and N. C. Hyatt, “Alteration layer formation of Ca- and Zn-oxide bearing alkali borosilicate glasses for immobilisation of UK high level waste: A vapour hydration study,” *J. Nucl. Mater.*, vol. 479, pp. 639–646, 2016.

[77] B. F. Dunnett, “Review of the Development of UK High Level Waste Vitrified Product,” 2007.

[78] M. T. Harrison, B. F. Dunnett, S. Morgan, C. R. Scales, and J. S. Small, “International Research on Vitrified HLW Long-Term Behavior: State of the Art,” 2009.

[79] Sellafield Ltd, “Technology Development and Delivery Summary: Review 2010-2011,” 2010.

[80] IAEA, *Geological Disposal of Radioactive Wastes*, vol. 2.

[81] C. L. Corkhill and N. C. Hyatt, *Nuclear Waste Management*. IOP Publishing, 2018.

[82] F. M. McEvoy, D. I. Schofield, R. P. Shaw, and S. Norris, “Tectonic and climatic considerations for deep geological disposal of radioactive waste: A UK perspective,” *Sci. Total Environ.*, vol. 571, pp. 507–521, 2016.

[83] Nuclear Decommissioning Authority, “Geological Disposal: Steps towards implementation,” 2010.

[84] IAEA, “Storage and Handling of Plutonium,” Vienna, 1998.

[85] Pöyry Energy Ltd and Nuclear Decommissioning Authority, “Production of the Derived Inventory for Uranium and Plutonium,” 2010.

[86] N. C. Hyatt, “Plutonium management policy in the United Kingdom: The need for a dual track strategy,” *Energy Policy*, vol. 101, pp. 303–309, 2017.

[87] A. Klung, “Management of Seperated Plutonium,” 1998.

[88] C. on the B. E. of I. Radiations, *Health Risks of Radon and Other Internally Deposited Alpha-Emitters*. Washington, D.C.: National Academy Press, 1988.

[89] S. A. Romanov *et al.*, “Plutonium production and particles incorporation into the human body,” *J. Environ. Radioact.*, vol. 211, no. October 2019, p. 106073, 2020.

[90] C. Burns, “Overview of Plutonium and Its Health Effects,” Worcester, MA, 2002.

[91] D. M. Taylor, “Environmental plutonium in humans,” *Appl. Radiat. Isot.*, vol. 46, no. 11, pp. 1245–1252, 1995.

[92] R. H. Clarke, J. Dunster, J. C. Nenot, H. Smith, and G. Voeltz, “The environmental safety and health implications of plutonium,” *J. Radiol. Prot.*, vol. 16, no. 2, pp. 91–105, 1996.

[93] S. M. Thornber, L. M. Mottram, A. R. Mason, P. Thompson, C. Stennett, and N. C. Hyatt, “Solubility, speciation and local environment of chlorine in zirconolite glass–ceramics for the immobilisation of plutonium residues,” *RSC Adv.*, vol. 10, pp. 32497–32510, 2020.

[94] N. C. Hyatt, “Safe management of the UK separated plutonium inventory: a challenge of materials degradation,” *npj Mater. Degrad.*, vol. 4, no. 28, 2020.

[95] R. C. Ewing, W. J. Weber, and J. Lian, “Nuclear waste disposal-pyrochlore ($A_2B_2O_7$): Nuclear waste form for the immobilization of plutonium and ‘minor’ actinides,” *J. Appl. Phys.*, vol. 95, no. 11, pp. 5949–5971, 2004.

[96] R. C. Ewing, “Nuclear waste forms for actinides,” in *Proc. Natl. Acad. Sci. USA*, 1999, vol. 96, pp. 3432–3439.

[97] E. Vance, “Development of Ceramic Waste Forms for High-Level Nuclear Waste over the Last 30 Years,” in *Mater. Res. Soc. Symp. Proc.*, 2007, vol. 985.

[98] W. E. Lee, M. I. Ojovan, M. C. Stennett, and N. C. Hyatt, “Immobilisation of radioactive waste in glasses, glass composite materials and ceramics,” *Adv. Appl. Ceram.*, vol. 105, no. 1, pp. 3–12, 2006.

[99] W. Miller, R. Alexander, N. Chaoman, P. McKinley, and J. Smellie, *Natural Analogue Studies in the Geological Disposal of Radioactive Wastes*. 1994.

[100] K. P. Hart, G. R. Lumpkin, R. Giere, C. T. Williams, P. J. McGlinn, and T. E. Payne, “Naturally-Occurring Zirconolites - Analogues for the Long-Term Encapsulation of Actinides in Synroc,”

Radiochim. Acta, vol. 74, pp. 309–312, 1996.

[101] P. A. Bingham, R. J. Hand, M. C. Stennett, N. C. Hyatt, and M. T. Harrison, “The Use of Surrogates in Waste Immobilization Studies: A Case Study of Plutonium,” in *Mater. Res. Soc. Symp. Proc.*, 2008, vol. 1107.

[102] B. L. Metcalfe *et al.*, “The Relative Merits of Oxides of Hafnium, Cerium and Thorium as Surrogates for Plutonium Oxide in Calcium Phosphate Ceramics,” in *Mater. Res. Soc. Symp. Proc.*, 2009, vol. 1193.

[103] Nikoloski, Gilligan, Squire, and Maddrell, “Chemical Stability of Zirconolite for Proliferation Resistance under Conditions Typically Required for the Leaching of Highly Refractory Uranium Minerals,” *Metals (Basel).*, vol. 9, no. 10, p. 1070, 2019.

[104] G. Wen, K. Zhang, D. Yin, and H. Zhang, “Solid-state reaction synthesis and aqueous durability of Ce-doped zirconolite-rich ceramics,” *J. Nucl. Mater.*, vol. 466, pp. 113–119, 2015.

[105] B. D. Begg and E. R. Vance, “The Incorporation of Cerium in Zirconolite,” in *Mat. Res. Soc. Symp. Proc.*, 1997, vol. 465, pp. 333–340.

[106] M. V. Zamoryanskaya and B. E. Burakov, “Feasibility Limits in Using Cerium as a Surrogate for Plutonium Incorporation in Zircon, Zirconia and Pyrochlore,” in *Mat. Res. Soc. Symp. Proc.*, 2001, vol. 663, pp. 1–6.

[107] B. M. Clark, S. K. Sundaram, and S. T. Misture, “Polymorphic Transitions in Cerium-Substituted Zirconolite ($CaZrTi_2O_7$),” *Sci. Rep.*, vol. 7, no. 1, pp. 2–10, 2017.

[108] J. Cachia *et al.*, “Enhancing cerium and plutonium solubility by reduction in borosilicate glass,” *J. Nucl. Mater.*, vol. 352, pp. 182–189, 2006.

[109] C. Lopez, X. Deschanels, J. M. Bart, J. M. Boubals, C. Den Auwer, and E. Simoni, “Solubility of actinide surrogates in nuclear glasses,” *J. Nucl. Mater.*, vol. 312, no. 1, pp. 76–80, 2003.

[110] J. C. Marra, A. D. Cozzi, R. A. Pierce, J. M. Pareizs, A. R. Jurgensen, and D. M. Missimer, “Cerium as a Surrogate for Plutonium in the Immobilized Form,” in *Environmental Issues and Waste Management Technologies in the Ceramic and Nuclear Industries VII*, 2002, pp. 381–388.

[111] E. R. Vance *et al.*, “Incorporation of Uranium in Zirconolite ($CaZrTi_2O_7$),” *J. Am. Ceram. Soc.*, vol. 85, no. 7, pp. 1853–1859, 2002.

[112] B. D. Begg, R. A. Day, and A. Brownscombe, “Structural Effect of Pu Substitutions on the Zr-site in Zirconolite,” in *Mat. Res. Soc. Symp. Proc.*, 2001, vol. 663, pp. 1–8.

[113] S. E. Kesson, W. J. Sinclair, and A. E. Ringwood, “Solid Solution Limits in Synroc Zirconolite,” *Nucl. Chem. Waste Manag.*, vol. 4, pp. 259–265, 1983.

[114] Y. Zhang, M. W. A. Stewart, H. Li, M. L. Carter, E. R. Vance, and S. Moricca, “Zirconolite-rich

titanate ceramics for immobilisation of actinides - Waste form/HIP can interactions and chemical durability," *J. Nucl. Mater.*, vol. 395, pp. 69–74, 2009.

[115] C. Lopez, X. Deschanels, C. Den Auwer, J. Cachia, S. Peuget, and J. Bart, "X-ray Absorption Studies of Borosilicate Glasses Containing Dissolved Actinides or Surrogates," *Phys. Scr.*, vol. T115, pp. 342–345, 2005.

[116] R. D. Shannon, "Revised Effective Ionic Radii and Systematic Studies of Interatomic Distances in Halides and Chalcogenides," *Acta Cryst.*, vol. A 32, pp. 751–767, 1976.

Chapter 3

Literature Review

Authorship Contribution Statement

3.1) ‘Actinide Immobilisation in Dedicated Ceramic Wasteforms: An Alternative Pathway for the Long Term Management of Existing Actinide Stockpiles’. L. Blackburn was responsible for conceptualisation, original draft preparation, reviewing and editing.

3.2) ‘Review of Zirconolite Crystal Chemistry and Aqueous Durability’. L. Blackburn was responsible for conceptualisation, original draft preparation, reviewing and editing.

3.3) ‘Solid Solution Limits of Plutonium and Neutron Poisons in Zirconolite Ceramics – A Literature Review and Gap Analysis for Immobilisation of UK Inventory’. L. Blackburn was responsible for conceptualisation, original draft preparation, reviewing and editing.

Actinide Immobilization in Dedicated Wasteforms: An Alternative Pathway for the Long-Term Management of Existing Actinide Stockpiles

Lewis R. Blackburn and Neil C. Hyatt, NucleUS Immobilisation Science Laboratory, Department of Materials Science and Engineering, University of Sheffield, Sheffield, United Kingdom

Abbreviations

ALSEP Actinide Lanthanide Separation
FP Fission Product(s)
GDF Geological Disposal Facility
HAL High Activity Liquor
HLW High Level Waste
IAEA International Atomic Energy Agency
ILW Intermediate Level Waste
LLW Low Level Waste
MA Minor Actinide(s)
MOX Mixed Oxide Fuel
NPT Nuclear Non-Proliferation Treaty
PWR Pressurized Water Reactor
RTG Radioisotope Thermoelectric Generator
SNF Spent Nuclear Fuel
TALSPEAK Trivalent Actinide Lanthanide Separation with Phosphorus-Reagent Extraction from Aqueous Komplexes
TBP Tributyl-phosphate
TRU Transuranic

Actinide production and inventories

Actinide elements, whilst a valuable resource for scientific study due to their rich chemistry, present a unique challenge with respect to radioactive waste management, due to their long half-lives, high radiogenic heat output, and chemical toxicity (see Table 1). With the exception of U and Th, which exist primordially in appreciable quantities, the actinide series is produced synthetically, as the result of either transmutation and decay processes occurring within commercial and experimental nuclear reactors. The production of Pu isotopes poses an aggrandized risk, insofar as these isotopes are separated in considerable quantities, with relatively small critical masses capable of sustaining a fission reaction, and are therefore subject to proliferation safeguards. Under conventional operating parameters, a civilian reactor operating in the burn-up range 35–45 MWd kgU^{-1} will produce around 1 at.% Pu, among other transuranic (TRU) elements at around 0.1 at.% (Ewing, 2015). It should be noted that the isotope distribution of Pu at discharge is a generally a function of reactor design, fuel type, initial ^{235}U enrichment, and burn up (Table 2). The remaining spent nuclear fuel (SNF) matrix is comprised of approximately 96 at.% U, with 3–4 at.% entrained fission products (FP). Notable high yield constituents that require consideration for immobilization include

Encyclopedia of Nuclear Energy, 2021, 650–662

Table 1 Properties of some actinide isotopes in the range ^{227}Ac–^{246}Cm.

Actinide	*Atomic number*	*Isotopes*	*Half-life*	*Specific activity (Ci g^{-1})*	*Primary decay mode*	*Decay product*
Ac	89	^{227}Ac	21.7 (year)	72	β^-	^{227}Th
		^{228}Ac	6.13 (h)	2.2×10^6	β^-	^{228}Th
Th	90	^{227}Th	18.7 (day)	3.2×10^4	α	^{223}Ra
		^{228}Th	1.9 (year)	820	α	^{224}Ra
		^{230}Th	7.5×10^4 (year)	190	α	^{226}Ra
		^{231}Th	25.5 (h)	5.2×10^3	β^-	^{231}Pa
		^{232}Th	1.4×10^{10} (year)	1.1×10^{-7}	α	^{228}Ra
		^{234}Th	24.1 (day)	2.4×10^4	β^-	^{234m}Pa
Pa	91	^{230}Pa	17.4 (day)	3.2×10^4	β^+	^{230}Th
		^{231}Pa	3.3×10^4 (year)	4.5×10^{-2}	α	^{227}Ac
		^{232}Pa	1.3 (day)	2.1×10^4	β^-	^{232}U
U	92	^{230}U	20.8 (day)	2.7×10^4	α	^{226}Th
		^{232}U	68.9 (day)	21	α	^{228}Th
		^{233}U	1.6×10^5 (year)	9.5×10^{-3}	α	^{229}Th
		^{234}U	2.5×10^5 (year)	6.2×10^{-6}	α	^{230}Th
		^{235}U	7.0×10^8 (year)	2.1×10^{-6}	α	^{231}Th
		^{236}U	2.3×10^7 (year)	6.5×10^{-5}	α	^{232}Th
		^{238}U	4.5×10^9 (year)	3.3×10^{-7}	α	^{234}Th
Np	93	^{237}Np	2.1×10^6 (year)	6.9×10^{-4}	α	^{233}Pa
		^{239}Np	2.4 (day)	2.3×10^5	β^-	^{239}Pu
Pu	94	^{238}Pu	87.7 (year)	17	α	^{234}U
		^{239}Pu	2.4×10^4 (year)	6.2×10^{-2}	α	^{235}U
		^{240}Pu	6.6×10^3 (year)	0.23	α	^{236}U
		^{241}Pu	14.3 (year)	110	β^-	^{241}Am
		^{242}Pu	3.8×10^5 (year)	3.9×10^{-3}	α	^{238}U
Am	95	^{241}Am	432.2 (year)	3.2	α	^{237}Np
		^{243}Am	7370 (year)	0.19	α	^{239}Np
Cm	96	^{242}Cm	182.2 (day)	3.3×10^3	α	^{238}Pu
		^{243}Cm	29.1 (year)	4.2	α	^{239}Pu
		^{244}Cm	18.1 (year)	82	α	^{240}Pu
		^{245}Cm	8.5×10^3 (year)	0.1	α	^{241}Pu
		^{246}Cm	4.8×10^3 (year)	0.4	α	^{242}Pu

Table 2 Plutonium isotope distribution on discharge.

Pu Source	*Mean fuel burn up (MWd/tHM)*	*Pu isotope on discharge*				
		^{238}Pu	*^{239}Pu*	*^{240}Pu*	*^{241}Pu*	*^{242}Pu*
Magnox	5000	0.1	70.0	24.9	3.9	1.1
AGR	30,000	1.1	53.5	27.9	12.3	5.2
PWR	45,000	2.2	54.3	22.4	14.9	6.2
WG[a]	N/A	~0	<92	>8	~0	~0

[a]MoD reporting in 2000.

^{129}I ($t_{1/2} = 15.7$ My) and ^{137}Cs ($t_{1/2} = 30.2$ y), and activation products originating from neutron activation of cladding materials e.g., ^{55}Fe ($t_{1/2} = 2.7$ y). Operating a reactor to a higher burn-up affords a greater yield of minor actinide (MA) species, which form a significant contribution to the overall radioactive output of the SNF matrix, often with considerable half-lives. Notable examples of MA species, for which immobilization options have been considered include ^{241}Am ($t_{1/2} = 433$ y), ^{239}Pu ($t_{1/2} = 21{,}400$ y), ^{237}Np ($t_{1/2} = 1.2$ My) and ^{237}Cm ($t_{1/2} = 1.56$ My). At fuel discharge there remains the option to implement an aqueous reprocessing procedure, whereby the SNF matrix is dissolved and actinides are targeted for solvent extraction, thus decreasing the radiogenic output associated with the fuel matrix, and allowing the separation and recovery of fissile material. Currently, only the PUREX (plutonium-uranium-reduction-extraction) process has been deployed at the industrial scale, examples of which are reprocessing plants integrated into the back-end of commercial fuel cycles in France (La Hague; capacity ~1600 tIHM/year) and the United Kingdom (Magnox; capacity ~1500 tIHM/year). During the reprocessing stage, the irradiated UO_2 pellets are sheared of cladding, prior to dissolution in a hot solution of 3–6 M HNO_3. Pu^{4+} and U^{6+} may then be extracted to an organic phase via complexation with 20–40 vol.% tri-butyl-phosphate (TBP) diluted in inert kerosene, and separated from the residual

Table 3 International inventories of Pu as reported to IAEA under INFCIRC/549 (reporting as of 2018).

Nation	*Unirradiated Pu (teHM)*	*Pu Contained in Spent Fuel (teHM)*
United States	49.3	716
Russia	61.3	167
United Kingdom	138.9	26
France	83.2	299.6
China	–	–
Japan	9.0	169
Germany	–	123.1
Belgium	$<$50 kg	44
Switzerland	$<$2 kg	20

high activity liquor (HAL) containing the remaining MA and FP contaminants. Pu is subsequently separated from U through a reductive backwash, and reclaimed via formation of insoluble $Pu^{4+}(C_2O_4)_3 \cdot 6H_2O$ and $Pu^{3+}{}_2(C_2O_4)_3 \cdot 10H_2O$ precipitates with the addition of oxalic acid, prior to calcination and storage as PuO_2. It should be noted that the PUREX process, and subsequent separation of U & Pu has formed the most significant contribution to existing actinide stockpiles internationally, as this is the only process demonstrated on any industrial scale. Indeed, the development of future nuclear fuel cycles may necessitate the implementation of advanced MA recovery separations, significantly reducing the radiothermal output associated with high level waste (HLW) packages prior to geological disposal. Concepts for integrated MA reprocessing cycles include TALSPEAK (trivalent actinide-lanthanide separations by phosphorous-reagent extraction from aqueous complexes) and ALSEP (actinide-lanthanide separations process). However, as such MA solvent extraction processes only occur on small scale, in particular the separation of ^{237}Np as a precursor for ^{238}Pu production for radioisotope thermoelectric generators (RTG), and are not stockpiled in considerable quantities, it is largely the isotopes of separated Pu that are considered when discussing the stockpiling of actinides. Nevertheless, the development of advanced materials capable of acting as immobilization hosts for MA constituents remains an active area of research. For a comprehensive discussion of advanced reprocessing techniques pertaining to separation and partitioning of actinides, the reader is referred to Nash and Nilsson (2015).

Internationally, over 340 metric tonnes of Pu were declared as holdings to the International Atomic Energy Agency (IAEA) in 2017, reported under INFCIRC/549 obligations of the Treaty on the Non-Proliferation of Nuclear Weapons (NPT) (**Table 3**). Some nations have implemented a management strategy whereby Pu is reintegrated into the fuel cycle, through the fabrication of mixed oxide (MOX) fuels for reuse in existing reactor fleets. However, it is disconcerting to note that there exist some significant inventories of unirradiated Pu held at surface facilities. For example, the United Kingdom is in a unique position insofar as it holds an inventory of unirradiated Pu forecast to reach approximately 140 teHM (tonnes heavy metal equivalent) currently held under civil safeguards. There is a growing consensus that the indefinite storage of such material is not a satisfactory approach to long term management, as this is in contravention of security and non-proliferation safeguards. Hence, it is necessary to implement a strategy favoring either reuse or prompt disposal. For example, the bulk of the United Kingdom. civil inventory could be utilized to support a campaign of energy production, through fueling a fleet of a three 1100 MWe Pressurized Water Reactors (PWR) for around 60 years. For a comprehensive review of Pu management policy in the context of the United Kingdom inventory, see (Hyatt, 2020). Nonetheless, the implementation of such a strategy is controlled by commercial appetite for MOX fuel, which has not been presented in the United Kingdom In some instances, the accumulation and long-term storage of Pu presents an additional challenge of materials degradation. For example, it is estimated that $\sim$5 t of United Kingdom Pu has succumbed to contamination through radiolytic degradation of the interim storage containment, hence regardless of the chosen pathway to disposition, it is advisable to develop long-term management strategy that can account for some portion, if not bulk inventories, to be designated as waste for disposal. There is a generic consensus that the end point of all ILW and HLW waste-streams, including actinide inventories, is geological disposal, subsequent to the design of a suitable wasteform.

Purpose and design requirements of nuclear wasteforms

As a precursor to the long-term disposition of nuclear waste inventories, it is necessary to convert, encapsulate or solidify the feedstock into a product with improved chemical and physical stability than the source material, offering improved characteristics with respect to handling, transport and disposal. To convert material in such a manner is termed *immobilization*, with the product referred to as the *wasteform*. Demonstrated practices of immobilization include vitrification, cementation, bitumenization and ceramification (Ojovan and Lee, 2005). The conditioning of waste in such a manner is a precursor towards ultimate disposition, the foreseen pathway for which is disposal in an engineered facility. The geological disposal facility (GDF) concept is considered to be the only technically mature option for the permanent disposition of intermediate and high level wastes, whereas surface disposal routes are deemed applicable to wastes with low levels of activity ($<$4 GBq/t α). The safety case for geological disposal is underpinned through the multi-barrier concept, a system whereby the encapsulation or immobilization matrix acts as the primary layer of containment,

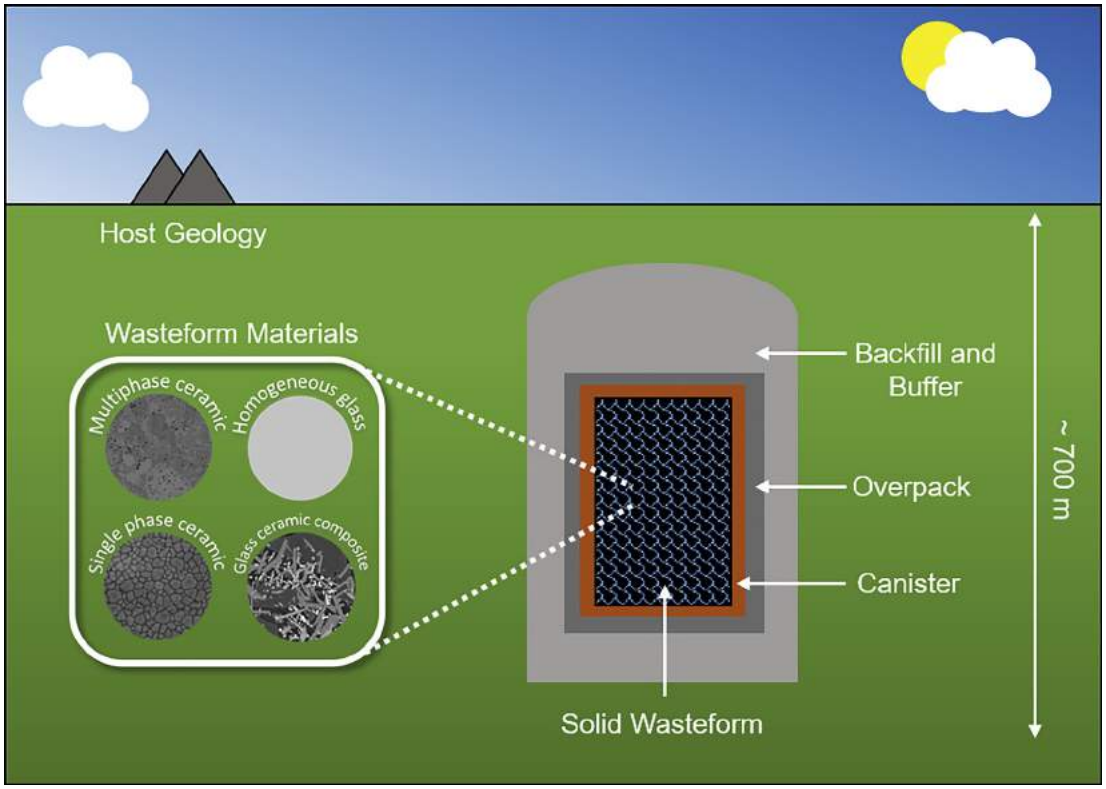

Fig. 1 Multibarrier concept for the immobilization and geological disposal of ILW, HLW and actinide-rich material.

which is subsequently over-packed and backfilled to retard water groundwater ingress, obviate corrosion and extend the lifetime of the package integrity, ultimately mitigating the release of radionuclide material into the near field environment, for such a time period that the overall activity of the waste is comparable to that of the natural uranium ore from which it was derived (Fig. 1). A sound disposal strategy stipulates that the choice of wasteform is tailored to suit the physical and chemical properties of the feedstock, as the immobilization matrix itself is considered to act as the primary containment, with the fundamental objective the reduce the potential for radionuclide dispersion into the near field environment. A set of generic wasteform design criteria is outlined below. For HLW wastes, typically concentrated raffinate derived from the reprocessing of SNF matrices, the thermal treatment of choice is calcination prior to vitrification in a borosilicate glass matrix (Table 4). Glass is a suitable candidate on the basis that a wide array of constituent elements comprising HLW are soluble in the glass matrix, either through substitution within the glass network (Si^{2+}, B^{3+}, P^{5+}) or as network modifiers (Cs^{+}, Na^{+}, Li^{+}, Mg^{2+}). The vitrification process is continuous, utilizes relatively low melting temperatures ($\sim$1050 °C) and is relatively insensitive to the nature of the wastestream, allowing the glass composition to be easily modified to accommodate small variations in feedstock. Upon cooling, the wasteform is a homogeneous product with a relatively high chemical durability ($NL_{Si} = 0.011 \pm 0.004$ g m^{-2} day^{-1} based on 1:3 Magnox-ThORP blend with 25% simulant waste loading at $T = 23$ °C and pH = 8; see (Cassingham et al., 2015). Despite the efficacy of borosilicate glass to accommodate HLW, the solubility of actinide-rich feedstocks in glass is relatively low. Using Ce as a surrogate for Pu, (Lopez et al., 2003) determined that Ce solubility in borosilicate glass was a function of temperature and Ce^{3+}/Ce_{total}, increasing from 0.25 wt.% at 1100 °C to 15 wt.% at 1400 °C, corresponding to an increase in the Ce^{3+}/Ce_{total} ratio from 0.5 to 0.9. This reduction protocol was utilized by (Cachia et al., 2006) to increase the solubility of PuO_2 from $\sim$2 wt.% to $\sim$4 wt.%. However, through the success of the SYNROC wasteform, alternative crystalline wasteform materials are favored for actinide immobilization, as it is considered these will offer superior wasteloading and durability.

Table 4 Compositions of selected nuclear waste glasses (wt.%).

Waste glass	*SiO_2*	*B_2O_3*	*Al_2O_3*	*CaO*	*MgO*	*Na_2O*	*Other*	*Waste loading*
R7T7 (France)	47.2	14.9	4.4	4.1	–	10.6	18.8	<28
Magnox (United Kingdom)	47.2	16.9	4.8	–	5.3	8.4	17.4	< 25
DWPF (United States)	49.8	8.0	4.0	1.0	–	8.7	27.1	<33
PAMELA (Germany)	52.7	13.2	2.7	4.6	2.2	5.9	18.7	<30

Ceramic wasteforms for actinide immobilization

Multiphase SYNROC

Despite the suitability of borosilicate glasses for the vitrification of chemically heterogeneous HLW waste streams, single and multiphase ceramic phase assemblages are generally considered to offer superior durability in the geological environment, alongside, in some instances, greater wasteloading of actinides. Ceramics offer a high performance solution for separated elements, as an alternative to vitrified wasteforms, and pertain to the substitution of the waste cations into a specific lattice sites within a crystalline structure, whilst retaining long-range order. Hence, tailoring ceramic materials for the effective immobilization of radionuclides requires additional considerations with respect to the relative size and accessible valence state compatibility between waste cations, and the targeted substitution site within the host structure. Such a design philosophy essentially allows the waste constituents to adopt the physical and chemical properties of the host material, hence ceramic immobilization is typically informed through the study of natural mineral analogs in the wider environment. Mineral specimens that remain present in the environment, having exhibited resistance to natural weathering processes over 10^6 years, are therefore excellent candidates from which to design synthetic ceramic materials for actinide immobilization. Ringwood et al. (1979) developed and proposed SYNROC (*synthetic-rock*) as alternative candidate ceramic wasteform for HLW and actinides. The SYNROC wasteform is a collection of thermodynamically stable titanate ceramic phases, chosen due to their extensive geochemical stability in the natural environment, and ability to accommodate the vast majority of elements comprising HLW waste streams. The dominant phases present in most variations of SYNROC are hollandite, zirconolite, perovskite and rutile. Hollandite, ideally $Ba_x(Al,Ti)_{2x}Ti_{8-2x}O_{16}$, is predominantly included as a host for processing contaminants and fission products. The hollandite structure is comprised of a framework of corner and edge sharing TiO_6 and AlO_6 polyhedra parallel to the c-axis of the tetragonal unit cell, allowing large mono or divalent A-site cations (Na^+, Ba^+, Cs^+, Sr^{2+}, Pb^{2+}) to reside in the tunnel centers, whilst the B and C sites can accommodate a variety of di- tri- and pentavalent species such as Mg^{2+}, Cr^{3+}, Cu^{2+}, Zn^{2+} and Sb^{5+} (Lutze and Ewing, 1988). Zirconolite, prototypically $CaZrTi_2O_7$, is the most durable of the SYNROC phases, and is the primary tri- and tetravalent actinide-bearing host. The anion deficient fluorite superstructure of zirconolite permits substitution of tetravalent actinides U^{4+}, Pu^{4+}, and Th^{4+} for Ca^{2+} in eightfold coordination, alongside moderate substitution for Zr^{4+} and a range of di- tri- and pentavalent substitution for Ti^{4+} (e.g., Mg^{2+}, Fe^{3+}, Al^{3+} and Nb^{5+}). The structure of perovskite (ideally $CaTiO_3$) permits a wide array of Ca^{2+} substitution, including Sr^{2+}, Ba^{2+}, REE^{3+}, Cm^{3+}, and Pu^{3+}, hence is included in SYNROC primarily to uptake Sr and minor actinides. The partitioning of key HLW elements in the constituent SYNROC phases is summarized in **Table 5**. Comprehensive discussions of SYNROC mineralogy, fabrication and disposability are provided by (Ringwood, 1985; Lutze and Ewing, 1988).

Wasteloading: Wasteform chemistry should be tailored such that solubility of waste material in the host phase is as extensive as reasonably possible, without promoting the formation of deleterious secondary phases, or breaching criticality limits. This will alleviate GDF volume requirements through the reduction in the number of overall waste packages produced.

Chemical flexibility: The ideal immobilization matrix should demonstrate the ability to accommodate variations in feedstock chemistry without the formation of detrimental accessory phases that may compromise performance in the disposal environment. This may include fluctuations in processing contaminants and additives. Multiphase ceramic, or glass-ceramic composite materials may be preferable to single phase ceramic materials in this respect.

Synthesis: Wasteform processing should favor rugged and established processing techniques, promoting compatibility with existing technology. Where possible, exotic syntheses routes and high temperature thermal treatments should be avoided, so as to prolong the lifetime of equipment, and suppress the potential for volatilization. These processes should also consider the environmental and economic impact of any secondary effluents that may be produced.

Aqueous durability: Leaching of the wasteform matrix in saturated groundwater compositions is considered to be the primary mechanism by which radionuclides begin to migrate into the near field environment. The wasteform should exhibit high chemical durability under such conditions, with the formulation optimized in laboratory trials to ensure the leach resistance is maximized. The aqueous durability of the chosen wasteform may be established through a variety of field tests, establishing a measure of the corrosion rate. However, the selection of wasteforms with existing natural analogs is preferable, as these specimens provide a true measure of corrosion resistance under geological timescales, and therefore act as a useful reference to support the safety case for geological disposal.

Radiation tolerance: The wasteform should exhibit resistance against amorphization due to the effects of self-irradiation. The formation and accumulation of decay products within the bulk wasteform may impact the overall mechanical integrity of the waste package, leading to volume swelling and cracking. This may, in turn, decrease the long-term durability by increasing the available surface area available for leaching.

Table 5 Distribution of key HLW elements in SYNROC phases.

Hollandite	*Zirconolite*	*Perovskite*	*Metal*
Cs^+	U^{4+}	Na^+	Ru
Rb^+	Th^{4+}	Sr^{2+}	Tc
K^+	Pu^{4+}	Pu^{3+}	Mo
Ba^{2+}	Cm^{4+}	Am^{3+}	Ni
Fe^{2+}	Am^{4+}	Cm^{3+}	Pd
Cr^{3+}	Np^{4+}	Np^{3+}	Rh
Ni^{2+}	Sr^{2+}	–	Te
Mo^{4+}	–	–	S

Table 6 Mineralogy of various SYNROC formulations.

	Ideal mineral composition (wt.%)						
Formulation	*Zirconolite*	*Hollandite*	*Rutile*	*Perovskite*	*Alloy phases*	*Spinel*	*Nepheline*
SYNROC-C	30	30	15	20	5	–	–
SYNROC-D	19	3	–	15	–	46	17
SYNROC-E	7[a]	5	79	7	–	–	–
SYNROC-F	90	5	5	–	–	–	–
SYNROC-Z	10	35	20	30	5	–	–

[a]Plus approximately 2% pyrochlore.

The conventional method of SYNROC fabrication involves the addition of ~2% Ti metal, due to the reducing conditions imposed during hot pressing. As the oxidation of the Ti reduces some portion of the Ti^{4+} inventory to Ti^{3+}, rutile, and related Magnelli phases TiO_{2-n} are included to provide an excess of Ti^{4+}, thus preventing the stabilization of Ti-poor phases such as $CsAlTiO_4$ that may be detrimental to wasteform performance in the disposal environment (Ringwood, 1985). The mineralogy of SYNROC may be varied, such that the relative proportions of the host ceramic phases are tailored to complement specific waste-streams (Table 6).

For example, whereas SYNROC-C was developed for as an alternative to borosilicate glass as an immobilization matrix for HLW waste streams, SYNROC-D is a unique variation developed specifically for the immobilization of defense wastes produced at the Savannah River Plant, favoring the replacement of hollandite with nepheline, and an inert spinel phase. Confidence in the SYNROC approach as a viable alternative to glass was largely supported by field durability studies. Development work by (Oversby and Ringwood, 1981) compared the release rates of key elements from 0.5 g disks of SYNROC and PNL-76-68 borosilicate glass (loaded with 33% simulant HLW), at both 85 °C and 200 °C. Based the concentrations of Ca, Cs and U in the distilled H_2O leaching solution, it was determined that whilst the PNL-76-68 wasteform had average leach rates of 1.4 and 8.9 g m^{-2} day^{-1} at 85 °C and 200 °C, respectively, the upper limit of the SYNROC leach rate was several orders of magnitude lower at <0.005 g m^{-2} day^{-1}. Subsequent work by (Ringwood et al., 1981) confirmed that whilst the retention of Cs in SYNROC was 500 times greater than PNL-76-68 at 95 °C, over a period between 10 and 30 days, the leach rate of U from SYNROC was 10^5 times lower than for corresponding borosilicate formulations (Fig. 2). The long term durability of SYNROC has also been established, with monoliths of SYNROC-C containing 10 wt.% simulated PW-4b-D HLW, containing 0.62 wt.% ^{239}Pu subjected to leaching in deionized water at 70 °C for a total of 2472 days. The normalized release rate of Pu from these samples was observed to be $\sim 5 \times 10^{-5}$ g m^{-2} day^{-1} (Smith et al., 1997). The radiation stability of SYNROC wasteforms is largely informed by in situ (i.e., doping with short lived actinides such as ^{238}Pu) and/or ex situ (i.e., charged ion-irradiation or gamma/neutron irradiation) response testing of the constituent actinide

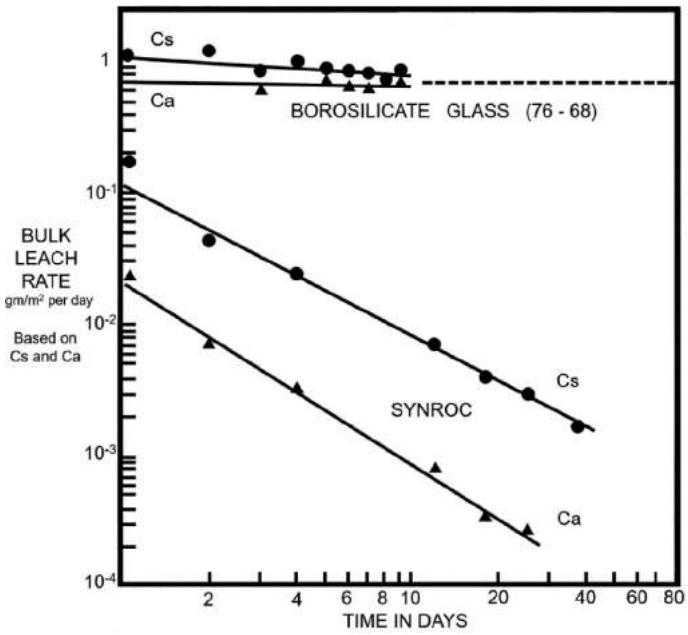

Fig. 2 Bulk leach rates of Cs and Ca from SYNROC and PNL-76-68 borosilicate glass. From Ringwood AE, et al. (1981) Immobilization of high-level nuclear reactor wastes in synroc: A current appraisal. *Nuclear Waste Management* 2: 287–305.

bearing phases, e.g., zirconolite and perovskite, which are discussed in the following sections. However, several pertinent examples of SYNROC radiation testing have been reported. For example specimens of SYNROC-C were subjected to neutron irradiation dose of 4.8×10^{20} n cm^{-2}, corresponding to a simulated aging of 2×10^5 year (Woolfrey et al., 1982). Specimens remained physically intact, yet with micro-cracking observed at volume expansions $\geq$4%. The microstructure of SYNROC-C doped with ^{238}Pu and ^{244}Cm, with ages in excess of 20 years and estimated experienced dose of 3×10^{19} α g^{-1}, were characterized by (Hambley et al., 2008). Micro-cracking was present across hollandite and rutile-rich regions of the microstructure yet did not extend across regions of zirconolite-perovskite intergrowths. As Pu was exclusively located, as expected, in the zirconolite and perovskite phases, the resultant swelling of these grains was proposed as the cause for the cracking. For a comprehensive review of radiation effects in SYNROC, and related titanate phases, the reader is referred to (Weber et al., 1998).

Single phase wasteforms

Whilst the original motivation for ceramic wasteform development was to develop alternative matrices to conventional borosilicate glasses, for the conditioning of heterogeneous reprocessing wastes, the past several decades have seen some nations strengthen reprocessing efforts, affording greater quantities of separated Pu and other actinides. Moreover, strategic arms reductions between the United States and the former Soviet Union has afforded some 100 metric tonnes of Pu designated as waste for disposal. Hence, the nature of wasteform development has evolved to favor the study of designated single-phase ceramic materials as immobilisation matrices for high purity actinide inventories. This rationale has seen many crystalline phases proposed for actinides (**Table 7**), justified by high durability and radiation stability, informed by natural analogs and laboratory field tests. For brevity, we shall provide a brief discussion of the crystallography and chemical properties of the titanate phases: pyrochlore, zirconolite, brannerite and perovskite.

Pyrochlore ($A_2B_2O_7$)

The pyrochlore family of minerals conforming to $^{VIII}A_2{}^{VI}B_2{}^{IV}X_6{}^{IV}Y_1$ stoichiometry have been proposed as wasteforms for the immobilization of actinides, including Pu, either through solid solution with the 16(d) B^{4+} site e.g., $Gd_2Ti_{2-x}Pu_xO_7$ or replacement of the 16(c) A site e.g., $CaPuTi_2O_7$. The cubic pyrochlore structure (ideally $A_2B_2O_7$—space group Fd-3 m) is described as a defect fluorite superstructure, related to the ideal AX_2 fluorite unit cell with one eight of the oxygen atoms replaced by ordered vacancies on the anion sublattice. Over 500 distinct compositional variations of this phase have been reported through control of A and B-site cations, hence single phase pyrochlore materials certainly offer the requisite structural flexibility to act as nuclear wasteforms for actinides. Typically, the A-site is able to incorporate formal valence states between +1 and +6, and the B-site between +3 and +6, although the mineralogy of pyrochlore typically favors the occupation of the eightfold coordinated A site with large tri- and tetravalent actinide and rare earth cations (e.g., Th^{4+}, U^{4+}, Gd^{3+}, Y^{3+}, Sm^{3+}) and smaller cation modifiers on the B-site (Zr^{4+}, Ti^{4+}, Ta^{5+}, Sb^{5+}). The long term durability of pyrochlore is supported by the existence of naturally altered specimens, many of which exist with primordial U/Th inventories, up to 30 wt.% and 9 wt.%, respectively, although the durability of these analogs is thought to be slightly lower than that of zirconolite (Lumpkin, 2001). Wang et al. (2019) tested the durability of $(Gd,Sm)_2(Zr,Ce)_2O_7$ pyrochlore materials through static leaching in distilled water for 7 day at 90 °C, with the leaching rates of all elements between 10^{-6} and 10^{-7} g m^{-2} day^{-1}. Icenhower et al. (2000) investigated the corrosion resistance of $Lu_2Ti_2O_7$ and $Gd_2Ti_2O_7$ through dissolution under dynamic SPFT conditions at pH = 2, confirming that even at under highly acidic conditions, dissolution rates remained low, in the range 1.3×10^{-3}–7.0×10^{-4} g m^{-2} day^{-1}. The stability and radiation response of pyrochlore-structured phases is dictated by the relative size ratio of A and B-site cations, with the cubic-forming region determined experimentally to be $1.46 < r_A/r_B < 1.78$. Compositions for which $r_A/r_B < 1.46$ form destabilize to form the defect fluorite structure, in which A and B-site cations become randomly distributed, and oxygen vacancies become disordered along the anion sublattice (Lang et al., 2010). (Reid et al., 2012) synthesized the $Gd_2Zr_{2-x}Ce_xO_7$ with the view to simulate Pu^{4+} immobilization, identifying three distinct phases corresponding to pyrochlore ($x < 0.25$), defect fluorite ($0.5 < x < 0.75$) and an incommensurate C*-type structure for $x = 1.00$. The response to radiation is significantly improved for Zr based pyrochlores, as is shown in **Fig. 3** for the $Gd_2Ti_{2-x}Zr_xO_7$ binary system.

Table 7 Candidate ceramic wasteforms for actinide immobilization.

Ceramic phase	*Ideal formula*	*Space group*	*Unit cell parameters (Å, °)*	*Calculated density (g cm^{-3})*
Zirconolite	$CaZrTi_2O_7$	C2/c	$a = 12.44$; $b = 7.27$; $c = 11.38$; $\alpha = \gamma = 90$; $\beta = 100.56$	4.44
Pyrochlore (Zr)	$Gd_2Zr_2O_7$	$Fm\bar{3}m$	$a = b = c = 5.27$; $\alpha = \beta = \gamma = 90$	6.91
Pyrochlore (Ti)	$Gd_2Ti_2O_7$	$Fd\bar{3}m$	$a = b = c = 10.18$; $\alpha = \beta = \gamma = 90$	6.57
Zirconia	ZrO_2	$P2_1/c$	$a = 4.15$; $b = 5.21$, $c = 5.32$, $\alpha = \gamma = 90$; $\beta = 99.21$	5.82
Zircon	$ZrSiO_4$	$I4_1/amd$	$a = b = 6.60$; $c = 5.98$; $\alpha = \beta = \gamma = 90$	4.66
Monazite	$CePO_4$	$P2_1/c$	$A = 6.77$; $b = 7.00$; $c = 6.44$; $\alpha = \gamma = 90$; $\beta = 103.42$	5.26
Xenotime	YPO_4	$I4_1/amd$	$a = b = 6.89$; $c = 6.03$; $\alpha = \beta = \gamma = 90$	4.26
Brannerite	UTi_2O_6	C2/m	$a = 9.81$; $b = 3.77$; $c = 6.93$; $\alpha = \gamma = 90$; $\beta = 118.96$	6.36
Kosnarite	$KZr_2(PO_4)_3$	$R\bar{3}c$	$a = b = 8.73$; $c = 23.20$; $\alpha = \beta = 90$; $\gamma = 120$	4.38
Perovskite	$CaTiO_3$	Pbnm	$a = 5.38$; $b = 5.44$; $c = 7.64$; $\alpha = \beta = \gamma = 90$	4.04

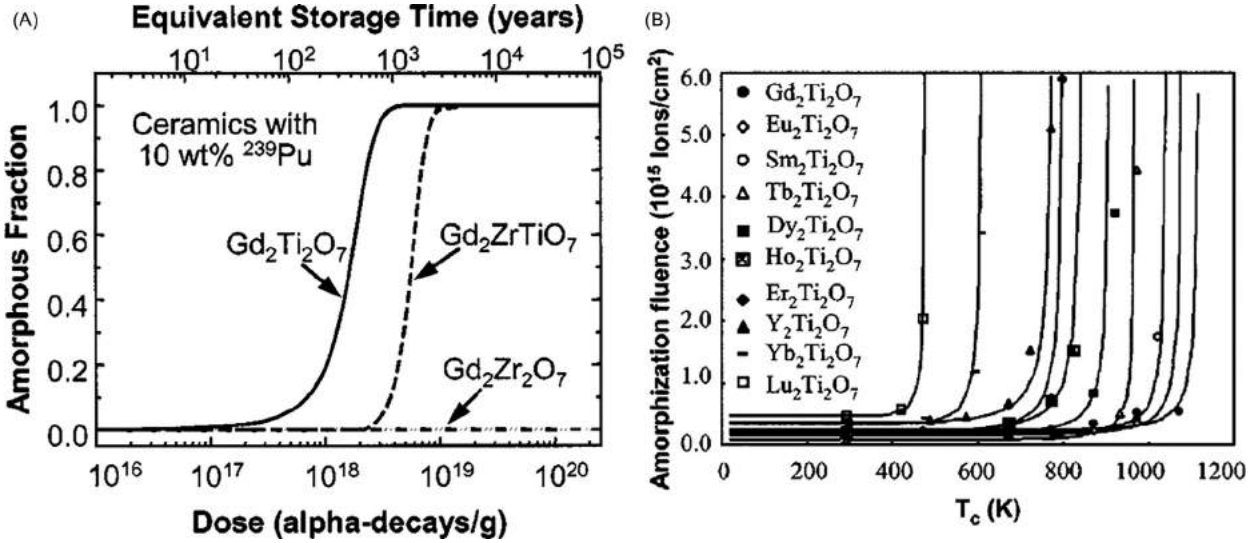

Fig. 3 Dependence of amorphisation dose rate on x parameter in $Gd_2Ti_{2-x}Zr_xO_7$ pyrochlore (A) and choice of REE^{3+} cation (B). Reproduced from Ewing RC, Weber WJ and Lian J (2004) "Nuclear waste disposal-pyrochlore ($A_2B_2O_7$): Nuclear waste form for the immobilization of plutonium and 'minor' actinides". *Journal of Applied Physics* 95(11): 5949–5971, with the permission of AIP Publishing.

Zirconolite ($CaZrTi_2O_7$)

Zirconolite, nominally $CaZrTi_2O_7$, is a relatively rare accessory mineral located in a variety of geological formations, and is included as the primary actinide bearing phase in the SYNROC wasteform. However, in recent years there has been a renewed interest in the development of single phase zirconolite ceramic materials for the immobilization of stockpiled Pu inventories, and zirconolite glass-ceramic composites for the conditioning of Pu residues, in the United Kingdom. Zirconolite has a demonstrated affinity for extensive substitution of several actinides ($Pu^{3+/4+}$, Np^{3+}, $U^{4+/6+}$, Th^{4+}), rare earth (Y^{3+}, Sm^{3+}, Nd^{3+}, Gd^{3+}) and alkaline/transition (Mg^{2+}, Al^{3+}, Fe^{3+}, Cr^{3+}) elements. Zirconolite, related to $A_2B_2O_7$ pyrochlore by a compression along the (111) plane, is an anion deficient fluorite-type structure, with cation ordering on planes parallel to the superstructure c-axis. A projection of the zirconolite unit cell is displayed in Fig. 4. The zirconolite-2M parent structure, stabilized over the compositional range $CaZr_xTi_{3-x}O_7$ ($0.8 < x < 1.3$), crystallizes with monoclinic symmetry in the space group (C2/c, $Z = 8$). The unit cell forms a lamellar structure comprised of alternating layers of Ca^{2+}/Zr^{4+} polyhedra, coordinated eight- and sevenfold to oxygen, respectively, interspaced 1:1 along the (001) plane with sheets of Ti^{4+} octahedra arranged in a hexagonal tungsten bronze (HTB) type topology.

Ti^{4+} is present in three distinct crystallographic sites, two of which, Ti(I) and Ti(III), are contained in sixfold coordination, whilst Ti(II) forms an unusual trigonal bipyramidal TiO_5 site, located off-center from the six membered ring, statistically 50% occupied. The chemistry of zirconolite permits solid solution of actinides and charge compensator species across the five distinct cation receptor sites ^{VIII}Ca, ^{VII}Zr, $^{VI}Ti(I)$, $^{V}Ti(II)$ and $^{VI}Ti(III)$, and hence allows for accommodation of multiple cations in conjunction. Several substitution regimes have been proposed and demonstrated for both tri- and tetravalent actinide species. For example, (Begg et al., 2001)

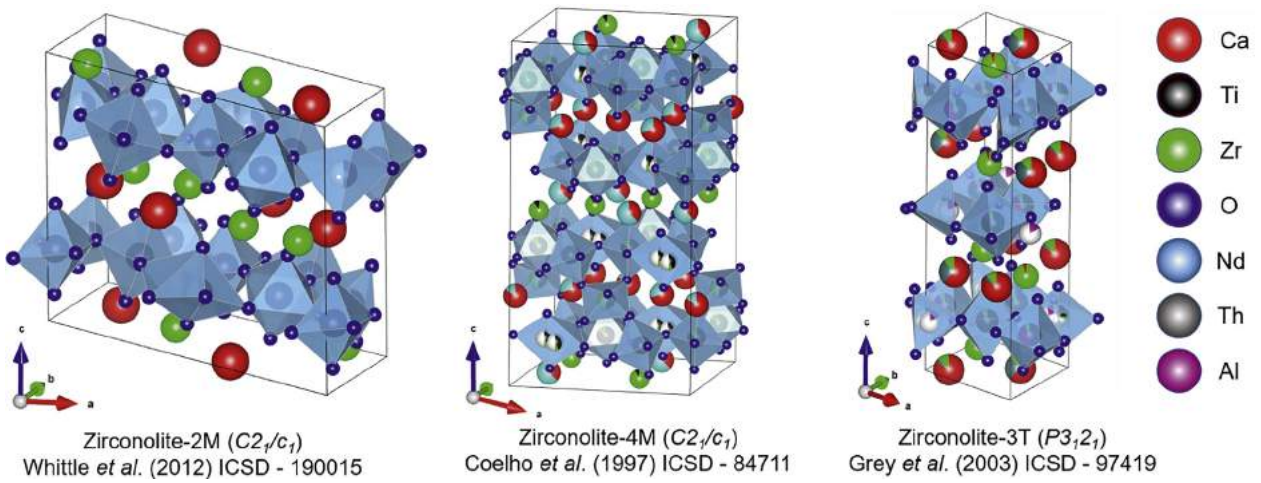

Fig. 4 Crystal structures of zirconolite-2M, 4M and 3T polytypes.

demonstrated that Pu^{4+} may be accepted in solid solution via isovalent substitution for Zr^{4+}, i.e., $CaZr_{1-x}Pu_xTi_2O_7$. Alternatively, it has been demonstrated that heterovalent tri- and tetravalent substitution for Ca^{2+} is also feasible, with a lower valence charge balancing species such as Al^{3+} accommodated across Ti^{4+} sites, e.g., $Ca_{1-x}Pu_xZrTi_{2-2x}Al_{2x}O_7$ and $Ca_{1-x}Pu_xZrTi_{2-x}Al_xO_7$ for Pu^{4+} and Pu^{3+}, respectively (Vance et al., 1994). The progressive substitution of foreign elements, depending on the chosen substitution regime and processing conditions, has been shown to stabilize a variety of crystallographically distinct polytype variants of zirconolite, most notably zirconolite-4M and zirconolite-3T (formerly recognized as zirkelite (Bayliss et al., 1989)). Successive zirconolite polytypes are characterized by variations in stacking sequence of Ca/Zr and HTB layers. For example, the structure of zirconolite-4M resembles intergrowths of zirconolite-2M and pyrochlore-type modules, resulting in lattice expansion along the c-axis and stacking of four Ca/Zr—HTB interlayers to comprise the unit cell. Isovalent substitution of U^{4+}, Ce^{4+} and Pu^{4+} for Zr^{4+} targeting $CaZr_{1-x}(Ce,U,Pu)_xTi_2O_7$ has been shown to favor zirconolite-4M as the dominant actinide phase above a threshold of $x = 0.15$, with further substitution to $x = 0.50$ yielding the pyrochlore phase (Begg et al., 2001; Vance et al., 2002; Blackburn et al., 2020a). Interestingly, it was recently reported that the $CaZr_{1-x}Th_xTi_2O_7$ did not give rise to the zirconolite-4M intermediate phase, rather a Th-rich pyrochlore phase was preferred in the interval $0.10 \leq x \leq 0.50$, forming a single phase at $x = 0.60$ (Blackburn et al., 2021). Targeting tetravalent substitution for Ca^{2+}, coupled with a charge balancing species has been shown to extend the formation range of zirconolite-2M. For example, (Vance et al., 2002) confirmed the formation of single phase 2M when targeting $Ca_{0.80}U_{0.20}ZrTi_{1.60}Al_{0.40}O_7$, with complementary data by (Deschanels et al., 2006) targeting, $Ca_{0.87}Pu_{0.13}ZrTi_{1.73}Al_{0.30}O_7$ confirming the 2M structure. Using Ce as a surrogate, (Blackburn et al., 2020b) confirmed the 2M polytype could be stabilized up to $x = 0.35$ in the $Ca_{1-x}Ce_xZrTi_{2-2x}Cr_{2x}O_7$, however, partial Ce^{3+} speciation promoted the formation of a Ce-rich perovskite phase. Furthermore, (Gilbert et al., 2010) reported the formation of the 3T polytype for the corresponding $Ca_{1-x}Pu_xZrTi_{2-2x}Fe_{2x}O_7$ solid solution. Incorporation of trivalent actinide species may be accomplished through equimolar substitution of a trivalent charge balancing species such as Al^{3+}, extending the solid solution range over which the zirconolite-2M polytype is stabilized. For example, the $Ca_{1-x}Nd_xZrTi_{2-x}Al_xO_7$ solid solution was fabricated by Ma et al., confirming that zirconolite-2M remained single phase for $x \leq 0.6$, after which the orthorhombic zirconolite-3O polytype was produced (Ma et al., 2018). The radiation stability of zirconolite is comparable to that of $Gd_2Ti_2O_7$ through doping with 3 wt.% ^{244}Cm (Weber, Wald and Matzke, 1986), with an amorphisation dose corresponding to $0.47 \times 10^{16}\ \alpha\ mg^{-1}$ causing bulk swelling between 6–6.5 vol.%. Similar results have been reported by ion irradiation with 1.3×10^{21} keV cm^{-1} Au^+ (Deschanels et al., 2014). A comprehensive report on the radiation response of zirconolite was provided by (Strachan et al., 2008), concluding that a dose rate of 2.6×10^{18} α/g was necessary to amorphize ^{238}Pu doped zirconolite. Furthermore, the forward dissolution rate at pH = 2 was experimentally determined as 1.7×10^{-3} g m^{-2} day^{-1}, showing no dependence on the amount of induced radiation damage. Other studies have concluded that the leaching of elements is not affected by amorphisation, whereas the release rates from fully amorphous pyrochlore specimens, have in some instances, been shown to increase by a factor of 10–15 (Smith et al., 2003). Durability studies have demonstrated that release rates of actinide surrogates from zirconolite specimens are typically of the order 10^{-6} g m^{-2} day^{-1}. Zhang et al. (2017) determined that the release of Ce from monoliths of zirconolite, with nominal composition $CaZr_{0.70}Ce_{0.30}Ti_2O_7$, was as low as 2.3×10^{-6} g m^{-2} day^{-1} over a 42 day period in deionized H_2O. Similar results were reported by (Wen et al., 2015) with Ce leach rates of 2.3×10^{-6} g m^{-2} day^{-1} over a 28 day period. Exceptionally low Gd^{3+} release rates of 4.72×10^{-7} g m^{-2} day^{-1} were recently reported by Zhang et al. (2019) from $Ca_{1-x}Hf_{1-x}Gd_{2x}Ti_2O_7$ zirconolite, with Gd included as a trivalent actinide surrogate. A summary of pH dependent U leaching from zirconolite, relative to other candidate wasteforms, was provided by Weber et al. (2009) and is summarized in Fig. 5.

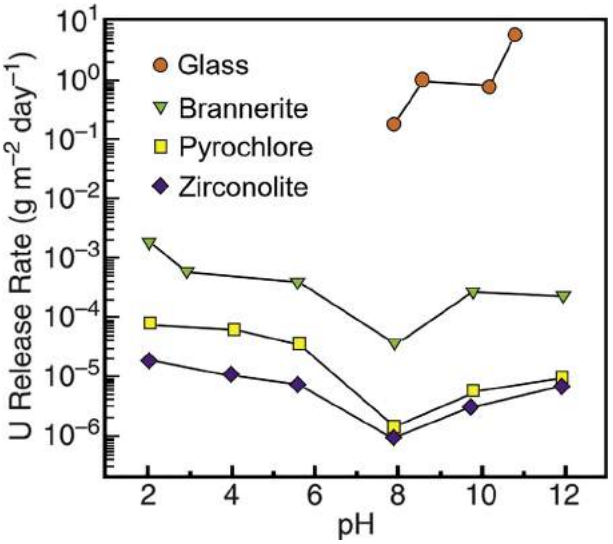

Fig. 5 Summary of U release rates (g m^{-2} day^{-1}) from a selection of candidate wasteforms. From Weber WJ, Navrotsky A, Stefanovsky S, Vance ER, and Vernaz E (2009) Materials science of high-level nuclear waste immobilization. *MRS Bulletin* 34 (01): 46–52.

Brannerite (UTi_2O_6)

Brannerite is a common accessory U-bearing accessory mineral, with a prototypical composition of UTi_2O_6, and in some areas is the principle uranium ore. As natural brannerites contain ~55 wt.% U, ceramics based on the UTi_2O_6 system may be suitable hosts matrices for wastes containing a high fraction of actinides, such as MOX residues (Bailey et al., 2018). UTi_2O_6 is a layered structure comprised of anatase-type sheets of edge-sharing distorted TiO_6, with chains of edge-sharing UO_6 octahedra connecting adjacent Ti-O layers. The ideal UTi_2O_6 structure crystallizes in monoclinic symmetry (space group C2/m) and is only formed under low partial oxygen pressure, in order to maintain U^{4+} valence. The preparation of UTi_2O_6 in air, to the correct stoichiometry, has been shown to produce a mixture of U_3O_8 and TiO_2. The U^{4+} site can be completely replaced by isovalent Ce/Th substitution, e.g., the isostructural thorutite structure $ThTi_2O_6$, however, the counterpart Ce brannerite was shown to be non-stoichiometric, *viz* $Ce_{0.975}Ti_2O_{5.95}$, with cerium and oxygen vacancies, as determined by powder neutron diffraction (Stennett et al., 2012). The incorporation of higher valence actinide species in brannerite is permitted through the co-substitution of lower valence charge balance species. For example, $U_{1-x}Y_xTi_2O_6$ and $Th_{1-x}Y_xTi_2O_{6-\delta}$ solid solutions were synthesized in air at 1400 °C by (James et al., 2003) and it was determined that the accommodation of Y^{3+} was greater in UTi_2O_6, due to the formation of charge balancing U^{5+} centers. Y^{3+} accommodation in $ThTi_2O_6$ is considerably lower, permitted by the formation of oxygen vacancies due to the stability of Th^{4+} in air. The chemical durability of brannerite is consistently lower than that of related zirconolite and pyrochlore phases, yet 3–4 orders of magnitude more durable than some glass matrices. Amorphous specimens of natural brannerite from the El Cabril mine (Spain) have been recrystallized by annealing at a range of temperatures by (Zhang et al., 2006) prior to durability testing. U release rates in weakly acid conditions (pH = 4) at 30 °C were observed to be $\sim 1 \times 10^{-3}$ g m^{-2} day^{-1} when annealed at 500 °C. Synthetic UTi_2O_6 was produced and dissolved over the pH range 2–12 by (Roberts et al., 2000) at 25 °C, 50 °C and 75 °C. The dissolution rate increased with temperature, yet the magnitude of the increase was observed to vary with pH, reaching a minimum near pH = 8. Whilst the dissolution rates for brannerite were in some instances a factor of 30 greater than zirconolite under the same conditions, the release rates for U were moderately low, between 10^{-3} and 10^{-5} g m^{-2} day^{-1}. Nevertheless, brannerite may act as a buffer phase to accommodate excess actinides that may exceed the solubility limit in targeted phases, and its inclusion not expected to significantly impact the overall performance of wasteform materials for actinides in the geological environment.

Perovskite ($CaTiO_3$)

Perovskite (ABO_3) structured materials are extensively studied, and have a wide field of applications, particularly in the development of photonic functional materials, and as a primary constituent of the SYNROC wasteform. Oxide perovskites have the general structure ABO_3, in which BO_6 octahedra form a three-dimensional corner sharing framework, with large A-site cations (i.e., Ca^{2+}, Sr^{2+}) residing in the cavity, 12-fold coordinated with oxygen. Although ABO_3 perovskites ideally have cubic symmetry in the Pm-3m space group, most perovskites are distorted due to tilting of BO_6 octahedra, caused by variation in cation radii r_A and r_B, and may undergo reversible, phase dependent transitions. For example, the $CaTiO_3$ unit cell distorts with orthorhombic symmetry in the space group Pbnm at room temperature, to tetragonal I4/mcm at 1225 °C, with a further transition to cubic Pm-3m observed at 1361 °C. The binary system $Ca_{1-x}Sr_xTiO_3$ exhibits complete solid solubility, with a structural transformation from Pbnm to the I4/mcm structure at $x = 0.6$, followed by transformation to Pm-3m with additional Sr^{2+} content (Qin et al., 2002). $CaTiO_3$ has been proposed as a host phase for Pu^{3+} and Pu^{4+} due to high radiation tolerance. $(Ca_{0.9}Nd_{0.1})(Ti_{0.9}Al_{0.1})O_3$ was synthesized by (Davoisne et al., 2011) with Nd^{3+} employed as a structural simulant for Pu^{3+}, and irradiated with a dose of 2 MeV Kr^+ at 5×10^{15} ions cm^{-2} with the view to simulate Pu recoil damage during α-decay. A well-defined damage region of 0.8–1.1 μm was observed, however only some of this was amorphous; the number of displacements per atom (dpa) was estimated at around 4 dpa (**Fig. 6**).

The incorporation of Ce^{3+} and Ce^{4+} within the $CaTiO_3$ was investigated by (Begg et al., 1998b) with Ce acting as a structural simulant for Pu. Ce^{3+} was successfully incorporated within the Ca^{2+} site with Al^{3+} charge compensation targeting $Ca_{0.9}Ce_{0.1}Ti_{0.9}Al_{0.1}O_3$ under both oxidizing and reducing conditions, with the partial formation of Ce^{4+} formed in air charge balanced by Ti^{4+} vacancies. Ce^{4+} was fully accommodated into single phase when targeting $Ca_{0.9}Ce_{0.1}Ti_{0.8}Al_{0.2}O_3$ under oxidizing conditions, however Ce was distributed as 80% Ce^{4+}, with the excess negative charge apparently compensated by oxygen vacancies. Moreover, Ce^{3+} was fully accommodated into single phase $Ca_{0.9}Ce_{0.1}TiO_3$ with lower valence species available for charge compensation, demonstrating the formation of cation vacancies. These solid solutions were later verified by (Begg et al., 1998a), using $Pu^{3+/4+}$; in all instances minor undigested PuO_2 (<2%) was evidenced. Investigations of Pu incorporation within $Ca_{0.9}Pu_{0.1}Ti_{0.9}Al_{0.1}O_3$ (targeting Pu^{3+}), $Ca_{0.9}Pu_{0.1}Ti_{0.8}Al_{0.2}O_3$ (targeting Pu^{4+}) and $Ca_{0.9}Pu_{0.1}TiO_3$ (targeting Pu^{3+}) yielded near single phase perovskite when sintering in air, with Pu uniformly present as Pu^{4+}; annealing in 3.5% H_2/N_2 resulted in 80–90% Pu^{3+} and the subsequent formation of a minor $CaPu(Ti,Al)_2O_7$ pyrochlore, at ~2 wt.% in each instance. The preferential incorporation of Ce within the $CaTiO_3$ phase is likely the result of increased reduction potential with respect to Pu, although the extent of Pu solubility on the Ca site has not been explicitly determined. $CaTiO_3$ has also demonstrated the ability to successfully accommodate both Np in both Np^{3+} and Np^{4+} valence states through tailoring the oxygen fugacity during synthesis (Begg et al., 1998a). Similar to related Pu compositions, targeting Np^{3+} incorporation in the absence of charge balancing additives did not prevent the formation of near single phase $Ca_{0.90}Np_{0.10}TiO_3$ when reacting in both air and 5% H_2/N_2. Np^{4+} remained the dominant valence state when targeting $Ca_{0.90}Np_{0.10}Ti_{0.80}Al_{0.20}O_3$ regardless of the sintering atmosphere, yielding >99% perovskite, demonstrating the ability of the phase to successfully immobilize both tri- and tetravalent actinides. The fundamental disadvantage hindering the deployment of single phase perovskite as an actinide wasteform pertains to its aqueous durability. Despite greater radiation tolerance relative to the actinide-designated zirconolite

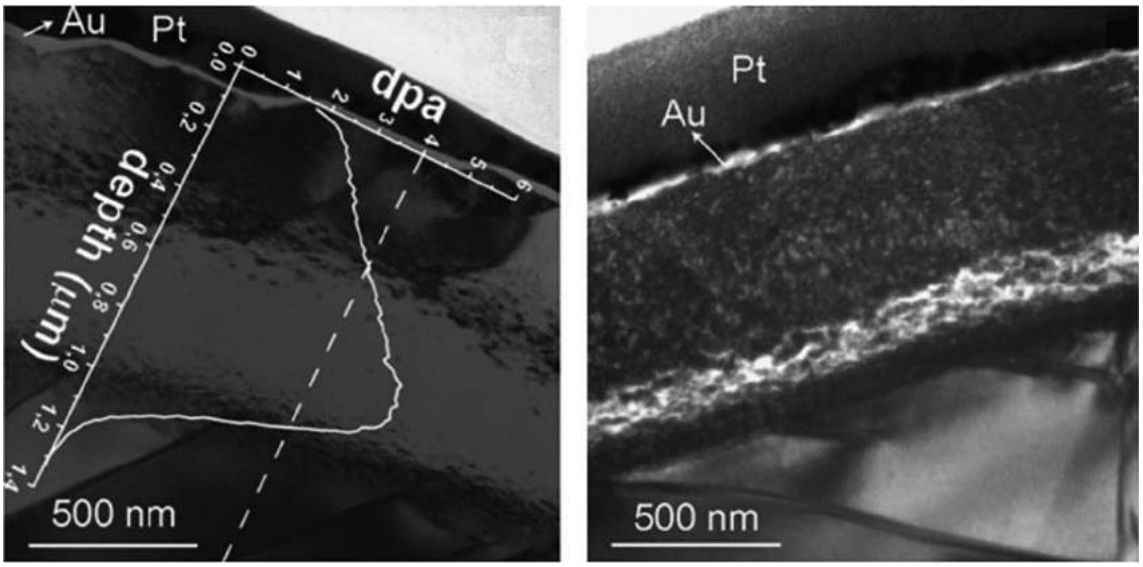

Fig. 6 TEM micrograph of damage region of Nd-doped perovskite irradiated with 2 MeV Kr^{+} at a dose of 5×10^{15} ions cm^{-2}, detailing a well-defined damage region between 0.8–1.1 μm, in agreement with TRIM calculations. From Davoisne C, Stennett MC, Hyatt NC, Peng N, Jeynes C, and Lee WE (2011) Krypton irradiation damage in Nd-doped zirconolite and perovskite. *Journal of Nuclear Materials* 415 (1): 67–73.

phase, perovskite is considered the most soluble of the SYNROC phases under hydrothermal conditions. Durability tests on disks of well characterized SYNROC-C in de-ionized water, bicarbonate and silicate solutions saturated at 150 °C up to 84 days confirmed that the dissolution rates of the SYNROC phases followed the order perovskite > hollandite > zirconolite, with the percentage of initial Al, Ca and Ce distributed across the SYNROC phases released after 337 days in 150 °C deionized water determined to be 0.10%, 0.068% and 0.045%, respectively (Lumpkin et al., 1991; Smith et al., 1992). Given the lower relative durability of perovskite with respect to zirconolite, and the common presence of $CaTiO_3$ as an ancillary phase during zirconolite synthesis, it is often desirable to reformulate precursor compositions with an excess of ZrO_2 and TiO_2 to preclude the ingrowth of perovskite.

Summary

Actinides, once chemically partitioned and separated from nuclear reactor wastes, pose an acute security and proliferation risk when stored *en masse* as unirradiated inventories. A credible pathway towards actinide disposition is immobilization in dedicated ceramic matrices, the design of which is largely informed by the study of naturally occurring mineral analogs that are robust against geological weathering. The SYNROC approach to wasteform development, comprised of durable titanate crystalline phases each targeting specific radionuclides present in HLW waste streams, demonstrated that ceramic immobilization is a feasible pathway to disposition, whilst offering superior aqueous durability compared to conventional borosilicate glass wasteforms under a range of standardized corrosion tests. A wide variety of titanate, zirconate and silicate-based mineral species have since been proposed as single phase wasteforms for separated actinides, including zirconolite, pyrochlore, perovskite and brannerite. The chemistry of these materials permits solid solution with actinides, allowing waste cations to adopt the properties of the host lattice, thus stabilizing and solidifying the waste prior to geological disposal, alleviating difficulties associated with storage, transport and nuclear non-proliferation. Wasteform selection trials, commonly utilizing actinide surrogates with similar chemistry, are fundamental in underpinning this approach, with rare-earth ($Ce^{3+/4+}$, Gd^{3+}, Sm^{3+}, Eu^{3+}) and in some cases U^{4+} and Th^{4+} commonly deployed as simulants. It should be noted, however, that with the exception of recent advances in the SYNROC program, the deployment of ceramic wasteform technology has not been demonstrated at the industrial scale. For example, whilst it is envisaged that ceramic matrices will be utilized to immobilize of some portions of the United Kingdom Pu stockpile, there is still considerable development of industrial-scale processes necessary before such a program can be implemented.

Acknowledgments

LRB and NCH are grateful for financial support from the Nuclear Decommissioning Authority and EPSRC (No. EP/L014041/1, EP/S01019X/1, EP/R511754/1 and EP/T011424/1).

References

Bailey, D.J., et al., 2018. Synthesis and characterisation of brannerite compositions $(U_{0.9}Ce_{0.1})_{1-x}M_xTi_2O_6$ ($M = Gd^{3+}$, Ca^{2+}) for the immobilisation of MOX residues. RSC Advances 8 (4), 2092–2099. https://doi.org/10.1039/C7RA11742F. Royal Society of Chemistry.

Bayliss, P., et al., 1989. Mineral nomenclature: zirconolite. Mineralogical Magazine 53 (December), 565–569.

Begg, B., Vance, E., Conradson, S., 1998a. The incorporation of plutonium and neptunium in zirconolite and perovskite. Journal of Alloys and Compounds 271–273, 221–226. https://doi.org/10.1016/S0925-8388(98)00058-9.

Begg, B.D., Vance, E.R., Lumpkin, G.R., 1998b. Charge compensation and the incorporation of cerium in zirconolite and perovskite. Materials Research Society Symposium Proceedings 79–86. https://doi.org/10.1557/PROC-506-79.

Begg, B.D., Day, R.A., Brownscombe, A., 2001. Structural effect of Pu substitutions on the Zr-site in zirconolite. Materials Research Society Symposium Proceedings 663, 259–266.

Blackburn, L.R., Sun, S., et al., 2020a. A systematic investigation of the phase assemblage and microstructure of the zirconolite $CaZr_{1-x}Ce_xTi_2O_7$ system. Journal of Nuclear Materials 535, 152137. https://doi.org/10.1016/j.jnucmat.2020.152137.

Blackburn, L.R., et al., 2020b. Synthesis and characterisation of $Ca_{1-x}Ce_xZrTi_{2-2x}Cr_{2x}O_7$: Analogue zirconolite wasteform for the immobilisation of stockpiled UK plutonium. Journal of the European Ceramic Society 40 (15), 5909–5919. https://doi.org/10.1016/j.jeurceramsoc.2020.05.066. Elsevier Ltd.

Blackburn, L.R., Sun, S.-K., et al., 2021. Synthesis, structure and characterisation of the thorium zirconolite $CaZr_{1-x}Th_xTi_2O_7$ system. Journal of the American Ceramic Society 1–15. https://doi.org/10.1111/jace.17627.

Cachia, J., et al., 2006. Enhancing cerium and plutonium solubility by reduction in borosilicate glass. Journal of Nuclear Materials 352, 182–189. https://doi.org/10.1016/j.jnucmat.2006.02.052.

Cassingham, N., et al., 2015. The initial dissolution rates of simulated UK Magnox–ThORP blend nuclear waste glass as a function of pH, temperature and waste loading. Mineralogical Magazine 79 (6), 1529–1542. https://doi.org/10.1180/minmag.2015.079.6.28.

Davoisne, C., et al., 2011. Krypton irradiation damage in Nd-doped zirconolite and perovskite. Journal of Nuclear Materials 415 (1), 67–73. https://doi.org/10.1016/j.jnucmat.2011.05.043. Elsevier B.V.

Deschanels, X., et al., 2006. Plutonium incorporation in phosphate and titanate ceramics for minor actinide containment. Journal of Nuclear Materials 352 (1–3), 233–240. https://doi.org/10.1016/j.jnucmat.2006.02.059.

Deschanels, X., et al., 2014. Swelling induced by alpha decay in monazite and zirconolite ceramics: A XRD and TEM comparative study. Journal of Nuclear Materials 448 (1–3), 184–194. https://doi.org/10.1016/j.jnucmat.2014.02.003. Elsevier B.V.

Ewing, R.C., 2015. Long-term storage of spent nuclear fuel. Nature Materials 14 (3), 252–257. https://doi.org/10.1038/nmat4226. Nature Publishing Group.

Gilbert, M.R., et al., 2010. Synthesis and characterisation of Pu-doped zirconolites—$(Ca_{1-x}Pu_x)Zr(Ti_{2-2x}Fe_{2x})O_7$. In: IOP Conference Series: Materials Science and Engineering, 9. https://doi.org/10.1088/1757-899X/9/1/012007, 012007.

Hambley, M., et al., 2008. Characterisation of 20 year old Pu 238-doped Synroc C. Materials Research Society Symposium Proceedings.

Hyatt, N.C., 2020. Safe management of the UK separated plutonium inventory: A challenge of materials degradation. npj Materials Degradation 4 (28). https://doi.org/10.1038/s41529-020-00132-7. Springer US.

Icenhower, J.P., Mcgrail, B.P., Schaef, H.T., Rodriguez, E.A., 2000. Dissolution kinetics of titanium pyrochlore ceramics at 90°C by single-pass flow-through experiments. Materials Research Society Symposium Proceedings 608, 373–378.

James, M., Carter, M.L., Watson, J.N., 2003. The synthesis, crystal chemistry and structures of Y-doped brannerite $(U_{1-x}Y_xTi_2O_6)$ and thorutite $(Th_{1-x}Y_xTi_2O_{6-\delta})$ phases. Journal of Solid State Chemistry 174 (2), 329–333. https://doi.org/10.1016/S0022-4596(03)00230-5.

Lang, M., et al., 2010. Review of $A_2B_2O_7$ pyrochlore response to irradiation and pressure. Nuclear Instruments & Methods in Physics Research, Section B: Beam Interactions with Materials and Atoms 268 (19), 2951–2959. https://doi.org/10.1016/j.nimb.2010.05.016. Elsevier B.V.

Lopez, C., et al., 2003. Solubility of actinide surrogates in nuclear glasses. Journal of Nuclear Materials 312 (1), 76–80. https://doi.org/10.1016/S0022-3115(02)01549-0.

Lumpkin, G.R., 2001. Alpha-decay damage and aqueous durability of actinide host phases in natural systems. Journal of Nuclear Materials 289 (1–2), 136–166. https://doi.org/10.1016/S0022-3115(00)00693-0.

Lumpkin, G.R., Smith, K.L., Blackford, M.G., 1991. Electron microscope study of Synroc before and after exposure to aqueous solutions. Journal of Materials Research 6 (10), 2218–2233. https://doi.org/10.1557/JMR.1991.2218.

Lutze, W., Ewing, R.C., 1988. Radioactive Wasteforms for the Future. North Holland Physics Publishing, Amsterdam.

Ma, S., et al., 2018. Effects of ionic radius on phase evolution in Ln-Al co-doped $Ca_{1-x}Ln_xZrTi_{2-x}Al_xO_7$ (Ln = La, Nd, Gd, ho, Yb) solid solutions. Ceramics International 44 (13), 15124–15132. https://doi.org/10.1016/j.ceramint.2018.05.149.

Nash, K.L., Nilsson, M., 2015. Reprocessing and Recycling of Spent Nuclear Fuel. Woodhead. https://doi.org/10.1016/C2013-0-16483-5.

Ojovan, M.I., Lee, W.E., 2005. An Introduction to Nuclear Waste Immobilisation, 1st edn. Elsevier, Oxford.

Oversby, V.A., Ringwood, A.E., 1981. Leach testing of synroc and glass samples at 85 and 200°C. Nuclear and Chemical Waste Management 2, 201–206.

Qin, S., et al., 2002. Micro-Raman study of perovskites in the $CaTiO_3$-$SrTiO_3$ system. Journal of the Chemical Society, Dalton Transactions 19, 3751–3755. https://doi.org/10.1039/b207228a.

Reid, D.P., Stennett, M.C., Hyatt, N.C., 2012. The fluorite related modulated structures of the Gd $_2(Zr_{2-x}Ce_x)O_7$ solid solution: An analogue for Pu disposition. Journal of Solid State Chemistry 191, 2–9. https://doi.org/10.1016/j.jssc.2011.12.039. Elsevier.

Ringwood, A.E., 1985. Disposal of high-level nuclear wastes: A geological perspective. Mineralogical Magazine 49 (2), 159–176. https://doi.org/10.1180/minmag.1985.049.351.04.

Ringwood, A.E., Kesson, S.E., Ware, N.G., 1979. The SYNROC process: A geochemical approach to nuclear waste immobilization. Geochemical Journal 13, 141–165.

Ringwood, A.E., et al., 1981. Immobilization of high-level nuclear reactor wastes in synroc: A current appraisal. Nuclear Waste Management 2, 287–305.

Roberts, S.K., Bourcier, W.L., Shaw, H.F., 2000. Aqueous dissolution kinetics of pyrochlore, zirconolite and brannerite at 25, 50, and 75 °C. Radiochimica Acta 88 (9–11), 539–543. https://doi.org/10.1524/ract.2000.88.9-11.539.

Smith, K.L., et al., 1992. The durability of Synroc. Journal of Nuclear Materials 190, 287–294. https://doi.org/10.1016/0022-3115(92)90092-Y.

Smith, K.L., et al., 1997. Characterization and leaching behavior of plutonium-bearing Synroc-C. Materials Research Society Symposium Proceedings 465, 1267–1272.

Smith, K.L., et al., 2003. The effect of radiation damage on zirconolite dissolution. Materials Research Society Symposium Proceedings 757.

Stennett, M.C., et al., 2012. Crystal structure and non-stoichiometry of cerium brannerite: $Ce_{0.975}Ti_2O_{5.95}$. Journal of Solid State Chemistry 192, 172–178. https://doi.org/10.1016/j.jssc.2012.03.057. Elsevier.

Strachan, D.M., et al., 2008. Radiation damage effects in candidate titanates for Pu disposition: Zirconolite. Journal of Nuclear Materials 372 (1), 16–31. https://doi.org/10.1016/j.jnucmat.2007.01.278.

Vance, E.R., et al., 1994. Actinide and rare earth incorporation into zirconolite. Journal of Alloys and Compounds 213/214, 406–409. https://doi.org/10.1016/0925-8388(94)90945-8.

Vance, E.R., et al., 2002. Incorporation of uranium in Zirconolite ($CaZrTi_2O_7$). Journal of the American Ceramic Society 85 (7), 1853–1859. https://doi.org/10.1111/j.1151-2916.2002.tb00364.x.

Wang, J., et al., 2019. Order-disorder phase structure, microstructure and aqueous durability of (Gd, Sm)2(Zr,Ce)2O7 ceramics for immobilizing actinides. Ceramics International 45 (14), 17898–17904.

Weber, W.J., Wald, J.W., Matzke, H., 1986. Effects of self-radiation damage in cm-doped $Gd_2Ti_2O_7$ and $CaZrTi_2O_7$. Journal of Nuclear Materials 138 (2–3), 196–209. https://doi.org/10.1016/0022-3115(86)90006-1.

Weber, W.J., et al., 1998. Radiation effects in crystalline ceramics for the immobilization of high-level nuclear waste and plutonium. Journal of Materials Research 13 (6), 1434–1484. Available at: http://journals.cambridge.org.

Weber, W.J., et al., 2009. Materials science of high-level nuclear waste immobilization. MRS Bulletin 34 (01), 46–52.

Wen, G., et al., 2015. Solid-state reaction synthesis and aqueous durability of Ce-doped zirconolite-rich ceramics. Journal of Nuclear Materials 466, 113–119. https://doi.org/10.1016/j.jnucmat.2015.07.047. Elsevier B.V.

Woolfrey, J.L., Reeve, K.D., Cassidy, D.J., 1982. Accelerated irradiation testing of synroc and its constituent minerals using fast neutrons. Journal of Nuclear Materials 109, 739–747.

Zhang, Y., et al., 2006. Recrystallisation of amorphous natural brannerite through annealing: The effect of radiation damage on the chemical durability of brannerite. Journal of Nuclear Materials 350 (3), 293–300. https://doi.org/10.1016/j.jnucmat.2006.01.012.

Zhang, K., et al., 2017. Self-propagating synthesis and CeO_2 immobilization of zirconolite-rich composites using CuO as the oxidant. Ceramics International 43, 1415–1423. https://doi.org/10.1016/j.ceramint.2016.10.103. Elsevier.

Zhang, K., et al., 2019. Self-propagating synthesis and characterization studies of Gd-bearing Hf-zirconolite ceramic waste forms. Materials 12 (1). https://doi.org/10.3390/ma12010178.

ADVANCES IN APPLIED CERAMICS
https://doi.org/10.1080/17436753.2021.1877596

I·M3 Institute of Materials, Minerals & Mining
Taylor & Francis
Taylor & Francis Group

REVIEW

Review of zirconolite crystal chemistry and aqueous durability

Lewis R. Blackburn, Daniel J. Bailey, Shi-Kuan Sun, Laura J. Gardner, Martin C. Stennett, Claire L. Corkhill and Neil C. Hyatt

Immobilisation Science Laboratory, Department of Materials Science and Engineering, University of Sheffield, Sheffield, UK

ABSTRACT

Zirconolite ($CaZrTi_2O_7$) has been identified as a candidate ceramic wasteform for the immobilisation and disposal of Pu inventories, for which there is no foreseen future use. Here, we provide an overview of relevant zirconolite solid solution chemistry with respect to Ce, U and Pu incorporation, alongside a summary of the available literature on zirconolite aqueous durability. The zirconolite phase may accommodate a wide variety of tri- and tetravalent actinide and rare-earth dopants through isovalent and heterovalent solid solution, e.g. $CaZr_{1-x}Pu_xTi_2O_7$ or $Ca_{1-x}Pu_xZrTi_{2-2x}Fe_{2x}O_7$. The progressive incorporation of actinides within the zirconolite-2M parent structure is accommodated through the formation of zirconolite polytypoids, such as zirconolite-4M or 3T, depending on the choice of substitution regime and processing route. A variety of standardised durability tests have demonstrated that the zirconolite phase exhibits exceptional chemical durability, with release rates of constituent elements typically $<10^{-5}$ $gm^{-2}{\cdot}d^{-1}$. Further work is required to understand the extent to which polytype formation and surrogate choice influence the dissolution behaviour of zirconolite wasteforms.

ARTICLE HISTORY
Received 18 November 2020
Revised 16 December 2020
Accepted 8 January 2021

KEYWORDS
Wasteform; zirconolite; ceramics; plutonium; immobilisation

Introduction

The resurgence of nuclear power, as a driver towards cleaner energy production, will necessitate the implementation of advanced spent fuel management strategy, and development of advanced nuclear materials capable of safely conditioning highly radioactive waste [1–3]. After nuclear fuel is removed from a reactor, nation states have the option to chemically recover a significant portion of the fissile inventory, or treat the fuel as waste for disposal. These fuel cycle options are considered *closed* or *open* respectively; the unit operations associated with these are illustrated in Figure 1. For many years the U.K. has operated a closed fuel cycle, in which a PUREX (plutonium-uranium-reduction-extraction) reprocessing step is implemented, with the primary motive to recover U/Pu from spent fuel. In the PUREX process, nuclear fuel pins are stripped of cladding and dissolved in 9M HNO_3; the aqueous nitric solution is then contacted with tri-butylphosphate (TBP). U^{6+} and Pu^{4+} form TBP complexes and are extracted to the organic phase; U^{6+} and Pu^{4+} are converted to oxides and calcined before storage. The remaining aqueous nitrate solution is comprised predominantly of high fission products and metalloids (Cs, I, Sr, As, Nd, Pd, Pr, Eu, La, Gd), minor actinides (Cm, Am, Np, Th), corrosion products (Mn, Ni, Cr), and entrained U/Pu. This effluent is referred to as high level liquid waste (HLLW) and is stored on the Sellafield site, before blending and calcination, prior thermal conditioning. The HLLW remains highly radioactive due to the long halflife of certain elements (e.g. $t_{1/2}$ $^{237}Np = 2.1 \times 10^6$ y, $t_{1/2}$ $^{129}I = 1.57 \times 10^7$ y). The current baseline thermal treatment for HLLW is vitrification in alkali borosilicate glass. In the vitrification process, HLLW is calcined and melted with glass forming additives, allowing complete dissolution of waste species into the vitrified network via incorporation into the glass forming structure; incorporation as network modifiers; and incorporation by encapsulation [4]. Although borosilicate glasses can incorporate a wide variety of elements, and vitrification is a well-established process that remains relatively insensitive to variations in feedstock chemistry, it is not the optimal choice for waste streams consisting of high actinide fractions, such as waste PuO_2. Actinides have exhibited low solubility in borosilicate glass matrices, alongside leach rates that are considerably higher than alternate wasteforms such as crystalline ceramics. The Pu^{4+} solubility in the French R7T7 glass has been limited at around 1.5 wt-% [5]. Several notable publications have indicated the solubility of plutonium can be increased to 4 wt-% when reduced to the Pu(III) species [5–7]. A series of borosilicate glasses containing 1 wt-% PuO_2 were fabricated Wellman et al. in order to elucidate the effect of self-irradiation on the elemental dissolution of the glass phase. Although it

CONTACT Lewis R. Blackburn lewis.blackburn@sheffield.ac.uk Immobilisation Science Laboratory, Department of Materials Science and Engineering, University of Sheffield, Sir Robert Hadfield Building, Mappin Street, S1 3JD, UK; Neil C. Hyatt n.c.hyatt@sheffield.ac.uk Immobilisation Science Laboratory, Department of Materials Science and Engineering, University of Sheffield, Sir Robert Hadfield Building, Mappin Street, S1 3JD, UK

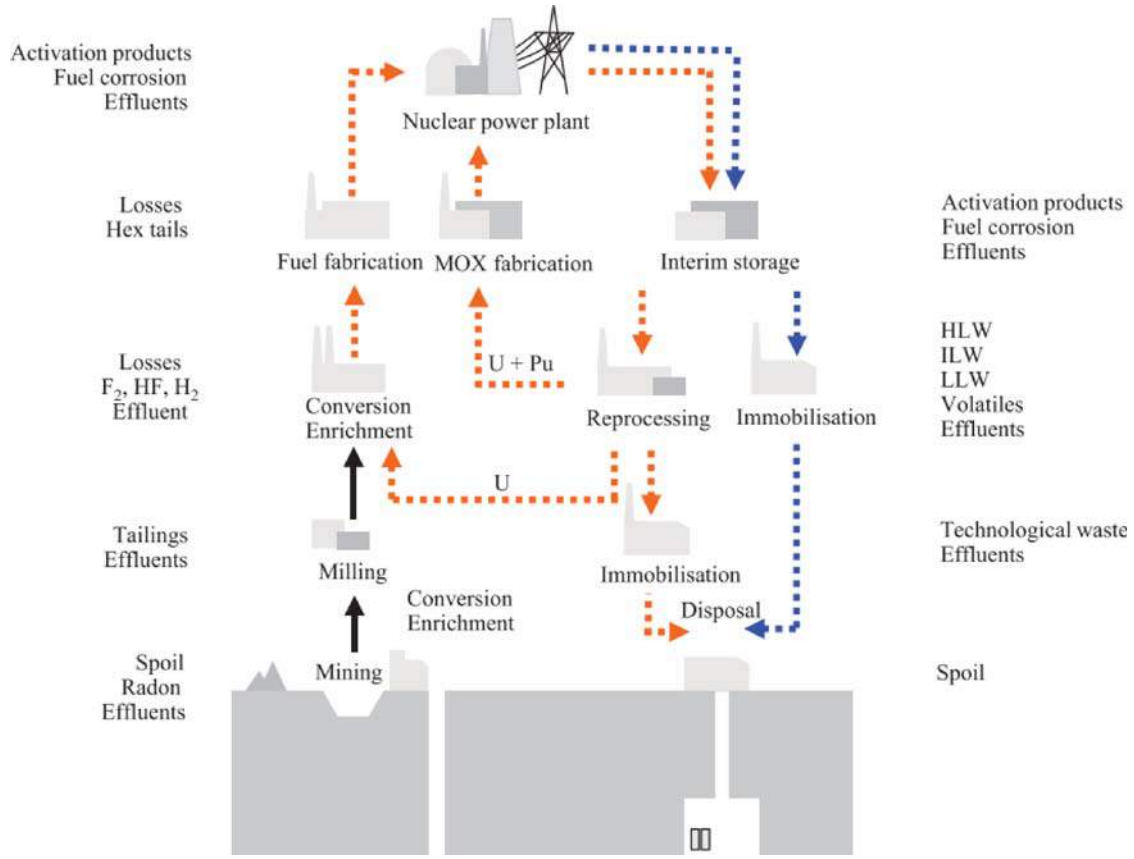

Figure 1. Illustration of unit operations associated with open and closed nuclear fuel cycles. Orange arrows indicate closed fuel cycle operations, while blue arrows represent those for an open fuel cycle (© IOP Publishing. Reproduced with permission. All rights reserved. [10]).

was determined that the release rate of Pu into the extraction phase was insensitive to dose rate (measured by $^{238}Pu/^{239}Pu$ ratio), temperature, and pH, was of the order 10^{-3} $gm^{-2}d^{-1}$ [8]. The development of SYNROC technology (synthetic-rock) in the 1980s has led to development of alternative waste-forms for nuclear waste based on ceramic systems [9]. The SYNROC formulation comprises an assemblage of chemically durable titanate crystalline phases (zirconolite, hollandite, perovskite, pyrochlore), based on natural mineral hosts that have demonstrated resistance to weathering on geological timescales; these can act as dedicated hosts for specific elements via accommodation in specific lattice sites in the host phase, providing a marked increase in solubility and chemical durability. The host phase for actinides is zirconolite – nominally $CaZrTi_2O_7$. The aim of this work is to provide an extensive literature review into the suitability of the zirconolite phase as a host for PuO_2. An assessment of the current UK situation regarding Pu will first be outlined, followed by a critical assessment of zirconolite as a ceramic host phase for Pu.

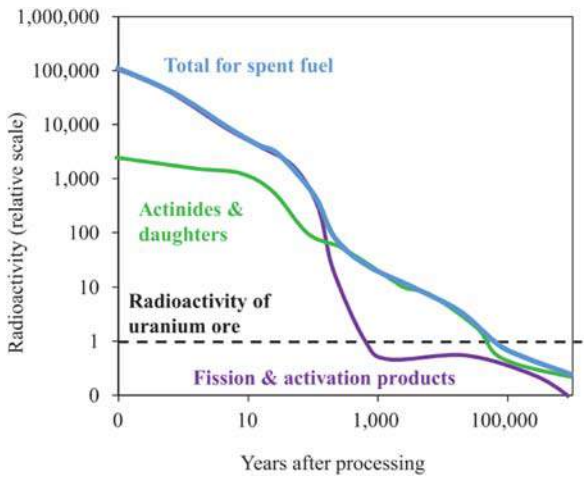

Figure 2. Illustration of timescales necessary for geological disposal (© IOP Publishing. Reproduced with permission. All rights reserved [10]).

Actinide immobilisation in ceramic materials

Owing to their relatively long half-lives and radiotoxicity, radionuclides must be separated from the biosphere and permanently disposed. The current intended disposal route for many countries is deep geological disposal, in an engineered repository known as a geological disposal facility (GDF). A GDF utilises the multibarrier concept, wherein a series of engineered barriers are constructed to prevent the egress of radionuclides until the radioactive output of the waste has decayed to levels comparable to the original uranium ore from which uranium fuel is

Table 1. Mineral host phases for actinide species.

Mineral	Ideal composition	Mineral space group	Calculated density (g/cm^3)	References
Pyrochlore	$A_2B_2O_7$ (e.g. $Gd_2Ti_2O_7$)	Fd-3m	6.57	[27–36]
Zircon	$ZrSiO_4$	$I4_1/amd$	4.66	[37–42]
Zirconia	ZrO_2	$P2_1/c$	5.82	[43–49]
Zirconolite	$CaZrTi_2O_7$	C2/c	4.44	[33,50–64]
Monazite	$CePO_4$	$P2_1/n$	5.26	[65–74]
Perovskite	$CaTiO_3$	Pbnm	4.04	[75–81]
Brannerite	UTi_2O_6	C2/m	6.37	[82–90]

derived, see Figure 2. The primary containment for radionuclides in this scenario is known as the *waste-form*, a passively safe material designed to prevent the release of radionuclides. Proposed wasteforms include cementitious, glass, ceramic, and glass-ceramic composite materials. Comprehensive analyses of these materials for nuclear waste applications are provided elsewhere [4,11–20]. In the context of the immobilisation of actinides, e.g. Pu, ceramic materials are considered to offer performance, including waste-loading and aqueous durability, when compared to cement-based systems, typically used for encapsulation of intermediate level wastes (ILW) and borosilicate glasses used for high level waste (HLW) immobilisation [12,16,19,21,22]. There have been many notable publications investigating potential single phase and multiphase ceramic wasteforms for the immobilisation of actinides, a selection of proposed host matrices for actinides is given in Table 1. Titanate and zirconate minerals have been particularly well-studied as a result of their excellent resistance to chemical alteration, and relatively high degree of resistance to radiation induced amorphisation [23–26]. Actinide incorporation in ceramic phases is achieved by allowing the waste component to be readily accepted into solid solution in the host lattice, either by direct substitution or partial incorporation with an appropriate charge compensation mechanism. Generally, the choice of solid solution mechanism is dictated by the relative ionic radii of the radionuclide and host cation site, and accessible valence states. For example, the zirconolite structure may accept Pu^{4+} in solid solution via homovalent substitution for Zr^{4+}, i.e. $CaZr_{1-x}Pu_xTi_2O_7$, or by a coupled substitution if Pu^{4+} is substituted for Ca^{2+}, with a secondary lower valence cation included to maintain charge balance, i.e. $Ca_{1-x}Pu_xZrTi_{2-x}Mg_xO_7$.

The design and implementation of ceramic actinide wasteforms is contingent on the following criteria:

- **Wasteloading**: The ceramic composition should be tailored such that solubility of waste material in the host phase is as extensive as reasonably possible, without the formation of deleterious secondary phases. This will alleviate space requirements in a geological disposal facility, through the reduction in the number of overall waste packages produced. The ceramic should also be able to incorporate appropriate quantity of Gd^{3+} and/or Hf^{4+}, to act as a neutron poison in the final Pu-bearing wasteform.
- **Fabricability**: Advantage should be taken of established manufacturing techniques, placing emphasis on the utilisation of continuous and simple processes. The use of exotic processing routes and high temperature thermal treatments should be avoided, if feasible.
- **Criticality**: The prevention of post immobilisation criticality must be ensured by the addition of a suitable quantity of neutron poison (e.g. Hf, Gd). The wasteform must be able to accommodate the co-incorporation of these species, and without significantly altering the waste package integrity or the host phase assemblage. There is currently no defined standard in the UK for the concentration of neutron poisons present in ceramic wasteforms for Pu immobilisation.
- **Proliferation Resistance**: The resulting waste package must demonstrate suitable resistance against illicit recovery of fissile material. This could potentially be achieved by a combination of the use of a multi-barrier overpack, and the production of a ceramic from which Pu extraction would be difficult and undesirable.
- **Aqueous Durability**: The chemical durability of the host material is essential in understanding the dissolution and long-term release rates of radionuclides to the wider environment. Wasteforms should be designed such that corrosion via groundwater ingress to the waste package occurs in manner that is minimised, controlled and predictable. Considering the halflife of ^{239}Pu is approximately 24,100 years, a containment period of at least 10 half-lives would be required, thus 241,000 years. The wasteform must therefore demonstrate high resistance to leaching under repository conditions for timescales of this magnitude.
- **Radiation Tolerance**: Ceramic wasteforms should demonstrate suitable resistance to the effects of irradiation induced by radioactive decay of waste components contained within the host structure.

Zirconolite ceramics for Pu immobilisation

Crystal structure of zirconolite

Zirconolite, ideal composition $CaZrTi_2O_7$ (ρ = 4.44 g·cm^{-3}, Z = 8, space group C2/c) is a relatively rare accessory mineral that has been located in a variety of terrestrial geologies, with a demonstrated affinity for, but not limited to, U^{4+}, Th^{4+}, Ce^{3+4+}, Al^{3+}, $Pu^{3+/4+}$, Gd^{3+} and Hf^{4+}. Confidence in the zirconolite

wasteform to successfully act as a host for actinides is largely underpinned through the existence of nature specimens, which have demonstrated excellent resistance to natural weathering effects over geological timescales, with several specimens found to retain significant portions of their primordial actinide inventories (~ 20 wt-% U/Th) [33, 91–94]. The ideal zirconolite structure is an anion-deficient fluorite superstructure, and is considered to be a derivative of the pyrochlore family of minerals, with approximate formulation $(Ca,Na,Ce,Th)_2(Nb,Ta,Ti)_2O_6(OH,F)$, however this often generalised to $A_2B_2O_7$ (Z = 8, space group Fd-3m) where A is typically some trivalent REE^{3+} species and B^{4+} = Ti, Zr [30,95,96]. During the development of the SYNROC wasteform, zirconolite was included as the host phase for actinides, due to its high aqueous durability [26,97–100]. Accordingly, a significant body of work has since been undertaken in order to determine the solubility of a wide array of actinide and rare-earth cation species within the zirconolite framework, particularly Ce and U as surrogates for Pu. The ideal zirconolite unit cell is comprised of planes of corner sharing CaO_8 and ZrO_7 polyhedra, interleaved by hexagonal tungsten bronze (HTB) type layers along (001). Ti^{4+} is distributed across three distinct sites in the HTB plane, two of which are TiO_6 octahedra, and one of which is a 50% statistically occupied TiO_5, giving rise to trigonal biprymidal coordination [101]. In this idealised structural description (see Figure 3), cation and HTB layers are integrated 1:1 along (001), related by a 180° rotation along the c^* axis. Owing to this two-layer repeat, stoichiometric $CaZrTi_2O_7$ is commonly referred to as zirconolite-2M, with reference to the two layer lamellar monoclinic motifs comprising the unit cell. The zirconolite-2M polytype has been since been demonstrated to form over the compositional range $CaZr_xTi_{3-x}O_7$ for $0.83 \leq x \leq 1.33$, indicating considerable flexibility with regards to [Ti]/[Zr] ratio [102]. The distribution of Ti across cation sites in zirconolite has also been shown to be controlled as a function of sample preparation temperature [52]. Zirconolite also exhibits a number of crystallographically distinct polytype structures, the formation of which is observed to be controlled by the chosen substitution regime and oxygen fugacity during synthesis. Zirconolite polytyoids are characterised by variation in stacking sequence of adjacent Ca/Zr and HTB layers, for example, the zirconolite-4M structure was solved by Coelho et al. as a four layer repeating sequence, comprised of alternating zirconolite-2M and pyrochlore-type layers, resulting in a doubling of the unit cell along the c-axis, retaining monoclinic symmetry [103]. Extensive substitution of Pu within the Ca^{2+} site, facilitated by co-substitution of Fe^{3+} was reported by Gilbert et al. to produce the trigonal zirconolite-3T variation (space group $P3_121$) [104]. Polytypes adopting three and six-layer orthorhombic symmetry have also been reported, but detailed structural solutions are lacking [64]. Ca^{2+} and Zr^{4+} sites are of particular interest as both have been shown to readily accept a range of actinide and rare-earth elements [53,55,56,64,78,105–108]. Extensive solubility of Mg^{2+}, Al^{3+}, Ti^{3+}, Fe^{3+}, and Nb^{5+} species within the Ti^{4+} site has also been demonstrated, with the view to charge balance substitutions which do not exhibit isovalence across the structure, e.g. the accommodation of Pu within the Ca^{2+} site could be achieved by the co-substitution of Al^{3+} via $Ca_{1-x}Pu_xZrTi_{2-2x}Al_{2x}O_7$, assuming all Pu is present as Pu^{4+} [55,98,104,109]. The simultaneous substitution of trivalent species within both Ca^{2+} and Zr^{4+}, negating the need for charge balancing species, has also been demonstrated [110–113]. As the manipulation of Pu in wasteform development trials is not often possible, due to the stringent handling requirements associated with radiotoxicity and the handling of fissile material, the remainder of this review will aim to provide a comprehensive discussion of Ce and U surrogate incorporation in zirconolite.

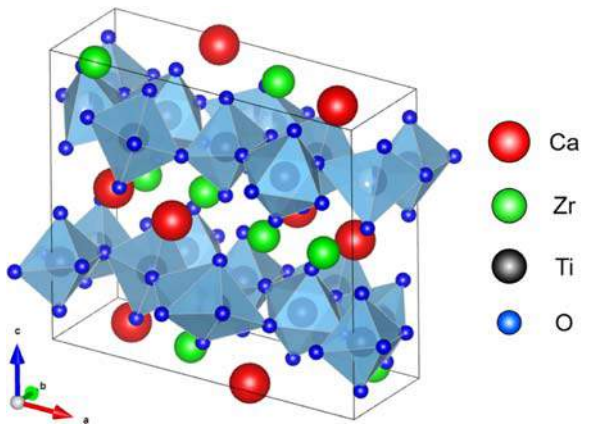

Figure 3. Crystal structure of zirconolite-2M ($CaZrTi_2O_7$).

Incorporation of Ce in zirconolite

Incorporation of Ce within Zr^{4+} site

The formation of zirconolite with Ce targeted in the Zr^{4+} site ($CaZr_{0.8}Ce_{0.2}Ti_2O_7$) was attempted by Begg and Vance [114]. Two distinct zirconolite phases were observed to form (zirconolite-2M and zirconolite-4M) alongside a secondary perovskite phase with considerable incorporated Ce (calculated stoichiometry $Ca_{0.72}Ce_{0.24}Zr_{0.02}Ti_{1.03}O_3$). Ce L_{III} edge X-ray absorption spectra (XANES) confirmed the presence of 35% Ce^{3+}, despite extended sintering under oxidising conditions. Further annealing in air at lower temperatures resulted in total conversion to Ce^{4+}, inferring the excess positive charge in the zirconolite-2M species may be self-compensated by cation vacancies. This work was complemented by Blackburn et al.

with the $CaZr_{1-x}Ce_xTi_2O_7$ system synthesised under both oxidising and reducing conditions [115]. It was determined that sintering at 1350°C under oxidising conditions produced a transformation to zirconolite-4M above $x = 0.20$, although failed to stabilise the entire Ce inventory as Ce^{4+}, with 28% Ce manifested as Ce^{3+}. Synthesising the solid solution under a 5% H_2/N_2 mixture promoted the formation of a Ce-rich perovskite phase, bypassing the formation of zirconolite-4M at the result of uniform Ce^{3+} speciation. Blackburn et al. also fabricated a sample corresponding to nominal composition $CaZr_{0.80}Ce_{0.20}Ti_2O_7$ by hot isostatic pressing (1300°C dwell temperature, maintained for 4 h with isostatic pressure 100 MPa) [116]. The bulk matrix was of near theoretical density, with zirconolite-2M comprising ~ 81 wt-% of the phase assemblage, with the remainder comprised of zirconolite-4M and Ce-perovskite. Similar phase fields were reported in the $CaZr_{1-x}Ce_xTi_2O_7$ system by Clark et al. utilising both conventional sintering and spark plasma sintering (SPS) [56]. Accommodation of Ce ($x \geq 0.20$) resulted in the formation of zirconolite-4M. EDS measurements confirmed that greater Ce content was concentrated in the zirconolite-4M phase, with a secondary Ce-bearing perovskite phase produced due to partial Ce^{3+} speciation. At extensive targeted Ce-substitution ($x = 0.5$), zirconolite-4M was present at high concentration (96 wt-%). The reducing conditions imposed by the SPS process promoted Ce^{4+} reduction to Ce^{3+}, destabilising zirconolite-4M in favour of Ce-rich perovskite. The $CaZr_{1-x}Ce_xTi_2O_7$ solid solution was extended by Li et al. [51]. A structural transformation from the zirconolite-2M to the zirconolite-4M polytype was observed, alongside accessory perovskite, in line with previous observations. Further attempted incorporation of Ce within the Zr site yielded a cubic pyrochlore phase (ideal composition $CaCeTi_2O_7$), and the total solubility limit of Ce was determined to be approximately $x = 0.80$. X-ray photoelectron spectroscopy (XPS) analysis confirmed the ratio of Ce^{3+}/Ce^{4+} to decrease from 1.24 at low concentration ($x = 0.20$) to 0.45 at maximum Ce concentration ($x = 1.00$).

Incorporation of Ce in Ca^{2+} site with charge compensators

Ce substitutions into zirconolite were undertaken by Begg and Vance, with the successful synthesis of $Ca_{0.8}Ce_{0.2}ZrTi_{1.6}Al_{0.4}O_7$ by sintering in air at 1400°C [114]. XANES measurements confirmed that Ce^{4+} was present at only 70%. Minor Al_2O_3 was also formed, hence Al^{3+} charge compensation was only therefore sufficient for 70% Ce^{4+}. Furthermore, re-formulation targeting Ce^{3+} on the Ca^{2+} site, producing a stoichiometry of $Ca_{0.8}Ce_{0.2}ZrTi_{1.8}Al_{0.2}O_7$ formed a single phase zirconolite, in which Ce^{3+} was accommodated entirely on the Ca^{2+} site. Further work by Begg et al. determined that zirconolite could undergo self-charge compensation via the formation of cation vacancies and trivalent Ti^{3+}, under oxidising and reducing conditions respectively [80]. This was demonstrated by the synthesis of single phase $Ca_{0.9}Ce_{0.1}ZrTi_2O_7$ under both oxidising and reducing conditions (i.e. the incorporation of Ce^{3+} and Ce^{4+} on the Ca^{2+} site), displaying an apparent excess charge. Vance et al. confirmed that Ce^{3+} may be overwhelmingly incorporated into the Ca^{2+} site, when reacting under reducing conditions, forming a single phase up to 0.3 f.u., i.e. $Ca_{0.70}Ce_{0.30}ZrTi_{1.70}Al_{0.30}O_7$ [117]. Similar results were obtained by Kaur et al. targeting $Ca_{0.80}Ce_{0.20}ZrTi_{1.80}Al_{0.20}O_7$, with synthesis under air at 1400°C. Ce was observed to fully accommodate within the zirconolite-2M phase, with XPS analysis confirming the formation of 75% Ce^{3+}, with sufficient Al^{3+} to charge balance [118]. Similar processing techniques were utilised by Pöml et al. targeting Ce^{4+} and Al^{3+} accommodation; specimens were sintered at 1400°C for 2 d [119]. Near single phase specimens with nominal composition $Ca_{0.85}Ce_{0.15}ZrTi_{1.70}Al_{0.30}O_7$ and $Ca_{0.87}Ce_{0.13}ZrTi_{1.74}Al_{0.36}O_7$ were fabricated by solid state synthesis, with EELS data confirming the formation of 80% Ce^{3+}, without a change in phase assemblage. A complementary investigation of the efficacy of Cr^{3+} as a charge balancing species was reported by Blackburn et al., with the $Ca_{1-x}Ce_xZrTi_{2-2x}Cr_{2x}O_7$ solid solution synthesised in air at 1350°C [120]. Single phase specimens were produced in the interval $0.05 \leq x \leq 0.20$, after which Cr_2O_3, CeO_2 and a Ce-rich perovskite phase were observed in the microstructure, although when targeting $x = 0.35$ the zirconolite-2M phase remained present at ~ 94 wt-%. Selected area electron diffraction confirmed that the 2M polytype structure was maintained throughout the phase evolution. Ce L_3 XANES data confirmed partial reduction to Ce^{3+} varying between 15% and 27%, similar to previous studies.

Incorporation of U/Pu in zirconolite

Incorporation of U/Pu in Zr^{4+} site

During development of SYNROC technology, U and Pu were observed to partition overwhelmingly into the zirconolite phase, although explicit discussion of zirconolite polytype formations were not provided [99,121,122]. Although more recent attempts to fabricate titanate phase assemblages by hot isostatic pressing, targeting a high zirconolite fraction, report agreeable data [123,124], it is necessary to discuss the structural effects of U/Pu incorporation within the zirconolite phase in isolation. Kesson et al. reported the solid solution limits of U within the zirconolite structure, targeting substitution on the Zr^{4+} site [98]. Compositions corresponding to $CaZr_{0.75}U_{0.25}Ti_2O_7$, $CaZr_{0.50}U_{0.50}Ti_2O_7$ were fabricated by

hot pressing at 1400°C; zirconolite and pyrochlore were yielded in each instance. Attempting to partition a greater amount of U within the Zr^{4+} site promoted the formation of the pyrochlore phase, alongside secondary (Ti,Zr,U)O_2 solid solutions. Initial work by Vance et al. reported the incorporation of 0.5 f.u. of U within the Zr^{4+} site, targeting $CaZr_{0.5}U_{0.5}Ti_2O_7$, by hot pressing at 1250°C, followed by a 1400°C heat treatment under reducing conditions, with a view to stabilise U^{4+} [106]. Further substitution of U appeared to stabilise the pyrochlore structure, while a minor U-containing rutile was also formed in all concentrations. The crystal chemistry of the uranium pyrochlore ($CaU^{4+}Ti_2O_7$ – betafite) is discussed elsewhere [125]. The $CaZr_{0.80}U_{0.20}Ti_2O_7$ composition was also produced by HIP (1300°C, 100 MPa) by Blackburn et al. yielding a significant fraction of zirconolite-2M (~ 97 wt-%), alongside minor unincorporated UO_2 and a (Zr,U)O_2 solid solution [116]. A detailed investigation of U^{4+} accommodation in the zirconolite $CaZr_{1-x}U_xTi_2O_7$ system was performed by Vance et al. in 2002 [55]. Synthesis of the solid solution under inert conditions produced single phase zirconolite-2M when targeting $x = 0.10$, with the zirconolite-4M phase preferred above $x = 0.20$. Further U^{4+} concentration increased the relative yield of the zirconolite-4M phase, with extensive incorporation (~0.5 f.u. U^{4+}) producing the U-pyrochlore phase, in line with previous data. Oxidation of samples corresponding to $CaZr_{0.9}U_{0.1}Ti_2O_7$ and $CaZr_{0.8}U_{0.2}Ti_2O_7$ promoted the formation of U^{5+}, causing the destabilisation of the zirconolite-4M phase with respect to the zirconolite-2M structure. Shrivastava, Kumar and Sharma have provided an excellent structural refinement of the zirconolite-2M $CaZr_{0.95}U_{0.05}Ti_2O_7$ and $CaZr_{0.90}U_{0.10}Ti_2O_7$ compositions [126]. More recently, the $CaZr_{1-x}U_xTi_2O_{7+x}$ solid solution was prepared by Subramani et al., with all compositions prepared in air at 1400°C [127]. Interestingly, zirconolite-2M was observed to form as a single phase at each level of targeted U concentration, with the average oxidation state of U close to U^{6+} in all instances, as determined by U L_3 XANES. The incorporation of Pu^{4+} within the Zr^{4+} site appears to yield broadly similar results to the corresponding U solid solution, demonstrating the efficacy of U^{4+} as a structural surrogate under inert conditions. Structural effects of Pu^{4+} substitution within the Zr^{4+} site in zirconolite were investigated by Begg et al. [105]. When sintering in air, $CaZr_{0.9}Pu_{0.1}Ti_2O_7$ was successfully synthesised as a single phase, with a secondary Pu-rich zirconolite-4M phase formed above $x = 0.20$. The yield of zirconolite-4M was increased with further Pu^{4+} substitution; a pyrochlore phase was observed to crystallise for the phase corresponding to $CaZr_{0.60}Pu_{0.40}Ti_2O_7$. Annealing specimens under reducing conditions (3.5% H_2/N_2 – 1200°C) promoted the formation of Pu^{3+}, similar to Ce, however this reduction mechanism is not available for U, highlighting a caveat for the deployment of U as a Pu surrogate under reducing conditions. The accompanying increase in ionic radius was considered to cause the destabilisation of the zirconolite-4M phase, with respect to zirconolite-2M, stabilising a deleterious perovskite phase in agreement with cerium doped specimens, in which targeting Zr^{4+} substitution for Ce^{3+} promoted the formation of perovskite. Complementary results were obtained by Vance et al. targeting $CaZr_{0.50}Pu_{0.50}Ti_2O_7$; hot pressing the sample (i.e. reducing conditions) yielded approximately 50 wt-% Pu-perovskite attributed to the formation of Pu^{3+} [106]. Further work by Begg et al. confirmed that hot pressing the $CaZr_{0.80}Pu_{0.20}Ti_2O_7$ composition failed to produce a single phase product, with only 50 wt-% zirconolite yield attributed to uniform Pu^{3+} speciation [26,128]. Nevertheless, annealing the composition in air at 1300°C produced significant modifications to the phase assemblage, yielding ~ 80 wt-% zirconolite, alongside a Pu-rich pyrochlore phase, eliminating the perovskite phase.

Incorporation of U/Pu in Ca^{2+} site with charge compensators

A selection of zirconolites targeting U^{4+} incorporation within the $Ca_{1-x}U_xZrTi_{2-2x}Al_{2x}O_7$ system were synthesised by Vance et al. with a view to further extend U^{4+} solubility without structural transformation to the closely related pyrochlore phase [117]. The solubility limit was determined to be $0.3 \leq x \leq 0.4$, after which further accommodation of U^{4+} resulted in the formation of UO_2–ZrO_2 solid solutions, and minor Al_2O_3. Further work demonstrated that imposing reducing conditions by hot pressing yielded a secondary brannerite phase, at appreciable quantity [106]. A more systematic approach was later undertaken, in which both Al^{3+} and Mg^{2+} were targeted on the Ti^{4+} site in order to provide sufficient charge compensation for both U^{4+} and U^{5+} [55]. It was determined that single phase zirconolite-2M was formed in both instances when targeting values $x = 0.1$, 0.2, after which secondary formation of UTi_2O_6, ZrO_2 and UO_2 phases was observed. The use of Mg^{2+} to charge balance approximately 26 wt-% U^{4+} in the zirconolite structure was reported by Kesson et al. with U apparently distributed between Ca^{2+} and Zr^{4+} sites [98]. The targeted zirconolite stoichiometry was not reported. Pu-bearing zirconolites targeting Ca^{2+} substitution without charge compensation (i.e. $Ca_{0.9}Pu_{0.1}HfTi_2O_7$ – Zr^{4+} entirely replaced by Hf^{4+}) were prepared by Begg, Vance and Conradson [78]. Pu was accommodated across both Ca^{2+} and Hf^{4+} sites, contrary to design; annealing under reducing conditions did not stabilise the formation of a secondary perovskite phase, despite 80% reduction to Pu^{3+}. Deschanels

et al. confirmed the synthesis of single phase $Ca_{0.87}Pu_{0.13}ZrTi_{1.73}Al_{0.30}O_7$, exhibiting the zirconolite-2M structure, when targeting Pu^{4+} [53]. A similar composition was synthesised by Vance et al.: $Ca_{0.80}Pu_{0.20}ZrTi_{1.80}Al_{0.20}O_7$, configured to accomodate Pu^{3+} [106]. While conventional sintering yielded a single phase zirconolite specimen, hot pressing at 1250°C yielded a secondary perovskite phase. Begg et al. determined the influence of processing atmosphere in the formulation of Pu^{3+} and Pu^{4+} doped zirconolites targeting $Ca_{0.80}Pu_{0.20}HfTi_{1.80}Al_{0.20}O_7$ and $Ca_{0.80}Pu_{0.20}HfTi_{1.60}Al_{0.40}O_7$, respectively, with Hf in place of Zr [128]. Targeting $Ca_{0.80}Pu_{0.20}HfTi_{1.80}Al_{0.20}O_7$ while sintering under a 3.5% H_2/N_2 mixture promoted uniform Pu^{3+} speciation, yielding approximately 88% zirconolite, alongside a Pu-perovskite phase. Sintering under air was sufficient to allow uniform Pu^{4+} valence, with ~ 96% zirconolite yield. Synthesis of the $Ca_{0.80}Pu_{0.20}HfTi_{1.60}Al_{0.40}O_7$ composition, requiring Pu^{4+}, failed to yield above 77% zirconolite when sintered under reducing conditions, whereas 94% zirconolite yield was produced in air. Fe^{3+} was deployed as a charge compensator in Pu-doped zirconolite, investigated by Gilbert et al. targeting $Ca_{1-x}Pu_xZrTi_{2-2x}Fe_{2x}O_7$ [104]. A transformation from zirconolite-2M to zirconolite-3T was reported for compositions above $x = 0.20$, with separated PuO_2 identified above $x = 0.40$.

Chemical durability of zirconolite

In the geological disposal scenario, aqueous dissolution of the immobilisation matrix, through contact with groundwater, will be the dominant mechanism by which radionuclides are released into the near field environment. Therefore, the design philosophy of nuclear wasteforms stipulates that chemical durability should be a primary factor when considering immobilisation matrices for actinides. Assessing the relative durability of potential wasteforms on timescales comparable to those likely to be imposed in geological timescales presents a significant technical challenge in a laboratory setting, as these tests typically occur on the timescale of several weeks to months. A further challenge is posed by the refractory nature of many oxide ceramics, for which the durability may be several orders of magnitude greater than vitrified or cementitious matrices, depending on the material of choice [129]. Nevertheless, information regarding the long-term behaviour may be extrapolated through the use of accelerated leaching techniques, in which the wasteform is contacted with low pH solution and increased saturation temperatures. A summary of established wasteform durability tests commonly applied to ceramic and vitrified materials is listed in Table 2. Normalised leach rates of constituent elements are typically quoted in $gm^{-2}{\cdot}d^{-1}$.

Table 2. Examples of dissolution methodologies used to ascertain the durability of candidate nuclear wasteforms.

Durability test	Summary of conditions
MCC-1	Saturation of monolith in ASTM-Type I H_2O (S.A./V = 10 m^{-1}) at 40, 70 or 90°C for 7 d.
MCC-2	As with MCC-1, yet environmental temperature may be raised to 110, 150 or 190°C.
PCT-B	1 g powdered substrate (75–150 μm) in 10 mL ASTM-Type I H_2O. 90°C for 7 d.
SPFT	Dynamic solution ingress permitted by peristaltic pump, with variable flow rate, temperature and solution pH.
VHT	Monolith suspended in saturated water vapour to promote accelerated surface alteration.

As zirconolite comprised a significant portion of many SYNROC variations, as the primary actinide-bearing phase, a measure of zirconolite durability was obtained through evaluation of SYNROC dissolution studies. Early work by Oversby and co-workers demonstrated the comparative success of SYNROC with respect to borosilicate glasses for the immobilisation of HLW. Samples of SYNROC and PNL-76-68 waste glass (borosilicate glass with 33% simulated HLW) were studied on 0.5 g discs with distilled water at 85 and 200°C [130]. Release rates of 1.4 and 8.9 $gm^{-2}{\cdot}d^{-1}$ were reported for the PNL-76-68 glass at 85 and 200°C respectively, while the upper limit for the SYNROC leach rate was determined to be several orders of magnitude lower, at <0.005 $gm^{-2}{\cdot}d^{-1}$. Tests were repeated with powdered samples in the 100–200 μm size fraction to accelerate leaching; it was determined that the leach rates of U were between a factor of 5–9 lower for SYNROC at 200°C. In 1981, specimens of SYNROC (comprising ~ 35% zirconolite) was crystallised by hot pressing with the addition of 20% HLW calcine readily accepted into solid solution with the constituent phases [122]. A more comprehensive investigation was performed in this instance, with variations in both temperature and leaching duration, allowing improved comparability between ceramic and glass phases for HLW immobilisation. With respect to leaching rates, SYNROC specimens were observed to decrease by approximately two orders of magnitude between 10–30 days, whereas borosilicate specimens were observed to dissolve at a consistent rate (see Figure 4). At 95°C the leachability of U from the SYNROC specimen was determined to be smaller than for the borosilicate glass by a factor of 100,000. A specimen of SYNROC with added 10 wt-% HLW (0.62 wt-% ^{239}Pu) was hot pressed, and subject to MCC-1 durability testing by Smith et al. with extensive leach periods of 52 d and 2472 d at 70°C in deionised water, alongside carbonate and silicate leachates [100]. After 52 d, ^{239}Pu release rates for carbonate and silicate leachates were an order of magnitude greater than for deionised water (10^{-4}, 10^{-4}, and 10^{-5} $gm^{-2}{\cdot}d^{-1}$, respectively). However, after 2472 d,

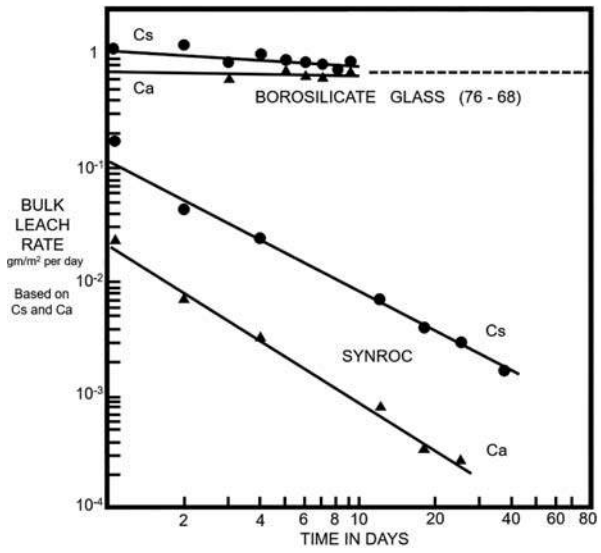

Figure 4. Bulk leach rate of SYNROC specimen in comparison to borosilicate glass (This article was published in A. E. Ringwood et al., "Immobilization of High-Level Nuclear Reactor Wastes in Synroc: A Current Appraisal," Nucl. Waste Manag., vol. 2, pp. 287–305, 1981, copyright Elsevier [122]).

the normalised leach rate of ^{239}Pu dropped to 10^{-6} $gm^{-2}{\cdot}d^{-1}$ in deionised water, demonstrating exceptional durability over extensive time periods. Further work by Smith et al. on the SYNROC wasteform was performed using an MCC-2 dissolution assessment using deionised water, at 150°C [131].

Samples were loaded with 10 wt-% simulated HLW, and after 532 d, SEM analysis determined that surface layer grains of major phases exhibited no corrosion. It was confirmed that after 337 d, 0.0045% of the original Ce inventory had been released to the leachate. These early investigations were considered sufficient to demonstrate the suitability of ceramic phases for the immobilisation of nuclear wastes. However, incongruent dissolution was a key consideration, as each phase in the SYNROC assemblage did not present comparable leach rates. A variety of zirconolite-rich and pyrochlore compositions containing approximately 12 wt-% Pu (alongside 15 wt-% Hf/Gd) were synthesised by Hart et al. with release rates of Pu were measured by MCC-1 analysis at 90°C [23]. 7-day release rates for Pu were measured to be between 10^{-5} and 10^{-6} $gm^{-2}d^{-1}$ after 300 d, with similar release rates observed for Hf. These data provide a significant contribution towards underpinning the safety case for geological disposal of Pu in the zirconolite wasteform, as the congruent release of Pu and neutron poisons is essential towards suppressing post-closure criticality. A zirconolite-rich titanate assemblage containing U/Th and Pu was synthesised by hot isostatic pressing by Zhang et al. yielding a zirconolite phase fraction of approximately 89 vol.-%. A secondary hollandite phase (nominally $BaAl_2Ti_6O_{16}$) and UTi_2O_6 brannerite phase (~ 2 vol.-%) were also formed, yet U and Th were incorporated overwhelmingly into zirconolite, with minor uptake in the brannerite phase [123]. Pu was successfully localised within the zirconolite phase, co-substituted with Gd and Hf as neutron poisons. Both samples were subject to MCC-1 durability testing in deionised H_2O at 90°C, however experimental framework was modified such that the leachate was replaced after 7 and 35 days, and the test was extended to 84 days. The normalised leach rates of key elements are summarised in Figure 5. After 35 days, a normalised release rate of 10^{-5} $gm^{-2}{\cdot}d^{-1}$ for Pu was measured, with similar accompanying release rates of included neutron poison species. Zirconolite-rich ceramics were synthesised by Zhang et al. by self-propagating synthesis, targeting a nominal $CaZr_{1-x}Ce_xTi_2O_7$ composition, with a view to assess the chemical durability of the composition corresponding to $CaZr_{0.7}Ce_{0.3}Ti_2O_7$ by a monolithic MCC-1 test in deionised H_2O [132]. The normalised leach rate of Ce over the 42 d period was measured to be 2.26×10^{-6} $gm^{-2}{\cdot}d^{-1}$, demonstrating exceptional resistance to alteration, despite the formation of a secondary Ce-bearing perovskite phase, accounting for approximately 35 wt-% of the phase assemblage. Meng et al. attempted the accommodation of Ce within both Ca^{2+} and Zr^{4+} sites, i.e. $Ca_{1-x}Zr_{1-x}Ce_{2x}Ti_2O_7$, anticipating the auto-reduction of Ce species may provide self-charge balance across the zirconolite structure [133]. Samples were synthesised by conventional solid state reaction and the durability was measured by PCT-B methodology. Despite a low normalised mass loss of Ce ranging between 10^{-6} and 10^{-7} $gm^{-2}{\cdot}d^{-1}$, an increased order of magnitude for Ce was observed for compositions containing a greater accompanying portion of perovskite. Cerium was applied as a surrogate for Pu targeting the zirconolite phase $CaZr_{1-x}Ce_xTi_2O_7$ system by Wen et al. synthesised by a solid state route [134]. MCC-1 leaching

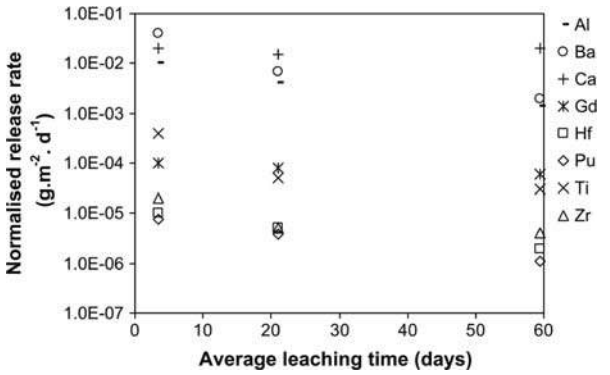

Figure 5. Normalised release rates of key elements for zirconolite-rich titanate assemblage processed by HIP (Reprinted from Y. Zhang et al., "Zirconolite-rich titanate ceramics for immobilisation of actinides - Waste form/HIP can interactions and chemical durability," J. Nucl. Mater., vol. 395, pp. 69–74, 2009, with permission from Elsevier [123]).

was performed on the sample pertaining to composition $Ca_{0.76}Zr_{0.64}Ce_{0.48}Ti_{2.03}O_7$; the normalised leach rate for Ce was measured to be approximately 2.3×10^{-4} $gm^{-2}{\cdot}d^{-1}$ up to 10 days of exposure; after 28 days the leach rate decreased by two orders of magnitude to 2.3×10^{-6} $gm^{-2}{\cdot}d^{-1}$. A Ce-bearing perovskite with composition $Ca_{0.84}Ce_{0.10}Ti_{1.03}O_3$ was also stabilised, which may have attributed to a greater release fraction of Ce, hence it is unlikely that the release rates for Ce could be attributed solely to the zirconolite phase. As the formation of perovskite is a common secondary phase in the fabrication of zirconolite wasteforms, formulations must be tailored such that the accompanying fraction is minimalised. This is an issue commonly associated with cerium surrogacy, as the tendency of Ce to undergo partial reduction, despite reaction under oxidising conditions, to form Ce^{3+} is commonly observed to promote the formation of a Ce-bearing perovskite [51,56,60,114]. Perovskite (nominally $CaTiO_3$) is present as a major constituent of the SYNROC assemblage, as a host for Sr^{2+}, despite markedly lower resistance to alteration with respect to the zirconolite phase. The relative leach rates of perovskite and zirconolite, with respect to pH dependence, was elucidated by McGlinn et al. subsequent to the demonstration of SYNROC for HLW immobilisation, as a precursor towards to implementation of single phase ceramic wasteforms. The formation of TiO_2 (anatase) at 90°C on the surface of perovskite specimens was observed at low and neutral pH levels, indicating hydrothermal alteration of the perovskite phase; no evidence of dissolution was observed with XRD or SEM techniques for the zirconolite phase [135]. It has since been proposed that precipitation of TiO_2 in subsequent dissolution trials was attributed to the dissociation of $CaTiO_3$ [81,136].

Potential zirconoliteformulations for Pu must incorporate sufficient buffer phases such that the formation of Pu-perovskite is not thermodynamically or kinetically favourable, as this may exacerbate the rate of Pu extraction from the wasteform in the geological disposal environment. Begg et al. synthesised perovskite incorporated with Pu under oxidising and reducing conditions, with a view to elucidate the substitution mechanism of Pu^{4+} and Pu^{3+}, respectively, within $CaTiO_3$ [78]. Attempting to form $Ca_{0.9}Pu_{0.1}Ti_{1.9}Al_{0.1}O_3$ under reducing conditions yielded two perovskite phases, accounting for an 80% reduction to the trivalent species. It was determined that Pu^{4+} can be substituted into the perovskite structure as a single phase in excess, with Ti vacancies allowing for charge neutrality to be preserved. Moreover, the perovskite phase was observed to accommodate a considerable amount of Pu^{3+} and Pu^{4+} without the addition of charge balancing species. Further work by Begg et al. confirmed that the release of Pu from $CaTiO_3$ under acidic conditions was indiscriminate of Pu valence [79]. More recently, the chemical durability of near single phase zirconolite has been elucidated. A sample of zirconolite with nominal composition $Ca_{0.80}Nd_{0.20}ZrTi_{1.80}Al_{0.20}O_7$ was synthesised by hydrolysis of alkoxide nitrate precursor material, before calcination and sintering at 1400°C in air. An excess of 1.5 wt-% Ti/Zr oxides were added to discourage perovskite formation; a dense microstructure of zirconolite-2M with minor $ZrTiO_4$ was yielded at 0.5%. MCC-2 analysis at 150°C in deionised water reported a normalised mass loss of Nd between 10^{-3} and 10^{-4} over 80 d. Single phase zirconolite doped with 0.15 f.u. of Nd (trivalent actinide surrogate) were recently fabricated by Cai et al. Subsequent to confirmation of a single product in the $Ca_{1-x}Zr_{1-x}Gd_{2x}Ti_2O_7$ system, the sample with nominal composition $Ca_{0.925}Zr_{0.925}Gd_{0.15}Ti_2O_7$ was selected for PCT analysis. The durability was measured in pH 5, 7, and 9 at 90°C. The single phase specimen demonstrated a normalised Nd leach rate of 3.13×10^{-5} $gm^{-2}{\cdot}d^{-1}$ after 42 d, proving insensitive to extraction under varying pH [137]. Recent work by Zhang et al. utilised Gd^{3+} and Hf^{4+} as trivalent and tetravalent actinide surrogates, with a view to eliminate the issues typically caused by Ce reduction, targeting the composition $Ca_{1-x}Hf_{1-x}Gd_{2x}Ti_2O_7$ [138]. Release rates of 4.72×10^{-7} and 1.59×10^{-8} $gm^{-2}{\cdot}d^{-1}$ were measured for Gd and Hf respectively.

Critical gap analysis

Zirconolite-rich wasteforms satisfy many of the design criteria commonly applied in the design of nuclear wasteform materials, not least high chemical durability and moderate wasteloading. Nevertheless, an in-depth review of the literature has identified several gaps that have not been conclusively addressed:

- **Polytype formation**: It has been demonstrated that the choice of substitution scheme, surrogate and thermal processing route are controlling factors in the formation of crystallographically distinct zirconolite polytype structures. However, although the acceptance criteria do not stipulate the preferred formation of a specific polytype, it has not been determined whether the formation of any specific zirconolite structure (i.e. 2M, 3 T) will result in improved performance in the disposal environment.
- **Charge compensation species**: The incorporation of high valence cation (e.g. Ce^{4+}/U^{6+}) within the Ca^{2+} site in zirconolite can be achieved by the accommodation of a lower valence cation within the Ti^{4+} site in a ratio sufficient to offset any apparent excess charge. A host of charge compensation species have been utilised in various studies,

including Mg^{2+}, Al^{3+}, Fe^{3+}, and Nb^{5+}. There is a need for a systematic evaluation as to whether any of these charge compensation species may afford increased durability relative to one another.

- **The use of chemical surrogates**: It has been highlighted that the use of chemical surrogates is necessary the development of wasteforms for actinides. Nevertheless, no surrogate species can sufficiently reproduce the chemical and physical properties required to reproduce Pu behaviour to a satisfactory level. The problems associated with Ce have been highlighted, and the tendency of Ce to undergo auto-reduction to Ce^{3+} at high temperatures has been demonstrated to promote the formation of undesirable secondary phases such as perovskite, making the elicitation of Ce release rates from the zirconolite phase difficult. The use of surrogates across the literature is typically limited to the use of a single analogous species, it is therefore necessary to use several surrogates in conjunction to allow a suite of behaviours analogous to Pu to be evaluated. As Pu exhibits a range of oxidation states, a multi-surrogate approach should be undertaken, with elements displaying a strong preference for (III) and (IV) oxidation states, that are relatively insensitive to imposed redox conditions. Furthermore, a detailed, systematic investigation of surrogates in the zirconolite system is necessary to support the safety case for geological disposal.
- **Processing methods:** Zirconolite is relatively unstable under reducing conditions, often resulting in the formation of parasitic perovskite phases that are determined to reduce the overall chemical durability of the wasteform. When assessing the durability of zirconolite compositions, variations in atmospheric processing conditions, synthesis temperature, and synthesis route (e.g. cold sintering, hot pressing, hot isostatic pressing) must be taken into consideration. As a result, it is difficult meaningful comparisons between data published regarding the synthesis and aqueous durability of zirconolite wasteforms for Pu immobilisation.

Conclusions

The zirconolite wasteform is currently a candidate host phase for Pu, should U.K. Government policy adopt a strategy of immobilisation and disposal of the bulk inventory. Zirconolite chemistry permits the acceptance of a wide variety of REE^{3+}/Ac^{4+} (U^{4+}, $Pu^{3+/4+}$, Th^{4+}, $Ce^{3+/4+}$, Sm^{3+}) within solid solution, alongside a considerable selection of charge balancing species (Al^{3+}, Mg^{2+}, Fe^{3+}, Nb^{5+}) for the formation of heterovalent compositions, and neutron poison species (Gd^{3+}, Hf^{4+}). A review of the literature has identified that the incorporation of Pu^{4+} may be best achieved by homovalent substitution for Zr^{4+}, and/or heterovalent substitution for Ca^{2+}, with the addition of a suitable charge balancing species such as Al^{3+} or Mg^{2+}. In the case of the former mechanism, the substitution would likely be facilitated by the formation of the polytypical zirconolite-4M structure above 0.15 f.u. Pu^{4+}, a hybrid intergrowth between the nominal $CaZrTi_2O_7$ aristotype and the $CaPuTi_2O_7$ pyrochlore-structured phase. However, it is apparent that the 2M polytype may be stabilised over a wider solid solution range when favouring substitution for Ca^{2+}, with appropriate charge compensation. The formation of deleterious secondary phases such as perovskite is shown to be dependent on the method of substitution utilised and the valence of the surrogate element, which is in turn is controlled by processing conditions rather than crystallographic design. A survey of the literature confirms zirconolite exhibits exceptional chemical durability with normalised release rates for constituent elements typically of the order 10^{-5} to 10^{-8} $gm^{-2}{\cdot}d^{-1}$ under simulated disposal conditions.

Acknowledgements

We acknowledge financial support from the Nuclear Decommissioning Authority (NDA) and EPSRC under grant numbers EP/S01019X/1, EP/S011935/1, EP/S020659/1, EP/P013600/1 and EP/R511754/1. This research utilised the HADES/MIDAS facility at the University of Sheffield established with financial support from EPSRC and BEIS [139].

Disclosure statement

No potential conflict of interest was reported by the author (s).

Funding

We acknowledge financial support from the Nuclear Decommissioning Authority (NDA) and EPSRC under grant numbers EP/S01019X/1, EP/S011935/1, EP/S020659/1, EP/P013600/1 and EP/R511754/1.

ORCID

Lewis R. Blackburn http://orcid.org/0000-0002-5889-2035
Laura J. Gardner http://orcid.org/0000-0003-3126-2583
Neil C. Hyatt http://orcid.org/0000-0002-2491-3897

References

[1] Donald IW. Waste immobilization in glass and ceramic based hosts. Chichester: Wiley; 2010.
[2] Ojovan MI, Lee WE. An Introduction to nuclear waste immobilisation. 1st ed. Oxford: Elsevier; 2005.

[3] Oh Chang H. Hazardous and radioactive waste treatment technologies handbook. Boca Raton: CRC Press; 2001.
[4] Ojovan MI, Batyukhnova OG. Glasses for nuclear waste immobilization, In WM '07 Conference, Tuscon, AZ. 2007. p. 15.
[5] Lopez C, Deschanels X, Den Auwer C, et al. X-ray absorption studies of borosilicate glasses containing dissolved actinides or surrogates. Phys Scr. 2005; T115:342–345.
[6] Cachia J, Deschanels X, Den Auwer C, et al. Enhancing cerium and plutonium solubility by reduction in borosilicate glass. J Nucl Mater. 2006;352:182–189. doi:10.1016/j.jnucmat.2006.02.052.
[7] Lopez C, Deschanels X, Bart JM, et al. Solubility of plutonium surrogates in nuclear glasses. In Scientific Research on the Back-End of the Fuel Cycle for the 21. Century, Avignon, France. 2000. p. 1–5.
[8] Wellman DM, Icenhower JP, Weber WJ. Elemental dissolution study of Pu-bearing borosilicate glasses. J Nucl Mater. 2005;340:149–162. doi:10.1016/j.jnucmat.2004.10.166.
[9] Lutze W, Ewing RC. Radioactive wasteforms for the future. Amsterdam: North Holland Physics Publishing; 1988.
[10] Corkhill CL, Hyatt NC. Nuclear waste management. Bristol, UK: IOP Publishing; 2018.
[11] McMaster SA, Ram R, Faris N, et al. Radionuclide disposal using the pyrochlore supergroup of minerals as a host matrix – a review. J Hazard Mater. 2018;360:257–269. doi:10.1016/j.jhazmat.2018.08.037.
[12] Harrison MT, Scales CR. Durability of borosilicate glass compositions for the immobilisation of the UK's separated plutonium stocks. Mater Res Soc Symp Proc. Pittsburgh, PA. 2008;1107.
[13] Lee WE, Ojovan MI, Stennett MC, et al. Immobilisation of radioactive waste in glasses, glass composite materials and ceramics. Adv Appl Ceram. 2006;105(1):3–12. doi:10.1179/174367606X81669.
[14] Ewing RC. Ceramic matrices for plutonium disposition. Prog Nucl Energy. 2007;49:635–643. doi:10.1016/j.pnucene.2007.02.003.
[15] Ewing RC. Nuclear waste forms for actinides. Proc Natl Acad Sci USA. 1999;96:3432–3439. doi:10.1073/pnas.96.7.3432.
[16] Wang L, Liang T. Ceramics for high level radioactive waste solidification. J Adv Ceram. 2012;1(3):194–203. doi:10.1007/s40145-012-0019-8.
[17] Weber WJ, Navrotsky A, Stefanovsky S, et al. Materials Science of high-level Immobilization. MRS Bull. 2009;34(01):46–52.
[18] Stewart M, Begg B, Day R, et al. Low-risk alternative waste forms for actinide immobilization. In WM'05 Conference, Tuscon, AZ. 2004.
[19] Gray LW, Kan T, Mckibbert JM. Immobilization as a route to surplus fissile materials disposition, vol. UCRL-JC–1, Lansdowne, VA. 1996.
[20] Burakov BE, Ojovan MI, Lee WE. Crystalline materials for actinide immobilisation. 1st ed. London, UK: Imperial College Press; 2011.
[21] Lumpkin GR. Ceramic waste forms for actinides. Elements. 2006;2(6):365–372. doi:10.2113/gselements.2.6.365.
[22] Orlova AI, Ojovan MI. Ceramic mineral waste-forms for nuclear waste immobilization. Materials (Basel). 2019;12(16):2638, doi:10.3390/ma12162638.
[23] Hart KP, Zhang Y, Loi E, et al. Aqueous durability of titanate ceramics designed to immobilise excess plutonium. Mat Res Soc Symp Proc. 2000;608:353–358.
[24] Vance ER, Agrawal DK. Incorporation of radionuclides in crystalline titanates. Nucl Chem Waste Manag. 1982;3(4):229–234. doi:10.1016/0191-815X(82)90004-3.
[25] Strachan DM, Scheele RD, Buck EC, et al. Radiation damage effects in candidate titanates for Pu disposition: zirconolite. J Nucl Mater. 2008;372(1):16–31. doi:10.1016/j.jnucmat.2007.01.278.
[26] Vance ER, Angel PJ, Begg BD, et al. Zirconolite-rich titanate ceramics for high-level actinide wastes. Mat Res Soc Symp Proc. 1994;333:293–298.
[27] Zhang FX, Manoun B, Saxena SK. Pressure-induced order-disorder transitions in pyrochlore $RE_2Ti_2O_7$ (RE = Y, Gd). Mater Lett. 2006;60(21–22):2773–2776. doi:10.1016/j.matlet.2006.01.095.
[28] Kong L, Zhang Y, Karatchevtseva I. Preparation of $Y_2Ti_2O_7$ pyrochlore glass-ceramics as potential waste forms for actinides: the effects of processing conditions. J Nucl Mater. 2017;494:29–36. doi:10.1016/j.jnucmat.2017.07.004.
[29] Wei T, Zhang Y, Kong L, et al. Hot isostatically pressed $Y_2Ti_2O_7$ and $Gd_2Ti_2O_7$ pyrochlore glass-ceramics as potential waste forms for actinide immobilization. J Eur Ceram Soc. 2019;39(4):1546–1554. doi:10.1016/j.jeurceramsoc.2018.11.012.
[30] Lang M, Zhang F, Zhang J, et al. Review of $A_2B_2O_7$ pyrochlore response to irradiation and pressure. Nucl Instrum Methods Phys Res B: Beam Interact Mater At. 2010;268(19):2951–2959. doi:10.1016/j.nimb.2010.05.016.
[31] Cleave A, Grimes RW, Sickafus K. Plutonium and uranium accommodation in pyrochlore oxides. Philos Mag. 2005;85(9):967–980. doi:10.1080/14786430412331314672.
[32] Wang L, Xie H, Chen Q, et al. Study on the solubility of uranium in the pyrochlore lattice of $Nd_2Zr_2O_7$. Mater Sci. 2015;5(4):184–190.
[33] Lumpkin GR, Hart KP, McGlinn PJ, et al. Retention of actinides in natural pyrochlores and zirconolites. Radiochim Acta. 1994;66/67:469–474.
[34] Zhang Y, Li H, Moricca S. Pyrochlore-structured titanate ceramics for immobilisation of actinides: hot isostatic pressing (HIPing) and stainless steel/waste form interactions. J Nucl Mater. 2008;377:470–475. doi:10.1016/j.jnucmat.2008.03.022.
[35] McMaster SA, Ram R, Charalambous F, et al. Synthesis and characterisation of the uranium pyrochlore betafite $[(Ca,U)_2(Ti,Nb,Ta)_2O_7]$. J Hazard Mater. 2014;280:478–486. doi:10.1016/j.jhazmat.2014.07.062.
[36] Ewing RC, Weber WJ, Lian J. Nuclear waste disposal-pyrochlore ($A_2B_2O_7$): nuclear waste form for the immobilization of plutonium and 'minor' actinides. J Appl Phys. 2004;95(11):5949–5971. doi:10.1063/1.1707213.
[37] Ewing RC, Lutze W. Zircon: a host-phase for the disposal of weapons plutonium. J Mater Res. 1995;10(2):243–246. doi:10.1557/JMR.1995.0243.
[38] Cherniak DJ. Diffusion of helium in radiation-damaged zircon. Chem Geol. 2019;529. doi:10.1016/j.chemgeo.2019.119308.

[39] Ding Y, Lu X, Dan H, et al. Phase evolution and chemical durability of Nd-doped zircon ceramics designed to immobilize trivalent actinides. Ceram Int. 2015;41(8):10044–10050. doi:10.1016/j.ceramint.2015.04.092.

[40] Xie Y, Fan L, Shu X, et al. Chemical stability of Ce-doped zircon ceramics: influence of pH, temperature and their coupling effects. J Rare Earths. 2017;35(2):164–171. doi:10.1016/S1002-0721(17)60895-0.

[41] Horie K, Hidaka H, Gauthier-Lafaye F. Elemental distribution in apatite, titanite and zircon during hydrothermal alteration: durability of immobilization mineral phases for actinides. Phys Chem Earth. 2008;33(14–16):962–968. doi:10.1016/j.pce.2008.05.008.

[42] Trocellier P, Delmas R. Chemical durability of zircon. Nucl Instrum Methods Phys Res B: Beam Interact Mater At. 2001;181:408–412. doi:10.1016/S0168-583X(01)00377-9.

[43] Thomé L, Gentils A, Jagielski J, et al. Radiation stability of ceramics: test cases of zirconia and spinel. Vacuum. 2007;81(10):1264–1270. doi:10.1016/j.vacuum.2007.01.021.

[44] Yu N, Sickafus KE, Kodali P, et al. In situ observation of defect growth beyond the irradiated region in yttria-stabilized zirconia induced by 400 keV xenon ion-beam at –90 and 30°C. J Nucl Mater. 1997;244:266–272.

[45] Yasuda K, Kinoshita C, Matsumura S, et al. Radiation-induced defect clusters in fully stabilized zirconia irradiated with ions and/or electrons. J Nucl Mater. 2003;319:74–80. doi:10.1016/S0022-3115(03)00136-3.

[46] Costantini JM, Beuneu F, Weber WJ. Radiation damage in cubic-stabilized zirconia. J Nucl Mater. 2013;440(1–3):508–514. doi:10.1016/j.jnucmat.2013.02.041.

[47] Burakov BE, Yagovkina MA. A study of accelerated radiation damage effects in PuO_2 and gadolinia-stabilized cubic zirconia, $Zr_{0.79}Gd_{0.14}Pu_{0.07}O_{1.93}$, doped with ^{238}Pu. J Nucl Mater. 2015;467:534–536. doi:10.1016/j.jnucmat.2015.10.032.

[48] Kulkarni NK, Sampath S, Venugopal V. Studies on stabilised zirconia as host phase for the fixation of actinides, rare-earths and sodium. Ceram Int. 2001;27(8):839–846. doi:10.1016/S0272-8842(01)00038-4.

[49] Ding Y, Dan H, Lu X, et al. Phase evolution and chemical durability of $Zr_{1-x}Nd_xO_{2-x/2}$ ($0 \le x \le 1$) ceramics. J Eur Ceram Soc. 2017;37(7):2673–2678. doi:10.1016/j.jeurceramsoc.2017.02.053.

[50] Gilbert M, Davoisne C, Stennett M, et al. Krypton and helium irradiation damage in neodymium–zirconolite. J Nucl Mater. Sep. 2011;416(1–2):221–224. doi:10.1016/J.JNUCMAT.2010.11.089.

[51] Li W, Dong F, Bian L, et al. Phase relations, microstructure, and valence transition studies on $CaZr_{1-x}Ce_xTi_{2-}O_7$ ($0.0 \le x \le 1.0$) system. J Rare Earths. 2018;36(11):1184–1189. doi:10.1016/j.jre.2018.04.006.

[52] Gatehouse BM, Grey IE, Hill RJ, et al. Zirconolite, $CaZr_xTi_{3-x}O_7$; structure refinements for near-end-member compositions with x = 0.85 and 1.30. Acta Cryst. 1981;B37(1974):306–312. doi:10.1107/S0567740881002914.

[53] Deschanels X, Broudic V, Jegou C, et al. Pu-doped zirconolite for minor actinide containment. ATALANTE. 2004;2004:1–6.

[54] Bohre A, Avasthi K, Shrivastava OP. Synthesis, characterization, and crystal structure refinement of lanthanum and yttrium substituted polycrystalline 2M type zirconolite phases: $Ca_{1-x}M_xZrTi_2O_7$ (M = Y, La and x = 0.2),. J Powder Technol. 2014;2014:1–10. doi:10.1155/2014/902317.

[55] Vance ER, Lumpkin GR, Carter ML, et al. Incorporation of uranium in zirconolite ($CaZrTi_2O_7$). J Am Ceram Soc. 2002;85(7):1853–1859. doi:10.1111/j.1151-2916.2002.tb00364.x.

[56] Clark BM, Sundaram SK, Misture ST. Polymorphic transitions in cerium-substituted zirconolite ($CaZrTi_2O_7$). Sci Rep. 2017;7(1):2–10. doi:10.1038/s41598-017-06407-5.

[57] Caurant D, Loiseau P, Bardez I. Structural characterization of Nd-doped Hf-zirconolite $Ca_{1-x}Nd_xHfTi_{2-x-}Al_xO_7$ ceramics. J Nucl Mater. 2010;407(2):88–99. doi:10.1016/j.jnucmat.2010.09.033.

[58] Salamat A, McMillan PF, Firth S, et al. Structural transformations and disordering in zirconolite ($CaZrTi_2O_7$) at high pressure. Inorg Chem. 2013;52:1550–1558. doi:10.1021/ic302346g.

[59] Hyatt NC, Stennett MC, Maddrell ER, et al. Single phase ceramic wasteforms for plutonium disposition. Adv Sci Technol. 2006;45(2006):2004–2011. doi:10.4028/www.scientific.net/ast.45.2004.

[60] Thornber S, Stennett MC, Hyatt NC. Investigation of Ce incorporation in zirconolite glass-ceramics for UK plutonium disposition. In 2016 MRS Fall Meeting, Boston, MA. 2016.

[61] Bailey DJ, Lawson SM, Sun SK, et al. A new approach to the immobilisation of technetium and transuranics: Co-disposal in a zirconolite ceramic matrix. J Nucl Mater. 2019;528:151885, doi:10.1016/j.jnucmat.2019.151885.

[62] Sun S-K, Stennett MC, Corkhill CL, et al. Reactive spark plasma synthesis of $CaZrTi_2O_7$ zirconolite ceramics for plutonium disposition. J Nucl Mater. 2018 Mar;500:11–14. doi:10.1016/J.JNUCMAT.2017.12.021.

[63] Kong L, Karatchevtseva I, Chironi I, et al. Cazrti$_2$o$_7$ zirconolite synthesis: from ceramic to glass-ceramic. Int J Appl Ceram Technol. 2019;16(4):1460–1470. doi:10.1111/ijac.13203.

[64] Ma S, Ji S, Liao C, et al. Effects of ionic radius on phase evolution in Ln-Al co-doped $Ca_{1-x}Ln_xZrTi_{2-x-}Al_xO_7$ (Ln = La, Nd, Gd, Ho, Yb) solid solutions. Ceram Int. 2018;44(13):15124–15132. doi:10.1016/j.ceramint.2018.05.149.

[65] Arinicheva Y, Gausse C, Neumeier S, et al. Influence of temperature on the dissolution kinetics of synthetic $LaPO_4$-monazite in acidic media between 50 and 130 °C. J Nucl Mater. 2018;509:488–495. doi:10.1016/j.jnucmat.2018.07.009.

[66] Meng C, Ding X, Zhao J, et al. Preparation and characterization of cerium-gadolinium monazites as ceramics for the conditioning of minor actinides. Prog Nucl Energy. 2016;89:1–6. doi:10.1016/j.pnucene.2016.01.021.

[67] Schlenz H, Dellen J, Kegler P, et al. Structural and thermodynamic mixing properties of $La_{1-x}Nd_xPO_4$ monazite-type solid solutions. J. Solid State Chem. 2019;270(November 2018):470–478. doi:10.1016/j.jssc.2018.11.040.

[68] Rawat D, Phapale S, Mishra R, et al. Thermodynamic investigation of thorium and strontium substituted monazite solid-solution. Thermochim Acta.

2019;674(April 2018):10–20. doi:10.1016/j.tca.2019.01.031.
[69] Brandt F, Neumeier S, Schuppik T, et al. Conditioning of minor actinides in lanthanum monazite ceramics: a surrogate study with europium. Prog Nucl Energy. 2014;72:140–143. doi:10.1016/j.pnucene.2013.07.019.
[70] Heuser J, Bukaemskiy AA, Neumeier S, et al. Raman and infrared spectroscopy of monazite-type ceramics used for nuclear waste conditioning. Prog Nucl Energy. 2014;72:149–155. doi:10.1016/j.pnucene.2013.09.003.
[71] Gausse C, Szenknect S, Mesbah A, et al. Dissolution kinetics of monazite $LnPO_4$ (Ln = La to Gd): a multi-parametric study. Appl Geochemistry. 2018;93(April):81–93. doi:10.1016/j.apgeochem.2018.04.005.
[72] Zhao X, Li Y, Teng Y, et al. The effect of Ce content on structure and stability of $Gd_{1-x}Ce_xPO_4$: theory and experiment. J Eur Ceram Soc. 2019;39(4):1555–1563. doi:10.1016/j.jeurceramsoc.2018.11.009.
[73] Clavier N, Mesbah A, Szenknect S, et al. Monazite, rhabdophane, xenotime & churchite: vibrational spectroscopy of gadolinium phosphate polymorphs. Spectrochim Acta A: Mol Biomol Spectrosc. 2018;205:85–94. doi:10.1016/j.saa.2018.07.016.
[74] Zhao X, Li Y, Teng Y, et al. The structure properties, defect stability and excess properties in Am-doped $LnPO_4$ (Ln = La, Ce, Nd, Sm, Eu, Gd) monazites. J Alloys Compd. 2019;806:113–119. doi:10.1016/j.jallcom.2019.07.251.
[75] Proust V, Jeannin R, White FD, et al. Tailored perovskite waste forms for plutonium trapping. Inorg Chem. 2019;58(5):3026–3032. doi:10.1021/acs.inorgchem.8b02832.
[76] Kastrissos T, Stephenson M, Turner P, et al. Hydrothermal dissolution of perovskite ($CaTiO_3$): implications for synroc formulation. J Am Ceram Soc. 1987;70(7):144–146. doi:10.1007/BF01161185.
[77] Davoisne C, Stennett MC, Hyatt NC, et al. Krypton irradiation damage in Nd-doped zirconolite and perovskite. J Nucl Mater. 2011;415(1):67–73. doi:10.1016/j.jnucmat.2011.05.043.
[78] Begg B, Vance E, Conradson S. The incorporation of plutonium and neptunium in zirconolite and perovskite. J Alloys Compd. 1998;271–273:221–226. doi:10.1016/S0925-8388(98)00058-9.
[79] Begg BD, Zhang Y, Vance ER, et al. Effect of Pu valence on acid dissolution of perovskite ($CaTiO_3$). AIP Conf Proc. 2003;673:131–132. doi:10.1063/1.1594577.
[80] Begg BD, Vance ER, Lumpkin GR. Charge compensation and the incorporation of cerium in zirconolite and perovskite. Mat Res Soc Symp Proc. 1998;506:79–86. doi:10.1557/PROC-506-79.
[81] Pham DK, Neall FB, Myhra S, et al. Dissolution mechanisms of $CaTiO_3$ – solution analysis, surface analysis and electron microscope studies – implications for synroc. Mat Res Soc Symp Proc. 1989;127:231–240.
[82] Zhang Y, Karatchevtseva I, Qin M, et al. Raman spectroscopic study of natural and synthetic brannerite. J Nucl Mater. 2013;437(1–3):149–153. doi:10.1016/j.jnucmat.2013.02.004.
[83] Zhang Y, Lumpkin GR, Li H, et al. Recrystallisation of amorphous natural brannerite through annealing: the effect of radiation damage on the chemical durability of brannerite. J Nucl Mater. 2006;350(3):293–300. doi:10.1016/j.jnucmat.2006.01.012.
[84] Zhang Y, Thomas BS, Lumpkin GR, et al. Dissolution of synthetic brannerite in acidic and alkaline fluids. J Nucl Mater. 2003;321(1):1–7. doi:10.1016/S0022-3115(03)00203-4.
[85] Stennett MC, Freeman CL, Gandy AS, et al. Crystal structure and non-stoichiometry of cerium brannerite: $Ce_{0.975}Ti_2O_{5.95}$. J Solid State Chem. 2012;192:172–178. doi:10.1016/j.jssc.2012.03.057.
[86] James M, Carter ML, Watson JN. The synthesis, crystal chemistry and structures of Y-doped brannerite ($U_{1-x}Y_xTi_2O_6$) and thorutite ($Th_{1-x}Y_xTi_2O_{6-\delta}$) phases. J Solid State Chem. 2003;174(2):329–333. doi:10.1016/S0022-4596(03)00230-5.
[87] Bailey DJ, Stennett MC, Ravel B, et al. Synthesis and characterisation of brannerite compositions $(U_{0.9}Ce_{0.1})_{1-x}M_xTi_2O_6$ ($M = Gd^{3+}$, Ca^{2+}) for the immobilisation of MOX residues. RSC Adv. 2018;8(4):2092–2099. doi:10.1039/C7RA11742F.
[88] Valeš V, Matějová L, Matěj Z, et al. Crystallization kinetics study of cerium titanate $CeTi_2O_6$. J Phys Chem Solids. 2014;75(2):265–270. doi:10.1016/j.jpcs.2013.10.001.
[89] Gilligan R, Nikoloski AN. The extraction of uranium from brannerite – a literature review. Miner Eng. 2015;71:34–48. doi:10.1016/j.mineng.2014.10.007.
[90] Lumpkin GR, Leung SHF, Ferenczy J. Chemistry, microstructure, and alpha decay damage of natural brannerite. Chem Geol. 2012;291:55–68. doi:10.1016/j.chemgeo.2011.09.008.
[91] Lumpkin GR, Gao Y, Gieré R, et al. The role of Th-U minerals in assessing the performance of nuclear waste forms. Mineral Mag. 2014;78(5):1071–1095. doi:10.1180/minmag.2014.078.5.01.
[92] Williams CT, Gieré R. Zirconolite: a review of Localities worldwide, and a compilation of its chemical compositions. Bull Nat Hist Museum London. 1996;52:1–24.
[93] Hart KP, Lumpkin GR, Giere R, et al. Naturally-occurring zirconolites – analogues for the long-term encapsulation of actinides in synroc. Radiochim Acta. 1996;74:309–312. doi:10.1524/ract.1996.74.special-issue.309.
[94] Lumpkin GR. Alpha-decay damage and aqueous durability of actinide host phases in natural systems. J Nucl Mater. 2001;289(1–2):136–166. doi:10.1016/S0022-3115(00)00693-0.
[95] McCauley RA, Hummel FA. New pyrochlores of the charge-coupled type. J Solid State Chem. 1980;33(1):99–105. doi:10.1016/0022-4596(80)90552-6.
[96] Farmer JM, Boatner LA, Chakoumakos BC, et al. Structural and crystal chemical properties of rare-earth titanate pyrochlores. J Alloys Compd. 2014;605:63–70. doi:10.1016/j.jallcom.2014.03.153.
[97] Vance ER, Jostsons A, Day RA, et al. Excess Pu disposition in zirconolite-rich synroc. Mat Res Soc Symp Proc. 1996;412:41–47.
[98] Kesson SE, Sinclair WJ, Ringwood AE. Solid solution limits in synroc zirconolite. Nucl Chem Waste Manag. 1983;4:259–265.
[99] Buck EC, Ebbinghaus B, Bakel AJ, et al. Characterization of a Pu-bearing zirconolite-rich synroc. In MRS Fall Meeting, Boston, MA. 1996.
[100] Smith KL, Lumpkin GR, Blackford MG, et al. Characterization and leaching behavior of plutonium-bearing synroc-C. Mat Res Soc Symp Proc. 1997;465:1267–1272.

[101] White TJ, Segall RL, Hutchison JL, et al. Polytypic behaviour of zirconolite. Proc R Soc Lond A. 1984;392:343–358. doi:10.1098/rspa.1936.0060.
[102] Cheary RW, Coelho AA. A site occupancy analysis of zirconolite $CaZr_xTi_{3-x}O_7$. Phys Chem Miner. 1997;24:447–454.
[103] Coelho AA, Cheary RW, Smith KL. Analysis and structural determination of Nd-substituted zirconolite-4M. J Solid State Chem. 1997;129:346–359. doi:10.1006/jssc.1996.7263.
[104] Gilbert MR, Selfslag C, Walter M, et al. Synthesis and characterisation of Pu-doped zirconolites – $(Ca_{1-x}Pu_x)Zr(Ti_{2-2x}Fe_{2x})O_7$. IOP Conf Ser Mater Sci Eng. 2010;9(012007): doi:10.1088/1757-899X/9/1/012007.
[105] Begg BD, Day RA, Brownscombe A. Structural effect of Pu substitutions on the Zr-site in zirconolite. Mat Res Soc Symp Proc. 2001;663:1–8.
[106] Vance ER, Begg BD, Day RA, et al. Zirconolite-rich ceramics for actinide wastes. Mat Res Soc Symp Proc. 1995;353:767–774.
[107] Rossell HJ. Solid solution of metal oxides in the zirconolite phase CaZrTi2O7. II: the ternary phase $CaZr_xTi_{3-x}O_7$. J. Solid State Chem. 1992;99(1):52–57. doi:10.1016/0022-4596(92)90287-6.
[108] Liao CZ, Shih K, Lee WE. Crystal structures of Al-Nd Codoped zirconolite derived from glass matrix and powder sintering. Inorg Chem. 2015;54(15):7353–7361. doi:10.1021/acs.inorgchem.5b00847.
[109] Whittle KR, Hyatt NC, Smith KL, et al. Combined neutron and X-ray diffraction determination of disorder in doped zirconolite-2M. Am Mineral. 2012;97:291–298.
[110] Jafar M, Achary SN, Salke NP, et al. X-ray diffraction and Raman spectroscopic investigations on $CaZrTi_2O_7$ - $Y_2Ti_2O_7$ system: delineation of phase fields consisting of potential ceramic host materials. J Nucl Mater. 2016;475:192–199. doi:10.1016/j.jnucmat.2016.04.016.
[111] Jafar M, Sengupta P, Achary SN, et al. Phase evolution and microstructural studies in $CaZrTi_2O_7$-$Nd_2Ti_2O_7$ system. J Am Ceram Soc. 2014;97(2):609–616. doi:10.1111/jace.12664.
[112] Jafar M, Sengupta P, Achary SN, et al. Phase evolution and microstructural studies in $CaZrTi_2O_7$ (zirconolite)-$Sm_2Ti_2O_7$ (pyrochlore) system. J Eur Ceram Soc. 2014;34(16):4373–4381. doi:10.1016/j.jeurceramsoc.2014.07.001.
[113] Zhang YB, Wang J, Wang JX, et al. Phase evolution, microstructure and chemical stability of $Ca_{1-x}Zr_{1-x}Gd_{2x}Ti_2O_7$ $(0.0 \leq x \leq 1.0)$ system for immobilizing nuclear waste. Ceram Int. 2018;44(12):13572–13579. doi:10.1016/j.ceramint.2018.04.191.
[114] Begg BD, Vance ER. The incorporation of cerium in zirconolite. Mat Res Soc Symp Proc. 1997;465:333–340.
[115] Blackburn LR, Sun S, Gardner LJ, et al. A systematic investigation of the phase assemblage and microstructure of the zirconolite $CaZr_{1-x}Ce_xTi_2O_7$ system. J Nucl Mater. 2020;535:152137, doi:10.1016/j.jnucmat.2020.152137.
[116] Blackburn LR, Gardner LJ, Sun SK, et al. Hot Isostatically pressed zirconolite wasteforms for actinide immobilisation. IOP Conf Ser: Mater Sci Eng. 2020. doi:10.1088/1757-899X/818/1/012010.
[117] Vance ER, Ball CJ, Day RA, et al. Actinide and rare earth incorporation into zirconolite. J Alloys Compd. 1994;213/214:406–409. doi:10.1016/0925-8388(94)90945-8.
[118] Kaur R, Gupta M, Kulriya PK, et al. Phase analysis and reduction behaviour of Ce dopant in zirconolite. J Radioanal Nucl Chem. 2019 Mar. doi:10.1007/s10967-019-06536-3.
[119] Pöml P, Geisler T, Cobos-Sabaté J, et al. The mechanism of the hydrothermal alteration of cerium- and plutonium-doped zirconolite. J Nucl Mater. 2011;410(1–3):10–23. doi:10.1016/j.jnucmat.2010.12.218.
[120] Blackburn LR, Sun S, Lawson SM, et al. Synthesis and characterisation of $Ca_{1-x}Ce_xZrTi_{2-2x}Cr_{2x}O_7$: analogue zirconolite wasteform for the immobilisation of Stockpiled UK plutonium. J Eur Ceram Soc. 2020;40(15):5909–5919. doi:10.1016/j.jeurceramsoc.2020.05.066.
[121] Lumpkin GR, Smith KL, Blackford MG. Partitioning of uranium and rare earth elements in synroc: effect of impurities, metal additive, and waste loading. J Nucl Mater. 1995;224(1):31–42. doi:10.1016/0022-3115(95)00037-2.
[122] Ringwood AE, Oversby VM, Kesson SE, et al. Immobilization of high-level nuclear reactor wastes in synroc: a current appraisal. Nucl Waste Manag. 1981;2:287–305.
[123] Zhang Y, Stewart MWA, Li H, et al. Zirconolite-rich titanate ceramics for immobilisation of actinides - waste form/HIP can interactions and chemical durability. J Nucl Mater. 2009;395:69–74. doi:10.1016/j.jnucmat.2009.09.019.
[124] Li H, Zhang Y, McGlinn PJ, et al. Characterisation of stainless steel-synroc interactions under hot isostatic pressing (HIPing) conditions. J Nucl Mater. 2006;355(1–3):136–141. doi:10.1016/j.jnucmat.2006.05.014.
[125] Dickson FJ, Hawkins KD, White TJ. Calcium uranium titanate – a new pyrochlore. J Solid State Chem. 1989;82(1):146–150. doi:10.1016/0022-4596(89)90234-X.
[126] Shrivastava OP, Kumar N, Sharma IB. Synthesis, characterization and structural refinement of polycrystalline uranium substituted zirconolite $CaZr_{0.9}U_{0.1}Ti_2O_7$. Radiochim Acta. 2006;94(6–7):339–342. doi:10.1524/ract.2006.94.6.339.
[127] Subramani T, Baker J, Xu H, et al. Synthesis, characterization, and enthalpies of formation of uranium substituted zirconolites. ACS Earth Sp Chem. 2020;4(10):1878–1887. doi:10.1021/acsearthspacechem.0c00182.
[128] Begg BD, Vance ER, Day RA, et al. Plutonium and neptunium incorporation in zirconolite. Mater Res Soc Symp – Proc. 1997;465:325–332. doi:10.1557/proc-465-325.
[129] Hyatt NC, Ojovan MI. Special issue: materials for nuclear waste immobilization. Materials (Basel). 2019;12(21), doi:10.3390/ma12213611.
[130] Oversby VA, Ringwood AE. Leach testing of synroc and glass samples at 85 and 200°C. Nucl Chem. Waste Manag. 1981;2:201–206.
[131] Smith KL, Lumpkin GR, Blackford MG, et al. The durability of synroc. J Nucl Mater. 1992;190:287–294. doi:10.1016/0022-3115(92)90092-Y.
[132] Zhang K, Yin D, Peng L, et al. Self-propagating synthesis and CeO_2 immobilization of zirconolite-rich composites using CuO as the oxidant. Ceram Int. 2017;43:1415–1423. doi:10.1016/j.ceramint.2016.10.103.

[133] Meng C, Ding X, Li W, et al. Phase structure evolution and chemical durability studies of Ce-doped zirconolite–pyrochlore synroc for radioactive waste storage. J Mater Sci. 2016;51:5207–5215. doi:10.1007/s10853-016-9822-x.
[134] Wen G, Zhang K, Yin D, et al. Solid-state reaction synthesis and aqueous durability of Ce-doped zirconolite-rich ceramics. J Nucl Mater. 2015;466:113–119. doi:10.1016/j.jnucmat.2015.07.047.
[135] Mcglinn PJ, Hart KP, Loi EH, et al. Ph dependence of the aqueous dissolution rates of perovskite and zirconolite at 90 °C. Mat Res Soc Symp Proc. 1995;353(3):847–854.
[136] Zhang Z, Blackford MG, Lumpkin GR, et al. Aqueous dissolution of perovskite ($CaTiO_3$): effects of surface damage and [Ca^{2+}] in the leachant. J Mater Res. 2005;20(9):2462–2473. doi:10.1557/JMR.2005.0294.
[137] Cai X, Teng Y, Wu L, et al. The synthesis and chemical durability of Nd-doped single-phase zirconolite solid solutions. J Nucl Mater. 2016;479:455–460. doi:10.1016/j.jnucmat.2016.07.042.
[138] Zhang K, Yin D, Xu K, et al. Self-propagating synthesis and characterization studies of Gd-bearing Hf-zirconolite ceramic waste forms. Materials (Basel). 2019;12(1), doi:10.3390/ma12010178.
[139] Hyatt NC, Corkhill CL, Stennett MC, et al. The HADES facility for high activity decommissioning engineering & science : part of the UK National nuclear user facility. IOP Conf Ser: Mater Sci Eng. 2020;818:1–8. doi:10.1088/1757-899X/818/1/012022.

Solid Solution Limits of Plutonium and Neutron Poisons in Zirconolite Ceramics – A Literature Review and Gap Analysis for Immobilisation of UK Pu Inventory

Lewis R. Blackburn[a], Amber R. Mason[a], Shi-Kuan Sun[a,b], Laura J. Gardner[a], Merve Kuman[a], Daniel J. Bailey[a], Martin C. Stennett[a], Ewan R. Maddrell[b], Stephanie M. Thornber[b], Claire L. Corkhill[a] and Neil C. Hyatt[a]

[a]Immobilisation Science Laboratory, University of Sheffield, Department of Materials Science and Engineering, Sir Robert Hadfield Building, Mappin Street, S1 3JD, UK

[b]School of Electromechanical Engineering, Guangdong University of Technology, Guangzhou, 510006, China

[c]National Nuclear Laboratory, Workington, Cumbria, CA14 3YQ, UK

Abstract

Should the decision be made to implement a strategy of disposition for which the majority of the Pu inventory is immobilised through a campaign of Hot Isostatic Pressing (HIP) in a zirconolite matrix, prior to geological disposal, a suite of disposability criteria must be satisfied. Protection and prevention against an inadvertent chain reaction, instigated through long-term degradation of Pu waste packages, post-closure, is imperative, as to ensure the physical longevity of the disposal infrastructure is not compromised, and premature release of fissile material into the near field environment remain unlikely. In the case of ceramic wasteforms, the best means of criticality control may be the co-incorporation of a requisite quantity of a suitable neutron poison, either through co-immobilisation within the host structure, or encapsulation of discrete particles in grain structure. Following an initial screening of a range of potential neutron poisons, we present a preliminary literature-based assessment of the solid solution limits of a number of potential additives (Gd, Hf, Sm, In, Cd, B) in the candidate zirconolite ($CaZrTi_2O_7$) wasteform. A gap analysis is also provided, highlighting key areas that are in need of development to further support the safety case for nuclearized HIP for Pu inventories.

1 Status of UK Owned Pu

Upon completion of domestic reprocessing of spent nuclear fuel (SNF) derived from the civil reactor fleet, the United Kingdom is forecast to accumulate a PuO_2 inventory equivalent to approximately 140 teHM (tonnes-heavy-metal-equivalent) [1]. This inventory is the result of the PUREX reprocessing (plutonium-uranium-reduction-extraction) of spent nuclear fuel (SNF). In the PUREX process, irradiated fuel assemblies are discharged from a reactor, cooled, sheared and dissolved in HNO_3, with Pu/U subsequently recovered in a series of solvent extraction steps. Pu(IV) and Pu(III) nitrates are co-extracted from the aqueous raffinate by complexation with tributyl phosphate (TBP), followed by precipitation as Pu insoluble oxalates $Pu^{4+}(C_2O_4)_3{\cdot}6H_2O$ and $Pu^{3+}{}_2(C_2O_4)_3{\cdot}10H_2O$ *via* the addition of oxalic acid. The precipitated oxalates are subsequently converted to PuO_2 by calcination in either air or inert atmosphere, with calcination temperature and time generally inversely proportional to specific

Corresponding authors: lrblackburn2@sheffield.ac.uk; n.c.hyatt@sheffield.ac.uk

surface area (m^2/g), prior to interim storage awaiting a decision on long term management [2]. The Nuclear Decommissioning Authority (NDA) liable for the continued monitoring and ultimate disposal for all UK owned nuclear material, and as such, is responsible for implementing an effective long-term management strategy that places all Pu inventories beyond reach, whilst satisfying proliferation and safety concerns. Potential routes towards Pu recycling and/or disposal were defined in the Credible Options Analysis, utilising a life cycle approach to outline and evaluate pathways to disposition within the constraints of financial and socioeconomic benefit; safety and compatibility with the disposal environment; readiness and maturity of necessary technology [3]. Several iterations of the Credible Options framework have identified two high level options that are feasible: reuse of the bulk inventory as mixed oxide fuels (MOX), or chemical immobilisation of the inventory in a suitable matrix, ideally utilising a similar continuously operated process, similar to the Waste Vitrification Plant (WVP) used for the immobilisation of high level liquid reprocessing wastes (HLLW) [1]. In either case, it is accepted that the timescales for the implementation of any strategy will be several decades at a minimum, and consideration must be given to the quality and source. A summary of UK Pu stocks taken from Hyatt (2017) is listed in **Table 1**. Regardless of strategy, it is considered that this process may be streamlined by consolidating all Pu inventories at one site (Sellafield Ltd., Cumbria, UK), with the aim of maintaining interim storage awaiting the completion of the Sellafield Product and Residue Store (SPRS). Upon completion, it is envisaged that all Pu containers will be repackaged, and presumably categorized with respect to their condition, prior to storage at SPRS until a defined strategy can be implemented.

Table 1) Civil Pu inventory under UK safeguards (reprinted from Hyatt (2017) [4])

Source	Amount (teHM)
Unirradiated separated plutonium in product stores at reprocessing plants	112.1
Unirradiated separated plutonium in the course of manufacture or fabrication and plutonium contained in unirradiated semi-fabricated or unfinished products at fuel or other fabricating plants of elsewhere	0.8
Plutonium contained in unirradiated MOX fuel or other fabricated products at reactor sites or elsewhere	1.9
Unirradiated separated plutonium held elsewhere	1.5
Unirradiated separated plutonium owned by foreign bodies under UK safeguards	23.0
Total	**146.2**

As of 2019, UK Government placed preference on a strategy based on MOX fuel fabrication, with designation of any portion of the stockpile unsuitable for this purpose as waste. The merits of a MOX fuel-based strategy will not be discussed in this article, the reader is referred to NDA Credible Options strategy publications [5]. Legacy storage of PuO_2 inventories over the past ~ 60 y in unsuitable conditions has resulted in a significant portion (~ 5 t) of the inventory becoming unfit for reuse, due to halide contamination. Radiolytic degradation of the PVC liner used to contain powder PuO_2 inside the can-in-

Corresponding authors: lrblackburn2@sheffield.ac.uk; n.c.hyatt@sheffield.ac.uk

can configuration has resulted in HCl release and subsequent adsorption of Cl^- on the Pu surface [6]. Wastes comprised of separated Pu (both of high purity and contaminated status) will necessitate the need for specifically tailored ceramic and glass-ceramic wasteforms for prompt immobilisation. It is envisaged Pu waste packages will be dispositioned within a geological disposal facility (GDF) alongside remaining HLW inventories.

2 Criticality Safety and the Role of Neutron Poisons in Waste Packages

In order to construct a safety case for the geological disposal of all nuclear wastes in the UK, Radioactive Waste Management Ltd. (RWM), the body responsible for the design, construction and continued operation of the as yet un-sited GDF, is in the process of developing a generic disposal system safety case, with a subset of reports devoted to in-depth evaluation of key aspects of repository safety case. These status reports evidence the science and technology underpinning the deliverability of a GDF, a key aspect of which is a criticality safety assessment of waste packages during transport, GDF operation and post-closure [7]. Generic Criticality Safety Assessments (CSAs), as described by Hicks (2007), are considered for waste packages containing one or more of the following four waste components: irradiated natural and slightly enriched uranium, low enriched uranium, high enriched uranium and separated plutonium [8]. In the interest of brevity, this report will omit discussion of all scenarios apart from the latter case of separated Pu, however the reader is referred to Solano *et al.* (2012) for a comprehensive discussion of criticality control in ILW and SNF waste packages [9].

Criticality control measures guard against an inadvertent self-sustaining chain reaction within immobilised fissile material. During the construction and operational phase of the GDF, waste packages will be transported through civilian areas, delivered to the facility, and placed in a suitable geometrical arrangement in pre-designated areas. The safety of workers and the general public must therefore be ensured by two general approaches: producing waste packages that remain sub-critical by placing an upper-limit of the quantity of fissile material contained within, and by optimizing the physical form of the waste package such that a critical chain reaction is not possible, either through arrangement in specific dimensions and geometry that are capable of mitigating the accumulation and critical mass of fissile material, or through the addition of NP. The condition of criticality is met when radionuclides capable of undergoing fission are arranged in a fixed geometry, such that a self-sustaining chain reaction may occur. This is described by the notation $K_{eff} = 1$, *i.e.* the rate of neutrons produced by per fission and the rate of neutrons lost by absorption, or leakage, is equal to unity. Under this condition, a self-sustaining reaction will occur.

Following the closure of the GDF, criticality assurance may be provided through a series of engineered barriers, providing a layered defense, known as the multi-barrier concept [10]; however, it is accepted that on the timescale of > 10^3 years, water will slowly ingress, resulting in deterioration of the physical containment of waste packages. The release of radioactive material into the near field is inevitable, with the possibility of new configurations that result in criticality. An arrangement of material that is critical

Corresponding authors: lrblackburn2@sheffield.ac.uk; n.c.hyatt@sheffield.ac.uk

would likely produce a rapid increase in temperature and pressure, causing disruption to the surrounding infrastructure, and potentially compromising the structural integrity of the GDF by cracking the surrounding geosphere.

A NP is an additive with a high thermal neutron cross section that may be integrated into a wasteform to reduce the overall neutron flux, thus reducing K_{eff} < 1 and mitigating the possibility of criticality. Inhibiting the neutron flux by inclusion of NP's may also afford the opportunity to increase the upper wasteloading limit, improving the volume footprint of the repository environment and reducing the number of waste packages, in turn reducing the number of handling operations and associated dose uptake to workers. There are a number of candidates that have been proposed as suitable NPs for Pu-containing ceramics, for example Nadykto and Timofeeva (2001) [11] estimated that in the case of thermal neutrons, the NP:Pu nuclei ratio for B, Gd, Cd, Sm and Eu was 1.6, 0.023, 0.45, 0.2 and 0.25, respectively. The addition of the NP to the wasteform could be accomplished in a number of ways. For clarity, the engineering unit operations for a HIP based strategy are illustrated in **Fig. 1**.

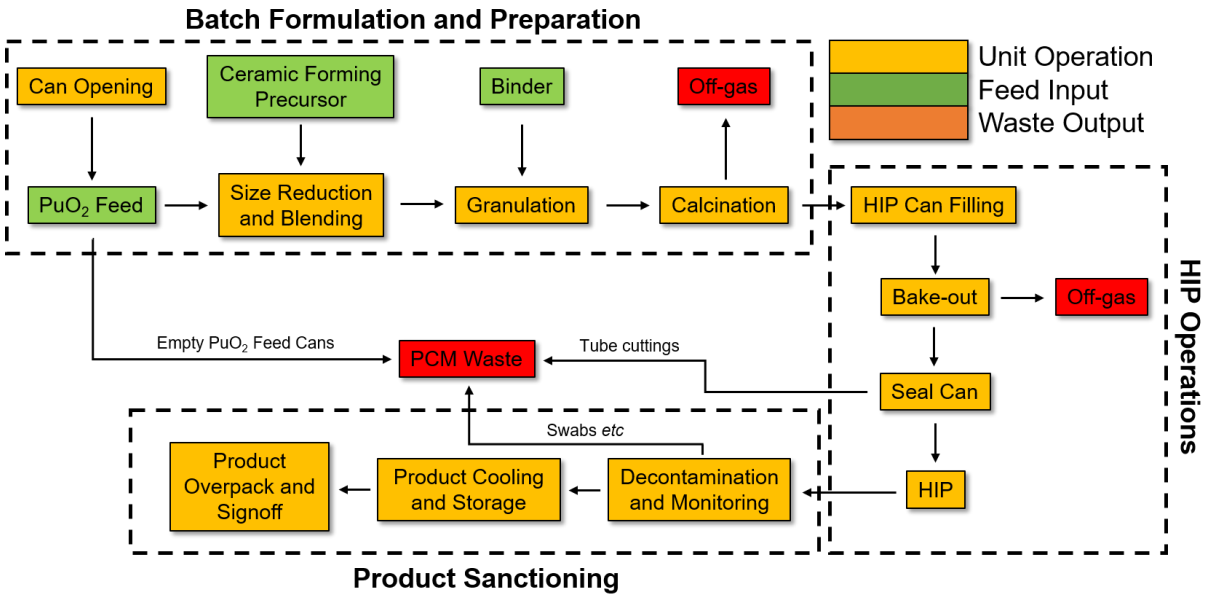

Fig. 1) Overview of primary unit operations associated with HIP immobilisation strategy for Pu

There is not currently a consensus regarding the most effective means of NP addition to a wasteform on an industrial scale, however the addition would likely have to be constrained within the batch formulation and powder preparation stage. There are three options that may be suitable, as they do not require additional handling or unit operations associated with them, and make use of existing pre-treatment parameters that are already essential to the HIP program. The three options are as follows:

Wasteform tailoring - The ceramic composition is tailored such that a pre-determined quantity of NP can be incorporated within the structure, without disrupting the phase assemblage, or resulting in formation of deleterious secondary phases. The addition of trivalent species, *e.g.* Gd^{3+} would necessitate tailoring of the nominal composition to account for excess/deficiency of charge units across

Corresponding authors: lrblackburn2@sheffield.ac.uk; n.c.hyatt@sheffield.ac.uk

the structure. An appropriate amount of NP is added in the oxide form directly to the milling stage as a function of the total wt. % of the waste package (*e.g.* direct addition of 2 wt. % Gd_2O_3). The inactive component of the ceramic precursor would require a pre-treatment stage consisting of homogenization and calcination, prior to addition of the PuO_2. This would be followed by a secondary milling stage to ensure complete oxide dispersion and size reduction to assist the sintering process. In this case, the NP source may be introduced alongside the PuO_2 at the secondary milling stage.

NP encapsulation - The NP additive may be incorporated into the waste microstructure as discrete particles by encapsulation. This may be more applicable for NP additives such as B, which due to its small ionic radius, may not be effectively accommodated in solid solution with the host ceramic phase. In this instance, a compound such as B_4C may be encapsulated at intergranular spaces and triple-points, forming discrete particulates within the microstructure. An additive such as B_4C has an extremely high Vickers hardness, hence in order to distribute homogeneously throughout the microstructure, the feed would have to be comprised of a fine powder that can easily be dispersed, or the process would need to take advantage of an aggressive milling stage.

Granule coating - There may also be potential to utilize the granulation step to contact the NP with a homogenized active precursor, prior to the can filling step, using a fluidized bed granulator. This would involve introduction of a water soluble NP compound, such as $Gd(NO_3)_3$, into the fluidized bed granulator rig to act as a binder. It should be noted that it is of debate whether there is a need for a granulation step in the HIP process, however from the perspective of large scale ceramic processing, it may be necessary to alleviate the difficulties associated with large scale powder flow. The granulation process serves to improve the followability properties of powders with poor handling characteristics, by enlarging primary particle size through agglomeration and coalescence. This is achieved by the introduction of a binder solution, the viscosity of which may greatly influence mean granule diameter, sphericity and compressive strength of the resultant agglomerates. The use of fluidized bed granulation serves to produce low density agglomerates of irregular shape with interstitial space, without mechanical agitation. During the subsequent calcination stage (a step which would be necessary prior to can-filling, irrelevant of an intermediate granulation operation) the temperature (> 600 ˚C) would result in adhesion of Gd_2O_3 nanocrystals to the granule surface, which would then act as the feed into the HIP canister. Nevertheless, this approach may be limited by the accompanied risk of Pu dispersion and glovebox contamination due to the use of the fluidized bed.

3 Review of Zirconolite Chemistry and Evaluation of Potential Solid Solution Regimes for Pu Immobilisation

Technical efforts in the U.K. to identify a suitable wasteform for separated Pu have considered single and multiphase ceramics based on derivatives of the titanate pyrochlore-rich wasteform developed for the U.S. DoE Plutonium Immobilisation Project (PIP); vitrified wasteforms based on variations of borosilicate glass (*e.g.* lanthanide borosilicate (LaBS), alkali-tin silicates (ATS)); encapsulation and

Corresponding authors: lrblackburn2@sheffield.ac.uk; n.c.hyatt@sheffield.ac.uk

dilution of PuO_2 in cementitious wasteforms is still also considered a technically feasible option on the basis of GDF compliance and simplicity [12], [13]. Following several years of inactive trials and deselection, occurring primarily in collaboration between the National Nuclear Laboratory (NNL) and the Immobilisation Science Laboratory (ISL), wasteforms favouring zirconolite has the host Pu phase have been selected as the preferred candidate, and as such a programme of systematic active and inactive trials aiming to maximise Pu wasteloading through tailoring a selection of baseline compositions, and further probe the underlying crystallography of the zirconolite structure, are underway [14]–[17]. Zirconolite (nominally $CaZrTi_2O_7$) is a rare accessory mineral that is present in a wide variety of terrestrial localities, demonstrating an affinity for extensive solid solution with, but not limited to: Mg^{2+}, Al^{3+}, $Fe^{2+/3+}$, Nb^{5+}, Ta^{5+}, Pb^{2+}, U^{4+}, Th^{4+}, $Ce^{3+/4+}$, Pr^{3+}, Gd^{3+}, Sm^{3+} and Nd^{3+} [18]. The ability of zirconolite analogues to incorporate such a wide variety of species, with five distinct cation receptor sites (Ca^{VIII}, Zr^{VII}, $Ti(I)^{VI}$, $Ti(II)^{V}$, $Ti(III)^{VI}$), makes it an ideal candidate for co-immobilisation of separated Pu, lower valence charge compensator cations such as Mg^{2+}, Al^{3+}, and an appropriate amount of a suitable neutron poison (*e.g.* Gd^{3+}) to suppress criticality. Zirconolite (ideally manifested in the form of the archetype 2M structure) has been recognized by NDA as a candidate ceramic phase for UK owned Pu, and as such has commissioned a body of work aiming to systematically validate potential solid solutions using a combination of surrogates (Ce/U/Th). It should also be noted that glass-ceramic wasteforms based on the $CaZrTi_2O_7$ – $Na_2Al_2Si_6O_{16}$ system are also proposed for Cl-contaminated Pu residues [6], [19]–[22]. The idealized zirconolite parent structure crystallizes in monoclinic symmetry (space group C2/c) and is comprised of two distinct cation layers; Ca^{2+} and Zr^{4+} polyhedra are 8 and 7-fold coordinated to oxygen (*i.e.* CaO_8 and ZrO_7), respectively, interspaced by layers of Ti-O polyhedra arranged in a topology closely related to that of hexagonal tungsten bronze (HTB) (see **Fig. 2**). In this theoretical description, Ti occupies three distinct sites within the HTB layer, two of which are 6-fold coordinated to oxygen forming six-membered rings. The remaining Ti is statistically distributed in the center of these rings, in a 50% occupied 5-fold coordinated trigonal bi-pyramidal site. In the zirconolite unit cell, planes of Ca/Zr polyhedra and HTB layers stacked 1:1 along parallel to [001], with HTB positioned at z = 0.25 and z = 0.75 related by a 180˚ rotation, offset along [130]; subsequent modules at z = 0.75 and z = 1.25 are offset in the [1-30] direction [23].

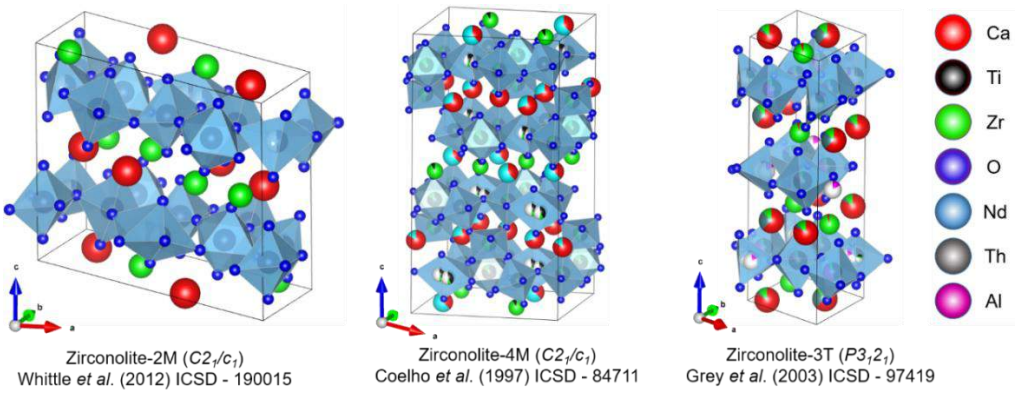

Fig. 2) Crystal structures of zirconolite-2M, 4M and 3T polytypes (images reproduced from the Vesta software using Crystallography Information Files (CIF) from Whittle *et al*. [24], Coelho *et al*. [25] and Grey *et al.* [26])

Corresponding authors: lrblackburn2@sheffield.ac.uk; n.c.hyatt@sheffield.ac.uk

This structure is referred to as zirconolite-2M, with reference to the two layer repeating lamellar structure comprising the monoclinic unit cell. A more comprehensive description is provided by Gatehouse *et al*. in which the zirconolite-2M structure remains stable over the solid solution $CaZr_xTi_{3-x}O_7$ constrained by $0.80 < x < 1.35$ [27], with mixed occupancy of Zr-Ti-O polyhedra also determined to be a function of temperature, between 1350 – 1500 ˚C [25]. Zirconolite structured materials are typically produced by high temperature sintering from a mixture of oxide precursors, and although sintering regimes are typically > 1300 ˚C and > 10 h, there does not seem to be any clear correlation between processing conditions and lattice dimensions. A selection of reported lattice parameters of $CaZrTi_2O_7$ and corresponding processing conditions are listed in **Table 2**. Due to the flexibility of the zirconolite structure, a variety of potential solid solution regimes for Pu immobilisation have been identified, both from survey of available literature, and hypothesized based on feasible (charge balanced) substitutions (**Table 3**). Depending on the substitution mechanism, and prevailing oxygen fugacity during the sintering process, zirconolite may crystallize in several distinct polytypes, characterized in principle by variation in stacking sequence of Ca/Zr and HTB layers. For example, the incorporation of > 0.15 f.u. of M^{4+} (Ce/U/Pu) promotes the formation of the zirconolite-4M polytype, described by Coelho *et al*. as a four-layer intergrowth of zirconolite-2M and pyrochlore-type modules, resulting in a doubling of the zirconolite unit cell along the c* axis [23]. The stacking of these modules is visualized in **Fig. 3**. Zirconolite-4M may also form as a result of near equimolar accommodation of trivalent species within the Ca^{2+} and Zr^{4+} sites, *i.e.* zirconolite-4M is essentially an intermediate phase between $CaZrTi_2O_7$ (zirconolite) and $REE^{3+}{}_2Ti_2O_7$ (pyrochlore) end-members [28]. Heavily disordered substitution regimes such targeting accommodation of M^{3+} and M^{4+} species between Ca^{2+} and Ti^{4+} sites may also result in the formation of more exotic polytypes, such as zirconolite-3T (trigonal unit cell, space group: Pbnm) or zirconolite-3O (orthorhombic unit cell, space group: Acam). For a comprehensive discussion of zirconolite polytypism, the reader is referred to White (1984) [29]. Generally, substitution schemes for entry of Pu^{4+} within the Ca^{2+} site is facilitated by a charge coupled substitution, by which a lower valence cation such as M = Fe^{3+}/Al^{3+} is accommodated within the Ti^{4+} site [30]. As stated, a simple isovalent substitution for Zr^{4+} has also been demonstrated and may allow greater wasteloading, however this results in a phase assemblage dominated by zirconolite-4M, using both Ce/U surrogates and indeed Pu [17], [31], [32].

Table 2) Reported unit cell parameters for zirconolite polytypes

Structure	**a** (Å)	**b** (Å)	**c** (Å)	**β** (˚)	Space Group	Origin	Ref.
2M	12.4435	7.2735	11.3748	10.563	C2/c	Synthetic	[15]
4M	12.553	7.248	23.081	84.799	C2/c	Synthetic	[23]
3T	7.228	-	16.805	-	$P3_121$	Synthetic	[26]
3O	10.31	14.48	7.41	-	Acam	Natural	[33]

Several of these solid solution regimes would necessitate Pu to be present as Pu^{3+}. This may not prove feasible, as it may involve conversion of the PuO_2 into Pu_2O_3 prior to ceramic processing, incurring

Corresponding authors: lrblackburn2@sheffield.ac.uk; n.c.hyatt@sheffield.ac.uk

additional feed preparation steps. The conversion of Pu^{3+} within the wasteform, *e.g.* through use of strongly reducing conditions during sintering will also likely drive the formation of deleterious accessory phases such as $CaTiO_3$. Furthermore, $CaTiO_3$ has demonstrated an affinity for trivalent M^{3+} incorporation, and has demonstrated a markedly lower chemical durability that the zirconolite phase, hence may significantly reduce overall wasteform performance through uptake and subsequent release of Pu^{3+} from $CaTiO_3$ [34]–[36].

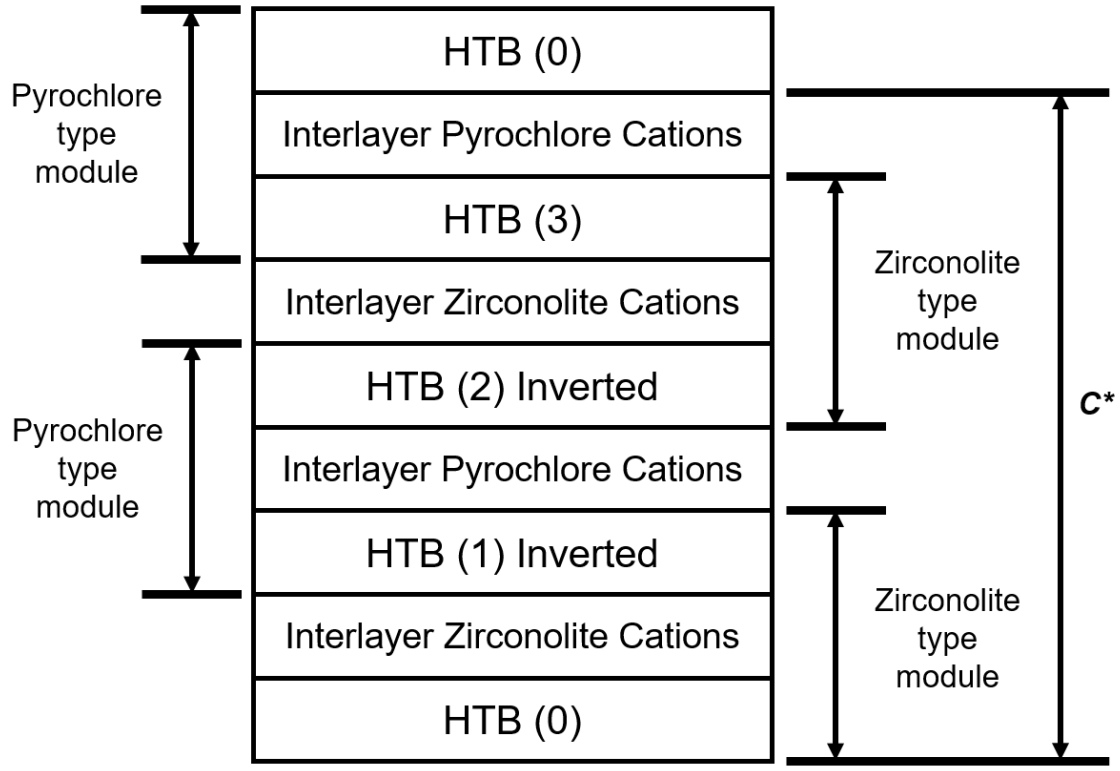

Fig. 3) Zirconolite-4M cation layers described by Coelho *et al*. (redrawn from [23])

Corresponding authors: lrblackburn2@sheffield.ac.uk; n.c.hyatt@sheffield.ac.uk

Table 3) List of feasible solid solution regimes for Pu in zirconolite and summary of expected polytype fields

Solid Solution Regime	Comments	References
$\mathbf{CaZr_{1-x}Pu^{4+}_xTi_2O_7}$	This system exhibits a polymorphic transition to 4M in the interval $0.10 \leq x \leq 0.20$. This has been demonstrated in several key works using Ce/U/Pu. A mixture of zirconolite-2M and zirconolite-4M could be expected in the compositional interval $0.20 \leq x \leq 0.40$. Zirconolite-4M is rarely stabilized as a single phase and exists over a narrow compositional range $0.40 \leq x \leq 0.50$, commonly twinned with pyrochlore. Transformation to the pyrochlore structure is common around $x = 0.60$, with solid solution limits of CeO_2 defined at $x \sim 0.80$ (this could also be expected for UO_2 and PuO_2).	[14], [17], [31], [32], [37], [38]
$\mathbf{Ca_{1-x}Pu^{4+}_xZrTi_{2-2x}M^{3+}_{2x}O_7}$	This solid solution appears to be the most common method of substitution, by which Ce/U/Pu are substituted within the Ca^{2+} site, and charge balanced by a small lower valence cation exchanged for Ti^{4+} (typically Al^{3+}, Fe^{3+}, Cr^{3+} or Mg^{2+}. *Note: in the case of Mg^{2+} the nominal composition becomes $Ca_{1-x}Pu_xZrTi_{2-x}Mg_xO_7$*). Zirconolite-2M phase is typically formed near single phase in the compositional range $0.00 \leq x \leq 0.20$, with secondary perovskite commonly observed for Ce surrogate compositions due to partial Ce^{3+} speciation. At elevated wasteloading (*i.e.* towards $x = 0.35$) free oxides may be observed. Furthermore, the dominant zirconolite polytype at extended wasteloading appears to be controlled by choice of M^{3+} species. For example, $Ca_{0.65}Ce_{0.35}ZrTi_{1.30}Cr_{0.70}O_7$ was reported as zirconolite-2M by Blackburn *et al*., yet the corresponding $Ca_{0.65}Pu_{0.35}ZrTi_{1.30}Fe_{0.70}O_7$ composition was reported as zirconolite-3T by Gilbert *et al*. This may be attributed to the different redox and/or site occupancy behavior between Ce/Pu, and/or ionic radii of Cr/Fe.	[15], [31], [39]–[44]
$\mathbf{Ca_{1-x}Pu^{3+}_xZrTi_{2-x}M^{3+}_xO_7}$	Systematic studies in the $Ca_{1-x}Ln_xZrTi_{2-x}(Al,Fe)_xO_7$ system have been reported for Ln = La, Nd, Gd, Ho and Yb, which may act as Pu^{3+} surrogates. The phase evolution of these ceramics is seemingly dictated by ionic radii, with increased solubility for smaller cations such as Gd^{3+}. Polytype transformation to zirconolite-3O could be expected at elevated substitution ($x = 0.60$) for some Ln^{3+} surrogates (*e.g.* Nd) but 2M phase stable up to $x = 0.80$ for others *e.g.* Gd^{3+}.	[45]–[48]
$\mathbf{Ca_{1-x}Zr_{1-x}Pu^{3+}_{2x}Ti_2O_7}$	Equimolar substitution of Pu^{3+} between Ca^{2+} and Zr^{4+} could be expected to produce a phase transformation to the pyrochlore structure with elevated Pu content $x \geq 0.60$, *via* formation of intermediate zirconolite-4M phase. This has been demonstrated for the corresponding Nd^{3+}, Y^{3+}, Sm^{3+} and Gd^{3+} solid solutions.	[49]–[52]
$\mathbf{Ca_{1-x}Pu^{4+}_{2x}Zr_{1-x}Pu^{4+}_xTi_{2-4x}M^{3+}_{4x}O_7}$	Currently under investigation as NNL 'HIP-1' formulation for small scale demonstration of Pu-zirconolite, crystallising as zirconolite-3T. Extensive doping scheme would likely incur polymorphic transition at low values of (x) and potentially uncontrolled secondary phase nucleation at small intervals $x + \delta x$.	[53]

Corresponding authors: lrblackburn2@sheffield.ac.uk; n.c.hyatt@sheffield.ac.uk

4 Solid Solution Limits of Potential Neutron Poisons in Zirconolite

4.1 Candidate Neutron Poisons and Cost Index Considerations

Initial calculations have provided a selection of candidate NPs, determined on the basis of atomic ratio of poison to Pu, cost per mole of material and thermal neutron absorption cross section necessary to effectively reduce K_{eff} < 0.9. This initial screening identified a selection of suitable NP species, as outlined in **Table 4**. Gd, Sm, Cd, In, Hf and B were identified as suitable candidates on the basis these criteria. The cost index as outlined in **Table 4** is taken from the current Alfa Aesar reagent catalogue, and therefore is not expected to be representative of the price for large quantities of constituent reagent materials. Nevertheless, these listings provide an order-of-magnitude comparison. Although wasteform design philosophy stipulates that the downselection of NP's should not be dictated by price, it is clear from **Table 4** that the cost index can vary by two orders of magnitude. Although the elements listed are not an exhaustive list of all potential poisons, an initial filter was applied such that any species with a cost index approximately 100 times greater than Gd were excluded.

Table 4) Data for evaluating candidate NP species *(* all elements are listed as oxides, with the exception of B which is anticipated to be B_4C)*

Element	Atom Ratio Pu:NP	NP g/kg of Pu	NP Cost £/mole	Cost Index (atom ratio × cost/mole)	Thermal Neutron Cross Section (σ_a/barns)
Gd	0.0115	7.59	110	1.27	4.90×10^4
Hf	0.2562	191.36	206	52.7	104
Sm	0.0220	13.82	79	1.74	5.92×10^3
Cd	0.0452	21.25	7.4	0.33	2.45×10^4
In	0.1295	62.19	396	51.26	194
B*	0.3091	13.98	3.8	1.17	767

4.2 Gadolinium Doped Zirconolite

Gd incorporation within zirconolite is common, as Gd^{3+} possesses physical characteristics also applicable to that of an effective minor actinide simulant. Nevertheless, Gd^{3+} may be accommodated in zirconolite to act as a NP. Gd has been included in a series of polycrystalline phase assemblages, such as the SYNROC wasteform, for criticality control. However, these studies did not intend to incorporate Gd^{3+} within specific lattice sites within the zirconolite parent structure, hence a meaningful discussion of the solid solution limits is not always possible. For example, a zirconolite-rich SYNROC composition was synthesized by HIP at 1280 ˚C in the work of Li *et al*., with 8.96 wt. % Gd_2O_3 added for criticality control [54], however the partitioning of Gd^{3+} between the obtained zirconolite, hollandite, pyrochlore and rutile phases was not discussed. The partitioning of Ln^{3+} species within a series of SYNROC compositions was investigated by Lumpkin *et al*., with the conclusion that the partitioning of these elements within the various crystalline phases was largely controlled by ionic radii [55]. Consequently, it was inferred that Ln^{3+} cations such as Gd^{3+} demonstrated an affinity for substitution within the large

Corresponding authors: lrblackburn2@sheffield.ac.uk; n.c.hyatt@sheffield.ac.uk

Ca^{2+} site in the zirconolite structure. Two zirconolite-rich SYNROC wasteforms were HIPed by Zhang *et al*. using both U/Th surrogates (targeting 90% zirconolite, 10% hollandite) and Pu (targeting 80% zirconolite, 10% hollandite, 10% rutile), with Gd and Gd + Hf added to each sample for criticality control, respectively [56]. In both instances, the zirconolite phase was observed to overwhelmingly accommodate both NP additives alongside U/Th and Pu. Leaching trials in deionized water at 90 ˚C demonstrated near congruent release of Gd/Hf with Pu from the wasteform, with normalized release rates < 10^{-5} $g \cdot m^{-2} \cdot d^{-1}$ after 35 d for Hf and Pu. It was concluded that the release of Pu from the wasteform would likely be accompanied by release of Hf/Gd, mitigating any potential localized criticality. The solid solution limits of Gd are more easily discussed when a series of specific solid solutions are targeted. Zhang *et al*. fabricated the $Ca_{1-x}Zr_{1-x}Gd_{2x}Ti_2O_7$ ($0.00 \leq x \leq 1.00$) solid solution by conventional sintering at 1400 ˚C for 48 h, from oxide precursors [49]. Zirconolite-2M was produced as the dominant phase in the range $0.00 \leq x \leq 0.20$, with a mixture of zirconolite-2M and zirconolite-4M obtained for $0.20 \leq x \leq 0.50$. A cubic pyrochlore phase was detected by powder XRD for $x \geq 0.40$, gradually progressing towards a single phase at x = 0.60. A 7-day PCT leaching test was performed for compositions corresponding to x = 0.20 (mixture of zirconolite-2M and 4M) and x = 0.40 (mixture zirconolite-2M, 4M and pyrochlore) using deionized water as the leachate. The normalized leach rate of Gd from each sample was exceptionally low, measured to be 4.96×10^{-7} $g \cdot m^{-2} \cdot d^{-1}$ and 1.78×10^{-7} $g \cdot m^{-2} \cdot d^{-1}$, respectively. Interestingly, this may infer that a mixture of zirconolite-2M and zirconolite-4M phases may slightly increase the overall chemical durability of wasteforms containing Gd. A systematic investigation was performed by Ma *et al*. [48] characterizing the incorporation of a variety of Ln^{3+} species in the zirconolite system $Ca_{1-x}Ln_xZrTi_{2-x}Al_xO_7$ (Ln = La, Nd, Gd, Ho, Yb, $0.10 \leq x \leq 1.00$) by sintering oxide precursors at 1400 ˚C for 100 h. Interestingly prevailing phase assemblage and dominant zirconolite polytype was controlled by the choice of Ln^{3+} species, with La^{3+} failing to form a complete solid solution past the limit of x = 0.20. When targeting the $Ca_{1-x}Gd_xZrTi_{2-x}Al_xO_7$ system, zirconolite-2M was maintained extensively over the range $0.00 \leq x \leq 0.80$, after which minor ZrO_2 became prominent as a secondary phase. Interestingly, the replication of this series with Nd^{3+} produced the zirconolite-3O phase at $x \geq 0.70$, inferring that Gd^{3+} does not distort the zirconolite structure as much as closely related Ln^{3+} species due to size constraints. Interestingly, the $Ca_{1-x}Gd_xZrTi_{2-x}Al_xO_7$ ($0.00 \leq x \leq 1.00$) solid solution synthesised at 1400 ˚C (5 h) by Stefanovsky *et al*. produced different phase fields than reported by Ma *et al*. [46]. Whilst the microstructure was comprised of a single phase zirconolite over the range $0.00 \leq x \leq 0.90$, at which point minor Gd-rich ZrO_2 was observed by SEM, electron diffraction data were consistent with the zirconolite phase transforming to 3T or 6T symmetry in the range $0.50 \leq x \leq 0.90$. When targeting x = 1.00, *i.e.* nominal composition $GdZrTiAlO_7$, electron diffraction analysis was consistent with zirconolite-3O. The solid solution limits of Gd within the following solid solutions was probed by Vance *et al*.: $Ca_{1-x}Gd_xZrTi_{2-x}Al_xO_7$, $Ca_{1-x}Zr_{1-x}Gd_{2x}Ti_2O_7$ and $CaZr_{1-x}Gd_xTi_{2-x}Nb_xO_7$, by conventional sintering at 1450 ˚C for 20 h [57]. When targeting $Ca_{1-x}Gd_xZrTi_{2-x}Al_xO_7$ the phase evolution was largely similar to related solid solutions, *e.g.* Ma *et al*. [48], with the formation of zirconolite-3O observed at x = 0.70. A transformation to the pyrochlore structure was identified at x = 0.50 for $Ca_{1-x}Zr_{1-x}Gd_{2x}Ti_2O_7$, similar to the phase fields observed by Zhang *et al*. for Gd, and indeed Nd, Sm [49]. Identical phase fields were also formed for the $CaZr_{1-x}Gd_xTi_{2-x}Nb_xO_7$, by which the pyrochlore phase was produced above x = 0.50. The $Ca_{1-x}Ln_xZrTi_{2-}$

Corresponding authors: lrblackburn2@sheffield.ac.uk; n.c.hyatt@sheffield.ac.uk

$_xFe_xO_7$ (Ln = La, Nd, Gd, Ho, Yb, 0.10 ≤ x ≤ 1.00) solid solution fabricated by Ji *et al*. [47] complements the data reported by Ma *et al*. [48] allowing a reasonable comparison to be made between $Ca_{1-x}Gd_xZrTi_{2-x}(Al,Fe)_xO_7$. The solid solution limits for the zirconolite-2M phase were largely similar for compositions charge balanced with Al, with the 2M phase stabilized over the range 0.10 ≤ x ≤ 0.80 for Fe-substituted compositions. Ji *et al*. concluded that zirconolte-3O was the dominant polytype over the compositional range 0.90 ≤ x ≤ 1.00, inferring that the end member $GdZrTiFeO_7$ may be a near single phase zirconolite-3O, however no electron diffraction data were provided. Phase relations in the pseudo-binary system $(1-x)CaZrTi_2O_7 – (x)GdAlO_3$ (x = 0.25, 0.50 and 0.75) were investigated by Mikhailenko *et al*. by a cold press and sinter method, at 1400 ˚C and 1500 ˚C [58]. Zirconolite was present as the major crystalline phase when targeting x = 0.25, with ~ 70 wt. % of the phase assemblage comprised of zirconolite with calculated stoichiometry $Ca_{0.36}Gd_{0.60}Zr_{1.12}Ti_{1.40}Al_{0.47}O_7$, however Gd was still concentrated in the secondary perovskite phase. Increasing the (x) parameter to 0.75 produced a phase assemblage comprised of 45 wt. % zirconolite, 45 wt. % perovskite and 10% hibonite. Interestingly, this pseudo-binary system produced a greater relative fraction of zirconolite than the corresponding Sm system also fabricated by Mikhailenko *et al*. when targeting x = 0.75 [59]. Leaching of these ceramics was performed according to the Australian Powder No. 1 (P1) test, with distilled water used as the leachate (0.2 g of material; 20 mL distilled water; static test at 95 °C for 6 h before solution replenished; continued for 10 d). The normalized leach rate of Gd was ~ 10^{-4} $g \cdot m^{-2} \cdot d^{-1}$ over the 10 d period when the nominal (x) parameter was 0.25; the release rate of Gd increased by an order of magnitude for x = 0.75, attributed to excess perovskite content.

Gadolinium Summary: The tendency of Gd^{3+} to incorporate within the zirconolite structure is relatively extensive, with a number of corroborating studies reporting high wasteloading within the Ca^{2+} site, alongside the possibility of equimolar substitution of Gd^{3+} between Ca^{2+} and Zr^{4+} sites, although this was reported to produce the zirconolite-4M phase at moderate levels of substitution. Considering the relatively low ratio of NP:Pu atoms necessary to reduce K_{eff} < 1 (refer to back to **Table 4**), the incorporation of Gd within zirconolite should not be expected to destabilise the zirconolite phase, or indeed produce a polytypical transformation, given that roughly 1 atom of Gd is necessary to offset 100 Pu atoms. Considering the dilution level of Gd needed to satisfy these neutronics requirements, the most effective means of Gd incorporation would likely be achieved by co-incorporation of Gd^{3+} across Ca^{2+} and Zr^{4+}, negating the need to alter the preferred formulation to accommodate for charge imbalance. Moreover, the cost index of Gd is attractive relative to Hf and In.

4.3 Hafnium Doped Zirconolite

From a solid solution perspective, Hf may be the most suitable NP, as Hf^{4+} readily forms a complete solid solution with Zr^{4+} in the zirconolite structure, on the basis of near identical ionic radii (0.78 Å vs. 0.76 Å for Zr^{4+} and Hf^{4+} in 7-fold coordination, respectively) [60]. Furthermore, the interchange of these species results in negligible impact on the overall structure properties. Three compositions corresponding to $CaZrTi_2O_7$, $CaHf_{0.5}Zr_{0.5}Ti_2O_7$ and $CaHfTi_2O_7$ were fabricated by Vance *et al*. with a

Corresponding authors: lrblackburn2@sheffield.ac.uk; n.c.hyatt@sheffield.ac.uk

sintering temperature of 1450 ˚C maintained for 20 h [57]. There was negligible variation in the unit cell parameters of the zirconolite phase (see **Table 5**) suggesting that in any optimized ceramic formulation for Pu, Zr^{4+} may be interchangeable with a requisite mol. % of Hf^{4+} to satisfy criticality concerns.

Table 5) Unit cell parameters for Hf-doped zirconolite (reproduced from Vance *et al*. [57])

Composition	Unit Cell Parameters			
	a (Å)	**b** (Å)	**c** (Å)	**β** (˚)
$CaZrTi_2O_7$	12.447	7.272	11.384	100.54
$CaHf_{0.5}Zr_{0.5}Ti_2O_7$	12.434	7.265	11.350	100.58
$CaHfTi_2O_7$	12.420	7.262	11.343	100.57

Complete replacement of Zr with Hf in the zirconolite structure was demonstrated by Putnam *et al*., with single phase $CaHfTi_2O_7$ synthesized from component oxides at 1300 ˚C, with intermittent regrinding to ensure phase homogeneity [61]. Furthermore, $CaHfTi_2O_7$ was determined to be more thermodynamically stable than stoichiometric $CaZrTi_2O_7$, hence partial replacement of Zr with Hf may be a favorable from a wasteform perspective, whilst satisfying criticality requirements. Hyatt *et al*. formulated a series of zirconolites with nominal stoichiometry $(Ca_{1-x/2}Gd_{x/2})(Zr_{1-5x/2}Ce_xHf_xGd_{x/2})Ti_2O_7$, with Ce acting as a structural simulant for Pu and Hf^{4+} included as a NP [62]. The following solid solution limits were systematically defined: zirconolite-2M ($0.00 \leq x \leq 0.15$); mixture of zirconolite-2M and zirconolite-4M ($0.15 \leq x \leq 0.25$); mixture of zirconolite-4M and pyrochlore ($0.25 \leq x \leq 0.30$). It is assumed that the equimolar substitution of Gd^{3+} across Ca^{2+} and Zr^{4+} was responsible for the formation of zirconolite-4M and pyrochlore, as very similar phase fields were observed for $Ca_{1-x}Zr_{1-x}Gd_{2x}Ti_2O_7$. This allows us to infer that the partial occupation of Hf^{4+} within the Zr^{4+} site does not disrupt the zirconolite-2M to zirconolite-4M phase transformation to any meaningful extent. The $CaZr_{1-x}Hf_xTi_2O_7$ ($0.00 \leq x \leq 1.00$) solid solution was fabricated by Zhang *et al*. using combustion synthesis combined with hot pressing for densification [63]. It was determined that the zirconolite-2M polytype was maintained over the phase evolution, with complete digestion of HfO_2 within a highly densified microstructure, at each compositional interval. The chemical durability of $CaZr_{0.4}Hf_{0.6}Ti_2O_7$ was investigated by the MCC-1 standard leaching test [64], over a 42 d period. The normalized leach rate after the 42 d period was significantly lower for Hf than Ca, corresponding to 1.11×10^{-8} $g \cdot m^{-2} \cdot d^{-1}$ and 0.25×10^{-2} $g \cdot m^{-2} \cdot d^{-1}$, respectively. As there was no Pu surrogate included in the targeted phase composition, no comment can be made as to whether there may be a congruent release of Pu/Hf from the wasteform. Complementary data was published by Zhang *et al*. utilizing the same combustion synthesis route to produce the $Ca_{1-x}Hf_{1-x}Gd_{2x}Ti_2O_7$ solid solution, with Gd^{3+} included as a surrogate for minor actinide species such as Pu^{3+} (although as discussed in the previous segment, Gd may also be included as an effective NP) [65]. The phase evolution consisted of a phase transition from $CaHfTi_2O_7$ (zirconolite-2M) to $Gd_2Ti_2O_7$ (cubic pyrochlore), with a solid solution limit of Gd_2O_3 defined at $x = 0.80$. Interestingly, the authors did not report the formation of an intermediate zirconolite-4M phase, as was observed in closely

Corresponding authors: lrblackburn2@sheffield.ac.uk; n.c.hyatt@sheffield.ac.uk

related solid solution regimes (*e.g.* $Ca_{1-x}Zr_{1-x}Gd_{2x}Ti_2O_7$ synthesized by Zhang *et al*. [49] or $Ca_{1-x}Zr_{1-x}Nd_{2x}Ti_2O_7$ synthesized by Coelho *et al.* [23]). After a 42 d leaching period (under MCC-1 conditions), the release of Gd and Hf was measured from the sample corresponding to nominal composition x = 0.60 (*i.e.* $Ca_{0.4}Hf_{0.4}Gd_{1.2}Ti_2O_7$). The release rates of Gd and Hf were measured to be 4.72×10^{-7} $g \cdot m^{-2} \cdot d^{-1}$ and 1.59×10^{-8} $g \cdot m^{-2} \cdot d^{-1}$ respectively, demonstrating that a similar cumulative dissolution trend may be preserved. However, inspection of the powder XRD data revealed that whilst exceptionally low leach rates were observed, the composition x = 0.6 was consistent with the sample adopting the pyrochlore structure, hence any meaningful discussion of the durability of a zirconolite structured material with a corresponding Gd/Hf concentration is not possible. The incorporation of Nd^{3+} in zirconolite was investigated by Caurant *et al*. targeting the solid solution $Ca_{1-x}Nd_xHfTi_{2-x}Al_xO_7$, with Nd^{3+} acting as a structural simulant for Pu^{3+} [66]. Compositions targeting x = 0.01 and x = 0.20 were fabricated by solid state reaction at 1460 ˚C between component oxides. It was confirmed that zirconolite remained in the 2M polytype for each targeted composition, alongside minor $CaTiO_3$ and Hf-Ti-O rich phases, accounting for a negligible portion of the phase assemblage. Mixed occupancy of Hf^{4+} and Ti^{4+} ions were confirmed, consistent with data reported for $CaZr_xTi_{3-x}O_7$, with Nd^{3+} exclusively entering the Ca^{2+} site, in accordance with the target composition. Loiseau *et al*. prepared the corresponding Zr solid solution ($Ca_{1-x}Nd_xZrTi_{2-x}Al_xO_7$, $x \leq 0.8$) allowing useful comparison between the Zr/Hf series [67]. In agreement with Caurant *et al*. the zirconolite-2M structure was stable in the corresponding compositional range ($x \leq 0.20$). Furthermore, zirconolite occupied the 2M structure until x = 0.7; when targeting a nominal Nd concentration of x = 0.8, the zirconolite-3O polytype was formed, with orthorhombic symmetry (space group Acam). Based on these observations, it would be expected that the Hf equivalent composition would also occupy 3O symmetry at elevated Nd^{3+} content. The solid solution limit for which zirconolite formed the 3O polytype was also consistent with the work of Ma *et al*. [48] discussed previously. Hf^{4+} was utilized in place of Zr^{4+} in the work of Begg *et al*., with the view to investigate the substitution of Pu for Ca^{2+} without the addition of a charge compensation cation, targeting $Ca_{0.9}Pu_{0.1}HfTi_2O_7$, however a slight excess of Pu was reported such that the actual concentration was < 0.1 f.u. [44]. Sintering in air at 1400 ˚C produced a near single phase zirconolite, alongside ~ 5 wt. % pyrochlore with composition $Ca_{0.92}Pu_{0.56}Hf_{0.75}Ti_{1.74}O_7$, and minor TiO_2/$HfTiO_4$. Annealing the sample in 3.5% H_2/N_2 was sufficient to reduce 80% Pu^{3+} however no disruption to the phase assemblage was observed, demonstrating the ability of the zirconolite phase to accommodate for changes in Pu valence, most likely compensated by Hf/Ti vacancies.

Hafnium Summary: Whilst the cost index and NP:Pu atomic ratio are an order of magnitude greater than Gd, there is an inherent advantage insofar as the ionic radius of Hf is near identical to that of Zr (Hf^{VII} = 0.76 Å; Zr^{VII} = 0.78 Å). In practice, the replacement of Zr^{4+} with Hf^{4+} should not impact zirconolite phase formation and moreover, the composition should not need tailoring to account for excess charge unit considerations. The primary drawback to the use of HfO_2 is the high cost index relative to Gd/Sm/B, hence whilst the complete replacement of Zr with Hf (*i.e.* $Ca_{0.80}Pu_{0.20}Hf_{0.90}Pu_{0.10}Ti_{1.60}Al_{0.40}O_7$) would likely incur a significant cost to head-end operations. Nevertheless, the partial replacement, with the

Corresponding authors: lrblackburn2@sheffield.ac.uk; n.c.hyatt@sheffield.ac.uk

view to only satisfy the NP:Pu ratio remains an attractive prospect, and it is reasonable to assume this substitution will not influence Pu partitioning or zirconolite phase formation.

4.4 Samarium Doped Zirconolite

We are aware of only several formal studies that have utilized Sm^{3+} as a surrogate for either minor actinide species, or indeed as a NP. It was demonstrated in early work, such as that of Kesson *et al*. zirconolite may incorporate Sm^{3+} with concentrations as high as 0.67 f.u. [30]. A zirconolite structured material with composition $(Ca_{0.55}Sm_{0.45})(Sm_{0.22}Zr_{0.71}Mg_{0.06})Ti_{1.99}O_7$ was produced from hot pressing a 1:1 molar mixture of $CaZrTi_2O_7$ – $Sm_2Ti_2O_7$ at 1400 ˚C and 1459 ˚C, producing a two phase mixture consisting of zirconolite (with the above composition) and pyrochlore. This work provided many initial insights into Ln^{3+} accommodation within the zirconolite structure, demonstrating that larger Ln^{3+} species were preferentially partitioned within the Ca^{2+} site on account of size constraints, whilst smaller Ln^{3+} may be accommodated in the Zr^{4+} site. Kesson *et al*. in the same work described for the formation of an Mg^{2+}/Nb^{5+} substituted zirconolite sample with composition $(Ca_{0.57}Sm_{0.32}Zr_{0.06})Zr_{1.00}(Ti_{1.14}Mg_{0.40}Nb_{0.40}Zr_{0.06})O_7$, demonstrating that Sm^{3+} may be incorporated into the zirconolite structure with considerable charge balance species retained on the Ti^{4+} site. Mikhailenko *et al*. fabricated zirconolite ceramics in the pseudobinary system $(1-x)CaZrTi_2O_7$ – $(x)SmAlO_3$, for x = 0.25, 0.50 and 0.75, by a conventional cold press and sinter method between 1400 – 1500 ˚C [59]. When targeting x = 0.25, a two phase mixture of zirconolite and perovskite was obtained, accounting for 80% and 20% of the overall phase fraction, respectively, with Sm^{3+} concentrated in the zirconolite phase. Increasing the (x) parameter served to greatly reduce the produced quantity of the zirconolite phase, with a mixture of zirconolite (25%), perovskite (60%) and free oxide (15%, Sm-stabilized ZrO_2) produced when targeting x = 0.75. Coincidently, Sm^{3+} was overwhelmingly concentrated in the perovskite phase, demonstrating the tendency of ABO_3 phases to accommodate Ln^{3+} species. At each interval of (x), powder diffraction data were consistent with zirconolite-3T of trigonal symmetry. Jafar *et al*. synthesized a series of zirconolites targeting the $Ca_{1-x}Zr_{1-x}Sm_{2x}Ti_2O_7$ solid solution, with $0.00 \leq x \leq 1.00$, by mixed oxide synthesis at 1300 ˚C [51]. Three distinct phase fields were identified, comprised of zirconolite-2M, zirconolite-4M and cubic pyrochlore. Specifically, a single phase zirconolite was produced when targeting x = 0.00, with a mixture of zirconolite-2M and a secondary perovskite phase obtained in the interval $0.05 \leq x \leq 0.10$. Zirconolite-2M and zirconolite-4M were observed to coexist (alongside the perovskite phase) in the range $0.15 \leq x \leq 0.25$). Zirconolite-4M was the only polytype present for $0.30 \leq x \leq 0.35$, with the appearance of a pyrochlore structured phase at x = 0.40; Sm-rich pyrochlore was produced as a single phase for $x \geq 0.60$. The presence of the $CaTiO_3$ secondary phase was attributed to the preferential occupation of Sm^{3+} within the 8-fold coordinated Ca^{2+} site, presumably due to ionic size compatibility ($_{VIII}Sm^{3+}$ = 1.07 Å). The behavior of Sm^{3+} in zirconolite in the $Ca_{1-x}Zr_{1-x}Sm_{2x}Ti_2O_7$ system is similar to that of analogous solid solutions containing Nd^{3+}, Gd^{3+}, Y^{3+} *etc*. hence, it could be expected that alternative substitution regimes would not significantly deviate from the expected phase evolution. Zhang *et al*. targeted two Sm^{3+} incorporation schemes: $Ca_{1-x}Sm_xZrTi_{2-x}Al_{2x}O_7$ ($0.00 \leq x \leq 0.50$), and $Ca_{1-x}Zr_{1-x}Sm_{2x}Ti_2O_7$ ($0.00 \leq x \leq 1.00$), using a combustion synthesis method as previously

Corresponding authors: lrblackburn2@sheffield.ac.uk; n.c.hyatt@sheffield.ac.uk

described [68]. The substitution scheme targeting Sm^{3+} incorporation within Ca^{2+} and Zr^{4+} was identical to that of Jafar *et al*. [51], however the phase fields were inconsistent, insomuch as zirconolite-4M was not identified as an intermediate phase in transition between $CaZrTi_2O_7$ – $Sm_2Ti_2O_7$. It is unclear as to why in this instance an Sm-rich zirconolite-4M phase was not produced, and it is possibly a result of discrepancy between fabrication parameters (Jafar *et al*. utilized a conventional solid state sintering method from component oxides, whereas Zhang *et al*. used the combustion synthesis method, with CuO as the oxidant). Synthesis of $Ca_{1-x}Sm_xZrTi_{2-x}Al_{2x}O_7$ produced a heterogeneous phase assemblage, in which undigested component oxides were present in the microstructure, at all levels of targeted Sm concentration. Furthermore, as the phase assemblage evolved towards x = 0.50, powder XRD data were consistent with zirconolite occupying the 3T polytype. These data were not consistent with the data produced by Ma *et al*. in the $Ca_{1-x}Ln_xZrTi_{2-x}Al_xO_7$ system for Ln = La, Nd, Gd, Ho and Yb, insomuch as zirconolite-3T was not detected [48]. As the ionic radii of Sm^{3+} (1.07 Å) falls between that of Nd^{3+} (1.11 Å) and Ho^{3+} (1.01 Å) in 8-fold coordination, this may infer that the zirconolite-3T phase in this system is stabilized over a very narrow compositional range.

Samarium Summary: A review of the literature has evidenced that whilst there are numerous studies that have successfully incorporated Sm^{3+} within zirconolite, this has typically been with the view to simulate MA^{3+} species, rather than as a NP. Nevertheless, despite some discrepancies as to polytype formation at extensive Sm substitution, the phase fields produced when incorporating Sm^{3+} in zirconolite are largely analogous to Gd^{3+}. The similarities between Sm and Gd (*i.e.* cost index; absorption cross section) mean that whilst both could be expected to be effective NP species, there is no apparent benefit that Sm would confer over Gd. Hence, it is reasonable that Sm should be discounted, on the basis of a greater preexisting knowledge base for Gd.

4.5 Cadmium Doped Zirconolite

We are not aware of any studies that have directly incorporated Cd^{2+} within the zirconolite structure. Nevertheless, the ionic radii of Ca^{2+} and Cd^{2+} are near identical (1.12 Å and 1.10 Å in 8-fold coordination, respectively) hence a continuous solid solution between $CaZrTi_2O_7$ – $CdZrTi_2O_7$ may form. Similar to Hf^{4+} zirconolite, this may allow substitution of a requisite quantity of Cd^{2+} within an optimized composition, with negligible impact on obtained structure. The only instance of Cd-zirconolite was reported by Leturcq *et al*., with the view to determine the influence of minor impurities on the phase formation in zirconolite [69]. Zirconolite with nominal composition $Ca_{0.863}Nd_{0.137}ZrTi_{1.863}Al_{0.137}O_7$ was homogenized, before the addition of 1 wt. % CdO and sintering as a pellet at 1450 ˚C in air for 4 h. SEM analysis confirmed that whilst Cd was partially incorporated within the zirconolite phase, Cd was also partitioned within a minor $CaTiO_3$ phase (presumably accommodated within the Ca^{2+} site in both instances). Nevertheless, confidence that Cd may be accommodated in zirconolite without significant disruption to the phase assemblage may be taken from the fact that several pertinent Ca/Cd analogues have been reported in the literature *e.g.* $CaTiO_3$ [70] and $CdTiO_3$ [71]; $Ca_2Nb_2O_7$ [72] and $Cd_2Nb_2O_7$ [73]; $CaMoO_4$ [74] and $CdMoO_4$ [75].

Corresponding authors: lrblackburn2@sheffield.ac.uk; n.c.hyatt@sheffield.ac.uk

Cadmium Summary: The advantage of Cd^{2+} within the formulation may be similar to that of Hf^{4+}, insofar as Cd^{2+} may be able to effectively replace Ca^{2+} as the A-site cation in zirconolite on the basis of ionic radii, though the phase $CdZrTi_2O_7$ has not yet been reported. Furthermore, Cd is an attractive poison due to a relatively low cost index in relation to Gd/Hf/In. The lack of literature regarding Cd-doped zirconolite may contribute significantly towards its down-selection. Moreover, the handling of Cd is accompanied by toxicity concerns, which would be a notable consideration during precursor production and downstream handling of powders. The reduction of CdO to Cd metal may also be a concern, particularly for compositions produced by HIP, for which the Fe-rich environment produces a reducing environment. On the basis of these stipulations, Cd may not be selected as a practically useful poison.

4.6 Indium Doped Zirconolite

Similar to Cd we are not aware of any studies that have incorporated In^{3+} in zirconolite with the view to simulate either a specific radionuclide, or indeed as a NP species. A suite of zirconolites targeting nominal compositions $CaZrTi_{2-x}In_xO_{7-x/2}$ (x = 0.25, 0.50 and 1.00) were prepared by Begg *et al*., reacted at 1400 ˚C for 40 h [76]. Here, In^{3+} was introduced as a surrogate for Ti^{3+} in order to simulate highly reducing conditions. Zirconolite was not produced as a single phase at any targeted level of In^{3+} concentration (with the exception of x = 0.00). Targeting a nominal concentration of x = 0.25 produced a two phase mixture of $Ca_{0.85}Zr_{1.16}Ti_{1.67}In_{0.33}O_7$ (zirconolite) and $Ca_{0.98}Zr_{0.01}Ti_{0.99}In_{0.01}O_3$ (perovskite), comprising 90 wt. % and 10 wt. % of the phase assemblage respectively. Increasing the nominal In^{3+} concentration to x = 0.50 significantly disrupted the phase assemblage, such that 20 wt. % of the overall yield was comprised of a $Ca_{0.17}Zr_{0.35}Ti_{0.33}In_{0.25}O_{1.9}$ fluorite-structured phase. Targeting the nominal composition $CaZrTiInO_{6.5}$ (*i.e.* x = 1.00) completely destabilized the zirconolite phase, with the phase assemblage comprised of 40 wt. % perovskite and 60 wt. % fluorite. Nevertheless, considering the estimated ionic radius of In^{3+} in 7-fold coordination (0.86 Å), In^{3+} may be more easily accommodated within the Zr^{4+} site, replacing half of the necessary Al^{3+} cations necessary in a substitution regime such as $Ca_{1-x}Pu_xZr_{1-x}In_xTi_{2-x}Al_xO_7$.

Indium Summary: The deployment of In^{3+} as a potential NP additive in zirconolite would be inhibited by the large associated cost that would be necessary to ensure successful poisoning. Furthermore, the NP:Pu ratio for In^{3+} is an order of magnitude greater than other trivalent species Gd/Sm. Considering the lack of systematic studies aiming to elucidate the solid solution limits of In^{3+} within zirconolite in a systematic manner, it may be stated that at the present time, there is not sufficient evidence to provide confidence in the ability of In^{3+} to successfully act as a NP in zirconolite.

Corresponding authors: lrblackburn2@sheffield.ac.uk; n.c.hyatt@sheffield.ac.uk

4.7 Boron Doped Zirconolite

Boron deviates from the above method of incorporating M^{3+} NP species due to the fact it may not be accommodated in solid solution with zirconolite, on the basis of ionic radii (B^{VI} = 0.27 Å), and must therefore be distributed as discrete intergranular particulates throughout the microstructure, most likely concentrated at grain boundaries and triple points. Furthermore, unlike the other NP considered, boron would be present as the carbine B_4C, rather than oxide. A thorough survey of the literature did not identify any reports detailing the inclusion of B_4C in zirconolite waste packages, although on the basis of the criteria evaluated in **Table 4**, the use of B_4C may prove attractive. Another consideration for B is related to the volume footprint of the wasteform; using the baseline formulation $(Ca_{0.80}Pu_{0.20})(Zr_{0.90}Pu_{0.10})Ti_{1.60}Al_{0.40}O_7$ (unit cell volume ~ 125 $Å^3$) it can be stated that 0.093 atoms of B would be required to achieve the required poisoning, occupying 0.85 $Å^3$. Consequently, addition of B_4C to zirconolite to this end will have a minimal effect on wasteloading, as the volume should only be expected to increase by < 1 vol. %.

5 Gap Analysis

The objective of this review was to provide an overview of established solid solution regimes for Pu incorporation in zirconolite, and insight into potential pathways towards formulation of a zirconolite-rich wasteform capable of accommodating a requisite quantity of a suitable NP. Nevertheless, there are several high level issues that have not been adequately discussed (at least in a manner that is systematic enough to provide confidence in the approach) within the wider literature to inform a decision regarding the most effective route towards disposal in a zirconolite matrix:

- The choice of solid solution regime appears to be favored towards a coupled A-site substitution, by which Pu^{4+} is accommodated in solid solution with Ca^{2+} sites, with a smaller lower valence cation such as Al^{3+} distributed across the available Ti^{4+} sites to provide charge balance. This is also an artefact of radioactive analogue zirconolite specimens, in which preferential accommodation of substituent elements occurs in the Ca^{2+} site, presumably due to larger ionic radius of Ca^{2+} (1.12 Å vs. 0.78 Å for Zr^{4+}, in 8- and 7-fold coordination, respectively). The choice of substitution scheme (and to a lesser extent, the partial oxygen pressure of the atmosphere introduced during the sintering process) has been shown to control polytype formation. Whilst it has not been explicitly defined as a criterion for the design of zirconolite wasteforms, it is generally accepted that maintaining zirconolite in its 2M form (or indeed, a single phase polytype of the 3O/3T species) may be preferable, rather than a mixture of polytypes. Despite this, we are not aware of any studies that conclusively determine that the chemically durability of zirconolite wasteforms is compromised, to any meaningful and quantifiable extent, by the presence of multiple zirconolite polytypes, and indeed whether any of the isolated polytypes exhibit any variation in leaching properties. **Gap analysis: it is undetermined which zirconolite polytype (if any) may exhibit superior/inferior dissolution and radiation**

Corresponding authors: lrblackburn2@sheffield.ac.uk; n.c.hyatt@sheffield.ac.uk

tolerance characteristics. Identification of particularly attractive polytypoid mixtures may allow for greater wasteloading and simpler solid solution regimes (this may also permit more facile modelling).

- In order to support an immobilisation program for Pu, the construction of a pilot scale facility is necessary, ideally allowing for the physical optimization of all chemical engineering aspects and processing parameters. As outlined in **Fig. 2**, there are several head-end powder handling operations that may need to be 1) optimized for handling of α-emitters such as Pu; 2) configured correctly to ensure efficient and homogeneous feed into downstream operations such as can-filling. One or more of the head end operations will make use of high intensity homogenization/size reduction techniques, in order to sufficiently mix the feed material and ensure PuO_2 is completely dispersed in the wasteform. Ball milling and attrition milling are both attractive options that take advantage of pre-existing ceramic processing technologies, and furthermore these operations may utilise a wet milling stage, whereby constituent precursors are agitated in the presence of a solvent such as methanol to improve mixing, or a dry-route, by which powders are mixed in the presence of a lubricant to aid the milling process before discharge. A variety of organic lubricants were utilised by Squire *et al*. in the attrition milling of zirconolite (target composition $Ca_{0.75}Ce_{0.25}ZrTi_{1.625}Fe_{0.375}O_7$), consolidated by HIP [77]. Examination of the product materials post-HIP evidenced poor densification due to incomplete lubricant burnout, resulting in incomplete formation of a single phase product. It was discussed that the use of fumed metal oxides may provide an inherent advantage, insofar as they may act as both a milling aid, and form part of the wasteform itself. Examples include the use of hydrophobic Al_2O_3 as a fumed powder, or indeed Ti_2O_3, which may, in turn, allow the use of Ti^{3+} as a charge compensation species, negating the need for Al^{3+}. **Gap analysis: there is currently no consensus regarding the optimal powder milling route, either by wet or dry methods. The potential use of Ti_2O_3 in the precursor formulation may alter the charge compensation mechanism such that accommodation of NP species within the zirconolite structure is lessened/heightened with respect to Al^{3+}.**

- The use of chemical surrogates is prevalent in most laboratory scale wasteform trials, as a precursor to active validation trials, on the basis of cost and expediency. Ce^{4+} and U^{4+} are typically employed as surrogates for Pu^{4+} in the immobilized form, both in ceramic and vitrified wasteforms. However, it is widely accepted that surrogates do not produce wasteform characteristics that can be directly translated to Pu-substituted compositions. Discrepancies between surrogate and 'real' compositions are typically a result of redox activity, with the tendency of Ce to reduce to the Ce^{3+} form considerably greater than Pu. For example, Blackburn *et al*. recently demonstrated that the partial oxygen pressure of the sintering environment applied for $CaZr_{1-x}Ce_xTi_2O_7$ ceramics significantly altered the obtained phase assemblage [17]. Vance *et al*. demonstrated that sintering of $CaZr_{1-x}U_xTi_2O_7$ ceramics in air significantly disrupted the phase assemblage due to the formation of U^{5+} [31]. As these behaviors were not replicated in the corresponding $CaZr_{1-x}Pu_xTi_2O_7$ solid solution synthesized by Begg *et*

Corresponding authors: lrblackburn2@sheffield.ac.uk; n.c.hyatt@sheffield.ac.uk

al. [32], the use of chemical surrogates must be done so with caution. The physical characteristics (such as morphology, density) of constituent oxide powders must also be taken into account. **Gap analysis: any potential substitution scheme proposed for Pu must be underpinned by use of several chemical surrogates in conjunction, accounting for redox conditions imposed by the HIP environment.**

6 Conclusions

The aim of the present work was to provide an overview of the current status of the U.K. immobilisation program for Pu inventories, with specific focus on efforts to optimise the baseline zirconolite formulation to accommodate a requisite quantity of NP. A detailed summary of Pu/NP solubility in a range of established zirconolite solid solution regimes was also provided, alongside a review of zirconolite crystallography. A selection of potential neutron poisons was then evaluated through an initial screening, with the view to down-select any candidates that did not appear attractive on the basis of cost and neutronics, and accordingly, a literature review of successful candidates Gd, Hf, Sm, Cd, In and B was performed, aiming to understand their respective solubility within the candidate Pu phase zirconolite. Where possible, a review of the solid solution limits with respect to polytype transformations and oxide solubility was provided. For each poison, we produced a high-level summary, identifying both Gd and Hf as the most promising oxide compounds, and highlighting the potential application of B_4C.

7 Acknowledgements

We acknowledge financial support from the Nuclear Decommissioning Authority (NDA) and EPSRC under grant numbers EP/S01019X/1, EP/N017870/1 and EP/R511754/1. This research utilised the HADES/MIDAS facility at the University of Sheffield established with financial support from EPSRC and BEIS, under grant EP/T011424/1 [78].

7 References

[1] Nuclear Decommissioning Authority (NDA), “Progress on Plutonium Consolidation, Storage and Disposition,” 2019.

[2] R. M. Orr, H. E. Sims, and R. J. Taylor, “A review of plutonium oxalate decomposition reactions and effects of decomposition temperature on the surface area of the plutonium dioxide product,” *J. Nucl. Mater.*, vol. 465, pp. 756–773, 2015.

[3] Nuclear Decommissioning Authority (NDA), “NDA Plutonium Options,” 2008.

[4] N. C. Hyatt, “Plutonium management policy in the United Kingdom: The need for a dual track strategy,” *Energy Policy*, vol. 101, pp. 303–309, 2017.

Corresponding authors: lrblackburn2@sheffield.ac.uk; n.c.hyatt@sheffield.ac.uk

[5] Nuclear Decommissioning Authority, “Progress on approaches to the management of separated plutonium,” 2014.

[6] A. R. Mason, S. M. Thornber, M. C. Stennett, L. J. Gardner, D. Lützenkirchen-Hecht, and N. C. Hyatt, “Preliminary investigation of chlorine speciation in zirconolite glass-ceramics for plutonium residues by analysis of Cl K-edge XANES,” in *MRS Advances*, 2020, vol. 5, no. 1–2, pp. 37–43.

[7] Nuclear Decommissioning Authority, “Geological Disposal: Criticality Safety Status Report,” 2016.

[8] T. W. Hicks, “Criticality Safety Assessment for Waste Packages Containing High-enriched Uranium,” 2007.

[9] J. M. Solano, T. Page, T. W. Hicks, and P. Thorne, “The use of Neutron-absorbing Materials in ILW and Spent Fuel Packages for Criticality Control,” 2012.

[10] Radioactive Waste Management Ltd, “Geological Disposal: Engineered Barrier System Status Report,” 2016.

[11] B. A. Nadykto and L. F. Timofeeva, “Storage of Plutonium and Nuclear Power Plant Actinide Wastes in the Form of Critical-Mass-Free Ceramics Containing Neutron Poisons,” in *Global 2001 international conference on: “‘back-end of the fuel cycle: from research to solutions,’”* 2001, pp. 1–8.

[12] M. T. Harrison, C. R. Scales, and E. R. Maddrell, “Progress in the Assessment of Wasteforms for the Immobilisation of UK Civil Plutonium,” in *WM2008 Conference*, 2008, vol. 1.

[13] Nuclear Decommissioning Authority (NDA), “Plutonium: Credible options analysis (Gate A),” 2010.

[14] L. R. Blackburn *et al.*, “Hot Isostatically Pressed Zirconolite Wasteforms for Actinide Immobilisation,” in *IOP Conf. Series: Materials Science and Engineering*, 2020.

[15] L. R. Blackburn *et al.*, “Synthesis and Characterisation of $Ca_{1-x}Ce_xZrTi_{2-2x}Cr_{2x}O_7$: Analogue Zirconolite Wasteform for the Immobilisation of Stockpiled UK Plutonium,” *J. Eur. Ceram. Soc.*, vol. 40, no. 15, pp. 5909–5919, 2020.

[16] L. R. Blackburn, S. K. Sun, L. J. Gardner, E. R. Maddrell, M. C. Stennett, and N. C. Hyatt, “Influence of Transition Metal Charge Compensation Species on Phase Assemblage in

Corresponding authors: lrblackburn2@sheffield.ac.uk; n.c.hyatt@sheffield.ac.uk

Zirconolite Ceramics for Pu Immobilisation," *MRS Adv.*, Feb. 2020.

[17] L. R. Blackburn, S. Sun, L. J. Gardner, E. R. Maddrell, M. C. Stennett, and N. C. Hyatt, "A systematic investigation of the phase assemblage and microstructure of the zirconolite $CaZr_{1-x}Ce_xTi_2O_7$ system," *J. Nucl. Mater.*, vol. 535, p. 152137, 2020.

[18] C. T. Williams and R. Gieré, "Zirconolite: A Review of Localities Worldwide, and a Compilation of its Chemical Compositions" *Bull. Nat. Hist. Museum London*, vol. 52, pp. 1–24, 1996.

[19] S. M. Thornber *et al.*, "A preliminary validation study of PuO_2 incorporation into zirconolite glass-ceramics," in *MRS Advances*, 2018, vol. 1, no. 4, pp. 1–7.

[20] S. Thornber, M. C. Stennett, and N. C. Hyatt, "Investigation of Ce incorporation in zirconolite glass-ceramics for UK plutonium disposition," in *2016 MRS Fall Meeting*, 2016.

[21] S. M. Thornber, L. M. Mottram, A. R. Mason, P. Thompson, C. Stennett, and N. C. Hyatt, "Solubility, speciation and local environment of chlorine in zirconolite glass–ceramics for the immobilisation of plutonium residues," *RSC Adv.*, vol. 10, pp. 32497–32510, 2020.

[22] E. Maddrell, S. Thornber, and N. C. Hyatt, "The influence of glass composition on crystalline phase stability in glass-ceramic wasteforms," *J. Nucl. Mater.*, vol. 456, pp. 461–466, 2015.

[23] A. A. Coelho, R. W. Cheary, and K. L. Smith, "Analysis and Structural Determination of Nd-Substituted Zirconolite-4M," *J. Solid State Chem.*, vol. 129, pp. 346–359, 1997.

[24] K. R. Whittle, K. L. Smith, N. C. Hyatt, and G. R. Lumpkin, "Neutron and Resonant X-ray Diffraction Studies of Zirconolite-2M," in *Mater. Res. Soc. Symp. Proc.*, 2008, vol. 1107.

[25] R. W. Cheary and A. A. Coelho, "A site occupancy analysis of zirconolite $CaZr_xTi_{3-x}O_7$," *Phys Chem Miner.*, vol. 24, pp. 447–454, 1997.

[26] I. E. Grey, W. G. Mumme, T. J. Ness, R. S. Roth, and K. L. Smith, "Structural relations between weberite and zirconolite polytypes - Refinements of doped 3T and 4M $Ca_2Ta_2O_7$ and 3T $CaZrTi_2O_7$," *J. Solid State Chem.*, vol. 174, no. 2, pp. 285–295, 2003.

[27] B. M. Gatehouse, I. E. Grey, R. J. Hill, and H. J. Rossell, "Zirconolite, $CaZr_xTi_{3-x}O_7$; Structure Refinements for Near-End-Member Compositions with x = 0.85 and 1.30," *Acta Cryst.*, vol. B37, no. 1974, pp. 306–312, 1981.

[28] D. S. Perera, M. W. A. Stewart, H. Li, A. Day, and E. R. Vance, "Tentative Phase Relationships

Corresponding authors: lrblackburn2@sheffield.ac.uk; n.c.hyatt@sheffield.ac.uk

in the System $CaHfTi_2O_7$-$Gd_2Ti_2O_7$ with up to 15 mol% Additions of Al_2TiO_5 and $MgTi_2O_5$," *J. Am. Ceram. Soc.*, vol. 85, no. 12, pp. 2919–2924, 2002.

[29] T. J. White, R. L. Segall, J. L. Hutchison, and J. C. Barry, "Polytypic behaviour of zirconolite," in *Proc. R. Soc. Lond. A*, 1984, vol. 392, pp. 343–358.

[30] S. E. Kesson, W. J. Sinclair, and A. E. Ringwood, "Solid Solution Limits in Synroc Zirconolite," *Nucl. Chem. Waste Manag.*, vol. 4, pp. 259–265, 1983.

[31] E. R. Vance *et al.*, "Incorporation of Uranium in Zirconolite ($CaZrTi_2O_7$)," *J. Am. Ceram. Soc.*, vol. 85, no. 7, pp. 1853–1859, 2002.

[32] B. D. Begg, R. A. Day, and A. Brownscombe, "Structural Effect of Pu Substitutions on the Zr-site in Zirconolite," in *Mat. Res. Soc. Symp. Proc.*, 2001, vol. 663, pp. 1–8.

[33] F. Mazzi and R. Munno, "Calciobetafite (new mineral of the pyrochlore group) and related minerals from Campi Flegrei, Italy: crystal structures of polymignyte and zirkelite: comparison with pyrochlore and zirconolite.," *Am. Mineral.*, vol. 68, no. 1–2, pp. 262–276, 1983.

[34] G. R. Lumpkin, K. L. Smith, and M. G. Blackford, "Electron microscope study of Synroc before and after exposure to aqueous solutions," *J. Mater. Res.*, vol. 6, no. 10, pp. 2218–2233, 1991.

[35] K. L. Smith, G. R. Lumpkin, M. G. Blackford, R. A. Day, and K. P. Hart, "The durability of Synroc," *J. Nucl. Mater.*, vol. 190, pp. 287–294, 1992.

[36] P. J. Mcglinn, K. P. Hart, E. H. Loi, and E. R. Vance, "pH Dependence of the Aqueous Dissolution Rates of Perovskite and Zirconolite at 90 °C," in *Mat. Res. Soc. Symp. Proc.*, 1995, vol. 353, no. 3, pp. 847–854.

[37] B. M. Clark, S. K. Sundaram, and S. T. Misture, "Polymorphic Transitions in Cerium-Substituted Zirconolite ($CaZrTi_2O_7$)," *Sci. Rep.*, vol. 7, no. 1, pp. 2–10, 2017.

[38] W. Li, F. Dong, L. Bian, H. Zou, and M. Song, "Phase relations, microstructure, and valence transition studies on $CaZr_{1-x}Ce_xTi_2O_7$ ($0.0 \leq x \leq 1.0$) system," *J. Rare Earths*, vol. 36, no. 11, pp. 1184–1189, 2018.

[39] M. R. Gilbert *et al.*, "Synthesis and characterisation of Pu-doped zirconolites - $(Ca_{1-x}Pu_x)Zr(Ti_{2-2x}Fe_{2x})O_7$," *IOP Conf. Ser. Mater. Sci. Eng.*, vol. 9, no. 012007, 2010.

[40] E. R. Vance *et al.*, "Actinide and rare earth incorporation into zirconolite," *J. Alloys Compd.*, vol.

Corresponding authors: lrblackburn2@sheffield.ac.uk; n.c.hyatt@sheffield.ac.uk

213/214, pp. 406–409, 1994.

[41] B. D. Begg, E. R. Vance, and G. R. Lumpkin, “Charge Compensation and the Incorporation of Cerium in Zirconolite and Perovskite,” in *Mat. Res. Soc. Symp. Proc.*, 1998, vol. 506, pp. 79–86.

[42] B. D. Begg and E. R. Vance, “The Incorporation of Cerium in Zirconolite,” in *Mat. Res. Soc. Symp. Proc.*, 1997, vol. 465, pp. 333–340.

[43] E. R. Vance, P. J. Angel, B. D. Begg, and R. A. Day, “Zirconolite-Rich Titanate Ceramics for High-Level Actinide Wastes,” in *Mat. Res. Soc. Symp. Proc.*, 1994, vol. 333, pp. 293–298.

[44] B. Begg, E. Vance, and S. Conradson, “The incorporation of plutonium and neptunium in zirconolite and perovskite,” *J. Alloys Compd.*, vol. 271–273, pp. 221–226, 1998.

[45] D. Caurant, P. Loiseau, and I. Bardez, “Structural characterization of Nd-doped Hf-zirconolite $Ca_{1-x}Nd_xHfTi_{2-x}Al_xO_7$ ceramics,” *J. Nucl. Mater.*, vol. 407, no. 2, pp. 88–99, 2010.

[46] S. V. Stefanovsky, A. Y. Troole, M. I. Lapina, B. S. Nikonov, A. V. Sivtsov, and S. V. Yudintsev, “XRD, SEM and TEM study of the Gd-doped zirconolites,” in *Materials Research Society Symposium - Proceedings*, 2002, vol. 713, no. January, pp. 345–350.

[47] S. Ji, Y. Li, S. Ma, C. Liu, K. Shih, and C. Z. Liao, “Synergistic effects of Ln and Fe Co-Doping on phase evolution of $Ca_{1-x}Ln_xZrTi_{2-x}Fe_xO_7$ (Ln = La, Nd, Gd, Ho, Yb) ceramics,” *J. Nucl. Mater.*, vol. 511, pp. 428–437, 2018.

[48] S. Ma, S. Ji, C. Liao, C. Liu, K. Shih, and W. He, “Effects of ionic radius on phase evolution in Ln-Al co-doped $Ca_{1-x}Ln_xZrTi_{2-x}Al_xO_7$ (Ln = La, Nd, Gd, Ho, Yb) solid solutions,” *Ceram. Int.*, vol. 44, no. 13, pp. 15124–15132, 2018.

[49] Y. B. Zhang *et al.*, “Phase evolution, microstructure and chemical stability of $Ca_{1-x}Zr_{1-x}Gd_{2x}Ti_2O_7$ ($0.0 \leq x \leq 1.0$) system for immobilizing nuclear waste,” *Ceram. Int.*, vol. 44, no. 12, pp. 13572–13579, 2018.

[50] M. Jafar, S. N. Achary, N. P. Salke, A. K. Sahu, R. Rao, and A. K. Tyagi, “X-ray diffraction and Raman spectroscopic investigations on $CaZrTi_2O_7$ - $Y_2Ti_2O_7$ system: Delineation of phase fields consisting of potential ceramic host materials,” *J. Nucl. Mater.*, vol. 475, pp. 192–199, 2016.

[51] M. Jafar, P. Sengupta, S. N. Achary, and A. K. Tyagi, “Phase evolution and microstructural studies in $CaZrTi_2O_7$ (zirconolite)-$Sm_2Ti_2O_7$ (pyrochlore) system,” *J. Eur. Ceram. Soc.*, vol. 34,

Corresponding authors: lrblackburn2@sheffield.ac.uk; n.c.hyatt@sheffield.ac.uk

no. 16, pp. 4373–4381, 2014.

[52] M. Jafar, P. Sengupta, S. N. Achary, and A. K. Tyagi, “Phase evolution and microstructural studies in $CaZrTi_2O_7$-$Nd_2Ti_2O_7$ system,” *J. Am. Ceram. Soc.*, vol. 97, no. 2, pp. 609–616, 2014.

[53] L. R. Blackburn *et al.*, “Influence of accessory phases and surrogate type on accelerated leaching of zirconolite wasteforms,” *npj Mater. Degrad.*, vol. 5, no. 24, pp. 1–11, 2021.

[54] H. Li, Y. Zhang, P. J. McGlinn, S. Moricca, B. D. Begg, and E. R. Vance, “Characterisation of stainless steel-synroc interactions under hot isostatic pressing (HIPing) conditions,” *J. Nucl. Mater.*, vol. 355, no. 1–3, pp. 136–141, 2006.

[55] G. R. Lumpkin, K. L. Smith, and M. G. Blackford, “Partitioning of uranium and rare earth elements in synroc: effect of impurities, metal additive, and waste loading,” *J. Nucl. Mater.*, vol. 224, no. 1, pp. 31–42, 1995.

[56] Y. Zhang, M. W. A. Stewart, H. Li, M. L. Carter, E. R. Vance, and S. Moricca, “Zirconolite-rich titanate ceramics for immobilisation of actinides - Waste form/HIP can interactions and chemical durability,” *J. Nucl. Mater.*, vol. 395, pp. 69–74, 2009.

[57] E. R. Vance, A. Jostsons, R. A. Day, C. J. Ball, B. D. Begg, and P. J. Angel, “Excess Pu Disposition in Zirconolite-Rich Synroc,” in *Mat. Res. Soc. Symp. Proc.*, 1996, vol. 412, pp. 41–47.

[58] N. P. Mikhailenko, A. V. Ochkin, S. V. Stefanovsky, and O. I. Kirjanova, “Phase relations and chemical durability of ceramics in the pseudo-binary system: $CaZrTi_2O_7$-$GdAlO_3$,” in *Materials Research Society Symposium Proceedings*, 2004, vol. 807, no. January 2011, pp. 327–331.

[59] N. Mikhailenko, S. Stefanovsky, and A. Ochkin, “Phase relations and elemental distribution among co-existing phases in the ceramics of the pseudobinary system $CaZrTi_2O_7$-$LnAlO_3$ (Ln= Nd, Sm),” in *Mat. Res. Soc. Symp. Proc.*, 2007, vol. 985, pp. 211–216.

[60] R. D. Shannon, “Revised Effective Ionic Radii and Systematic Studies of Interatomic Distances in Halides and Chalcogenides,” *Acta Cryst.*, vol. A 32, pp. 751–767, 1976.

[61] R. L. Putnam, A. Navrotsky, B. F. Woodfield, J. L. Shapiro, R. Stevens, and J. Boerio-Goates, “Thermochemistry of Hf-Zirconolite, $CaHfTi_2O_7$,” in *Mat. Res. Soc. Symp. Proc.*, 2011, no. 556.

[62] N. C. Hyatt, M. C. Stennett, E. R. Maddrell, and W. E. Lee, “Single Phase Ceramic Wasteforms for Plutonium Disposition,” *Adv. Sci. Technol.*, vol. 45, no. 2006, pp. 2004–2011, 2006.

Corresponding authors: lrblackburn2@sheffield.ac.uk; n.c.hyatt@sheffield.ac.uk

[63] K. Zhang, D. Yin, Z. He, B. Luo, and H. Zhang, “Combustion synthesis of Hf-doped zirconolite-rich composite waste forms and the aqueous durability,” *J. Adv. Ceram.*, vol. 8, no. 3, pp. 448–455, 2019.

[64] D. M. Strachan, R. P. Turcotte, and B. O. Barnes, “MCC-1: A Standard Leach Test for Nuclear Waste Forms,” *Nucl. Technol.*, vol. 56, no. 2, pp. 306–312, 1982.

[65] K. Zhang, D. Yin, K. Xu, and H. Zhang, “Self-propagating synthesis and characterization studies of Gd-bearing Hf-zirconolite ceramic waste forms,” *Materials (Basel).*, vol. 12, no. 1, 2019.

[66] D. Caurant, P. Loiseau, and I. Bardez, “Structural characterization of Nd-doped Hf-zirconolite $Ca_{1-x}Nd_xHfTi_{2-x}Al_xO_7$ ceramics,” *J. Nucl. Mater.*, vol. 407, no. 2, pp. 88–99, 2010.

[67] P. Loiseau, D. Caurant, N. Baffier, and C. Fillet, “Structural characterization of polycrystalline (Nd,Al)-substituted zirconolite,” in *Mat. Res. Soc. Symp. Proc.*, 2003, vol. 757, no. January 2003, pp. 243–250.

[68] K. Zhang, D. Yin, Z. He, J. Xue, W. Zhao, and H. Zhang, “Combustion synthesis and characterizations of Sm_2O_3 doped zirconolite-rich waste forms with CuO as oxidant,” *J. Rare Earths*, vol. 37, no. 12, pp. 1359–1365, 2019.

[69] G. Leturcq and B. Auzemerie, “Study of the Effects of Potential Impurities from Actinide Flux on the Zirconolite Microstructure,” in *Mat. Res. Soc. Symp. Proc.*, 2004, vol. 807, pp. 1–5.

[70] R. Ali and M. Yashima, “Space group and crystal structure of the Perovskite CaTiO3 from 296 to 1720 K,” *J. Solid State Chem.*, vol. 178, no. 9, pp. 2867–2872, 2005.

[71] S. Sasaki, C. T. Prewitt, and J. D. Bass, “Orthorhombic Perovskite $CaTiO_3$ and $CdTiO_3$: Structure and Space Group,” *Acta Crystallogr. Sect. C Struct. Chem.*, vol. 43, pp. 1668–1674, 1987.

[72] J. Yang, M. Zhao, M. Shahid, J. Feng, C. Wan, and W. Pan, “Electronic structure, anisotropic elastic and thermal properties of monoclinic $Ca_2Nb_2O_7$,” *Ceram. Int.*, vol. 42, no. 8, pp. 9426–9432, 2016.

[73] A. W. Sleight, “High Pressure Substitutions for Cd in $Cd_2Nb_2O_7$ and $Cd_2Ta_2O_7$,” *Mat. Res. Bull.*, vol. 9, pp. 1437–1442, 1974.

[74] G. Botelho, I. C. Nogueira, E. Moraes, and E. Longo, “Study of structural and optical properties of CaMoO4 nanoparticles synthesized by the microwave-assisted solvothermal method,” *Mater.*

Corresponding authors: lrblackburn2@sheffield.ac.uk; n.c.hyatt@sheffield.ac.uk

Chem. Phys., vol. 183, pp. 110–120, 2016.

[75] N. P. Singh *et al.*, “Effects of annealing temperature on structural and luminescence properties of $CdMoO_4$:Dy^{3+} phosphor synthesized at room temperature by co-precipitation method,” *Solid State Sci.*, vol. 102, no. March, p. 106172, 2020.

[76] B. D. Begg, E. R. Vance, B. A. Hunter, and J. V. Hanna, “Zirconolite transformation under reducing conditions,” *J. Mater. Res.*, vol. 13, no. 11, pp. 3181–3190, 1998.

[77] J. Squire, E. R. Maddrell, N. C. Hyatt, and M. C. Stennett, “Influence of lubricants and attrition milling parameters on the quality of zirconolite ceramics, consolidated by hot isostatic pressing, for immobilization of plutonium,” *Int. J. Appl. Ceram. Technol.*, vol. 12, no. S2, pp. E92–E104, 2015.

[78] N. C. Hyatt, C. L. Corkhill, M. C. Stennett, R. J. Hand, L. J. Gardner, and C. L. Thorpe, “The HADES Facility for High Activity Decommissioning Engineering & Science : part of the UK National Nuclear User Facility,” in *IOP Conf. Series: Materials Science and Engineering*, 2020, vol. 818, pp. 1–8.

Corresponding authors: lrblackburn2@sheffield.ac.uk; n.c.hyatt@sheffield.ac.uk

4 EXPERIMENTAL METHODOLOGY

4.1 Materials Synthesis

4.1.1 Batching and Milling

The majority of ceramic formulations presented in this thesis were initially prepared *via* a solid state synthesis, between a mixture of reagent grade (typically > 99.9% purity) oxide precursors. For each targeted composition, a batch calculation was performed in order to attain the required mass of each constituent precursor, to an accuracy of 0.0001 g. Prior to weighing, all precursors were dried at 180 °C (800 °C for particularly hygroscopic compounds such as CeO_2/HfO_2) in order to eliminate surface moisture and adsorbed impurities, the volatilisation of which during the sintering process may afford greater porosity. The handling and manipulation of radioactive precursor material, namely $^{238}UO_2$ and $^{232}ThO_2$, was performed where possible in a glovebox. When transferring material from the glovebox environment, all external surfaces of transport vessels were monitored to remove mobile contamination. The dried powders, weighed to the desired amount, were then placed into a milling jar (SiAlON for ~ 5 – 10 g batches, Y-stabilised ZrO_2 for > 20 g batches), with ZrO_2 milling media and a carrier fluid, typically isopropanol, acetone and/or deionised H_2O. The milling process serves to reduce the primary particle size of the constituent precursor materials, increasing the associated surface energy through modification of the primary morphology, promoting greater reactivity and thus resulting improved thermal treatment of ceramic materials. Mill pots were placed into a Fritsch P7 planetary mill (inactive materials) or Retsch PM100 (^{238}U/^{232}Th containing materials) and homogenised, typically with a milling cycle of a maximum rotational frequency of 400 rpm held for 20 min, with the direction of milling reversed after 10 min. However, for larger batches (*i.e.* material produced for HIP) the milling time was often doubled to 40 min. The milling jar was then removed and placed into a small drying oven set to 80 °C and dried for over 12 h, in order to evaporate excess solvent. The batch material was then discharged and the powder recovered and stored, prior to synthesis *via* cold pressing and sintering (CPS), hot isostatic pressing (HIP) or reactive spark plasma sintering (RSPS). For batches containing ^{238}U/^{232}Th, the powder recovery stage was performed either in a glovebox or dedicated fumehood rated for use with active material.

4.1.2 Cold Pressing and Sintering

Solid state cold pressing and sintering (CPS) is a commonly utilised and well understood method of ceramic processing, as it is relatively simple and affords a reasonable throughput. CPS is comprised of two steps, the first of which involves the compression of milled precursor material into loosely bound powder compacts (pellets) referred to as a green body, under uniaxial pressure using a die. As the die is filled with powder, a network of large and small voids is formed. The application of pressure serves to reduce the volume of granular voids through rearrangement, deformation and fragmentation processes. Green pellets are densified with approximately 30 – 40 vol. % porosity, the formation of which improves the mechanical properties of the powder compact, aids handling, and promotes sintering under high temperature in a furnace to achieve the desired grain growth and phase formation. The sintering of ceramic materials is a temperature and/or pressure driven process through which

loosely packed powder compacts are converted into a dense product, substantially improving the homogeneity of the ceramic microstructure and drastically increasing mechanical properties. A simplified illustration of the sintering process is given in **Fig. 25**. The process of solid state sintering generally occurs at elevated temperatures, below the melting point of the constituent material. The driving force for sintering is a reduction in the free surface area, and elimination of solid-vapour interfaces of a powder compact, achieved by atomic diffusion processes promoting either densification of the bulk powder body (causing shrinkage), or by microstructure coarsening (without shrinkage) [1]. The densification of the bulk material is also controlled by the primary particle size, sphericity, application of pressure and imposed atmospheric conditions. The mechanism of solid state sintering involves, at least, six distinct mass transport pathways, for a system of three particles (**Fig. 26**) however not all of these are densifying mechanisms. Surface diffusion, lattice diffusion and vapour transport (mechanisms 1, 2 and 3 in **Fig. 26**) from the surface of the particulates result in the formation of necks between primary particles, however, these mechanisms are non-densifying [2]. Diffusion of material from grain boundaries to pores promote neck growth, and is the leading densification mechanism during the sintering of polycrystalline ceramics (mechanisms 4 and 5 in **Fig. 26**). Plastic flow by dislocation motion may also contribute to densification however this is more typical for the sintering of metal powders.

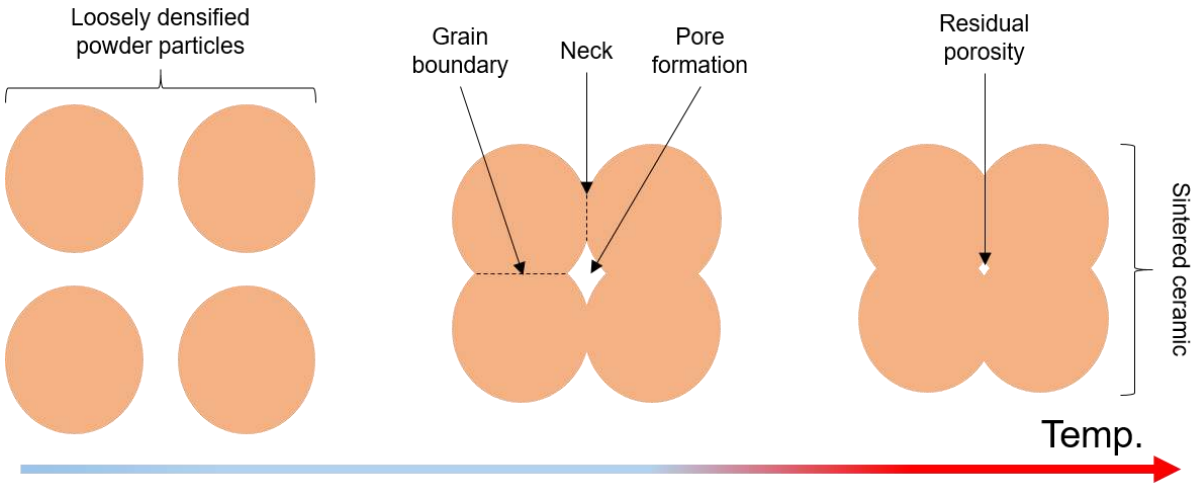

Fig. 25) Simplified illustration of ceramic powder sintering

The sintering of materials in the course of this thesis was typically as follows. Approximately 0.35 g of dried batch material was placed into a hardened steel die with 10 mm internal diameter and compressed under 3 t uniaxial pressure, for approximately 60 s. Each green body was produced in duplicate and were loaded onto a zirconia setter plate, or alumina crucible, and placed into a furnace for sintering. The choice of furnace was determined by the processing environment; a muffle furnace would be used for air sintering, and for synthesis under flowing argon or 5% H_2/N_2, an alumina tube furnace would be used. In these instances, the samples would be placed into the central hot-zone of the tube, which would then be sealed and purged for several hours to remove air, prior to sintering. In order to maintain consistency, all samples were reacted for 20 h in the required atmosphere, at 1350 °C, unless stated otherwise.

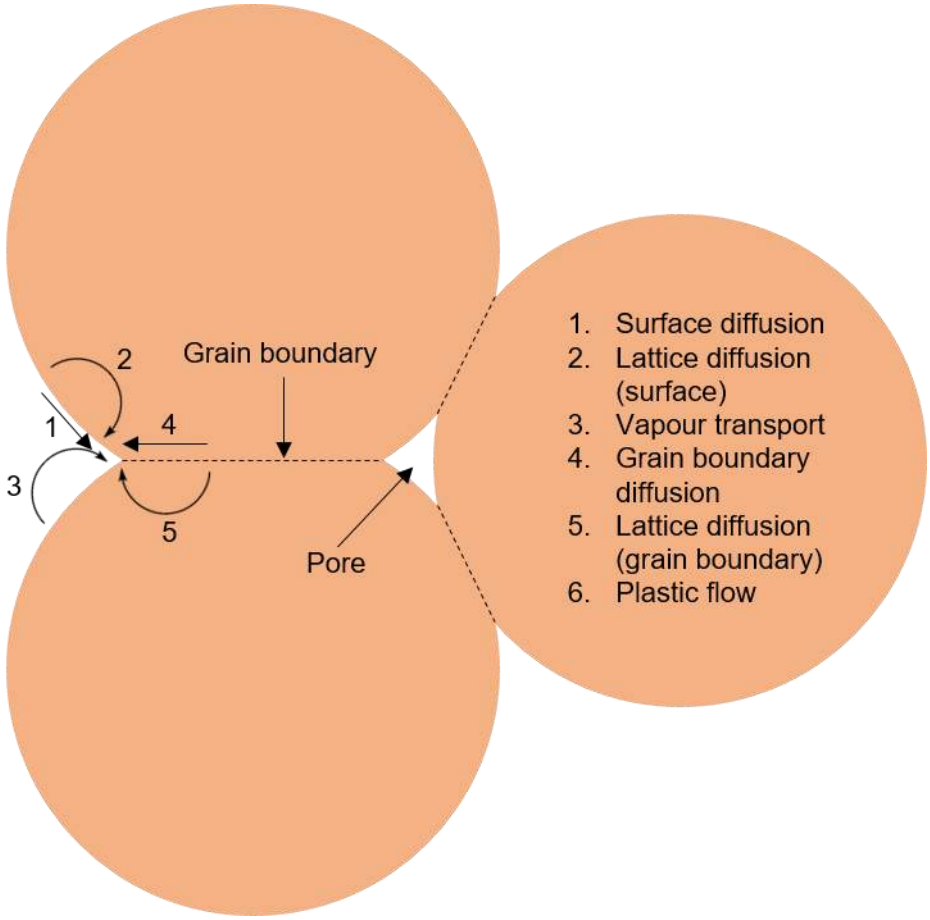

Fig. 26) Outline of the six distinct mechanisms that may contribute to the sintering of a consolidated mass of crystalline particulates comprising a ceramic compact (redrawn from [2])

4.1.3 Hot Isostatic Pressing

Hot Isostatic Pressing (HIP) is a pressure-assisted sintering technique that was originally developed for the diffusion bonding of dissimilar metals and nuclear fuel element assemblies. However, the technique is now commonly applied to a variety of metallic and ceramic components in many different industries [3]–[6]. The application of HIP for the thermal treatments of radioactive waste is relatively novel, however the HIP process has been proposed as the ideal processing route for a range of applications, such as Magnox sludge conditioning, and is a candidate thermal processing route for UK Pu inventories, should the decision be taken to implement a disposition strategy favouring immobilisation prior to disposal [7]. HIP utilises the simultaneous application of elevated heat and isostatic pressure to consolidate material, affording a significant reduction in bulk volume. The material is typically a loosely densified powder compact pressed into a protective overpack material such as stainless steel, allowing simultaneous sintering and densification into a dense monolith. Handling difficulties are also alleviated by this route, as the processed material is protected by an additional stainless steel overpack layer. The AIP6-30H HIP unit at the University of Sheffield is displayed in **Fig. 27**. The advantages of HIP, comparative to traditional ceramic processes such as CPS, are numerous. Predominantly, as the densification cycle is achieved through the introduction of an inert pressure transfer medium (typically argon gas), the HIP process is largely insensitive to the physical and chemical nature of the batch material. The operating

window for HIP is large, with temperatures of up to 2200 °C permitted by the interchange of the molybdenum furnace to graphite, with a maximum vessel pressure of 206 MPa attainable (30,000 psi). The process also produces a minimal volume of secondary effluent with no potential for volatile losses, is scale independent and can be used to process packages > 100 L.

Fig. 27) HIP control unit exterior (**a**); control unit interior pump (**b**); pressure vessel and argon manifold (**c**); example of processed canister, courtesy of NNL (**d**)

In order to prepare a sample for HIP, the batch material, milled according to the standard procedure as defined above, is first calcined at 600 °C for 12 h, in order to remove adsorbed surface moisture and entrained volatiles that may oppose the isostatic densification process [8]. Calcination was typically performed in air, although in the case of U containing samples, inert Ar gas was introduced to prevent oxidation. The calcined material was then pressed into the walls of a HIP canister under uniaxial pressure. The average dimensions of the in-house HIP canisters used for processing of inactive samples are given in **Fig. 28**. The inactive HIP cans were fabricated in-house from 316 stainless steel cut on the Buehler AbrasiMet™ 250 using SiC cutting blades.

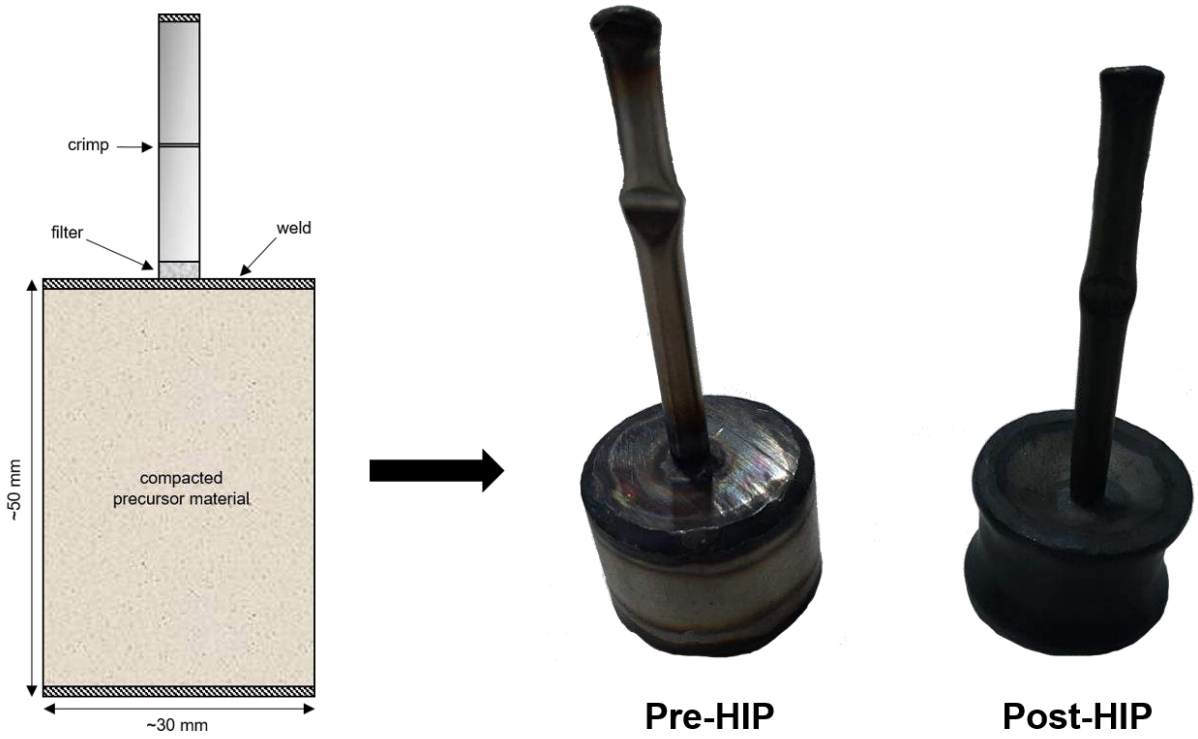

Fig. 28) Illustration of average HIP can dimensions (left) and photographs of canisters pre- and post-processing (right)

Active HIP canisters were externally supplied by AMEPT, machined to specific dimensions, with snap-lock lids that provide an additional layer of containment. The powder was manually compressed into the canister using a plunger, machined to the correct dimension to ensure high packing density, under uniaxial pressure using a hand-pump hydraulic press. For active samples, this stage was performed in a glovebox to protect against the dispersion of radioactive material; active HIP cans were monitored at each stage for mobile contamination and transported in multi-layered containment to the HIP nuclearized zone for HIPing. A labelled photograph of the nuclearized zone is shown in **Fig. 29**. Here, the canister lids, with steel wool added to the base of the evacuation tube, were welded to the body, prior to connection to a vacuum line. The purpose of the primary evacuation step was to remove all entrained air remaining in the canister, as any remaining air would contribute an external force opposing the densification process, producing porous specimens. Once a suitable vacuum was achieved, the

can (remaining connected to the vacuum line) was placed into a small furnace embedded within the bake-out station (see **Fig. 29b**) to eliminate adsorbed water and other volatiles. The furnace was set at 300 °C, and the canisters remained under heated vacuum (this process is referred to as the 'bake-out') until the vacuum recovered, or a suitable pressure of ~ 7 Pa was achieved. Remaining under vacuum, the cans were removed from the furnace and then crimped using a hydraulic press and vice (**Fig. 29b**). This was immediately followed by a second crimp above the first, at which the evacuation tube was quickly snapped and welded shut, to ensure a hermetic seal. At this point the cans were left to cool to room temperature, prior to HIPing. Once cooled, the pressure vessel was equilibrated to atmosphere, and the vessel lid removed using a small manual crane (**Fig. 27c**). The thermal barrier was removed, exposing the furnace. Sealed HIP canisters were then placed into a stainless steel overpack and placed into the base of the pressure vessel (this varied in the case of radioactive samples, for which the Active Furnace Isolation Chamber (AFIC) plug-in component was used (**Fig. 30**). The thermal barrier was then screwed back into place and the coolant lines were reconnected. The desired temperature and pressure parameters were then programmed using the HIP control computer. The operational parameters were dependent on whether the sample was active or inactive (in the case of the active samples, the temperature and pressure set points were staggered in order to maximise the lifetime of the AFIC unit). An example of a standard inactive HIP cycle is annotated in **Fig. 31**. After the HIP cycle was complete, the lid of the pressure vessel was lifted and samples were visually inspected to determine whether successful densification had occurred. In the case of active samples, this procedure was performed in tandem, with continuous monitoring was performed to ensure no dispersion of radioactive material had occurred. Once it had been established that no loss of containment had occurred, the processed canisters were retained for characterisation.

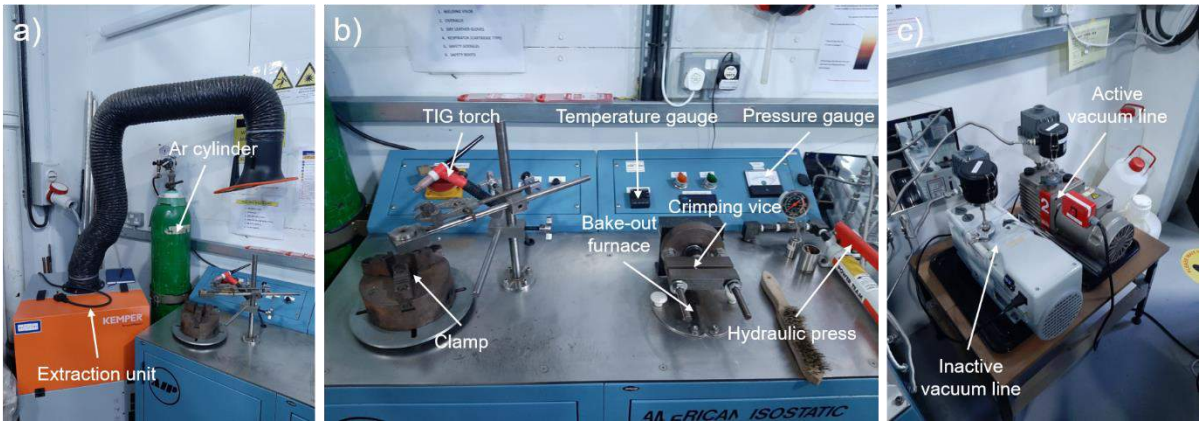

Fig. 29) Nuclearized zone: filtered extraction unit and Ar cylinder (**a**); bake-out station, with TIG torch, furnace and hydraulic vice (**b**); inactive and dedicated active vacuum line (**c**)

The AFIC plug in component allows the safe processing of wasteform materials containing ^{238}U and ^{232}Th, and represents a capability unique to the University of Sheffield [9]. The AFIC allows the processing of a single canister, permitted by a unique design ensuring that during the HIP cycle, no radioactive material is dispersed within the pressure vessel in the event of loss of containment. The AFIC is comprised of a two-layer filter house system integrated with sintered metal filters located outside of the hot zone of the furnace, hence this component does not see elevated temperature. The filters

allow gas flow in and out of the chamber whilst ensuring no powder can escape in the event of a canister rupture or rapid decompression stimulated by failure of the pressure vessel. The HIP canister itself is placed inside a boron nitride (or alumina) crucible, with a removable lid to aid sample retrieval. The modular design of the AFIC allows for facile deconstruction and inspection of the constituent components, maximising the lifetime of the unit, which is protected under patent number WO 2018/009782 A1.

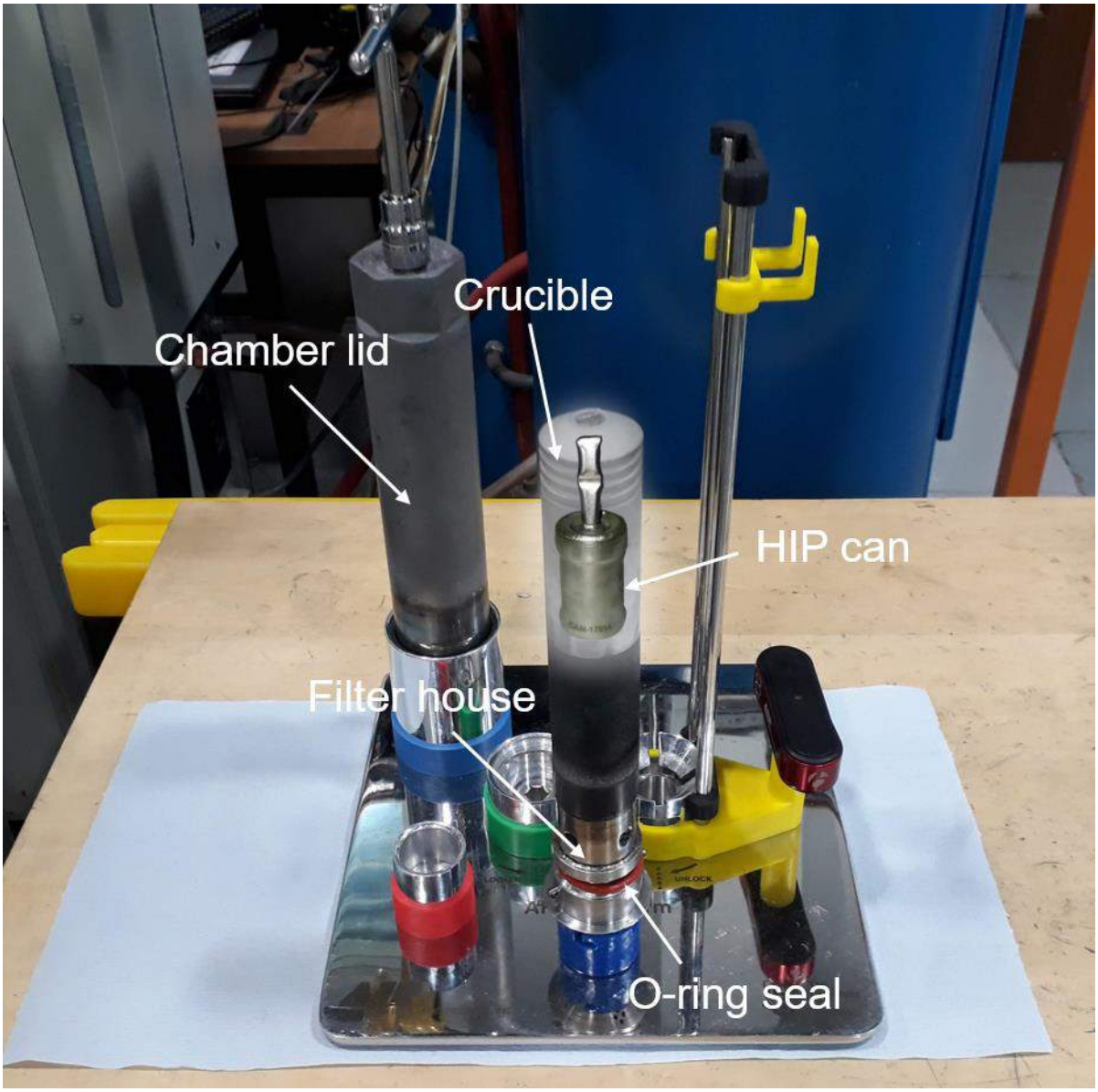

Fig. 30) Active furnace isolation chamber (AFIC) plug-in component for processing of radioactive samples, protected under patent number WO 2018/009782 A1

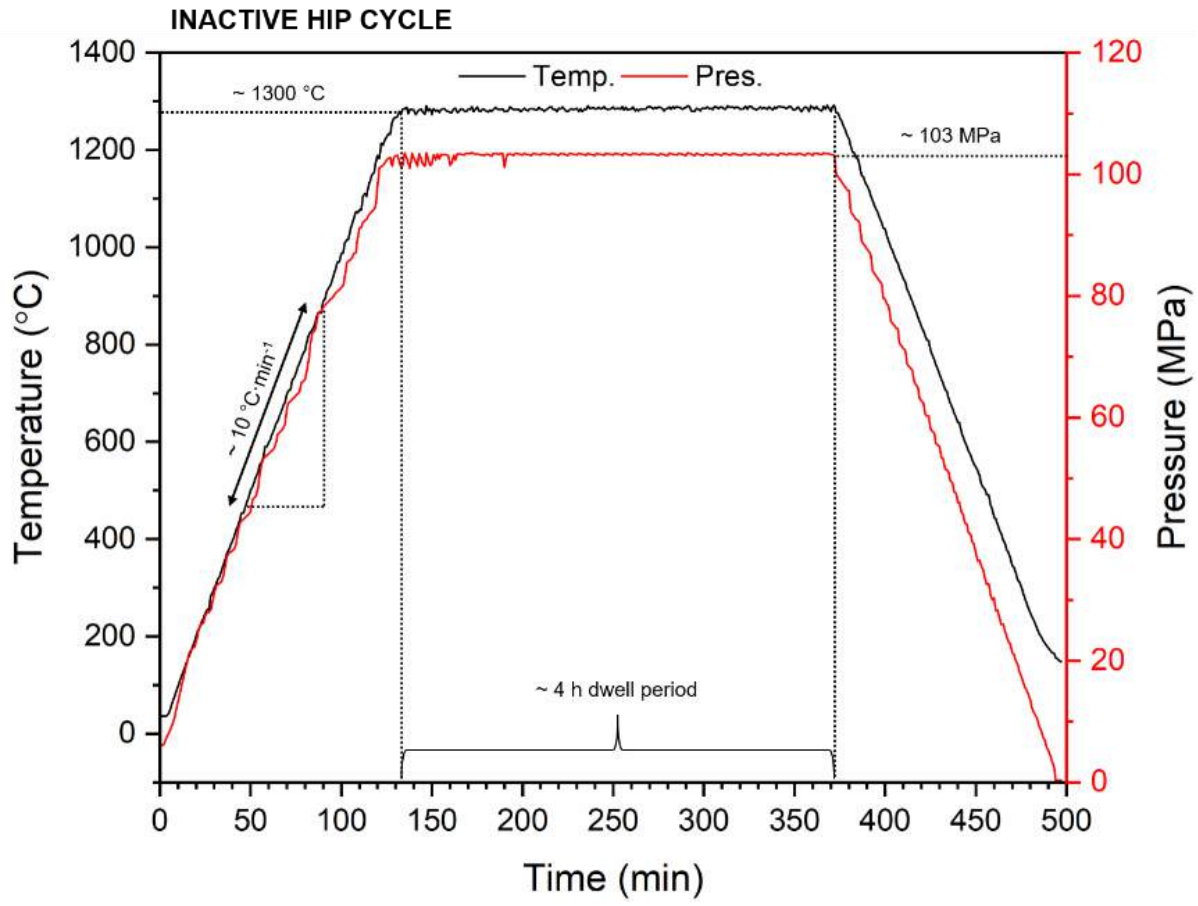

Fig. 31) Example of inactive HIP processing cycle, following a temperature ramp of 10 °C·min^{-1} to 1300 °C and ~ 103 MPa maintained for 4 h, before cooling to room temperature at 10 °C·min^{-1}

4.1.4 Spark Plasma Sintering

Spark plasma sintering (SPS), also referred to as electric field assisted sintering (EFAS) is a novel approach for the rapid synthesis, consolidation and densification of ceramic materials, largely informed through the successful deployment in the field of powder metallurgy processing [10]. More recently, the fabrication of high density ceramic materials for waste immobilisation and fuel composite purposes has been demonstrated by the SPS technique [11]–[13]. A primary advantage of the SPS process, over conventional CPS manufacturing, is the remarkable heating rates that may be achieved (up to ~ 1000 °C·min^{-1} in some instances) resulting in rapid throughput, safety and high reproducibility, producing ceramic monoliths of near-theoretical density with short processing times. The rate at which the heating occurs is primarily attractive for nanostructured ceramic applications whereby densification is required without grain coarsening. While the SPS technique is most commonly used to consolidate reacted crystalline phases to theoretical density, the technique may be applied to non-reacted precursor materials, permitting the formation of the desired phase and densification simultaneously. In this instance, the technique is referred to as reactive spark plasma sintering (RSPS). A conventional SPS arrangement is depicted in **Fig. 32**. The powder compact is compressed into a graphite (or in some

instances BN) die under a uniform uniaxial pressure, typically between 10 – 50 MPa, whilst a DC current is pulsed across the sample. As a spark discharges at the contact point between neighbouring particles, a discharge column is formed resulting in extremely high temperatures, up to 10,000 °C, momentarily generated in the vicinity of the spark, promoting the formation of necks due to surface melting and evaporation. Several controlling mechanisms for SPS-driven sintering have been proposed, including plasma generation, Joule heating and electrical field diffusion, however it is not clear which process is responsible for the SPS effect [14].

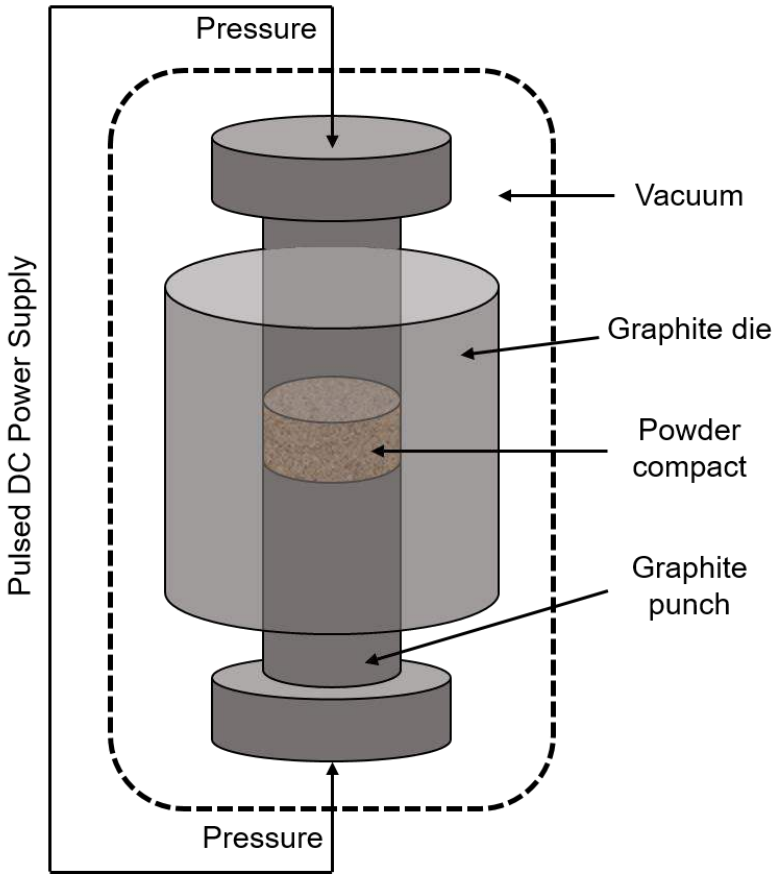

Fig. 32) Conventional spark plasma sintering configuration

In order to prepare material for reaction and/or consolidation by SPS, samples were first batched and milled. Between 5 – 7 g of precursor material was pressed into the walls a graphite die, and compacted under 3 t uniaxial pressure maintained for approximately 10 min. Thin graphite foil spacers were also inserted between the powder compact and die punch, as this is known to promote a more uniform current flow across the sample. The die was then loaded into a HP-D 1050 SPS (FCT Systeme GmBH) and sintered under vacuum. The temperature was increased a rate of 100 °C·min^{-1} to 1320 °C, with a dwell time of 30 min at 5 V and 1 kA. During sintering, a uniaxial pressure of 15 MPa was maintained.

Once cooled, the samples were removed from the die, with adhered graphite foil and surface contamination removed by lightly grinding with SiC paper.

4.2 Materials Characterisation

4.2.1 Powder X-ray Diffraction

Powder X-ray diffraction (XRD) is a fundamental characterisation technique in the field of crystallography and materials science, useful for phase identification, quantitative phase analysis, and structure refinement of crystalline materials. X-rays are a source of electromagnetic radiation with a frequency between 10^{16} – 10^{18} Hz, resulting in a wavelength of the order 10^{-10} m, or 1 Å. As the internal lattice spacing in crystal structures is typically of the same order, X-rays incident on a crystal lattice will interact with the sample and undergo diffraction, producing interference patterns that allow reconciliation of the crystal structure through the Bragg Law. The production of X-rays is permitted from transitions between electronic orbitals, stimulated by the interactions of an atom with charged particles. If a charged particle incident on an atom has sufficient kinetic energy, it is possible to displace a core electron, *e.g.* from the 1s shell into the continuum, leaving a core 'hole' (**Fig. 33**). This hole is immediately filled by an electron transitioning from an outer shell (*e.g.* 2p). This transition produces an X-ray photon of a well-defined wavelength characteristic of the target material, as the energy levels in the atomic orbitals are quantised. In the case of Cu, a 2p → 1s transition (Kα) produces X-rays with a wavelength of 1.5418 Å (averaged between contributions of $K\alpha_1$ and $K\alpha_2$ arising from the possible spin states of the transitioning electron). By studying the interaction of monochromatic X-rays with a crystalline sample, it is possible to reconcile the crystal structure of the material. The conditions necessary for X-ray diffraction are derived from Bragg's Law. The crystal structure of a material may be simplified and considered as a series of parallel planes separated by a distance **d**, that either reflect or partially transmit X-rays incident to the surface by an angle (θ) (**Fig. 34**).

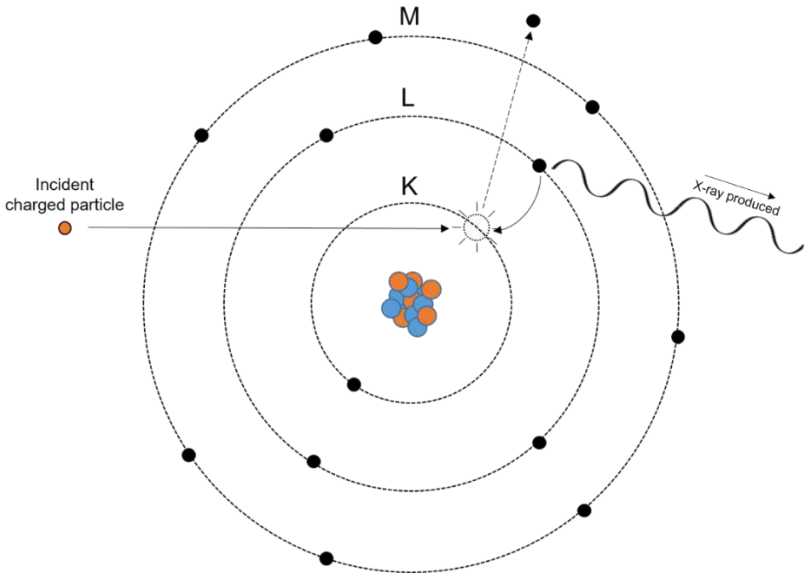

Fig. 33) Simplified illustration of the mechanism of Kα radiation emission *via* 2p → 1s emission

Considering X-rays 1 and 2 are incident upon a crystal plane separated by a distance **d**, for constructive phase interference to occur between X-rays 1 and 2, the extra distance travelled by X-ray 2, equal to **ABC**, must be equal to an integer number of wavelengths, *i.e.* **nλ**. The Bragg condition may then be derived (**Fig. 34**) as $n\lambda = 2 \cdot d \cdot \sin(\theta)$. When the reflected X-rays 1* and 2* are in phase, constructive interference occurs, however, when the Bragg condition is not met, destructive interference occurs. When performing diffraction measurements using a Bragg-Brentano arrangement, as is the case for all XRD data contained within this thesis, the X-ray source remains fixed, whilst the sample and detector are rotated around the axis perpendicular to the X-ray beam. In this parafocussing geometry, the detector records the diffracted X-ray intensity as sample is scanned through a range of angles θ, giving rise to an X-ray diffraction pattern. The width, height and position of reflections is representative of microstructural characteristics of the sample, for example crystallite size, lattice defects and unit cell parameters [15]. For example, a common observation pertaining to the effect of sample microstructure on diffraction peak shape arises from size and strain effects. The size and shape of crystallites (the distribution of which may also be an artefact of the grinding process) and lattice imperfections *e.g.* stacking faults, twinning, dislocations, vacancies and interstitials, typically give rise to peak broadening. Amorphous structures, such as glass networks, do not produce diffraction patterns due to the lack of long range order, rather a large region of diffuse scattering is observed. Glass-ceramic composite materials, *i.e.* glass matrices with entrained crystalline phases give rise to diffraction patterns consisting of both diffuse scattering and intense crystalline reflections. Peak position is largely dictated by the lattice dimensions (*i.e.* a, b, c, α, β, γ) of the specimen, as these parameters give rise to the d-spacing between diffraction will occur. A small change in the lattice parameters, by example through solid solution, will give rise to a change in the 2θ position of diagnostic reflections through the Bragg Law. An example of a diffraction pattern for CeO_2 is given in **Fig. 35**. CeO_2 has the fluorite structure (Fd-3m), powder XRD data in the range $20° \leq 2\theta \leq 55°$ gives rise to a number of sharp intense reflections, indicative of a highly crystalline material. The inset of **Fig. 35** demonstrates a variation in the 2θ position of (111) and (002) reflections in the CeO_2 structure when doped with 20 mol. % Gd_2O_3. The increased lattice parameter, resulting from ionic radii variation between Gd^{3+} (1.053 Å) and Ce^{4+} (0.97 Å) in 8-fold coordination, produces a shift in the observed reflections to a lower 2θ in accordance with the Bragg law. Assuming Gd^{3+} homogeneously replaces Ce^{4+} cations in the CeO_2 structure, the nominal composition can be assigned $Ce_{0.8}Gd_{0.2}O_{1.9}$.

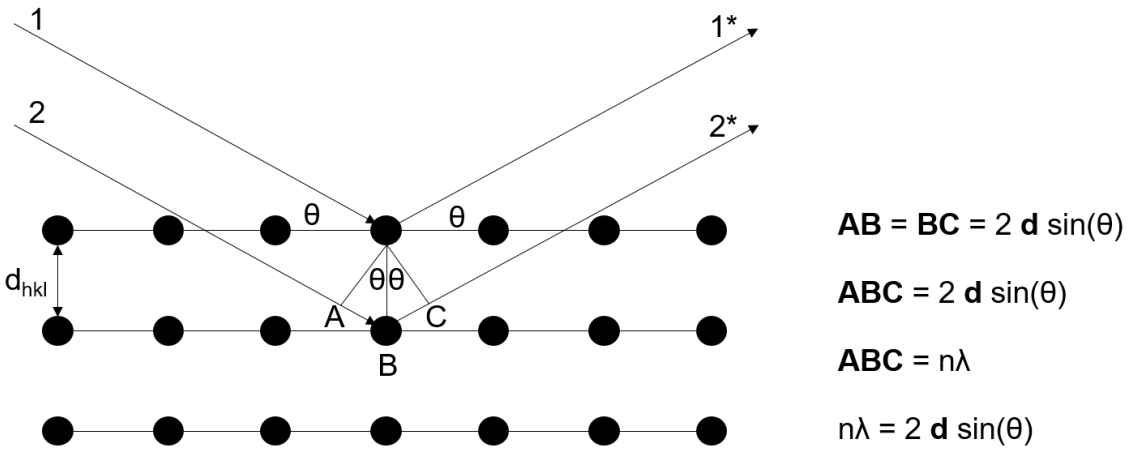

Fig. 34) Derivation of the Bragg law of diffraction

In order to prepare samples for analysis by powder X-ray diffraction, representative portions of ceramic samples were size reduced by manual grinding with isopropanol in an agate pestle and mortar. Aliquots of powder were homogenised to ensure randomised distribution of crystallites, and then mounted in a zero-background PMMA holder and pressed down with a glass slide to counteract surface roughness and preferred orientation effects. Analysis was performed using a Bruker D2 Phaser diffractometer, operating in Bragg-Brentano geometry, using a Cu Kα X-ray source (λ = 1.5418 Å) with a 10 mA current and 30 kV accelerating voltage. The diffractometer was also fitted with a Lynxeye position sensitive detector, and Ni foil to filter Kβ. Unless stated otherwise, data were collected in the range 5° ≤ 2θ ≤ 80°, with a step size of 0.02° 2θ and a count time of 2 s·step^{-1}. Phase identification was accomplished by comparison of peak position and intensities with published crystal structures recorded in the Crystallographic Open Database (COD) or Powder Diffraction File (PDF-4+) databases.

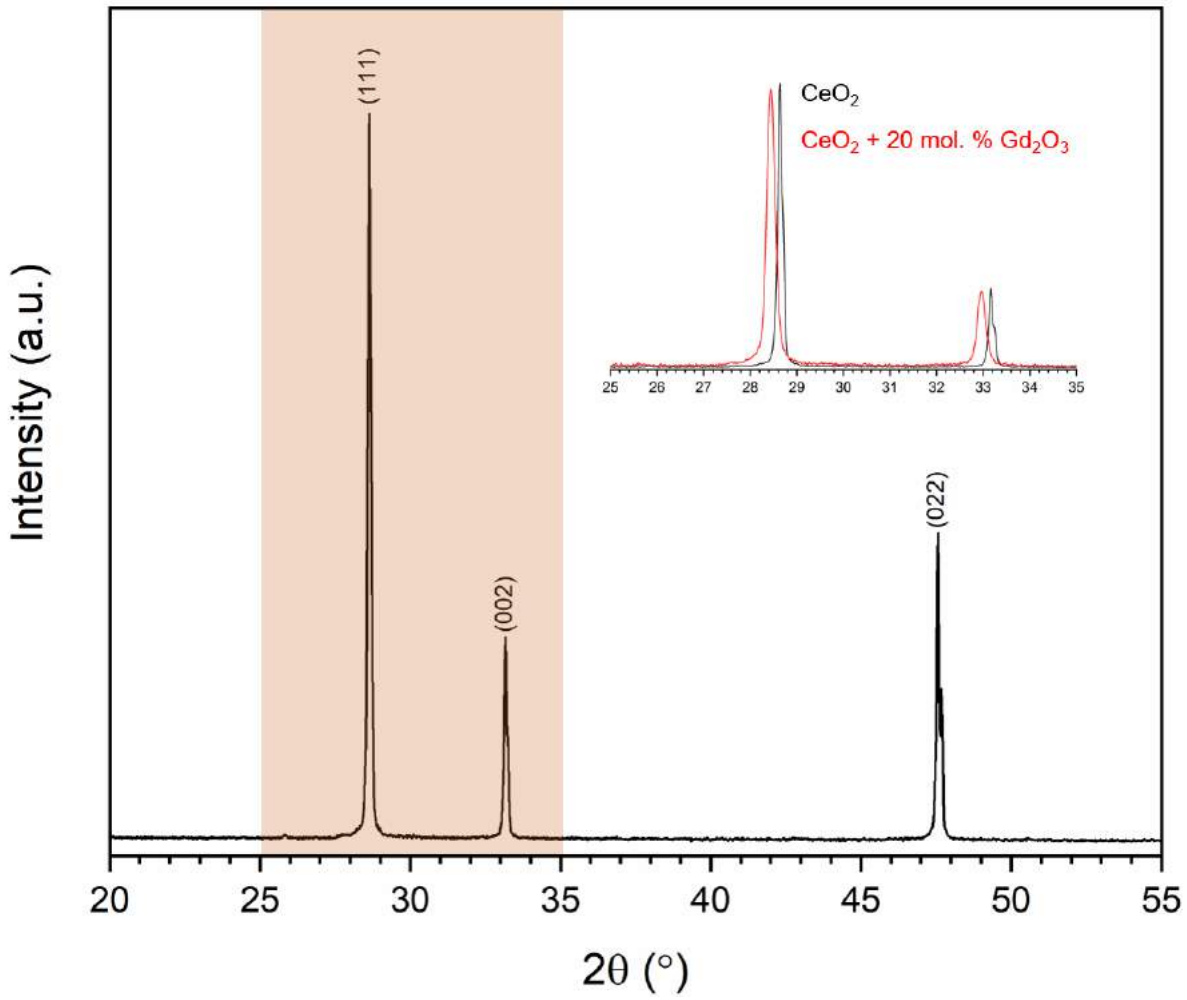

Fig. 35) Powder X-ray diffraction data for CeO_2 and CeO_2 – 20 mol. % Gd_2O_3 solid solution

4.2.2 Rietveld Analysis

Powder XRD data is commonly complemented by analysis *via* the Rietveld method. A Rietveld refinement is an analytical technique by which a least squares fitting of a crystallographic model is applied to an experimental data set, taking into account the relative height, width and 2θ position of diffraction peaks to elucidate, amongst other physical properties, the structural parameters of a crystalline phase [16]. Analysis of powder XRD data by the Rietveld method permits quantitative phase analysis (QPA), whilst refinement of the theoretical model against the experimental data allows the extraction of unit cell parameters and atomic coordinates of the target material. There are a number of measures to determine the quality of the refinement model, however the weighted profile residual (R_{wp}) is often quoted (**Eq. 10**).

$$R_{wp} = \sum_{i}^{n} \sqrt{\frac{w_i(Y_i^{obs} - Y_i^{calc})^2}{\sum_i^n w_i(Y_i^{obs})^2}} \times 100\% \qquad \text{Equation (10)}$$

Here, the least squares approach is used to minimise the weighted sum, denoted by $\boldsymbol{w}$, of a computed diffraction profile ($\boldsymbol{y_{i,calc}}$) and the observed diffraction profile ($\boldsymbol{y_{i,obs}}$). The magnitude of weighted profile residual R_{wp} is therefore a measure of the quality of the fit, where a smaller value indicates a more accurate fit of the model to the data. Rietveld analysis of powder XRD data was achieved using the GSAS package with EXPGUI interface, or the Bruker Topas package [17].

4.2.3 Scanning Electron Microscopy

Electron microscopy is a fundamental characterisation technique across many scientific disciplines. Scanning electron microscopy (SEM) utilises the interaction of an electron beam with a polished specimen, allowing improved resolution over traditional optical microscopic analysis due to the decreased wavelength of electrons with respect to visible light. The wavelength associated with the electron beam is calculated by the de Broglie principle. For example, an electron with kinetic energy 1 eV has a wavelength 1000 smaller than a 1 eV photon, hence with SEM, µm resolution can be achieved. An SEM image is generated by the interaction of a focussed electron beam onto the bulk sample. The electron beam is produced by thermionic emission from a tungsten filament, achieved by heating the filament such that the work function of the filament is exceeded, releasing electrons. Tungsten is commonly used for this application as it has a high melting point and low vapour pressure, and is relatively inexpensive. The stream of electrons is accelerated down the column under vacuum, and focussed on the sample using a series of lenses. The penetration range of the electrons through the sample is finite, due to gradual energy loss through inelastic scattering processes; this penetration is a function of both sample density, and accelerating voltage. The interaction of electrons with the sample surface produces several signals – secondary electrons (SE), backscattered electrons (BSE), Auger electrons (AE) and X-rays, these are the consequence of elastic and inelastic scattering processes (**Fig. 36**) [18]. Secondary electrons are produced between inelastic scattering of the incident electron beam with the sample, exceeding the work function and liberating low energy electrons which are easily attenuated. SE are produced from the first few nm of the probed sample, allowing for surface topology measurements. Electrons that penetrate further into the bulk of the sample can undergo elastic scattering and such can provide compositional analysis, these are backscattered electrons. The amount of scattering is proportional to the atomic number of the nucleus, hence contrast differences BSE micrographs are indicative of compositional variation [19]. X-ray photons are also produced as a result of electron interactions with the bulk sample, by the same principle demonstrated in **Fig. 33**. If the incident electron has sufficient energy to ionise a core electron in the sample, an outer shell electron transition occurs in order to fill the hole left in the core shell, accompanied by the release of an X-ray photon. Alternatively, an emitted X-ray may be absorbed by an outer shell electron, causing a second ionisation, known as an auger electron. The characteristics produced also form the basis of Energy Dispersive X-ray Spectroscopy (EDS – sometimes referred to as EDX). Using appropriate calibration, it is possible to collect the X-rays produced over a scanned surface and construct elemental distribution maps. It is also possible to collect semi-quantitative data, allowing the average composition of a given material based on the intensity of the X-rays produced in a bulk phase. However, the characteristic

wavelength of X-rays produced in elements for which A ≤ 20 is often too weak for most conventional detectors.

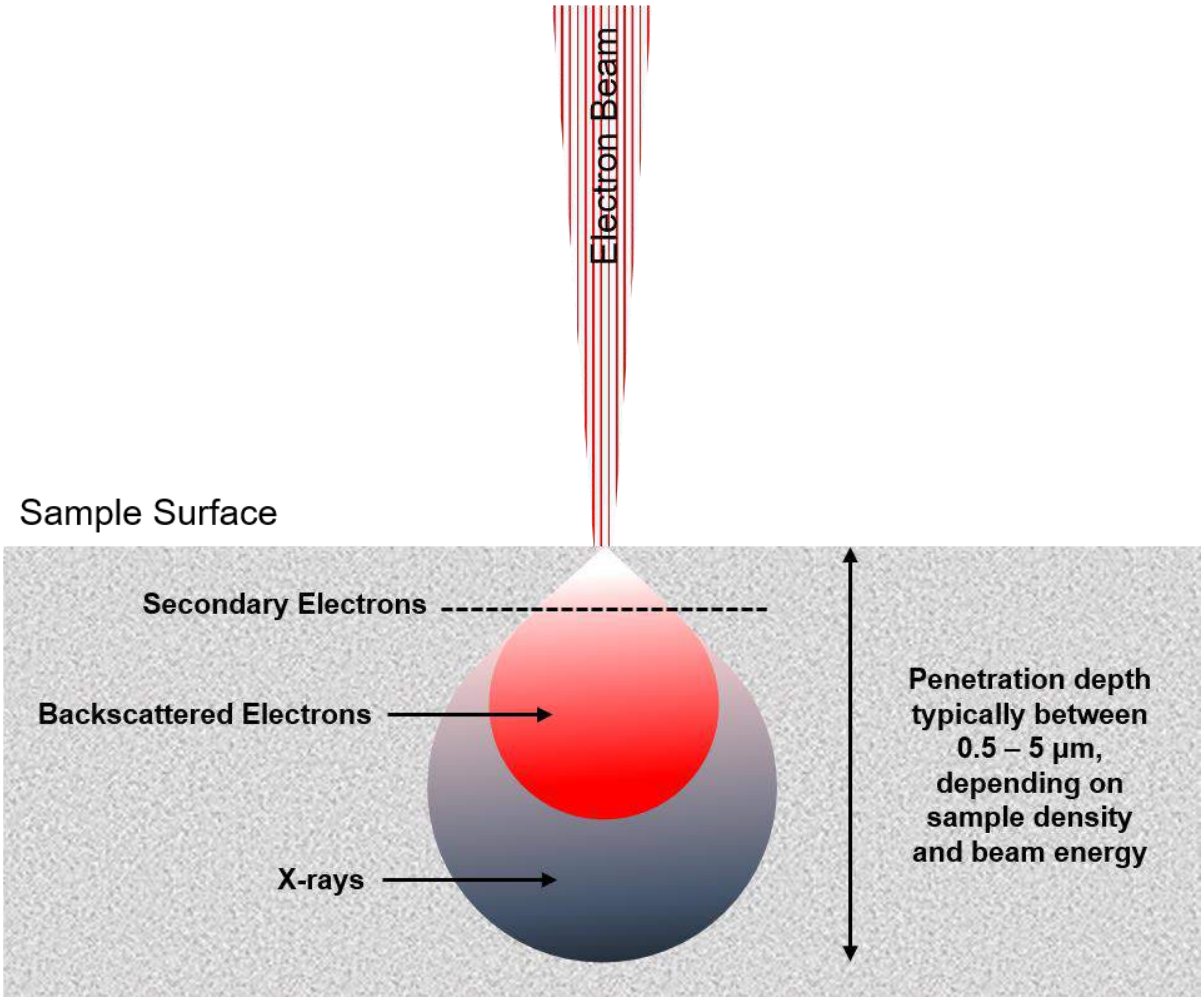

Fig. 36) Interaction between electron beam and bulk material, illustrating the origin of signals which may be used for analysis

Samples were prepared for SEM-EDS analysis by first mounting in a cold setting epoxy resin with a curing time of 24 h, poured into hardened plastic moulds. The resin stubs were freed from the moulds once cured, and the surface was ground with incremental grades of SiC paper (typically P400, P600, P800 and P1200) using a Kemet 300 Lapping and Polishing Wheel with isopropanol applied to the grinding surface. Once the desired finish was achieved, samples were polished to an optical finish with incremental grades of diamond suspension (6 µm, 3 µm and 1 µm). Prior to analysis, samples were sputter coated with a thin layer of carbon using an Agar Auto Carbon Coater, with a thin layer of Ag conductive paint also applied to reduce surface charging effects. Unless otherwise stated, SEM analysis was performed using a benchtop Hitachi TM3030, operating with a 15 kV accelerating voltage and a working distance of 8 mm. This was fitted with a Bruker Quantax Energy Dispersive X-ray spectrometer (EDS) component for compositional analysis.

4.2.4 X-ray Absorption Spectroscopy

X-ray absorption spectroscopy (XAS) is a powerful technique capable of providing local structure information for an absorbing atom in a crystalline lattice, allowing the study of the oxidation state and coordination environment of specific elements in a material. XAS is of particular importance in the design of wasteform materials, as the oxidation state and local coordination of waste cations in glass and ceramic materials is known to be a controlling factor in dissolution rates. Furthermore, the technique can be applied *in-situ* allowing time-resolved corrosion behaviour of wasteform materials to be investigated. XAS necessitates a source of incredibly bright light known as synchrotron radiation, which is the brightest known artificial source of X-rays. The production of synchrotron radiation requires a large particle accelerator, hence XAS and related absorption spectroscopy data are collected at external user facilities, such as the Diamond Light Source (Oxford, UK).

The source of synchrotron radiation arises from electrons travelling at relativistic speeds (*i.e.* close to the speed of light $c = 3 \times 10^8$ m·s^{-1}) are accelerated perpendicular to the direction of their velocity under a magnetic field. The result is the production of high intensity electromagnetic radiation normal to the direction of acceleration, which may be collimated and focussed onto a sample through a series of mirrors. The useful properties of synchrotron radiation, as opposed to laboratory based X-ray sources, include the broad and continuous spectral range of energy values that can be selected, from microwaves to hard X-rays; high photon brightness; high beam stability and collimation. An illustration of the UK national third generation synchrotron, Diamond Light Source, is given in **Fig. 37**.

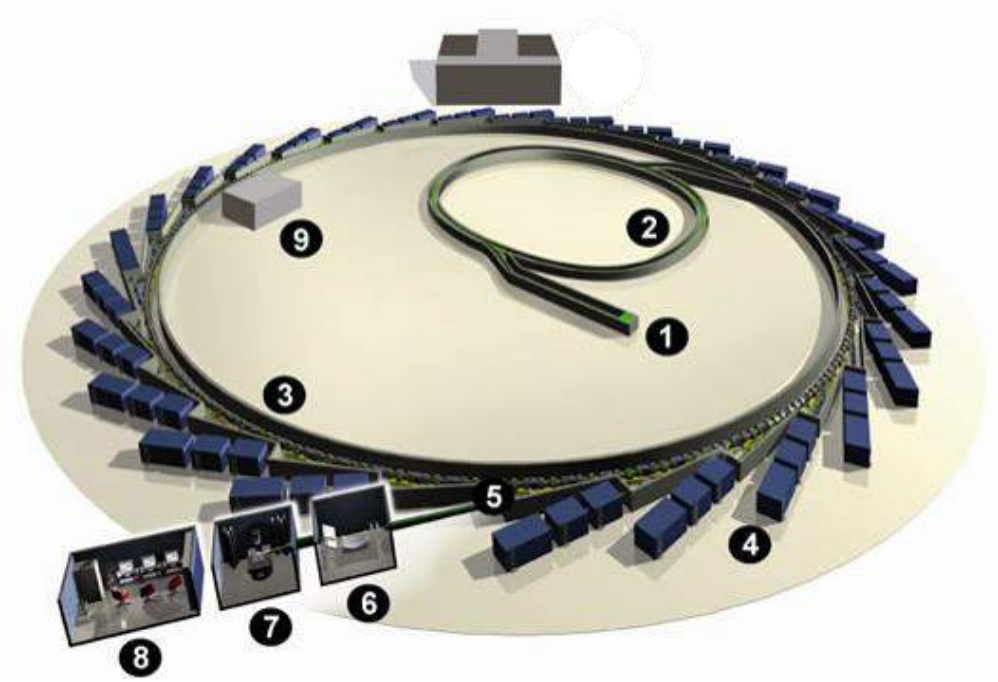

Fig. 37) Illustration of the Diamond Light Source Synchrotron [20]

Electrons that are introduced into the storage ring are first produced by an electron gun and accelerated to relativistic energy by a linear accelerator (**1**) known as a Linac. Electrons above a threshold energy *e.g.* 0.1 GeV are injected from the Linac into the booster synchrotron (**2**) which uses a series of bending magnets to raise the associated electron energy to 3 GeV. The electrons then enter the storage ring (**3**) comprised (in the above example) of 25 straight sections, angled together through an arc of 7.5° to form a closed loop. Large electromagnets (bending magnets) are used to curve the electron beam between straight sections. The acceleration of electrons produces the synchrotron radiation tangential to the direction of travel around the beam (**4**) which is extracted to beamline 'hutches' around the ring to perform experiments. At the interface between the light source and the hutch (**5**) the position of the beam is monitored and potential leaks are detected. The beam then passes to the optics hutch (**6**) which contains optical apparatus such as monochromators, diffraction gratings and mirrors to focus refine the beam footprint and scan across specific energies. Samples for measurement are introduced to the beam in the experimental hutch (**7**), and data acquisition and interface occurs at the control hutch (**8**). As the electrons circulate around the storage ring, energy is progressively lost on each rotation due to the emission of synchrotron radiation. This loss is replenished by passing the electrons through a radiofrequency cavity (**9**) which allows maintenance of a fixed orbit around the ring.

XAS operates on the principle that X-rays interacting with matter undergo scattering and absorption processes. When an atom absorbs X-ray photons, beyond the Fermi energy, electrons become excited and are promoted to a higher energy level, and undergo a transition either to an unoccupied orbital, or are ejected into the continuum as photoelectrons. The core hole is filled within an immediate time interval (~ 10^{-15} s). The anatomy of a conventional XAS experiment is illustrated in **Fig. 38**. Incident X-rays tuned to a specific energy are incident on a sample containing an element of interest, and in the case of a solid state system, constrained within a lattice site in a particular coordination and valence configuration. By comparing the intensity of the incident beam and the transmitted beam, it is possible to determine the absorption coefficient of the material. By scanning across a continuous range of energies below and above the absorption edge, it is possible to compose an absorption spectrum, such the example provided for the Dy L_3 absorption edge for Dy_2TiO_5 in **Fig. 39**.

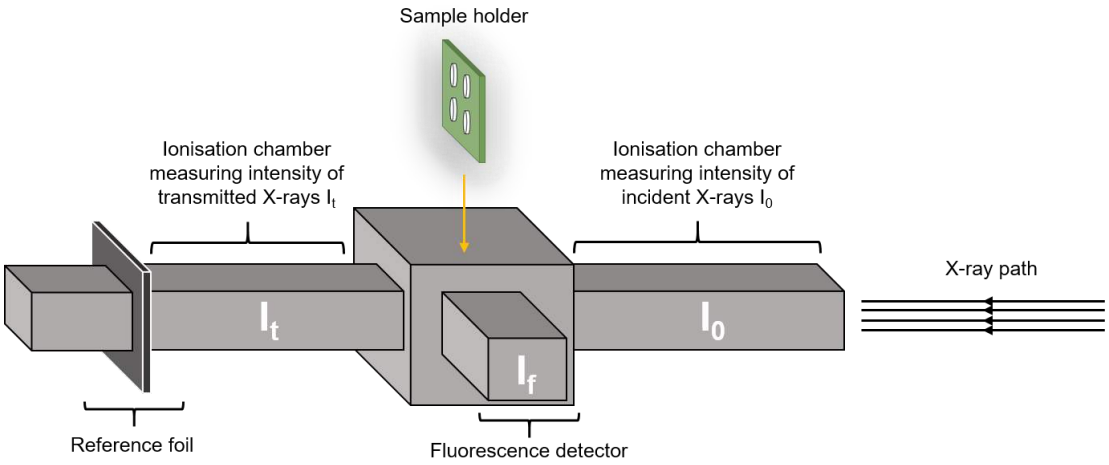

Fig. 38) Anatomy of a conventional XAS experiment

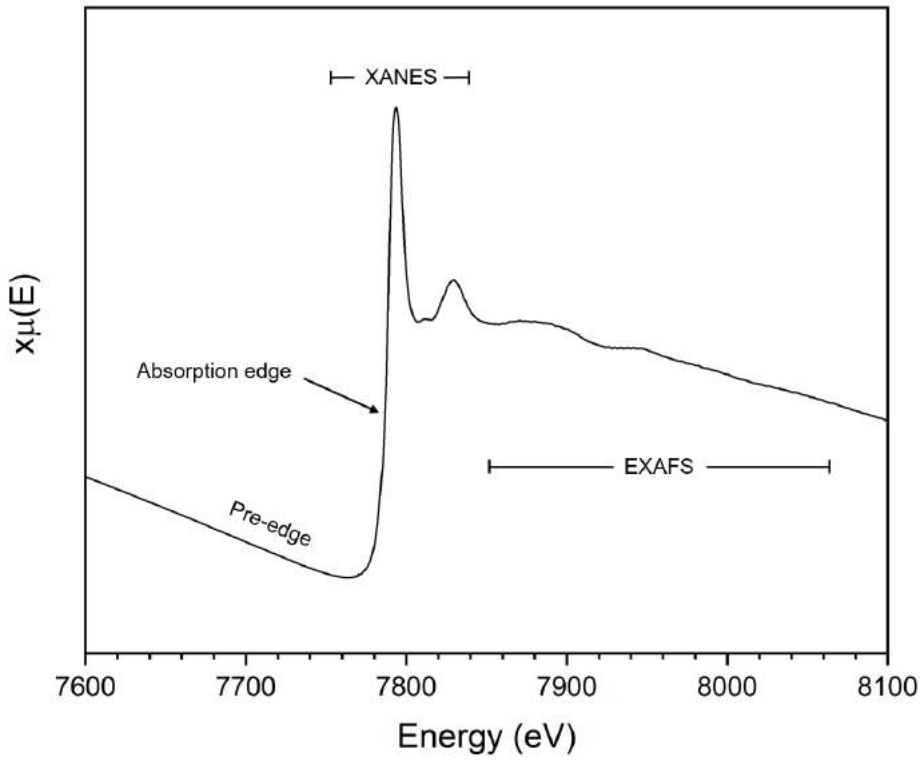

Fig. 39) Transmission X-ray absorption spectrum at the Dy L_3 edge (E_0 = 7790 eV) for Dy_2TiO_5, with pre-edge, XANES and EXAFS absorption features labelled

The XAS spectrum is categorised by four distinct regions [21]:

1. **Pre edge**) A linear trend towards lower absorption is observed as the scanned energy is increased. It is common to observe weak pre-edge features originating from bound state transitions, common especially for the K-edge of first row transition metals such as Cr, arising from 1s → 3d transitions.
2. **Absorption Edge**) As the energy is scanned across the binding regime for a core electron, the excitation process occurs leading to a sharp attenuation in the transmission spectrum, due to X-ray absorption. The edge is named according to the principle quantum number of the excited electron *e.g.* the L_1 edge represents a transition from the 2s orbital. The energy position of the absorption edge is unique to the absorbing element for a given transition, *e.g.* absorption at 17,116 eV is unique to the U L_3 edge.
3. **XANES**) The peaks and shoulders near the absorption edge are generally referred to as the XANES region (X-ray absorption near edge structure). The XANES regions is typically defined up to 50 eV higher than the edge position and is sensitive to oxidation state and coordination environment of the absorbing atom.
4. **EXAFS**) The EXAFS (extended X-ray absorption fine structure) region occurs for up to + 1000 eV after the XANES position, and is comprised of weak oscillations resulting from the interference between the emitted photoelectron and nearby atoms. Fitting of the EXAFS region

can provide information regarding the local structure environment of the absorbing atom, alongside interatomic distances and coordination.

By collecting X-ray absorption spectra for actinide surrogates *e.g.* Ce/U, alongside data for a series of reference compounds, containing Ce and U constrained in variety of oxidation states and coordination environments, it is possible to determine these properties in ceramic materials, either by direct comparison with standards or by linear combination fitting. Specimens were prepared for XAS analysis by dispersing an aliquot of finely ground powder within an X-ray transparent medium, polyethylene glycol (PEG), prior to homogenisation *via* gentle mixing in a pestle and mortar to ensure uniform distribution, before pressing into pellets of 13 mm diameter to a depth of one absorption length. Samples were then transferred to an external synchrotron user facility for measurement by XAS. Data were collected at Diamond Beamline B-18 (Oxford, UK) under proposal SP2407-1, Beamline 6-BM at the National Synchrotron Light Source II (Brookhaven, USA), a U.S. Department of Energy (DOE) Office of Science User Facility Operated for the DOE office of Science by Brookhaven National Laboratory under Contract No. DE-SC0012704, and Beamline BL-27B at the Photon Factory (PF) accelerator-based light source facility (Tsukuba, Japan) under proposal 2019G586. The Diamond synchrotron operates at 3 GeV with a ring current of 300 mA. Beamline B-18 is a versatile conventional XAS bending magnet beamline capable of producing soft to hard X-rays in the energy range 2 – 20 keV. The optical arrangement consists of a water cooled vertically collimated Si mirror, double crystal Si(111) monochromator, a double toroidal focussing mirror and harmonic rejection mirrors. Incident and transmitted beam intensities were measured using ionisation chambers filled with mixtures of He and N_2. Fluorescence emission was detected using a 36 chamber Ge solid state detector. A Cr foil was also measured to act as a reference for which to align the edge position. NSLS-II Beamline 6-BM is supplied by a 3 GeV storage ring operating with a 400 mA ring current, using a 3-pole wiggler to deliver X-rays between 4.5 – 23 keV. The optical arrangement was comprised of a parabolic collimating mirror and Si(111) monochromator, with a toroidal focussing mirror and harmonic rejection mirror. The intensity incident and transmitted beam energy was measured using an ionisation chamber. Fluorescence signal was collected using a SII Vortex ME4 Si drift detector. Beamline BL-27B at PF is supplied by a 2.6 GeV ring operating with a ring current 300 mA, affording X-ray energies between 4 – 20 keV *via* a bending magnet. All data manipulation and analyses were performed using the Demeter suite, comprised of the Artemis and Athena programmes [22]. The Athena component facilitates XANES data processing through appropriate background subtraction, energy calibration, normalisation, and statistical analysis such as linear combination fitting. Athena files, subsequent to such processing, can then be imported into Artemis for more sophisticated analysis of the EXAFS region.

4.2.5 Transmission Electron Microscopy

Transmission electron microscopy (TEM) operates on a similar principle to SEM. However, rather than constructing an image by viewing backscattered and/or secondary electrons, electrons are accelerated at high voltage through a vacuum, incident on a thin section of sample such that they are transmitted through the material. This permits high resolution imaging of the material, and can allow a determination of the crystal structure through the formation of electron diffraction patterns caused by electron transfer

through the material (this is known as selected area electron diffraction (SAED)). To perform TEM measurements, it is essential that the samples of interest are sufficiently thin, hence often analysis is performed on individual grains. A conventional TEM arrangement is shown in **Fig. 40**.

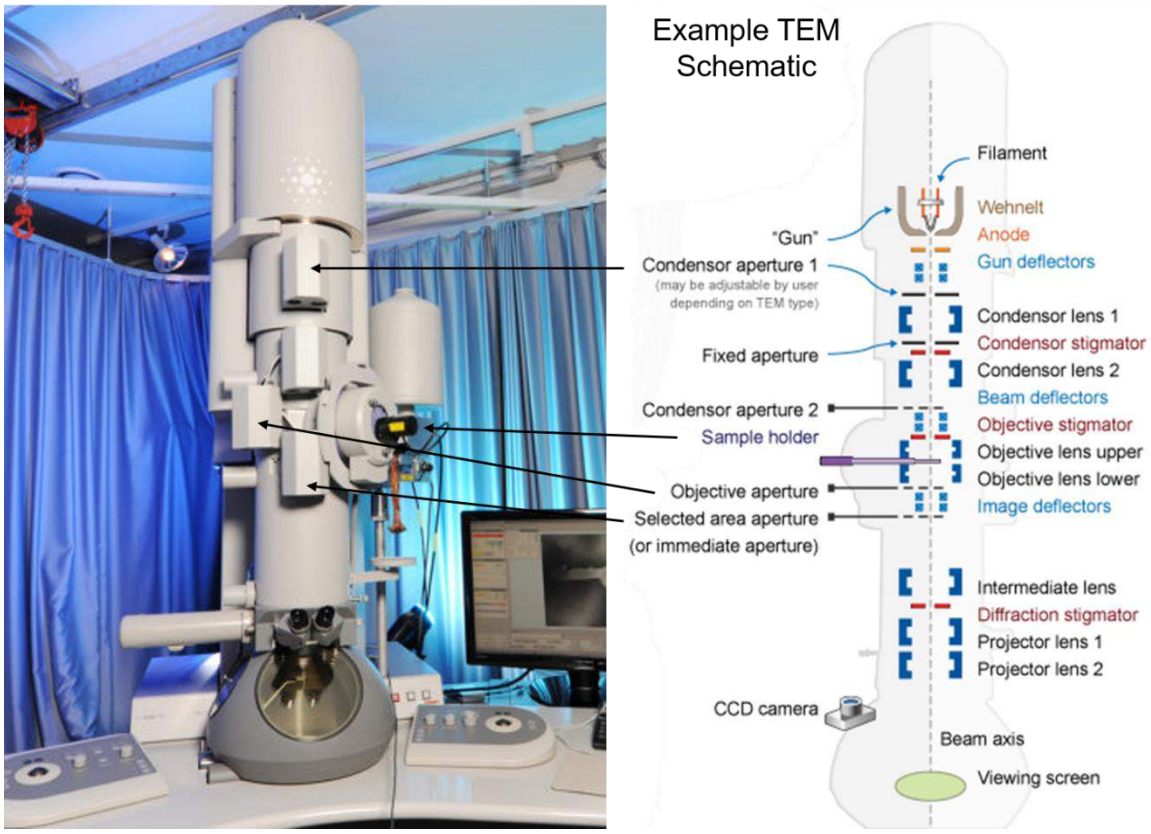

Fig. 40) Cut away diagram of a Philips Tecnai T20 200 kV electron microscope [23]

An electron emission source (often a single crystal source of LaB_6) is connected to a high voltage source to emit electrons which are then accelerated close to the speed of light through a series of condenser lenses such that they are impinged onto the sample. The sample itself is contained within a side entry single or double axis tilt holder, which can be manipulated externally by the operator to change the orientation of the material relative to the electron beam. As the wavelength of electrons at such high energy is significantly smaller than the atomic spacing in the material, the crystal structure acts as a diffraction grating, producing SAED diffraction patterns that are captured below by a CCD camera. An example of two SAED patterns for the pyrochlore structure are given in **Fig. 41**.

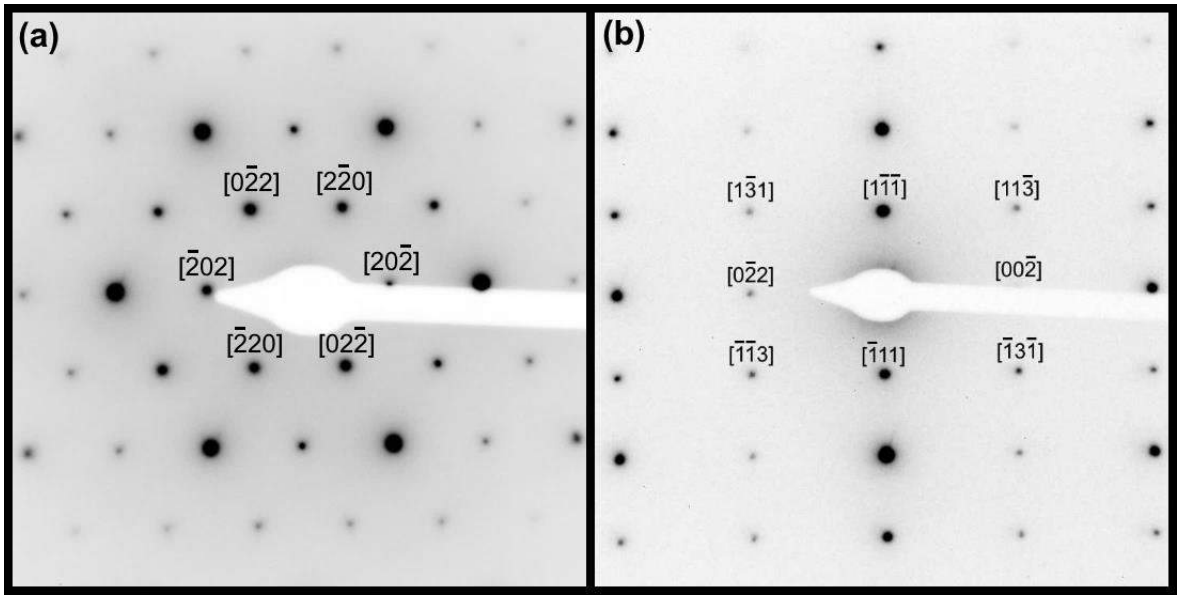

Fig. 41) Selected area electron diffraction patterns for the $Ca_{0.40}Zr_{0.40}Dy_{1.20}Ti_2O_7$ composition, adopting the cubic pyrochlore structure (space group Fd-3m), with the electron beam positioned down the (**a**) [111] and (**b**) [211] zone axes

As can be seen by **Fig. 41**, the electron diffraction pattern is comprised of a series of reflections or spots, with each spot representative of a satisfied diffraction condition related to the crystal structure of the material. It was possible to analyse and successfully index selected area electron diffraction patterns by comparing the collected data with simulated diffraction patterns generated by the Single Crystal software package. The Single Crystal program generates theoretical electron diffraction patterns for specific zone axis of a given crystal structure, by reading data inputted by the user from a CIF file. By comparing the relative position and intensity of the experimental data with the theoretical positions, and comparison with those published in the wider literature, it was possible to correctly assign the polytype regimes formed in a variety of zirconolite solid solutions. Samples were prepared for TEM analysis using the crushed grain method, providing material of the appropriate thickness with relative ease. However, this technique does not permit observations of surface implantation regions (*i.e.* those that might be attained from heavy ion implantation) or grain boundary structures. Preparation of crushed grain samples required a small quantity of the sample to be rapidly ground by hand in ethanol, using an agate pestle and mortar. This was typically performed for several minutes, before allowing the majority of particulates to flocculate and settle. An aliquot of liquid was siphoned from the top of the solvent layer using a pipette and deposited onto the surface of a 300 μm mesh holey Cu grid, and allowed to dry prior to analysis. Two different TEM configurations were utilised during the course of this thesis. For TEM analysis of $Ca_{1-x}Ce_xZrTi_{2-2x}Cr_{2x}O_7$ zirconolite ceramics, a FEI Tecnai F20 was utilised, operating at 200 kV, with selected area electron diffraction patterns captured using a CCD camera. TEM data were collected at the Sorby Centre for Electron Microscopy by Dr. Sebastian Lawson, at the University

of Sheffield. Crushed grain specimens of various $CaZr_{1-x}U_xTi_2O_7$ zirconolite compositions were prepared at the University of Sheffield and transferred to the NNL Central Laboratory facility, under the Advanced Fuel Cycle Programme (AFCP) Academic User Access 2020 Call. A JEOL JEM-2100 operating at 200 kV, equipped with an Oxford Instruments 80 mm^2 SSD EDS was utilised to capture dark field images of individual grains and collected selected area electron diffraction patterns. The authors are grateful to Dr. Peter Apps from the National Nuclear Laboratory for data collection and assistance with data analysis.

4.2.6 Raman Spectroscopy

Raman spectroscopy is a non-destructive technique used to determine the vibrational modes of molecular structures, revealing information regarding the crystal structure of a material [24]. The technique is more commonly applied as a fingerprinting technique for organic compounds, although it is emerging as a powerful technique to probe local defect chemistry in UO_2 compositions. Nevertheless, the technique is scarcely applied to the characterisation of ceramic wasteforms with low symmetry crystal structures, such as zirconolite. Therefore, during the course of this thesis, Raman spectra were routinely collected on zirconolite $CaZr_{1-x}(Ce,U,Th)_xTi_2O_7$ and $Ca_{1-x}(Ce,U)ZrTi_{2-2x}(Cr,Al,Fe)_{2x}O_7$ compositions, with a view to collate a small library of data that may serve as a useful resource to other researchers in the field. The Raman scattering process arises from the inelastic scattering of a monochromatic light source with a sample. The incident photons excite the atoms present in the sample to higher (virtual) energy states. In quantum theory, 'virtual' energy states are described as very short lived intermediate quantum states that cannot be observed, and serve to describe the excitation of atoms between the ground state and excited electronic state. In such processes, the vast majority of light is scattered at the same wavelength as the source beam, producing Rayleigh scattering. However, a very small portion of the light is in-elastically scattered producing a small increase in wavelength, giving rise to the Raman scattering (**Fig. 42**). Raman spectra were collected on powdered specimens. Samples were prepared for analysis by depositing a small quantity of material onto a glass slide and pressing flat to ensure an even surface. For ^{238}U and ^{232}Th containing samples, this was performed in a glovebox. The glass slide was then placed in a Horiba-XploRA Plus system with a motorised (x,y,z) sample stage. This system was equipped with a 532 nm air cooled Ar^+ laser line, with a laser power of approximately 5 mW. Raman spectra were collected from multiple different areas across the powder surface, in the range 100 – 1000 cm^{-1}.

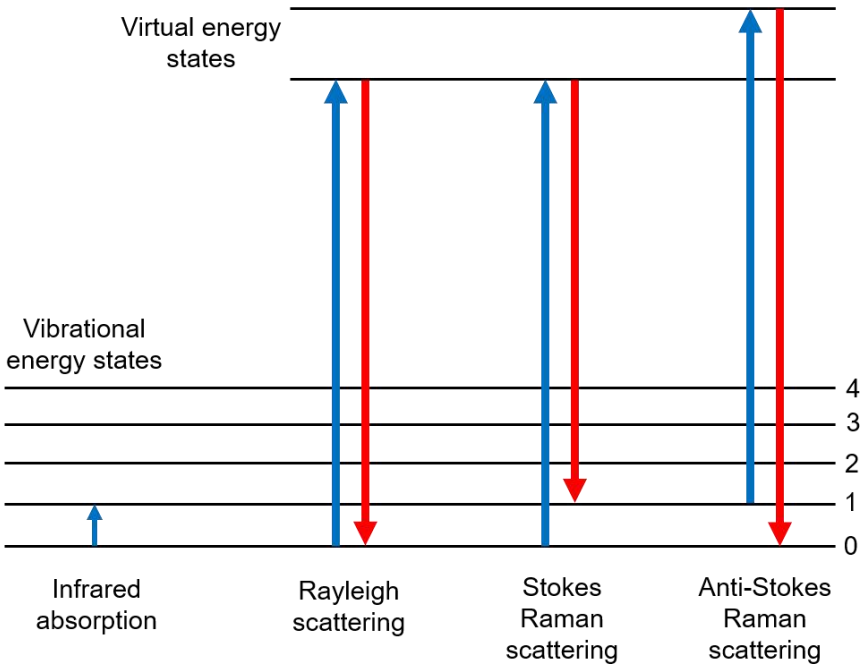

Fig. 42) Energy states involved in various scattering processes

4.2.7 Inductively Coupled Plasma Optical Emission Spectroscopy

Inductively Coupled Plasma Optical Emission Spectroscopy (ICP-OES) is a versatile technique that is used in many industries including environmental remediation and sampling, pharmaceuticals, and any field for which solution analysis is prevalent. ICP-OES allows the concentration of elements in a given solution to be determined, identified by their unique emission spectra [25]. This technique was used to determine the composition of leachate solutions recovered from aggressive dissolution of several distinct zirconolite compositions. Elemental concentration analysis is achieved through first converting the liquid to an aerosol before contacting with an Ar^+ plasma torch. An aliquot of solution is drawn from a reservoir by a peristaltic pump and delivered to a nebuliser, the role of which is to convert the bulk liquid into a fine mist, by pressurising the liquid through a small aperture under an overpressure of inert Ar gas. The liquid sample is therefore converted into a fine aerosol, with any residual liquid is discharged as waste. The aerosol is subsequently passed through an Ar^+ plasma torch, operating with a temperature between 7000 – 10,000 K. By passing an intense radiofrequency (RF) signal through a wrapped coil *via* an RF generator, and igniting and ionising the Ar gas stream, a Ar^+ plasma is generated and sustained in the torch. The aerosol is passed through the torch, promoting collisions of Ar^+ ions with the fine aerosol particles, resulting in complete atomisation and ionisation of the sample. As the elements contained within the sample are ionised, electronic relaxation transitions result in the emission of light. These emission spectra are correlated with standards of known concentration, allowing the concentration of elements in the test solution to be calculated. The author is grateful to Dr. Colleen Mann, Dr. Sam Walling, Dr. Laura Gardner, Rachel Crawford and Dr. Claire Corkhill for collection and quantitative analysis of ICP-OES data.

References

[1] T. A. Ring, *Fundamentals of Ceramic Powder Processing and Synthesis*. San Diego: Academic Press, 1979.

[2] M. N. Rahaman, *Ceramic Processing and Sintering*, 2nd ed. Marcel Dekker, Inc., 2003.

[3] M. H. Bocanegra-Bernal, “Hot isostatic pressing (HIP) technology and its applications to metals and ceramics,” *J. Mater. Sci.*, vol. 39, pp. 6399–6420, 2004.

[4] E. Maddrell, “Hot isostatically pressed wasteforms for future nuclear fuel cycles,” *Chem. Eng. Res. Des.*, vol. 91, pp. 735–741, 2013.

[5] P. G. Heath, M. W. A. Stewart, S. Moricca, and N. C. Hyatt, “Hot-isostatically pressed wasteforms for Magnox sludge immobilisation,” *J. Nucl. Mater.*, vol. 499, pp. 233–241, 2018.

[6] N. L. Loh and K. Y. Sia, “An overview of hot isostatic pressing,” *J. Mater. Process. Technol.*, vol. 30, no. 1, pp. 45–65, 1992.

[7] L. R. Blackburn *et al.*, “Hot Isostatically Pressed Zirconolite Wasteforms for Actinide Immobilisation,” in *IOP Conf. Series: Materials Science and Engineering*, 2020.

[8] S. M. Thornber, P. G. Heath, G. P. Da Costa, M. C. Stennett, and N. C. Hyatt, “The effect of pre-treatment parameters on the quality of glass-ceramic wasteforms for plutonium immobilisation, consolidated by hot isostatic pressing,” *J. Nucl. Mater.*, vol. 485, pp. 253–261, 2017.

[9] L. J. Gardner, S. A. Walling, and N. C. Hyatt, “Hot isostatic pressing: Thermal treatment trials of inactive and radioactive simulant UK intermediate level waste,” *IOP Conf. Ser. Mater. Sci. Eng.*, vol. 818, no. 1, 2020.

[10] M. Drahansky *et al.*, “Sintering and Reactive Sintering by Spark Plasma Sintering (SPS),” *Intech*, vol. i, no. tourism, p. 13, 2016.

[11] S.-K. Sun, M. C. Stennett, C. L. Corkhill, and N. C. Hyatt, “Reactive spark plasma synthesis of $CaZrTi_2O_7$ zirconolite ceramics for plutonium disposition,” *J. Nucl. Mater.*, vol. 500, pp. 11–14, Mar. 2018.

[12] B. M. Clark, S. K. Sundaram, and S. T. Misture, “Polymorphic Transitions in Cerium-Substituted Zirconolite ($CaZrTi_2O_7$),” *Sci. Rep.*, vol. 7, no. 1, pp. 2–10, 2017.

[13] L. R. Blackburn *et al.*, “Synthesis and Characterisation of $Ca_{1-x}Ce_xZrTi_{2-2x}Cr_{2x}O_7$: Analogue Zirconolite Wasteform for the Immobilisation of Stockpiled UK Plutonium,” *J. Eur. Ceram. Soc.*, vol. 40, no. 15, pp. 5909–5919, 2020.

[14] M. Suarez *et al.*, “Challenges and Opportunities for Spark Plasma Sintering: A Key Technology for a New Generation of Materials,” in *Sintering Applications*, 2013.

[15] R. E. Dinnebier and S. J. L. Billinge, *Powder Diffraction Theory and Practice*. RSC Publishing,

2008.

[16] R. A. Young, *The Rietveld Method*, vol. 1. Oxford: Oxford University Press, 1993.

[17] B. H. Toby, “EXPGUI, a graphical user interface for GSAS,” *J. Appl. Crystallogr.*, vol. 34, pp. 210–213, 2001.

[18] J. I. Goldstein, D. E. Newbury, J. R. Michael, N. W. M. Ritchie, J. H. J. Scott, and D. C. Joy, *Scanning Electron Microscopy and X-Ray Microanalysis*, 4th ed. New York: Springer, 2018.

[19] F. Zupanič, T. Bončina, and B. Markoli, “Use of electron backscattering coefficients for identification of Be-bearing phases,” *Microsc. Sci. Technol. Appl. Educ.*, pp. 1824–1829, 2010.

[20] “Storage Ring - - Diamond Light Source.” [Online]. Available: https://www.diamond.ac.uk/Science/Machine/Components/storagering.html. [Accessed: 22-Apr-2021].

[21] S. D. Kelly, D. Hesterberg, and B. Ravel, *Analysis of Soils and Minerals Using X-ray Absorption Spectroscopy*, no. 5. 2008.

[22] B. Ravel and M. Newville, “ATHENA, ARTEMIS, HEPHAESTUS: Data analysis for X-ray absorption spectroscopy using IFEFFIT,” *J. Synchrotron Radiat.*, vol. 12, pp. 537–541, 2005.

[23] “FEI Tecnai F20 – FELMI ZFE.” [Online]. Available: https://www.felmi-zfe.at/instrumentation/tem/fei-tecnai-f20/. [Accessed: 22-Apr-2021].

[24] P. J. Larkin, *IR and Raman Spectroscopy: Principles and Spectral Interpretation*. Elsevier, 2011.

[25] M. He, B. Hu, B. Chen, and Z. Jiang, “Inductively Coupled Plasma Optical Emission Spectrometry for Rare Earth Elements Analysis,” *Phys. Sci. Rev.*, vol. 2, no. 1, pp. 1–37, 2017.

Chapter 5

Systematic Comparison of Surrogates in the $CaZr_{1-x}M_xTi_2O_7$ Zirconolite System (M = Ce, U, Th)

Authorship Contribution Statement

5.1) ‘A Systematic Investigation of the Phase Assemblage and Microstructure of the Zirconolite $CaZr_{1-x}Ce_xTi_2O_7$ System’. L. Blackburn was responsible for conceptualisation, materials preparation and characterisation, formal analysis of data, original draft preparation, reviewing and editing.

5.2) ‘Synthesis and Characterisation of the $CaZr_{1-x}U_xTi_2O_7$ Zirconolite Solid Solution’. L. Blackburn was responsible for conceptualisation, materials preparation and characterisation, formal analysis of data, original draft preparation, reviewing and editing.

5.3) ‘Synthesis, Structure and Characterisation of the Thorium Zirconolite $CaZr_{1-x}Th_xTi_2O_7$ System’. L. Blackburn was responsible for conceptualisation, materials preparation and characterisation, formal analysis of data, original draft preparation, reviewing and editing.

Journal of Nuclear Materials 535 (2020) 152137

Contents lists available at ScienceDirect

Journal of Nuclear Materials

journal homepage: www.elsevier.com/locate/jnucmat

A systematic investigation of the phase assemblage and microstructure of the zirconolite $CaZr_{1-x}Ce_xTi_2O_7$ system

Lewis R. Blackburn [a], Shikuan Sun [a, **], Laura J. Gardner [a], Ewan R. Maddrell [b], Martin C. Stennett [a], Neil C. Hyatt [a, *]

[a] Immobilisation Science Laboratory, University of Sheffield, Department of Materials Science and Engineering, Sir Robert Hadfield Building, Mappin Street, S13JD, UK
[b] National Nuclear Laboratory, Workington, Cumbria, CA14 3YQ, UK

ARTICLE INFO

Article history:
Received 25 November 2019
Received in revised form
24 March 2020
Accepted 24 March 2020
Available online 7 April 2020

Keywords:
Cerium
Plutonium
Zirconolite
Immobilisation
Surrogate
Wasteform
Ceramic

ABSTRACT

A series of zirconolite ceramics with nominal stoichiometry $CaZr_{1-x}Ce_xTi_2O_7$ ($0.0 \leq x \leq 0.4$) were synthesised under oxidizing, inert and reducing conditions, by a conventional solid-state cold press and sinter method. The evolution of phase assemblage and microstructure were characterized by XRD, SEM-EDS, Ce-L_3 XANES and Raman spectroscopy techniques. It was determined that the relative yield of zirconolite-2M and zirconolite-4M polytypes, alongside secondary perovskite phases, was influenced by processing environment *via* the control of $Ce^{3+/4+}$ speciation. Oxidizing conditions produced a mixture of zirconolite-2M and zirconolite-4M polytypes due to the formation of Ce^{4+}. Inert and reducing conditions yielded predominantly zirconolite-2M and a Ce-bearing perovskite phase through favouring Ce^{3+} speciation.

1. Introduction

The United Kingdom holds a considerable quantity of separated plutonium derived from civil nuclear power generation. This inventory is expected to exceed 140 t at the completion of AGR and Magnox nuclear fuel reprocessing [1]. The current management strategy for stockpiled plutonium is onsite interim storage at Sellafield, pending future reuse in $(U,Pu)O_2$ mixed oxide (MOX) nuclear fuel, with a small quantity of plutonium unsuitable for reuse designated for immobilisation and disposal [2]. Thus, there is growing pressure on UK government to condition separated Pu inventories in such a manner that diversion for illicit purposes is not feasible. As a result, UK government, supported in policy by the Nuclear Decommissioning Authority (NDA), is in the process of refining several 'credible options' deemed appropriate for the long term management of separated plutonium. The viability of these options is primarily evaluated on the basis of technical maturity, proliferation resistance, cost, and compatibility with geological disposal conditions. However, in all scenarios it is accepted that some portion of this material will need to be immobilised in a chemically durable ceramic host phase, prior to disposal [3].

Zirconolite, prototypically $CaZrTi_2O_7$, is a candidate crystalline host for separated Pu. Zirconolite is the dominant actinide-bearing phase in the Synroc-C formulation, a suite of chemically durable titanate phases specifically formulated for the immobilisation of high level nuclear wastes [4]. Naturally occurring zirconolite specimens have been found to contain radionuclides and withstand the effects of self-irradiation, and metamictization, over geological timescales, whilst retaining actinide inventories (up to 20 wt % U/Th) [5]. $CaZr_xTi_{3-x}O_7$ (where $0.80 \leq x \leq 1.30$) is considered the prototypical formula with $x = 1.00$, and its crystal structure assigned the nomenclature zirconolite-2M with reference to the two fold repeat of constituent hexagonal tungsten bronze (HTB) motifs [6]. The zirconolite-2M unit cell thus consists of alternating layers of CaO_8 and ZrO_7 polyhedra aligned in parallel along (110). Parallel to the [001] direction, these polyhedral are interleaved 1:1

* Corresponding author.
** Corresponding author.
E-mail addresses: shikuan.sun@sheffield.ac.uk (S. Sun), n.c.hyatt@sheffield.ac.uk (N.C. Hyatt).

https://doi.org/10.1016/j.jnucmat.2020.152137
0022-3115/

with HTB motifs formed by corner sharing TiO_6 and TiO_5 polyhedra. Several zirconolite polytypes are known, for which definitive or approximate crystal structures are established, including: 4M, 3T and 3O (where M, T and O denote monoclinic, trigonal and orthorhombic unit cells, respectively) [7–9]. These polytypes are characterized by variations in stacking sequence with respect to Ca/Zr and HTB polyhedral layers; note, however, that the monoclinic zirconolite-4M structure is in fact best described as a 1:1 intergrowth of zirconolite-2M and pyrochlore structural units, parallel to the [001] direction of the unit cell. The crystallization of zirconolite polytypes is determined by compositional modification, in particular by solid solution of lanthanides or actinides for Ca and/or Zr, and the oxygen fugacity imposed during synthesis [10–12]. Plutonium can substitute within the zirconolite system *via* solid solution as Pu^{4+}, *i.e.* $CaZr_{1-x}Pu_xTi_2O_7$ or $Ca_{1-x}Pu_xZrTi_{2-2x}M_{2x}O_7$, where M^{3+} enters zirconolite as a charge balancing species *e.g.* Al^{3+}, Fe^{3+}. Co-substitution of Pu may also be achieved on both Ca^{2+} and Zr^{4+} sites, i.e. $Ca_{1-x}Zr_{1-x}Pu_{2x}Ti_2O_7$, where Pu is designed to enter the lattice as Pu^{3+} to ensure isovalence, as the incorporation of Ln^{3+} have been previously observed [13,14].

The use of surrogates for radioisotopes during wasteform design and formulation is common practice, so as to emulate the chemical and/or physical properties of radioactive element, for which no stable isotope is available. This avoids the hazard and cost of working with (highly) radioactive materials whilst enabling a more comprehensive investigation of structure-property relations to target subsequent research with radioisotopes. Whilst it is to be emphasized that a surrogate cannot fully replicate the physiochemical behavior of the element concerned, the use of several surrogates can allow useful insight to be gained, for example, in the crystal chemical factors controlling solid solution mechanisms. Surrogates are typically selected with regards to accessible oxidation states, ionic radii, oxide melting temperature and density. In the context of Pu, several active and inactive elements satisfy these criteria. Ce is typically utilised as an inactive surrogate on the basis of safety and expediency, and the availability of Ce^{3+}/Ce^{4+} as an analogue for Pu^{3+}/Pu^{4+} oxidation states, albeit with different redox potentials [15]. U and Th are less commonly used as Pu surrogates, due to the associated hazards of handling radioactive materials; however, U^{4+} and Th^{4+} are generally regarded as more applicable as Pu^{4+} surrogates, as they are actinide elements [15].

In developing a zirconolite ceramic formulation suitable for potential immobilisation of the UK plutonium stockpile, we are mindful of previous studies of solid solution mechanisms and phase diagrams which have primarily used surrogates but also plutonium. A challenge in the synthesis and application of this existing body of research is the different composition range, processing method, and synthesis conditions used in these studies, all of which may influence the limits and mechanisms of solid solution. Therefore, it was considered that a systematic comparison of plutonium surrogacy in zirconolite was required, using common solid solution mechanisms, processing methods and synthesis conditions. This contribution is therefore the first component of a body of work which aims to systematically evaluate Ce/U/Th solubility in the zirconolite system, targeting the substitution $CaZr_{1-x}M_xTi_2O_7$, where $M = Ce^{4+}/U^{4+}/Th^{4+}$, accounting for variations in surrogate redox chemistry and subsequent influence on partitioning behavior. Accordingly, three atmospheres representative of oxidizing, inert and reducing conditions (air, argon, and 5% H_2/N_2 respectively) were used to sinter zirconolite ceramic wasteforms. The relationship between phase assemblage and processing environment was also investigated as a function of Ce incorporation (x).

2. Experimental

2.1. Materials synthesis

All compositions were prepared by conventional solid state reaction between oxide precursors $CaTiO_3$ (Alfa Aesar, 99.9% trace metals basis), ZrO_2 (Alfa Aesar, 99.9% trace metals basis), TiO_2 - anatase (Alfa Aesar, 99.9% trace metals basis) and CeO_2 (Acros Organics, 99.9% trace metals basis). Precursor materials were batched (~5 g) according to stoichiometry $CaZr_{1-x}Ce_xTi_2O_7$, where $0.0 \leq x \leq 0.4$, and planetary milled at 400 rpm with approximately 5 mL of isopropanol as a carrier fluid. Slurried mixtures were discharged and dried overnight at 80 °C to remove excess solvent. The dried material was then collected and ~0.3 g was added into a 10 mm stainless steel die and compressed under a uniaxial pressure of 3 t for 1 min. Green bodies were reacted at 1350 °C for 20 h in one of the following atmospheres: air, flowing argon and a flowing 5% H_2/N_2 mixture.

2.2. Materials characterization

Reacted samples were finely ground and analyzed by powder X-ray diffraction using a Bruker D2 Phaser, with a Lynxeye position sensitive detector and Ni filter. Data were acquired within the range $5° \leq 2\theta \leq 80°$ using Cu K_α radiation ($\lambda = 1.5418$ Å). Phases were identified using the PDF-4+ database. Each diffraction pattern was analysed using the Rietveld method in order to extract lattice parameters and provide quantitative phase analysis, using the GSAS package [16]. Specimens were prepared for scanning electron microscopy (SEM) analysis by mounting in cold setting epoxy resin and polished to a 1 μm optical finish. Polished surfaces were sputter coated with carbon in order to reduce surface charging effects, prior to analysis using a Hitachi TM3030 analytical scanning electron microscope, with 15 kV accelerating voltage and a working distance of approximately 8 mm. This was fitted with the Bruker Quantax Energy Dispersive X-ray Spectrometer (EDS) for compositional analysis. Ce valence was measured for $CaZr_{0.6}Ce_{0.4}Ti_2O_7$, reacted in each atmosphere, by bulk X-ray absorption near edge spectroscopy (XANES) for the Ce-L3 edge (5723 eV) at NSLS-II (USA). Specimens were ground and mixed with polyethylene glycol (PEG), prior to uniaxial pressing in a 13 mm die to form pellets with depth of approximately one absorption length. Raman spectra of powdered specimens were collected using the Horiba-XploRA Plus system with 532 nm air cooled Ar^+ laser line and laser power of approximately 5 mW.

3. Results

3.1. $CaZr_{1-x}Ce_xTi_2O_7$ phase assemblage

3.1.1. Air sintering

Powder XRD data for specimens sintered in air are shown in Fig. 1. Near single phase zirconolite-2M was obtained for $x = 0.0$, however, a trace impurity of a titanium rich phase was observed when viewing polished surfaces. As the nominal Ce concentration was increased, a transformation from the zirconolite-2M to zirconolite-4M polytype was observed. This was characterized by the appearance of weak zirconolite-4M supercell reflections at approximately $2\theta = 7.7°$ and 31.1°; the relative intensities of zirconolite-4M reflections appeared to increase with further Ce incorporation.

Unit cell parameters were derived from Rietveld fitting of X-ray diffraction data (Fig. 2); for the parent phase with $x = 0.0$, the unit cell dimensions were in excellent agreement with previously reported determinations [17]. The unit cell parameters were observed

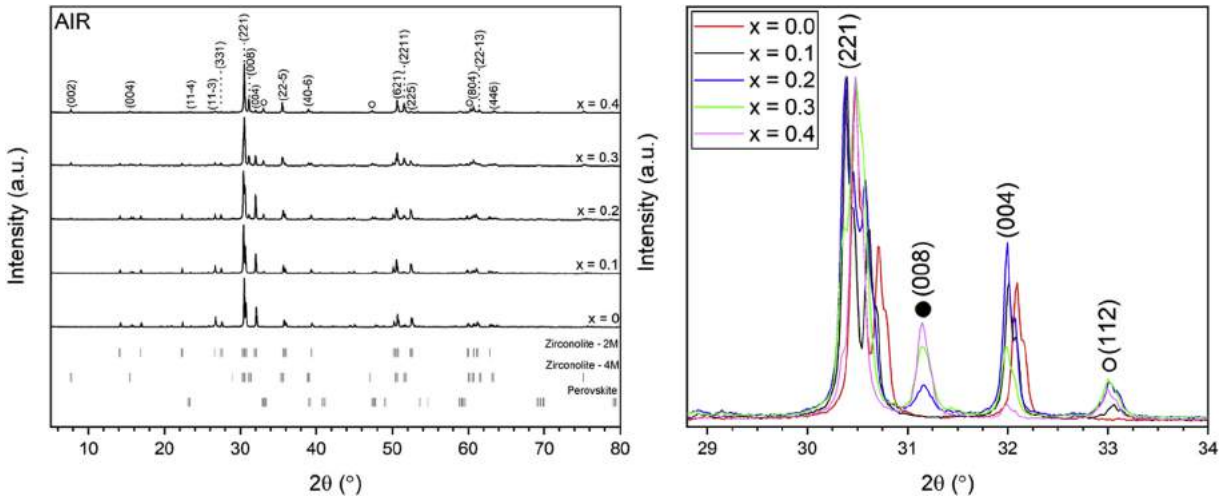

Fig. 1. Powder X-ray diffraction data for $CaZr_{1-x}Ce_xTi_2O_7$ specimens ($0.0 \leq x \leq 0.4$) sintered in air. Zirconolite-2M/4 M reflections are indexed by appropriate (hkl) values. Zirconolite-4M reflections are highlighted with closed circles (●); perovskite reflections are highlighted with open circles (○).

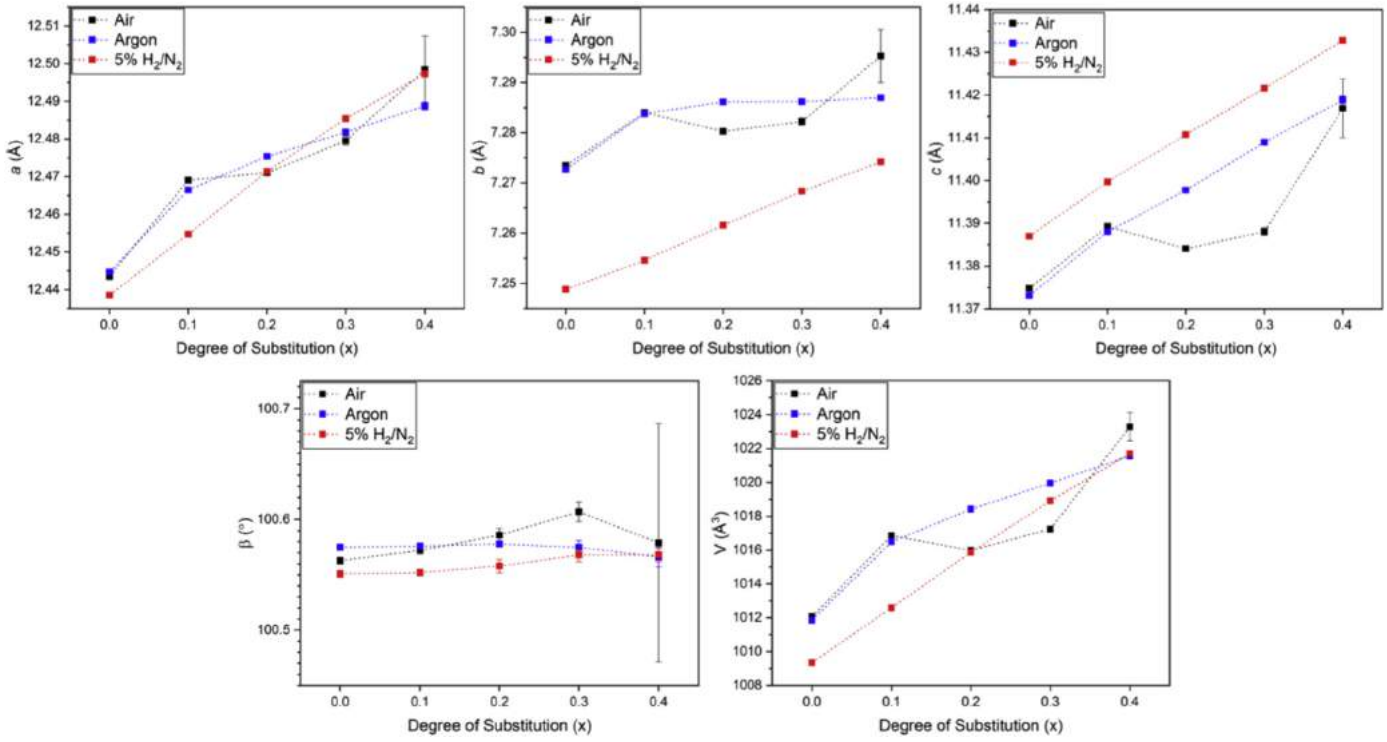

Fig. 2. Lattice parameter variations of the zirconolite-2M phase as a function of Ce concentration in $CaZr_{1-x}Ce_xTi_2O_7$ compositions for $0.0 \leq x \leq 0.4$.

to increase isotropically with Ce concentration, for all sintering atmospheres, consistent with successful incorporation of Ce into the zirconolite structure. The unit cell β angle remained essentially unchanged as a function of Ce content (x). Unit cell expansion can be attributed to variations in ionic radii between dopant (Ce) and host site (Zr), as discussed below.

Quantitative phase analysis (QPA) was also performed using the Rietveld method, the results of which are displayed in Table 1, in which the reported precision of derived phase fractions represents the uncertainty associated with parameter fitting in the Rietveld analysis (*i.e.* it represents the uncertainty in the refined parameter, minimized by the least squares algorithm, and, as such, underestimates the true uncertainty which is also subject to systematic error) [18]. Zirconolite-2M was identified as the major phase when $x = 0.1$ and $x = 0.2$, under air sintering. No evidence of zirconolite-4M formation was present when targeting $x = 0.1$. The fraction of the zirconolite-4M polytype increased from 16.4 ± 0.5 wt % to 67.7 ± 0.3 wt % as the nominal concentration of Ce was raised from $x = 0.2$ to $x = 0.4$. This analysis also confirmed the co-existence of an ancillary perovskite phase (prototypically $CaTiO_3$), identified by sharp reflections at $2\theta = 33.0°$, 47.5° and 59°; however, perovskite was not identified when targeting stoichiometric $CaZrTi_2O_7$. Perovskite ($CaTiO_3$) is present in many Synroc formulations and can act as a host phase for actinides, and the

Table 1
QPA (wt. %) results for $CaZr_{1-x}Ce_xTi_2O_7$ compositions sintered under oxidizing, inert and reducing conditions.

Nominal Composition	Processing Atmosphere	Phase Fraction (wt. %)			
		Zirconolite-2M	Zirconolite-4M	Perovskite	TiO_2
$CaZrTi_2O_7$	Air	96.5 ± 0.03	–	–	3.5 ± 0.27
$CaZrTi_2O_7$	Argon	99.6 ± 0.01	–	0.4 ± 0.19	–
$CaZrTi_2O_7$	5% H_2/N_2	92.4 ± 0.05	–	7.6 ± 0.26	–
$CaZr_{0.9}Ce_{0.1}Ti_2O_7$	Air	94.6 ± 0.04	–	3.7 ± 0.28	1.7 ± 0.38
$CaZr_{0.9}Ce_{0.1}Ti_2O_7$	Argon	93.6 ± 0.05	–	6.4 ± 0.28	–
$CaZr_{0.9}Ce_{0.1}Ti_2O_7$	5% H_2/N_2	84.3 ± 0.10	–	15.8 ± 0.29	–
$CaZr_{0.8}Ce_{0.2}Ti_2O_7$	Air	75.4 ± 0.21	16.4 ± 0.45	8.2 ± 0.34	–
$CaZr_{0.8}Ce_{0.2}Ti_2O_7$	Argon	82.2 ± 0.11	–	17.8 ± 0.28	–
$CaZr_{0.8}Ce_{0.2}Ti_2O_7$	5% H_2/N_2	75.4 ± 0.15	–	24.6 ± 0.29	–
$CaZr_{0.7}Ce_{0.3}Ti_2O_7$	Air	47.2 ± 0.43	43.1 ± 0.39	9.6 ± 0.37	–
$CaZr_{0.7}Ce_{0.3}Ti_2O_7$	Argon	70.6 ± 0.21	1.20 ± 0.32	28.2 ± 0.34	–
$CaZr_{0.7}Ce_{0.3}Ti_2O_7$	5% H_2/N_2	65.0 ± 0.20	–	35.0 ± 0.29	–
$CaZr_{0.6}Ce_{0.4}Ti_2O_7$	Air	21.6 ± 0.90	67.7 ± 0.32	9.6 ± 0.37	–
$CaZr_{0.6}Ce_{0.4}Ti_2O_7$	Argon	46.7 ± 0.42	16.0 ± 0.48	37.3 ± 0.40	–
$CaZr_{0.6}Ce_{0.4}Ti_2O_7$	5% H_2/N_2	52.4 ± 0.26	–	47.6 ± 0.28	–

preferential accommodation of Ce^{3+} in perovskite has been previously observed [12]. Bulk X-ray absorption near edge spectroscopy (XANES) data (Fig. 11) demonstrate that even under oxidizing conditions, Ce was not exclusively present as Ce^{4+}. Hence, some portion of Ce may be accommodated in the perovskite phase as Ce^{3+}.

3.1.2. Argon sintering

Sintering under argon produced a largely similar phase assemblage as for compositions sintered in air. Sharp reflections characteristic of zirconolite-2M were observed in all compositions, as shown in Fig. 3. Phase pure zirconolite was formed when targeting $CaZrTi_2O_7$ (*i.e.* x = 0.0) with no secondary phases readily identified. When targeting low Ce incorporation x = 0.1 and x = 0.2, an accessory perovskite was evident, as determined by the appearance of the (112) reflection at $2\theta = 33.0°$. The normalized intensity of reflections attributed to the accessory perovskite phase increased with Ce concentration. QPA analysis confirmed that the fraction of perovskite increased gradually from 6.4 ± 0.3 wt % for x = 0.1 to 37.3 ± 0.4 wt % for x = 0.4. Additionally, for the x = 0.4 composition, Rietveld analysis evidenced the presence of an additional zirconolite-4M phase, determined to be 16.0 ± 0.5 wt % of the phase assemblage.

3.1.3. 5% H_2/N_2 sintering

The sintering of $CaZr_{1-x}Ce_xTi_2O_7$ compositions under reducing conditions was not expected to produce the required Ce valence. Whilst oxidizing and inert sintering conditions produced a mixture of zirconolite polytypes, seemingly controlled by Ce speciation, processing under reducing conditions did not appear to stabilize the zirconolite-4M polytype, even when targeting high Ce concentration x = 0.4. Powder XRD data for these compositions are displayed in Fig. 4.

Sharp reflections characteristic of zirconolite-2M were readily identified in all samples. Perovskite was also present in considerable quantity (see Table 1). The formation of perovskite is evidently influenced by the reducing synthesis environment, as 7.6 ± 0.3 wt % $CaTiO_3$ was present when targeting stoichiometric zirconolite. This is understandable given that zirconolite has previously been observed to dissociate and transform into perovskite under reducing conditions, through the partial reduction of Ti^{4+} to Ti^{3+} [19]. As nominal Ce concentration was increased from x = 0.1 to x = 0.2, the associated quantity of secondary perovskite was observed to increase from 15.8 ± 0.3 to 24.6 ± 0.3 wt %. When targeting x = 0.4, perovskite was present at 47.6 ± 0.3 wt % in the phase assemblage. Considering Fig. 4, a clear shift in the diagnostic 2θ position is observed for perovskite, towards a lower angle; this is

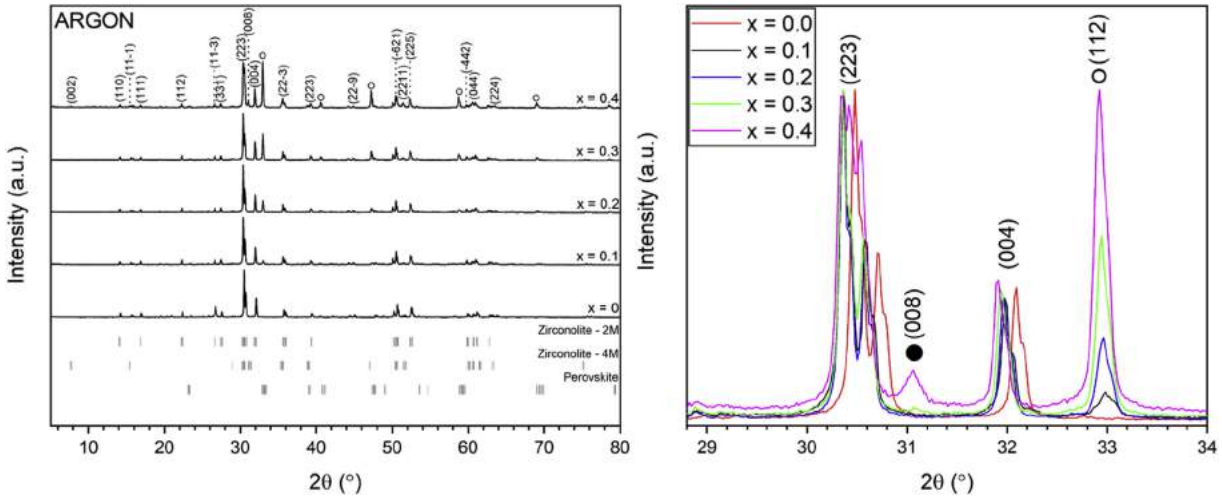

Fig. 3. Powder X-ray diffraction measurements for $CaZr_{1-x}Ce_xTi_2O_7$ specimens ($0.0 \leq x \leq 0.4$) sintered in argon. Zirconolite-2M reflections are indexed by appropriate (hkl) values. Zirconolite-4M reflections are highlighted with closed circles (●); perovskite reflections are highlighted with open circles (○).

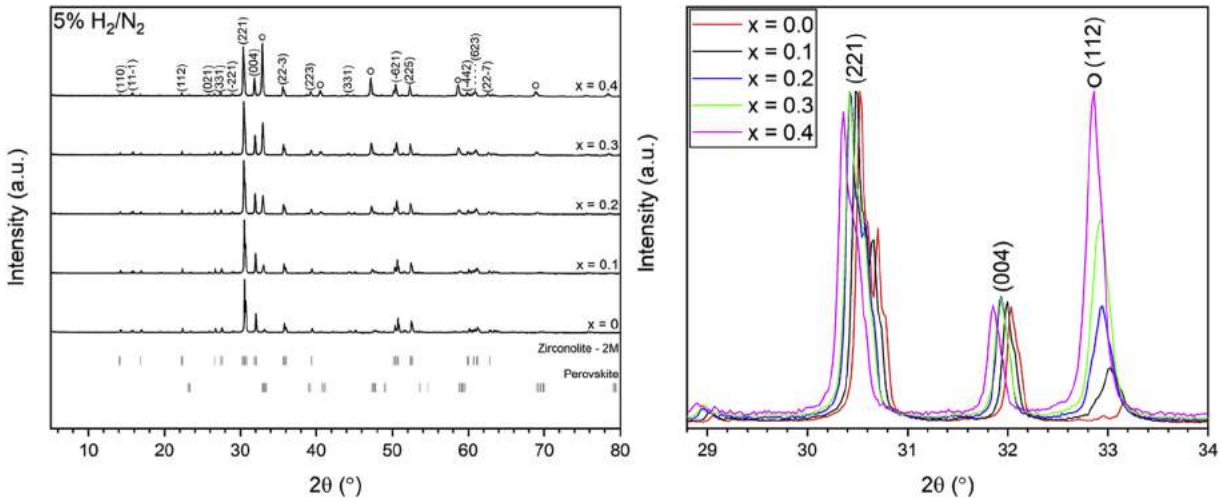

Fig. 4. Powder X-ray diffraction data for $CaZr_{1-x}Ce_xTi_2O_7$ specimens ($0.0 \leq x \leq 0.4$) sintered in 5% H_2/N_2. Zirconolite-2M reflections are indexed by appropriate (hkl) values. Perovskite reflections are highlighted with open circles (○).

consistent with an expansion in d-spacing, suggesting partial incorporation of a larger cation within either Ca and/or Ti sites in the nominal $CaTiO_3$ structure, consistent with incorporation of Ce^{3+} and/or Ti^{3+}. XANES data (Fig. 11) for the x = 0.4 composition confirmed that Ce is exclusively present as Ce^{3+} when sintering under reducing conditions, resulting in a phase assemblage in which a Ce-bearing perovskite is present at almost 50 wt %. Ce^{3+} incorporation into the zirconolite phase is likely to therefore occur *via* co-substitution within both Ca^{2+} and Zr^{4+} sites, negating the need for addition of charge balancing species.

3.2. $CaZr_{1-x}Ce_xTi_2O_7$ Microstructure observations

3.2.1. Air sintering

Scanning electron micrographs were collected on polished surfaces in order to verify the phase assemblage determined from XRD and undertake semi-quantitative micro-chemical analysis by EDS. BSE micrographs for air sintered specimens targeting nominal Ce concentration x = 0.1 and x = 0.2 are shown in Fig. 5.

For air sintered specimens, the observed microstructure was in good agreement with crystalline structures identified by XRD analysis. When nominal $CaZr_{0.9}Ce_{0.1}Ti_2O_7$ was targeted, a homogenous matrix of zirconolite-2M was identified, with small clusters of perovskite dispersed throughout the microstructure. A chemical composition of $Ca_{1.02(5)}Zr_{0.88(7)}Ce_{0.06(2)}Ti_{2.04(6)}O_7$ (normalized to seven oxygen atoms) was calculated for the zirconolite-2M phase from quantitative EDS data. The slight Ce deficiency with respect to target composition was attributed to formation of minor Ce-bearing perovskite. When targeting $CaZr_{0.8}Ce_{0.2}Ti_2O_7$, two bright Ce-bearing phases were observed, which were identified as zirconolite-2M and zirconolite-4M, with lower and higher Ce concentration, respectively, as determined by EDS analysis. The EDS spot analyses of zirconolite-2M and zirconolite-4M present in the microstructure for the x = 0.3 composition are displayed in Fig. 6; the composition of the zirconolite-2M phase was calculated to be $Ca_{1.05(11)}Zr_{0.80(15)}Ce_{0.14(4)}Ti_{2.01(9)}O_7$, whereas the 4M phase had average stoichiometry $Ca_{1.09(9)}Zr_{0.64(7)}Ce_{0.31(4)}Ti_{2.04(10)}O_7$. This is in close agreement with previous observations that Ce solubility in the $CaZr_{1-x}Ce_xTi_2O_7$ system reaches a maximum at approximately 0.15 f.u., after which a structural transformation to the zirconolite-4M polytype occurs to accommodate increased Ce content [11,12]. EDS data are summarized in Table 2. Due to small grain size, the quantitative EDS data obtained for perovskite grains must be considered with caution, as contribution from neighboring zirconolite grains may influence the obtained composition.

3.2.2. Argon sintering

Microstructures for specimens with targeted Ce concentration x = 0.1 and x = 0.2 sintered under flowing argon are displayed in Fig. 7, and coincide with phases identified by powder XRD data.

A mid grey matrix was observed in both microstructures that was confirmed as zirconolite-2M by EDS analysis. Calculated compositions from EDS analysis for x = 0.1 and x = 0.2 phases were $Ca_{1.02(7)}Zr_{0.85(8)}Ce_{0.07(2)}Ti_{2.06(5)}O_7$ and $Ca_{0.97(5)}Zr_{0.84(9)}Ce_{0.11(3)}Ti_{2.07(4)}O_7$ respectively. Stoichiometry for the 2M phase was close to nominal composition for low cerium content, but the actual Ce concentration was always lower than the nominal for x > 0.2, consistent with Ce partitioning into the perovskite phase. The site occupancy of

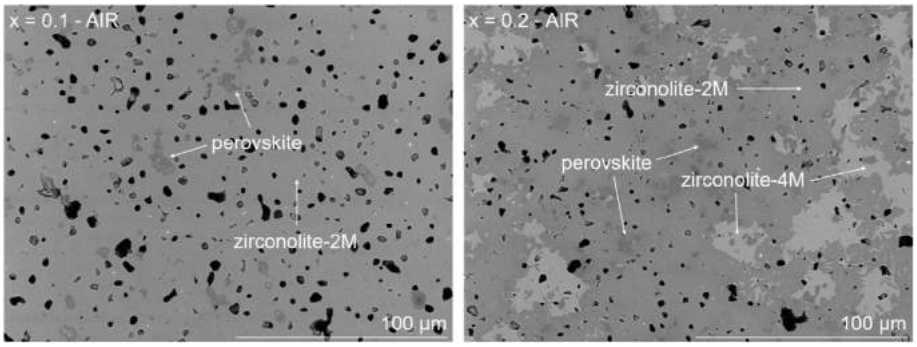

Fig. 5. Representative backscattered electron micrographs for $CaZr_{0.9}Ce_{0.1}Ti_2O_7$ (left) and $CaZr_{0.8}Ce_{0.2}Ti_2O_7$ (right) compositions sintered in air.

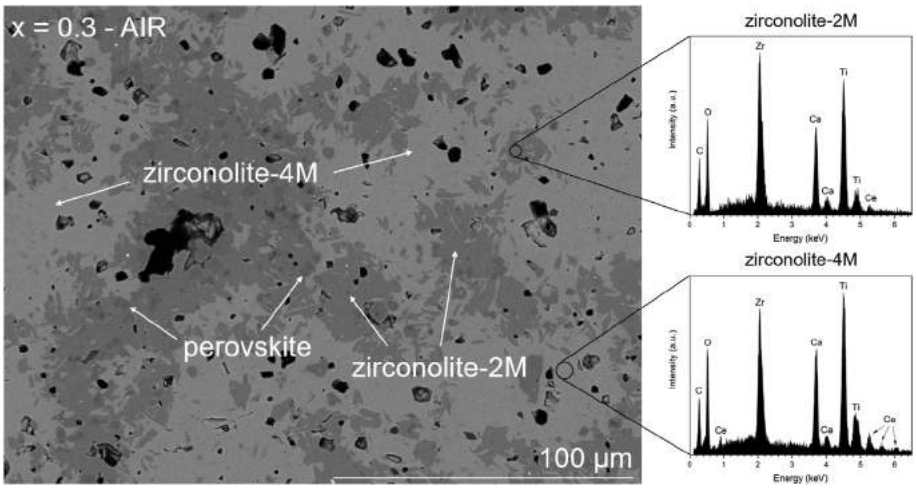

Fig. 6. EDS spot analysis of zirconolite-2M and zirconolite-4M regions present in the microstructure for nominal composition $CaZr_{0.7}Ce_{0.3}Ti_2O_7$ sintered in air.

Table 2
Calculated phase compositions for zirconolite-2M, zirconolite-4M and perovskite phases observed in $CaZr_{1-x}Ce_xTi_2O_7$ compositions, synthesised at 1350 °C for 20 h, under air, argon or 5% H_2/N_2. (* - identification not possible due to BSE contrast and/or grain size).

x	Nominal Composition	Atmosphere	Calculated composition from EDS analysis	
			Zirconolite-2M	Zirconolite-4M
0.1	$CaZr_{0.9}Ce_{0.1}Ti_2O_7$	Air	$Ca_{1.02(5)}Zr_{0.88(7)}Ce_{0.06(2)}Ti_{2.04(6)}O_7$	–
0.2	$CaZr_{0.8}Ce_{0.2}Ti_2O_7$	Air	$Ca_{1.05(8)}Zr_{0.81(7)}Ce_{0.10(3)}Ti_{2.04(8)}O_7$	$Ca_{1.01(6)}Zr_{0.63(10)}Ce_{0.31(5)}Ti_{2.05(9)}O_7$
0.3	$CaZr_{0.7}Ce_{0.3}Ti_2O_7$	Air	$Ca_{1.05(11)}Zr_{0.80(15)}Ce_{0.14(4)}Ti_{2.01(9)}O_7$	$Ca_{1.01(9)}Zr_{0.64(7)}Ce_{0.31(4)}Ti_{2.04(10)}O_7$
0.4	$CaZr_{0.6}Ce_{0.4}Ti_2O_7$	Air	*	$Ca_{0.98(5)}Zr_{0.59(6)}Ce_{0.35(2)}Ti_{2.07(7)}O_7$
			Zirconolite-2M	Perovskite
0.1	$CaZr_{0.9}Ce_{0.1}Ti_2O_7$	Argon	$Ca_{1.02(7)}Zr_{0.85(8)}Ce_{0.07}Ti_{2.06(5)}O_7$	*
0.2	$CaZr_{0.8}Ce_{0.2}Ti_2O_7$	Argon	$Ca_{0.97(5)}Zr_{0.84(9)}Ce_{0.11(3)}Ti_{2.07(4)}O_7$	$Ca_{0.62(2)}Ce_{0.19(4)}Ti_{1.19(3)}O_3$
0.3	$CaZr_{0.7}Ce_{0.3}Ti_2O_7$	Argon	$Ca_{1.06(7)}Zr_{0.77(17)}Ce_{0.18(8)}Ti_{1.99(10)}O_7$	$Ca_{0.60(1)}Ce_{0.20(4)}Ti_{1.21(2)}O_3$
0.4	$CaZr_{0.6}Ce_{0.4}Ti_2O_7$	Argon	*	*
			Zirconolite-2M	Perovskite
0.1	$CaZr_{0.9}Ce_{0.1}Ti_2O_7$	5% H_2/N_2	$Ca_{0.97(6)}Zr_{0.93(7)}Ce_{0.05(3)}Ti_{2.05(3)}O_7$	$Ca_{0.81(3)}Ce_{0.15(4)}Ti_{1.05(3)}O_3$
0.2	$CaZr_{0.8}Ce_{0.2}Ti_2O_7$	5% H_2/N_2	$Ca_{0.94(3)}Zr_{0.98(7)}Ce_{0.08(4)}Ti_{2.00(6)}O_7$	$Ca_{0.74(7)}Ce_{0.16(5)}Ti_{1.11(4)}O_3$
0.3	$CaZr_{0.7}Ce_{0.3}Ti_2O_7$	5% H_2/N_2	$Ca_{1.01(17)}Zr_{0.75(26)}Ce_{0.22(9)}Ti_{2.03(5)}O_7$	$Ca_{0.68(7)}Ce_{0.23(5)}Ti_{1.09(3)}O_3$
0.4	$CaZr_{0.6}Ce_{0.4}Ti_2O_7$	5% H_2/N_2	*	*

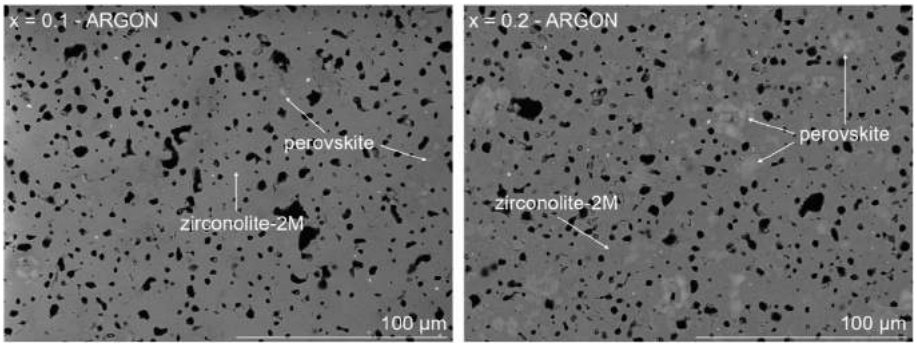

Fig. 7. Representative backscattered electron micrographs for $CaZr_{0.9}Ce_{0.1}Ti_2O_7$ (left) and $CaZr_{0.8}Ce_{0.2}Ti_2O_7$ (right) compositions sintered in argon.

dopants in nominal $CaZrTi_2O_7$ is controlled by ionic radii; the inert conditions imposed by the argon sintering environment was considered to have influenced Ce speciation (bulk XANES data later confirmed approximately 78% reduction to Ce^{3+} species - Fig. 11), hence the formation of Ce^{3+} may promote co-partitioning of Ce within both zirconolite and perovskite phases. Moreover, spot analysis of nominal microstructure x = 0.3 revealed high Ce content present in the perovskite phase (Fig. 8). The zirconolite-2M phase in this instance was calculated to have average composition $Ca_{1.06(7)}Zr_{0.77(17)}Ce_{0.18(8)}Ti_{1.99(10)}O_7$ (normalized to seven oxygen atoms). Furthermore, semi-quantitative analysis of the perovskite phase inferred a stoichiometry of $Ca_{0.62(2)}Ce_{0.21(5)}Ti_{1.17(5)}O_3$ (normalized to three oxygen atoms).

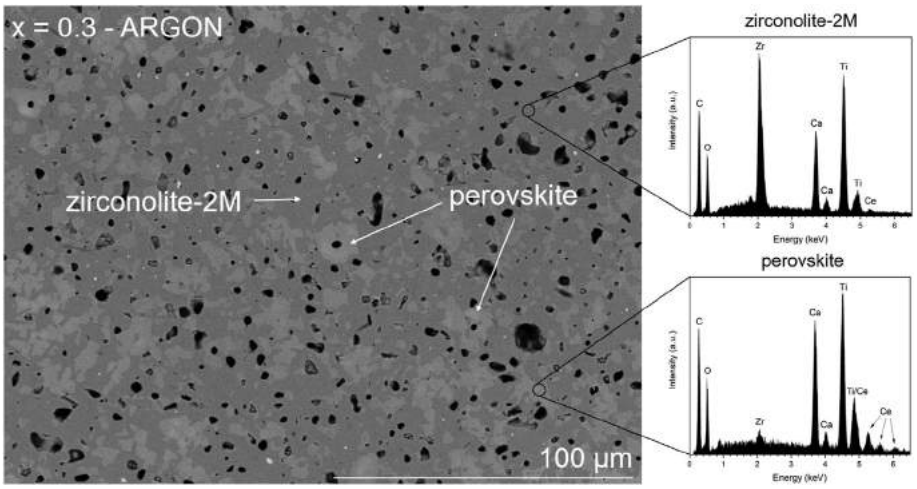

Fig. 8. EDS spot analysis of zirconolite-2M and perovskite regions present in the microstructure for nominal composition $CaZr_{0.7}Ce_{0.3}Ti_2O_7$ sintered in argon.

3.2.3. 5% H_2/N_2 sintering

Synthesis under reducing conditions resulted in a microstructure with elevated perovskite content (Fig. 9). Considering nominal $CaZr_{0.9}Ce_{0.1}Ti_2O_7$ and $CaZr_{0.8}Ce_{0.2}Ti_2O_7$ compositions, a homogeneous mid-grey matrix of zirconolite-2M was observed, with perovskite clusters distributed throughout the microstructure. No zirconolite-4M could be identified, in agreement with XRD data. It was noted that the relative BSE contrast between zirconolite-2M and perovskite phases in the interval x = 0.1 and x = 0.2 increased, with the perovskite phase appearing to become brighter. This was consistent with preferential Ce uptake in the perovskite phase. Furthermore, EDS spot analysis of perovskite grains (Fig. 10) demonstrated elevated Ce incorporation relative to zirconolite-2M. Quantitative EDS measurements were undertaken in order to investigate the stoichiometry of the formed perovskite phase when Ce concentration was targeted to x = 0.3 – $Ca_{0.68(7)}Ce_{0.23(5)}Ti_{1.09(3)}O_3$ (normalized to three oxygen atoms). Bulk XANES data determined that when sintering under reducing conditions, Ce is uniformly present as Ce^{3+}. It was presumed that electro-neutrality of the perovskite phase was maintained by a combination of Ti^{3+} and cation vacancies.

3.3. Oxidation state of Ce

The oxidation state of cerium in the samples with highest Ce content (nominally $CaZr_{0.6}Ce_{0.4}Ti_2O_7$) sintered in each environment was determined by X-ray absorption near edge spectroscopy (XANES). Normalized Ce-L_3 XANES data are shown in Fig. 11. These data were acquired alongside CeO_2 and $CePO_4$ reference compounds (Ce^{4+} and Ce^{3+} species respectively). The Ce-L_3 XANES of $CePO_4$ shows a single intense white-line feature, characteristic of Ce^{3+} speciation, whereas the Ce-L_3 XANES of CeO_2 exhibits a white-line comprising a doublet of two overlapping features (note: the term white-line refers to strong absorption feature(s) associated with the crest of the X-ray absorption edge). The electronic states associated with these features have been previously described [20–22]. The Ce-L_3 XANES for the air sintered specimen consisted of a white line and post-edge feature similar to the CeO_2 reference, suggesting that the dominant oxidation state of cerium is Ce^{4+}. The intensity of the peak on the low energy side of the doublet appears to increase relative to that on the high energy side, this suggested the presence of a small fraction of Ce^{3+}. A linear combination fit of measured XANES spectra with respect to CeO_2 and $CePO_4$ reference compounds was performed using the Athena package [23]. The speciation of Ce^{3+}/Ce^{4+} is expressed as a percentage in Table 3, alongside a corresponding R-factor. Sintering in air resulted in the formation of 28% Ce^{3+} species. The XANES spectrum for argon sintered compositions appeared to retain white-line features common to both CeO_2 and $CePO_4$ reference compounds. The white-line position was largely similar to $CePO_4$ yet there were features consistent with the doublet characteristic of the CeO_2 reference. Linear combination fitting determined that approximately 78% of Ce was present as Ce^{3+} when sintering in argon. The XANES spectrum obtained for the sample sintered under 5% H_2/N_2 had no features characteristic of CeO_2, and consisted of a single intense white-line feature. 100% reduction to the Ce^{3+} species was calculated from linear combination fitting.

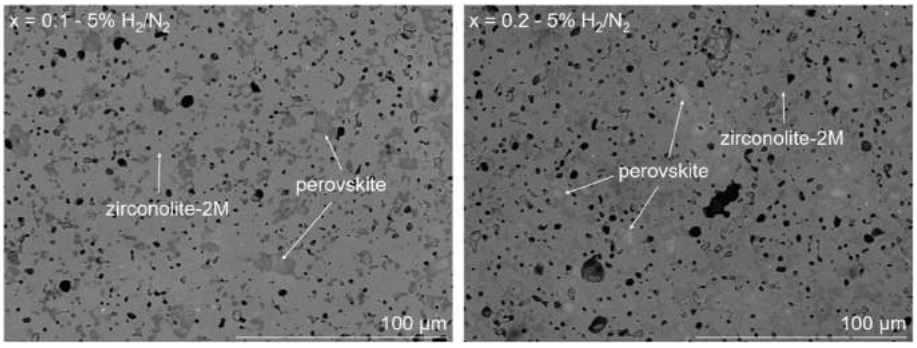

Fig. 9. Representative backscattered electron micrographs for $CaZr_{0.9}Ce_{0.1}Ti_2O_7$ (left) and $CaZr_{0.8}Ce_{0.2}Ti_2O_7$ (right) compositions sintered under 5% H_2/N_2.

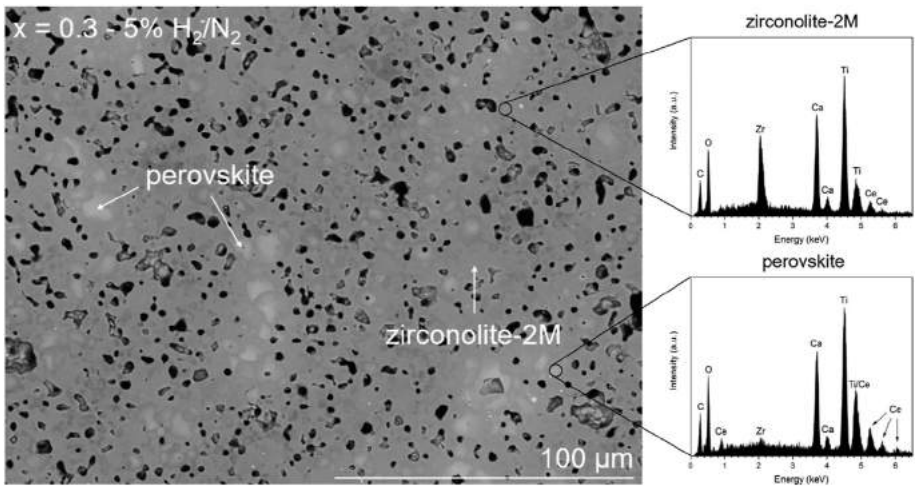

Fig. 10. EDS spot analysis of zirconolite-2M and perovskite regions present in the microstructure for nominal composition $CaZr_{0.7}Ce_{0.3}Ti_2O_7$ sintered in argon.

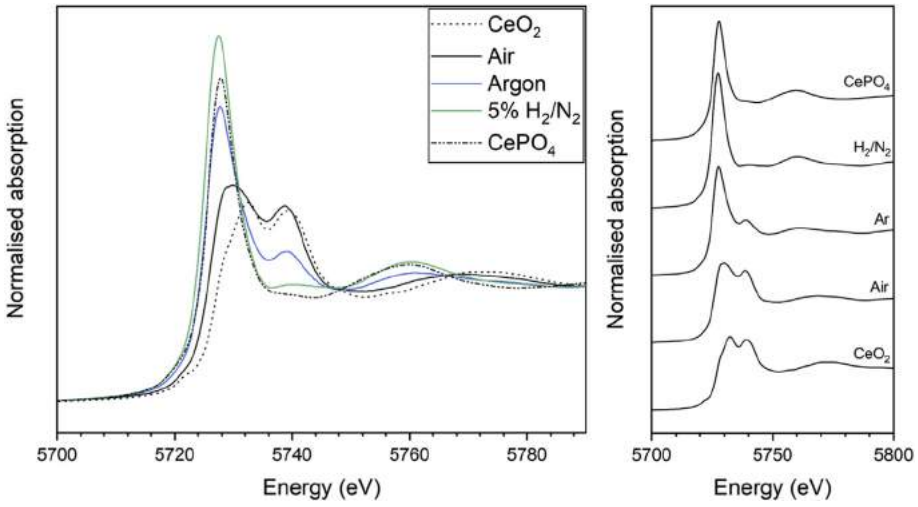

Fig. 11. Ce L_3 XANES spectra for $CaZr_{0.6}Ce_{0.4}Ti_2O_7$ specimens sintered in air, argon and 5% H_2/N_2, with respect to +3 and + 4 reference compounds ($CePO_4$ and CeO_2 respectively).

Table 3
Ce speciation as determined by linear combination fitting of Ce-L_3 XANES data relative to CeO_2 and $CePO_4$ reference compounds.

Nominal Composition	Processing Environment	Ce Speciation (%)		R-factor
		Ce^{3+}	Ce^{4+}	
$CaZr_{0.6}Ce_{0.4}Ti_2O_7$	Air	28.0 ± 1.0	72.0 ± 1.0	0.011
$CaZr_{0.6}Ce_{0.4}Ti_2O_7$	Argon	78.4 ± 1.0	21.6 ± 1.0	0.024
$CaZr_{0.6}Ce_{0.4}Ti_2O_7$	5% H_2N_2	100.0 ± 3.0	0.00 ± 3.0	0.055

3.4. Raman spectroscopy

Further evidence for the preferential accommodation of CeO_2 in zirconolite under oxidizing conditions was demonstrated using Raman spectroscopy. Fig. 12 shows observed Raman shift for $CaZr_{1-x}Ce_xTi_2O_7$ samples synthesised in air, argon and 5% H_2/N_2. As the prototypical zirconolite-2M structure (space group *C2/c*) has low symmetry due to the monoclinic unit cell, many Raman-active modes were observed. The measured spectrum for $CaZrTi_2O_7$ (*i.e.* x = 0) is in agreement with our previous observations [24]. The dominant vibrational mode at 780 cm^{-1} was assigned to the symmetric excitation of TiO_6 octahedra that constitute the HTB layers in the zirconolite structure [25]; vibrational modes observed at lower wavenumbers can be attributed to CaO_8 and ZrO_7 polyhedra, alongside lower intensity TiO_6 internal vibrations [26].

Considering air-fired specimens (Fig. 12(a)), there was no observable variation in peak position or intensity between x = 0 and x = 0.1 compositions, suggesting Ce retention in the zirconolite structure at 0.1 f.u. did not cause any significant structural modification. At higher targeted Ce incorporation (*i.e.* x = 0.2 and x = 0.3) some broadening of peaks between 200 and 400 cm^{-1} was observed; this is attributed to disorder induced by the occupation of Ce within the zirconolite-2M structure and subsequent emergence of the closely related zirconolite-4M polytype. There was also a marked decrease in the intensity associated with TiO_6 octahedra at 780 cm^{-1}; when high cerium loading was targeted (x = 0.4) this

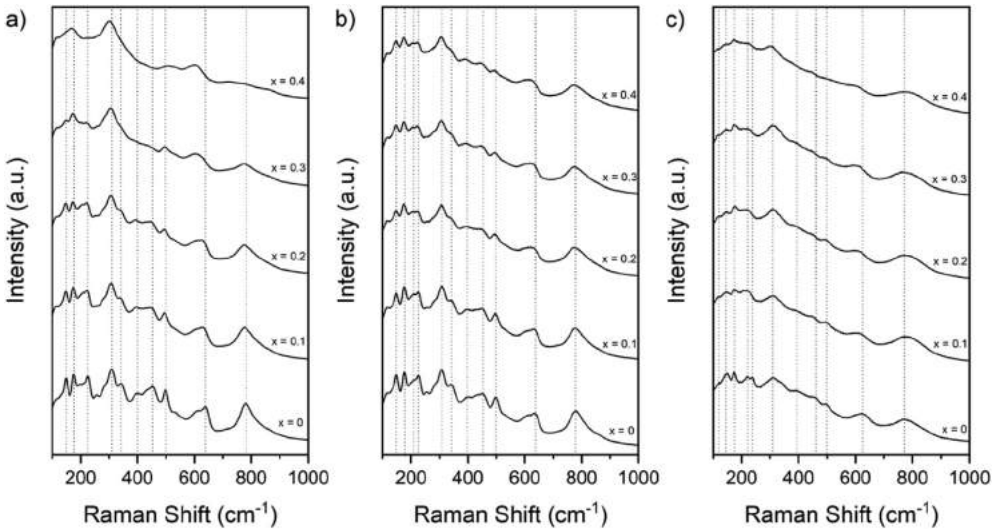

Fig. 12. Measured Raman shift for nominal compositions $CaZr_{1-x}Ce_xTi_2O_7$ reacted under a) air, b) argon, c) 5% H_2/N_2.

peak was no longer present. No weak Raman features remained and only three modes could be distinguished at this Ce concentration. This is consistent with previous measurements in the $CaZrTi_2O_7 - Y_2Ti_2O_7$ system investigated by Jafar et al. [25]. The evolution of this system results in the formation of zirconolite-4M as an intermediate phase between zirconolite-2M and the pyrochlore end member *via* nominal accommodation of Y^{3+} on both Ca^{2+} and Zr^{4+} sites. As the relative weight fraction of zirconolite-2M decreases in favour of zirconolite-4M and pyrochlore, broadening of weak features occurs, alongside total abatement of the TiO_6 vibrational mode. This is further evidence towards the coexistence of zirconolite-2M and zirconolite-4M polytypes in the $CaZr_{1-x}Ce_xTi_2O_7$ system for air sintered samples.

Raman spectra for compositions reacted under argon are shown in Fig. 12(b). Unlike compositions sintered in air, notable broadening of vibrational modes did not occur at any level of Ce incorporation. When targeting x = 0.1 there was no apparent shift in position of breadth or position of Raman peaks. Elevated Ce concentrations *i.e.* x = 0.3, 0.4 demonstrated a slight degree of broadening, yet weak features in the 150–250 cm^{-1} were still distinguished.

The dominant Raman mode at 780 cm^{-1} does seem to systematically decrease in relative intensity corresponding to increasing Ce concentration. QPA derived from powder XRD analysis confirmed the existence of approximately 16 wt % zirconolite-4M when targeting this composition. Therefore, as with the air-sintered specimen, the broadening of the TiO_6 vibrational mode can be attributed to the presence of the zirconolite-4M polytype.

$CaZr_{1-x}Ce_xTi_2O_7$ compositions reacted under reducing conditions did not appear to produce a strong Raman signal (Fig. 12(c)), and this was attributed to the partial reduction of Ti^{4+} to Ti^{3+}. The resulting oxygen vacancy-type defects that occur as part of the charge balancing mechanism are formed, resulting in the modification of oxygen stretching vibrational modes. The corresponding orientation of TiO_6 octahedra in the constituent HTB layers in the zirconolite structure is therefore altered, resulting in the broadening of the dominant Ti-O stretching mode at 780 cm^{-1}. The weak intensity of Raman features at a lower wavenumber can be attributed to a similar mechanism, as Ca and Zr are bonded to oxygen *via* 8-fold and 7-fold CaO_8 and ZrO_7 sites, respectively. The contribution of the secondary perovskite phases to the collected Raman spectra appeared negligible. The dominant O-Ti-O bending modes that contribute to the Raman signal for $CaTiO_3$ are present in the range 100–300 cm^{-1}, and are therefore masked by the signal from the zirconolite phase. Furthermore, the incorporation of Ce within the perovskite phase would be expected to significantly dampen the Raman features of the $CaTiO_3$ spectrum, as was observed in the case of Qin et al. in the $CaTiO_3 - SrTiO_3$ system [27].

4. Discussion

The preparation of specimens adopting the $CaZr_{1-x}Ce_xTi_2O_7$ stoichiometry, under oxidizing conditions, has been reported previously within the literature. Li et al. successfully synthesised a series of zirconolites with $CaZr_{1-x}Ce_xTi_2O_7$ ($0.0 \leq x \leq 1.0$) structures in air at 1250 °C [28]. A phase transition from zirconolite-2M, to zirconolite-4M, to pyrochlore ($CaCeTi_2O_7$) was observed with increasing Ce concentration, in agreement with the results presented here. The solubility limit of Ce in the Zr^{4+} site was found to be approximately 0.80 f.u., after which cerianite (CeO_2) was distributed within the microstructure. Notably, XPS measurements demonstrated the ratio of Ce^{3+}/Ce^{4+} decreased in accordance with partial reduction from Ce^{4+} to Ce^{3+}; the incorporation of Ce within an ancillary perovskite phase was also detected. Clark et al. reported the formation of nearly single phase zirconolite-4M (approximately 95.6 wt %) with $CaZr_{0.5}Ce_{0.5}Ti_2O_7$ stoichiometry, by reacting under oxidizing conditions [12]. However, consolidation *via* spark plasma sintering (SPS) of $CaZr_{0.5}Ce_{0.5}Ti_2O_7$ powder led to the destabilisation of the zirconolite-4M structure, resulting in the formation of zirconolite-2M and a Ce bearing perovskite phase ($Ca_{0.4}Ce_{0.4}TiO_3$). Ce-L_3 XANES data demonstrated a majority of Ce^{3+} in specimens processed by SPS, assumed to be a result of the reducing environment imposed by the graphite die. It was concluded that whilst at low concentrations *i.e.* x = 0.10, Ce^{4+} is accommodated successfully in the Zr^{4+} site, the formation of zirconolite-4M occurs as a result of Ce^{3+} retention on both Ca^{2+} and Zr^{4+} sites. This is accommodated by partial reduction of Ce^{4+} to Ce^{3+}, resulting in the liberation of Ca^{2+} to form an ancillary Ce-perovskite. Moreover, the incorporation of trivalent actinide surrogates in $Ca_{1-x}Zr_{1-x}M_{2x}Ti_2O_7$ (namely $M = Y^{3+}/Nd^{3+}$) has been shown to produce a phase transition from the zirconolite-2M polytype, to the cubic pyrochlore end member, with the formation of zirconolite-4M as an intermediate phase [13,25].

In this instance, the phase evolution of $CaZr_{1-x}Ce_xTi_2O_7$ is in

reasonably good agreement with data presented in the literature, although these studies have not applied a common set of synthesis conditions. The accommodation of Ce in the zirconolite phase is intrinsically determined by ionic radii and redox behavior, which is in turn controlled by processing environment *via* the speciation of $Ce^{3+/4+}$ and accompanying variations in size. Ce^{4+} has ionic radius of 0.92 Å, significantly larger than the Zr^{4+} host site (0.78 Å in 7-fold coordination). This substitution is not favourable considering incompatibility with regards to radii, hence it is expected only a small fraction of Ce^{4+} can be successfully accommodated in the zirconolite-2M structure before structural rearrangement occurs. Further incorporation favours the formation of zirconolite-4M, with an accompanying doubling of the unit cell along the c-axis, with alternate ordering of four HTB type layers interleaved with Ca/Zr polyhedra (as in the prototypical 2 M structure) and Ca/Ti polyhedra (as in pyrochlore). This is observed when sintering in oxidizing conditions (air); this polymorphic transition appeared to occur in the range $0.1 \leq x \leq 0.2$. This is in agreement with values previously reported within the literature [11,12,28,29]. Ce^{3+} is expected to be preferentially occupied on the Ca^{2+} site in zirconolite-2M, on the basis of compatibility between ionic radii (Ca^{2+} - 1.12 Å; Ce^{3+} - 1.14 Å; 8-fold coordinate). The co-partitioning of Ce onto both Ca/Zr sites would also provide a self-balancing charge mechanism, providing the substitution is equimolar. It has been reported that the formation of zirconolite-4M can be stabilised *via* the incorporation of 0.5–0.8 f.u. Nd^{3+} (and other trivalent species of appropriate ionic radius), due to co-substitution of Nd within both Ca/Zr sites [7]. This is consistent with our assumptions – for air sintered compositions, Ce^{4+} was partially reduced to produce the appropriate amount of Ce^{3+}, allowing retention on the Ca^{2+} site and stabilising the zirconolite-4M structure. As the design of the $CaZr_{1-x}Ce_xTi_2O_7$ system does not account for any Ce to be occupied on the Ca site, excess Ca is liberated, resulting in the stabilisation of a secondary perovskite phase; the formation of Ce perovskite is to be expected, both Ce^{3+}/Ca^{2+} share ionic radius of 1.34 Å in 12-fold coordination. It is proposed the partial reduction of Ti^{4+} to Ti^{3+} and Ti-vacancies facilitate the solubility of Ce in perovskite, by maintaining isovalence. Furthermore, the incorporation of both Ce and Pu in perovskites have been previously reported, without the need for co-doping of charge balancing species [30,31].

5. Conclusions

Zirconolite ceramics are currently under consideration as a host for stockpiled UK plutonium. A series of ceramics with composition $CaZr_{1-x}Ce_xTi_2O_7$, where $0.0 \leq x \leq 0.4$, were fabricated *via* solid state methods using Ce as a surrogate for Pu. Processing atmosphere has been found to influence Ce partitioning within zirconolite *via* the control of $Ce^{3+/4+}$ speciation. XRD and SEM analysis of air-fired samples suggest destabilisation of the zirconolite-2M structure with respect to the zirconolite-4M polytype with increasing Ce-content. Synthesis under inert Ar gas yielded some zirconolite-4M when targeting $x = 0.4$, with considerable accompanying perovskite. XRD and SEM analysis did not suggest any evidence of zirconolite-4M formation under reducing 5% H_2/N_2 gas. Bulk XANES spectra for $CaZr_{0.6}Ce_{0.4}Ti_2O_7$ compositions indicate that synthesis under oxidizing conditions promotes Ce^{4+} formation, resulting in a structural transition from zirconolite-2M to zirconolite-4M consistent with values previously observed in the literature. Inert and reducing conditions are observed to promote Ce^{3+} speciation, which facilitates the formation of Ce-bearing perovskite and zirconolite phases. Based on these measurements, several implications can be made for Pu in the $CaZr_{1-x}Pu_xTi_2O_7$ system; Pu^{4+} will likely be accommodated up to 0.15 f.u. in the zirconolite-2M structure, considering the similarities between ionic radii of Ce^{4+} and Pu^{4+} (0.92 Å and 0.91 Å in 7-fold coordination, respectively). Further substitution will result in the formation of two zirconolite polytypes (and possibly a small amount of Pu^{3+} partitioning within a secondary perovskite phase). If sintered in an inert or reducing environment, the $CaZr_{1-x}Pu_xTi_2O_7$ design is likely to produce a phase assemblage consisting of zirconolite-2M and a Pu-bearing perovskite. This is undesirable given the lower demonstrated aqueous durability of perovskite with respect to zirconolite. Nevertheless, the affinity for Ce to reduce is greater than that for Pu, as has been previously demonstrated in zirconia and titanate pyrochlores [32]. This work demonstrates that Ce speciation is a controlling factor for the fabrication of zirconolite wasteforms, and by analogy with this system, plutonium. However, it recognised that this can only be demonstrated by a plutonium validation study. This has implications for zirconolite ceramics formed by both conventional sintering and novel thermal treatments such as Hot Isostatic Pressing (HIP).

Declaration of competing interest

The authors declare that they have no known competing financial interests or personal relationships that could have appeared to influence the work reported in this paper.

CRediT authorship contribution statement

Lewis R. Blackburn: Conceptualization, Methodology, Formal analysis, Writing - original draft. **Shikuan Sun:** Formal analysis, Writing - review & editing. **Laura J. Gardner:** Formal analysis, Writing - review & editing. **Ewan R. Maddrell:** Supervision, Writing - review & editing. **Martin C. Stennett:** Supervision, Writing - review & editing. **Neil C. Hyatt:** Supervision, Writing - review & editing.

Acknowledgements

We are grateful for financial support from the Nuclear Decommissioning Authority and EPSRC under grant numbers EP/S01019X/1, EP/N017870/1 and EP/R511754/1. This research utilised the HADES/MIDAS facility at the University of Sheffield established with financial support from EPSRC and BEIS, under grant EP/T011424/1 [33]. This research used beamline BMM of the National Synchrotron Light Source II, a U.S. Department of Energy (DOE) Office of Science User Facility Operated for the DOE office of Science by Brookhaven National Laboratory under Contract No. DE-SC0012704.

Appendix A. Supplementary data

Supplementary data to this article can be found online at https://doi.org/10.1016/j.jnucmat.2020.152137.

References

[1] N.C. Hyatt, Plutonium management policy in the United Kingdom: the need for a dual track strategy, Energy Pol. 101 (2017) 303–309.
[2] Department of Energy & Climate Change, Management of the UK's Plutonium Stocks: A Consultation Response on the Proposed Justification Process for the Reuse of Plutonium, 2011.
[3] Nuclear Decommissioning Authority, NDA Plutonium Topic Strategy: Credible Options Technical Summary, 2009.
[4] E. Vance, Development of ceramic waste forms for high-level nuclear waste over the last 30 Years, Mater. Res. Soc. Symp. Proc. 985 (2007).
[5] G.R. Lumpkin, Alpha-decay damage and aqueous durability of actinide host phases in natural systems, J. Nucl. Mater. 289 (1–2) (2001) 136–166.
[6] G.R. Lumpkin, et al., Crystal chemistry and cation ordering in zirconolite 2M, Mater. Res. Soc. Symp. Proc. 932 (2006).
[7] A.A. Coelho, R.W. Cheary, K.L. Smith, Analysis and structural determination of

Nd-substituted zirconolite-4M, J. Solid State Chem. 129 (1997) 346–359.
[8] S. Ma, S. Ji, C. Liao, C. Liu, K. Shih, W. He, Effects of ionic radius on phase evolution in Ln-Al co-doped $Ca_{1-x}Ln_xZrTi_{2-x}Al_xO_7$ (Ln = La, Nd, Gd, Ho, Yb) solid solutions, Ceram. Int. 44 (13) (2018) 15124–15132.
[9] N.V. Zubkova, et al., The crystal structure of nonmetamict Nb-rich zirconolite-3T from the Eifel paleovolcanic region, Germany, Zeitschrift fur Krist. - Cryst. Mater. 233 (7) (2018) 463–468.
[10] E.R. Vance, et al., Incorporation of uranium in zirconolite ($CaZrTi_2O_7$), J. Am. Ceram. Soc. 85 (7) (2002) 1853–1859.
[11] B.D. Begg, R.A. Day, A. Brownscombe, Structural effect of Pu substitutions on the Zr-site in zirconolite, Mater. Res. Soc. Symp. Proc. 663 (2001) 1–8.
[12] B.M. Clark, S.K. Sundaram, S.T. Misture, Polymorphic transitions in cerium-substituted zirconolite ($CaZrTi_2O_7$), Sci. Rep. 7 (1) (2017) 2–10.
[13] M. Jafar, P. Sengupta, S.N. Achary, A.K. Tyagi, Phase evolution and microstructural studies in CaZrTi2O7-Nd2Ti2O7 system, J. Am. Ceram. Soc. 97 (2) (2014) 609–616.
[14] M. Jafar, P. Sengupta, S.N. Achary, A.K. Tyagi, Phase evolution and microstructural studies in $CaZrTi_2O_7$ (zirconolite)-$Sm_2Ti_2O_7$ (pyrochlore) system, J. Eur. Ceram. Soc. 34 (16) (2014) 4373–4381.
[15] P.A. Bingham, R.J. Hand, M.C. Stennett, N.C. Hyatt, M.T. Harrison, The use of surrogates in waste immobilization studies: a case study of plutonium, Mater. Res. Soc. Symp. Proc. 1107 (2008).
[16] B.H. Toby, EXPGUI, a graphical user interface for GSAS, J. Appl. Crystallogr. 34 (2001) 210–213.
[17] K.R. Whittle, et al., Combined neutron and X-ray diffraction determination of disorder in doped zirconolite-2M, Am. Mineral. 97 (2012) 291–298.
[18] R.E. Dinnebier, S.J.L. Billinge, Powder Diffraction Theory and Practice, RSC Publishing, 2008.
[19] B.D. Begg, E.R. Vance, B.A. Hunter, J.V. Hanna, Zirconolite transformation under reducing conditions, J. Mater. Res. 13 (11) (1998) 3181–3190.
[20] N.C. Hyatt, et al., Thermal treatment of simulant plutonium contaminated materials from the Sellafield site by vitrification in a blast-furnace slag, J. Nucl. Mater. 444 (2014) 186–199.
[21] D.J. Bailey, M.C. Stennett, B. Ravel, D. Grolimund, N.C. Hyatt, "Synthesis and characterisation of brannerite compositions $(U_{0.9}Ce_{0.1})_{1-x}M_xTi_2O_6$ ($M = Gd^{3+}$, Ca^{2+}) for the immobilisation of MOX residues, RSC Adv. 8 (4) (2018) 2092–2099.
[22] M.C. Stennett, C.L. Freeman, A.S. Gandy, N.C. Hyatt, Crystal structure and non-stoichiometry of cerium brannerite: $Ce_{0.975}Ti_2O_{5.95}$, J. Solid State Chem. 192 (2012) 172–178.
[23] B. Ravel, M. Newville, ATHENA, artemis, hephaestus: data analysis for X-ray absorption spectroscopy using IFEFFIT, J. Synchrotron Radiat. 12 (2005) 537–541.
[24] A. Salamat, et al., Structural transformations and disordering in zirconolite ($CaZrTi_2O_7$) at high pressure, Inorg. Chem. 52 (2013) 1550–1558.
[25] M. Jafar, S.N. Achary, N.P. Salke, A.K. Sahu, R. Rao, A.K. Tyagi, X-ray diffraction and Raman spectroscopic investigations on $CaZrTi_2O_7$ - $Y_2Ti_2O_7$ system: delineation of phase fields consisting of potential ceramic host materials, J. Nucl. Mater. 475 (2016) 192–199.
[26] Y.B. Zhang, et al., "Phase evolution, microstructure and chemical stability of $Ca_{1-x}Zr_{1-x}Gd_{2x}Ti_2O_7$ ($0.0 \leq x \leq 1.0$) system for immobilizing nuclear waste, Ceram. Int. 44 (2018) 13572–13579.
[27] S. Qin, X. Wu, F. Seifert, A.I. Becerro, Micro-Raman study of perovskites in the $CaTiO_3$-$SrTiO_3$ system, J. Chem. Soc., Dalton Trans. 19 (2002) 3751–3755.
[28] W. Li, F. Dong, L. Bian, H. Zou, M. Song, Phase relations, microstructure, and valence transition studies on $CaZr_{1-x}Ce_xTi_2O_7$ ($0.0 \leq x \leq 1.0$) system, J. Rare Earths 36 (11) (2018) 1184–1189.
[29] B.D. Begg, E.R. Vance, The incorporation of cerium in zirconolite, Mater. Res. Soc. Symp. Proc. 465 (1997) 333–340.
[30] B.D. Begg, E.R. Vance, G.R. Lumpkin, Charge compensation and the incorporation of cerium in zirconolite and perovskite, Mater. Res. Soc. Symp. Proc. 506 (1998) 79–86.
[31] B. Begg, E. Vance, S. Conradson, The incorporation of plutonium and neptunium in zirconolite and perovskite, J. Alloys Compd. 271 (273) (1998) 221–226.
[32] M.V. Zamoryanskaya, B.E. Burakov, Feasibility limits in using cerium as a surrogate for plutonium incorporation in zircon, zirconia and pyrochlore, Mater. Res. Soc. Symp. Proc. 663 (2001) 1–6.
[33] N.C. Hyatt, C.L. Corkhill, M.C. Stennett, R.J. Hand, L.J. Gardner, C.L. Thorpe, The HADES Facility for High Activity Decommissioning Engineering & Science: part of the UK National Nuclear User Facility, IOP Conf. Series: Mater. Sci. Eng. 818 (2020), 012022.

A Systematic Analysis of the $CaZr_{1-x}U_xTi_2O_7$ Zirconolite Solid Solution

Lewis R. Blackburn[a], Peter Apps[c], Shi-Kuan Sun[b], Kristina Kvashnina[d], Lucy M. Mottram[a], Laura J. Gardner[a], Amber R. Mason[a], Ewan R. Maddrell[e], Martin C. Stennett[a], Claire L. Corkhill[a], Neil C. Hyatt[*a]

[a] *Immobilisation Science Laboratory, University of Sheffield, Department of Materials Science and Engineering, Sir Robert Hadfield Building, Mappin Street, S13JD, UK*

[b] *School of Material Science and Energy Engineering, Foshan University, Foshan 528000, China*

[c] *National Nuclear Laboratory, Sellafield, Seascale, CA20 1PG, UK*

[d] *Rossendorf Beamline (BM20), The European Synchrotron (ESRF), 38000 Grenoble, France*

[e] *National Nuclear Laboratory, Workington, Cumbria, CA20 1PJ, UK*

Abstract

A series of zirconolite ceramics with stoichiometry $CaZr_{1-x}U_xTi_2O_7$ ($0 \leq x \leq 0.40$, $\Delta x = 0.10$) were synthesised at 1350 °C for 20 h in air, Ar and 5% H_2/N_2, using a conventional solid state cold press and sinter method. The progressive accommodation of U within the zirconolite phase was most readily achieved when synthesising under Ar atmosphere with U distributed predominantly as U^{4+}, confirmed by U L_3-edge XANES analysis. Accordingly, a transformation from zirconolite-2M to the zirconolite-4M polytype was observed in the compositional interval $0.10 \leq x \leq 0.20$, with polytype structures confirmed by high resolution TEM coupled with selected area electron diffraction. Synthesis in air promoted the formation of higher U oxidations states, with uniform U^{5+} speciation in single phase zirconolite-2M ($x = 0.10$) confirmed by U M_4 HERFD-XANES. Further U incorporated resulted in the formation of a U-substituted cubic ZrO_2 phase, apparently stabilised with additional Ca and Ti. Synthesis under 5% H_2/N_2 promoted an undesirable phase assemblage, despite uniform U^{4+} speciation, consisting of zirconolite-2M and a U-bearing perovskite phase at all targeted U concentration. A tertiary pyrochlore-structured phase was also present above $x \geq 0.30$. The implications for deployment of U as a chemical surrogate for Pu, in the context of wasteform development, is discussed with reference to existing literature.

1 Introduction

The 2019 UK Radioactive Material Inventory reported that 112 teHM (tonnes heavy metal equivalent) of PuO_2 has been separated from spent nuclear fuel by aqueous reprocessing [1]. In an effort to satisfy security requirements, all UK-owned Pu inventories are currently being consolidated at the Sellafield site, with provisions made for a further 2 teHM, forecast to arise from reprocessing the remaining portion of spent fuel currently in storage [2]. This stockpile represents a substantial burden to the UK nuclear sector, and in turn requires a long-term management strategy that alleviates proliferation concerns whilst providing a reasonable economic benefit and meeting disposal criteria. The Nuclear Decommissioning Authority (NDA) has outlined potential reuse and disposal options for the inventory

Corresponding Author: Lewis Blackburn – lewis.blackburn@sheffield.ac.uk

through the credible options framework, with consideration given to cost; technological maturity; human factors; socioeconomics and deliverability [3]. Several iterations of this framework with respect to these criteria have identified two high level disposition options, described as: fabrication of Mixed Oxide (MOX) fuel for loading in the current fleet of operational light water reactors (LWR), followed by geological disposal; immobilisation as a monolithic ceramic product (either by cold pressing and sintering of ceramic pellets, or by consolidation by Hot Isostatic Pressing (HIP)), followed prompt geological disposal. Whilst HM Government has concluded that reuse as MOX fuel is the preferred strategy, some fraction of the stockpile will not be suitable for this purpose, due to the progressive radiolysis of PVC containment used for the storage of some inventories, resulting in significant halide contamination [4]. Hence, it is accepted that the need for immobilisation for some of the Pu material will be required in all scenarios.

The immobilisation of radionuclides using cementitious and glass materials as the host matrix is the baseline thermal treatment for intermediate and high level liquid waste streams, respectively. For example, an alkali borosilicate glass wasteform is currently used for the vitrification of high level waste calcines (HLW) produced at Sellafield [5]. However, it is widely considered that ceramic wasteforms may offer superior mechanical properties and aqueous durability compared to the counterpart vitrified product, and therefore are the preferred immobilisation matrix for wastes containing a high-actinide fraction [6]. This confidence is largely based on the successful deployment of SYNROC technology. Ceramic immobilisation is typically achieved by dilution of waste species in solid solution, targeting specific atomic sites in the host lattice. Multiphase ceramic systems, such as the SYNROC wasteform, have also demonstrated the phase flexibility to ability to accommodate chemically heterogeneous waste streams, allowing for comparable variations in feedstock with vitrified materials, whilst retaining exceptional chemical durability [7]–[9].

Zirconolite (prototypically $CaZrTi_2O_7$) is a naturally occurring titanate mineral phase that has demonstrated extensive affinity for actinide incorporation and retention, and has subsequently been identified as a candidate host phase for UK owned Pu. Zirconolite is the host phase for actinides within the SYNROC-C wasteform, specifically developed for the immobilisation of chemically heterogeneous HLW streams [10]. Zirconolite has been identified as the most chemically durable SYNROC phase, evidenced by natural specimens which have retained significant actinide inventories (~ 20 wt. % U/Th) over geological timescales, demonstrating the necessary radiation tolerance and chemical durability required to act as a single phase host with a significant actinide fraction (such as PuO_2) [11]. Zirconolite exhibits a complex oxide structure that is closely related to that of the $A_2B_2O_7$ pyrochlore family of minerals, and is therefore, in turn, a derivative of the anion deficient fluorite superstructure. Zirconolite may also crystallise in a range of polytypical structures, the formation of which appears to be manipulated by variation of experimental parameters (in particular processing atmosphere) and cation substitution regimes. The ideal $CaZrTi_2O_7$ zirconolite structure is assigned the nomenclature zirconolite-2M, with reference to the two distinct cation layers that comprise the monoclinic lamellar unit cell (space group C2/c). It was demonstrated by Gatehouse *et al*. that the zirconolite-2M parent structure is actually

Corresponding Author: Lewis Blackburn – lewis.blackburn@sheffield.ac.uk

stabilized over the compositional range $CaZr_xTi_{3-x}O_7$ for $0.8 \leq x \leq 1.3$ [12]. The zirconolite-2M structure is comprised of alternating cation layers, with three distinct sites (Ca^{2+}, Zr^{4+}, Ti^{4+}) capable of cation substitution, allowing moderate solid solution of radionuclides within the structure. Planes of Ca^{2+} and Zr^{4+} atoms, 8 and 7-fold coordinated to oxygen respectively, are interleaved with sheets of Ti polyhedra adopting a HTB-type motif. Ti^{4+} cations are distributed in three distinct sites across the HTB plane, two of which consist of corner sharing TiO_6 octahedra, with the remaining Ti^{4+} occupying a statistically occupied trigonal biprymidal site, 5-fold coordinated to oxygen [13]. In the zirconolite-2M structure Ca/Zr and Ti planes are interleaved along [001], with successive HTB modules offset by a stacking vector corresponding to a 180˚ rotation offset in the [130] direction. Extensive substitution of actinides (U^{4+}, Pu^{4+}, Th^{4+}) and trivalent lanthanide elements (Gd^{3+}, Ce^{3+}, Sm^{3+}) within the zirconolite structure is generally accommodated by cation reordering and polytype formation. Zirconolite is capable of adopting a number of distinct polytypes, characterized by variations in stacking sequence of adjacent CaO_8/ZrO_7 and TiO_6 cation interlayers parallel to the [001] plane. For example, the accommodation of > 0.15 f.u. of Pu^{4+} within the Zr^{4+} site was facilitated by the formation of zirconolite-4M [14]. The zirconolite-4M polytype was described by Coelho *et al*. as an admixture of zirconolite-2M and pyrochlore like modules, with an expansion of the unit cell along the c-axis to accommodate cation reordering, resulting in a four HTB planes interspaced with Ca/Zr polyhedra (akin to zirconolite-2M) and Ca/Ti polyhedra (similar to pyrochlore) [15]. The 4M polytype has also been stabilized by incorporation of Ce^{4+} within the Zr^{4+} site in the same compositional interval, however the corresponding $CaZr_{1-x}Th_xTi_2O_7$ solid solution does not exhibit the same polytype transformation [16], [17].

We have recently demonstrated the incorporation of Ce within the Zr^{4+} site in $CaZrTi_2O_7$ was directly influenced by processing atmosphere, ultimately controlling Ce^{4+}/Ce^{3+} speciation and thus determining partitioning behavior. Synthesis in air at 1350 ˚C for 20 h produced the most favorable phase assemblage, in which Ce was mainly accommodated in zirconolite-2M and zirconolite-4M, whereas synthesis in argon and 5% H_2/N_2 conditions promoted the reduction of Ce^{4+} to Ce^{3+} and the subsequent formation of a deleterious Ce-bearing perovskite phase [16]. The limitations of Ce as a Pu surrogate have been largely realized (*e.g.* the tendency of Ce^{4+} to auto-reduce to Ce^{3+} at elevated processing temperature), and therefore in order to reliably understand the potential partitioning of Pu within the zirconolite parent structure, a series of chemical surrogates under identical processing conditions must be utilized in conjunction. The data presented here is complementary to our previously reported work on the $CaZr_{1-x}Ce_xTi_2O_7$ and $CaZr_{1-x}Th_xTi_2O_7$ systems, in which zirconolite polytype formation and secondary phase concentration was controlled by processing atmosphere. To ensure that a useful comparison between Pu surrogates may be elucidated, we have preserved the synthesis method used in our previous work on the $CaZr_{1-x}Ce_xTi_2O_7$ and $CaZr_{1-x}Th_xTi_2O_7$ solid solutions, targeting a consistent identical compositional range, and using the same mixed oxide synthesis technique. It is hoped these data will contribute towards a detailed understanding of zirconolite chemistry using a multi-surrogate approach, and further support the safety case for geological disposal of Pu materials within a zirconolite ceramic matrix.

Corresponding Author: Lewis Blackburn – lewis.blackburn@sheffield.ac.uk

2 Experimental

2.1 Materials Synthesis

All samples were fabricated by a mixed oxide synthesis, targeting $CaZr_{1-x}U_xTi_2O_7$. Compositions were batched in the range $0 \leq x \leq 0.40$ ($\Delta x = 0.10$) and synthesized by reaction between $CaTiO_3$ (Sigma Aldrich, 99.9% trace metals basis), TiO_2 (Sigma Aldrich, 99.9% trace metals basis), ZrO_2 (Sigma Aldrich, 99.9% trace metals basis) and UO_2 (depleted, ABSCO Ltd.). Precursors were dried, weighed according to desired composition, and homogenised by planetary ball milling at 400 rpm for 20 minutes, with isopropanol added as a carrier fluid. Powder slurries were discharged and dried overnight at 80 °C, in order to evaporate excess solvent, followed by recovery of the batch material. Approximately 0.35 g of each composition was pressed into the walls of a hardened steel die (ø = 10 mm), under 3 t uniaxial pressure to form loosely bound green bodies. The powder compacts were transferred to a ZrO_2 crucible and sintered at 1350 °C for 20 h in either air, a flowing Ar or 5% H_2/N_2 mixture, to represent oxidising, inert and reducing conditions, respectively, with a heating/cooling profile of 3 °C/min.

2.2 Materials Characterization

All samples were characterized by powder X-ray diffraction (XRD) using a Bruker D2 Phaser (Cu Kα - λ = 1.5418 Å, Ni filter), fitted with a Lynxeye position sensitive detector. Diffraction data were acquired in the range $5^\circ \leq 2\theta \leq 80^\circ$ with a scan rate of $0.02^\circ\ s^{-1}$. Phase matching was achieved using the PDF-4+ database, with analysis of powder XRD data performed using the Rietveld method, using the GSAS package with EXPGUI interface [18]. A section of each sintered pellet was prepared for scanning electron microscopy (SEM) analysis by mounting in cold setting resin, followed by polishing to a 1 µm optical finish. Surfaces were also coated with a thin layer of carbon and Ag-based conductive paint prior to analysis, to prevent charging effects. SEM analysis was performed using a Hitachi TM3030 analytical scanning microscope, operating at 15 kV accelerating voltage, with an approximate working distance of 8 mm. SEM hardware was also equipped with a Bruker Quantax system for elemental dispersive X-ray spectroscopy (EDS) analysis. X-ray absorption near edge spectroscopy (XANES) spectra at the U L_3 edge were collected at Diamond Light Source Beamline B-18 (Oxford, U.K.). U L_3 XANES spectra were acquired alongside a series of reference compounds UTi_2O_6, UO_2, $CrUO_4$, $CaUO_4$, representing U in a variety of coordination configuration and oxidation states. A Si(111) double crystal monochromator was used to fine-tune incident synchrotron radiation, with the intensity of the incident and transmitted beam measured using ionization chambers, filled with a mixture of N_2 and He gas, operated in a stable region of the I/V curve. U L_3 XANES spectra were collected from the fluorescence emission channel, detected using a four channel Si-drift detector with appropriate dead time correction [19]. Subsequent reduction and analysis of data was completed using the Athena component of the Demeter software package [20]. All specimens were prepared for XANES analysis by finely grinding into suspension with polyethylene glycol (PEG). Mixtures were then compacted into the walls of a 6 mm

Corresponding Author: Lewis Blackburn – lewis.blackburn@sheffield.ac.uk

stainless steel die under uniaxial pressure, and pressed to a depth corresponding to approximately one absorption length. The average oxidation state of U in the zirconolite samples was determined by linear regression of the normalized and aligned E_0 position with respect to reference compounds. U M_4-edge XANES measurements were performed at beamline BM20 [21] of the European Synchrotron Radiation Facility (ESRF) in Grenoble. The incident energy was selected using the <111> reflection from a double Si crystal monochromator. XANES spectra was measured in high-energy-resolution fluorescence detected (HERFD) mode using an X-ray emission spectrometer [22]. The sample, analyzer crystal and photon detector (silicon drift detector) were arranged in a vertical Rowland geometry. The U HERFD spectra at the M_4 edge were obtained by recording the maximum intensity of the U Mb emission line (~3337 eV) as a function of the incident energy. The emission energy was selected using the <220> reflection of five spherically bent striped Si crystal analyzers (with 1m bending radius) aligned at 75° Bragg angle. The intensity was normalised to the incident flux. A combined (incident convoluted with emitted) energy resolution of 0.7 eV was obtained as determined by measuring the full width at half maximum (FWHM) of the elastic peak. The paths of the incident and emitted X-rays through air were minimized in order to avoid losses in intensity due to absorption. Data was collected at the room temperature. Samples have been sealed in a sample holder and protected by 13 µm of Kapton film at the University of Sheffield and transported to ESRF for the HERFD measurements. Samples were prepared for high resolution transmission electron microscopy (HR-TEM) coupled with selected area electron diffraction (SAED) by the crushed grain method, wherein a small quantity of powered sample was rapidly ground in a pestle and mortar in ethanol. An aliquot of liquid was siphoned from the top of the solvent layer using a pipette and deposited onto the surface of a 300 µm mesh holey Cu grid, and allowed to dry prior to analysis. A JEOL JEM-2100 operating at 200 kV, equipped with an Oxford Instruments 80 mm^2 SSD EDS was utilised to capture dark field images of individual grains and collected selected area electron diffraction patterns.

3 Results and Discussion

3.1 $CaZr_{1-x}U_xTi_2O_7$ Phase Evolution

3.1.1 Air Sintering

Powder X-ray diffraction measurements for $CaZr_{1-x}U_xTi_2O_7$ specimens reacted in air are shown in **Fig. 1a**. Phase pure zirconolite-2M (space group C2/c, ICSD – 190015) was formed when targeting x = 0. Refinement of the powder XRD data were accomplished using the Rietveld method, allowing calculation of the zirconolite-2M unit cell parameters to be: ***a*** = 12.4435(4) Å, ***b*** = 7.2735(3) Å, ***c*** = 11.3748(4) Å, ***β*** = 100.563(3)˚ and ***V*** = 1012.06(4) $Å^3$. These are in excellent agreement with previously reported values [23]. When targeting x = 0.10, weak additional reflections were observed at 2θ = 30.4˚ and 35.6˚, corresponding to reflections in the (111) and (002) planes, respectively, for $ZrTiO_4$ (space group Pbcn, ICSD – 153939). As the targeted U substitution was increased to x = 0.30, zirconolite underwent a partial phase transformation to the zirconolite-4M polytype, noted by the appearance of weak supercell

Corresponding Author: Lewis Blackburn – lewis.blackburn@sheffield.ac.uk

reflections at 2θ = 7.8˚ and 31.1˚ corresponding to the (002) and (008) reflections of the 4M superstructure, respectively. The diffraction pattern for x = 0.30 also evidenced a phase that was not representative of the zirconolite-2M or 4M structures, distinguished by the appearance of a prominent additional reflection at approximately 2θ = 30.6˚ (see **Fig. 1b**). When targeting x = 0.40, the intensity of this reflection was such that it appeared to the dominant phase with respect to zirconolite phase(s). Inspection of position and intensity of this phase in the powder XRD data was consistent with cubic ZrO_2, stabilised (herein referred to as c-ZrO_2) by moderate substitution of Ca, U and Ti. Within **Fig. 1b** the calculated diffraction pattern for $(Ca_{0.22}Ti_{0.22}Zr_{0.56})O_{1.78}$ (space group Fm-3m, ICSD – 56300) is also plotted demonstrating that the 2θ position of the major reflection for this phase is in good agreement with the position of the cubic phase observed for x = 0.30 and x = 0.40. It is certainly conceivable that such as phase would be able to accommodate moderate U content, as was later inferred by SEM-EDS analysis. Moreover, there has been recent evidence for U-stabilised c-ZrO_2 in simulant Chernobyl lava-like fuel-containing (LCFM) material, hence it is conceivable that U stabilised c-ZrO_2 may form in the present system.

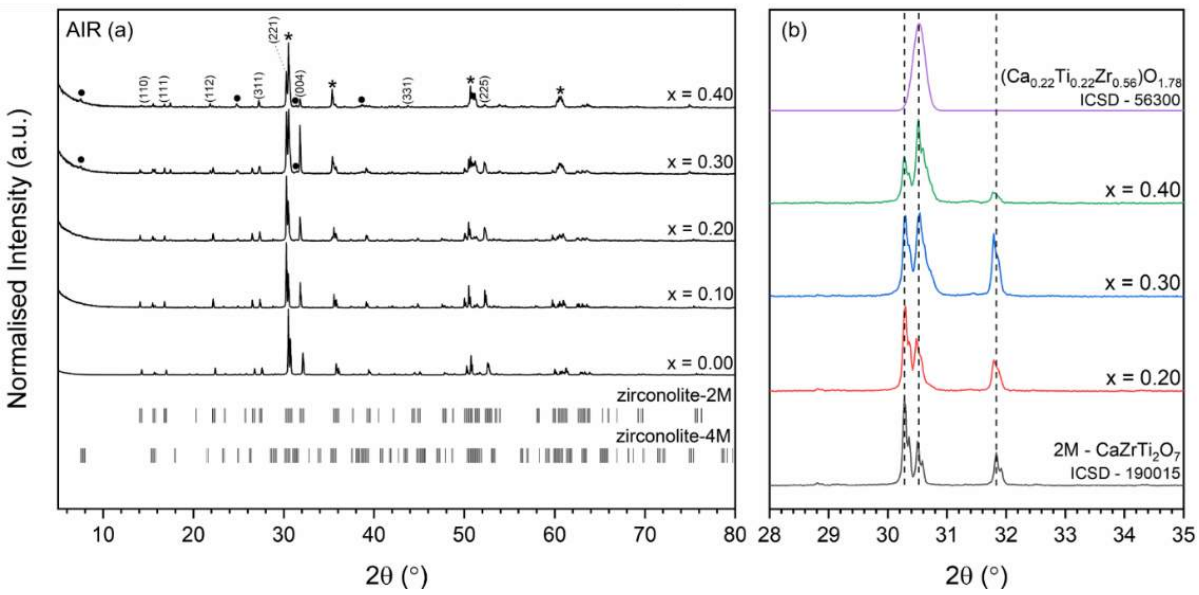

Fig. 1) Powder X-ray diffraction measurements for $CaZr_{1-x}U_xTi_2O_7$ ($0 \leq x \leq 0.40$) compositions, sintered in air at 1350 ˚C for 20 h, in the range $5^\circ \leq 2\theta \leq 80^\circ$. Zirconolite-2M reflections are highlighted with (hkl) values. Zirconolte-4M reflections are labelled by filled circles. Defect fluorite reflections are highlighted by asterisk (*).

3.1.2 Argon Sintering

It was determined from powder XRD analysis that progressive incorporation of U within the zirconolite phase under inert conditions (argon) produced a mix of zirconolite polytypes (**Fig. 2**). When targeting nominal x = 0.00 and x = 0.10 compositions, reflections attributed to single-phase zirconolite-2M were clearly distinguished, forming as single phases in both instances. The unit cell parameters (**Table 1**) for the single phase zirconolite with composition x = 0.10, corresponding to $CaZr_{0.90}U_{0.10}Ti_2O_7$, were in excellent agreement with unit cell dimensions reported by Shrivastava *et al* [25]. Targeting a nominal U

Corresponding Author: Lewis Blackburn – lewis.blackburn@sheffield.ac.uk

concentration of x = 0.20 resulted in the formation of zirconolite-4M, comprising 30.3 ± 0.5 wt. % of the phase assemblage, evidenced by the appearance of supercell reflections at 2θ = 7.8˚ and 31.1˚ corresponding to (002) and (008) reflections of the 4M structure, respectively. The unit cell dimensions of the zirconolite-4M phase produced for 0.20 ≤ x ≤ 0.40 and quantitative phase analysis are also listed in **Table 1**. As the nominal concentration of U was elevated to x = 0.30, the relative quantity of zirconolite-4M increased to 63.0 ± 0.3 wt. %. The intensity of zirconolite-4M supercell reflections also increased relative to the diagnostic zirconolite-2M reflection (labelled by (*) on **Fig. 2**). When targeting x = 0.40 zirconolite-4M comprised 90.7 ± 0.1 wt. % of the phase assemblage. Selected area electron diffraction data for $CaZr_{0.90}U_{0.10}Ti_2O_7$ and $CaZr_{0.60}U_{0.40}Ti_2O_7$ are displayed in **Fig. 3**. The electron diffraction data of $CaZr_{0.90}U_{0.10}Ti_2O_7$ was indexed to the [010] zone axis in the zirconolite-2M structure in agreement with the powder XRD data. Representative electron diffraction patterns for $CaZr_{0.60}U_{0.40}Ti_2O_7$ revealed noticeable stacking disorder in the [110] direction, consistent with the characteristic streaking previously reported for zirconolite-4M. These data are in excellent agreement with Vance *et al* [26], and as such it is expected that further accommodation of U within the Zr^{4+} site would be expected to produce a mixture of zirconolite-4M and pyrochlore. Similar phase fields in the $CaZr_{1-x}Pu_xTi_2O_7$ solid solution were reported by Begg *et al.* [11], however recent data for the corresponding $CaZr_{1-x}Th_xTi_2O_7$ solid solution recently published by Blackburn *et al.* revealed that the zirconolite-4M polytype did not form in the corresponding solid solution regime when doped with Th^{4+} under identical synthesis conditions [17].

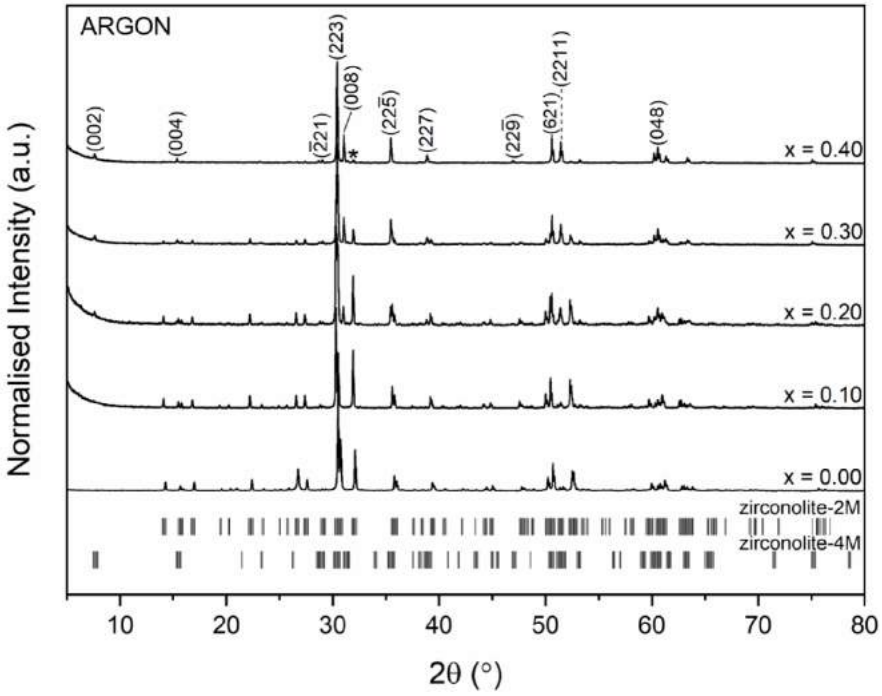

Fig. 2) Powder X-ray diffraction data for $CaZr_{1-x}U_xTi_2O_7$ (0.00 ≤ x ≤ 0.40) compositions, sintered in argon at 1350 ˚C for 20 h. Zirconolite-4M reflections are highlighted by (hkl) values. The residual zirconolite-2M (004) reflection is highlighted with (*).

Corresponding Author: Lewis Blackburn – lewis.blackburn@sheffield.ac.uk

Table 1) Unit cell parameters and quantitative phase data for the zirconolite-2M phase and 4M phases, calculated from Rietveld analysis of $CaZr_{1-x}U_xTi_2O_7$ ($0 \leq x \leq 0.40$, $\Delta x = 0.10$) sintered in argon at 1350 ˚C for 20 h

Nominal Composition	Unit Cell Dimensions					R_{wp} (%)	Wt. %
	a (Å)	b (Å)	c (Å)	β (˚)	V (Å^3)		
x = 0.00	12.4447(3)	7.2727(2)	11.3731(3)	100.575(3)	1011.854(3)	7.37	100*
x = 0.10	12.4746(5)	7.2838(2)	11.3953(3)	100.583(3)	1017.792(4)	7.70	100*
x = 0.20	12.4786(6) – 2M 12.4757(40) – 4M	7.2830(3) – 2M 7.2034(21) – 4M	11.3928(5) – 2M 23.1373(21) – 4M	100.588(3) – 2M 84.785(18) – 4M	1017.786(6) – 2M 2070.672(270) – 4M	7.49	69.7 ± 0.3 (2M) 30.3 ± 0.5 (4M)
x = 0.30	12.4773(9) – 2M 12.4746(19) – 4M	7.2811(5) – 2M 7.2036(10) – 4M	11.3850(7) – 2M 23.1030(11) – 4M	100.595(6) – 2M 84.791(9) – 4M	1016.676(9) – 2M 2067.502(117) – 4M	7.26	37.0 ± 0.5 (2M) 63.0 ± 0.3 (4M)
x = 0.40	12.4831(71) – 2M 12.4797(17) – 4M	7.2850(42) – 2M 7.2056(9) – 4M	11.3926(53) – 2M 23.0937(8) – 4M	100.638(66) – 2M 84.798(9) – 4M	1018.228(708) – 2M 2068.118(93) – 4M	8.03	9.3 ± 0.1 (2M) 90.7 ± 0.1 (4M)

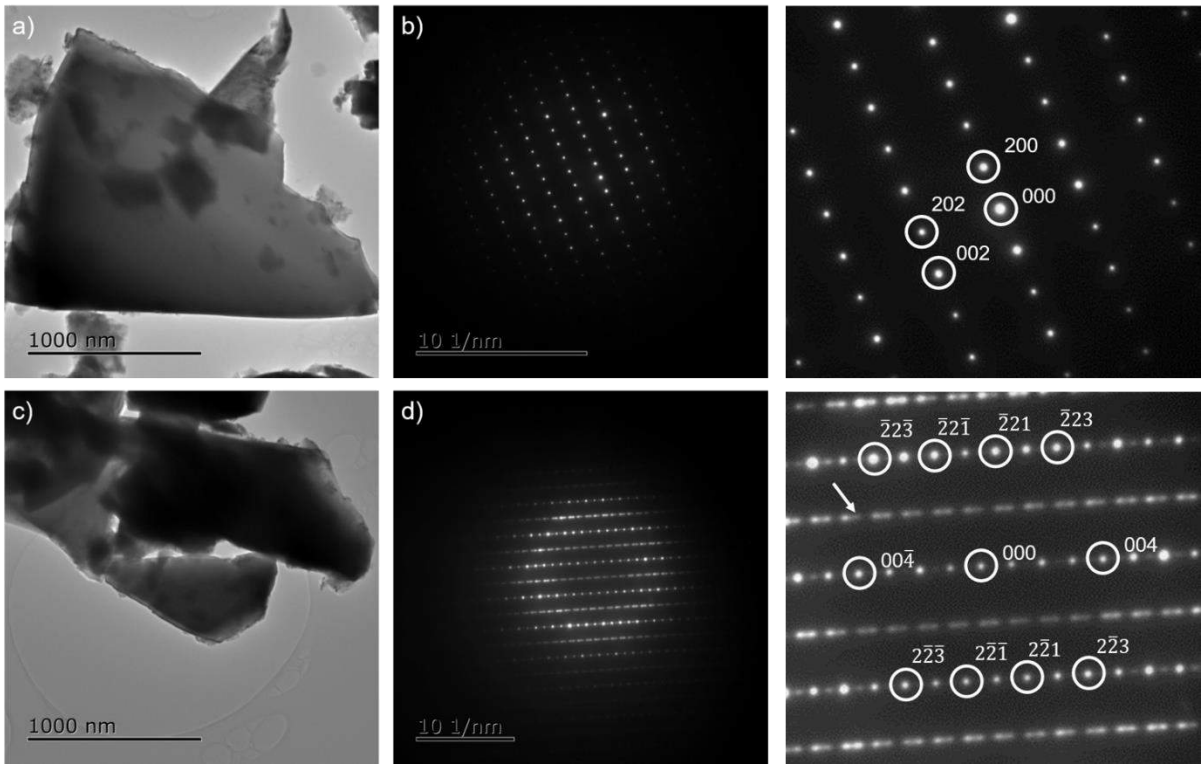

Fig 3) Bright field micrograph and electron diffraction data collected for $CaZr_{0.90}U_{0.10}Ti_2O_7$ (**a – b**) down [010] zone axis, and $CaZr_{0.60}U_{0.40}Ti_2O_7$ (**c – d**) down [110] zone axis, confirming the structures of zirconolite-2M and zirconolite-4M, respectively.

3.1.3 5% H_2/N_2 Sintering

Powder XRD data for $CaZr_{1-x}U_xTi_2O_7$ compositions sintered under reducing 5% H_2/N_2 are displayed in **Fig. 4**. When targeting x = 0.00, the phase assemblage was comprised of zirconolite-2M and perovskite (ideally $CaTiO_3$), accounting for 92.4 ± 0.04 and 7.6 ± 0.3 wt. % of the phase assemblage, respectively. The perovskite phase was identified by the dominant reflection at 2θ = 33.1˚, corresponding to (112) reflection. When U incorporation was increased to x = 0.10, no additional reflections were observed, yet the phase fraction corresponding to the perovskite phase increased to 10.4 ± 0.3 wt. %. The zirconolite-2M unit cell volume (**Table 2**) was observed to increase from ~ 1009.3 Å^3 to ~ 1014.7 Å^3, consistent with U incorporation (Zr^{4+}: 0.78 Å, U^{4+}: 0.95 Å in 7-fold coordination). Increasing the nominal

Corresponding Author: Lewis Blackburn – lewis.blackburn@sheffield.ac.uk

U content to x = 0.20 did not produce any additional diffraction peaks, however the corresponding perovskite content increased to ~ 11.6 wt. % and the unit cell volume of the zirconolite-2M phase expanded to ~ 1020.9 Å^3. As the targeted U^{4+} content was increased to x = 0.30 and x = 0.40 additional reflections were distinguished, representative of the pyrochlore structure, indexed as (111), (113), (004) and (044) reflections. Through Rietveld analysis it was determined that the pyrochlore phase comprised 6.9 ± 0.8 wt. % and 29.6 ± 0.4 wt. % at x = 0.30 and x = 0.40, respectively (see **Table 3**). The unit cell volume of the pyrochlore phase was calculated to be ~ 1049.5 Å^3 and ~ 1049.7 Å^3 at x = 0.30 and x = 0.40, in good agreement with published crystal structure data reported by Dickson *et al*., who reported a cell volume of 1048.1 Å^3 [27]. Further substitution of U^{4+} within the Zr^{4+} site would be expected to yield the $CaUTi_2O_7$ phase (betafite, space group Fd-3m), however above x > 0.70, it is reported that hot pressing is required to yield a (near) single phase material [26]. The unit cell dimensions of the zirconolite-2M phase were observed to increase in the compositional range 0 ≤ x ≤ 0.20, consistent with U incorporation. However, above the solid solution value x = 0.30, at which the pyrochlore phase became prominent in the phase assemblage, the 2M unit cell parameters remained largely constant, suggesting that U solid solution in the zirconolite phase was reached, and further U was preferentially accommodated in the pyrochlore structure. **Fig. 5** displays bright field TEM image and corresponding selected area diffraction data for the sample with the highest pyrochlore content (x = 0.40). Electron diffraction data were characteristic of the [110] zone axis in the pyrochlore structure, and in good agreement with those previously published [26]. Superlattice spots were clearly visible between dominant diffraction reflections (**Fig. 5b**) arising from the cell doubling of the fluorite sub-cell, giving rise to the pyrochlore structure [28].

Table 2) Unit cell parameters for the zirconolite-2M phase derived from Rietveld refinement of $CaZr_{1-x}U_xTi_2O_7$ (0 ≤ x ≤ 0.40, Δx = 0.10) sintered in 5% H_2/N_2 at 1350 ˚C for 20 h

Nominal (x)	a (Å)	b (Å)	c (Å)	β (˚)	V (Å^3)	R_{wp} (%)
0.00	12.4386(4)	7.2488(2)	11.3870(3)	100.551(3)	1009.346(36)	6.88
0.10	12.4656(5)	7.2600(3)	11.4052(5)	100.556(3)	1014.703(54)	8.39
0.20	12.5032(8)	7.2660(4)	11.4308(7)	100.568(9)	1020.849(81)	8.50
0.30	12.5180(14)	7.2662(7)	11.4338(9)	100.605(12)	1022.236(123)	9.18
0.40	12.5239(16)	7.2672(8)	11.4243(11)	100.593(15)	1022.032(150)	8.36

Table 3) Quantitative phase analysis for $CaZr_{1-x}U_xTi_2O_7$ (0 ≤ x ≤ 0.40, Δx = 0.10) sintered in 5% H_2/N_2 at 1350 ˚C for 20 h

Nominal (x)	Wt. %			R_{wp}
	Zirconolite-2M	Perovskite	Pyrochlore	
0.00	92.4 ± 0.1	7.6 ± 0.3	-	6.88
0.10	89.6 ± 0.1	10.4 ± 0.4	-	8.39
0.20	88.4 ± 0.1	11.6 ± 0.4	-	8.50
0.30	81.3 ± 0.3	11.8 ± 0.5	6.9 ± 0.8	9.18
0.40	61.1 ± 0.5	9.3 ± 0.5	29.6 ± 0.4	8.36

Corresponding Author: Lewis Blackburn – lewis.blackburn@sheffield.ac.uk

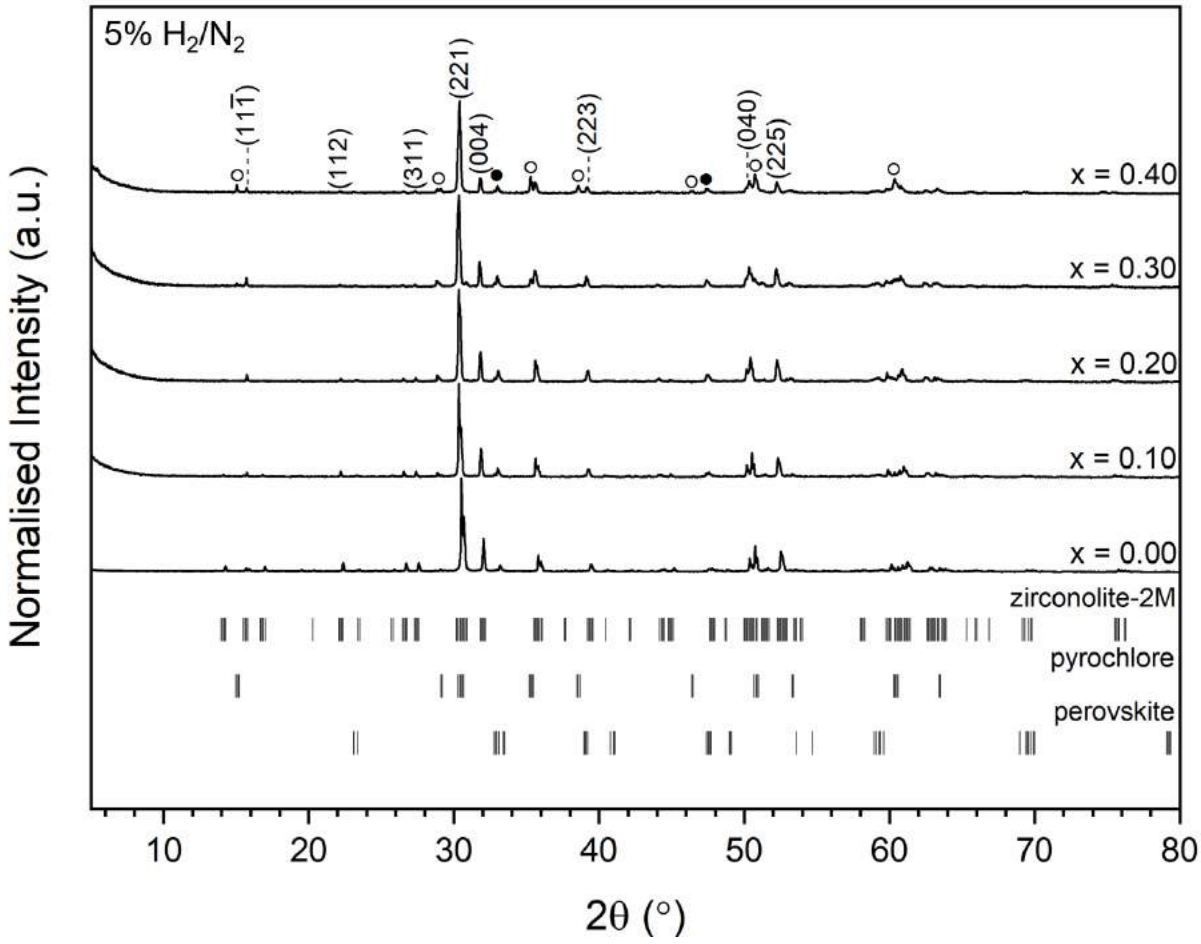

Fig. 4) Powder X-ray diffraction data for $CaZr_{1-x}U_xTi_2O_7$ ($0.00 \leq x \leq 0.40$) compositions, sintered in 5% H_2M_2 mixture at 1350 ˚C for 20 h. Zirconolite-2M reflections are indexed by (hkl) values. Pyrochlore reflections are labelled with open circles. Perovskite reflections are labelled with filled circles.

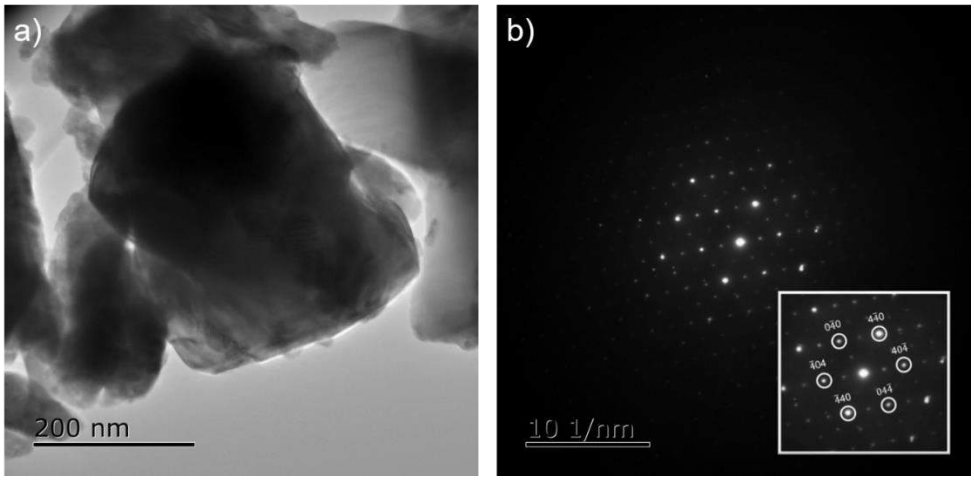

Fig 5) Bright field micrograph (**a**) and electron diffraction data (**b**) for $CaZr_{0.60}U_{0.40}Ti_2O_7$ down [110] zone axis indexed to pyrochlore structure

Corresponding Author: Lewis Blackburn – lewis.blackburn@sheffield.ac.uk

3.2 Microstructure and Compositional Analysis

3.2.1 Air Sintering

A sample of each microstructure for $CaZr_{1-x}U_xTi_2O_7$ ($0.10 \leq x \leq 0.40$) is presented in **Fig. 6**. When targeting x = 0.10, a bulk matrix of near-single phase zirconolite-2M was observed, with $ZrTiO_4$ inclusions, in agreement with XRD analysis. EDS analysis confirmed an average approximate ratio of 80:20 Ti/Zr (at. %) which was consistent with the reported phase diagrams [29]. Furthermore, it was determined by EDS analysis that U did not substitute within the $ZrTiO_4$ phase at any targeted level of U incorporation (**Fig. S1**). The microstructure for x = 0.20 was comprised of three distinct phases, distinguished by variation in backscattered electron contrast. The additional phase was considered to represent the U-substituted c-ZrO_2 phase, consistent with powder XRD analysis. As the nominal U content was increased, the visible fraction of the accompanying c-ZrO_2 clearly increased, such that the microstructure for x = 0.40 was clearly dominated by this phase. Analysis of x = 0.30 and x = 0.40 microstructures proved difficult, as the backscattered electron contrast between zirconolite-2M and zirconolite-4M polytypes rendered these phases practically indistinguishable. The assignment of zirconolite phases was assisted in part by a change in morphology, with elongated grains generally a consistent feature of zirconolite-4M [16]. It was assumed that the quantity of U substituted within the Zr^{4+} site was just greater than 0.15 f.u., resulting in near-identical composition, and indistinguishable contrast between 2M and 4M phases. The phase assignment was further complicated by the presence of a Zr-rich oxide with minor incorporated Ti (assumed composition $Zr_{1-x}Ti_xO_2$) identified in the microstructure for x = 0.40, which in turn presented a near-identical backscattered electron contrast both zirconolite phases. The elemental distribution for the x = 0.40 sample is illustrated in **Fig. 7**. Vance *et al*. synthesized a series of $CaZr_{1-x}U_xTi_2O_7$ zirconolites under argon, prior to annealing under oxidizing conditions, resulting in the partial decomposition of the zirconolite-4M phase to produce a 'zirconolite-2M phase' with stoichiometry $Ca_{1.11}U^{5+}_{0.46}Zr_{0.53}Ti_{1.84}O_7$ [26]. We propose that the zirconoite-2M phase reported by Vance *et al*. was likely consistent with the c-ZrO_2 phase observed in the present work. The composition of the oxidized material observed reported by Vance *et al*. was found to be very close to the stoichiometry reported for the defect fluorite phase in the present work. Furthermore, it would later be determined in that U was present as > U^{5+} when sintering in air, in agreement with the calculated composition.

Corresponding Author: Lewis Blackburn – lewis.blackburn@sheffield.ac.uk

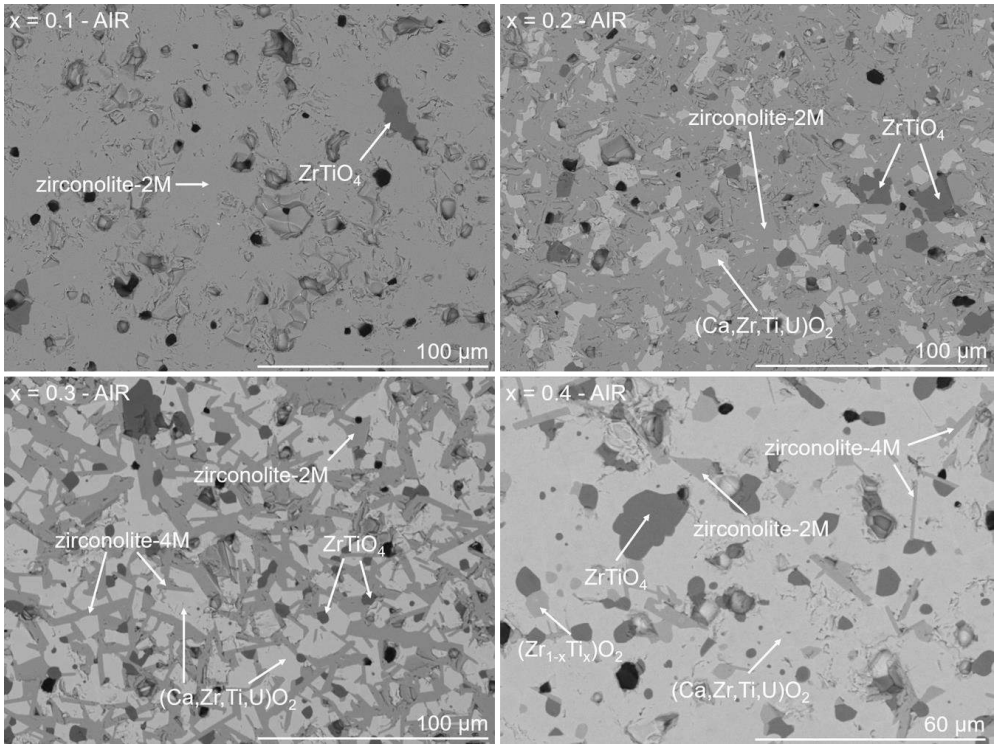

Fig. 6) Representative backscattered electron micrographs for $CaZr_{1-x}U_xTi_2O_7$ ($0.10 \leq x \leq 0.40$) sintered in air at 1350 ˚C for 20 h.

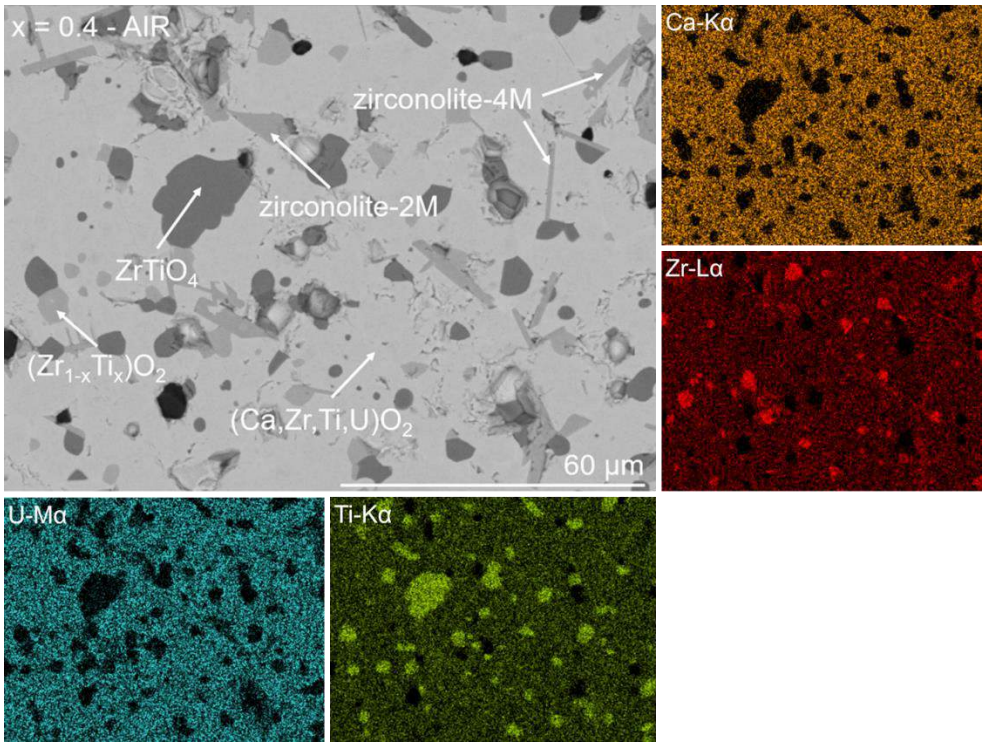

Fig. 7) Representative backscattered electron micrograph and corresponding elemental distribution for x = 0.40 sintered in air at 1350 ˚C for 20 h.

Corresponding Author: Lewis Blackburn – lewis.blackburn@sheffield.ac.uk

3.3.2 Argon Sintering

The microstructure of argon sintered specimens with compositions x = 0.1 and 0.2 are displayed in **Fig. 8**. In agreement with powder XRD measurements, single phase zirconolite-2M was observed when targeting nominal composition x = 0.10. EDS measurements confirm that the observed stoichiometry $Ca_{1.01(5)}Zr_{0.81(7)}U_{0.09(1)}Ti_{2.08(6)}O_7$, was close to target composition. When targeting x = 0.20, two phases were observed in the microstructure. These were distinguished by backscattered electron contrast due to compositional variation, with the zirconolite-4M phase appearing brighter relative to 2M grains, due to greater solubility of U within the 4M structure. SEM-EDS analyses of zirconolite-2M and zirconolite-4M grains present in the microstructure of x = 0.30 are displayed in **Fig. 9**. The zirconolite-4M phase was consistently enriched in U with respect to the zirconolite-2M phase, with average compositions $Ca_{0.98(8)}Zr_{0.76(8)}U_{0.15(3)}Ti_{2.12(9)}O_7$ and $Ca_{1.04(5)}Zr_{0.55(6)}U_{0.35(2)}Ti_{2.05(7)}O_7$ for the 2M and 4M phase when targeting x = 0.30, respectively. When x = 0.40, only a small fraction of the zirconolite-2M phase was observed in the microstructure, with the average composition of zirconolite-4M determined to be $Ca_{1.04(4)}Zr_{0.50(6)}U_{0.40(3)}Ti_{2.06(6)}O_7$, in good agreement with the targeted stoichiometry. The compositions of each phase observed in the microstructure for the $CaZr_{1-x}U_xTi_2O_7$ solid solution are summarised in **Table 4**.

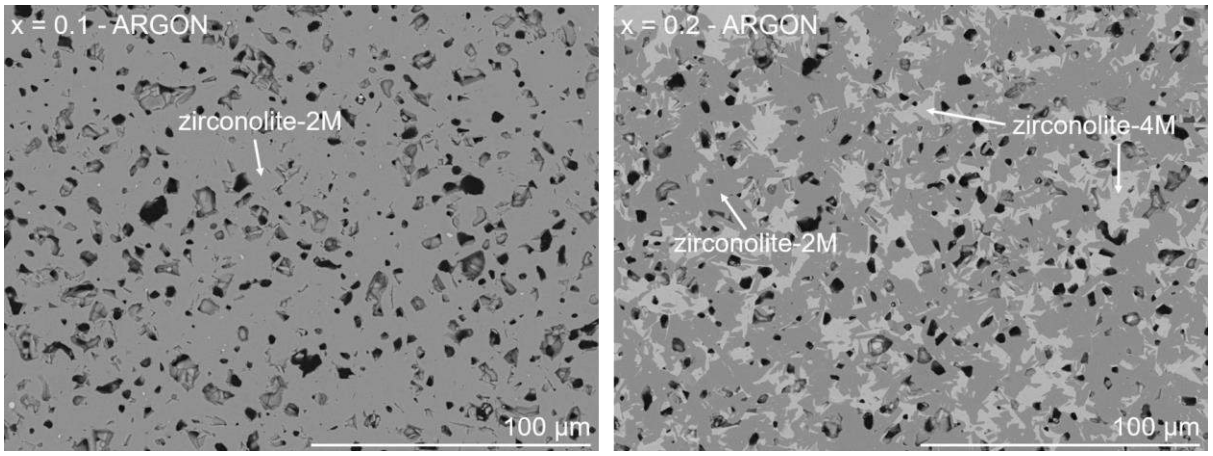

Fig. 8) Representative backscattered electron micrographs for x = 0.10 (left) and x = 0.20 (right) compositions sintered under flowing argon at 1350 ˚C for 20 h.

Table 4) Average compositions of zirconolite-2M, zirconolite-4M and pyrochlore phases formed in the $CaZr_{1-x}U_xTi_2O_7$ ($0.10 \leq x \leq 0.40$) under argon and 5% H_2/N_2 determined by semi-quantitative EDS analysis (* - data not obtained due to grain size).

Nominal (x)	Semi-Quantitative EDS Analysis			
	Argon		5% H_2/N_2	
	Zirconolite-2M	Zirconolite-4M	Zirconolite-2M	Pyrochlore
x = 0.10	$Ca_{1.01(5)}Zr_{0.82(7)}U_{0.09(1)}Ti_{2.08(6)}O_7$	-	$Ca_{0.89(6)}Zr_{0.90(9)}U_{0.09(1)}Ti_{2.11(8)}O_7$	-
x = 0.20	$Ca_{0.97(6)}Zr_{0.82(11)}U_{0.12(2)}Ti_{2.08(9)}O_7$	$Ca_{1.03(6)}Zr_{0.59(3)}U_{0.31(4)}Ti_{2.07(7)}O_7$	$Ca_{0.86(5)}Zr_{0.79(5)}U_{0.18(3)}Ti_{2.15(5)}O_7$	-
x = 0.30	$Ca_{0.98(8)}Zr_{0.76(8)}U_{0.15(3)}Ti_{2.12(9)}O_7$	$Ca_{1.04(5)}Zr_{0.55(6)}U_{0.35(2)}Ti_{2.05(7)}O_7$	$Ca_{0.94(9)}Zr_{0.74(9)}U_{0.22(2)}Ti_{2.09(4)}O_7$	$Ca_{1.01(5)}Zr_{0.45(7)}U_{0.52(7)}Ti_{2.03(8)}O_7$
x = 0.40	*	$Ca_{1.04(4)}Zr_{0.50(6)}U_{0.40(3)}Ti_{2.06(6)}O_7$	$Ca_{0.88(1)}Zr_{0.69(1)}U_{0.25(3)}Ti_{2.17(1)}O_7$	$Ca_{1.00(1)}Zr_{0.35(2)}U_{0.57(1)}Ti_{2.08(2)}O_7$

Corresponding Author: Lewis Blackburn – lewis.blackburn@sheffield.ac.uk

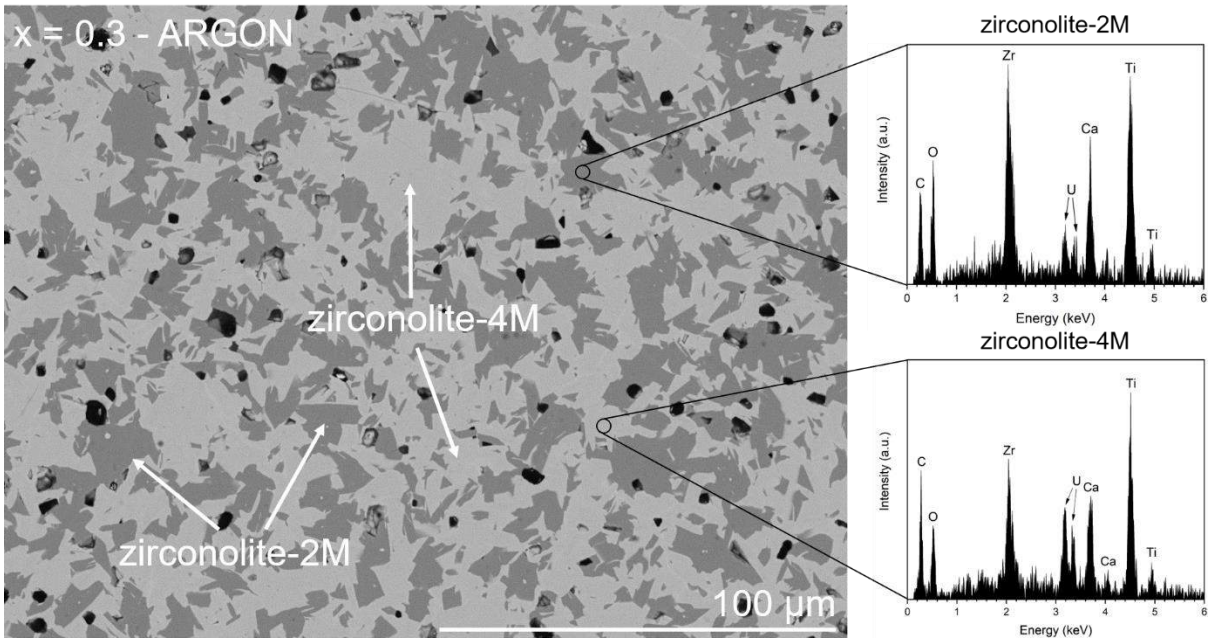

Fig. 9) EDS analysis of zirconolite-2M and zirconolite-4M phases present in microstructure of x = 0.30 composition, sintered in argon at 1350 ˚C for 20 h.

3.2.3 5% H_2/N_2 Sintering

SEM analysis of $CaZr_{1-x}U_xTi_2O_7$ compositions synthesized under reducing conditions confirmed the formation of a secondary perovskite phase for all targeted compositions. The microstructure for x = 0.10 and x = 0.20 compositions are displayed in **Fig. 10**. The perovskite was distinguished from the bulk zirconolite-2M matrix by decreased backscattered electron contrast, due to compositional variation. EDS analysis confirmed that U was partitioned between both the zirconolite-2M and perovskite phases (see **Fig. S2**). This is consistent with our previous observations when sintering $CaZr_{1-x}Th_xTi_2O_7$ solid solutions under reducing conditions, whereby a small amount of Th^{4+} was located in the perovskite phase [17]. In the absence of charge balancing cations such as Al^{3+}, it is likely that the charge balancing mechanism for U^{4+} in the perovskite phase is satisfied by the formation of some Ti^{3+}, as has been previously described by Vance *et al* [30]. When targeting x = 0.30, a third phase was distinguished in the microstructure by backscattered electron contrast, (**Fig. 11**), in agreement with powder XRD data, consistent with a pyrochlore structured phase, nominally $CaUTi_2O_7$ (betafite). EDS analysis confirmed that the U inventory was preferentially partitioned within the pyrochlore phase, rather than the target zirconolite-2M phase, with EDS spot analyses of both phases displayed in **Fig. 11**. The average composition of the pyrochlore phase was determined to be $Ca_{1.01(5)}Zr_{0.45(7)}U_{0.52(7)}Ti_{2.03(8)}O_7$ and $Ca_{1.00(1)}Zr_{0.35(2)}U_{0.57(1)}Ti_{2.08(2)}O_7$ for nominal U content x = 0.30 and x = 0.40, respectively (**Table 7**).

Corresponding Author: Lewis Blackburn – lewis.blackburn@sheffield.ac.uk

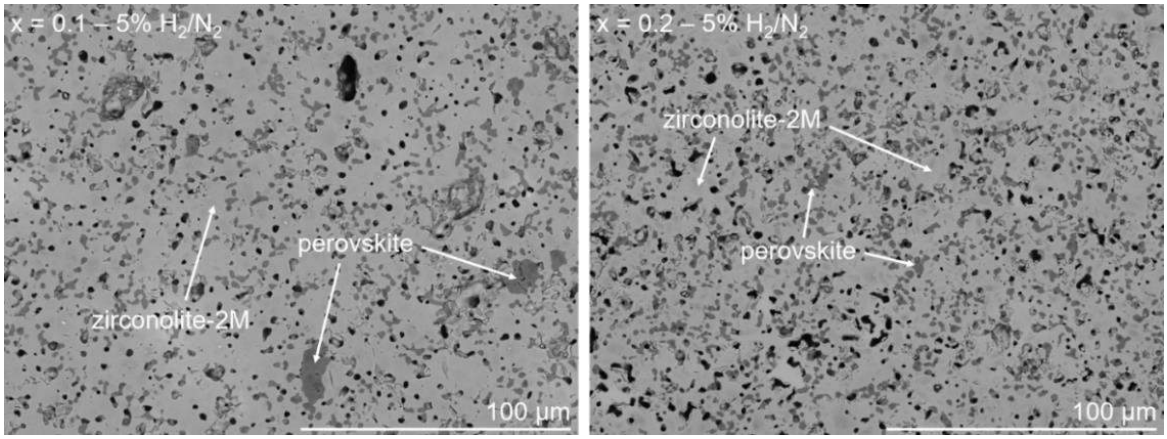

Fig. 10) Representative backscattered electron micrographs for x = 0.1 (left) and x = 0.2 (right) compositions synthesized under 5% H_2/N_2 at 1350 ˚C for 20 h.

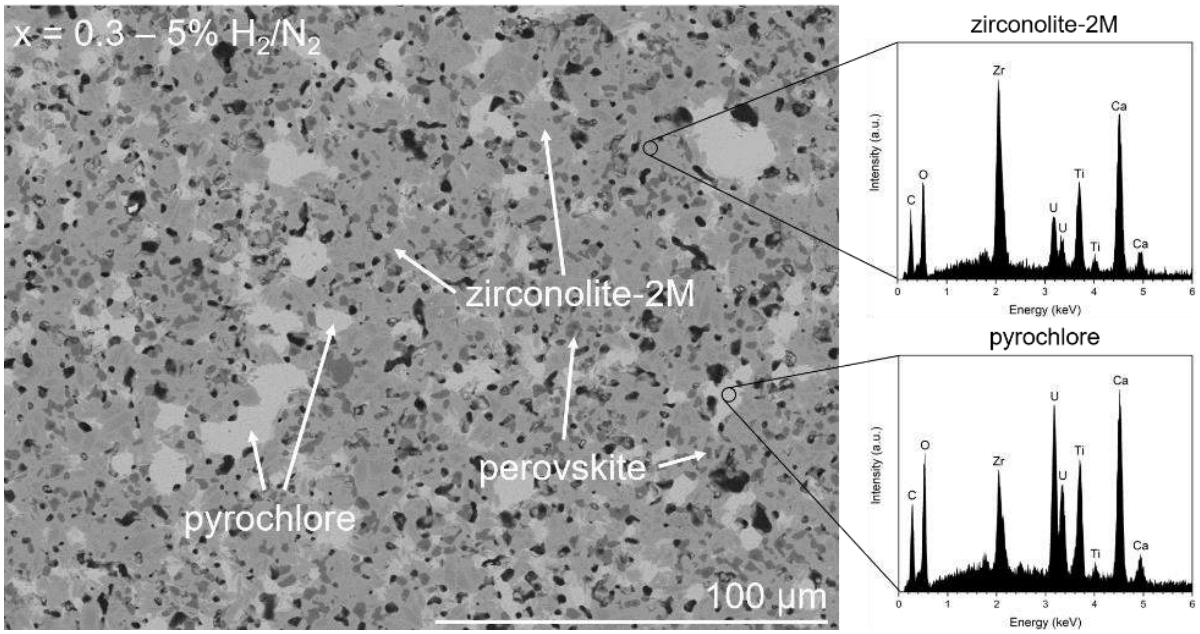

Fig. 11) EDS analysis of zirconolite-2M and pyrochlore phases present in microstructure of x = 0.30 composition sintered in 5% H_2/N_2 at 1350 ˚C for 20 h.

3.3 Oxidation State of U

3.3.1 U L_3-edge X-ray Absorption Near Edge Structure

The average oxidation state of U in the $CaZr_{1-x}U_xTi_2O_7$ zirconolite specimens synthesized in air, argon and 5% H_2/N_2 was determined by X-ray absorption near edge structure (XANES) spectroscopy (**Fig. 12**), with incident synchrotron energy scanned over the U L_3-edge, alongside reference compounds UO_2, $LaUO_4$ and $CaUO_4$, representing U^{4+}, U^{5+} and U^{6+}, respectively. The absorption features for all reference compounds remain largely similar, with a single intense white line feature and post-edge

Corresponding Author: Lewis Blackburn – lewis.blackburn@sheffield.ac.uk

oscillations of lower relative intensity (*note*: white-line refers to the strong absorption features associated with the crest of the absorption edge). The features of the U L_3 absorption edge originate from the promotion of a core $2p_{3/2}$ electron to a partially occupied valence 6d valence shell. For U^{4+}, U^{5+} and U^{6+} compounds these transitions are, theoretically, $(2p^63d^{10})5f^26d^0 \rightarrow (2p^53d^9)5f^26d^1$, $(2p^63d^{10})5f^16d^0 \rightarrow (2p^63d^9)5f^16d^1$ and $(2p^63d^{10})5f^06d^0 \rightarrow (2p^63d^9)5f^06d^1$, respectively. For further discussion of electronic contributions to U L_3 absorption features, the reader is referred to Bès *et al* [31]. It was evident from visual inspection of the normalized and aligned XANES data that the average oxidation state of U in the synthesized zirconolite samples was controlled by the prevailing oxygen partial pressure during the sintering process. The spectra for samples reacted in air displayed features indicative of > U^{5+} valence, or possibly mixed $U^{4+/6+}$, whereas material synthesized in argon and 5% H_2/N_2 exhibited absorption features generally consistent with U^{4+}. The average oxidation state of U was determined by linear regression with respect to the E_0 position of reference compounds, with E_0 calibrated to the energy position of the maxima for the first derivative of the absorption edge, these data are displayed in **Fig. 13** and summarised in **Table 5**. It was demonstrated that the average oxidation state of U in the synthesised specimens was correlated to the processing environment. The average oxidation state of U within the bulk 5% H_2/N_2 samples calculated to be between 3.9 – 4.1 ± 0.2 whilst the average oxidation state of U in the argon sintered specimens was slightly higher, measured to be between 4.0 – 4.6 ± 0.2, and synthesis in air resulted in an average oxidation state between 5.4 – 5.7 ± 0.2. However, the presence of accessory phases containing U (cubic ZrO_2 in the case of air sintered samples; perovskite and pyrochlore in the 5% H_2/N_2 sintered samples) did not allow the oxidation state of U solely within the zirconolite phase to be determined.

Table 5) Mean oxidation state of U in $CaZr_{1-x}U_xTi_2O_7$ ceramics ($0.10 \leq x \leq 0.40$) determined from linear regression of E_0 position with respect to UO_2, $LaUO_4$ and $CaUO_4$ reference compounds

Composition	Mean U Oxidation State		
	Air	Argon	5% H_2N_2
$CaZr_{0.90}U_{0.10}Ti_2O_7$	5.7 ± 0.2	4.6 ± 0.2	4.2 ± 0.2
$CaZr_{0.80}U_{0.20}Ti_2O_7$	5.5 ± 0.2	4.3 ± 0.2	4.1 ± 0.2
$CaZr_{0.70}U_{0.30}Ti_2O_7$	5.4 ± 0.2	4.1 ± 0.2	4.0 ± 0.2
$CaZr_{0.60}U_{0.40}Ti_2O_7$	5.4 ± 0.2	4.0 ± 0.2	3.9 ± 0.2

Corresponding Author: Lewis Blackburn – lewis.blackburn@sheffield.ac.uk

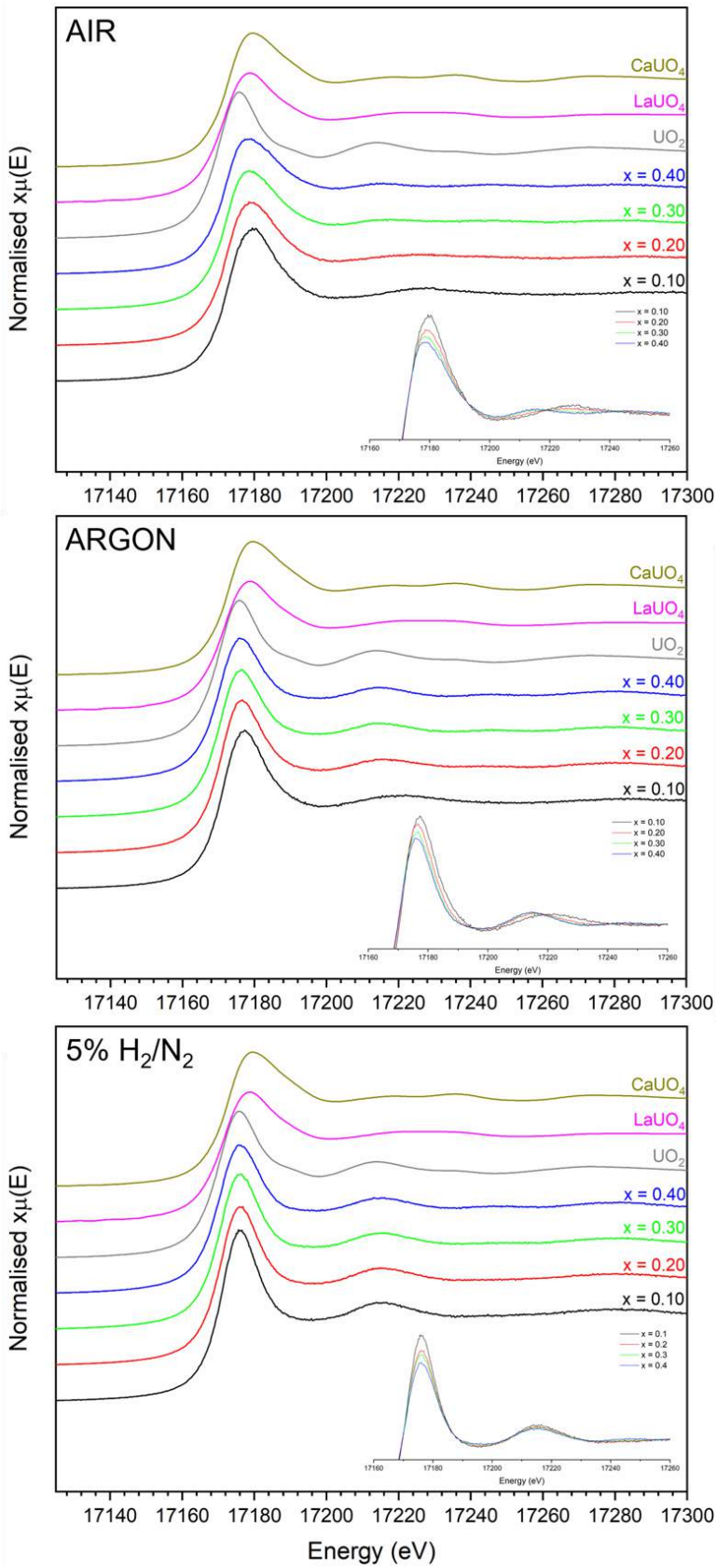

Fig. 12) U L_3 XANES spectra of $CaZr_{1-x}U_xTi_2O_7$ ($0 \leq x \leq 0.40$) compounds sintered at 1350 ˚C for 20 h in air, argon and 5% H_2/N_2, collected alongside UO_2, $LaUO_4$ and $CaUO_4$ reference compounds

Corresponding Author: Lewis Blackburn – lewis.blackburn@sheffield.ac.uk

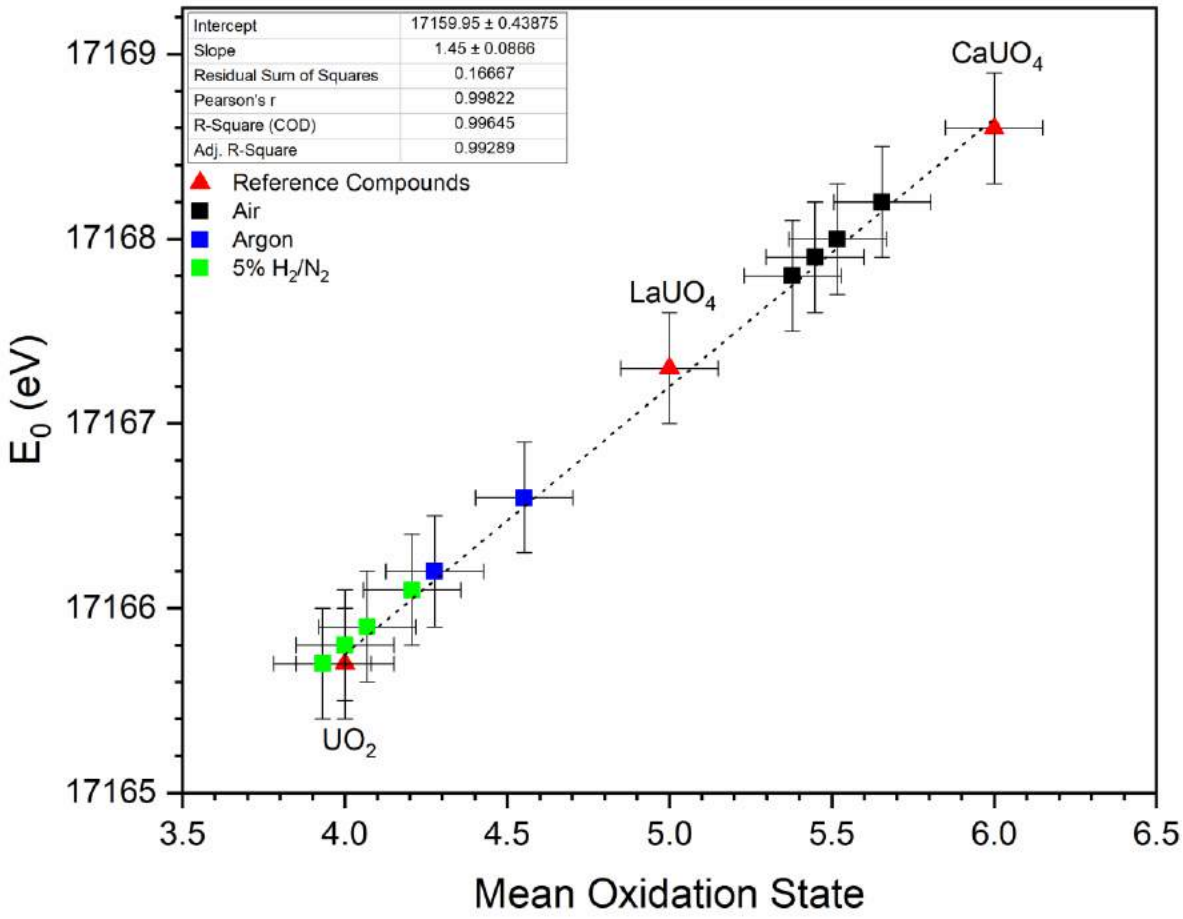

Fig. 13) Oxidation state of $CaZr_{1-x}U_xTi_2O_7$ ($0 \leq x \leq 0.40$) calculated by linear regression of E_0 position relative to reference compounds

3.3.2 U M_4-edge HERFD-XANES

With the view to determine the oxidation state of U in the single phase zirconolite-2M sample formed in air (nominal composition $CaZr_{0.90}U_{0.10}Ti_2O_7$) the electronic structure was probed by U M_4-edge HERFD-XANES [32], which probes directly the f-orbitals through $3d_{3/2} \rightarrow 5f_{5/2}$ electronic transitions. The appearance of the main HERFD transitions at different incident energy in X-ray spectroscopy process is generally attributed to the change of the oxidation state, which produce the chemical shift of the detected 3d-5f transitions. The U M_4 spectrum of $CaZr_{0.90}U_{0.10}Ti_2O_7$ (air sintered) was collected alongside UTi_2O_6 and $BaUO_4$ reference compounds, containing U^{4+} and U^{6+}, respectively. The recorded HERFD-XANES spectrum (Fig. 14) show the characteristic profile of the pentavalent uranium ion, confirming the existence of U^{5+} in zirconolite-2M.

Corresponding Author: Lewis Blackburn – lewis.blackburn@sheffield.ac.uk

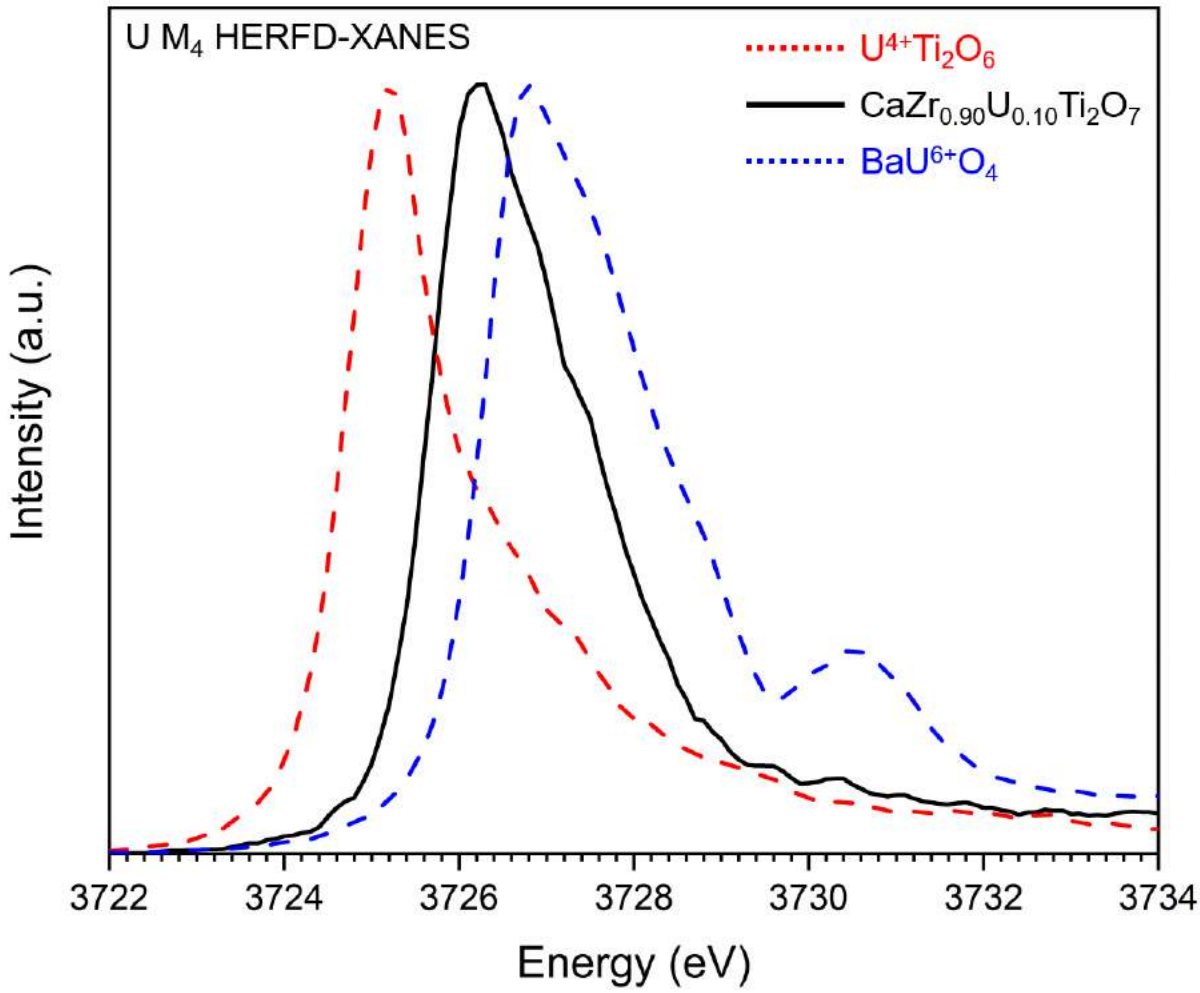

Fig. 14) U M_4 HERFD-XANES data for $CaZr_{0.90}U_{0.10}Ti_2O_7$ (air sintered) alongside $U^{4+}Ti_2O_6$ and $BaU^{6+}O_4$ reference compounds

4 Discussion

The accommodation of U within the target zirconolite phase was ultimately controlled by the prevailing sintering environment, consistent with previous observations by Blackburn *et al*. in the closely related $CaZr_{1-x}Ce_xTi_2O_7$ system [16]. Under reducing conditions Ce was also partitioned within a secondary perovskite phase, whereas the use of oxidizing conditions was sufficient to maintain ~ 80% Ce^{4+}, allowing incorporation within the zirconolite-2M phase, and a subsequent transformation to zirconolite-4M for $x \geq 0.20$. It was demonstrated here that the phase evolution of $CaZr_{1-x}U_xTi_2O_7$ was largely sensitive to atmospheric conditions during processing, with respect to phase formation and subsequent U partitioning. Synthesis in air produced a mixture of zirconolite-2M and 4M polytypes in the compositional interval $0.3 \leq x \leq 0.4$ alongside a U-substituted cubic ZrO_2 structure, with assumed stoichiometry related to $(Ca,Zr,Ti,U)O_{2-x}$ and space group Fm-3m, in the compositional range $0.2 \leq x \leq 0.4$. U L_3-edge XANES data confirmed that U valence was consistently > U^{5+}, demonstrating an apparent excessive of positive charge across the zirconolite structure(s), facilitated by either cation

Corresponding Author: Lewis Blackburn – lewis.blackburn@sheffield.ac.uk

vacancies or oxygen excess. Studies on closely related analogue systems in which excess positive charge across the zirconolite structure, formulated by Pu^{4+} was accommodated on the Ca^{2+} site with no charge compensation, was likely balanced by Hf/Ti vacancies (*i.e.* $Ca_{0.9}Pu_{0.1}HfTi_2O_7$) [33]. A similar charge compensation mechanism would therefore be expected, for example in the x = 0.10 sample, in which U^{5+} was incorporated within single phase zirconolite-2M under oxidising conditions. Accommodation of U in the target zirconolite phase was favored under inert conditions, in which the oxidation state was consistently > U^{4+}. These findings are consistent with data reported in analogue systems *e.g.* $CaZr_{1-x}Ce_xTi_2O_7$, $CaZr_{1-x}Pu_xTi_2O_7$, in which a structural transformation to the zirconolite-4M polytype was observed in the compositional range $0.10 \leq x \leq 0.20$, capable of accommodating elevated Ce/U/Pu with respect to the 2M phase [14], [34]. Solid solutions targeting $CaZr_{1-x}U_xTi_2O_7$ were also reported by Vance *et al*. when synthesizing under near-identical processing conditions to those utilised in the current study. U^{4+} accommodation in the zirconolite phase favored under inert conditions, with U distributed predominantly as U^{4+}, confirmed by diffuse reflectance spectroscopy [26]. Synthesis under reducing conditions produced an undesirable phase assemblage, in which U^{4+} was co-partitioned within an accessory $CaTiO_3$ perovskite phase. The formation of $CaTiO_3$ under reducing conditions is to be expected, as zirconolite is known to be unstable with respect to perovskite under reducing conditions [35]. Furthermore, the $CaTiO_3$ phase has demonstrated reduced aqueous durability under extraction conditions, with respect to the highly refractory $CaZrTi_2O_7$ phase [6], [36]. The co-retention of U within this phase was therefore considered undesirable, and would impair wasteform performance, ultimately leading to premature release of U to the near field environment under geological disposal conditions. Clearly, the immobilisation of U, as a surrogate for Pu, was most readily achieved under inert atmosphere.

5 Conclusions

The phase assemblage of $CaZr_{1-x}U_xTi_2O_7$ was found to be modified by oxygen fugacity during the sintering process, by which a solid solution of heterogeneous U-bearing phases were obtained when sintering in both air and 5% H_2/N_2. Processing under Ar gas produced a polytype transformation from zirconolite-2M to zirconolite-4M in the compositional range $0.10 \leq x \leq 0.20$, in agreement with data previously reported for the analogous Ce system [16], and indeed the corresponding Pu solid solution synthesised by Begg *et al* [14]. The relative partitioning of U between phases was therefore considered to be an artefact of prevailing U valence during sintering, which was supported by U L_3 XANES. The substitution of U in the zirconolite phase appeared most favorable in argon with U distributed as U^{4+}, promoting isovalent substitution within the target Zr^{4+} site, whilst presumably maintaining Ti as Ti^{4+}. Modification of the U valence state to > U^{5+}, by sintering in air, resulted in the formation of parasitic cubic ZrO_2 phase for $x \geq 0.20$, with extensive U solubility with respect to the target zirconolite phase. Arguably, the phase evolution was most significantly disrupted when processing under reducing conditions (5% H_2/N_2), promoting the formation of a deleterious U-substituted perovskite phase at all levels of U concentration, alongside a pyrochlore structured phase of the $CaUTi_2O_7$ (betafite) type for $x \geq 0.30$. This would be expected to significantly decrease resistance to chemical alteration of the

Corresponding Author: Lewis Blackburn – lewis.blackburn@sheffield.ac.uk

wasteform, as the presence of perovskite has been demonstrated to significantly reduce the overall aqueous durability of zirconolite wasteforms, by means of preferential accommodation and subsequent premature release of actinides. The inclusion of the pyrochlore phase would not be expected to significantly modify wasteform durability, as the betafite phase has demonstrated highly refractory behavior in both synthetic and mineral samples [37], [38], although it was recently demonstrated that zirconolite had a comparatively higher resistance to proliferation under accelerated leaching conditions [39]. These data confirmed that under inert and reducing conditions, U acted as a reasonable surrogate for Pu, with the exhibited phase assemblage analogous with comparable solid solution data reported in the wider literature. The presence of higher oxidation states in air sintered samples is considered a limiting factor with respect to the use of U as a surrogate, as higher Pu valences states have not been reported in zirconolite under comparable processing conditions.

6 Declaration of Competing Interest

The authors declare that they have no known competing financial interests or personal relationships that could have appeared to influence the work reported in this paper

7 Authorship Contribution Statement

Lewis R. Blackburn: Conceptualisation; design of experimental methodology; sample fabrication; data acquisition; formal analysis; original draft preparation.

Shi-Kuan Sun: Formal analysis; reviewing and editing.

Laura J. Gardner: Formal analysis; reviewing and editing.

Amber R. Mason: Formal analysis; reviewing and editing.

Ewan R. Maddrell: Supervision; reviewing and editing.

Peter Apps: Data acquisition, reviewing and editing.

Kristina Kvashnina: Data acquisition, reviewing and editing.

Martin C. Stennett: Supervision; reviewing and editing.

Claire L. Corkhill: Supervision; reviewing and editing.

Neil C. Hyatt: Supervision; reviewing and editing.

Corresponding Author: Lewis Blackburn – lewis.blackburn@sheffield.ac.uk

8 Acknowledgements

LRB, NCH, SKS and LJG are grateful for financial support from the Nuclear Decommissioning Authority and EPSRC under grant numbers EP/M026566/1, EP/S01019X/1, EP/N017870/1 and EP/R511754/1. This research utilised the HADES/MIDAS facility at the University of Sheffield established with financial support from EPSRC and BEIS, under grant EP/T011424/1 [40]. We acknowledge Diamond Light Source for allocation of beam-time at Beamline B18 (Proposal No. SP17243). A portion of this work was performed using the EPSRC funded (EP/I034106/1) JEOL JEM-2100 (S)TEM at NNL's Central Laboratory at Sellafield and funded via the BEIS Advance Fuel Cycle Programme and the EPSRC ROYCE grant (EP/R00661X/1).

9 References

[1] Nuclear Decommissioning Authority (NDA), "2019 UK Radioactive Waste Inventory," 2019.

[2] Nuclear Decommissioning Authority (NDA), "Progress on Plutonium Consolidation, Storage and Disposition," 2019.

[3] Nuclear Decommissioning Authority (NDA), "NDA Plutonium Topic Strategy: Credible Options Technical Summary," 2009.

[4] A. R. Mason, S. M. Thornber, M. C. Stennett, L. J. Gardner, D. Lützenkirchen-Hecht, and N. C. Hyatt, "Preliminary investigation of chlorine speciation in zirconolite glass-ceramics for plutonium residues by analysis of Cl K-edge XANES," in *MRS Advances*, 2020, vol. 5, no. 1–2, pp. 37–43.

[5] M. T. Harrison, "Vitrification of High Level Waste in the UK," *Procedia Mater. Sci.*, vol. 7, pp. 10–15, 2014.

[6] K. L. Smith, G. R. Lumpkin, M. G. Blackford, R. A. Day, and K. P. Hart, "The durability of Synroc," *J. Nucl. Mater.*, vol. 190, pp. 287–294, 1992.

[7] A. E. Ringwood, "Disposal of high-level nuclear wastes: A geological perspective," *Miner. Mag.*, vol. 49, no. 2, pp. 159–176, 1985.

[8] E. C. Buck, B. Ebbinghaus, A. J. Bakel, and J. K. Bates, "Characterization of a Pu-Bearing Zirconolite-Rich Synroc," in *MRS Fall Meeting*, 1996.

[9] A. Jostsons and E. R. Vance, "Synroc for Plutonium Disposal," in *Fourth Conference on Nuclear Science and Engineering in Australia*, 2001, pp. 61–66.

Corresponding Author: Lewis Blackburn – lewis.blackburn@sheffield.ac.uk

[10] M. C. Stennett, N. C. Hyatt, M. Gilbert, F. R. Livens, and E. R. Maddrell, “Towards a Single Host Phase Ceramic Formulation for UK Plutonium Disposition,” in *Mater. Res. Soc. Symp. Proc.*, 2008, vol. 1107, pp. 1–6.

[11] N. V. Zubkova *et al.*, “The crystal structure of nonmetamict Nb-rich zirconolite-3T from the Eifel paleovolcanic region, Germany,” *Zeitschrift fur Krist. - Cryst. Mater.*, vol. 233, no. 7, pp. 463–468, 2018.

[12] B. M. Gatehouse, I. E. Grey, R. J. Hill, and H. J. Rossell, “Zirconolite, $CaZr_xTi_{3-x}O_7$; Structure Refinements for Near-End-Member Compositions with x = 0.85 and 1.30,” *Acta Cryst.*, vol. B37, no. 1974, pp. 306–312, 1981.

[13] T. J. White, “Microstructure and Microchemistry of Synthetic Zirconolite, Zirkelite and Related Phases.,” *Am. Mineral.*, vol. 69, pp. 1156–1172, 1984.

[14] B. D. Begg, R. A. Day, and A. Brownscombe, “Structural Effect of Pu Substitutions on the Zr-site in Zirconolite,” in *Mat. Res. Soc. Symp. Proc.*, 2001, vol. 663, pp. 1–8.

[15] A. A. Coelho, R. W. Cheary, and K. L. Smith, “Analysis and Structural Determination of Nd-Substituted Zirconolite-4M,” *J. Solid State Chem.*, vol. 129, pp. 346–359, 1997.

[16] L. R. Blackburn, S. Sun, L. J. Gardner, E. R. Maddrell, M. C. Stennett, and N. C. Hyatt, “A systematic investigation of the phase assemblage and microstructure of the zirconolite $CaZr_{1-x}Ce_xTi_2O_7$ system,” *J. Nucl. Mater.*, vol. 535, p. 152137, 2020.

[17] L. R. Blackburn *et al.*, “Synthesis, Structure and Characterisation of the Thorium Zirconolite $CaZr_{1-x}Th_xTi_2O_7$ System,” *J. Am. Ceram. Soc.*, vol. 00, pp. 1–15, 2021.

[18] B. H. Toby, “EXPGUI, a graphical user interface for GSAS,” *J. Appl. Crystallogr.*, vol. 34, pp. 210–213, 2001.

[19] J. C. Woicik, B. Ravel, D. A. Fischer, and W. J. Newburgh, “Performance of a four-element Si drift detector for X-ray absorption fine-structure spectroscopy: Resolution, maximum count rate, and dead-time correction with incorporation into the ATHENA data analysis software,” *J. Synchrotron Radiat.*, vol. 17, no. 3, pp. 409–413, 2010.

[20] B. Ravel and M. Newville, “ATHENA, ARTEMIS, HEPHAESTUS: Data analysis for X-ray absorption spectroscopy using IFEFFIT,” *J. Synchrotron Radiat.*, vol. 12, pp. 537–541, 2005.

Corresponding Author: Lewis Blackburn – lewis.blackburn@sheffield.ac.uk

[21] A. C. Scheinost *et al.*, “ROBL-II at ESRF: A synchrotron toolbox for actinide research,” *J. Synchrotron Radiat.*, vol. 28, p. 333, 2021.

[22] K. O. Kvashnina and A. C. Scheinost, “A Johann-type X-ray emission spectrometer at the Rossendorf beamline,” *J. Synchrotron Radiat.*, vol. 23, no. 3, pp. 836–841, 2016.

[23] K. R. Whittle *et al.*, “Combined neutron and X-ray diffraction determination of disorder in doped zirconolite-2M,” *Am. Mineral.*, vol. 97, pp. 291–298, 2012.

[24] S. McCaugherty and A. P. Grosvenor, “Low-temperature synthesis of $CaZrTi_2O_7$ zirconolite-type materials using ceramic, coprecipitation, and sol-gel methods,” *J. Mater. Chem. C*, pp. 23–25, 2019.

[25] O. P. Shrivastava, N. Kumar, and I. B. Sharma, “Synthesis, characterization and structural refinement of polycrystalline uranium substituted zirconolite $CaZr_{0.9}U_{0.1}Ti_2O_7$,” *Radiochim. Acta*, vol. 94, no. 6–7, pp. 339–342, 2006.

[26] E. R. Vance *et al.*, “Incorporation of Uranium in Zirconolite ($CaZrTi_2O_7$),” *J. Am. Ceram. Soc.*, vol. 85, no. 7, pp. 1853–1859, 2002.

[27] F. J. Dickson, K. D. Hawkins, and T. J. White, “Calcium uranium titanate-A new pyrochlore,” *J. Solid State Chem.*, vol. 82, no. 1, pp. 146–150, 1989.

[28] M. C. Stennett, N. C. Hyatt, E. R. Maddrell, F. G. F. Gibb, G. Moebus, and W. E. Lee, “Microchemical and Crystallographic Characterisation of Fluorite-Based Ceramic Wasteforms,” in *Mat. Res. Soc. Symp. Proc.*, 2006, vol. 932.

[29] U. Troitzsch, A. G. Christy, and D. J. Ellis, “The crystal structure of disordered $(Zr,Ti)O_2$ solid solution including srilankite: Evolution towards tetragonal ZrO2 with increasing Zr,” *Phys. Chem. Miner.*, vol. 32, no. 7, pp. 504–514, 2005.

[30] E. R. Vance, M. L. Carter, Z. Zhang, K. S. Finnie, S. J. Thomson, and B. . Begg, “Uranium Valences in Perovskite,” in *Environmental Issues and Waste Management Technologies in the Ceramic and Nuclear Industries IX*, 2012.

[31] R. Bès, M. Rivenet, P. L. Solari, K. O. Kvashnina, A. C. Scheinost, and P. M. Martin, “Use of HERFD-XANES at the U L3- and M4-Edges to Determine the Uranium Valence State on $[Ni(H_2O)_4]_3[U(OH,H_2O)(UO_2)_8O_{12}(OH)_3]$,” *Inorg. Chem.*, vol. 55, no. 9, pp. 4260–4270, 2016.

[32] K. O. Kvashnina, S. M. Butorin, P. Martin, and P. Glatzel, “Chemical state of complex uranium

Corresponding Author: Lewis Blackburn – lewis.blackburn@sheffield.ac.uk

oxides," *Phys. Rev. Lett.*, vol. 111, no. 253002, 2013.

[33] B. . Begg, E. . Vance, and S. . Conradson, "The incorporation of plutonium and neptunium in zirconolite and perovskite," *J. Alloys Compd.*, vol. 271–273, pp. 221–226, 1998.

[34] B. M. Clark, S. K. Sundaram, and S. T. Misture, "Polymorphic Transitions in Cerium-Substituted Zirconolite ($CaZrTi_2O_7$)," *Sci. Rep.*, vol. 7, no. 1, pp. 2–10, 2017.

[35] B. D. Begg, E. R. Vance, B. A. Hunter, and J. V. Hanna, "Zirconolite transformation under reducing conditions," *J. Mater. Res.*, vol. 13, no. 11, pp. 3181–3190, 1998.

[36] P. J. Mcglinn, K. P. Hart, E. H. Loi, and E. R. Vance, "pH Dependence of the Aqueous Dissolution Rates of Perovskite and Zirconolite at 90 °C," in *Mat. Res. Soc. Symp. Proc.*, 1995, vol. 353, no. 3, pp. 847–854.

[37] S. A. McMaster, R. Ram, N. Faris, M. I. Pownceby, J. Tardio, and S. K. Bhargava, "Uranium leaching from synthetic betafite: $[(Ca,U)_2(Ti,Nb,Ta)_2O_7]$," *Int. J. Miner. Process.*, vol. 160, pp. 58–67, 2017.

[38] S. A. McMaster, R. Ram, M. I. Pownceby, J. Tardio, and S. Bhargava, "Characterisation and leaching studies on the uranium mineral betafite $[(U,Ca)_2(Nb,Ti,Ta)_2O_7]$," *Miner. Eng.*, vol. 81, pp. 58–70, 2015.

[39] Nikoloski, Gilligan, Squire, and Maddrell, "Chemical Stability of Zirconolite for Proliferation Resistance under Conditions Typically Required for the Leaching of Highly Refractory Uranium Minerals," *Metals (Basel).*, vol. 9, no. 10, p. 1070, 2019.

[40] N. C. Hyatt, C. L. Corkhill, M. C. Stennett, R. J. Hand, L. J. Gardner, and C. L. Thorpe, "The HADES Facility for High Activity Decommissioning Engineering & Science : part of the UK National Nuclear User Facility," in *IOP Conf. Series: Materials Science and Engineering*, 2020, vol. 818, pp. 1–8.

Corresponding Author: Lewis Blackburn – lewis.blackburn@sheffield.ac.uk

Supplementary Information: A Systematic Investigation of the Phase Assemblage and Microstructure of $CaZr_{1-x}U_xTi_2O_7$ Zirconolite

Lewis R. Blackburn[a], Peter Apps[c], Shi-Kuan Sun[b], Kristina Kvashnina[d], Lucy M. Mottram[a], Laura J. Gardner[a], Amber R. Mason[a], Ewan R. Maddrell[e], Martin C. Stennett[a], Claire L. Corkhill[a], Neil C. Hyatt[*a]

[a] *Immobilisation Science Laboratory, University of Sheffield, Department of Materials Science and Engineering, Sir Robert Hadfield Building, Mappin Street, S13JD, UK*

[b] *School of Material Science and Energy Engineering, Foshan University, Foshan 528000, China*

[c] *National Nuclear Laboratory, Sellafield, Seascale, CA20 1PG, UK*

[d] *Rossendorf Beamline (BM20), The European Synchrotron (ESRF), 38000 Grenoble, France*

[e] *National Nuclear Laboratory, Workington, Cumbria, CA20 1PJ, UK*

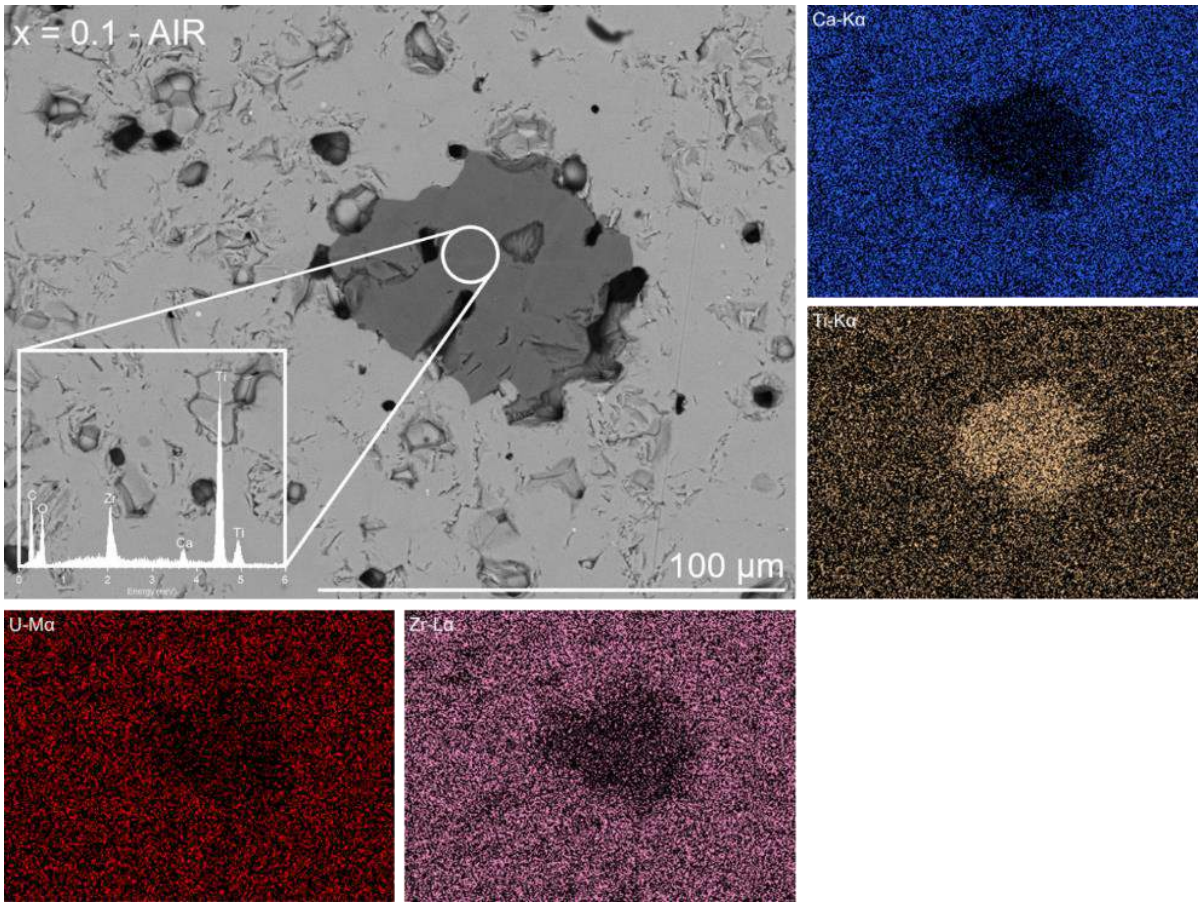

Fig. S1) EDS spot analysis and corresponding elemental distribution of secondary $ZrTiO_4$ phase present in the x = 0.10 sample, reacted in air at 1350 ˚C for 20 h.

Corresponding Author: Lewis Blackburn – lewis.blackburn@sheffield.ac.uk

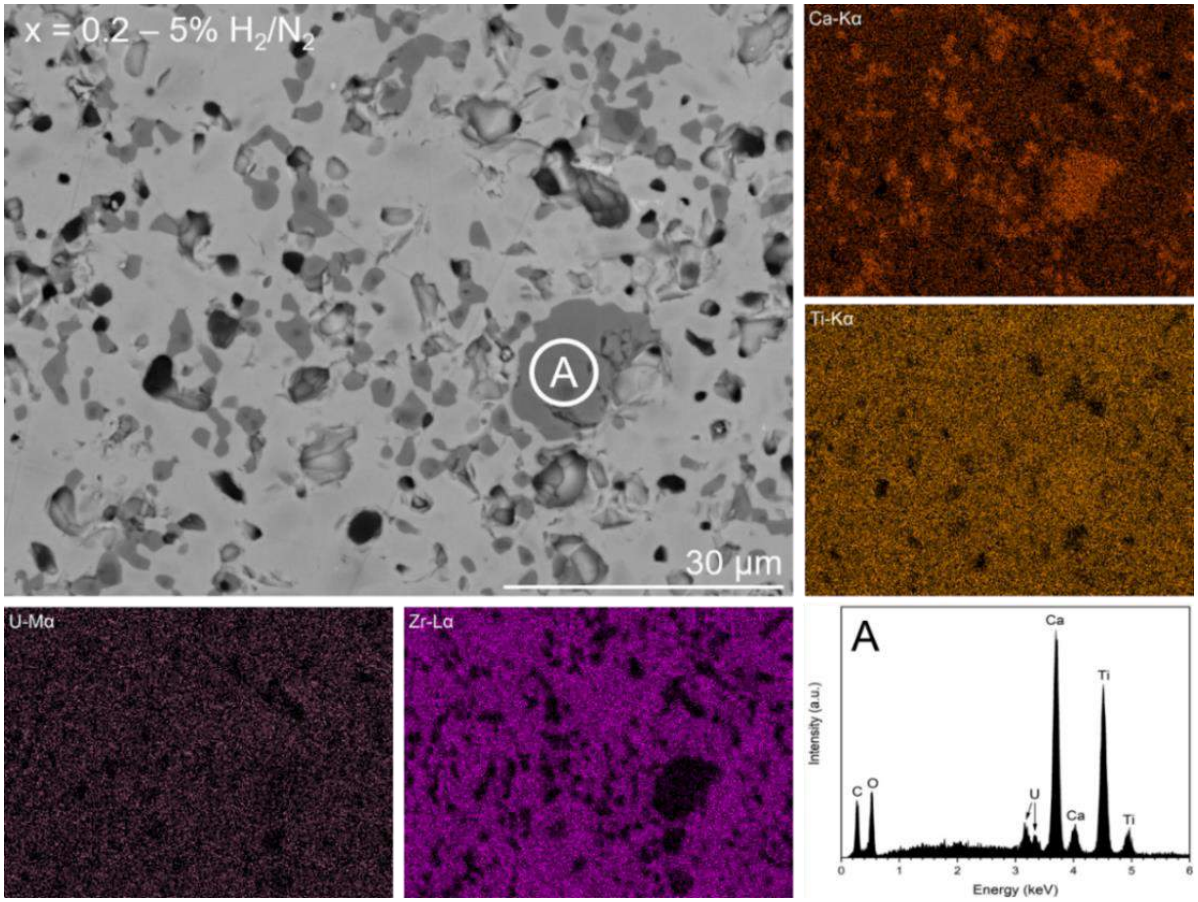

Fig. S2) EDS spot analysis of perovskite phase present in microstructure of x = 0.20 composition sintered in 5% H_2/N_2 at 1350 ˚C for 20 h. The perovskite grain was determined by EDS analysis to have the composition $Ca_{0.93}U_{0.04}Ti_{1.03}O_3$, assuming full oxygen stoichiometry

Corresponding Author: Lewis Blackburn – lewis.blackburn@sheffield.ac.uk

Received: 14 October 2020 | Revised: 3 December 2020 | Accepted: 3 December 2020

DOI: 10.1111/jace.17627

Journal of the American Ceramic Society

ORIGINAL ARTICLE

Synthesis, structure, and characterization of the thorium zirconolite $CaZr_{1-x}Th_xTi_2O_7$ system

Lewis R. Blackburn[1] | **Shi-Kuan Sun**[1,2] | **Laura J. Gardner**[1] | **Ewan R. Maddrell**[3] | **Martin C. Stennett**[1] | **Claire L. Corkhill**[1] | **Neil C. Hyatt**[1]

[1]Immobilisation Science Laboratory, Department of Materials Science and Engineering, University of Sheffield, Sheffield, UK

[2]School of Material Science and Energy Engineering, Foshan University, Foshan, Guangdong, PR China

[3]National Nuclear Laboratory, Workington, Cumbria, UK

Correspondence
Neil C. Hyatt and Shi-Kuan Sun, Immobilisation Science Laboratory, Department of Materials Science and Engineering, University of Sheffield, Sheffield S13JD, UK.
Emails: n.c.hyatt@sheffield.ac.uk (N. C. H.) and shikuan.sun@sheffield.ac.uk (S.-K. S.)

Funding information
Engineering and Physical Sciences Research Council, Grant/Award Number: EP/S01019X/1, EP/N017870/1, EP/R511754/1 and EP/T011424/1; Department for Business, Energy and Industrial Strategy, UK Government

Abstract

A series of zirconolite ceramics with composition $CaZr_{1-x}Th_xTi_2O_7$ ($\Delta x = 0.10$) were reactively sintered at 1350°C for 20 h, in air ($0 \leq x \leq 0.60$) and 5% H_2/N_2 ($0 \leq x \leq 0.40$). A sample with composition corresponding to $x = 0.20$ was also produced by hot isostatic pressing (HIP) at 1300°C and 100 MPa for 4 hours. Th^{4+} immobilization was most readily achieved under oxidizing conditions, with Th^{4+} preferentially incorporated within a pyrochlore-structured phase in the range $0.10 \leq x \leq 0.50$, yet formation of the zirconolite-4M polytype was not observed. We report the novel synthesis of single-phase pyrochlore with nominal composition $CaZr_{0.40}Th_{0.60}Ti_2O_7$ when targeting $x = 0.60$. Th^{4+} incorporation under reducing conditions produced a secondary Th-bearing perovskite, comprising 24.2 ± 0.6 wt% of the phase assemblage when targeting $x = 0.40$, alongside 8.8 ± 0.3 wt% undigested ThO_2. Under reducing conditions, powder XRD data were consistent with zirconolite adopting the 3T polytype structure. The sample produced by HIP presented a nonequilibrium phase assemblage, yielding a major phase of zirconolite-2M alongside accessory Th^{4+}-bearing phases $ThTi_2O_6$, ThO_2, and perovskite. These data highlight the efficacy of Th^{4+} as a Pu^{4+} surrogate, with implications for the formation of Zr-stabilized Th-pyrochlore phases as matrices for waste with elevated Th^{4+} content.

KEYWORDS

immobilization, plutonium, pyrochlore, thorium surrogate, zirconolite wasteform

1 | INTRODUCTION

The United Kingdom is in the process of consolidating all civil Pu inventories at the Sellafield site, in an effort to satisfy security and proliferation requirements, presenting a significant decommissioning challenge in terms of materials degradation.[1] The Nuclear Decommissioning Authority (NDA) is liable for the management and disposition of all nuclear wastes under UK safeguards, and has commissioned a credible options analysis to identify technically mature reuse and disposition options, one of which is a strategy of immobilization and disposal.[2] Zirconolite (nominally $CaZrTi_2O_7$) is the proposed candidate ceramic wasteform for the immobilization of Pu oxides.[3-7] The zirconolite-2M parent structure is derived from the anion-deficient fluorite unit cell, and is closely related to the $A_2B_2O_7$ pyrochlore structure (Fd-3m) by a compression along the (111) direction. Furthermore, a range of polytypical zirconolite structures (e.g., 4M, 3O, 3T) have been reported, the formation of which is controlled by cation substitution and processing conditions.[8-10] The zirconolite-2M unit cell is considered the archetype, with observed stability over the compositional range $CaZr_xTi_{3-x}Ti_2O_7$ ($0.8 < x < 1.3$), with a lamellar unit cell crystallizing in the space group C2/*c*.[11] The nomenclature "2M" is a

reference to the two-layer repeating modules that comprise the monoclinic unit cell. In the idealized 2M structure, Ca^{2+} and Zr^{4+} are arranged in CaO_8 and ZrO_7 polyhedra layered between sheets of TiO_6 and TiO_5 polyhedra. Ti^{4+} sites are arranged in modular symmetry alike to the hexagonal tungsten bronze (HTB) motif. Statistically, one of the octahedra in the HTB layer is collapsed to unusual trigonal bipyramidal symmetry (i.e., TiO_5) to satisfy bonding criteria.[12] In the zirconolite-2M structure, adjacent cation layers are layered in a 1:1 along [001], with HTB layers at $z = 0.25$ and $z = 0.75$ positions related by a 180° rotation, offset by a stacking vector of approximately 60° in the [130] direction; successive HTB layers at z = 0.75 and z = 1.25 positions are subsequently offset in the [130] direction.[8]

Successive zirconolite polytypes (the crystal structures of zirconolite-2M, zirconolite-3T, and pyrochlore are displayed in Figure 1) are stabilized through progressive substitution within Ca^{2+}, Zr^{4+}, and Ti^{4+} sites, and characterized according to variation in stacking sequence of adjacent Ca/Zr and HTB planes. The accommodation of dopants within zirconolite has been shown to produce a phase transition to the pyrochlore structure, generally *via* the zirconolite-4M structure with increasing dopant concentration, either by extensive M^{4+} substitution within the Zr^{4+} site (e.g., U, Ce, Pu) [13-15], or isovalent accommodation of M^{3+} within the Ca^{2+} and Zr^{4+} site (e.g., Y, Gd, Nd) [16-18]. The zirconolite-4M polytype is thus considered an intergrowth of zirconolite-2M and pyrochlore modules, with a four-layer repeating sequence and subsequent doubling of the unit cell along c^* due to cation ordering.[8] Further doping of tri- and tetravalent species within the Ca^{2+} and Zr^{4+} sites in zirconolite produces a transformation to the pyrochlore structure (ideally $A_2B_2O_7$ – space group Fd-3m, where A^{3+} and B^{4+} are typically rare-earth and transition-metal elements, respectively). The pyrochlore supergroup of minerals encompasses a wide range of compositions (> 500 reported) and is considered a suitable matrix for the immobilization of actinides. The pyrochlore structure is related to that of the ideal fluorite structure, with one-eighth of the oxygen anions removed, resulting in two distinct cation sites [19]. Extensive doping within the zirconolite structure produced a phase transformation to the pyrochlore structure in the work of Vance et al. for which the $CaZr_{1-x}U_xTi_2O_7$ system stabilized the pyrochlore structure at $x > 0.60$.[13] Begg et al. reported the same solid solution limit for pyrochlore formation in the $CaZr_{1-x}Pu_xTi_2O_7$ system.[15] Zirconolite-3T is the trigonal polytype of zirconolite, however, detailed structural characterization of the 3T phase is rarely reported in the literature. The 3T polytype typically occurs in natural specimens with extensive substitution of REE^{3+}, Fe, Hf, Th, Nb, such as those reported by Zubkova et al.[20] Nevertheless, there are solid solution regimes that have been reported to form the zirconolite-3T polytype, such as the $Ca_{1-x}Pu_xZrTi_{2-2x}Fe_{2x}O_7$ system, for which Gilbert et al. reported the stabilization of the 3T polytype between $0.30 \leq x \leq 0.40$ [21]. Despite this, the zirconolite-3T phase was not produced at the same compositional level in the $Ca_{1-x}Ce_xZrTi_{2-2x}Cr_{2x}O_7$ suggesting that the formation of the 3T polytype structure is sensitive to both the different redox and/or site occupancy behavior between Ce/Pu, and/or ionic radii of Cr/Fe as charge compensators.[22] The synthesis and structural characterization of synthetic zirconolite-3T was reported by Grey et al., with single-crystal X-ray diffraction data produced for $Ca_{0.80}Th_{0.15}Zr_{1.30}Ti_{1.35}Al_{0.40}O_7$ indexed to the space group $P3_121$, with excess Zr accommodated on the Ca and Ti sites.[10] In order to predict the long-term stability and overall performance of zirconolite-rich wasteforms, it is essential to fully understand the structure of the target polytype, and characterize any polytypical transitions that may occur due to cation substitution. It is currently not yet determined whether any manifestations of the zirconolite structure (i.e., 2M, 4M, 3T) exhibit superior properties that may contribute to improved radiation tolerance and aqueous durability.

The aim of the current work was to characterize the structural transitions accompanying the substitution of Th^{4+} (as a surrogate for Pu^{4+}) within the Zr^{4+} site in zirconolite, under oxidizing and reducing conditions, as this system has not

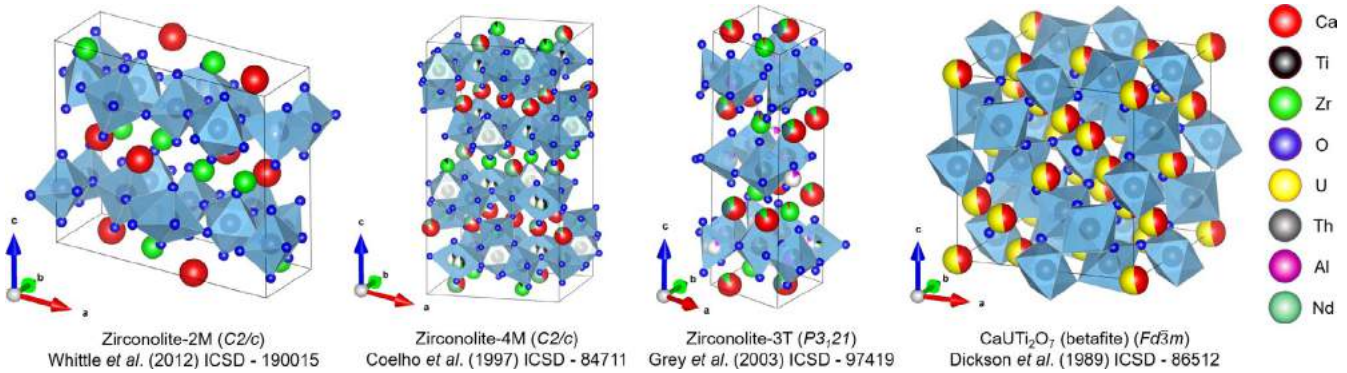

FIGURE 1 Crystal structure of zirconolite 2M, 4M, and 3T polytypes, alongside $CaUTi_2O_7$ pyrochlore

been systematically investigated. We have recently demonstrated that the phase assemblage of $CaZr_{1-x}Ce_xTi_2O_7$ was controlled by the processing atmosphere during the synthesis process, with Ce acting as a structural simulant for Pu.[23] It was revealed that synthesis under oxidizing conditions produced a phase transformation to the zirconolte-4 M polytype with progressive Ce accommodation (in the compositional interval $0.10 \leq x \leq 0.20$), however, this was not observed under reducing conditions, for which Ce^{3+} was preferentially accommodated in an accessory perovskite phase. We acknowledge that a truly representative study of the zirconolite system, producing reliable data that may be transferred to Pu active trails, must utilize several surrogate species in conjunction. Although Ce is commonly deployed as a Pu surrogate, the tendency of Ce to partially reduce to Ce^{3+} under oxidative sintering environments is a behavior not representative of Pu. Hence, as Th remains stable in the Th^{4+} configuration under oxidizing conditions, we consider this to be an effective choice of surrogate. Understanding the effects of compositional modification and subsequent phase transitions that may occur is essential to underpin the safe and effective immobilization of plutonium. Hence, the data presented here allow a direct comparison of ThO_2 and CeO_2 surrogates in the zirconolite system, $CaZr_{1-x}M_xTi_2O_7$ (M = Ce or Th).

2 | EXPERIMENTAL METHODOLOGY

2.1 | Materials synthesis

All compositions targeting $CaZr_{1-x}Th_xTi_2O_7$ ($0 \leq x \leq 0.60$, $\Delta x = 0.10$) were produced by a mixed oxide route between $CaTiO_3$, ZrO_2, TiO_2 (Sigma Aldrich, 99.9% trace metals basis) and ThO_2 (ABSCO Ltd.). Samples were batched according to desired composition and homogenized by planetary milling at 400 rpm for 20 min, with isopropanol added as a carrier fluid and ZrO_2 milling media. Slurries were dried at 80°C overnight. Approximately 0.5 g of each composition was pressed into the walls of a 10 mm stainless steel die and compressed under 3 t of uniaxial pressure. Pellets were then sintered at 1350°C for 20 hours in air (muffle furnace) or flowing 5% H_2/N_2 (BOC, Al_2O_3 tube furnace), representing oxidizing and reducing conditions, respectively. A sample with nominal composition $CaZr_{0.80}$ $Th_{0.20}Ti_{2.00}O_7$ was also produced by Hot Isostatic Pressing (HIP).[44] Milled precursor powder from the x = 0.20 batch was calcined in air at 600°C in air for 12 hours to remove adsorbed water and volatiles prior to HIP. The powder was then pressed into the walls of a stainless steel HIP canister (Grade 310 stainless steel) under uniaxial pressure. The canister was heated at 300°C under vacuum until a suitable pressure was achieved (~ 7 Pa). The canister was then hermetically sealed, placed into an AIP 630-H HIP unit, and processed at 1300°C for 4 hours at 100 MPa. The HIPing of radioactive materials was made possible through the use of the active furnace isolation chamber (AFIC) plug-in component, unique to the University of Sheffield, protected under patent number WO 2018/009782 A1 [24]. The AFIC is capable of processing a single HIP canister loaded with U/Th-containing wasteforms while providing a multi-layered protection approach, preventing dispersion of radioactive material to the HIP pressure vessel and surrounding workspace in the event of a canister breach.

2.2 | Materials characterization

Post synthesis, a representative portion of each sample was finely ground in an agate pestle and mortar with isopropanol prior to powder X-ray diffraction (XRD) analysis. For the HIPed sample, this involved the use of a Buehler IsoMet 1000 Low Speed Saw; the canister was sectioned and a representative portion was removed. XRD was performed using a Bruker D2 Phaser (Cu$K\alpha$, λ = 1.5418 Å, Ni filter), fitted with a Lynxeye position-sensitive detector. Data were acquired in the range $5° \leq 2\theta \leq 80°$ with a step size of 0.02° s^{-1}. XRD data were refined by the Rietveld method using the GSAS package with EXPGUI interface.[25] Prior to analysis by scanning electron microscopy (SEM), samples were sectioned and a representative section of each composition was mounted in cold setting resin, with a curing time of 24 hours. Samples were polished to a 1 μm optical finish using incremental grades of SiC grinding paper and diamond suspension. Surfaces were also coated with carbon and conductive Ag-based paint to reduce surface-charging effects. SEM analysis was performed using a Hitachi TM3030, operating at 15 kV accelerating voltage, at a working distance of 8 mm. This was also fitted with a Bruker Quantax Energy Dispersive X-ray Spectrometer (EDS) for compositional analysis. Semi-quantitative cation compositions of observed zirconolite phases were determined based on 10 independent EDS data points, normalized to seven oxygen atoms.

3 | RESULTS

3.1 | Synthesis under oxidizing conditions

3.1.1 | Phase assemblage

Powder XRD data for $CaZr_{1-x}Th_xTi_2O_7$ compositions reacted in air are displayed in Figure 2. When targeting x = 0.00, phase pure zirconolite-2M (space group C2/*c*) was observed. Rietveld analysis of the powder diffraction profile for x = 0.00 produced unit cell parameters that were in excellent agreement with previously reported unit cell

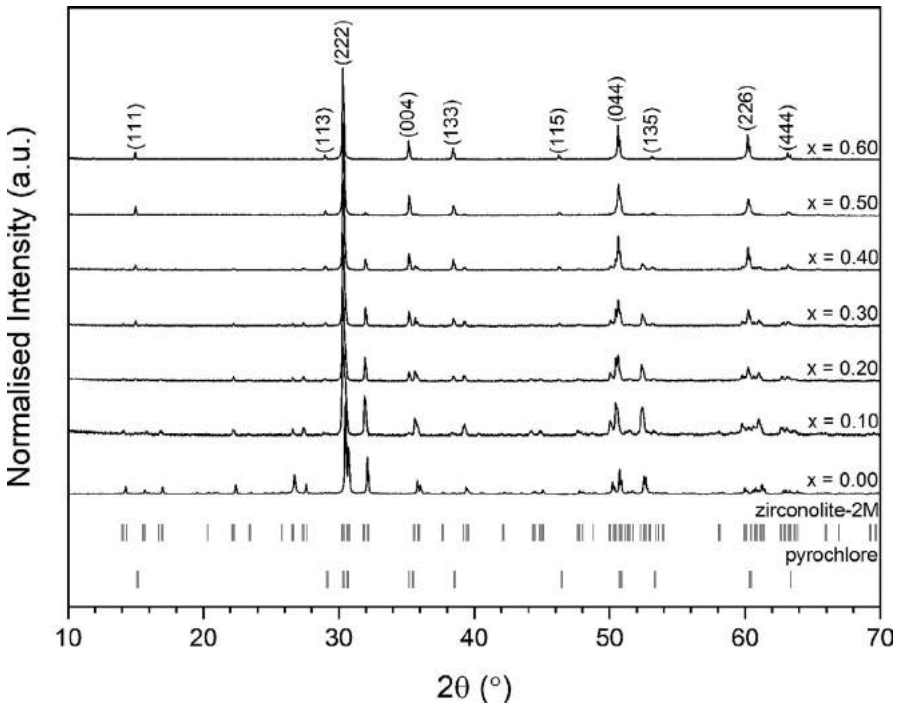

FIGURE 2 Powder XRD analyses of $CaZr_{1-x}Th_xTi_2O_7$ ($0 \leq x \leq 0.60$) reacted in air at 1350°C for 20 h. Pyrochlore reflections are labeled by *(hkl)* indices

TABLE 1 Unit cell dimensions and quantitative phase analysis (QPA) of $CaZr_{1-x}Th_xTi_2O_7$ compositions reacted at 1350°C for 20 h in air

x	Phase	a (Å)	b (Å)	c (Å)	β (°)	V (Å^3)	QPA (wt. %)	R_{wp} (%)	χ^2
0.10	Zirconolite-2M	12.4800 (10)	7.2771 (6)	11.3853 (9)	100.588 (9)	1016.40 (11)	92.1 ± 0.1	8.81	1.274
	Pyrochlore	10.1898 (29)	-	-	-	1058.04 (91)	6.8 ± 0.6		
	Perovskite	-	-	-	-	-	1.1 ± 0.5		
0.20	Zirconolite-2M	12.4798 (9)	7.2747 (5)	11.3811 (8)	100.597 (9)	1015.63 (9)	74.8 ± 0.3	8.33	1.202
	Pyrochlore	10.1813 (6)	-	-	-	1055.95 (12)	23.9 ± 0.5		
	Perovskite	-	-	-	-	-	1.3 ± 0.5		
0.30	Zirconolite-2M	12.4782 (3)	7.2717 (5)	11.3659 (8)	100.613 (6)	1013.68 (11)	62.0 ± 0.5	8.30	1.308
	Pyrochlore	10.1772 (3)	-	-	-	1054.09 (10)	38.0 ± 0.5		
0.40	Zirconolite-2M	12.4833 (16)	7.2712 (9)	11.3716 (11)	100.625 (12)	1014.49 (16)	41.5 ± 0.7	7.87	1.154
	Pyrochlore	10.1820 (3)	-	-	-	1055.59 (8)	58.5 ± 0.3		
0.50	Zirconolite-2M	12.4854 (62)	7.2733 (34)	11.3696 (42)	100.624 (45)	1014.78 (6)	14.4 ± 1.0	8.57	1.546
	Pyrochlore	10.1794 (3)	-	-	-	1054.78 (8)	85.7 ± 0.1		
0.60	Zirconolite-2M	-	-	-	-	-	-	9.72	1.728
	Pyrochlore	10.1843 (2)	-	-	-	1056.32 (20)	100*		

*Indicates phase purity.

dimensions for undoped $CaZrTi_2O_7$ [26]: $a = 12.44808(11)$ Å, $b = 7.27366(6)$ Å, $c = 11.37383(1)$ Å, $\beta = 100.5782(7)$,° and $V = 1012.321(16)$ Å^3. It should be noted that the reported precision of the unit cell parameters presented here represents the uncertainty associated with parameter fitting in the Rietveld refinement analysis. The diffraction data for the undoped x = 0.00 composition are indexed to the zirconolite-2M structure in Supplementary Figure S1. For x = 0.10, a mixture of zirconolite-2M and a pyrochlore-structured phase was confirmed by XRD analysis. The unit cell parameters for zirconolite-2M and pyrochlore phases are summarized in Table 1. The existence of the pyrochlore phase (space group Fd-3m) was rationalized by the appearance of diagnostic supercell reflections at 2θ = 15.2°, 29.2°, 35.4°, 38.7°, and 46.5°, corresponding the (111), (113), (004), (133), and (115) reflections, respectively. As the nominal Th^{4+} concentration was increased to x = 0.10 and x = 0.20, the relative intensity of these reflections increased relative to the diagnostic 2M reflections, suggesting a greater phase fraction. Close inspection of the powder diffraction profile also revealed the

presence of a perovskite ($CaTiO_3$) impurity, identified by a weak reflection at $2\theta = 33.1°$, although only comprising 1.1 ± 0.5 and 1.3 ± 0.5 wt% of the overall phase assemblage for $x = 0.10$ and 0.20 (see Table 1), respectively, however, the lattice dimensions for this impurity were not included in the refinement output. Rietveld analysis of the powder XRD data confirmed that the relative fraction of the pyrochlore phase increased linearly as a function of Th^{4+} incorporation. In the compositional interval $0.10 \leq x \leq 0.50$, the phase assemblage evolved such that pyrochlore became the dominant phase at $x \geq 0.40$. For $x = 0.60$, powder XRD were consistent with phase assemblage being comprised of phase pure pyrochlore with nominal composition $CaZr_{0.4}Th_{0.6}Ti_2O_7$. We are not aware of this phase being reported elsewhere. This will be discussed later in Section 3.1.3. We note that this would correspond approximately to 33.5 wt% Pu for the corresponding $CaZr_{0.4}Pu_{0.6}Ti_2O_7$ composition.

3.1.2 | Microstructure analysis

Figure 3 shows the microstructure for $x = 0.10$ and $x = 0.20$ compositions. Two phases were clearly distinguished by backscattered electron contrast, consistent with zirconolite-2M and pyrochlore in agreement with powder XRD data. Although Th^{4+} was accommodated within both phases in the microstructure, EDS analysis demonstrated that Th^{4+} was preferentially distributed within the bright contrast pyrochlore phase. The zirconolite-2M phase present in the $x = 0.10$ microstructure had an average composition of $Ca_{0.98(6)}Zr_{0.89(8)}Th_{0.05(2)}Ti_{2.07(8)}O_7$, with the excess Th^{4+} presumably concentrated in the pyrochlore grains, which were too small to accurately measure. The average compositions of the zirconolite-2M and pyrochlore phases produced for $0.10 \leq x \leq 0.60$, calculated from EDS analysis, are listed in Table 2. The occupation of each phase in the microstructure was consistent with the quantitative phase analysis (Table 1); as the level of Th^{4+} substitution was elevated in the interval $0.10 \leq x \leq 0.50$, the pyrochlore phase comprised a greater proportion of the visible microstructure. A representative section of the microstructure corresponding to the composition $x = 0.40$ is displayed in Figure 4, alongside the corresponding elemental distribution. EDS data clearly demonstrated that the zirconolite-2M phase was deficient in Th^{4+} and rich in Zr^{4+} with respect to the pyrochlore phase. It was also evident that grains of zirconolite-2M appeared lath-like in morphology. As the Th^{4+} concentration reached $x = 0.60$, the microstructure produced for the pyrochlore phase was homogeneous in BSE contrast, consistent with the formation of single-phase $CaZr_{0.4}Th_{0.6}Ti_2O_7$ as inferred by powder XRD analysis (Figure 2). A representative section of the microstructure is displayed in Figure 5. SEM analysis also evidenced grains of a Th-Ti-O rich phase, occasionally distributed across the surface, consistent with $ThTi_2O_6$ from EDS analysis (however, it should be noted that this phase was not detected by XRD). Despite this trace impurity, it was considered that the pyrochlore formed as a single phase at $x = 0.60$, as no reflections consistent with $ThTi_2O_6$ could be reconciled by XRD analysis.

3.1.3 | Initial refinement of $CaZr_{0.40}Th_{0.60}Ti_2O_7$

All prominent reflections in the XRD pattern of $CaZr_{0.4}Th_{0.6}Ti_2O_7$ could be indexed assuming the structure to be isostructural with that of $CaUTi_2O_7$ (space group: Fd-3m; ICSD 40264, see Figure 1). With the exception of negligible $ThTi_2O_6$ (as indicated in Figure 5) no secondary phases were identified by SEM analysis, and quantitative EDS analyses confirmed the average stoichiometry to be $Ca_{1.00(2)}Zr_{0.33(2)}Th_{0.54(1)}Ti_{2.13(2)}O_7$, demonstrating an apparent excess of Ti. Structure refinement initially assumed the ideal stoichiometry of $CaZr_{0.4}Th_{0.6}Ti_2O_7$ adopting the space group Fd-3m, consistent with the published crystal structure of $CaUTi_2O_7$.[27] Refinements quickly converged yet produced negative isotropic thermal parameters for the Ti site; the fits were, however, improved after setting 0.1 f.u. of Zr occupying the Ti site. In this instance, the refinement quickly converged to a satisfactory fit (displayed in Figure 6) with Rwp =9.72% and $\chi^2 = 1.728$ for 22 variables, including six structural parameters. As shown in Table 3, the isotropic thermal parameter (U_{iso}) of the mixed occupancy 16d site was significantly larger than that of the Ca cation, inferring the presence of Ti vacancies with charge compensation provided by oxygen vacancies, or Ti reduction

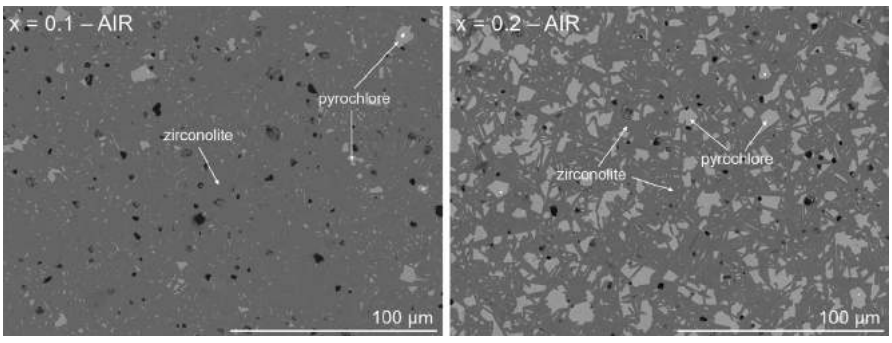

FIGURE 3 Representative BSE micrographs for $x = 0.10$ (left) and $x = 0.20$ (right) microstructures reacted at 1350°C for 20 h in air

TABLE 2 Average composition of zirconolite-2M and pyrochlore phases determined from EDS analyses, assuming complete oxygen stoichiometry, reacted at 1350°C for 20 h in air, normalized to seven oxygen atoms

	Observed Composition	
Nominal Composition	**Zirconolite−2M**	**Pyrochlore**
$CaZr_{0.9}Th_{0.1}Ti_2O_7$	$Ca_{0.99(7)}Zr_{0.82(8)}Th_{0.06(1)}Ti_{2.12(9)}O_7$	*
$CaZr_{0.8}Th_{0.2}Ti_2O_7$	$Ca_{0.99(8)}Zr_{0.84(13)}Th_{0.07(2)}Ti_{2.10(13)}O_7$	$Ca_{0.94(22)}Zr_{0.55(24)}Th_{0.51(6)}Ti_{1.99(10)}O_7$
$CaZr_{0.7}Th_{0.3}Ti_2O_7$	$Ca_{0.91(8)}Zr_{0.84(10)}Th_{0.07(2)}Ti_{2.17(9)}O_7$	$Ca_{0.93(16)}Zr_{0.37(5)}Th_{0.58(7)}Ti_{2.13(10)}O_7$
$CaZr_{0.6}Th_{0.4}Ti_2O_7$	*	$Ca_{1.04(7)}Zr_{0.38(4)}Th_{0.55(7)}Ti_{2.03(11)}O_7$
$CaZr_{0.5}Th_{0.5}Ti_2O_7$	*	$Ca_{1.00(3)}Zr_{0.39(6)}Th_{0.51(5)}Ti_{2.10(6)}O_7$
$CaZr_{0.4}Th_{0.6}Ti_2O_7$	-	$Ca_{1.00(2)}Zr_{0.33(2)}Th_{0.54(1)}Ti_{2.13(2)}O_7$

*Composition determination not possible due to grain size.

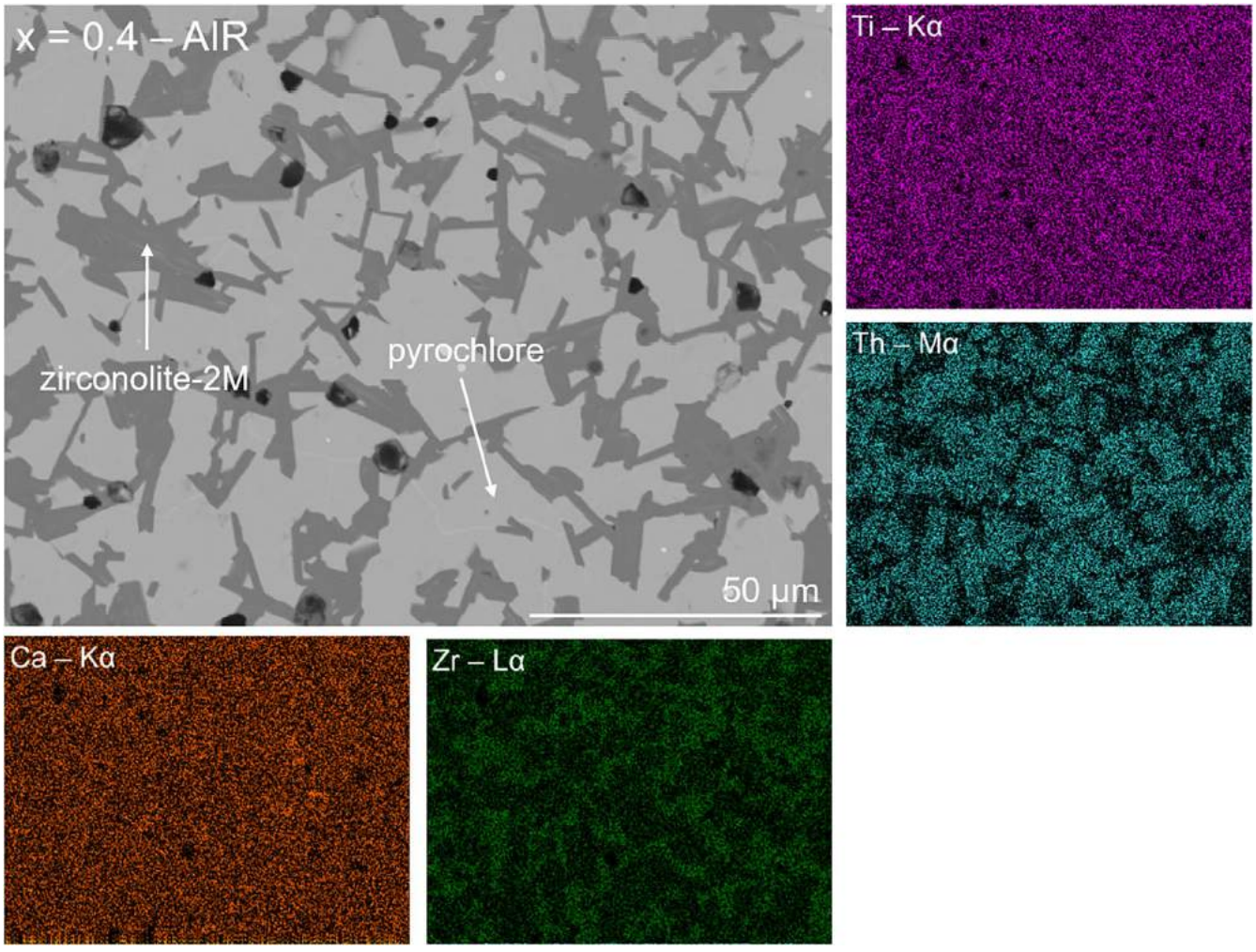

FIGURE 4 BSE and EDS analysis of x = 0.40 microstructure reacted at 1350 °C for 20 h in air

to Ti^{3+}. Complementary structural refinement studies of the specimens studied here are underway.

Pyrochlore compounds with significant U/Ce incorporation, corresponding to compositions $Ca_{1.46}U^{4+}{}_{0.23}U^{6+}{}_{0.46}Ti_{1.85}O_7$ and $Ca_{0.93}Ce_{1.00}Ti_{2.04}O_7$ have been previously reported.[28] In contrast, here we hypothesize Th-pyrochlore may be stabilized by the occupation of Zr within the Ti site. Considering the ionic radii of Ca (1.12 Å, CN = 8), Th (1.05 Å, CN = 8 and 0.94 Å, CN = 6), Zr (0.84 Å, CN = 8 and 0.72 Å, CN = 6), and Ti (0.74 Å, CN = 8 and 0.605 Å, CN = 6), the substitution of Ca by Th may be preferable, alongside the reduction in coordination number from

8 to 6, which likely drove zirconolite (C2/c) to a higher symmetry space group (Fd-3m).[29]

3.2 | Synthesis under reducing conditions

3.2.1 | Phase assemblage

Powder XRD data for $CaZr_{1-x}Th_xTi_2O_7$ compositions reacted under 5% H_2/N_2 are displayed in Figure 7, quantitative phase analysis data for all compositions sintered under 5% H_2/N_2 are summarized in Table 4. When targeting x = 0.00, zirconolite-2M was formed as the major phase, occupying 92.4 ± 0.1 wt% of the total phase assemblage. The diagnostic reflection at $2\theta = 33.1^\circ$ confirmed that perovskite was also formed as a secondary phase, comprising 7.6 ± 0.3 wt% of the assemblage (Table 4). As the nominal Th^{4+} concentration was increased to x = 0.10, the relative yield of perovskite increased to 11.3 ± 0.5 wt%. Minor reflections at $2\theta = 27.5^\circ$, 45.7° and 54.2° corresponding to reflections in the (111), (022), and (113) plane for ThO_2 were also visible, indicating incomplete digestion of Th^{4+} within the target zirconolite phase. The intensity of perovskite and ThO_2 reflections were observed to increase when targeting x = 0.20, accounting for 15.4 ± 0.5 wt% and 0.9 ± 0.1 wt%, respectively. For x ≥ 0.20, the powder diffraction profiles for zirconolite compositions were consistent with the zirconolite-3T polytype, adopting trigonal symmetry in the space group $P3_121$. The lattice parameters for the zirconolite-3T phase (Table 5) corresponding to x = 0.20 were derived from Rietveld fitting: $a = 7.2511(2)$ Å, $c = 16.826(1)$ Å, $V = 766.17(3)$ Å^3. These unit cell dimensions were in general agreement with previously reported values for the zirconolite-3T phase when doped with similar levels of Th^{4+}.[10] However, as can be seen from the data provided in Table 5, there did not appear to be a trend between the zirconolite-3T unit cell parameters and the targeted level of substitution (x). The proportion of the perovskite phase increased linearly, which further increased at x = 0.30 and x = 0.40 to 18.9 ± 0.6 and 24.2 ± 0.6 wt%, respectively. The relative quantity of unincorporated ThO_2 in the microstructure was also further elevated, with an increase from 0.9 ± 0.1 to 8.8 ± 0.3 wt% in the interval 0.20 ≤ x ≤ 0.40.

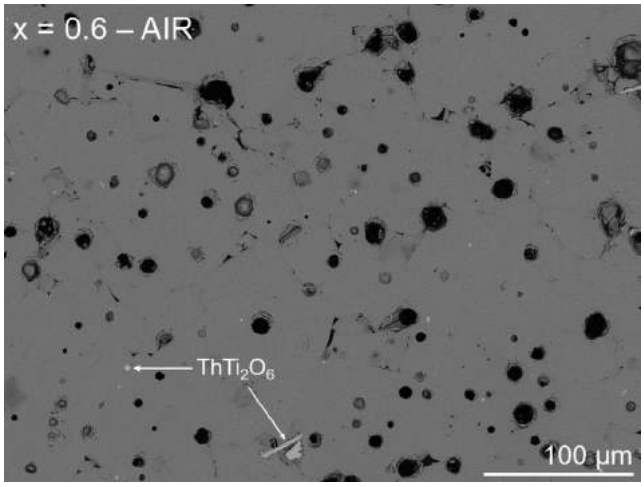

FIGURE 5 Representative BSE micrograph for single-phase Th-rich pyrochlore with nominal composition $CaZr_{0.4}Th_{0.6}Ti_2O_7$ reacted at 1350°C for 20 h in air

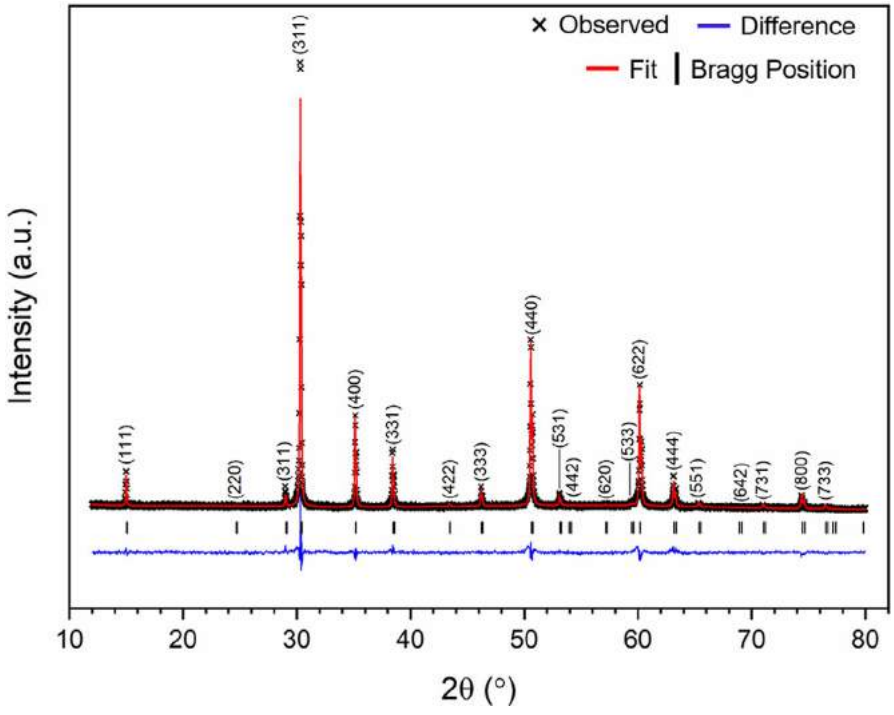

FIGURE 6 Rietveld analysis of powder diffraction profile for $CaZr_{0.4}Th_{0.6}Ti_2O_7$ reacted in air at 1350°C for 20 h. Bragg positions of the pyrochlore structure are labeled by vertical indices. Rwp = 9.72%, $\chi^2 = 1.728$

TABLE 3 Refined structural parameters for $CaZr_{0.40}Th_{0.60}Ti_2O_7$

Space Group: Fd-3m a = 10.1843(2) Å						
Atom	**Site**	**x**	**y**	**z**	**Occupancy**	**U_{iso} ×10² (Å²)**
Ca	16c	0	0	0	0.50	0.10(6)
Th	16c	0	0	0	0.27	0.10(6)
Zr	16c	0	0	0	0.07	0.10(6)
Ti	16c	0	0	0	0.24	0.10(6)
Ti	16d	0.5	0.5	0.5	0.90	1.00(12)
Zr	16d	0.5	0.5	0.5	0.10	1.00(12)
O1	48f	0.4220(7)	0.125	0.125	1.00	3.69(33)
O2	8a	0.125	0.125	0.125	1.00	4.05(99)

Powder Statistics: $\chi^2 = 1.728$, R_{wp} =9.72%, R_p =7.65%.

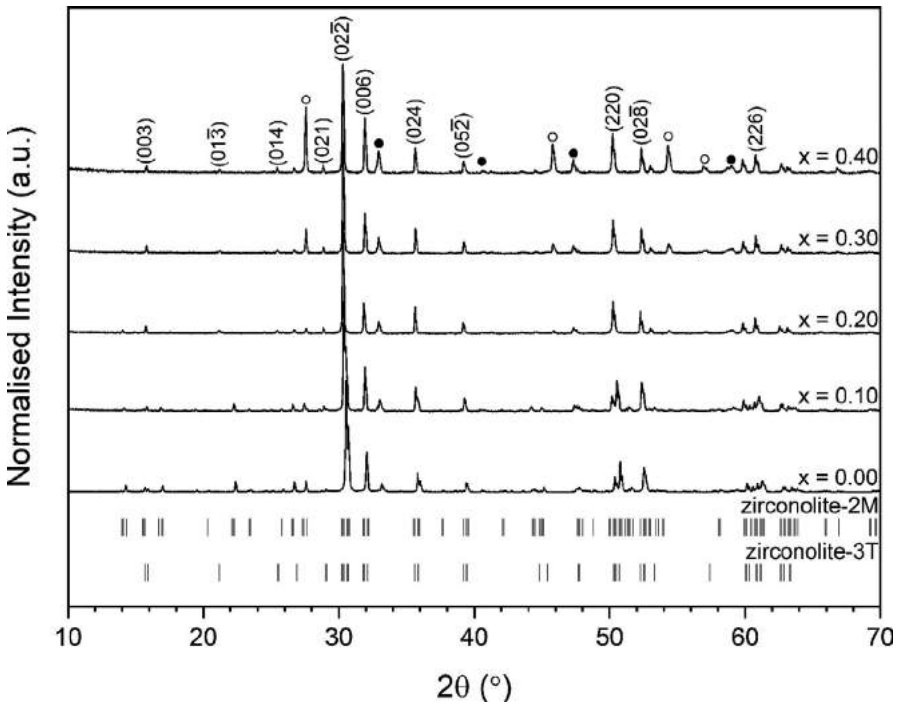

FIGURE 7 Powder XRD analyses of $CaZr_{1-x}Th_xTi_2O_7$ ($0.00 \leq x \leq 0.40$) reacted under flowing 5% H_2/N_2 at 1350°C for 20 h. Zirconolite-3T reflections are indexed by appropriate (*hkl*) indices. ThO_2 reflections are highlighted with open circles. Perovskite reflections are highlighted with closed circles

TABLE 4 Quantitative phase analysis for $CaZr_{1-x}Th_xTi_2O_7$ ($0 \leq x \leq 0.40$) compositions reacted at 1350°C for 20 h in 5% H_2/N_2

	QPA (wt%)			
Nominal composition	**Zirconolite-2M**	**Zirconolite-3T**	**Perovskite**	**ThO_2**
$CaZrTi_2O_7$	92.4 ± 0.1	-	7.6 ± 0.3	-
$CaZr_{0.9}Th_{0.1}Ti_2O_7$	88.6 ± 0.1	-	11.3 ± 0.5	0.2 ± 0.1
$CaZr_{0.8}Th_{0.2}Ti_2O_7$	-	83.6 ± 0.1	15.4 ± 0.5	0.9 ± 0.1
$CaZr_{0.7}Th_{0.3}Ti_2O_7$	-	77.2 ± 0.2	18.9 ± 0.6	3.9 ± 0.1
$CaZr_{0.6}Th_{0.4}Ti_2O_7$	-	67.0 ± 0.3	24.2 ± 0.6	8.8 ± 0.3

When targeting x = 0.40, the zirconolite-3T phase, while still forming the dominant portion of the phase assemblage, accounted for only ~67 wt%. Hence, the imposition of reducing conditions during the sintering of $CaZr_{1-x}Th_xTi_2O_7$ was not favorable compared to sintering in air.

3.2.2 | Microstructure analysis

The microstructure for x = 0.10 and x = 0.20 compositions is displayed in Figure 8, with x = 0.40 presented in Figure 9. In all instances, a homogenous mid-gray matrix was observed

TABLE 5 Unit cell dimensions of zirconolite-2M and zirconolite-3T from *Rietveld* analysis of powder X-ray diffraction profile of $CaZr_{1-x}Th_xTi_2O_7$ ($0 \leq x \leq 0.40$) reacted at 1350°C for 20 h under 5% H_2/N_2

x	Zirconolite Polytype	Unit Cell Parameter					R_{wp} (%)	χ^2
		a (Å)	b (Å)	c (Å)	β (°)	V (Å^3)		
0.1	2M	12.4759 (5)	7.2656 (3)	11.3982 (5)	100.58 (3)	1015.63 (6)	8.03	1.369
0.2	3T	7.2511 (2)	-	16.8262 (6)	-	766.17 (3)	8.26	1.423
0.3	3T	7.2524 (2)	-	16.7950 (7)	-	765.01 (4)	8.06	1.168
0.4	3T	7.2525 (2)	-	16.7847 (11)	-	765.56 (5)	8.02	1.125

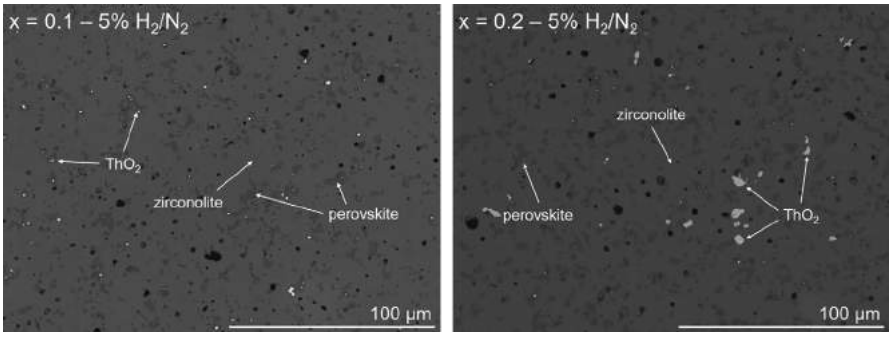

FIGURE 8 Representative BSE micrographs for x = 0.10 (left) and x = 0.20 (right) microstructures reacted at 1350°C for 20 h under flowing 5% H_2/N_2

representative of zirconolite-2M or 3T, with two secondary phases evidenced by variation in backscattered electron contrast. These were consistent with perovskite (dark gray) and ThO_2 (bright gray). Close inspection of EDS data confirmed that Th^{4+} was partitioned between all three phases, contrary to experimental design. The average composition of the zirconolite-2M and zirconolite-3T phases are summarized in Table 6. The zirconolite phase(s) were consistently deficient in Th^{4+}, relative to the target composition, for all values of x, coinciding with unincorporated ThO_2 in the microstructure. In agreement with powder XRD data, the accompanying quantity of perovskite and ThO_2 in the microstructure was elevated for x = 0.30 and x = 0.40 samples.

The elemental distribution for the sample with composition x = 0.40 is displayed in Figure 9. EDS analysis of perovskite grains also evidenced incorporation of Th^{4+} (see Supplementary Figure S2). The formation of perovskite in this system is undesirable, and would be considered detrimental to Pu wasteform performance, due to inferior chemical durability with respect to the target zirconolite phase.[30] The accommodation of Th^{4+} within the Ca^{2+} site in perovskite would also demonstrate an apparent excess of positive charge, typically necessitating the necessitating the formation of (or the co-accommodation of a lower valence charge balancing species, such as in the case of Begg et al. where Ce was used as a Pu surrogate[31]). However, in this instance, the imposition of reducing conditions would be considered sufficient to drive the reduction of Ti^{4+} to Ti^{3+}, providing charge balance by 5%-10% Ti^{3+}. When targeting x = 0.40, the average composition of the accompanying perovskite phase was calculated from EDS data to be $Ca_{0.77(2)}Th_{0.13(1)}Zr_{0.09(2)}Ti_{1.01(3)}O_3$, normalized to three oxygen atoms.

3.3 | Hot isostatic pressing of $CaZr_{0.80}Th_{0.20}Ti_{2.00}O_7$

A specimen with nominal composition $CaZr_{0.80}Th_{0.20}Ti_{2.00}O_7$ (*i.e.*, x = 0.20) was also produced by HIP, with the view to determine whether the obtained phase assemblage would be greatly disrupted by the in-canister containment necessary for HIP, with respect to conventional sintering processes. Processing *via* HIP appeared to negatively impact the phase assemblage with respect to both air and 5% H_2/N_2 sintered samples, largely due to the increased occupation of perovskite within the phase assemblage (increasing from ~1 wt% to ~14 wt% in the case of the air-sintered composition), and through the production of a non-equilibrium microstructure. Figure 10 displays the powder diffraction data obtained for $CaZr_{0.80}Th_{0.20}Ti_{2.00}O_7$. A reasonable fit was achieved, with the diffraction profile refined to a phase assemblage of zirconolite-2M (74.0 ± 0.3 wt%), ZrO_2 (3.1 ± 0.4 wt%), ThO_2 (3.6 ± 0.1 wt%), $ThTi_2O_6$ (5.3 ± 0.3 wt%), and $CaTiO_3$ (14.1 ± 0.6 wt%). The existence of $ThTi_2O_6$ was confirmed by reflections at $2\theta = 14.3°$, $18.4°$, and $25.4°$ corresponding to reflections in the (001), ($20\bar{1}$), and (110) reflections of the $ThTi_2O_6$ structure, respectively.

A representative section of the microstructure for the $CaZr_{0.80}Th_{0.20}Ti_{2.00}O_7$ sample processed by HIP is displayed in Figure 11. A mid-gray matrix of zirconolite-2M was observed, with several secondary phases identified by variation

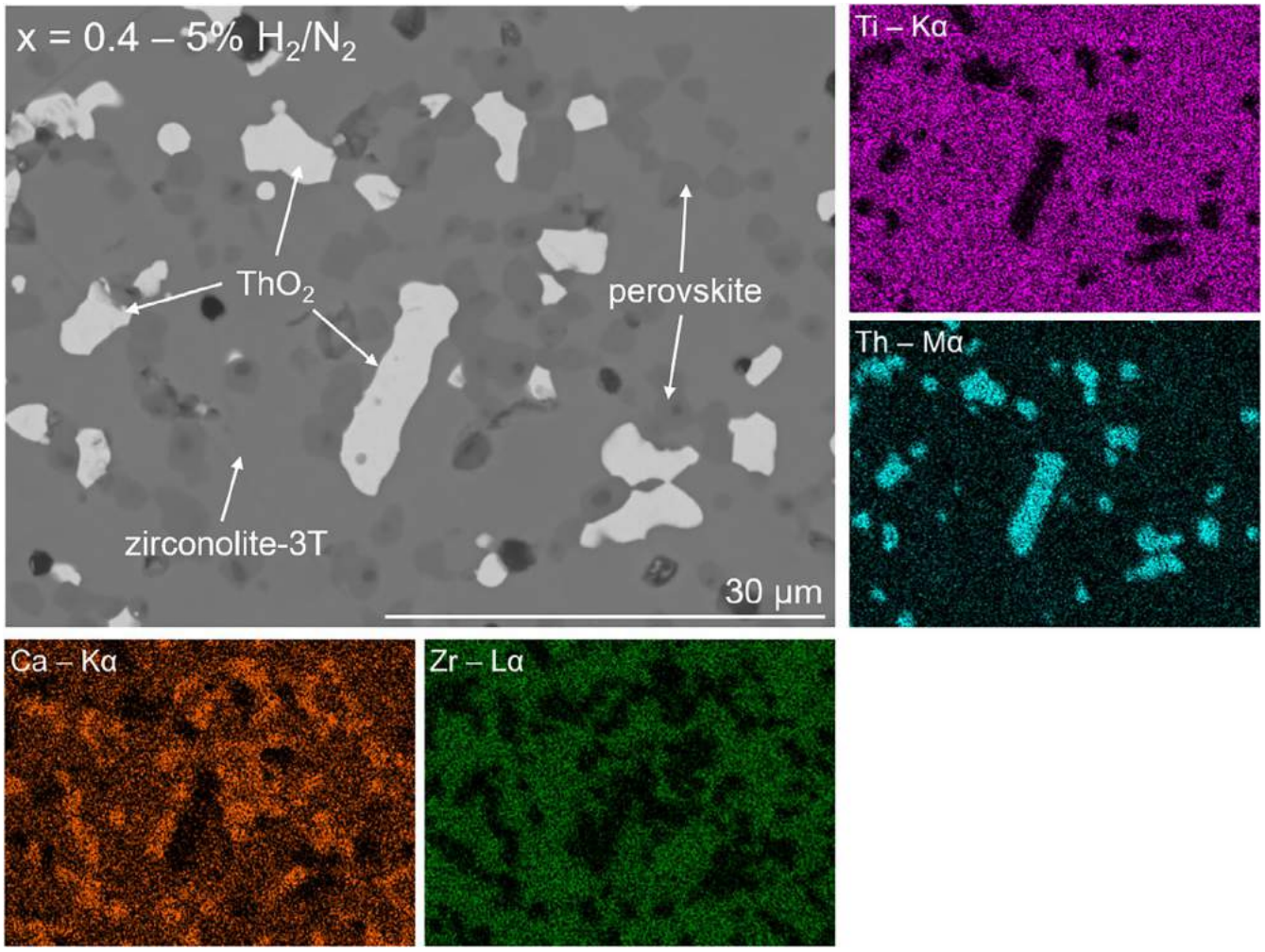

FIGURE 9 BSE-EDS analysis of x = 0.40 microstructure reacted at 1350 °C for 20 h under flowing 5% H_2/N_2

TABLE 6 Observed compositions for zirconolite phase in $CaZr_{1-x}Th_xTi_2O_7$ compositions reacted under flowing 5% H_2/N_2 at 1350°C for 20 h, calculated by EDS analysis, normalized to seven oxygen

	Observed Composition	
Nominal Composition	**Zirconolite-2M**	**Zirconolite-3T**
$CaZr_{0.9}Th_{0.1}Ti_2O_7$	$Ca_{0.88(9)}Zr_{0.94(9)}Th_{0.06(3)}Ti_{2.11(7)}O_7$	-
$CaZr_{0.8}Th_{0.2}Ti_2O_7$	-	$Ca_{0.83(7)}Zr_{0.88(11)}Th_{0.15(2)}Ti_{2.15(11)}O_7$
$CaZr_{0.7}Th_{0.3}Ti_2O_7$	-	$Ca_{0.92(9)}Zr_{0.72(8)}Th_{0.22(4)}Ti_{2.14(7)}O_7$
$CaZr_{0.6}Th_{0.4}Ti_2O_7$	-	$Ca_{0.88(8)}Zr_{0.77(11)}Th_{0.21(4)}Ti_{2.13(7)}O_7$

in backscattered electron contrast. Clusters of perovskite were distributed throughout, with a contrast darker than that of the bulk matrix. Reliable EDS analysis of individual perovskite grains was not possible due to small grain size, yet it is assumed that, similar to the compositions sintered under 5% H_2/N_2, Th^{4+} was also located within this phase, presumably accommodated within the Ca^{2+} site. The incorporation of Th^{4+} within the more abundant perovskite phase (~14 wt%) would be considered highly undesirable, as the lower durability of perovskite with respect to the target zirconolite phase may negatively impact the overall performance of the wasteform, resulting in accelerated release of Th^{4+} (and Pu, by analogy) from the ceramic phase into solution in the disposal environment.[32] Undigested ThO_2 was observed in the microstructure, clearly visible in Figure 11 as relics with bright contrast, with a clear reaction rim surrounding the ThO_2 cores. The composition of these reaction rims was consistent with both XRD and EDS analyses as $ThTi_2O_6$ (*i.e.*, thorutite), evidencing that the reactions did not reach equilibrium under the imposed conditions (1300°C dwell temperature maintained for

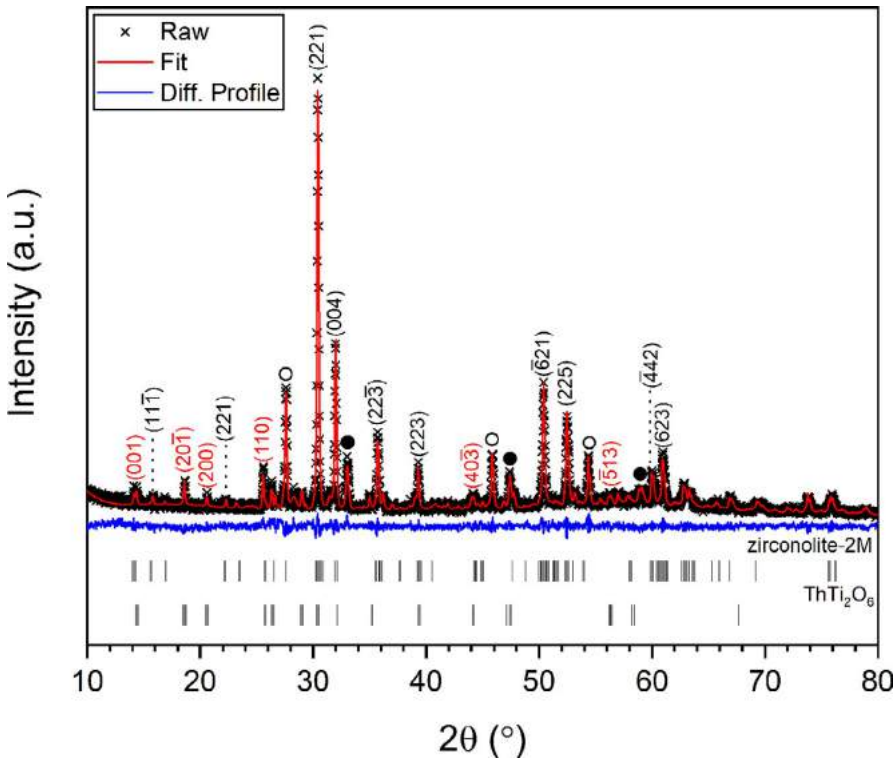

FIGURE 10 Rietveld analysis of powder XRD data for $CaZr_{0.80}Th_{0.20}Ti_{2.00}O_7$ processed by HIP at 1300°C at 100 MPa for 4 h. Zirconolite-2M reflections are highlighted by (*hkl*) values (black). $ThTi_2O_6$ reflections are highlighted by (*hkl*) values (red). ThO_2 reflections are highlighted by open circles. Perovskite reflections are highlighted by filled circles

4 hours). This is clear when comparing Figures 9 and 11, the former of which does not contain these features, despite ThO_2 being prevalent in the microstructure. In this instance, the difficulty in attaining an equilibrated microstructure through the use of HIP was considered to be the result of variations between HIP (1300°C, 4 hours) and CPS (1350°C, 20 hours) processing parameters, the latter of which provided more suitable equilibrium conditions due to extended dwell time at high temperature. Although the partitioning of Th^{4+} within an ancillary phase was generally considered undesirable, $ThTi_2O_6$ is known to be highly durable in aggressive leaching environments, with Zhang et al. reporting normalized release rates of Th $<10^{-5}$ g m^{-2} d^{-1} over a cumulative time of 60 d, in pH =2 solution.[33] It should be noted that while this microstructure is not representative of a wasteform that would be considered suitable for the disposition of Pu, its inclusion in the present work may serve as a useful comparison for future Ce/U/Pu compositions processed in a similar manner.

4 | DISCUSSION

4.1 | Influence of processing environment on phase evolution of $CaZr_{1-x}Th_xTi_2O_7$

There exists a narrow scope of literature concerned with the incorporation of Th^{4+} within the zirconolite structure, making any reasonable comparison with published solid solution data limited. Kesson et al. discussed the incorporation of Th^{4+} within the Zr^{4+} site, with compositions corresponding to $CaZr_{0.90}Th_{0.10}Ti_{2.00}O_7$ and $CaZr_{0.80}Th_{0.20}Ti_{2.00}O_7$ fabricated by hot pressing in a graphite die at 1400°C.[34] When targeting x = 0.10, a single-phase zirconolite was reported, in contrast to the data presented here for the air-sintered solid solution, with a two-phase mixture of zirconolite and a "*fine-grained face-centered cubic phase*" produced for x = 0.20 (further Th^{4+} doping was not attempted). However, it is accepted that the discrepancies in solid solution limit on the Zr^{4+} site, with reference to the current work, may be rationalized by the use of a graphite die, which would be expected to yield conditions similar to sintering under a reducing H_2/N_2 mixture, rather than air. By making comparison to the data presented in this work, it may be reasonable to assume that the cubic phase reported by Kesson et al. was ThO_2, however, as no unit cell parameters were reported, this cannot be confirmed. We are not aware of any other studies that have accommodated Th^{4+} within the Zr^{4+} site of zirconolite.

Sintering the $CaZr_{1-x}Th_xTi_2O_7$ solid solution in air produced a pseudo-binary system comprised of $Ca(Zr,Th)Ti_2O_7$ zirconolite and a pyrochlore-structured phase, requiring mixed Th/Zr occupancy, with the pyrochlore phase favored with increasing Th-content, without the formation of the expected zirconolite-4M intermediate phase. Replacement of Zr^{4+} by 0.60 f.u. of Th^{4+} stabilized a composition retaining the pyrochlore structure, however, targeting a higher Th^{4+} concentration would be expected to destabilize the pyrochlore phase in favor of ancillary phases. This was informed by the work of Vance et al., who reported zero yield of the "$CaThTi_2O_7$" phase when sintering in air between 1300 and 1500°C, rather a mixture of Th-brannerite and perovskite.[35]

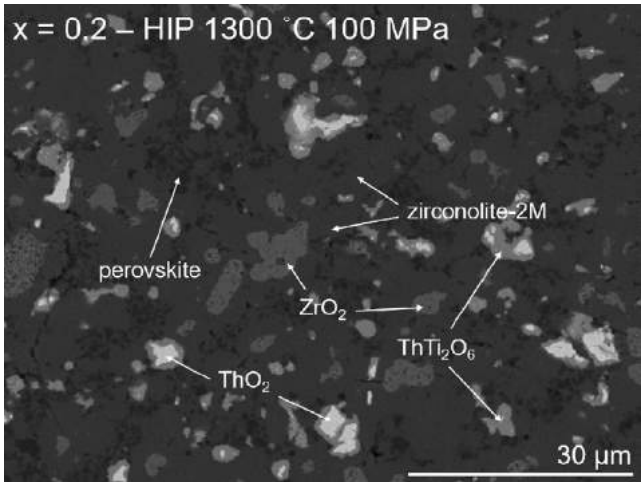

FIGURE 11 Backscattered electron micrograph detailing a representative section of the microstructure for $CaZr_{0.80}Th_{0.20}Ti_{2.00}O_7$ processed by HIP at 1300°C at 100 MPa for 4 h

Furthermore, McCauley et al. attempted to form $CaThTi_2O_7$ by reacting at 1700°C for 8 hours in a sealed Pt-Rh tube, yet this failed to yield the pyrochlore structure.[36] The formation of $A_2B_2O_7$ pyrochlores is generally limited by the relative size difference of constituent A- and B-site cations (8- and 6-fold coordinated, respectively), with the pyrochlore phase stabilized in the range $1.46 < r_A/r_B < 1.78$; compositions for which $r_A/r_B < 1.46$ crystallize with the defect fluorite unit cell, whereas $r_A/r_B > 1.78$ produces a layered perovskite-type structure with monoclinic symmetry [37]. Considering the relative ionic radii of Ca^{2+}, Th^{4+}, and Ti^{4+} in the relevant coordination environment (see Supplementary Table S1), the average A-site radius for $CaThTi_2O_7$ is calculated to be 1.085, resulting in $r_A/r_B = 1.79$, hence slightly too large to satisfy the pyrochlore formation criterion. It is logical to conclude the inclusion of Zr^{4+} within the Ca/Th-site reduced the average ionic radius of the A-site, allowing the stabilization of the pyrochlore phase with 0.4 f.u. Zr^{4+} and 0.60 f.u. Th^{4+}. This is in good agreement with Vance et al. when considering the size limitations for $Ca(A)Ti_2O_7$ pyrochlores, who concluded that 0.7 f.u. Th^{4+} could be accommodated on the A site of the titanate pyrochlore, facilitated by co-incorporation of Zr^{4+}.[38] Furthermore, published thermodynamic data for a selection of pyrochlore ceramic phases relevant to the immobilization of Pu indicate that the $CaThTi_2O_7$ may not be thermodynamically stable.[39,40]

Sintering of the $CaZr_{1-x}Th_xTi_2O_7$ solid solution under flowing 5% H_2/N_2 produced an undesirable phase assemblage due to the presence of a deleterious perovskite phase, expected to be detrimental to the overall wasteform performance due to the inferior aqueous durability of this structure relative to the zirconolite phase. The reduced compositions were comprised of zirconolite (of the 3T polytype structure, space group $P3_121$, above $x \geq 0.20$), undigested ThO_2 and the perovskite phase, accepting Th^{4+} in dilute solid solution. Considering the average compositions of the zirconolite-3T phase e.g. $Ca_{0.88(8)}Zr_{0.77(11)}Th_{0.21(4)}Ti_{2.13(7)}O_7$ as calculated for the $x = 0.40$ sample, it is clear that to maintain charge balance, Ti would be partially reduced to Ti^{3+} (5%-10% Ti^{3+}). The formation of Ti^{3+} is likely under the reducing sintering conditions imposed (5% H_2/N_2), hence it may be inferred that $CaZr_{1-x}Th_xTi_2O_7$ zirconolite-2M is unstable with respect to perovskite and zirconolite-3T under reducing conditions. The $CaZr_{1-x}Pu_xTi_2O_7$ solid solution sintered in air by Begg et al. was annealed in a 3.5% H_2/N_2 mixture at 1200°C for 12 hours, and while this was sufficient to produce powder XRD data consistent with zirconolite-3T and a perovskite phase, in agreement with the current work, no free PuO_2 was observed.[15] Despite zirconolite-3T occupying a moderate portion of the overall phase fraction at low-targeted Th concentration, under reducing conditions, the perovskite and ThO_2 phases occupied more than 30 wt% of the phase assemblage combined, when targeting $x = 0.40$. We consider this would render the wasteform significantly more susceptible to accelerated dissolution, due to the relatively low chemical durability of the perovskite phase[30] relative to the target zirconolite phase, and indeed ThO_2.[41,42] Although it is accepted that relics of unincorporated PuO_2 would be practically unavoidable on a large scale, as a consequence of localized incomplete milling, this would fall within the envelope of the expected wasteform product. In the present work, however, the abundance of ThO_2 throughout the microstructure was considered to be a consequence of the high thermal stability, low redox activity (i.e., Th present only as Th^{4+}) and high melting point of the component oxide. In summary, the immobilization of Th^{4+} in the $CaZr_{1-x}Th_xTi_2O_7$ was best achieved when sintering under oxidizing conditions, as while the composition favors a pyrochlore structure as the dominant phase for $x \geq 0.4$, no perovskite or undigested ThO_2 remained present in the microstructure.

4.2 | Implications for use of Th^{4+} as surrogate for Pu^{4+} wasteform development

The data presented in this study demonstrate the need for careful use of chemical surrogates in the context of wasteform development, as the use of Th^{4+} produced a phase evolution in the $CaZr_{1-x}Th_xTi_2O_7$ system that was inconsistent with respect to closely related analogue solid solutions. Blackburn et al. fabricated a series of zirconolite samples targeting $CaZr_{1-x}Ce_xTi_2O_7$ under identical processing conditions with those used in the current work, demonstrating that the progressive accommodation of Ce^{4+} within the Zr^{4+} site, during oxidative sintering, was consistent with a polymorphic transition to the zirconolite-4M polytype in the compositional range $0.10 \leq x \leq 0.20$.[23] The extension of this solid

solution to $x \geq 0.5$ was reported by Li et al. to form the pyrochlore structure.[43] Analogous phase fields were reported by Vance et al. for the $CaZr_{1-x}U_xTi_2O_7$ solid solution, in which a transition to the zirconolite-4M polytype was observed at $x = 0.15$, with inert Ar gas introduced during the sintering process to maintain U^{4+}.[13] Akin to the Ce system, the U-pyrochlore phase was obtained alongside the 4M phase for $x \geq 0.5$. It is advantageous that for this solid solution there are published Pu data that can provide validation as to the effectiveness of each surrogate. The findings of Begg et al[15] confirmed that oxidative sintering of the $CaZr_{1-x}Pu_xTi_2O_7$ solid solution produced a phase transition from zirconolite-2M to pyrochlore, *via* the formation of Pu-rich zirconolite-4M in the compositional interval $0.1 \leq x \leq 0.6$. Moreover, single-phase Pu pyrochlore was obtained at $x = 0.60$ (i.e., corresponding to a nominal composition $CaZr_{0.4}Pu_{0.6}Ti_2O_7$), identical to the present work. The dataset presented in the current work provides a notable contribution toward the comparative study of plutonium surrogates in the zirconolite system (a summary of which is provided in Table 7), highlighting an important caveat for the application of Th^{4+} as a Pu^{4+} surrogate in the development of zirconolite wasteforms. The zirconolite-4M polytype transformation at higher wasteloading was not observed under oxidizing conditions, presumably as a consequence of size restrictions, due to the large ionic radius of Th^{4+}, compared to U^{4+}, Ce^{4+}, and Pu^{4+} (1.05 Å vs 1.00, 0.97, and 0.96 Å, respectively, for 8-fold coordinate species). Nevertheless, these findings may support the deployment of Th as a Pu surrogate on the basis of safety and expediency, considering the specific activity of ^{239}Pu (2.30×10^2 Bq/μg) is significantly greater than that of ^{232} Th, approximately 4.1 Bq/μg. Hence, these data confirm that Th may act as a suitable radioactive surrogate for Pu in the zirconolite system, and indeed would be beneficial for the investigation of the stability and durability of pyrochlore wasteforms.

5 | CONCLUSIONS

The phase assemblage, microstructure development, and substitution boundary of Th^{4+} within the Zr^{4+} site in $CaZrTi_2O_7$ zirconolite was investigated, by sintering the $CaZr_{1-x}Th_xTi_2O_7$ at 1350°C for 20 hours, under oxidizing and reducing conditions (air and 5% H_2/N_2, respectively). A specimen with nominal composition $CaZr_{0.80}Th_{0.20}Ti_{2.00}O_7$ was also produced by HIP, with a dwell temperature of 1300°C maintained for 4 hours at 100 MPa. Synthesis of $CaZr_{1-x}Th_xTi_2O_7$ compositions in air produced a polycrystalline phase assemblage of zirconolite-2M and pyrochlore in the compositional interval $0.10 \leq x \leq 0.50$, with no observed formation of zirconolite-4M as an intermediate phase. Single-phase pyrochlore with nominal composition $CaZr_{0.4}Th_{0.6}Ti_2O_7$ was stabilized when targeting $x = 0.60$. The $CaZr_{0.4}Th_{0.6}Ti_2O_7$ pyrochlore may be deployed as a suitable phase for the immobilization of wastes with a high Th^{4+} fraction, given the relative ease of processing with moderate Zr^{4+} content with respect to the $CaThTi_2O_7$ end-member. Although, further analysis is necessary to provide a detailed structural refinement of this phase. Synthesis under reducing conditions produced an undesirable phase assemblage consisting of zirconolite-2M and a perovskite phase in the compositional range $0.10 \leq x \leq 0.20$. Sintering under reducing conditions also resulted in considerable unincorporated ThO_2, occupying 3.9 ± 0.1 and 8.8 ± 0.3 wt% of the phase assemblage, respectively. XRD data of the reduced solid solution for which $0.2 \leq x \leq 0.4$ were consistent with zirconolite adopting the 3T polytype. At $x = 0.40$, the perovskite phase and residual ThO_2 accounted for 24.2 and 8.8 wt% of the total phase fraction, respectively. EDS analysis of perovskite inclusions confirmed partial Th^{4+} incorporation, with charge balance presumably facilitated by the formation of Ti^{3+}. The phase assemblage formed by HIP was similar to the counterpart synthesized in 5% H_2/N_2, with a major phase of zirconolite-2M, alongside 3.6 ± 0.1 wt% ThO_2, 5.3 ± 0.3 wt% $ThTi_2O_6$, and 14.1 ± 0.6 wt% perovskite. It was concluded that the immobilization of Th^{4+} in the Zr^{4+} site in zirconolite was best accommodated by synthesis under oxidizing conditions, although a deviation from the expected phase evolution was observed, insofar as the zirconolite-4M intermediate phase was not produced. Nevertheless, the zirconolite-2M to pyrochlore phase transformation was reproduced in the same solid solution range as for Pu, hence under oxidizing conditions, Th^{4+} acted as an effective surrogate for Pu^{4+}. Due to the absence of the trivalent Th species (i.e., Th^{3+}), Th^{4+} could not accurately reproduce the behavior of Pu^{4+} under reducing conditions. The work

TABLE 7 Summary of reported phase fields for $CaZr_{1-x}M_xTi_2O_7$ zirconolites in the compositional range $0.10 \leq x \leq 0.60$ (M^{4+} = Ce/U/Th/Pu, *denotes single phase).

M^{4+} Cation	0.10	0.20	0.30	0.40	0.50	0.60	Ref.
Ce^{4+}	2 M*	2 M + 4 M	2 M + 4 M	2 M + 4 M	2 M + 4 M + P	4 M + P	23,43
U^{4+}	2 M*	2 M + 4 M	2 M + 4 M	4 M + P	4 M + P	4 M + P	13
Th^{4+}	2 M + P	2 M + P	2 M + P	2 M + P	2 M + P	P*	*This work*
Pu^{4+}	2 M*	2 M + 4 M	2 M + 4 M	4 M + P	4 M + P	P*	15

presented hitherto demonstrates the need for multiparametric approach to wasteform development, utilizing several surrogates in conjunction.[44]

ACKNOWLEDGMENTS

We acknowledge financial support from the Nuclear Decommissioning Authority (NDA) and EPSRC under grant numbers EP/S01019X/1, EP/N017870/1, and EP/R511754/1. This research utilized the HADES/MIDAS facility at the University of Sheffield established with financial support from EPSRC and BEIS, under grant EP/T011424/1. The authors declare that they have no known competing financial interests or personal relationships that could have appeared to influence the work reported in this paper.

ORCID

Lewis R. Blackburn https://orcid.org/0000-0002-5889-2035
Shi-Kuan Sun https://orcid.org/0000-0002-1688-5072
Laura J. Gardner https://orcid.org/0000-0003-3126-2583
Martin C. Stennett https://orcid.org/0000-0002-8363-9103
Claire L. Corkhill http://orcid.org/0000-0002-7488-3219
Neil C. Hyatt http://orcid.org/0000-0002-2491-3897

REFERENCES

1. Hyatt NC. Safe management of the UK separated plutonium inventory: a challenge of materials degradation. npj Mater Degrad.. 2020;4(28):2.
2. Nuclear Decommissioning Authority (NDA). Plutonium strategy: Current position paper. 2011.
3. Vance ER, Angel PJ, Begg BD, Day RA. Zirconolite-rich titanate ceramics for high-level actinide wastes. Mater Res Soc Symp Proc. 1993;333:293.
4. Begg BD, Vance ER, Conradson SD. The incorporation of plutonium and neptunium in zirconolite and perovskite. J Alloys Compd. 1998;271–273:221–6.
5. Zhu H, Wang F, Liao Q, Zhu Y. Synthesis and characterization of zirconolite-sodium borosilicate glass-ceramics for nuclear waste immobilization. J Nucl Mater. 2020;532:152026.
6. Kong L, Wei T, Zhang Y, Karatchevtseva I. Phase evolution and microstructure analysis of $CaZrTi_2O_7$ zirconolite in glass. Ceram Int. 2018;44(6):6285–92.
7. Bailey DJ, Lawson SM, Sun SK, Stennett MC, Lee TH, Ravel B, et al. A new approach to the immobilisation of technetium and transuranics: Co-disposal in a zirconolite ceramic matrix. J Nucl Mater. 2020;528:151885.
8. Coelho AA, Cheary RW, Smith KL. Analysis and structural determination of Nd-substituted zirconolite-4M. J Solid State Chem. 1997;129(2):346–59.
9. Ma S, Ji S, Liao C, Liu C, Shih K, He W. Effects of ionic radius on phase evolution in Ln-Al co-doped $Ca_{1-x}Ln_xZrTi_{2-x}Al_xO_7$ (Ln = La, Nd, Gd, Ho, Yb) solid solutions. Ceram Int. 2018;44(13):15124–32.
10. Grey IE, Mumme WG, Ness TJ, Roth RS, Smith KL. Structural relations between weberite and zirconolite polytypes–refinements of doped 3T and 4M $Ca_2Ta_2O_7$ and 3T $CaZrTi_2O_7$. J Solid State Chem. 2003;174(2):285–95.
11. Gatehouse BM, Grey IE, Hill RJ, Rossell HJ. Zirconolite $CaZr_xTi_{3-x}O_7$; structure refinements for near-end-member compositions with x = 0.85 and 1.30. Acta Crystallogr Sect B. 1981;37(2):306–12.
12. White TJ. The microstructure and microchemistry of synthetic zirconolite, zirkelite and related phases. Am Mineral. 1984;69(11–12):1156–72.
13. Vance ER, Lumpkin GR, Carter ML, Cassidy DJ, Ball CJ, Day RA, Begg BD. Incorporation of uranium in zirconolite ($CaZrTi_2O_7$). J Am Ceram Soc. 2002;85(7):1853–59.
14. Clark BM, Sundaram SK, Misture ST. Polymorphic transitions in cerium-substituted zirconolite ($CaZrTi_2O_7$). Sci Rep. 2017;7(1):5920.
15. Begg BD, Day RA, Brownscombe A. Structural effect of Pu substitutions on the Zr-site in zirconolite. Mater Res Soc Symp Proc. 2000;663:259.
16. Jafar M, Achary SN, Salke NP, Sahu AK, Rao R, Tyagi AK. X-ray diffraction and Raman spectroscopic investigations on $CaZrTi_2O_7$–$Y_2Ti_2O_7$ system: Delineation of phase fields consisting of potential ceramic host materials. J Nucl Mater. 2016;475:192–9.
17. Zhang Y-B, Wang J, Wang J-X, Huang Y, Luo P, Liang X-F, et al. Phase evolution, microstructure and chemical stability of $Ca_{1-x}Zr_{1-x}Gd_{2x}Ti_2O_7$ ($0.0 \le x \le 1.0$) system for immobilizing nuclear waste. Ceram Int. 2018;44(12):13572–9.
18. Jafar M, Sengupta P, Achary SN, Tyagi AK. Phase evolution and microstructural studies in $CaZrTi_2O_7$–$Nd_2Ti_2O_7$ system. J Am Ceram Soc. 2014;97(2):609–16.
19. Lang M, Zhang F, Zhang J, Wang J, Lian J, Weber WJ, et al. Review of $A_2B_2O_7$ pyrochlore response to irradiation and pressure. Nucl Instrum Methods Phys Res Sect B. 2010;268(19):2951–9.
20. Zubkova NV, Chukanov NV, Pekov IV, Ternes B, Schüller W, Ksenofontov DA, et al. The crystal structure of nonmetamict Nb-rich zirconolite-3T from the Eifel paleovolcanic region. Germany. Z Kristallogr Cryst Mater. 2018;233(7):463–8.
21. Gilbert MR, Selfslag C, Walter M, Stennett MC, Somers J, Hyatt NC, et al. Synthesis and characterisation of Pu-doped zirconolites – $(Ca_{1-x}Pu_x)Zr(Ti_{2-2x}Fe_{2x})O_7$. IOP Conf Ser Mater Sci Eng. 2010;9:012007.
22. Blackburn LR, Sun S-K, Lawson SM, Gardner LJ, Ding H, Corkhill CL, et al. Synthesis and characterisation of $Ca_{1-x}Ce_xZrTi_{2-2x}Cr_{2x}O_7$: Analogue zirconolite wasteform for the immobilisation of stockpiled UK plutonium. J Eur Ceram Soc. 2020;40(15):5909–19.
23. Blackburn LR, Sun S, Gardner LJ, Maddrell ER, Stennett MC, Hyatt NC. A systematic investigation of the phase assemblage and microstructure of the zirconolite $CaZr_{1-x}Ce_xTi_2O_7$ system. J Nucl Mater. 2020;535:152137.
24. Gardner LJ, Walling SA, Hyatt NC. Hot isostatic pressing: Thermal treatment trials of inactive and radioactive simulant UK intermediate level waste. IOP Conf Ser Mater Sci Eng. 2020;818:012009.
25. Toby B. EXPGUI, a graphical user interface for GSAS. J Appl Crystallogr. 2001;34(2):210–3.
26. Whittle KR, Hyatt NC, Smith KL, Margiolaki I, Berry FJ, Knight KS, et al. Combined neutron and X-ray diffraction determination of disorder in doped zirconolite-2M. Am Mineral. 2012;97(2–3):291–8.
27. Dickson FJ, Hawkins KD, White TJ. Calcium uranium titanate–A new pyrochlore. J Solid State Chem. 1989;82(1):146–50.
28. Helean KB, Navrotsky A, Vance ER, Carter ML, Ebbinghaus B, Krikorian O, et al. Enthalpies of formation of Ce-pyrochlore, $Ca_{0.93}Ce_{1.00}Ti_{2.035}O_{7.00}$, U-pyrochlore,

$Ca_{1.46}U^{4+}_{0.23}U^{6+}_{0.46}Ti_{1.85}O_{7.00}$ and Gd-pyrochlore, $Gd_2Ti_2O_7$: Three materials relevant to the proposed waste form for excess weapons plutonium. J Nucl Mater. 2002;303(2):226–39.

29. Shannon RD. Revised effective ionic radii and systematic studies of interatomic distances in halides and chalcogenides. Acta Cryst. 1976;A32:751–67
30. McGlinn PJ, Hart KP, Loi EH, Vance ER. pH dependence of the aqueous dissolution rates of perovskite and zirconolite at 90°C. Mater Res Soc Symp Proc. 1994;353:847.
31. Begg BD, Vance ER, Lumpkin GR. Charge compensation and the incorporation of cerium in zirconolite and perovskite. Mater Res Soc Symp Proc. 1997;506:79.
32. Kastrissios T, Stephenson M, Turner PS, White TJ. Hydrothermal dissolution of perovskite: implications for synroc formulation. J Am Ceram Soc. 1987;70(7):144–6.
33. Zhang Y, Loi E, Blackford M, McLeod T, Li H, Begg B. Effects of pH and uranium valence state on the aqueous dissolution of brannerite. Mater Res Soc Symp Proc. 2003;807:279.
34. Kesson SE, Sinclair WJ, Ringwood AE. Solid solution limits in synroc zirconolite. Nucl Chem Waste Manage. 1983;4(3):259–65.
35. Vance ER, Carter ML, Day RA. Interim report on Task 1.1: Single-phase sample production to Lawrence Livermore National Laboratory for Contract B345772, United States. UCRL-CR-139059. 1998. https://doi.org/10.2172/15007251.
36. McCauley RA, Hummel FA. New pyrochlores of the charge-coupled type. J Solid State Chem. 1980;33(1):99–105.
37. Shamblin J, Tracy CL, Ewing RC, Zhang F, Li W, Trautmann C, et al. Structural response of titanate pyrochlores to swift heavy ion irradiation. Acta Mater. 2016;117:207–15.
38. Vance ER, Carter ML, Stewart MWA, Day RA, Begg BD, Ball CJ. Ionic size limits for A ions in brannerite (ATi_2O_6) and pyrochlore ($CaATi_2O_7$) titanate structures (A = tetravalent rare earths and actinides). Mater Res Soc Symp Proc. 2002;716:2–7.
39. Xu H, Wang Y. Use of linear free energy relationship to predict Gibbs free energies of formation of pyrochlore phases ($CaMTi_2O_7$). J Nucl Mater. 1999;275(2):216–20.
40. Putnam RL, Gallegos UF, Ebbinghaus BB, Navrotsky A, Helean KB, Ushakov SV, et al. Formation energetics of ceramic phases related to surplus plutonium disposition. Ceram Trans. 2001;119:147–58.
41. Nikoloski AN, Gilligan R, Squire J, Maddrell ER. Chemical stability of zirconolite for proliferation resistance under conditions typically required for the leaching of highly refractory uranium minerals. Metals. 2019;9:1070.
42. Corkhill CL, Myllykylä E, Bailey DJ, Thornber SM, Qi J, Maldonado P, et al. Contribution of energetically reactive surface features to the dissolution of CeO_2 and ThO_2 analogues for spent nuclear fuel microstructures. ACS Appl Mater Interfaces. 2014;6(15):12279–89.
43. Li W, Dong F, Bian L, Zou H, Song M. Phase relations, microstructure, and valence transition studies on $CaZr_{1-x}Ce_xTi_2O_7$ ($0.0 \leq x \leq 1.0$) system. J Rare Earths. 2018;36(11):1184–9.
44. Hyatt NC, Corkhill CL, Stennett MC, Hand RJ, Gardner LJ, Thorpe CL. The HADES facility for High Activity Decommissioning Engineering & Science: part of the UK National Nuclear User Facility. IOP Conf Ser Mater Sci Eng. 2020;818:012022.

SUPPORTING INFORMATION

Additional supporting information may be found online in the Supporting Information section.

How to cite this article: Blackburn LR, Sun SK, Gardner LJ, et al. Synthesis, structure, and characterization of the thorium zirconolite $CaZr_{1-x}Th_xTi_2O_7$ system. *J Am Ceram Soc*. 2021;00:1–15. https://doi.org/10.1111/jace.17627

Supplementary Information

Synthesis, Structure and Characterisation of the Thorium Zirconolite $CaZr_{1-x}Th_xTi_2O_7$ System

Lewis R. Blackburn[a], Shi-Kuan Sun[a,b], Laura J. Gardner[a], Ewan R. Maddrell[c], Martin C. Stennett[a], Claire L. Corkhill[a], Neil C. Hyatt[a]

[a]*Immobilisation Science Laboratory, Department of Materials Science and Engineering, University of Sheffield, Sheffield, S13JD, UK*

[b] *School of Material Science and Energy Engineering, Foshan University, Foshan, Guangdong, 528000, PR China*

[c] *National Nuclear Laboratory, Workington, Cumbria, CA14 3YQ, UK*

Corresponding authors – n.c.hyatt@sheffield.ac.uk (N. C. Hyatt); shikuan.sun@sheffield.ac.uk (S.-K. Sun).

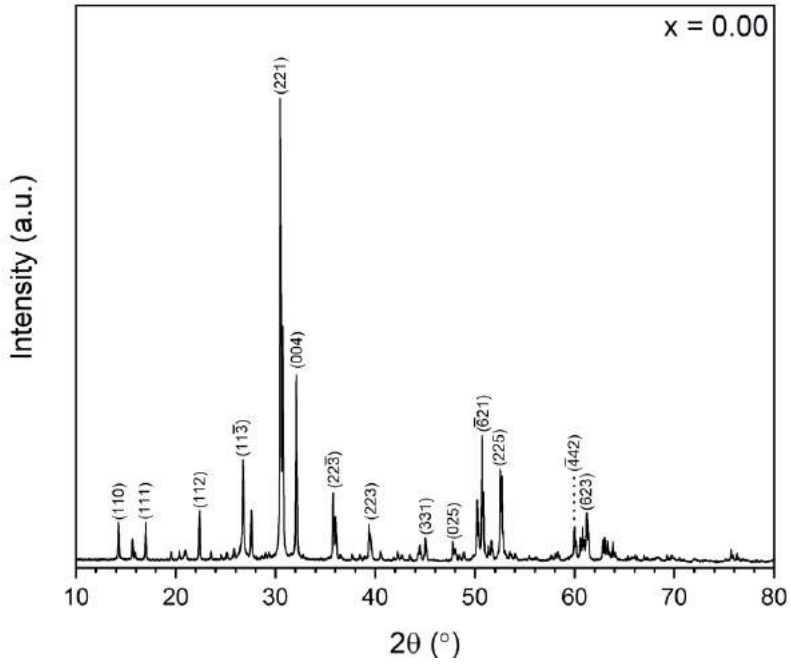

Fig. S1) XRD pattern of the undoped $CaZrTi_2O_7$ (x =0) composition reacted in air at 1350 ˚C for 20 h.

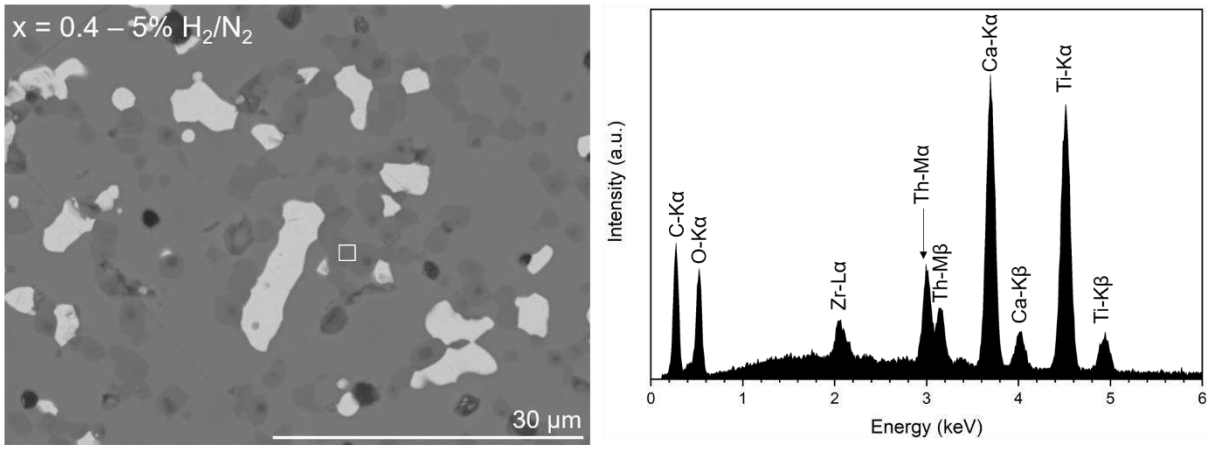

Fig. S2) EDS analysis of perovskite grain present in x = 0.40 composition, demonstrating partial incorporation of Th^{4+}.

Table S1) Ionic radii of elements relevant to $CaThTi_2O_7$ formation [Ref. 1].

	Ionic Radius (Å)	
Element	**8-fold coordination**	**6-fold coordination**
Th^{4+}	1.05	0.94
Ca^{2+}	1.12	1.00
Zr^{4+}	0.84	0.72
Ti^{4+}	0.74	0.605

Ref. 1: Shannon RD. Revised effective ionic radii and systematic studies of interatomic distances in halides and chalcogenides. Acta Cryst. 1976;A32: 751–67.

Chapter 6

Incorporation of Ce within Ca^{2+} Site of Zirconolite via Charge Coupled Substitution

Authorship Contribution Statement

6.1) ‘Influence of Transition Metal Charge Compensation Species on Phase Assemblage in Zirconolite Ceramics for Pu Immobilisation’. L. Blackburn was responsible for conceptualisation, materials preparation and characterisation, formal analysis of data, original draft preparation, reviewing and editing.

6.2) ‘Synthesis and Characterisation of $Ca_{1-x}Ce_xZrTi_{2-2x}Cr_{2x}O_7$: Analogue Zirconolite Wasteform for the Immobilisation of Stockpiled UK Plutonium’. L. Blackburn was responsible for conceptualisation, materials preparation and characterisation, formal analysis of data, original draft preparation, reviewing and editing.

MRS Advances

Influence of Transition Metal Charge Compensation Species on Phase Assemblage in Zirconolite Ceramics for Pu Immobilisation

L.R. Blackburn[1], S.K. Sun[1], L.J. Gardner[1], E.R. Maddrell[2], M.C. Stennett[1], N.C. Hyatt[1]

[1]*Immobilisation Science Laboratory, University of Sheffield, Department of Materials Science and Engineering, Sir Robert Hadfield Building, Mappin Street, S13JD, UK*

[2]*National Nuclear Laboratory, Workington, Cumbria, CA14 3YQ, UK*

ABSTRACT

Immobilisation of Pu in a zirconolite matrix ($CaZrTi_2O_7$) is a viable pathway to disposition. A-site substitution, in which Pu^{4+} is accommodated into the Ca^{2+} site in zirconolite, coupled with sufficient trivalent M^{3+}/Ti^{4+} substitution (where M^{3+} = Fe, Al, Cr), has been systematically evaluated using Ce^{4+} as a structural analogue for Pu^{4+}. A broadly similar phase assemblage of zirconolite-2M and minor perovskite was observed when targeting low levels of Ce incorporation. As the targeted Ce fraction was elevated, secondary phase formation was influenced by choice of M^{3+} species. Co-incorporation of Ce/Fe resulted in the stabilisation of a minor Ce-containing perovskite phase at high wasteloading, whereas considerable phase segregation was observed for Cr^{3+} incorporation. The most favourable substitution approach appeared to be achieved with the use of Al^{3+}, as no perovskite or free CeO_2 was observed. However, high temperature treatments of Al containing specimens resulted in the formation of a secondary Ce-containing hibonite phase.

INTRODUCTION

The United Kingdom Nuclear Decommissioning Authority (NDA) is responsible for the safe and long term management of waste derived from the reprocessing of spent fuel from civil power generation [1]. Reprocessing of nuclear fuels in the UK has resulted in a significant stockpile of civil separated Pu, forecast to reach 140 teHM [2]. The default strategy for this material is continuous interim storage (subject to periodic repackaging) at the Sellafield site. However, NDA is currently in the process of refining the ‘credible options’ framework, exploring potential reuse and disposal options for UK stockpiled Pu. The UK Government has

placed preference on the fabrication of $(U/Pu)O_2$ mixed oxide fuels (MOX) for use in a fleet of civil light water reactors [3]. Yet, some portion of the stockpile may not meet the requirements for the manufacture of MOX fuel due to degradation and contamination, hence, prompt immobilisation and disposal in a suitable glass or ceramic matrix is considered a viable and proliferation resistant management strategy for this material.

Alkali borosilicate glass wasteforms are currently operational for the immobilisation of chemically heterogeneous calcines derived from aqueous reprocessing operations, however, ceramic matrices are considered a more suitable option for wastes with a high actinide fraction. Zirconolite, with ideal composition $CaZrTi_2O_7$, is a naturally occurring titanate phase that is the candidate host for Pu in the UK [4]. Natural zirconolites have demonstrated excellent resistance to extensive weathering and self-irradiation over geological timescales (10^9 years), whilst retaining significant actinide inventories (in some instances approximately 20 wt. %). In the ideal zirconolite-2M structure, planes of Ca^{2+} and Zr^{4+} (8 and 7-fold oxygen coordinated respectively) are arranged between sheets of Ti arranged in hexagonal tungsten bronze type (HTB) motifs. The Ca/Zr layers and HTB units alternate parallel to (001), whilst HTB layers at z = 0.25 and z = 0.75 are orientated by a 180˚ rotation, along the [130] direction [5]. The nomenclature '2M' refers to the two layer repeating sequence forming the unit cell. With reference to the prototypical composition $CaZr_xTi_{3-x}O_7$, the zirconolite-2M polytype is found to be stable over the compositional range $0.83 < x < 1.33$ [6]. Further zirconolite polytypes (*e.g.* 4M, 3T, 3O) have been reported, the formation these polytypes, is postulated to be controlled by the level of targeted Ln^{3+}/An^{4+} incorporation, processing temperature and target site [7–9]. Pu^{4+} can enter the zirconolite lattice *via* solid solution with either Ca^{2+} and/or Zr^{4+} sites, which can create charge imbalance. Co-substitution of a lower valence cation such as Al^{3+} on the Ti^{4+} sites is necessary for Ca^{2+} substitution, in order to maintain isovalence across the structure. In the present work, we aim to systematically evaluate the influence of trivalent charge compensation species Fe^{3+}, Cr^{3+} and Al^{3+} on zirconolite phase evolution. In this instance, Ce^{4+} is used as a structural surrogate for Pu^{4+}.

EXPERIMENTAL

A series of zirconolite ceramics were batched according to composition $Ca_{1-x}Ce_xZrTi_{2-2x}M_{2x}O_7$ ($0.05 \leq x \leq 0.35$, 0.05 increments) with M^{3+} = Cr/Al/Fe as a charge balancing species. $CaTiO_3$, ZrO_2, CeO_2, M_2O_3, and TiO_2 (Alfa Aesar, 99.9% purity, trace metals basis) were batched according to nominal stoichiometry and mixed by high speed planetary milling (Fritsch P7, 400 rpm, 20 min, IPA carrier fluid). Approximately 0.3 g of homogenised precursor material was pressed into the walls of a 10 mm hardened steel die and pressed under 3 t uniaxial pressure. Green bodies were sintered in air at 1350 ˚C for 20 h. Specimens were prepared for powder X-ray diffraction using a Bruker D2 Phaser, fitted with Lynxeye position sensitive detector, using a Cu Kα source (λ = 1.5418 Å, Ni filter). Identified phases were refined using the Rietveld method. Samples were mounted in cold setting resin and polished to a 1 μm finish prior to SEM analysis using a Hitachi TM3030 scanning electron microscope, operating at 15 kV with a working distance of approximately 8 mm. Semi-quantitative analysis was performed using a Bruker Quantax Energy Dispersive X-ray Spectrometer (EDS).

RESULTS AND DISCUSSION

$Ca_{1-x}Ce_xZrTi_{2-2x}Fe_{2x}O_7$

When targeting a nominal composition x = 0.10, zirconolite-2M was identified as the dominant crystalline phase (space group *C2/c*). This was determined by powder X-ray diffraction measurements (**Fig. 1**), and later confirmed by zone axis electron diffraction techniques (not shown). Intense reflections indicative of prototypical zirconolite-2M were observed alongside a minor perovskite phase, nominally $CaTiO_3$, identified by diagnostic reflection 2θ = 33.1˚. This was consistent with the microstructure observed in SEM analysis of well-sintered regions (**Fig. 2**). Perovskite clusters were observed to be distributed throughout the ceramic, observed as darker grey particulates in **Fig. 2**. At x = 0.10, perovskite comprised 1.72 ± 0.24 wt. % of the overall phase assemblage. EDS analysis also demonstrated partial retention of Ce and Fe within the perovskite phase whilst zirconolite-2M exhibited an average composition in good agreement with the nominal stoichiometry. This was confirmed by semi-quantitative EDS measurements (**Table 1**). As the targeted level of Ce/Fe incorporation was elevated, no significant phase separation was observed. When the nominal concentration of Ce was elevated to x = 0.35, perovskite remained present as a secondary phase, accounting for 3.46 ± 0.60 wt. % of the overall phase assemblage. No free CeO_2 or Fe_2O_3 oxides were readily identified by XRD analysis (**Fig. 3**) or by SEM analysis, where only a matrix of zirconolite-2M with considerable perovskite was present (**Fig. 4**).

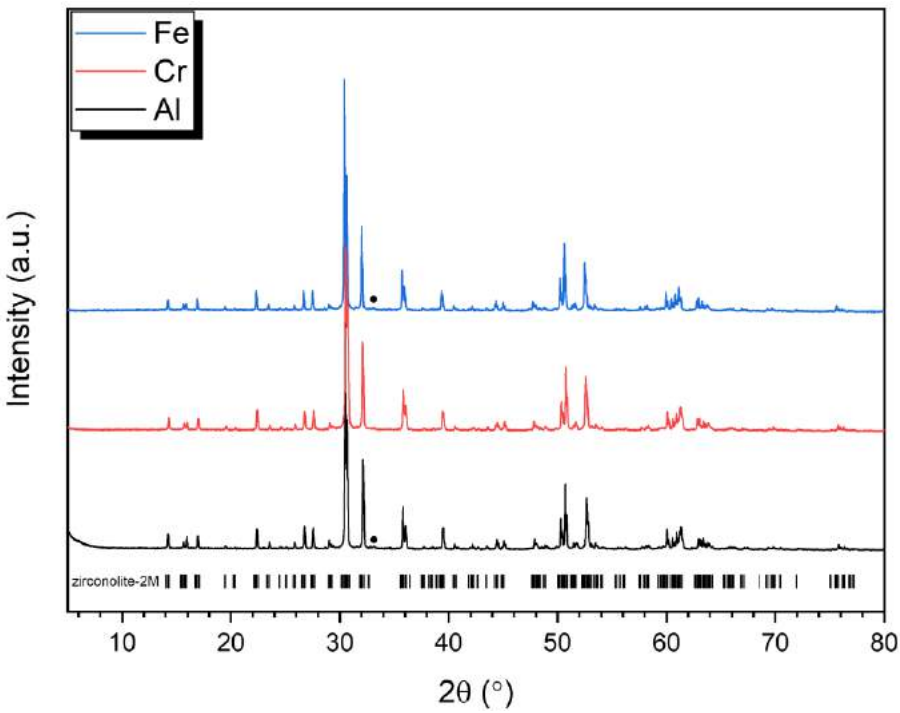

Fig. 1) Powder X-ray diffraction measurements for $Ca_{0.90}Ce_{0.10}ZrTi_{1.80}M_{0.20}O_7$ where M^{3+} = Al/Fe/Cr. Nominal zirconolite-2M reflections are indicated. Minor perovskite inclusions are indexed by (●).

$Ca_{1-x}Ce_xZrTi_{2-2x}Cr_{2x}O_7$

Single phase zirconolite-2M was attained when targeting nominal stoichiometry $Ca_{0.90}Ce_{0.10}ZrTi_{1.80}Cr_{0.20}O_7$, with no perovskite indexed by powder XRD measurements (**Fig. 1**). This was confirmed by zone axis electron diffraction measurements. A homogeneous matrix was observed when viewing polished surfaces (**Fig. 2**). It was, however, noted that all specimens doped with chromium formed with considerable porosity, with respect to the Fe/Al samples (**Fig. 2** and **Fig. 5**). The observed composition is in general agreement with the nominal stoichiometry – **Table 1**. No perovskite was observed when targeting low Ce/Cr substitution ($x < 0.15$). SEM evidenced several secondary phases as the concentration of Ce/Cr was further increased; XRD measurements evidenced free Cr_2O_3 and perovskite for $x = 0.35$ (**Fig. 3**). These phases comprised 2.50 ± 0.26 wt. % and 3.22 ± 0.33 wt. % of the overall phase assemblage, respectively. EDS analysis confirmed co-partitioning of some Ce and Cr in the perovskite phase at $x = 0.35$. SEM analysis also revealed minor ZrO_2 and CeO_2 to be present in the microstructure, these were not readily evidenced by powder XRD due to overlap of diagnostic peaks. Typical phase segregation and elemental distribution for $Ca_{0.65}Ce_{0.35}ZrTi_{1.30}Cr_{0.70}O_7$ is shown in **Fig. 5**.

Table 1) Average zirconolite-2M compositions determined from semi-quantitative EDS analysis (normalized to seven oxygen units).

	Observed Average Composition		
Nominal composition	$Ca_{1-x}Ce_xZrTi_{2-2x}Al_{2x}O_7$	$Ca_{1-x}Ce_xZrTi_{2-2x}Fe_{2x}O_7$	$Ca_{1-x}Ce_xZrTi_{2-2x}Cr_{2x}O_7$
x = 0.10	$Ca_{0.94(4)}Ce_{0.08(4)}Zr_{0.95(7)}Ti_{1.82(6)}Al_{0.22(4)}O_7$	$Ca_{0.95(4)}Ce_{0.07(2)}Zr_{0.93(8)}Ti_{1.86(8)}Fe_{0.19(3)}O_7$	$Ca_{0.94(5)}Ce_{0.07(1)}Zr_{0.93(12)}Ti_{1.89(28)}Cr_{0.17(3)}O_7$
x = 0.35	$Ca_{0.78(6)}Ce_{0.31(10)}Zr_{0.97(10)}Ti_{1.49(10)}Al_{0.44(7)}O_7$	$Ca_{0.69(12)}Ce_{0.28(6)}Zr_{1.04(11)}Ti_{1.41(11)}Fe_{0.57(7)}O_7$	$Ca_{0.68(7)}Ce_{0.30(4)}Zr_{1.01(10)}Ti_{1.46(8)}Cr_{0.52(6)}O_7$

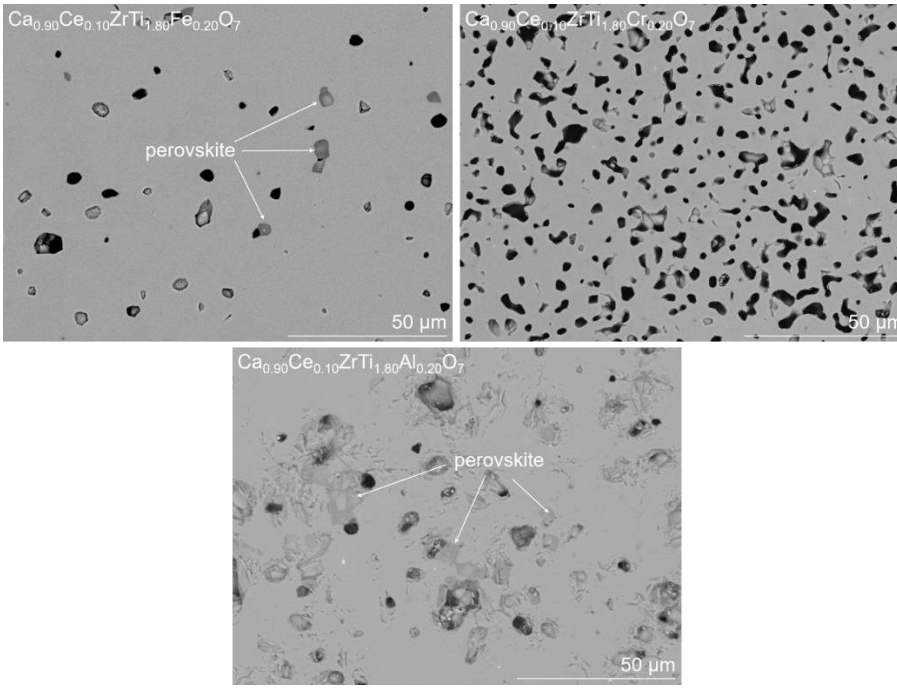

Fig. 2) Representative backscattered electron micrographs for specimens with nominal composition x = 0.10.

$Ca_{1-x}Ce_xZrTi_{2-2x}Al_{2x}O_7$

Intense reflections indicative of prototypical zirconolite-2M were observed for nominal stoichiometry $Ca_{0.90}Ce_{0.10}ZrTi_{1.80}Al_{0.20}O_7$, alongside a minor perovskite phase as indexed in **Fig. 1**, comprising 1.72 ± 0.24 wt. % of the phase assemblage. Electron diffraction techniques inferred that zirconolite remained present in the 2M polytype. The phase assemblage identified by powder XRD was confirmed by SEM analysis of the polished surfaces to be a matrix of zirconolite-2M, with minor Al_2O_3 present at high wasteloading. **Fig. 2** displays a dense matrix of zirconolite-2M, with perovskite inclusions evidenced by variation in backscattered electron contrast, with brighter grains indicating overall greater Ce fraction. EDS analysis confirmed Ce accommodation in the perovskite phase, suggesting the formation of Ce^{3+}. As the Ce/Al fraction was elevated to x = 0.35, the separation of a secondary Al_2O_3 phase was observed, this is evidenced by reflections at approximately 2θ = 25.6˚ and 35.2˚, accounting for 4.01 ± 0.54 wt. % of the phase assemblage. In contrast to the Fe and Cr systems, no perovskite was observed in the microstructure when targeting maximum Ce concentration x = 0.35. A representative microstructure for $Ca_{0.65}Ce_{0.35}ZrTi_{1.60}Al_{0.40}O_7$ is displayed in **Fig. 6**, with a minor amount of $(Ce,Zr)O_2$ present (< 1 wt. %). Whilst perovskite is a common accessory phase in the fabrication of zirconolite specimens (attributed to the partial formation of Ce^{3+}), perovskite has a markedly lower resistance to hydrothermal alteration with respect to zirconolite [10,11]. Therefore, the accommodation of Ce within the Ca^{2+} site of zirconolite-2M may be best achieved *via* the co-partitioning of Al^{3+} on the Ti^{4+} site, in order to inhibit perovskite formation. It was however noted, in separate trials on the same precursor, that a sintering regime in which 1450 ˚C was reached, resulted in the crystallization of a Ce-bearing hibonite phase (ideally $CaAl_{12}O_{19}$). This was not evidenced in the current work, as the formation temperature of nominal $CaAl_{12}O_{19}$ is quoted to be approximately 1500 ˚C [12].

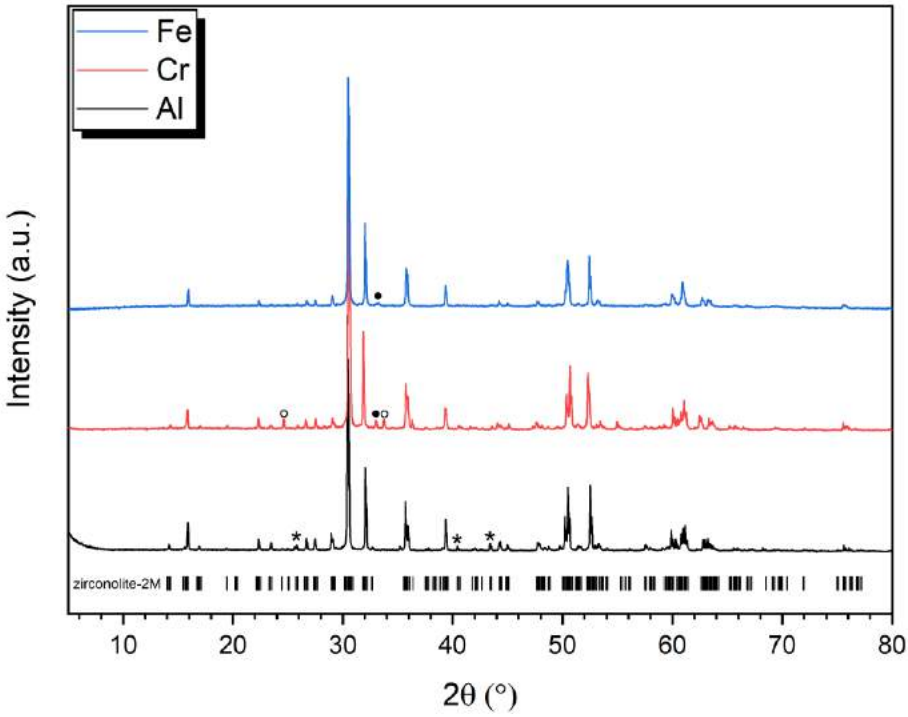

Fig. 3) Powder X-ray diffraction measurements for $Ca_{0.65}Ce_{0.35}ZrTi_{1.30}M_{0.70}O_7$ where M^{3+} = Al/Fe/Cr. Nominal zirconolite-2M reflections are indicated. Minor perovskite and Cr_2O_3 inclusions are indexed by (●) and (o) respectively. Al_2O_3 phases are denoted by (*)

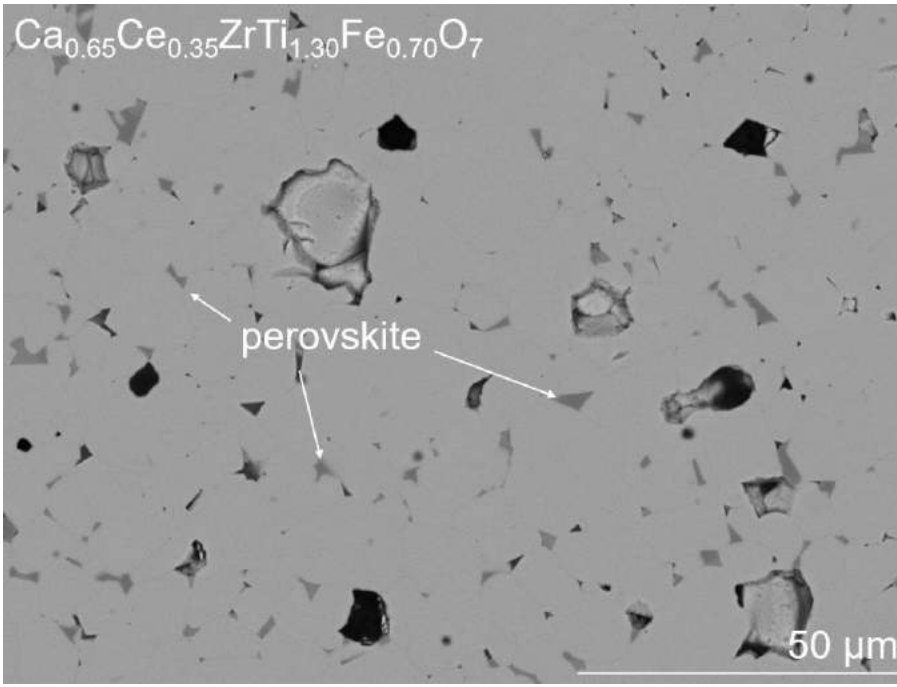

Fig. 4) Backscattered electron micrograph for Fe-doped specimen with nominal x = 0.35 composition.

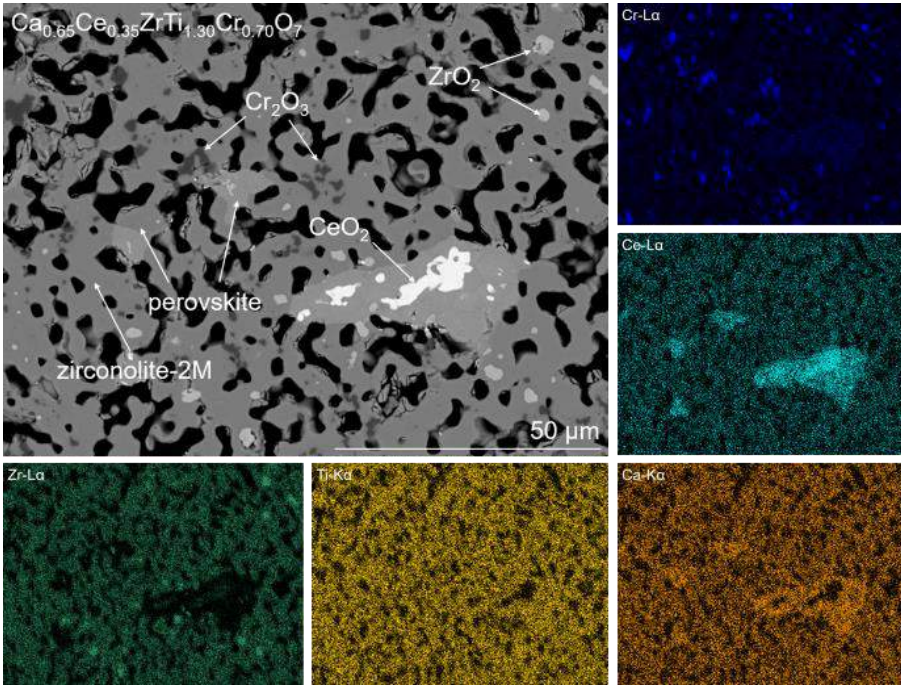

Fig. 5) Representative BSE micrograph and corresponding EDS maps for Ce/Cr doped specimen with nominal composition $Ca_{0.65}Ce_{0.35}ZrTi_{1.30}Cr_{0.70}O_7$.

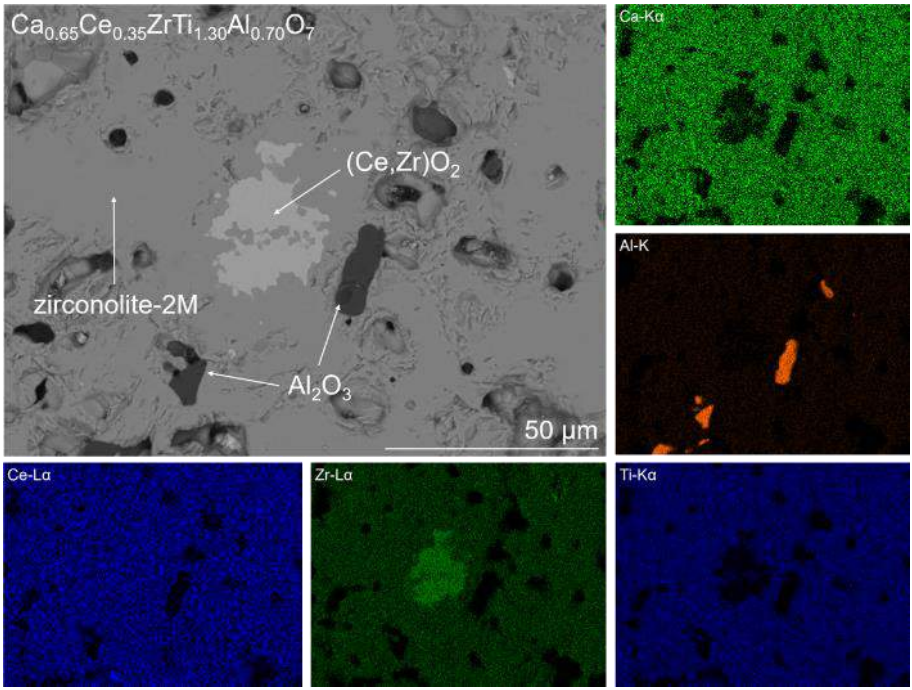

Fig. 6) Representative BSE micrograph and corresponding EDS maps for Ce/Al doped specimen with nominal composition $Ca_{0.65}Ce_{0.35}ZrTi_{1.30}Al_{0.70}O_7$.

CONCLUSIONS

Zirconolite ceramics are under consideration as a host matrix for the immobilisation of civil UK Pu that does not meet the requirements for MOX fuel fabrication. Pu^{4+} may enter the zirconolite system *via* $Ca_{1-x}Pu_xZrTi_{2-2x}M_{2x}O_7$ with the co-substitution of some M^{3+} trivalent species to provide charge balance. The prevailing phase assemblage was likely controlled by size constraints between Ti^{4+} and M^{3+} sites, alongside thermodynamic considerations. When targeting relatively low Ce incorporation (*i.e.* $x \geq 0.15$) a broadly similar phase assemblage and microstructure was observed when utilizing Fe/Cr/Al charge compensation species. When attempting to a substitute high Ce fraction ($x = 0.35$), Fe charge compensation favored the formation of a minor Ce-containing perovskite phase, whilst considerable phase separation and perovskite inclusions were observed for Cr^{3+} samples. Specimens formed with Al^{3+} produced the most favorable phase assemblage due to the lack of secondary $CaTiO_3$. The suppression of secondary perovskite phases is desirable, given the lower aqueous durability of this phase with respect to the target zirconolite phase. Based on the current work, Al^{3+} and Fe^{3+} charge compensation produced wasteforms with the lowest accessory perovskite fraction, and may therefore be considered superior candidates for charge balance than Cr^{3+}. Considerations with respect to temperature should, however, be noted. These results are promising towards the refinement and evaluation of a single phase ceramic host for Pu.

ACKNOWLEDGEMENTS

We are grateful for financial support from the Nuclear Decommissioning Authority and EPSRC under grant numbers EP/M026566/1, EP/S01019X/1, EP/N017870/1 and

EP/R511754/1. This research utilized the MIDAS facility at the University of Sheffield established with financial support from the Department for Energy and Climate Change, now incorporated within the Department for Business, Energy and Industrial Strategy.

References

1. Nuclear Decommissioning Authority, *NDA Plutonium Options* (2008).
2. N.C. Hyatt, Energy Policy **101**, 303 (2017).
3. Nuclear Decommissioning Authority, *NDA Plutonium Topic Strategy: Credible Options Technical Summary* (2009).
4. M.C. Stennett, N.C. Hyatt, M. Gilbert, F.R. Livens, and E.R. Maddrell, in *Mater. Res. Soc. Symp. Proc.* (2008), pp. 1–6.
5. A.A. Coelho, R.W. Cheary, and K.L. Smith, J. Solid State Chem. **129**, 346 (1997).
6. B.M. Gatehouse, I.E. Grey, R.J. Hill, and H.J. Rossell, Acta Cryst. **B37**, 306 (1981).
7. B.M. Clark, S.K. Sundaram, and S.T. Misture, Sci. Rep. **7**, 2 (2017).
8. S. Ma, S. Ji, C. Liao, C. Liu, K. Shih, and W. He, Ceram. Int. **44**, 15124 (2018).
9. N. V. Zubkova, N. V. Chukanov, I. V. Pekov, B. Ternes, W. Schüller, D.A. Ksenofontov, and D.Y. Pushcharovsky, Zeitschrift Fur Krist. - Cryst. Mater. **233**, 463 (2018).
10. K.L. Smith, G.R. Lumpkin, M.G. Blackford, R.A. Day, and K.P. Hart, J. Nucl. Mater. **190**, 287 (1992).
11. S. Myhra, H.E. Bishop, J.C. Rivière, and M. Stephenson, J. Mater. Sci. **22**, 3217 (1987).
12. J. Li, E.A. Medina, J.K. Stalick, A.W. Sleight, and M.A. Subramanian, Prog. Solid State Chem. **44**, 107 (2016).

Journal of the European Ceramic Society 40 (2020) 5909–5919

Contents lists available at ScienceDirect

Journal of the European Ceramic Society

journal homepage: www.elsevier.com/locate/jeurceramsoc

Original Article

Synthesis and characterisation of $Ca_{1-x}Ce_xZrTi_{2-2x}Cr_{2x}O_7$: Analogue zirconolite wasteform for the immobilisation of stockpiled UK plutonium

Lewis R. Blackburn[a], Shi-Kuan Sun[a,*], Sebastian M. Lawson[a], Laura J. Gardner[a], Hao Ding[a], Claire L. Corkhill[a], Ewan R. Maddrell[b], Martin C. Stennett[a], Neil C. Hyatt[a,*]

[a] Immobilisation Science Laboratory, University of Sheffield, Department of Materials Science and Engineering, Sir Robert Hadfield Building, Mappin Street, S1 3JD, UK
[b] National Nuclear Laboratory, Workington, Cumbria, CA14 3YQ, UK

ARTICLE INFO

Keywords:
Zirconolite
Immobilisation
Plutonium
Surrogate
Wasteform

ABSTRACT

A series of $Ca_{1-x}Ce_xZrTi_{2-2x}Cr_{2x}O_7$ zirconolite ceramics ($0 \le x \le 0.35$) were reactively sintered in air at 1350 °C for 20 h. Single phase zirconolite-2M was formed for $x \le 0.15$, with Cr_2O_3 and an undesirable Ce-bearing perovskite phase present above $x = 0.20$. Electron diffraction analysis confirmed that the zirconolite-2M polytype was maintained over the solid solution. X-ray absorption near edge structure (XANES) data determined that between 10–20% Ce was speciated as Ce^{3+}, and Cr was present uniformly as Cr^{3+} with near edge features consistent with occupation of octahedral sites within the zirconolite-2M structure. A sample corresponding to $x = 0.20$ was processed by reactive spark plasma sintering (RSPS), with a rapid processing time of less than 1 h. XANES data confirmed complete reduction to Ce^{3+} during RSPS, promoting the formation of a Ce-bearing perovskite, comprising 19.3 ± 0.4 wt. % of the phase assemblage.

1. Introduction

The safe handling and conditioning of highly radioactive materials derived from nuclear fuel reprocessing operations is an issue of scientific and socioeconomic importance. In the United Kingdom, a large stockpile of separated civil plutonium oxide (PuO_2) has amassed from spent fuel reprocessing *via* the PUREX (Plutonium-Uranium-Reduction-Extraction) process [1]. This stockpile is forecast to peak at 140 teHM (tonnes of heavy metal equivalent), following cancellation of the Fast Neutron Reactor programme in 1994, which has led to the need for other Pu management strategies, for example reuse as mixed oxide (U, Pu)O_2 (MOX) fuel in light water reactors [2]. Currently, MOX fuel presents a commercially unattractive prospect in the UK. The Nuclear Decommissioning Authority (NDA, UK) have assessed it to be a credible option, although appetite for offtake from commercial operators is weak [2]. A fraction of the Pu stockpile has also been declared unsuitable for MOX fabrication, due to chlorine contamination arising from long term storage in polyvinyl chloride (PVC) packaging [3]. An alternative approach is the conditioning of the Pu stockpile and waste material *via* immobilisation within a ceramic matrix.

Immobilisation within ceramic matrices is considered a viable option for the conditioning of actinides such as Pu, since crystalline materials generally offer superior aqueous durability with respect to borosilicate glasses currently used for the vitrification of high level nuclear waste calcines [4–6]. Zirconolite is a naturally occurring titanate ceramic closely related to the pyrochlore family of minerals, with general structure $A_2B_2O_7$ [7]. Zirconolite has nominal stoichiometry $CaZr_xTi_{3-x}O_7$, and crystallises in the zirconolite-2M polytype for $0.85 \le x \le 1.30$, in space group C2/*c* [8]. This structure consists of ZrO_7 and CaO_8 polyhedra integrated between corner sharing TiO_6/TiO_5 polyhedra arranged in a hexagonal tungsten bronze-style motif. This two-layer repeat constitutes the zirconolite-2M unit cell [9]. Zirconolite can exhibit extensive polytypical behaviours which are characterised by the stacking sequence between CaO_8/ZrO_7 polyhedra and TiO_6 layers; the crystallisation of zirconolite polytypes occurs as a result of lanthanide/actinide incorporation and partial oxygen pressure. For example, the zirconolite-4M polytype was observed to form as an intermediate phase in $Ca_{1-x}Zr_{1-x}Nd_{2x}Ti_2O_7$ system and is described as an intercalated sequence of zirconolite-2M and pyrochlore type modules [10,11]. The flexibility of zirconolite and its respective polytypes to incorporate a wide variety of lanthanide and actinides within its structure makes it an ideal candidate for the disposition of excess Pu. The aim of this work is to evaluate the effectiveness of Cr^{3+} as a charge balancing species for the immobilisation of Ce; in this instance, Ce^{4+} is applied as a surrogate for Pu^{4+}. Cerium is justified as a suitable surrogate on the basis of safety and expediency, however, the variations with respect to redox

* Corresponding authors.
E-mail addresses: shikuan.sun@sheffield.ac.uk (S.-K. Sun), n.c.hyatt@sheffield.ac.uk (N.C. Hyatt).

https://doi.org/10.1016/j.jeurceramsoc.2020.05.066
Received 22 April 2020; Received in revised form 25 May 2020; Accepted 26 May 2020
Available online 29 May 2020

potential have been largely realised [12]. Compositions were fabricated by conventional solid state reaction – sintering of the compositional range $Ca_{1-x}Ce_xZrTi_{2-2x}Cr_{2x}O_7$ ($0.00 \leq x \leq 0.35$) and the phase evolution of zirconolite was characterised to determine the incorporation of Ce, using Cr^{3+} to maintain electro-neutrality across the target zirconolite phase. The solid solution parameter x was limited at x = 0.35 as this would correspond to an upper Pu content of ~ 20 wt. %, which is of interest for application. Reactive Spark Plasma Sintering (RSPS) [13] was successfully applied to produce $Ca_{0.80}Ce_{0.20}ZrTi_{1.60}Cr_{0.40}O_7$ (x = 0.20) ceramics of near theoretical density, however, this afforded complete reduction to Ce^{3+}, with a deleterious impact on the phase assemblage, as a result of the use of graphite die and vacuum in the SPS system [14].

2. Experimental

2.1. Materials synthesis

All compositions were synthesised by conventional solid state reaction – sintering between $CaTiO_3$ (Sigma Aldrich, 99.9 % trace metals basis), ZrO_2 (Sigma Aldrich, 99.9 % trace metals basis), Cr_2O_3 (Sigma Aldrich, 99.9 % trace metals basis), TiO_2 (anatase, Sigma Aldrich, 99.9 % trace metals basis) and CeO_2 (Acros Organics, 99.9 % trace metals basis). Precursor materials were dried and weighed according to $Ca_{1-x}Ce_xZrTi_{2-2x}Cr_{2x}O_7$ where $0.00 \leq x \leq 0.35$ ($\Delta x = 0.05$ increments). Batches were homogenised by planetary milling at 400 rpm for 20 min, using isopropanol as a milling agent. Slurries were discharged and left for 12 h at 90 °C to evaporate excess solvent. Approximately 0.3 g of dried material was uniaxially pressed into 10 mm green body pellets under a force of 3 t (~ 260 MPa), and reacted for 20 h in air at 1350 °C. A specimen was also produced by reactive spark plasma sintering (RSPS). Powder mixture with nominal composition $Ca_{0.80}Ce_{0.20}ZrTi_{1.60}Cr_{0.40}O_7$ (x = 0.20) was pressed into a graphite die (with graphite foil spacers) then sintered using a HP-D 1050 SPS system at 1320 °C under vacuum with a dwell time of 30 min (100 °C/min, 5 V and 1 kA at maximum sintering temperature). During the sintering process, the uniaxial pressure was maintained at 15 MPa.

2.2. Materials characterisation

Samples were prepared for powder X-ray diffraction (XRD) by hand grinding the reacted specimens in an agate pestle and mortar using IPA. A Bruker D2 Phaser diffractometer fitted with Lynxeye position sensitive detector was used; diffraction data were acquired in the range $5^\circ \leq 2\theta \leq 80^\circ$, with step size of 0.02° and 1 s per step, using Cu Kα radiation (λ = 1.5418 Å, Ni filter). Unit cell parameters for the zirconolite unit cell and quantitative phase analysis (QPA) were calculated using the Rietveld method, using the GSAS software with EXPGUI interface [15]. Samples were sectioned, mounted in cold setting resin, and polished to a 1 μm optical finish with diamond suspension prior to microstructure analysis using a Hitachi TM3030 scanning electron microscope (SEM), operating with a 15 kV accelerating voltage and a working distance of approximately 8 mm. Energy dispersive X-ray spectroscopy (EDS) was undertaken using a Bruker Quantax Energy Dispersive X-ray Spectrometer for compositional analysis.

Ce L_3 XANES and Cr K XANES (X-ray absorption near edge structure) spectra for cold pressed and sintered samples (CPS) were acquired on beamline B18 at the Diamond Light Source (Oxford, UK) which operates at 3 GeV with a ring current of 300 mA. B18 is a bending magnet beamline producing X-rays in the energy range 2–20 keV. The optical arrangement consists of a water cooled vertically collimated Si mirror, a double crystal Si(111) monochromator, a double toroidal focusing mirror, and harmonic rejection mirrors. Samples were measured in QuEXAFS mode with simultaneous collection of transmission and fluorescence data. Cr K-edge spectra were recorded between 5789 and 6550 eV in energy steps of 0.2 eV using an acquisition time of 35 ms step^{-1}. Ce L_3-edge spectra were recorded between 5523 and 6154 eV in energy steps of 0.25 eV using an acquisition time of 50 ms step^{-1}. To improve data quality, the beam spot size was defocused to *ca.* 1.0 mm and multiple scans were acquired and averaged. Incident and transmitted beam intensities were measured using ionisation chambers which were filled with mixtures of He and N_2 gas. Fluorescence emission was detected using a 36 channel Ge solid state detector. In order to ensure energy reproducibility (± 0.05 eV) and allow absolute energy calibration, a Cr foil was measured in the reference measurement position; the edge position (measured as the first inflection point in the derivative of the absorption) was aligned to the expected value of 5989 eV [16].

XANES data for the sample processed by RSPS was acquired at the Ce L_3-edge on beamline BL-27B at the Photon Factory (PF) accelerator-based light source facility (Tsukuba, Japan). The PF operates at 2.5 GeV with a ring current of 300 mA, and supplies beamline BL-27B with radiation energy in the energy range 4–20 keV *via* a bending magnet. The optical arrangement consists of a double crystal Si(111) monochromator and slits were used to reduce the size of the beam to 3 mm in the horizontal and 1 mm in the vertical. The incident and transmitted photon spectra were measured with ionisation chambers which were gas filled to absorb *ca.* 20 % of the X-rays in the front chamber and 90 % in the second chamber [17]. Spectra were recorded between 5590 and 5990 eV with energy steps of 5 eV (5590–5690), 0.5 eV (5690–5790), 1 eV (5790–5890) and 5 eV (5890–5990). An accumulation time of 1 s step^{-1} was used for all regions and multiple scans were acquired and averaged to improve the signal to noise. To ensure energy reproducibility (± 0.05 eV) a spectrum was collected from a $CePO_4$ standard between each sample.

Specimens were prepared for measurement by homogenising and suspended in polyethylene glycol (PEG) to produce samples with a thickness of approximately one absorption length. Spectra were also acquired from a selection of standards: CeO_2, $CePO_4$, $KCrO_3$, Cr_2O_3 and CrO_2. Data reduction and analysis was performed using the Demeter software package [18]. A linear combination fit of Ce L_3-edge XANES spectra was performed with respect to standards, in order to determine the relative amount of $Ce^{3+/4+}$ species. The corresponding R-factor (mean square sum of the residual for each data point) was determined. The pre-edge region in the Cr XANES spectra were deconvoluted by an edge step (modelled by an arctangent function) and three pre-edge features (fitted by Gaussian functions). To ensure fitting quality, the R-factor was optimised below 0.001. This methodology was based on the work of Wilke et al. [19].

Raman spectra of powdered specimens were collected using the Horiba-XploRA Plus system with 532 nm air cooled Ar^+ laser line and laser power of approximately 5 mW. Specimens for transmission electron microscopy were prepared *via* the powder route. Powders derived from the grinding of the sintered pellets were dispersed with isopropanol, with a small amount of the mixture pipetted from the top of the solvent line onto a holey lined Cu grid (Agar). Selected Area Electron Diffraction patterns (SAED) were acquired for specimens with nominal composition x = 0.05 and x = 0.35, using an FEI Tecnai T20 operating at 200 keV. SAEDPs were captured using a CCD camera.

3. Results and discussion

3.1. Phase assemblage

It was determined from powder X-ray diffraction data (Fig. 1) that zirconolite-2M crystallised as the major phase for each composition in the range $0 \leq x \leq 0.35$ (space group C2/*c*, Z = 8). The Bragg position of theoretical zirconolite-2M reflections (ICSD – 190015) are in excellent agreement with experimental data. In Fig. 1, prominent reflections for the 2M phase are indexed with appropriate (hkl) indices. Secondary phases $CaTiO_3$ (perovskite) and Cr_2O_3 are highlighted by open and closed circles, respectively. When targeting nominal

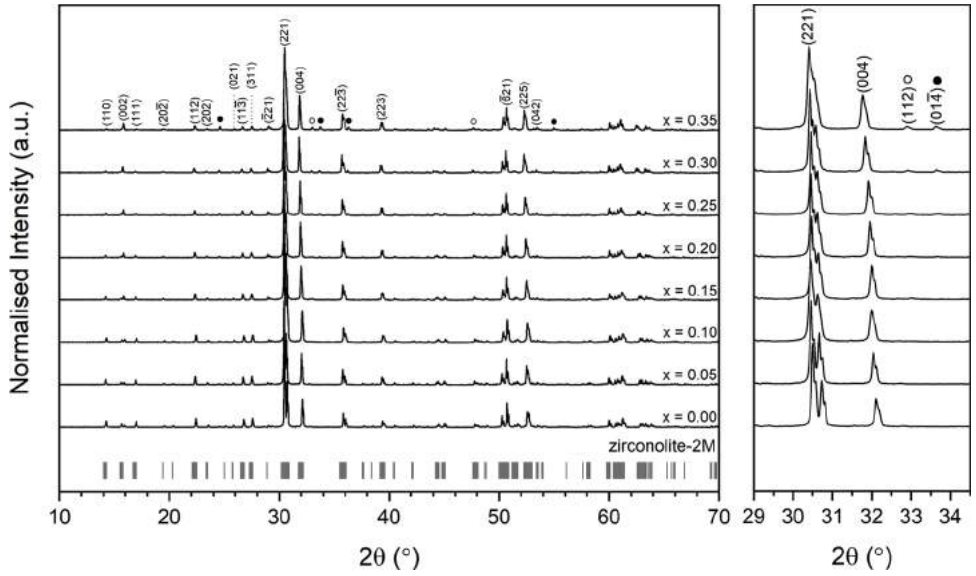

Fig. 1. Powder X-ray diffraction data of $Ca_{1-x}Ce_xZrTi_{2-2x}Cr_{2x}O_7$ ($0.00 \leq x \leq 0.35$) compositions synthesised at 1350 °C for 20 h in air. $CaTiO_3$ reflections are labelled by open circles; Cr_2O_3 reflections are labelled by black filled circles; vertical marks indicate Bragg positions of $CaZrTi_2O_7$ (ICSD – 190015).

$CaZrTi_2O_7$, single phase zirconolite adopting the 2M polytype was formed; unit cell parameters for x = 0.00 were derived from Rietveld fitting (Fig. 2) of XRD data: $\boldsymbol{a}$ = 12.4435(4) Å, $\boldsymbol{b}$ = 7.2735(3) Å, $\boldsymbol{c}$ = 11.3748(4) Å, $\boldsymbol{\beta}$ = 100.563(3)° and $\boldsymbol{V}$ = 1012.06(4) Å^3. These are in good agreement with previous reports [20]. The unit cell parameters for the zirconolite phase over the range $0 \leq x \leq 0.35$ are listed in Table 1. Zirconolite-2M was formed as a single phase in the compositional range $0 \leq x \leq 0.15$, indicating substitution of Ce and Cr into the host phase was achieved. However, minor reflections at 2θ = 33.1° and 2θ = 33.7° were evidenced for x = 0.20, which were attributed to $CaTiO_3$ and Cr_2O_3, comprising 1.2 ± 0.2 wt. % and 0.6 ± 0.2 wt. % of the total phase assemblage, respectively, as determined from the Rietveld analysis. With increased Ce/Cr content, $0.20 \leq x \leq 0.35$, greater relative proportions of $CaTiO_3$ and Cr_2O_3 secondary phases were found to be present, indicating the Ce and Cr were not fully substituted within the zirconolite-2M structure above x = 0.15. Despite the minor phase separation, zirconolite-2M remained present at approximately 94 wt. % when targeting x = 0.35, with perovskite accounting for ~ 3 wt. % of the total phase assemblage. Refinement of the powder diffraction data for the specimen corresponding to x = 0.35 is also displayed in Fig. 2.

Selected area electron diffraction (SAED) patterns for the $Ca_{0.95}Ce_{0.05}ZrTi_{1.90}Cr_{0.10}O_7$ (x = 0.05) and $Ca_{0.65}Ce_{0.35}ZrTi_{1,30}Cr_{0.70}O_7$ (x = 0.35) compositions are presented down the [010] direction in Fig. 3**a** and **b** and down the [111] direction in Fig. 3**c** and **d**, respectively. In both instances, the patterns indexed to the zirconolite-2M polytype (space group C2/c), in agreement with XRD data. There was no indication of polymorphic transitions to the zirconolite-4M or other polytypes, which has been previously observed when partitioning Ce/U in the Zr^{4+} site. For example, in the case of Vance et al., extensive "streaking" of crystalline reflections was observed in diffraction data for compositions of zirconolite-4M in the range $CaZr_{1-x}U_xTi_2O_7$ ($0.20 \leq x \leq 0.30$) [21].

3.2. Microstructure analysis

Polished surfaces for each composition were analysed by SEM-EDS analysis. A representative micrograph for x = 0.05 is displayed in Fig. 4. A matrix with homogeneous BSE contrast was observed, confirming the formation of single phase zirconolite-2M, with an average composition of $Ca_{1.01(7)}Ce_{0.03(1)}Zr_{0.88(9)}Ti_{2.00(5)}Cr_{0.08(1)}O_7$ determined by EDS analysis (oxygen content was assumed to be stoichiometric, given the poor sensitivity of EDS towards oxygen determination). The compositional analysis was in good agreement with targeted stoichiometry, considering the associated error of EDS analysis (quoted in parentheses to 1 s.d.). It was observed that all specimens exhibited a sintered microstructure but with high internal porosity; Archimedes density measurements and EDS data for each composition are summarised in Table 2. The high internal porosity would be undesirable from a disposability perspective, if replicated in a corresponding Pu solid solution. The porosity would result in an increased contact surface area available for dissolution, and this may be reduced by increasing the sintering temperature and/or applying the external pressure. It should be noted that with reference to the prototypical $CaZr_xTi_{3-x}O_7$ composition, the site occupancy and distribution of [Ti]/[Zr] is known to be sensitive to processing temperature: ratios between 1.31 and 2.75 at 1500 °C and 1300 °C have been reported, respectively [8]. Considering the processing temperature used (1350 °C), the observed [Ti]/[Zr] ratio falls within the expected range of values, considering the associated error of EDS analysis (quoted in parenthesis to 1 s.d.).

In agreement with powder XRD, no other phases were observed in the microstructure for x = 0.10 and x = 0.15 compositions (data not shown). Phase separation was observed in the microstructure at x = 0.20, shown in Fig. 5. Cr_2O_3 and perovskite were distinguished from the bulk matrix by BSE contrast. EDS analysis confirmed that Ce and Cr were also incorporated within the perovskite phase. The accommodation of Ce within the perovskite phase suggests partial Ce reduction to Ce^{3+}, as the formation of Ce^{3+} is known to promote and stabilise Ce-bearing perovskite [22,23]. A comparison of the EDS spectra of the perovskite phase and zirconolite-2M in the x = 0.35 composition is given in Fig. 6. Begg et al. reported that Ce^{3+} substituted within the Ca site in perovskite up to 0.1 f.u. without the need for charge balancing species [24]. However, in this instance, Cr^{3+} may provide sufficient charge compensation such that more Ce^{3+} can be incorporated within the perovskite phase. Indeed, $Ca_{0.9}Pu_{0.1}Ti_{0.8}Al_{0.2}O_3$ perovskite has been previously synthesised, hence the formation of Ce and Cr substituted counterparts is considered plausible, considering the similar electronegativity and size constraints for Ce/Pu and Cr/Al [25]. The microstructure for $0.25 \leq x \leq 0.35$ compositions displayed further phase separation, with Cr_2O_3 comprising 1.1 ± 0.2, 1.9 ± 0.2 and 2.5 ± 0.3 wt. % of the total phase assemblage, respectively. The zirconolite-2M phase fraction remained high, corresponding to 97.4 ± 0.02, 96.3 ± 0.03 and 93.5 ± 0.05 wt. % for x = 0.25, 0.30 and 0.35, respectively. A representative microstructure for the x = 0.35 sample, and elemental distributions, are

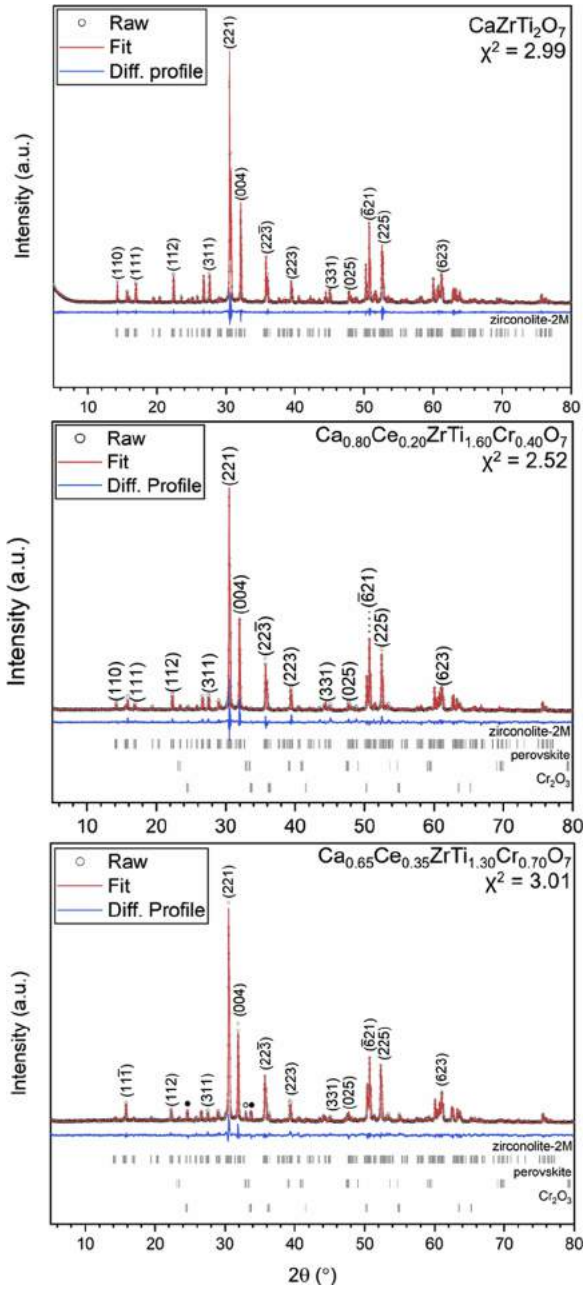

Fig. 2. Rietveld profile fit x = 0.00, x = 0.20 and x = 0.35. Recorded data is displayed in black; fit data is displayed in red; difference profile is displayed in blue. $CaTiO_3$ reflections are labelled by open circles; Cr_2O_3 reflections are labelled by black filled circles. Vertical marks indicate Bragg positions of $CaZrTi_2O_7$ (ICSD – 190015), $CaTiO_3$ (ICSD – 183209) and Cr_2O_3 (ICSD – 167268). (For interpretation of the references to colour in this figure legend, the reader is referred to the web version of this article).

displayed in Fig. 7. A minor fraction of unincorporated CeO_2 was evidenced in the x = 0.35 specimen by SEM analysis of the microstructure, yet, this was not detected by XRD. A ZrO_2 phase was also detected, however this constituted < 1 wt. % of the overall phase assemblage.

3.3. Oxidation state and local environment of Ce and Cr

Ce has been observed to exist as Ce^{4+} and Ce^{3+} in zirconolite wasteforms despite processing under oxidizing conditions. The oxidation state of cerium was determined through the use Ce L_3 XANES, acquired alongside Ce^{3+} and Ce^{4+} reference compounds ($CePO_4$ and CeO_2, respectively). These data are displayed in Fig. 8. The $CePO_4$ (monazite) spectrum was comprised of a single intense white line feature characteristic of Ce^{3+} speciation (in $CePO_4$ (monazite), Ce^{3+} is coordinated as a CeO_9 polyhedron). The white line features for CeO_2 consisted of an asymmetric doublet with lower relative intensity than observed for $CePO_4$ (in CeO_2, Ce^{4+} is coordinated as a CeO_8 polyhedron). The initial and final state electron configurations associated with the white line features for both reference compounds are discussed elsewhere [26]. It was apparent from visual inspection of normalised XANES spectra that Ce was present mainly as Ce^{4+} in $Ca_{1-x}Ce_xZrTi_{2-2x}Cr_{2x}O_7$ compositions, remaining analogous to Pu^{4+}. However closer inspection of XANES data revealed a small shift in the edge position toward lower energy (with respect to the CeO_2 reference compound) and a small change in the relative intensity of the asymmetric doublet features, consistent with a minor fraction of Ce^{3+}. Linear combination fitting (LCF) of each composition was performed using the CeO_2 and $CePO_4$ reference compounds, the results are summarised in Table 3, which confirmed the presence of 15–30% Ce^{3+} depending on the composition. Reduction of Ce^{4+} to Ce^{3+} results in an increase in average ionic radius (0.97 Å–1.143 Å for 8-fold coordinated species [27]), favoring partitioning within the Ca^{2+} site in the perovskite phase, as was confirmed by SEM/EDS data.

XANES analysis at the Cr K-edge was undertaken on all compositions, and a series of Cr reference compounds representing various oxidation states and coordination environments. XANES spectra acquired at the Cr K-edge are displayed in Fig. 9. It was evident that all Cr-zirconolite specimens retained very similar edge features, consisting of an intense white line at approximately E_0 = 6002 eV (E_0 derived from the maxima of the first derivative). For all zirconolite spectra a minor pre-edge feature was also observed. The E_0 position of the Cr_2O_3 XANES spectrum was lower at approximately E_0 = 6000 eV, and the Cr_2O_3 white line also featured a significant shoulder on the absorption edge and a moderately intense pre-edge feature, which were not observed in the measured zirconolite spectra. The E_0 position and white line features for $YCrO_3$ were more consistent with features observed in the zirconolite XANES data, inferring similar Cr speciation and chemical environment. It was evident, therefore, that Cr was present primarily in a single dominant Cr environment, for all zirconolite compositions similar to that in $YCrO_3$, in which Cr^{3+} adopts octahedra coordination by oxygen. Furthermore, the XANES spectrum for K_2CrO_4 (in which Cr^{6+} adopts tetrahedral coordination by oxygen) is characterised by an intense pre-edge feature, which exists at ~ 15 eV prior to the main absorption edge. This feature was not observed for any Cr-containing zirconolite specimens, confirming the absence of Cr^{6+}. Several isosbestic points were also revealed as the concentration of *x* was increased – these are labelled as **A**, **B**, **C** and **D** on Fig. 9. The presence of isosbestic points in a closed system is attributed to the contribution of the absorbing atom (*i.e.* Cr) in two or more chemical environments. Considering the reference spectra for Cr_2O_3, the formation of isosbestic points is a result of increased contribution of free Cr_2O_3 present in the sample. Upon closer inspection, points **A**, **B**, **C** and **D** become apparent at some nominal composition in the interval $0.15 \leq x \leq 0.20$. This was clearly distinguished by the appearance of the feature at 6012 eV (between points **B** and **C** in Fig. 9) which was common to both Cr_2O_3 and zirconolite spectra. The intensity of this feature increased with elevated Cr content, $x > 0.15$, suggesting the presence of Cr_2O_3. This is in agreement with powder XRD data and microscopic analysis, in which a secondary Cr_2O_3 phase was observed in the microstructure for compositions where $x > 0.15$. The pre-edge features in the XANES of Cr_2O_3, $YCrO_3$ and the x = 0.15 sample were deconvoluted by subtraction of a modelled arctangent function, and the features fitted by Gaussian functions. Considering Fig. 10, there are three distinct contributions to the Cr^{3+} pre-edge features in each instance. There were clear similarities between the features for the zirconolite pre-edge and $YCrO_3$ standard. The origin of the doublet feature for Cr^{3+} compounds in the pre-edge region are from quadrupolar 1 s → 3d transitions, as a result of

Table 1
Zirconolite-2M unit cell parameters for $Ca_{1-x}Ce_xZrTi_{2-2x}Cr_{2x}O_7$ ($0.00 \leq x \leq 0.35$) derived from Rietveld refinement fitting of powder X-ray diffraction data. Statistical errors are quoted in parentheses to 1 s.d.

Composition	Zirconolite-2M Unit Cell Parameters					
	a (Å)	*b* (Å)	*c* (Å)	*β* (°)	*V* (Å^3)	R_p (%), R_{wp} (%), χ^2
x = 0.00	12.4435(4)	7.2735(3)	11.3748(4)	100.563(3)	1012.06(4)	8.17, 6.28, 2.99
x = 0.05	12.4441(2)	7.2635(2)	11.3742(3)	100.580(3)	1010.62(3)	7.31, 5.75, 2.09
x = 0.10	12.4483(4)	7.2581(2)	11.3819(4)	100.582(3)	1010.88(4)	6.70, 5.15, 2.04
x = 0.15	12.4459(4)	7.2508(2)	11.3834(4)	100.582(3)	1009.79(4)	7.25, 5.65, 2.32
x = 0.20	12.4540(3)	7.2530(2)	11.3993(3)	100.569(3)	1012.23(4)	7.18, 5.54, 2.52
x = 0.25	12.4628(3)	7.2566(2)	11.4195(3)	100.548(3)	1015.31(4)	7.14, 5.47, 2.41
x = 0.30	12.4629(4)	7.2548(2)	11.4368(3)	100.518(3)	1016.69(4)	7.41, 5.70, 2.61
x = 0.35	12.4693(5)	7.2560(3)	11.4532(5)	100.500(3)	1018.89(5)	7.56, 5.74, 3.01

hybridisation of Cr-3d energy levels [28]. These data are in agreement with Cabaret et al. in which three local electric quadrupole transitions were predicted for K pre-edge features of octahedrally coordinated Cr^{3+} species from first principles [29]. The normalised intensity and energy centroid of the fitted Gaussian contributions to the pre-edge features of the x = 0.15 sample and $YCrO_3$ were determined to be similar. In the ideal $YCrO_3$ structure, CrO_6 octahedtra are arranged in a corner sharing motif, analogous to the hexagonal tungsten bronze layers of TiO_6 octahedra in the zirconolite structure. Cr_2O_3 also contains Cr^{3+} in octahedral coordination, however, the face and edge sharing of CrO_6 octahedra results in fitted Gaussian contributions to the pre-edge feature that are dissimilar in normalised intensity and centroid energy, compared to those of the x = 0.15 and $YCrO_3$. Thus, the Cr K-edge XANES analysis presented here is consistent with Cr substitution within the octahedral TiO_6 sites of the zirconolite structure.

Raman spectra in the wavenumber range 100 – 1000 cm^{-1} are presented in Fig. 11. Many active Raman vibrational modes are observed due to the low symmetry of the monoclinic unit cell. A prominent Raman mode at 780 cm^{-1} was observed for all samples, and a variety of intense modes were evidenced in the 150 – 400 cm^{-1} range.

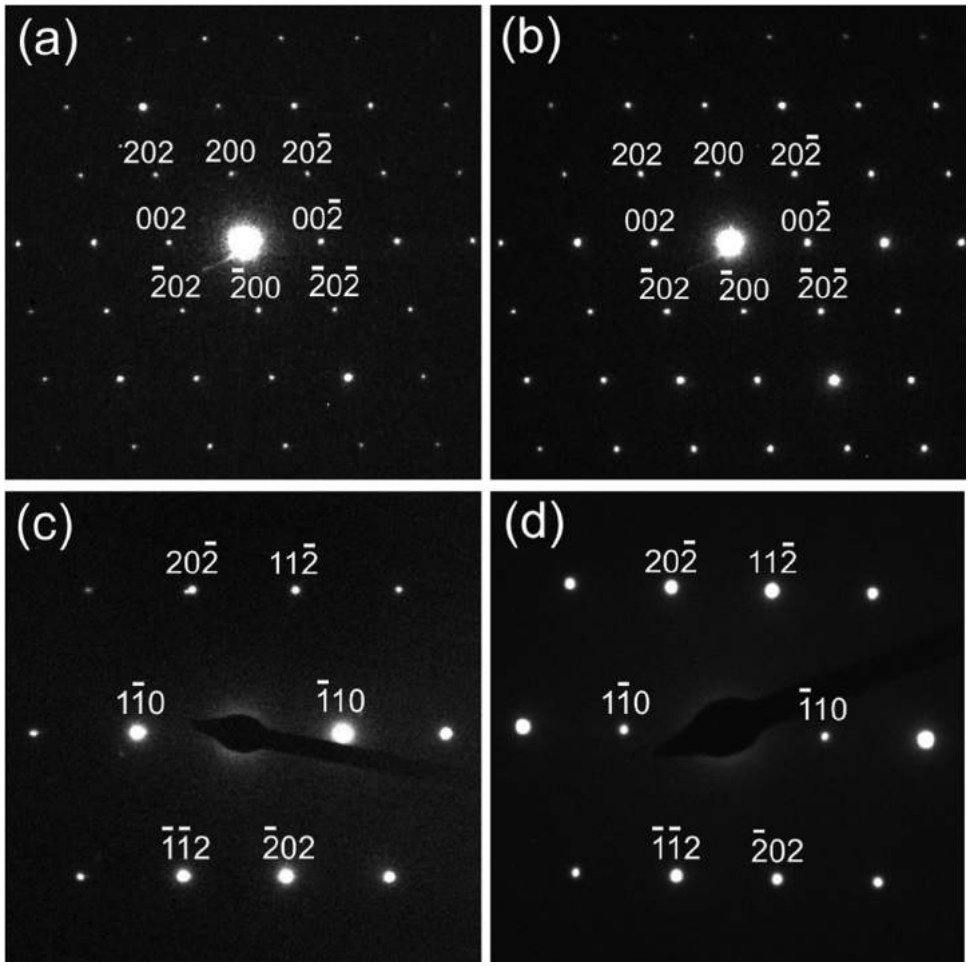

Fig. 3. Selected area electron diffraction patterns for (a) $Ca_{0.95}Ce_{0.05}ZrTi_{1.90}Cr_{0.10}O_7$; [010], (b) $Ca_{0.65}Ce_{0.35}ZrTi_{1.30}Cr_{0.70}O_7$; [010], (c) $Ca_{0.95}Ce_{0.05}ZrTi_{1.90}Cr_{0.10}O_7$; [111] and (d) $Ca_{0.65}Ce_{0.35}ZrTi_{1.30}Cr_{0.70}O_7$; [111].

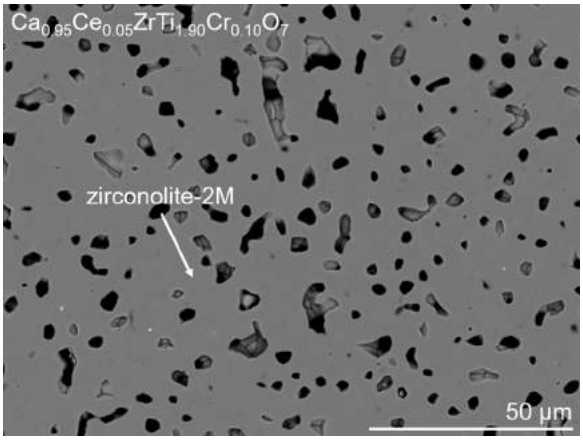

Fig. 4. Representative backscattered electron micrograph for specimen with nominal composition x = 0.05. Black regions are porosity.

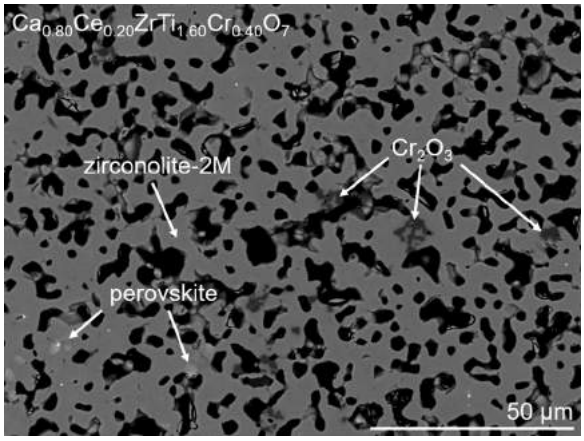

Fig. 5. Representative backscattered electron micrograph for specimen with nominal composition $Ca_{0.80}Ce_{0.20}ZrTi_{1.60}Cr_{0.40}O_7$ shows a mixture of zirconolite-2M, with minor $CaTiO_3$ and Cr_2O_3. Black regions are porosity.

At low concentrations *e.g.* x = 0.05, the spectrum is in good agreement with the active Raman modes observed in our previous studies for the zirconolite-2M structure [30]. As the substituted concentration is elevated, many of these features undergo broadening, in particular those at a lower Raman shift. This is attributed to disorder induced by Cr^{3+} and $Ce^{4+/3+}$ partitioning in Ti^{4+} and Ca^{2+} sites respectively. The degree of broadening does not appear to change beyond x ≥ 0.20, consistent with the observations that Cr^{3+} was not fully incorporated into the zirconolite-2M structure beyond this concentration. Whilst it is known that the dominant vibrational mode at 780 cm^{-1} is attributed to the symmetric vibrations of TiO_6 octahedra, we are not aware of any studies that have directly assigned other prominent modes to specific bonds in the zirconolite structure [31]. However, it is generally accepted that vibrational modes below 700 cm^{-1} are attributed to CaO_8 and ZrO_7 polyhedral vibrations, and TiO_6 bending and stretching vibrations [30]. Jafar et al. performed Raman spectroscopic studies on the $CaZrTi_2O_7$ – $Y_2Ti_2O_7$ system, where a structural transition from zirconolite-2M to cubic pyrochlore was observed, with the formation of the zirconolite-4M polytype as an intermediate phase [32]. A characteristic feature of the transition to the zirconolite-4M and pyrochlore structures was the abatement of the TiO_6 peak at 780 cm^{-1}. This feature remains prominent in this instance, inferring zirconolite crystallised in the 2M configuration throughout the solid solution.

3.4. Reactive spark plasma sintering

In order to overcome poor densification observed in reactively sintered specimens, a sample of milled precursor with nominal composition x = 0.20 was processed by reactive spark plasma sintering (RSPS). It should be noted that this is not the same as *consolidation via* SPS, as in this instance, the reaction and consolidation occur simultaneously. Rather, here, we report the formation of heavily-doped zirconolite with a rapid processing time of less than 60 min. We have previously reported the formation of nearly single phase $CaZrTi_2O_7$ using this technique [13]. Whilst zirconolite wasteforms with incorporated Ce were reported by Clark et al., these were only consolidated by SPS subsequent to zirconolite formation *via* solid state reaction [22,33]. Powder XRD data comparing the phase assemblage of the RSPS and CPS product are displayed in Fig. 12. The sample processed by RSPS formed zirconolite-2M as the major phase, comprising 64.9 ± 0.2 wt. % of the overall phase assemblage. It was noted that relative phase fraction of perovskite (labelled with closed circles on Fig. 12) significantly increased in comparison to the CPS sample, from 1.2 ± 0.2 wt. % to 19.3 ± 0.4 wt % of the phase assemblage. There was also an increase in the quantity of ZrO_2 (labelled by open circles on Fig. 12), however this was still < 3 wt. % of the overall phase assemblage. A relative increase in Cr_2O_3 was also observed, from 0.6 ± 0.2 wt. % to 2.1 ± 0.3 wt. %. An accessory pyrochlore-structured phase with prototypical composition $Ca_2Ti_2O_6$ (JCPDS No. 04-0103, space group *Fd-3m*) was formed, with an intense reflection at 2θ = 31.1° [34]. It was not possible to resolve the $Ca_2Ti_2O_6$ by SEM, presumably due similar backscattered electron coefficient to the accompanying perovskite and/or zirconolite-2M phase, yet the phase comprised 10.9 ± 0.5 wt. %. It is likely that partial incorporation of Ce occurred within both $CaTiO_3$ and $Ca_2Ti_2O_6$ phases, producing similar BSE contrast. Our previous attempts to form $CaZrTi_2O_7$ by RSPS resulted in approximately 2.1 wt. % $CaTiO_3$, with partial Ti^{3+} speciation confirmed by paramagnetic electron resonance measurements [13]. Furthermore, in the case of Clark et al., a sample of $CaZr_{0.5}Ce_{0.5}Ti_2O_7$ was sintered in air, and subsequently consolidated by SPS [22]. During this process, a perovskite fraction with stoichiometry $Ca_{0.40}Ce_{0.40}TiO_3$

Table 2
Comparison between nominal and calculated zirconolite-2M composition derived from quantitative EDS data, normalised to seven oxygen atoms. Errors are quoted in parentheses to 1 s.d.

Degree of Substitution	Nominal Composition	Observed Composition from EDS	Archimedes Density (g/cm^3)	Theoretical Density (g/cm^3)
x = 0.05	$Ca_{0.95}Ce_{0.05}ZrTi_{1.90}Cr_{0.10}O_7$	$Ca_{1.01(7)}Ce_{0.03(1)}Zr_{0.88(9)}Ti_{2.00(5)}Cr_{0.08(1)}O_7$	3.991 ± 0.032	4.528 ± 0.0001
x = 0.10	$Ca_{0.90}Ce_{0.10}ZrTi_{1.80}Cr_{0.20}O_7$	$Ca_{0.96(4)}Ce_{0.07(1)}Zr_{0.89(5)}Ti_{1.90(4)}Cr_{0.17(3)}O_7$	3.949 ± 0.083	4.598 ± 0.0002
x = 0.15	$Ca_{0.85}Ce_{0.15}ZrTi_{1.70}Cr_{0.30}O_7$	$Ca_{0.89(6)}Ce_{0.12(1)}Zr_{0.94(9)}Ti_{1.79(5)}Cr_{0.26(1)}O_7$	4.071 ± 0.071	4.674 ± 0.0002
x = 0.20	$Ca_{0.80}Ce_{0.20}ZrTi_{1.60}Cr_{0.40}O_7$	$Ca_{0.88(6)}Ce_{0.15(2)}Zr_{0.97(9)}Ti_{1.70(8)}Cr_{0.29(4)}O_7$	4.045 ± 0.035	4.734 ± 0.0002
x = 0.25	$Ca_{0.75}Ce_{0.25}ZrTi_{1.50}Cr_{0.50}O_7$	$Ca_{0.82(5)}Ce_{0.21(2)}Zr_{0.92(8)}Ti_{1.67(7)}Cr_{0.39(4)}O_7$	3.881 ± 0.055	4.790 ± 0.0002
x = 0.30	$Ca_{0.70}Ce_{0.30}ZrTi_{1.40}Cr_{0.60}O_7$	$Ca_{0.77(7)}Ce_{0.25(3)}Zr_{0.99(13)}Ti_{1.56(8)}Cr_{0.44(4)}O_7$	3.874 ± 0.040	4.855 ± 0.0002
x = 0.35	$Ca_{0.65}Ce_{0.35}ZrTi_{1.30}Cr_{0.70}O_7$	$Ca_{0.68(7)}Ce_{0.30(4)}Zr_{1.01(10)}Ti_{1.46(8)}Cr_{0.52(6)}O_7$	3.895 ± 0.032	4.915 ± 0.0002

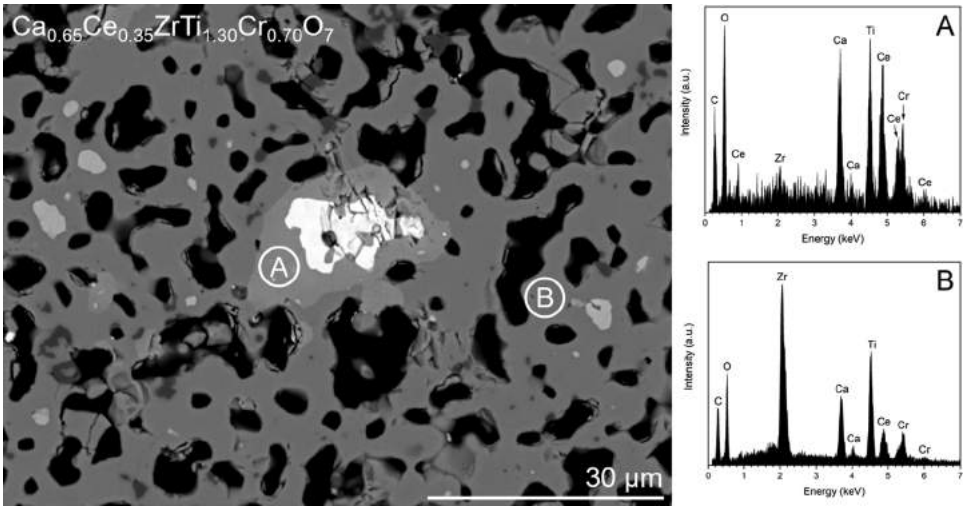

Fig. 6. EDS spot analysis of A) Ce-bearing perovskite; B) zirconolite-2M.

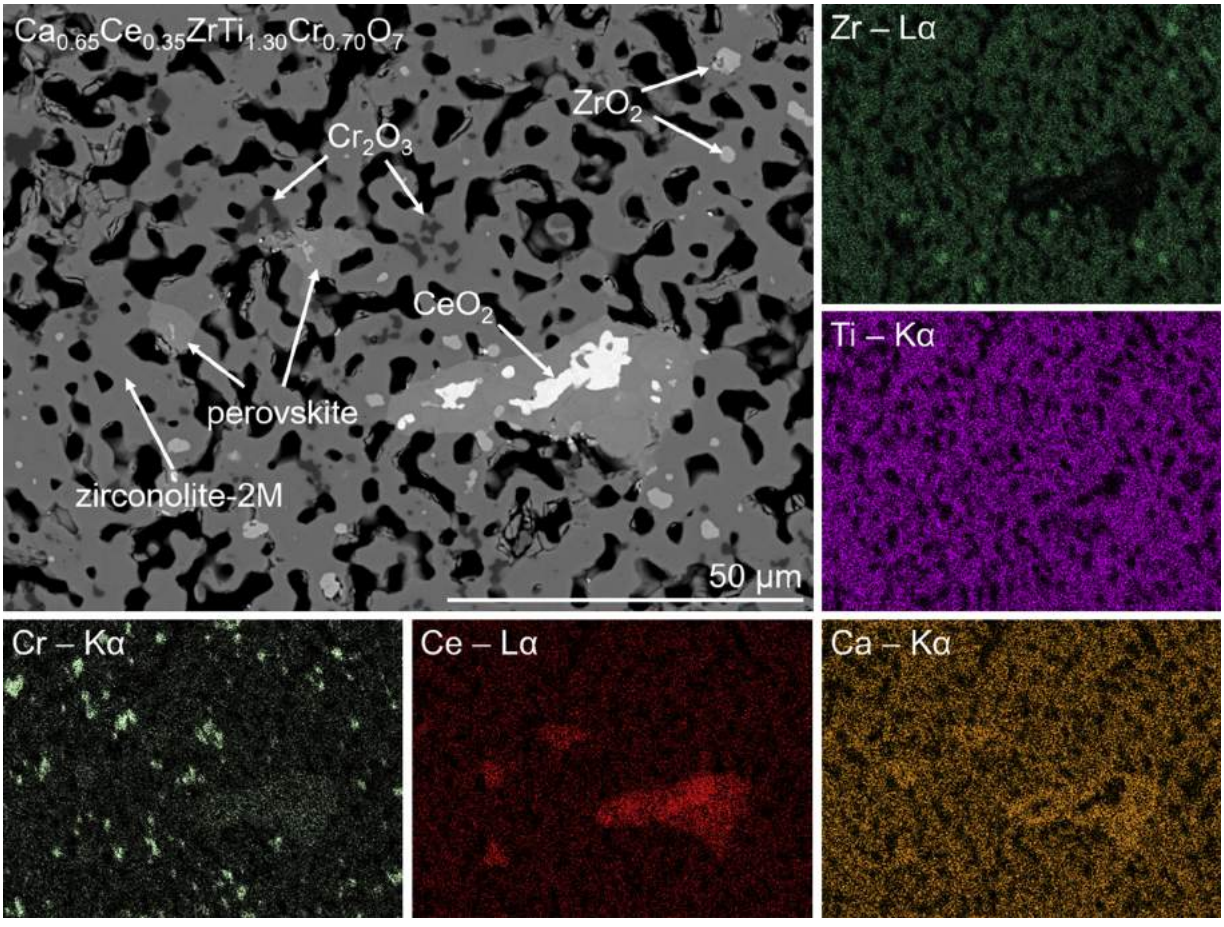

Fig. 7. Representative backscattered electron micrograph and corresponding elemental distribution for specimen with nominal composition x = 0.35. Black regions are porosity. (For interpretation of the references to colour in this figure legend, the reader is referred to the web version of this article).

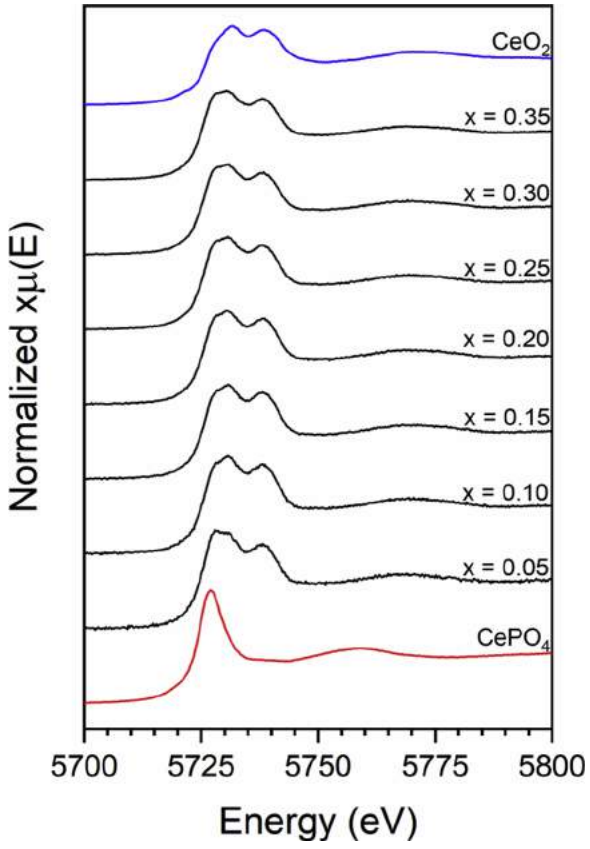

Fig. 8. XANES spectra at the Ce L_3-edge for compositions in the range $Ca_{1-x}Ce_xZrTi_{2-2x}Cr_{2x}O_7$ ($0.05 \leq x \leq 0.35$), in comparison to Ce^{4+} and Ce^{3+} standards (CeO_2 and $CePO_4$ respectively).

Table 3
Linear combination fitting of Ce L_3 XANES data relative to CeO_2 and $CePO_4$ standards.

Composition	Cerium Speciation (%)		R-factor
	Ce^{3+}	Ce^{4+}	
$Ca_{0.95}Ce_{0.05}ZrTi_{1.90}Cr_{0.10}O_7$	27.3 ± 1.1	72.7 ± 1.5	0.0119
$Ca_{0.90}Ce_{0.10}ZrTi_{1.80}Cr_{0.20}O_7$	15.7 ± 1.0	84.3 ± 1.5	0.0108
$Ca_{0.85}Ce_{0.15}ZrTi_{1.70}Cr_{0.30}O_7$	14.9 ± 0.9	85.1 ± 1.4	0.0073
$Ca_{0.80}Ce_{0.20}ZrTi_{1.60}Cr_{0.40}O_7$	16.4 ± 1.1	83.6 ± 1.5	0.0108
$Ca_{0.75}Ce_{0.25}ZrTi_{1.50}Cr_{0.50}O_7$	18.7 ± 1.0	81.3 ± 1.5	0.0096
$Ca_{0.70}Ce_{0.30}ZrTi_{1.40}Cr_{0.60}O_7$	20.4 ± 0.9	79.6 ± 1.4	0.0075
$Ca_{0.65}Ce_{0.35}ZrTi_{1.30}Cr_{0.70}O_7$	21.9 ± 0.8	78.1 ± 1.4	0.0079

was stabilised due to the reducing conditions imposed by the SPS graphite die, with 90 % reduction to the Ce^{3+} species determined by XANES. Therefore, it was understood that the SPS environment caused the partial reduction of Ce^{4+} to Ce^{3+} promoting the formation of a Ce-perovskite phase. XANES spectra for the sample corresponding to x = 0.20 processed by air sintering and RSPS, with respect to Ce^{3+} and Ce^{4+} reference compounds, are displayed in Fig. 13. The XANES features for the RSPS sample consisted of a single intense feature consistent with the Ce^{3+} reference compound. Linear combination analysis determined that a complete reduction to the Ce^{3+} species was achieved. In consideration of the reduction during SPS, the reduction of Ce^{4+} or Pu^{4+} and formation of undesirable perovskite phase may be suppressed by use of a boron nitride die [35], instead of graphite die used in this work. SEM-EDS analysis of the polished RSPS surface was in good agreement with XRD data, demonstrated in Fig. 14. A dense matrix of zirconolite-2M was observed, with multiple secondary phases

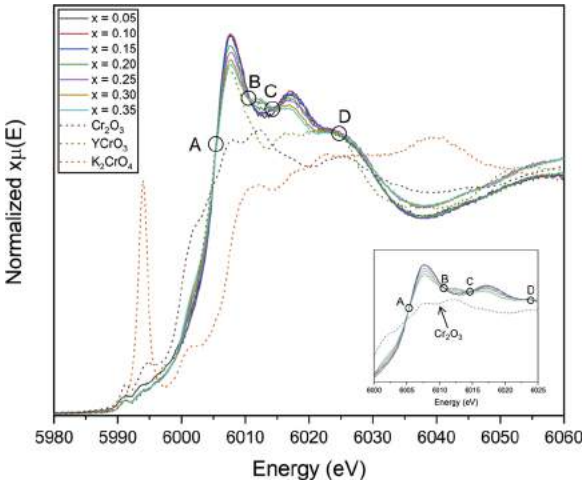

Fig. 9. Cr K XANES in the range 5980 – 6060 eV with Cr_2O_3, $YCrO_3$ and K_2CrO_4 reference compounds.

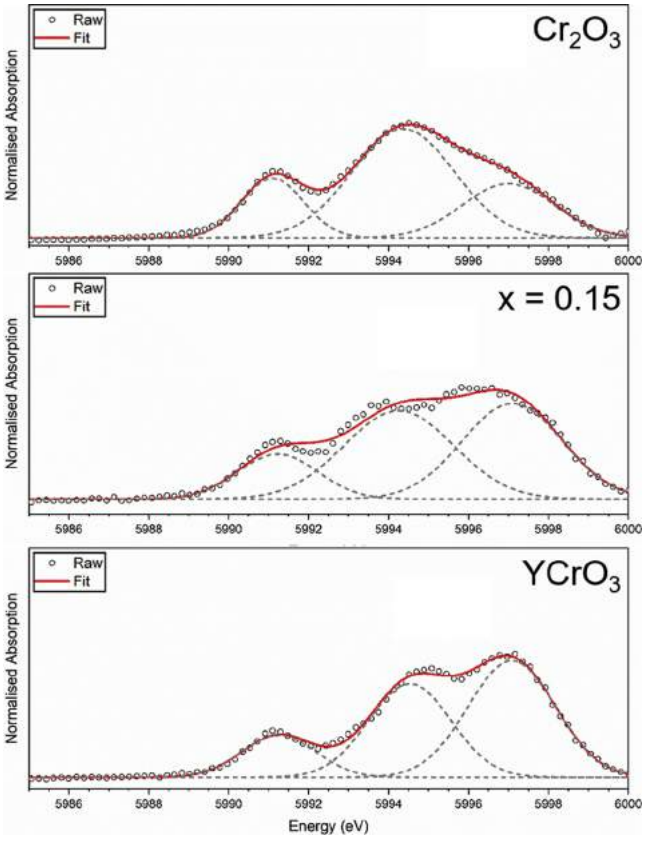

Fig. 10. Deconvolution of Cr K pre-edge region for Cr_2O_3, 'x = 0.15', and $YCrO_3$.

distinguished by variation in backscattered electron contrast. These were confirmed by EDS analysis to be Cr_2O_3, ZrO_2 and (Ca,Ce)TiO_3. Ce incorporation in the perovskite phase (or $Ca_2Ti_2O_6$) was evidenced by backscattered electron contrast, as brighter grains indicated a high Ce-fraction.

4. Conclusions

The incorporation of Ce within $CaZrTi_2O_7$ zirconolite, with Cr acting as a charge compensation species, was investigated for the Ca_{1-}

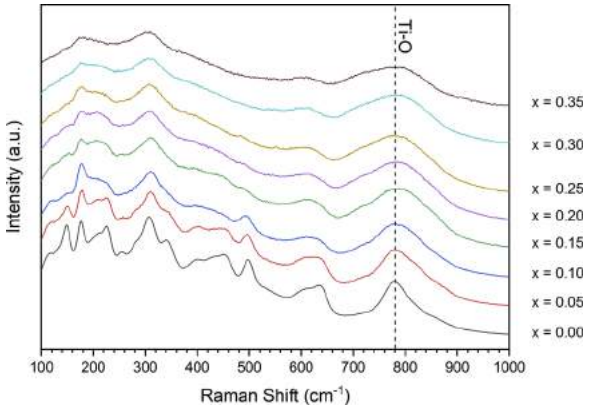

Fig. 11. Raman shift in the range 100 – 1000 cm^{-1} for $Ca_{1-x}Ce_xZrTi_{2-2x}Cr_{2x}O_7$ compositions.

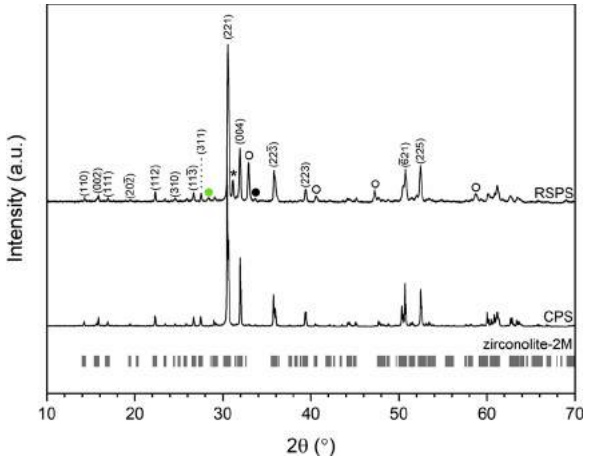

Fig. 12. Comparison of powder X-ray diffraction data of x = 0.20 composition synthesised by RSPS and CPS. $CaTiO_3$ reflections are labelled by open circles; ZrO_2 reflections are labelled by green filled circles; $Ca_2Ti_2O_6$ reflections are labelled by asterisk (*); Cr_2O_3 reflections are labelled by black filled circles. (For interpretation of the references to colour in this figure legend, the reader is referred to the web version of this article).

$_xCe_xZrTi_{2-2x}Cr_{2x}O_7$ system. The densification achieved by a cold-press and sinter method was poor, and therefore this is not a practical choice of solid solution for Pu^{4+} immobilisation from the perspective of the ceramic microstructure, despite the efficacy of Cr as a charge compensator. High porosity was evidently overcome by the application of reactive spark plasma sintering, yet a significant disruption to the phase assemblage was observed, attributed to the total reduction of Ce to Ce^{3+} and subsequent increase in the Ce-perovskite phase fraction. Electron diffraction analyses were consistent with zirconolite adopting the 2M polytype at all levels of Ce incorporation for the CPS solid solution. Powder XRD and SEM analysis confirmed that zirconolite-2M was formed as a single phase for $0.00 \leq x \leq 0.15$. Cr^{3+} was fully incorporated within the zirconolite phase up to x = 0.15, after which phase separation occurred. Ce incorporation within the perovskite phase was observed for $x > 0.15$, yet even at maximum targeted wasteloading, the phase assemblage was comprised of ~ 94 wt. % zirconolite-2M. Ce L_3 XANES data and linear combination fitting with reference compounds confirmed ~ 80 % Ce^{4+}. It was concluded from Cr K-edge XANES data that Cr was incorporated into the zirconolite phase as Cr^{3+}. Deconvolution of the Cr K XANES pre-edge region for zirconolite produced features consistent with $YCrO_3$ reference compound, inferring octahedral coordination in the zirconolite phase as expected. The potential behaviour of a Pu bearing zirconolite ceramic charge balanced with Cr^{3+} could be hypothesised using this data. Pu can be present as trivalent and tetravalent cations, similar to Ce. It was inferred from Ce L_3 XANES that Ce was distributed mainly as Ce^{4+}. Accounting for discrepancies in redox behaviour, Pu is expected to be uniformly present as Pu^{4+}, as Ce has a greater propensity to undergo auto-reduction at high processing temperatures. At values for which $0.05 \leq x \leq 0.15$, Pu^{4+} could be expected to fully partition within zirconolite-2M. However, these data imply that a conventional sintering route using Cr as a charge compensating cation may produce a microstructure with elevated porosity. This paper also highlights an important caveat for the deployment of reactive spark plasma sintering for Pu-bearing zirconolites, demonstrating the need for careful compositional design and atmosphere selection to control redox reactions.

Declaration of Competing Interest

The authors declare that they have no known competing financial interests or personal relationships that could have appeared to influence the work reported in this paper.

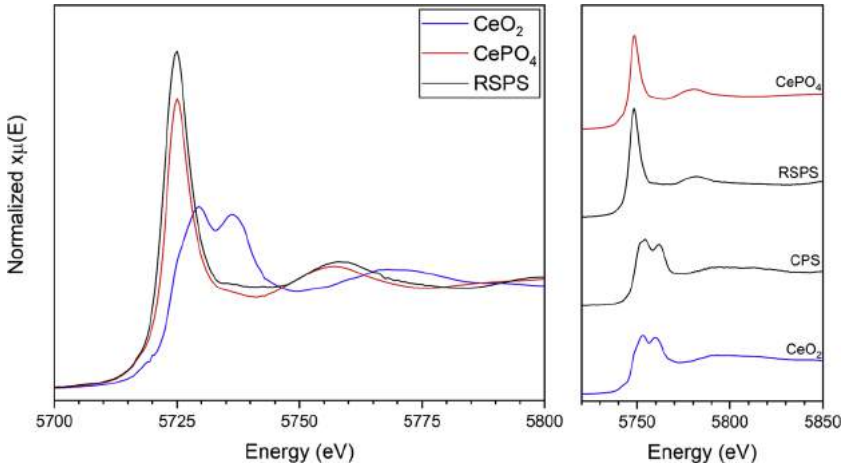

Fig. 13. Ce L_3 XANES data corresponding to $Ca_{0.80}Ce_{0.20}ZrTi_{1.60}Cr_{0.40}O_7$ processed by air sintering and RSPS, alongside CeO_2 and $CePO_4$ reference compounds.

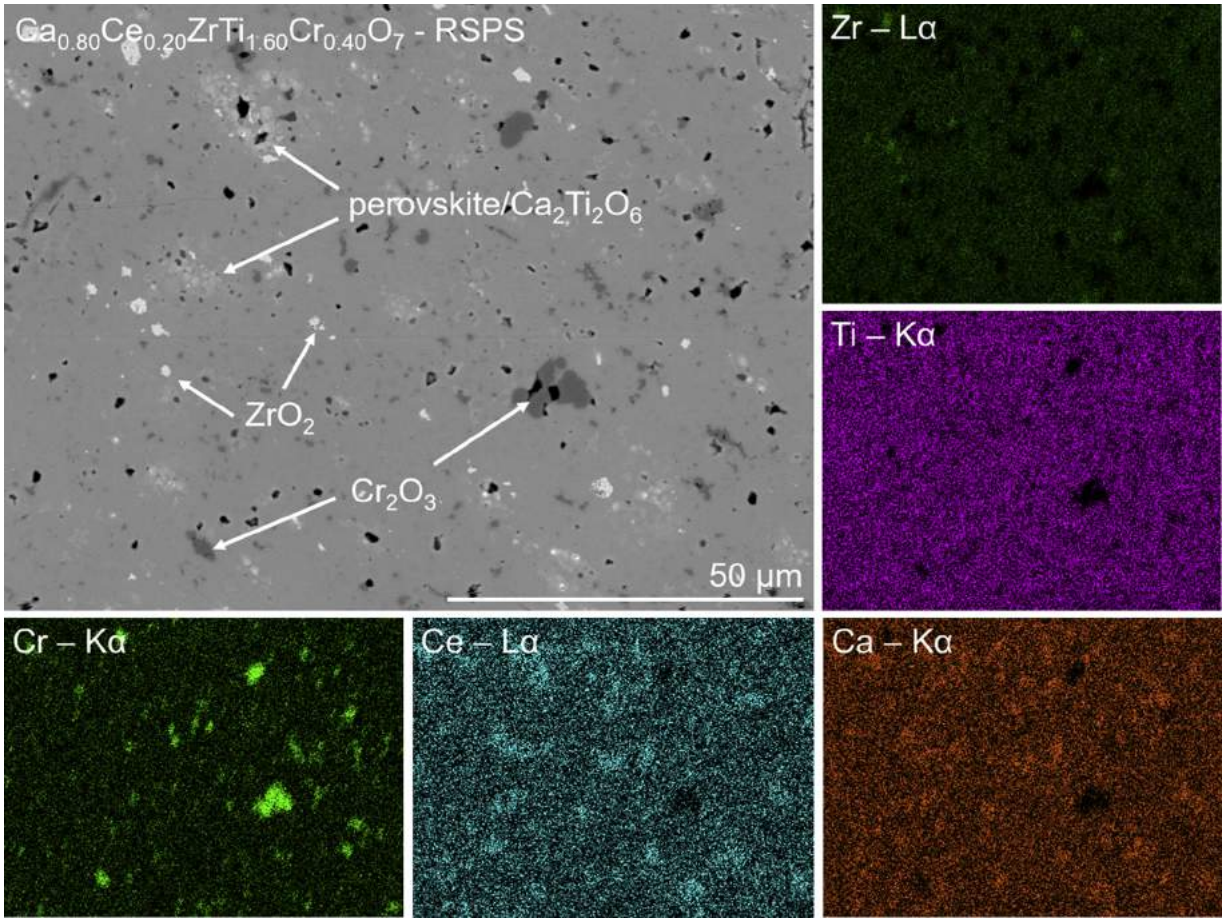

Fig. 14. Representative backscattered electron micrograph and corresponding elemental distribution for $Ca_{0.80}Ce_{0.20}ZrTi_{1.60}Cr_{0.40}O_7$ produced by RSPS.

Acknowledgements

LRB, NCH, SKS and LJG are grateful for financial support from the Nuclear Decommissioning Authority and EPSRC under grant numbersEP/M026566/1, EP/S01019X/1, EP/N017870/1 and EP/R511754/1. CLC and SML acknowledge EPSRC for funding under grant number EP/N017374/1. This research utilised the MIDAS/HADES facility at The University of Sheffield established with financial support from EPSRC and BEIS, under grant EP/T011424/1 [36]. We acknowledge Diamond Light Source for allocation of beam-time at Beamline B18 (Proposal SP24074-1). We acknowledge the Photon Factory Advisory Committee (Proposal No. 2019G586) for allocation of beam-time; the support of Yoshihiro Okamoto (Japan Atomic Energy Agency) and Noriko Usami (High Energy Accelerator Research Organization), during the experiment, is gratefully acknowledged.

References

[1] M.I. Ojovan, W.E. Lee, Introduction to Nuclear Waste Immobilisation, Elsevier Science Publishers, Amsterdam, Netherlands, 2005.
[2] N.C. Hyatt, Plutonium management policy in The United Kingdom: the need for a dual track strategy, Energy Policy 101 (2017) 303–309, https://doi.org/10.1016/j.enpol.2016.08.033.
[3] Nuclear Decommissioning Authority (UK), NDA plutonium Topic Strategy: Credible Options Technical Analysis, SAF/081208/006.2 (2009).
[4] K.P. Hart, Y. Zhang, E. Loi, Z. Aly, M.W.A. Stewart, A. Brownscombe, B.B. Ebbinghaus, W. Bourcier, Aqueous durability of titanate ceramics designed to immobilise excess plutonium, MRS Proc. 608 (1999) 353–358, https://doi.org/10.1557/proc-608-353.
[5] R.C. Ewing, Ceramic matrices for plutonium disposition, Prog. Nucl. Energy 49 (2007) 635–643, https://doi.org/10.1016/j.pnucene.2007.02.003.
[6] K.L. Smith, G.R. Lumpkin, M.G. Blackford, R.A. Day, K.P. Hart, The durability of synroc, J. Nucl. Mater. 190 (1992) 287–294, https://doi.org/10.1016/0022-3115(92)90092-y.
[7] R.C. Ewing, W.J. Weber, J. Lian, Nuclear waste disposal-pyrochlore ($A_2B_2O_7$): nuclear waste form for the immobilization of plutonium and 'minor' actinides, J. Appl. Phys. 95 (2004) 5949–5971, https://doi.org/10.1063/1.1707213.
[8] B.M. Gatehouse, I.E. Grey, R.J. Hill, H.J. Rossell, Zirconolite, $CaZr_xTi_{3-x}O_7$; Structure refinements for near-end-member compositions with x = 0.85 and 1.30, Acta Cryst. 37 (1981) 306–312, https://doi.org/10.1107/S0567740881002914.
[9] T.J. White, R.L. Segall, J.L. Hutchison, J.C. Barry, P.B. Hirsch, Polytypic behaviour of zirconolite, Proc. R. Soc. Lond. Ser. A 392 (1984) 343–358, https://doi.org/10.1098/rspa.1984.0035.
[10] A.A. Coelho, R.W. Cheary, K.L. Smith, Analysis and structural determination of Nd-substituted zirconolite-4M, J. Solid State Chem. 129 (1997) 346–359, https://doi.org/10.1006/jssc.1996.7263.
[11] M. Jafar, P. Sengupta, S.N. Achary, A.K. Tyagi, Phase evolution and microstructural studies in $CaZrTi_2O_7$-$Nd_2Ti_2O_7$ system, J. Am. Ceram. Soc. 97 (2014) 609–616, https://doi.org/10.1111/jace.12664.
[12] P.A. Bingham, R.J. Hand, M.C. Stennett, N.C. Hyatt, M.T. Harrison, The use of surrogates in waste immobilization studies: a case study of plutonium, MRS Proc. 1107 (2008) 421–428, https://doi.org/10.1557/proc-1107-421.
[13] S.-K. Sun, M.C. Stennett, C.L. Corkhill, N.C. Hyatt, Reactive spark plasma synthesis of $CaZrTi_2O_7$ zirconolite ceramics for plutonium disposition, J. Nucl. Mater. 500 (2018) 11–14, https://doi.org/10.1016/j.jnucmat.2017.12.021.
[14] A. Prasad, L. Malakkal, L. Bichler, J. Szpunar, Challenges in spark plasma sintering of cerium (IV) oxide, in: N.P. Bansal, R.H. Castro, M. Jenkins, A. Bandyopadhyay, S. Bose, A. Bhalla, J.P. Singh, M.M. Mahmoud, G. Pickrell, S. Johnson (Eds.), Processing, Properties, and Design of Advanced Ceramics and Composites II, John Wiley & Sons, Inc., New Jersey, 2018, pp. 217–224, , https://doi.org/10.1002/9781119423829.ch19.
[15] B.H. Toby, EXPGUI, a graphical user interface for GSAS, J. Appl. Crystallogr. 34 (2001) 210–213, https://doi.org/10.1107/S0021889801002242.
[16] J.A. Bearden, A.F. Burr, Reevaluation of X-ray atomic energy levels, Rev. Mod. Phys. 39 (1967) 125–142, https://doi.org/10.1103/revmodphys.39.125.
[17] H. Konishi, A. Yokoya, H. Shiwaku, H. Motohashi, T. Makita, Y. Kashihara, S. Hashimoto, T. Harami, T.A. Sasaki, H. Maeta, H. Ohno, H. Maezawa, S. Asaoka, N. Kanaya, K. Ito, N. Usami, K. Kobayashi, Synchrotron radiation beamline to study radioactive materials at the Photon Factory, Nucl. Instruments Methods Phys. Res. Sect. A 372 (1996) 322–332, https://doi.org/10.1016/0168-9002(95)01241-9.
[18] B. Ravel, M. Newville, ATHENA, ARTEMIS, HEPHAESTUS: data analysis for X-ray absorption spectroscopy using IFEFFIT, J. Synchrotron Radiat. 12 (2005) 537–541, https://doi.org/10.1107/S0909049505012719.

[19] M. Wilke, F. Farges, P.E. Petit, G.E. Brown, F. Martin, Oxidation state and coordination of Fe in minerals: an Fe K-XANES spectroscopic study, Am. Mineral. 86 (2001) 714–730, https://doi.org/10.2138/am-2001-5-612.
[20] K.R. Whittle, N.C. Hyatt, K.L. Smith, I. Margiolaki, F.J. Berry, K.S. Knight, G.R. Lumpkin, Combined neutron and X-ray diffraction determination of disorder in doped zirconolite-2M, Am. Mineral. 97 (2012) 291–298, https://doi.org/10.2138/am.2012.3848.
[21] E.R. Vance, G.R. Lumpkin, M.L. Carter, D.J. Cassidy, C.J. Ball, R.A. Day, B.D. Begg, Incorporation of uranium in zirconolite ($CaZrTi_2O_7$), J. Am. Ceram. Soc. 85 (2002) 1853–1859, https://doi.org/10.1111/j.1151-2916.2002.tb00364.x.
[22] B.M. Clark, S.K. Sundaram, S.T. Misture, Polymorphic transitions in cerium-substituted zirconolite ($CaZrTi_2O_7$), Sci. Rep. 7 (2017) 5920, https://doi.org/10.1038/s41598-017-06407-5.
[23] B.D. Begg, E.R. Vance, The incorporation of cerium in zirconolite, MRS Proc. 465 (1996) 333–340, https://doi.org/10.1557/proc-465-333.
[24] B.D. Begg, E.R. Vance, G.R. Lumpkin, Charge compensation and the incorporation of cerium in zirconolite and perovskite, MRS Proc. 506 (1997) 79–86, https://doi.org/10.1557/proc-506-79.
[25] B.D. Begg, E.R. Vance, S.D. Conradson, The incorporation of plutonium and neptunium in zirconolite and perovskite, J. Alloys Compd. 271–273 (1998) 221–226, https://doi.org/10.1016/S0925-8388(98)00058-9.
[26] N.C. Hyatt, R.R. Schwarz, P.A. Bingham, M.C. Stennett, C.L. Corkhill, P.G. Heath, R.J. Hand, M. James, A. Pearson, S. Morgan, Thermal treatment of simulant plutonium contaminated materials from the Sellafield site by vitrification in a blast-furnace slag, J. Nucl. Mater. 444 (2014) 186–199, https://doi.org/10.1016/j.jnucmat.2013.08.019.
[27] R.D. Shannon, Revised effective ionic radii and systematic studies of interatomie distances in halides and chaleogenides, Acta Cryst. 32 (1976) 751–767, https://doi.org/10.1107/s0567739476001551.
[28] S. Ould-Chikh, O. Proux, P. Afanasiev, L. Khrouz, M.N. Hedhili, D.H. Anjum, M. Harb, C. Geantet, J.-M. Basset, E. Puzenat, Photocatalysis with chromium-doped TiO_2: bulk and surface doping, ChemSusChem 7 (2014) 1361–1371, https://doi.org/10.1002/cssc.201300922.
[29] D. Cabaret, A. Bordage, A. Juhin, M. Arfaoui, E. Gaudry, First-principles calculations of X-ray absorption spectra at the K-edge of 3d transition metals: an electronic structure analysis of the pre-edge, Phys. Chem. Chem. Phys. 12 (2010) 5619–5633, https://doi.org/10.1039/b926499j.
[30] A. Salamat, P.F. McMillan, S. Firth, K. Woodhead, A.L. Hector, G. Garbarino, M.C. Stennett, N.C. Hyatt, Structural transformations and disordering in zirconolite ($CaZrTi_2O_7$) at high pressure, Inorg. Chem. 52 (2013) 1550–1558, https://doi.org/10.1021/ic302346g.
[31] R. Kaur, M. Gupta, P.K. Kulriya, S.S. Ghumman, Phase analysis and reduction behaviour of Ce dopant in zirconolite, J. Radioanal. Nucl. Chem. 322 (2019) 183–192, https://doi.org/10.1007/s10967-019-06536-3.
[32] M. Jafar, S.N. Achary, N.P. Salke, A.K. Sahu, R. Rao, A.K. Tyagi, X-ray diffraction and Raman spectroscopic investigations on $CaZrTi_2O_7$ - $Y_2Ti_2O_7$ system: delineation of phase fields consisting of potential ceramic host materials, J. Nucl. Mater. 475 (2016) 192–199, https://doi.org/10.1016/j.jnucmat.2016.04.016.
[33] B.M. Clark, P. Tumurugoti, S.K. Sundaram, J.W. Amoroso, J.C. Marra, K.S. Brinkman, Microstructures of melt-processed and spark plasma sintered ceramic waste forms, Metall. Mater. Trans. E 1 (2014) 341–348, https://doi.org/10.1007/s40553-014-0035-4.
[34] M. Sato, R. Tu, T. Goto, Preparation of pyrochlore $Ca_2Ti_2O_6$ by metal-organic chemical vapor deposition, Mater. Trans. 47 (2006) 2603–2605 https://www.jim.or.jp/journal/e/47/10/2603.html.
[35] O. Guillon, J. Gonzalez-Julian, B. Dargatz, T. Kessel, G. Schierning, J. Räthel, M. Herrmann, Field-assisted sintering technology/spark plasma sintering: mechanisms, materials, and technology developments, Adv. Eng. Mater. 16 (2014) 830–849, https://doi.org/10.1002/adem.201300409.
[36] N.C. Hyatt, C.L. Corkhill, M.C. Stennett, R.J. Hand, L.J. Gardner, C.L. Thorpe, The HADES facility for high activity decommissioning engineering & science: part of the UK national nuclear user facility, IOP Conf. Ser. Mater. Sci. Eng. 818 (2020) 012022, , https://doi.org/10.1088/1757-899x/818/1/012022.

Chapter 7

Hot Isostatic Pressing of Zirconolite Wasteforms

Authorship Contribution Statement

7.1) ‘Hot Isostatically Pressed Zirconolite Wasteforms for Actinide Immobilisation’. L. Blackburn was responsible for conceptualisation, materials preparation and characterisation, original draft preparation, reviewing and editing.

7.2) ‘Synthesis and Characterisation of HIP $Ca_{0.80}Ce_{0.20}ZrTi_{1.60}Cr_{0.40}O_7$ Zirconolite and Observations of the Ceramic-Canister Interface. L. Blackburn was responsible for conceptualisation, materials preparation and characterisation, original draft preparation, reviewing and editing.

IOP Conf. Series: Materials Science and Engineering **818** (2020) 012010 doi:10.1088/1757-899X/818/1/012010

Hot Isostatically Pressed Zirconolite Wasteforms for Actinide Immobilisation

L R Blackburn[1], L J Gardner[1], S K Sun[1], E R Maddrell[2], M C Stennett[1], C L Corkhill[1], N C Hyatt[1*]

[1]Immobilisation Science Laboratory, Department of Materials Science and Engineering, University of Sheffield, S1 3JD, UK.
[2]National Nuclear Laboratory, Workington, Cumbria, CA14 3YQ, UK.

*n.c.hyatt@sheffield.ac.uk

Abstract. In order to demonstrate the deployment of Hot Isostatic Pressing (HIP) for the immobilisation of Pu stocks and residues, a series of active and inactive zirconolite formulations have been processed and characterised. In this instance, Ce, U, and Th have been applied as chemical surrogates for Pu^{4+}. A range of formulations targeting isovalent Zr^{4+} site substitution (*i.e.* to simulate $CaZr_{1-x}Pu_xTi_2O_7$) have been processed by HIP and characterised by powder X-ray diffraction, and scanning electron microscopy, in order to determine surrogate partitioning between the host zirconolite phase, and accessory phases that may have formed during the HIP process.

1. Introduction

The United Kingdom holds a stockpile of civil separated plutonium that is forecast to exceed 140 teHM (tonnes equivalent heavy metal), subsequent to the completion of domestic reprocessing operations [1]. Immobilisation of Pu within a ceramic matrix such as zirconolite, prototypically $CaZrTi_2O_7$, may be a suitable pathway to disposition. Zirconolite has demonstrated extensive chemical flexibility with regards to feedstock chemistry, and as such is the dominant actinide-bearing phase in the Synroc formulation, developed for the immobilisation of high level waste (HLW) [2]. Pu^{4+} may be accepted into solid solution through Zr^{4+} site, *i.e.* $CaZr_{1-x}Pu_xTi_2O_7$ [3]. The Ca^{2+} site has also been demonstrated to accommodate Pu^{4+} through the addition of a suitable lower valence charge balancing species such as Al^{3+} (*e.g.* $Ca_{0.9}Pu_{0.1}ZrTi_{1.8}Al_{0.2}O_7$) [4]. The preferred final wasteform for Pu would require a robust processing route, insensitive to feed chemistry, with high throughput and waste loading.

Hot Isostatic Pressing (HIP) utilizes the simultaneously application of high temperature and isostatic pressing (typically through the use of an inert medium such as Ar gas) to consolidate and sinter materials to near-theoretical density. The HIP process is insensitive to the chemical properties of the feedstock, and produces minimal secondary waste, and is therefore a good candidate thermal treatment for the immobilisation of Pu stocks and residues [5]. In the current work, we report laboratory scale trials for zirconolite wasteforms processed by HIP. In this instance, CeO_2, UO_2 and ThO_2 were employed as chemical surrogates for PuO_2.

2. Materials synthesis and characterisation

2.1. Materials synthesis

Zirconolites were batched from oxide precursors ($CaTiO_3$, ZrO_2, TiO_2, CeO_2, ThO_2, UO_2) targeting nominal stoichiometry $CaZr_{0.8}Ce_{0.2}Ti_2O_7$, $CaZr_{0.8}U_{0.2}Ti_2O_7$ and $CaZr_{0.8}Th_{0.2}Ti_2O_7$. Precursor materials were optimised for HIP according to our previous investigations considering zirconolite glass-ceramic wasteforms [6]. Materials were batched and homogenised by high intensity ball milling (400 rpm, ~ 40 min), with the addition of isopropanol as a milling agent. Powder cakes were dried and passed through a sieve to break up agglomerates. Materials were then calcined at 600 ˚C in air for 12 h (Ar gas was used in the case of $CaZr_{0.8}U_{0.2}Ti_2O_7$ in order to maintain U^{4+}), before being pressed into the walls of a HIP can (316 stainless steel), under ~ 1 t uniaxial pressure. The cans were then evacuated at 300 ˚C for a further 12 h until approximately 50 mTorr pressure was achieved. The HIP cans were then hermetically sealed and placed into a AIP 630-H HIP unit and consolidated at 1300 ˚C and 100 MPa for 4 h.

2.2. Materials characterisation

A portion of the bulk ceramic was cut free from stainless steel containment and prepared for microchemical analysis using a Hitachi TM3030 scanning electron microscopy (SEM), fitted with a Bruker Quantax Energy Dispersive X-ray Spectrometer (EDS) for compositional analysis. The sample was mounted in cold setting resin and polished to a 1 μm optical finish using incremental grades of diamond suspension paste. SEM analysis was undertaken with a 15 kV accelerating voltage, and a working distance of ~ 8mm. A specimen was also mechanically ground prior to powder X-ray diffraction analysis using a Bruker D2 Phaser, using Cu Kα radiation ($\lambda = 1.5418$ Å). This was fitted with a Lynxeye position sensitive detector. Data were acquired in the range $5^\circ \leq 2\theta \leq 80^\circ$, with step size 0.02˚.

3. Results

3.1. $CaZr_{0.8}Ce_{0.2}Ti_2O_7$

The HIPing process was successful in all instances, and an example of a canister pre and post-processing is displayed in Figure 1. Powder X-ray diffraction data for $CaZr_{0.8}Ce_{0.2}Ti_2O_7$ are displayed in Figure 2. Refinement of the powder diffraction profile determined that zirconolite-2M was formed as the major crystalline phase – these reflections are indexed by relevant (hkl) values. Reflections consistent with the zirconolite-4M polytype phase were also observed, noted by (002) and (008) supercell reflections at $2\theta = 7.8^\circ$ and $2\theta = 31.1^\circ$, respectively. The formation of the zirconolite-4M polytype is consistent with previous observations, with the incorporation of tetravalent species within the Zr^{4+} site [7,8]. A considerable inventory of perovskite (parent structure $CaTiO_3$) was also stabilised; the formation of accessory perovskite phases is commonly attributed to the partial reduction of Ce^{4+} to Ce^{3+} [7,9]. XANES data (not shown) confirmed that a considerable fraction of Ce^{4+} was reduced to the Ce^{3+} species. EDS spotmap analysis of the perovskite phase, in this instance, confirmed the partial retention of Ce. Microscopic analyses (Figure 3) were consistent with powder XRD data. Zirconolite-4M and perovskite were clearly identified, distinguished by variation in backscattered electron contrast; these phases were consistently enriched in Ce.

Figure 1. Photograph of HIP canister pre and post-processing at 1300 ˚C and 100 MPa for 4 h.

3.2. $CaZr_{0.8}U_{0.2}Ti_2O_7$

When targeting nominal stoichiometry $CaZr_{0.8}U_{0.2}Ti_2O_7$, zirconolite-2M was formed as the dominant U-bearing phase, as determined by powder X-ray diffraction (Figure 2). Weak reflections indicative of a $(Zr,U)O_2$ solid solution were also identified. An ancillary perovskite phase was evidenced by powder XRD data (diagnostic reflection 2θ = 33.1˚) however, this was not clearly identified by SEM analysis. The zirconolite-4M polytype was not observed to form, contrary to experimental design and previous observations by Vance *et al*. [8]. Furthermore, UO_2 did not appear to be fully accommodated within the zirconolite phase, inferred by reflections consistent with the cubic UO_2 structure present in XRD analyses; SEM observations confirmed that free UO_2 was distributed throughout the microstructure (Figure 4). The $(Zr,U)O_2$ solid solution appeared to form at the rim of undigested UO_2 relics within the microstructure.

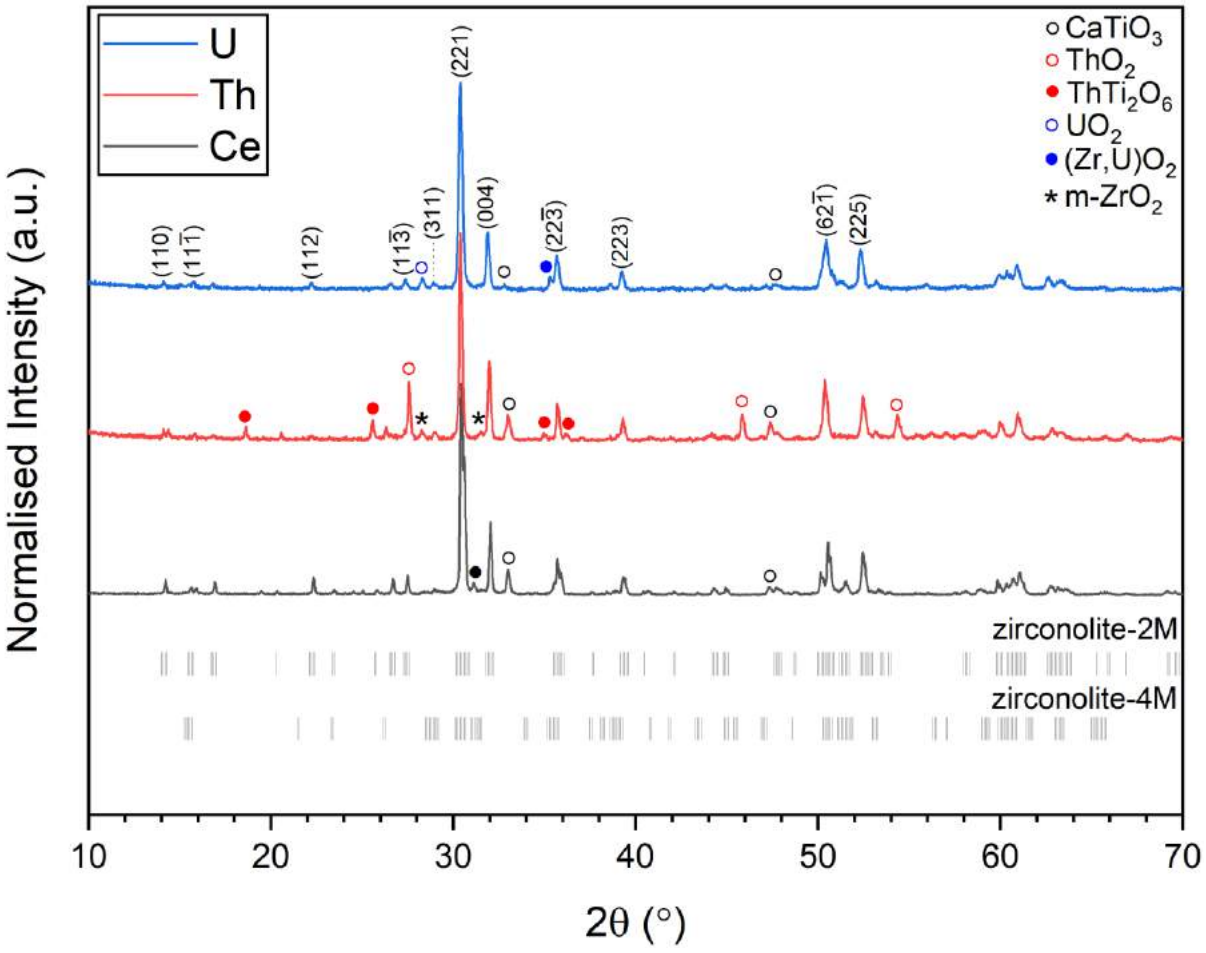

Figure 2. Powder X-ray diffraction data for $CaZr_{0.8}Ce_{0.2}Ti_2O_7$, $CaZr_{0.8}U_{0.2}Ti_2O_7$ and $CaZr_{0.8}Th_{0.2}Ti_2O_7$ processed by HIP at maximum temperature 1300 ˚C, at 100 MPa for 4 h. Zirconolite-2M reflections are labelled by (hkl) values; zirconolite-4M reflections are labelled by closed circles (●).

3.3. $CaZr_{0.8}Th_{0.2}Ti_2O_7$

Phase determination for $CaZr_{0.8}Th_{0.2}Ti_2O_7$ from powder XRD data are displayed in Figure 2. Diagnostic reflections consistent with zirconolite-2M were identified; these are labelled by appropriate (hkl) values. Intense (111) and (022) reflections, coherent with the fluorite structured ThO_2 phase, were clearly evidenced at 2θ = 27.5˚ and 2θ = 45.7˚, showing that ThO_2 was not fully incorporated within the zirconolite phase. This was confirmed by SEM analyses – see Figure 5. An ancillary perovskite phase was also clearly evidenced by powder XRD and SEM measurements. The zirconolite-4M polytype did not appear to form; a secondary thorutite phase, with ideal stoichiometry $ThTi_2O_6$, was stabilized. This phase was distributed around the rim of undigested ThO_2 within the microstructure as is illustrated in Figure 5.

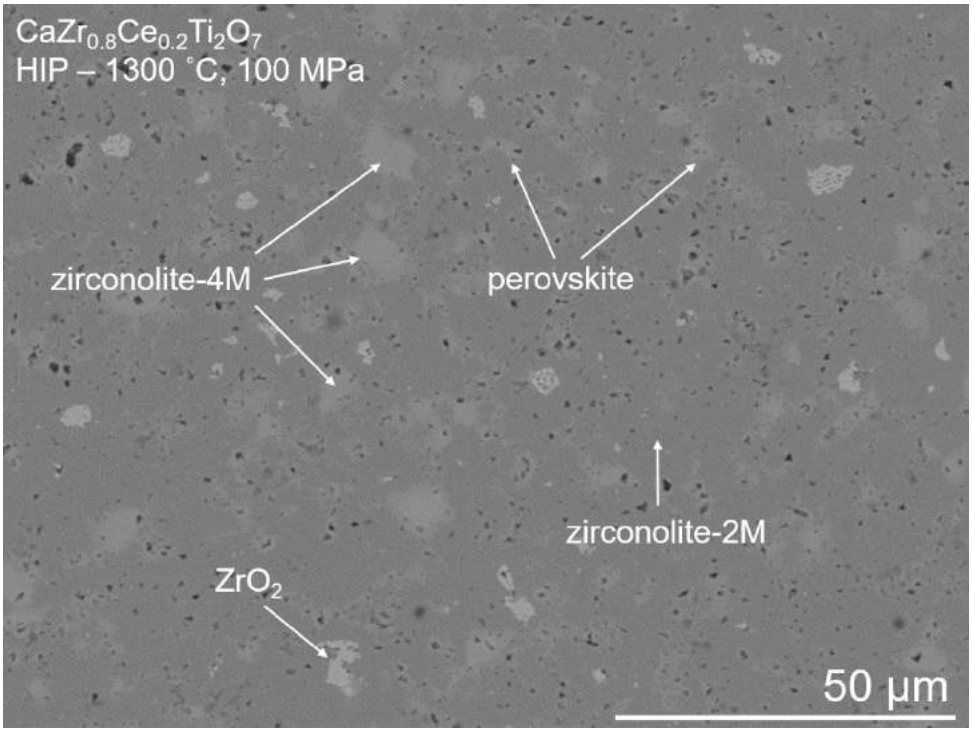

Figure 3. Representative backscattered electron micrograph of the $CaZr_{0.8}Ce_{0.2}Ti_2O_7$ microstructure formed by HIP at 1300 ˚C at 100 MPa

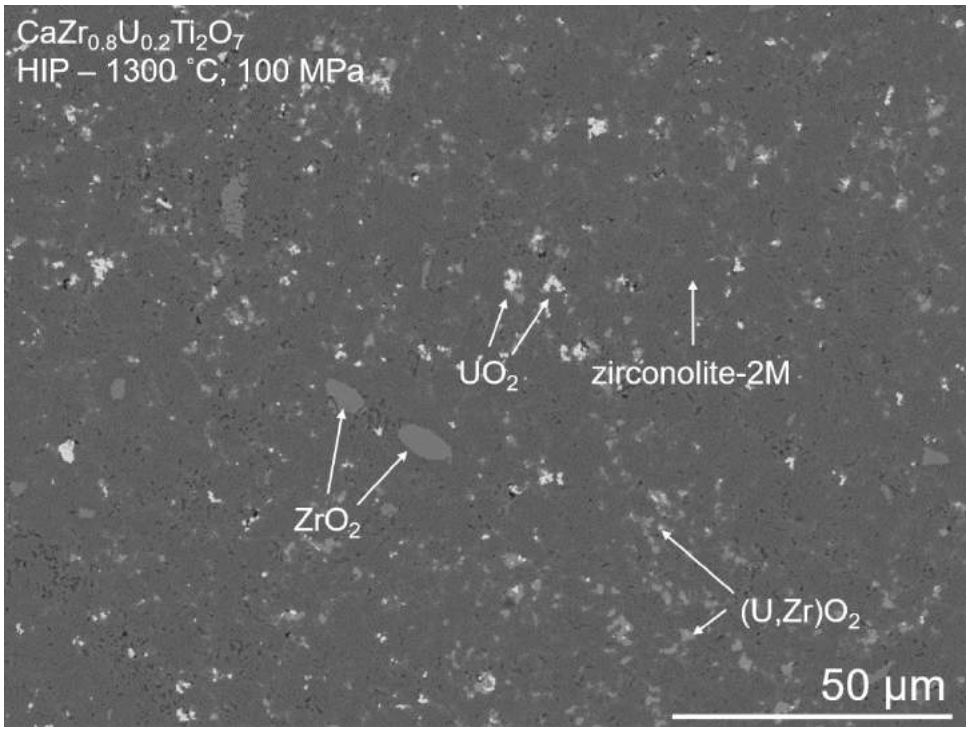

Figure 4. Representative backscattered electron micrograph of the $CaZr_{0.8}U_{0.2}Ti_2O_7$ microstructure formed by HIP at 1300 ˚C at 100 MPa

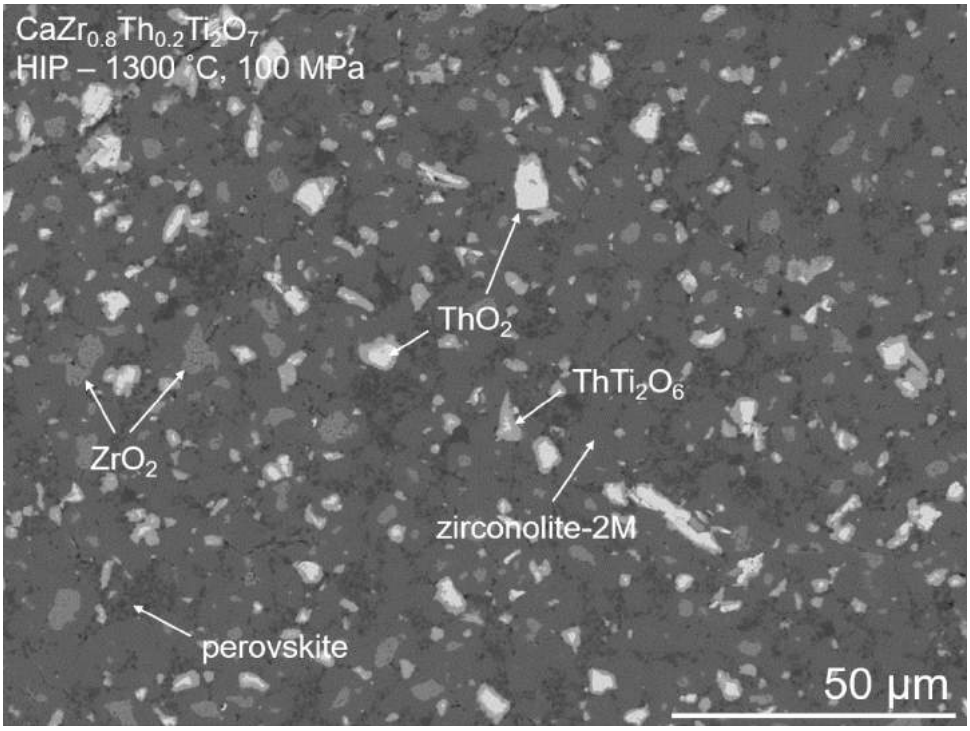

Figure 5. Representative backscattered electron micrograph of the $CaZr_{0.8}Th_{0.2}Ti_2O_7$ microstructure formed by HIP at 1300 ˚C at 100 MPa

4. Conclusions

Zirconolite wasteforms incorporated with CeO_2, UO_2 and ThO_2, chemical surrogates for PuO_2, have been processed by laboratory scale HIP. The processing parameters utilised a maximum temperature of 1300 ˚C, under an Ar pressure of 100 MPa; these conditions were held for a dwell time of 4 h. A mixture of zirconolite-2M and zirconolite-4M polytypes were observed when targeting nominal formulation $CaZr_{0.8}Ce_{0.2}Ti_2O_7$; a notable fraction of Ce-perovskite was also stabilised. The formation of perovskite is undesirable, due to inferior chemical durability with respect to the target zirconolite phase [10]. The crystallisation of zirconolite-4M was not observed in the case of $CaZr_{0.8}U_{0.2}Ti_2O_7$ or $CaZr_{0.8}Th_{0.2}Ti_2O_7$, due to the incomplete accommodation of UO_2 and ThO_2 within the zirconolite phase. The incorporation of UO_2 and ThO_2 within zirconolite stabilized secondary $(Zr,U)O_2$ and $ThTi_2O_6$ phases, respectively. The use of multiple surrogates may allow the imply the possible localization of Pu within a similar system. The reducing conditions imposed by the HIP environment may promote the formation of Pu^{3+}, and subsequent partitioning within the ancillary perovskite phase, decreasing the wasteform stability under hydrothermal conditions. These data demonstrate the need for careful phase design, in order to suppress the formation of deleterious accessory phases.

5. References

[1] Nuclear Decommissioning Authority (NDA), *Progress on Plutonium Consolidation, Consolidation, Storage and Disposition*, 2019.
[2] Ringwood A E, Oversby V M, Kesson SE, Sinclair W, Ware N, Hibberson W and Major A 2005 *Nucl. Waste Manag.* **2** 287.
[3] Begg B D, Day R A and Brownscombe A 2001 *Mat. Res. Soc. Symp. Proc*. **663** 1.
[4] Begg B, Vance E. and Conradson S. 1998 *J Alloys Compd.* **271–273**, 221.
[5] Maddrell E. 2012 *Chem. Eng. Res. Des.* **91** 735.
[6] Thornber S, Maddrell E, Stennett M C and Hyatt N C, 2016, in *Proceedings of the Waste Management Symposium 2016*, Phoenix, AZ, USA, 6 – 10 March 2016, 16581.

[7] Clark B M, Sundaram S K and Misture S T 2017 *Sci. Rep.* **7** 2.
[8] Vance E R, Lumpkin G R, Carter M L, Cassidy D J, Ball C J, Day R A and Begg B, 2002 *J. Am. Ceram. Soc.* **85** 1853.
[9] Begg B D and Vance E R, 1997 *Mat. Res. Soc. Symp. Proc.* **465** 333.
[10] McGlinn P J, Hart K P, Loi E H and Vance E R, 1995 *Mat. Res. Soc. Symp. Proc.* **353** 847.

Acknowledgement
We are grateful for financial support from the Nuclear Decommissioning Authority and EPSRC under grant numbers EP/201019X/1, EP/N017870/1 and EP/R511754/1. This research utilised the HADES/MIDAS facility at the University of Sheffield established with financial support from EPSRC and BEIS, under grant EP/T011424/1.

MRS Advances
https://doi.org/10.1557/s43580-021-00055-8

ORIGINAL PAPER

Synthesis and characterisation of HIP $Ca_{0.80}Ce_{0.20}ZrTi_{1.60}Cr_{0.40}O_7$ zirconolite and observations of the ceramic–canister interface

Lewis R. Blackburn[1] · Max R. Cole[1] · Laura J. Gardner[1] · Daniel J. Bailey[1] · Merve Kuman[1] · Amber R. Mason[1] · Shi-Kuan Sun[1] · Ewan R. Maddrell[2] · Martin C. Stennett[1] · Claire L. Corkhill[1] · Neil C. Hyatt[1]

Received: 24 December 2020 / Accepted: 2 April 2021

Abstract

A sample of zirconolite with nominal composition $Ca_{0.80}Ce_{0.20}ZrTi_{1.60}Cr_{0.40}O_7$ was processed via Hot Isostatic Pressing (HIP), with a dwell temperature and pressure of 1320 °C/100 MPa maintained for 4 h. The produced wasteform was characterised by powder XRD, SEM–EDS, Ce L_3 and Cr K-edge XANES. A significant portion of the Ce inventory did not fully partition within the zirconolite phase, instead remaining as CeO_2 within the microstructure. Inspection of the stainless steel–ceramic interface detailed the presence of an interaction region dominated by a Cr-rich oxide layer. No significant Cr or Fe migration was observed, although a greater concentration of perovskite was observed at the periphery, relative to the bulk ceramic matrix. The X-ray absorption features of Cr remained analogous with Cr^{3+} accommodation within TiO_6 octahedra in the zirconolite matrix. The absorption edge of Ce was comprised of contributions from zirconolite-2M and unincorporated CeO_2, with an average oxidation state of $Ce^{3.9+}$. As zirconolite-2M accounted for > 92 wt% of the overall phase assemblage, it is clear that the dominant oxidation state of Ce in this phase was Ce^{4+}.

Introduction

In the United Kingdom, aqueous reprocessing of spent nuclear fuel (SNF) has afforded a significant inventory of PuO_2, forecast to amount to 140 teHM (tonnes heavy metal equivalent), representing a significant decommissioning effort and a unique challenge with respect materials degradation [1]. Immobilisation of the bulk Pu inventory through a campaign of hot isostatic pressing (HIP), prior to geological disposal, is considered a credible pathway to disposition. Zirconolite ceramics (ideally $CaZrTi_2O_7$) are considered a potential host matrix for immobilisation of Pu; the crystal structure may accept a wide variety of tri- and tetravalent rare earth and actinide species in solid solution, with aqueous durability superior to that of closely related pyrochlore ($Gd_2Ti_2O_7$) and brannerite (UTi_2O_6) phases [2]. Zirconolite is considered to be a derivative of the anion-deficient fluorite superstructure, with the parent zirconolite-2M structure crystallising with monoclinic symmetry over the compositional range $CaZr_xTi_{3-x}O_7$ ($0.8 < x < 1.3$), in the space group C2/c [3]. The aristotype is comprised of alternating layers of Ca^{2+} and Zr^{4+} cation polyhedra, coordinated 8- and sevenfold to oxygen, respectively, interspaced with corner sharing TiO_6 arranged in a topology similar to that of hexagonal tungsten bronze (HTB). Zirconolite may accept actinide cations, such as Pu^{4+} in solid solution via isovalent substitution i.e. $CaZr_{1-x}Pu_xTi_2O_7$ or by a coupled substitution by which Pu^{4+} is accommodated in the Ca^{2+} site, facilitated by the incorporation of a lower valence charge balancing species e.g. $Ca_{1-x}Pu_xZrTi_{2-2x}Cr_{2x}O_7$. We recently investigated the feasibility of Cr^{3+} as a charge balancing species, targeting $Ca_{1-x}Ce_xZrTi_{2-2x}Cr_{2x}O_7$, utilising Ce as a Pu surrogate, through two distinct ceramic processing routes: a conventional cold press and sinter method (CPS), and a novel reactive spark plasma sintering (RSPS) methodology [4]. Whilst the CPS route yielded a single phase product in the range $0.05 \leq x \leq 0.15$, further substitution of Ce promoted the formation of a Ce-rich perovskite ($CaTiO_3$) phase, facilitated by partial Ce^{3+} speciation, and unincorporated CeO_2 and Cr_2O_3 above $x = 0.25$. The formation of an accessory perovskite

✉ Lewis R. Blackburn
lewis.blackburn@sheffield.ac.uk

✉ Neil C. Hyatt
n.c.hyatt@sheffield.ac.uk

[1] Immobilisation Science Laboratory, Department of Materials Science and Engineering, University of Sheffield, Sir Robert Hadfield Building, Mappin Street, Sheffield S13JD, UK

[2] National Nuclear Laboratory, Workington CA201PJ, Cumbria, UK

phase would reduce the overall wasteform performance, as this phase is known to exhibit reduced aqueous durability relative to zirconolite [5]. Nevertheless, a yield of ~ 94 wt% zirconolite-2M was obtained when targeting $x = 0.35$, corresponding to approximately 25 wt% Pu loading in the corresponding solid solution. All specimens prepared by the CPS method presented a highly porous microstructure. RSPS was therefore applied to achieve complete sintering, since this technique has previously been utilised to produce zirconolite with near theoretical density [6]. Whilst RSPS produced ceramic bodies with no significant porosity, the conditions were sufficient to entirely reduce the Ce inventory to Ce^{3+}, resulting in disruption of the target phase assemblage, favouring Ce-perovskite as an accessory phase. Hot isostatic pressing is the favoured thermal processing route for disposition of the bulk Pu inventory, and has recently been investigated for both zirconolite ceramic and glass–ceramic matrices, using a multitude of Pu surrogates, and indeed Pu validation trials have been performed [7–10]. HIP processing involves the simultaneous application of high temperatures (> 1300 °C) and isostatic pressure (> 100 MPa) via an inert Ar gas medium, to a loosely packed ceramic precursor material pressed into the walls of a hermetically sealed overpack, typically Ni metal or high grade stainless steel. This offers distinct advantages with respect to conventional sintering and RSPS, as the application of isostatic pressure during processing affords elimination of porosity, whilst producing minimal secondary effluent streams and remaining insensitive to the physical and chemical nature of the feedstock material [11]. In the present work, we investigate the feasibility of Cr^{3+} as a charge compensation species, targeting $Ca_{0.80}Ce_{0.20}ZrTi_{1.60}Cr_{0.40}O_7$ as to remain analogous to our previous studies of this system. We also provide a characterisation of the ceramic–canister interface.

Experimental methods

Materials synthesis

A zirconolite ceramic with nominal composition $Ca_{0.80}Ce_{0.20}ZrTi_{1.60}Cr_{0.40}O_7$ was fabricated by hot isostatic pressing, with the view to use Ce^{4+} as a structural surrogate for Pu^{4+}. This composition was selected since it would afford an approximate 15 wt% incorporation rate of Pu. Commercial metal oxide precursors $CaTiO_3$ (Sigma-Aldrich, > 99.9%), ZrO_2 (Sigma-Aldrich, > 99.9%), CeO_2 (Acros Organics, > 99.9%), TiO_2 (rutile, Sigma-Aldrich, > 99.9%) and Cr_2O_3 (Sigma-Aldrich, > 99.9%) were dried and batched according to desired composition, intimately mixed by planetary milling at 500 rpm for 20 min, using ZrO_2 milling media and isopropanol as a milling agent. Powder slurries were discharged and dried at 80 °C overnight to evaporate excess solvent, prior to calcination at 600 °C for 12 h. Compositions were then pressed into the walls of a 316 stainless steel HIP canister under uniaxial pressure, ensuring uniform packing density. The HIP canisters were machined with internal diameter 22 mm and can wall thickness of 2 mm. The canisters were then heated under vacuum at 300 °C until an internal canister pressure of ~ 7 Pa was reached, before crimping and welding shut to attain a hermetic seal. The canisters were then placed into a AIP6-30H HIP unit and processed at 1320 °C, with a 100 MPa dwell pressure maintained for 4 h, with inert Ar gas introduced into the pressure vessel as the pressure transfer medium.

Materials characterisation

The processed canister was retrieved and sectioned using a Buelher IsoMet 1000 low speed saw, with material extracted from the bulk and the stainless steel-ceramic interface preserved for analysis. Powder X-ray diffraction (XRD) analysis was performed using a Bruker D2 Phaser fitted with a Lynxeye position sensitive detector and Ni filter. Data were acquired using a Cu Kα source ($\lambda = 1.5418$ Å) in the range $5° \leq 2\theta \leq 80°$ with a stepsize of 0.02°. Powder XRD data were refined by the Rietveld method, using the GSAS package with EXPGUI interface [12]. The bottom section of the canister was set in epoxy resin and polished to a 1 µm optical finish, permitting microanalysis of both the bulk ceramic material and the exterior can–ceramic interface. Scanning electron microscopy (SEM) analysis was performed using a FEI Inspect f50 operating at 20 kV accelerating voltage and 10.6 mm working distance. Ce L_3 and Cr K-edge X-ray absorption near edge spectroscopy (XANES) data were collected at beamline BL-27 at the Photon Factory (PF) accelerator light source (Tsukuba, Japan). The optical arrangement consists of a double crystal Si(111) monochromator and slits were used to reduce the size of the beam to 3 mm in the horizontal and 1 mm in the vertical. Spectra were recorded between 5590–5990 eV and 5523–6154 eV in energy steps of 0.25 eV using an acquisition time of 50 ms $step^{-1}$ for Cr K and Ce L_3 edges, respectively. Data were collected alongside a series of reference compounds, representative of Ce and Cr in a variety of valence states and coordination environments.

Results and discussion

Characterisation of bulk zirconolite ceramic matrix by XRD and SEM

The HIP processing cycle produced a high density monolith, visually black in colour, with no evidence of loss of containment. Powder XRD data for material retrieved

from the bulk of the HIP can is displayed in Fig. 1. Intense reflections, corresponding in position and intensity to the target zirconolite-2M phase, were identified. The lattice parameters corresponding to the zirconolite-2M phase were calculated by Rietveld refinement to be: $a = 12.4499(7)$ Å, $b = 7.2457(4)$ Å, $c = 11.3798(6)$ Å, $\beta = 100.591(6)°$ and $V = 1009.06(8)$ Å^3. Accessory phases $CaTiO_3$ (~ 0.8 wt%), ZrO_2 (~ 1.1 wt%), CeO_2 (~ 3.9 wt%) and Cr_2O_3 (~ 1.9 wt%) were also distinguished (precision ± 0.1 wt%). Whilst the material densified with a comparable quantity of perovskite reported for the corresponding CPS sample (~ 1.2 wt%) [4], incomplete digestion of the CeO_2 surrogate inventory within the wasteform was observed to an unsatisfactory degree. SEM analysis of the bulk microstructure detailed a dense morphology consistent with those previously characterised for zirconolite produced by HIP [7]. A matrix of zirconolite-2M was observed with medium grey-scale contrast, with accessory phases clearly distinguished from the bulk through backscattered electron contrast, alongside some minor porosity (black regions in Fig. 2). Relics of undigested CeO_2 were clearly evidenced with bright contrast throughout the ceramic matrix, with a clear reaction rim indicating that the reaction did not achieve equilibrium under the imposed HIP conditions. The composition of the reaction rims was consistent with Ce-rich perovskite $(Ca,Ce)TiO_3$, in agreement with powder XRD data, or potentially $CaCeTi_2O_7$, although reflections consistent with this pyrochlore structured phase were not evidenced by diffraction data.

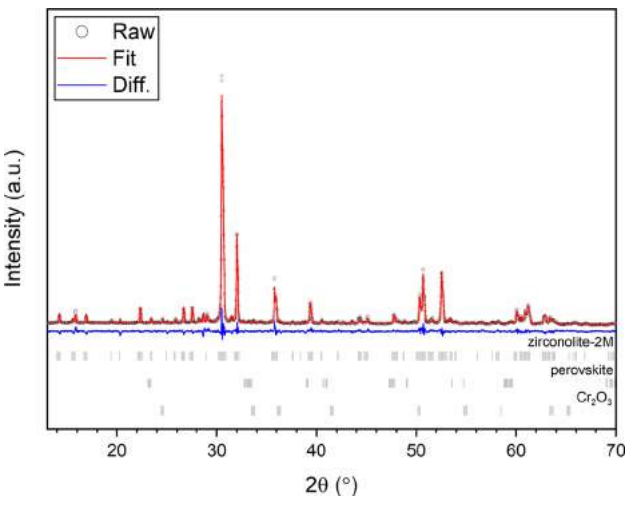

Fig. 1 Powder XRD data for $Ca_{0.80}Ce_{0.20}ZrTi_{1.60}Cr_{0.40}O_7$ processed via HIP at 1320 °C with a dwell pressure of 100 MPa maintained for 4 h

Examination of ceramic–canister interface

A cross-sectional backscattered electron micrograph, and corresponding elemental mapping of the interface between the stainless steel HIP-canister and the ceramic matrix is shown in Fig. 3, allowing a detailed interpretation of the interaction region. The interior HIP-can region did not evidence any significant diffusion of constituent elements beyond the layer marked 'interface' in Fig. 3, as demonstrated by Ni and Fe element maps. The HIP can did contain some discrete Cr_2O_3 oxides scattered adjacent to the interface. The interface region was consistently measured to be 5–8 µm in width across the specimen, and was dominated in composition by a Cr-rich oxide, with minor Fe and trace Ti evidenced by EDS analysis. The formation of the Cr-rich interface layer was considered to be the effect of Cr/Fe diffusion from the HIP canister and subsequent oxidation, as had been previously described for stainless steel–SYNROC interactions under comparable conditions [13]. Nevertheless, the composition of the interface region was not entirely consistent with those described previously for pyrochlore-rich SYNROC and zirconolite-rich wasteforms. For example, Li et al. confirmed that Fe^{2+} was the main element to diffuse from the can material, partitioning within zirconolite and hollandite ($BaAl_2Ti_6O_{16}$), replacing Ca/Ti and Al, respectively, however it was noted that Fe^{2+} preferentially entered the Ti site in zirconolite [13]. Zhang et al. described similar features, with Fe and Cr diffusion into the zirconolite phase [14]. The composition of the interface region is generally more heterogeneous than the data presented in the present work, dominated by Fe diffusion into the wasteform. For example, Zhang et al. described five distinct subsections of the interface, one of which was rich in Fe adjacent to the bulk ceramic matrix, whereas the interface for $Ca_{0.80}Ce_{0.20}ZrTi_{1.60}Cr_{0.40}O$ appears to be comprised of just three distinct layers [15]. Close inspection of the Fe EDS data did reveal a thin reaction layer rich in Fe relative to Cr, however Fe diffusion did not appear to influence the local chemistry of the zirconolite phase. The distinct lack of an Fe-rich region in the interaction layer is presumably due to the high concentration of Cr present in the wasteform matrix, with subsequent diffusion into the interface. The primary observation from these data is that the diffusion and subsequent oxidation of Cr and Fe from the canister material did not appear to significantly destabilise the local phase assemblage in the ceramic microstructure, although it is evident that undigested CeO_2 was concentrated towards the bulk of the ceramic matrix, likely the result of local redox chemistry favouring slightly reducing conditions at the periphery, resulting from Cr and Fe oxidation. The reducing environment may have promoted reduction of the local Ce inventory to Ce^{3+} and subsequent partitioning within a perovskite phase. Moreover, clusters of perovskite

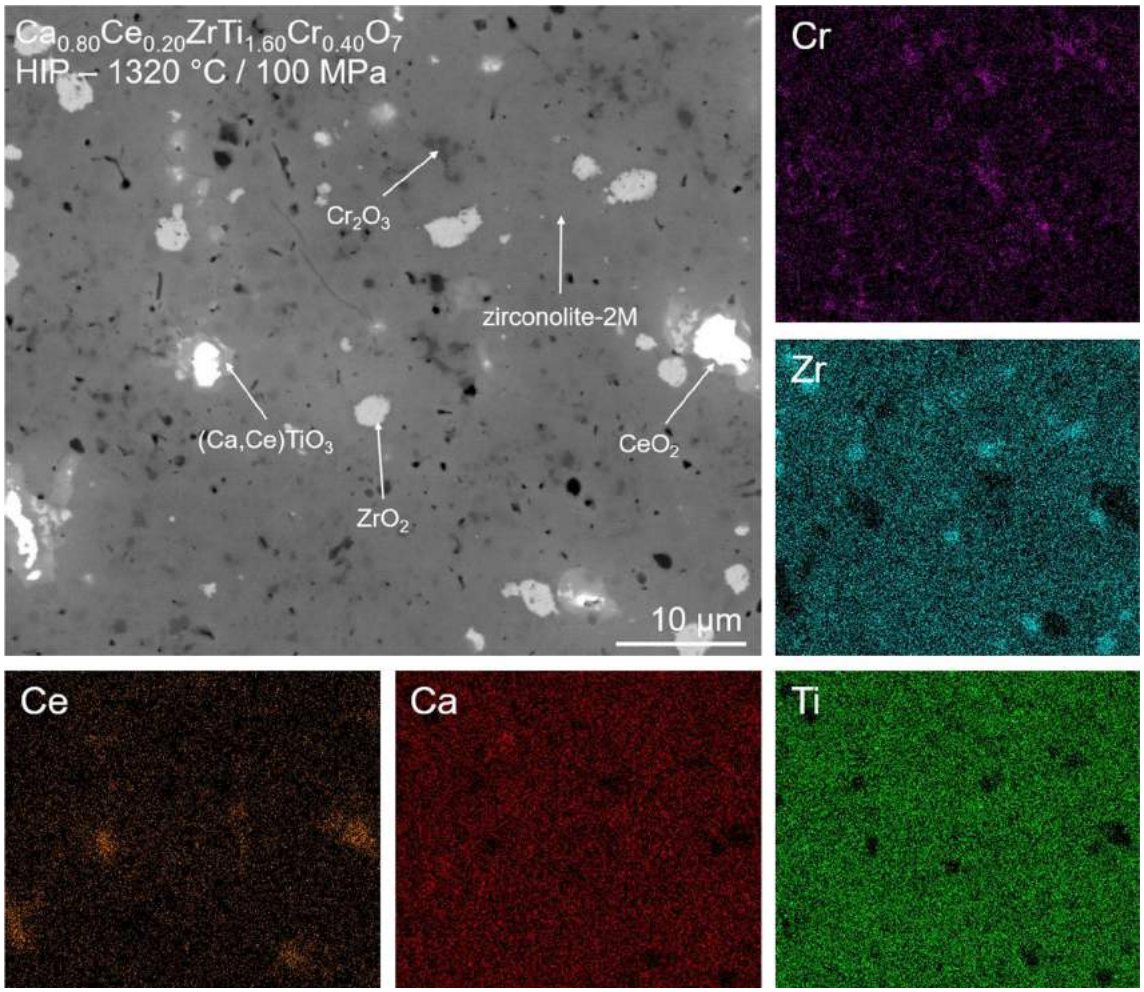

Fig. 2 SEM–EDS analysis of HIPed $Ca_{0.80}Ce_{0.20}ZrTi_{1.60}Cr_{0.40}O_7$ matrix

appeared more readily formed near the Cr-rich oxide layer, with EDS analysis confirming greater Cr concentration (likely substituted for $Ti^{3+/4+}$ in perovskite) relative to the perovskite reaction rims located around undigested CeO_2 in the bulk material. It is important to note, however, that there is no clear indication that the stainless steel–wasteform interface will lead to the formation of non-durable phases or free actinides.

Cr K- and Ce L_3-edge XANES

X-ray absorption spectroscopy (XAS) is a fundamental technique in support of nuclear waste management, as an effective means to probe the local structure and valence chemistry of radionuclides in immobilisation matrices, supporting the safety case towards geological disposal through underpinning the underlying crystal chemistry of actinide-containing wasteforms [16–18]. Accordingly, Ce L_3 and Cr K-edge X-ray absorption near edge structure (XANES) data were collected alongside a series of reference compounds representing Ce and Cr in a variety of oxidation states and coordination environments, allowing the speciation and local environment of Ce and Cr to be inferred. Cr K edge XANES is displayed in Fig. 4, alongside Cr_2O_3, $YCrO_3$ and K_2CrO_4 (representing Cr^{3+}, Cr^{3+} and Cr^{6+}, respectively). The XANES region for K_2CrO_4, in which Cr^{6+} adopts tetrahedral coordination to neighbouring oxygen atoms, was dominated by an intense pre-edge feature, with a centroid position approximately 15 eV from the main absorption edge. This feature was not present in the XANES spectrum for the HIPed zirconolite specimen, inferring the absence of Cr^{6+}. Inspection of the Cr K-edge data revealed white line features comparable with Cr^{3+} reference compounds ($YCrO_3$ and Cr_2O_3), consistent with a similar edge position and low intensity pre-edge feature [19]. Through modelling of the pre-edge feature, it was previously observed that Cr^{3+} adopts the octahedral coordination in the zirconolite structure, consistent with substitution within TiO_6 polyhedra. The absorption features for HIPed $Ca_{0.80}Ce_{0.20}ZrTi_{1.60}Cr_{0.40}O_7$ were consistent with those reported previously for the

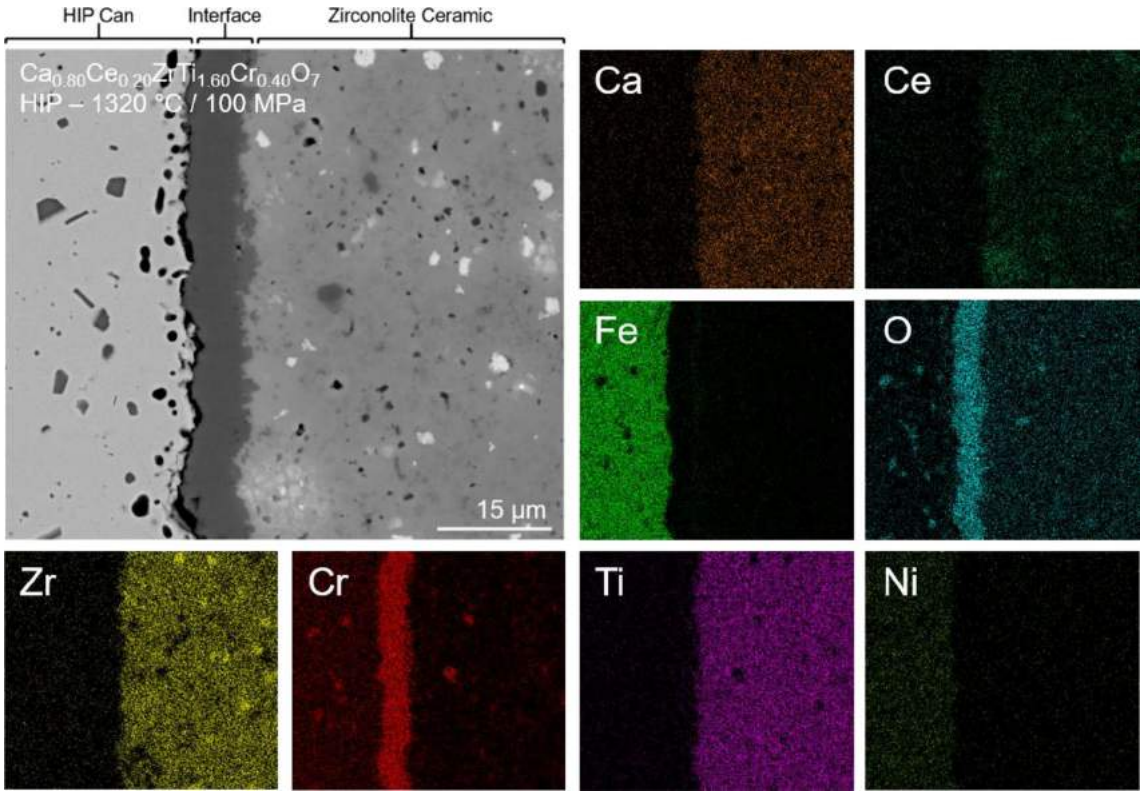

Fig. 3 Backscattered SEM micrograph and elemental distribution maps for the stainless steel-ceramic interface

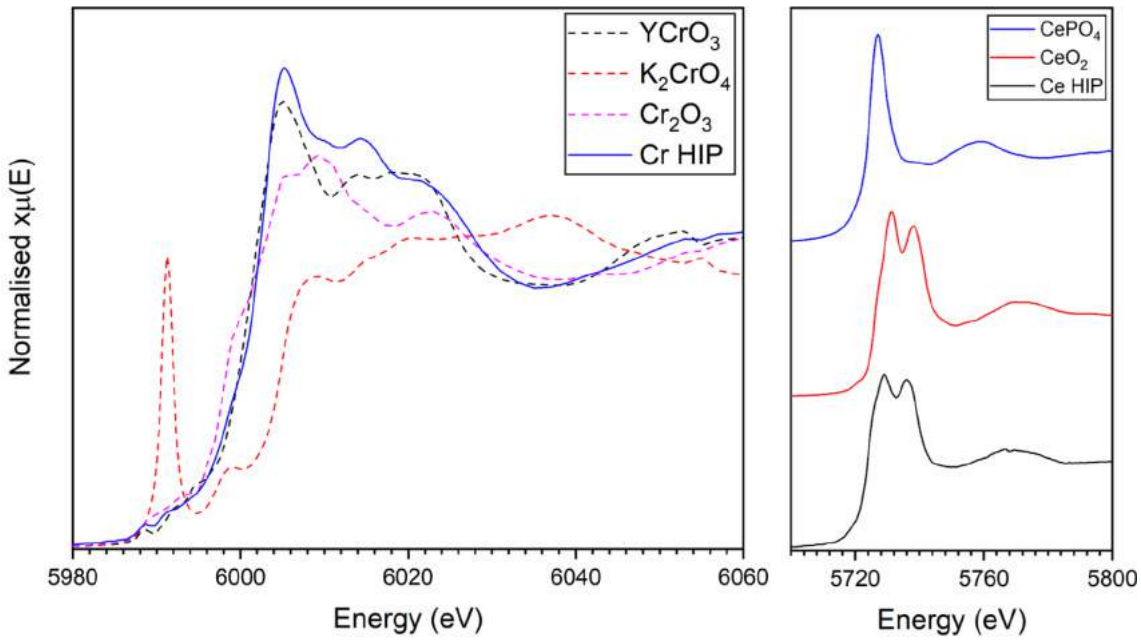

Fig. 4 Cr K (left) and Ce L_3-edge (right) XANES data for HIPed $Ca_{0.80}Ce_{0.20}ZrTi_{1.60}Cr_{0.40}O_7$, alongside $YCr^{3+}O_3$, $K_2Cr^{6+}O_4$, $Cr_2{}^{3+}O_3$, $Ce^{4+}O_2$ and $Ce^{3+}PO_4$ reference compounds

corresponding CPS composition [4], hence by analogy, it can be assumed that the same substitution mechanism occurred for the HIPed sample. Ce L_3 XANES were collected alongside CeO_2 and $CePO_4$, representing Ce^{4+} and Ce^{3+} in eight and ninefold coordination to oxygen, respectively [20]. The Ce absorption edge for the HIPed zirconolite composition was comprised of an asymmetric doublet, similar in energy position to that of the CeO_2 reference compound, inferring that the available Ce inventory remained present as Ce^{4+}, analogous to Pu^{4+}. A linear combination fit was performed to determine the average oxidation state of Ce, confirming that $93.3 \pm 2\%$ of the Ce remained present as Ce^{4+}, inferring an average oxidation state of approximately $Ce^{3.9+}$ (data fit with an R-factor of 0.017). However, powder XRD and SEM data confirmed that considerable unincorporated CeO_2 remained present in the microstructure, hence the XANES signal for the HIPed specimen is comprised of contributions from two distinct Ce chemical environments. Nevertheless, as the zirconolite-2M phase accounted for approximately 92 wt% of the overall phase assemblage, it is clear that the dominant oxidation state of Ce in the zirconolite phase is Ce^{4+}.

Conclusions

A sample of zirconolite with nominal composition $Ca_{0.80}Ce_{0.20}ZrTi_{1.60}Cr_{0.40}O_7$ was produced by HIP, with a densification cycle of 1320 °C and 100 MPa maintained for 4 h. The resulting wasteform was characterised by powder XRD, detailing that whilst the target zirconolite-2M phase accounted for 92.3 ± 0.1 wt% of the total phase assemblage, a significant fraction of the available Ce inventory, equivalent to approximately 3.9 wt% (acting as a surrogate for Pu) was unincorporated into the zirconolite matrix. SEM–EDS data also revealed the presence of Ce within an accessory perovskite phase, presumably incorporated as Ce^{3+}, in line with previous observations. Observations of the interface region between the HIP canister and the bulk ceramic matrix revealed the presence of a Cr-rich oxide layer, with a thickness comparable to those previously detailed for SYNROC that was HIPed in stainless steel canisters. Whilst diffusion of Cr and Fe did not appear to significantly destabilise the phase assemblage at the canister-ceramic interface, Cr was observed to partition within the accessory perovskite phase, potentially providing a charge balancing mechanism permitting greater Ce loading. The formation of a Ce-bearing perovskite expected to be detrimental to the overall wasteform performance. Cr K edge XANES data were consistent with our previous observations, in which Cr^{3+} was largely accommodated in TiO_6 octahedra. The Ce L_3 XANES spectrum presented features consistent with the Ce^{4+} reference sample, although as a significant portion of the available Ce inventory remained present in the microstructure as CeO_2, we do not consider the XANES spectrum obtained to be entirely representative of Ce speciation in the zirconolite phase.

Acknowledgments We acknowledge financial support from the Nuclear Decommissioning Authority (NDA) and EPSRC under Grant Numbers EP/S01019X/1, EP/P013600/1 and EP/R511754/1. This research utilised the HADES/MIDAS facility at the University of Sheffield established with financial support from EPSRC and BEIS, under grant EP/T011424/1 [21]. Collection of the Ce L_3 and Cr K-edge XAS data was performed under the approval of the Photon Factory Advisory Committee (Proposal No. 2019G586); the support of Yoshihiro Okamoto (Japanese Atomic Energy Agency) and Noriko Usami (The High Energy Accelerator Research Organisation—Kō Enerugī Kasokuki Kenkyū Kikō) during the experiment is gratefully acknowledged.

Data availability The data that support these findings cannot be shared at the present time, as they form part of an ongoing study.

References

1. N.C. Hyatt, Safe management of the UK separated plutonium inventory: a challenge of materials degradation. NPJ Mater. Degrad. (2020). https://doi.org/10.1038/s41529-020-00132-7
2. S.K. Roberts, W.L. Bourcier, H.F. Shaw, Aqueous dissolution kinetics of pyrochlore, zirconolite and brannerite at 25, 50, and 75 °C. Radiochim. Acta **88**(9–11), 539–543 (2000)
3. B.M. Gatehouse, I.E. Grey, R.J. Hill, H.J. Rossell, Zirconolite, $CaZr_xTi_{3-x}O_7$; structure refinements for near-end-member compositions with x = 0.85 and 1.30. Acta Crystallogr. **B37**(1974), 306–312 (1981)
4. L.R. Blackburn et al., Synthesis and characterisation of $Ca_{1-x}Ce_xZrTi_{2-2x}Cr_{2x}O_7$: analogue zirconolite wasteform for the immobilisation of stockpiled UK plutonium. J. Eur. Ceram. Soc. **40**(15), 5909–5919 (2020)
5. G.R. Lumpkin, K.L. Smith, M.G. Blackford, Electron microscope study of Synroc before and after exposure to aqueous solutions. J. Mater. Res. **6**(10), 2218–2233 (1991)
6. S.-K. Sun, M.C. Stennett, C.L. Corkhill, N.C. Hyatt, Reactive spark plasma synthesis of $CaZrTi_2O_7$ zirconolite ceramics for plutonium disposition. J. Nucl. Mater. **500**, 11–14 (2018)
7. L. R. Blackburn et al., Hot isostatically pressed zirconolite wasteforms for actinide immobilization. IOP Conf. Ser. Mater. Sci. Eng. **818**(1), 012010 (2020)
8. S. Thornber, M.C. Stennett, N.C. Hyatt, Investigation of Ce incorporation in zirconolite glass-ceramics for UK plutonium disposition, in 2016 MRS Fall Meeting (2016)

9. S.M. Thornber et al., A preliminary validation study of PuO_2 incorporation into zirconolite glass-ceramics. MRS Adv. **1**(4), 1–7 (2018)
10. D.J. Bailey et al., A new approach to the immobilisation of technetium and transuranics: co-disposal in a zirconolite ceramic matrix. J. Nucl. Mater. **528**, 151885 (2019)
11. E. Maddrell, Hot isostatically pressed wasteforms for future nuclear fuel cycles. Chem. Eng. Res. Des. **91**, 735–741 (2013)
12. B.H. Toby, EXPGUI, a graphical user interface for GSAS. J. Appl. Crystallogr. **34**, 210–213 (2001)
13. H. Li, Y. Zhang, P.J. McGlinn, S. Moricca, B.D. Begg, E.R. Vance, Characterisation of stainless steel-synroc interactions under hot isostatic pressing (HIPing) conditions. J. Nucl. Mater. **355**(1–3), 136–141 (2006)
14. Y. Zhang, M.W.A. Stewart, H. Li, M.L. Carter, E.R. Vance, S. Moricca, Zirconolite-rich titanate ceramics for immobilisation of actinides - Waste form/HIP can interactions and chemical durability. J. Nucl. Mater. **395**, 69–74 (2009)
15. Y. Zhang, H. Li, S. Moricca, Pyrochlore-structured titanate ceramics for immobilisation of actinides: Hot isostatic pressing (HIPing) and stainless steel/waste form interactions. J. Nucl. Mater. **377**, 470–475 (2008)
16. L.M. Mottram et al., A feasibility investigation of laboratory based X-ray absorption spectroscopy in support of nuclear waste management. MRS Adv. **XLIII**, 27–35 (2020)
17. S.M. Thornber, L.M. Mottram, A.R. Mason, P. Thompson, C. Stennett, N.C. Hyatt, Solubility, speciation and local environment of chlorine in zirconolite glass–ceramics for the immobilisation of plutonium residues. RSC Adv. **10**, 32497–32510 (2020)
18. D.J. Bailey et al., Ce and U speciation in wasteforms for thermal treatment of plutonium bearing wastes, probed by L3 edge XANES. IOP Conf. Ser. Mater. Sci. Eng. **818**(1), 012019 (2020)
19. M. Tromp, J. Moulin, G. Reid, J. Evans, Cr K-edge XANES spectroscopy: Ligand and oxidation state dependence—what is oxidation state? AIP Conf. Proc. **882**, 699–701 (2007)
20. L.R. Blackburn, S. Sun, L.J. Gardner, E.R. Maddrell, M.C. Stennett, N.C. Hyatt, A systematic investigation of the phase assemblage and microstructure of the zirconolite $CaZr_{1-x}Ce_xTi_2O_7$ system. J. Nucl. Mater. **535**, 152137 (2020)
21. N.C. Hyatt, C.L. Corkhill, M.C. Stennett, R.J. Hand, L.J. Gardner, C.L. Thorpe, The HADES facility for high activity decommissioning engineering & science : part of the UK National Nuclear User Facility. *IOP Conf. Ser. Mater. Sci. Eng.* **818**, 1–8 (2020)

Chapter 8

Influence of Accessory Phases and Surrogate Type on Accelerated Leaching of Zirconolite

Authorship Contribution Statement

8) ‘Influence of Accessory Phases and Surrogate Type on Accelerated Leaching of Zirconolite Wasteforms’. L. Blackburn was responsible for conceptualisation, materials preparation and characterisation, original draft preparation, reviewing and editing.

npj | Materials Degradation

www.nature.com/npjmatdeg

ARTICLE OPEN

Check for updates

Influence of accessory phases and surrogate type on accelerated leaching of zirconolite wasteforms

Lewis R. Blackburn[1], Rachel Crawford[1], Samuel A. Walling[1], Laura J. Gardner[1], Max R. Cole[1], Shi-Kuan Sun[1], Clémence Gausse[1], Amber R. Mason[1], Martin C. Stennett[1], Ewan R. Maddrell[2], Neil C. Hyatt[1] and Claire L. Corkhill[1]✉

A fraction of the UK Pu inventory may be immobilised in a zirconolite ceramic matrix prior to disposal. Two zirconolite compositions, targeting $CaZr_{0.80}Ce_{0.20}Ti_2O_7$ and $CaZr_{0.80}U_{0.20}Ti_2O_7$, were fabricated by hot isostatic pressing, alongside a reformulated composition, nominally $Ca_{0.80}Zr_{0.90}Ce_{0.30}Ti_{1.60}Al_{0.40}O_7$, with an excess of Ti and Zr added to preclude the formation of an accessory perovskite phase. Materials were subjected to accelerated leaching in a variety of acidic and alkaline media at 90 °C, over a cumulative period of 14 d. The greatest Ce release was measured from $CaZr_{0.80}Ce_{0.20}Ti_{2.00}O_7$ exposed to 1 M H_2SO_4, for which 14.7 ± 0.2% of the original Ce inventory was released from the wasteform into solution. The extent of Ce leaching into the solution was correlated with the quantity of perovskite present in the wasteform, and associated with the incorporation and preferential dissolution of Ce^{3+}. $CaZr_{0.80}U_{0.20}Ti_{2.00}O_7$ exhibited improved leach resistance relative to $CaZr_{0.80}Ce_{0.20}Ti_{2.00}O_7$, attributed to the decreased proportion of accessory perovskite, with 7.1 ± 0.1% U released to in 8 M HNO_3 after 7 d. The $Ca_{0.80}Zr_{0.90}Ce_{0.30}Ti_{1.60}Al_{0.40}O_7$ composition, with no accessory perovskite phase, presented significantly improved leaching characteristics, with < 0.4%Ce released in both 8 M HNO_3 and 1 M H_2SO_4. These data demonstrate the need for careful compositional design for zirconolite wasteforms with regard to accessory phase formation and surrogate choice.

npj Materials Degradation (2021)5:24; https://doi.org/10.1038/s41529-021-00171-8

INTRODUCTION

Reprocessing of spent Magnox and advanced gas-cooled reactor (AGR) fuels in the UK has resulted in an inventory of PuO_2 forecast to amount to 140 tonnes heavy metal equivalent (teHM). This material is the liability of the Nuclear Decommissioning Authority (NDA), which is supporting the UK government in the Pu management strategy through identifying solutions that put UK civil inventories beyond reach[1]. One approach that satisfies the fundamental criteria of potential disposition pathways is immobilisation within a chemically durable ceramic matrix that incorporates Pu at the atomic scale within a crystalline material, while remaining resistant to the effects of self-irradiation.

Zirconolite, prototypically $CaZrTi_2O_7$, is a naturally occurring titanate mineral that has been identified as a candidate crystalline host phase for Pu immobilisation. The zirconolite-2M polytype (monoclinic unit cell — space group C2/c), where '2M' refers to a two-layer repeated arrangement of cation layers within the unit cell, is stabilised over the solid solution $CaZr_xTi_{3-x}O_7$, with stoichiometry $0.80 \le x \le 1.30$, and is considered the archetype structure[2]. Other zirconolite polytypes are observed as a consequence of the structural rearrangement due to substitution on Ca^{2+}, Zr^{4+}, and Ti^{4+} sites, e.g. 4M, 3T and 3O[3–5]. Substitution of Pu^{4+} on the Zr^{4+} site in zirconolite above 0.15 formula units (f.u.) produces a transformation from a 2 M to 4 M polytype, as reported by Begg et al[6]. Increasing the Pu content in excess of 0.4 f.u. yields the pyrochlore structure, whilst the end member $CaPuTi_2O_7$ is reported to be a fluorite-derivative structure with a reported X-ray amorphisation dose of 1.3×10^{25} α·m^{-3} [7,8]. Zirconolite can also accommodate Pu^{4+} in solid solution through Ca^{2+} site substitution, coupled with co-immobilisation of a suitable charge-balancing species, e.g. $Ca_{1-x}Pu_xZrTi_{2-2x}Al_{2x}O_7$, where Al^{3+} acts as a charge balancing species[9].

The durability of zirconolite for Pu immobilisation (using surrogates for Pu) under conditions relevant for geological disposal is estimated to be of the same order of magnitude as spent nuclear fuel. For example, Meng et al. recently reported the normalised mass loss of Ce in the $Ca_{1-x}Zr_{1-x}Ce_{2x}Ti_2O_7$ system to be of the order 10^{-6}–10^{-7} g m^{-2} when leached in H_2O at 90 °C[10]. The normalised release rate of Nd from single-phase Nd-doped zirconolite-2M was reported to be 10^{-5} g m^{-2} d^{-1} by Cai et al. over a 42-d period[11]. Since the dissolution rate is inherently low, accelerated leaching methods can be utilised to rapidly evaluate the dissolution of zirconolite ceramics of different compositions and structures. Such acceleration could be promoted by increasing the reactive surface area exposed to the solution, by increasing the temperature, or by using aggressive leaching media, such as strong acid or alkali solutions. For example, Strachan et al.[12] and Icenhower et al.[13] undertook the assessment of the forward rate of dissolution of Pu and Ce in zirconolite and less-durable pyrochlore materials, respectively, at pH 2, since this was the only solution condition under which elements were measurable. The latter approach is also of relevance to understand the recovery of fissile inventory from such a material, should there be a future need to rework the wasteform or reverse the decision to immobilise in favour of reuse.

While the durability of zirconolite is relatively high, should processing conditions result in the formation of accessory phases that readily partition Pu, the rate of Pu release during dissolution may be enhanced. $CaTiO_3$ perovskite is one such accessory phase that is postulated to increase the release of Pu to aqueous leaching media, largely informed by early durability trials of the SYNROC-C wasteform, for which zirconolite and perovskite were included as hosts for actinides[14]. The extent of perovskite formation can also be dependent on the choice surrogate used

[1]Immobilisation Science Laboratory, University of Sheffield, Department of Materials Science and Engineering, Sheffield, UK. [2]National Nuclear Laboratory, Workington, Cumbria, UK. ✉email: c.corkhill@sheffield.ac.uk

for Pu, typically Ce or U, and the prevailing oxygen fugacity during synthesis[3,15].

In this study, we aim to quantify the release of Pu surrogates from zirconolite to a range of aggressive leaching media, to provide a greater understanding of the effect of (i) media composition; (ii) contribution of perovskite accessory phase; and (iii) Pu surrogate choice (Ce or U) on the durability of zirconolite ceramics. To achieve this, three different zirconolite compositions were investigated. Firstly, a 'non-ideal' formulation of $CaZr_{0.80}M_{0.20}Ti_{2.00}O_7$, with a minor perovskite accessory phase, was investigated, with $M = Ce^{4+}$ or $M = U^{4+}$ as surrogates for Pu^{4+}. The third composition targeted $Ca_{0.80}Zr_{0.90}Ce_{0.30}Ti_{1.60}Al_{0.40}O_7$, reformulated with approximately 0.10 f.u. excess each of both Ti and Zr, added to preclude the formation of perovskite and accommodate partial Ce^{3+} speciation, resulting in a nominal composition of $Ca_{0.80}Zr_{1.00}Ce_{0.30}Ti_{1.70}Al_{0.40}O_7$. The characterisation of these phases is first described, followed by an evaluation of their leaching behavior.

RESULTS AND DISCUSSION

Phase assemblage and redox chemistry

Monoclinic zirconolite-2M (space group C2/c) was identified as the major crystalline phase (~80 wt.%) for the $CaZr_{0.80}Ce_{0.20}Ti_{2.00}O_7$ formulation (Fig. 1a and Table 1). The unit cell parameters were determined by Rietveld analysis of the powder diffraction profile to be $a = 12.4898(2)$ Å, $b = 7.2807(1)$ Å, $c = 11.3979(2)$ Å, $\beta = 100.593(1)^\circ$ and $V = 1018.81(2)$ Å^3. Inspection of the powder diffraction profile revealed reflections attributed to other, minor, phases. The first of these was zirconolite-4M (~10 wt.%), which was distinguished via the presence of diagnostic supercell reflections (002) and (008) at $2\theta = 7.8^\circ$ and $2\theta = 31.1^\circ$, respectively. This phase was also apparent in SEM images, clearly distinguished by the contrast variation in the back-scattered electron image and by a cerium enrichment, as shown in the Ce-Lα EDS data (Supplementary Fig. 1).

Ce-bearing perovskite (nominal composition $(Ca,Ce)TiO_3$) was also identified. This phase, preferentially accommodating Ce in reduced form (Ce^{3+}), has previously been observed to form during HIP synthesis of zirconolite, as a result of the reducing environment imposed by the in-canister containment[16]. The presence of Ce^{3+} was confirmed by X-ray absorption near-edge structure (XANES) spectroscopy; linear combination analysis revealed that 59 ± 3 at.% of the Ce inventory was reduced to the Ce^{3+} species (Supplementary Fig. 2). A small amount of unreacted ZrO_2 (<1 wt.%) and trace CeO_2 (identified by SEM/EDS only), considered to be artefacts of the milling process, were also observed.

The phase assemblage obtained for the U-bearing zirconolite counterpart, $CaZr_{0.80}U_{0.20}Ti_{2.00}O_7$, comprised primarily zirconolite-2M (~97 wt.%—Table 1) with unit cell dimensions $a = 12.4779(27)$ Å, $b = 7.2424(21)$ Å, $c = 11.3899(30)$ Å, $\beta = 100.651(33)^\circ$ and $V = 1011.58(27)$ Å^3 (Fig. 1b). A number of other XRD reflections were distinguished, corresponding to trace phases of perovskite and UO_2. Two distinct ZrO_2 phases were also observed by SEM, consistent with ZrO_2, and a $(Zr,U)O_2$ dilute solid solution (Supplementary Fig. 3). Given the pseudo-binary phase diagram of PuO_2-ZrO_2, it is plausible that Pu counterpart formulations may contain a $(Zr,Pu)O_2$ solid solution[17,18]. However, to our knowledge, no such phases have previously been reported in the literature pertaining to Pu-zirconolite, even at relatively high Pu loadings[4].

It is possible that a portion of the available U may have been accommodated within the accessory perovskite phase, with U stabilised as U^{4+}. In such a case, charge balance is provided by partial reduction of Ti^{4+} to Ti^{3+} in the $CaTiO_3$ structure, as was reported by Vance et al[19]. However, it was not possible to reliably distinguish perovskite grains from the bulk zirconolite-2M phase by SEM (Supplementary Fig. 3) due to a combination of fine grain structure, low occupation within the microstructure (<1 wt.%), and similar backscattered electron coefficient. Therefore, the incorporation, and extent thereof, of U in the perovskite phase could not be definitively confirmed.

Uranium L_3 XANES spectra were obtained to determine whether the redox environment in the canister was sufficient to maintain

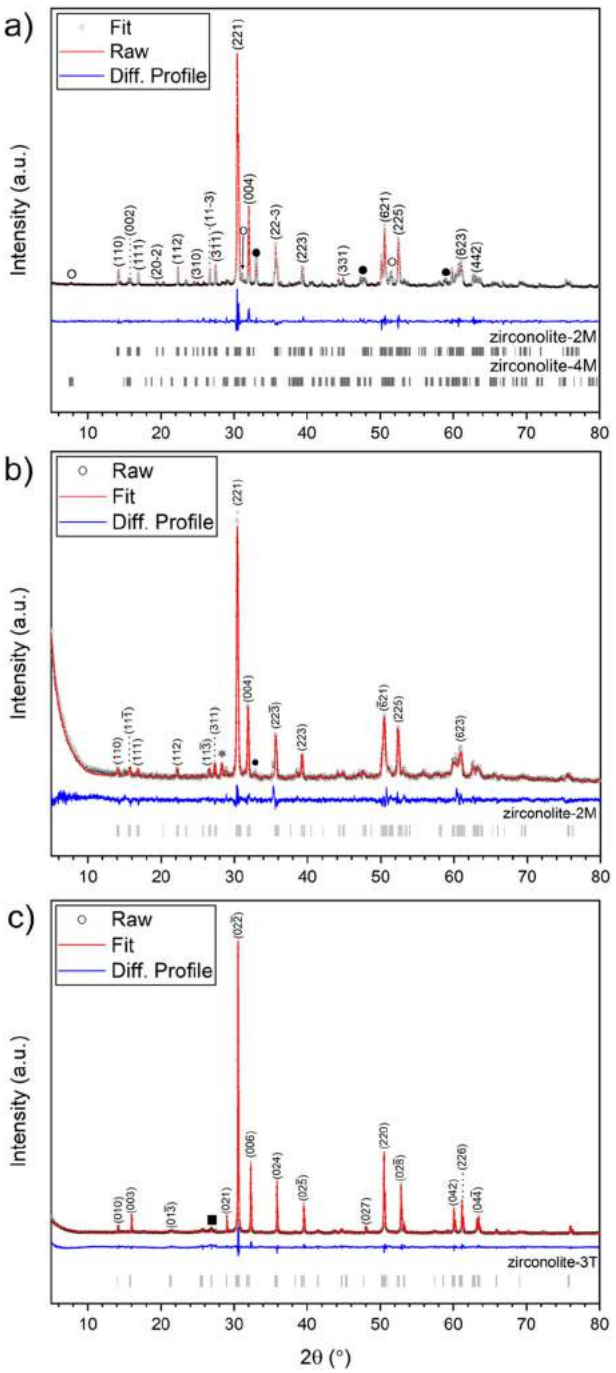

Fig. 1 Refined powder diffraction profiles of zirconolite ceramic materials. Showing **a** HIPed $CaZr_{0.80}Ce_{0.20}Ti_{2.00}O_7$; **b** HIPed $CaZr_{0.80}U_{0.20}Ti_{2.00}O_7$; and **c** CPS $Ca_{0.80}Zr_{0.90}Ce_{0.30}Ti_{1.60}Al_{0.40}O_7$. Zirconolite-2M, 4 M, and 3T reflections are indexed with corresponding (hkl) values. Diagnostic zirconolite-4M reflections are labelled with open circles (o). Perovskite reflections are labelled with closed circles. UO_2 reflections are labelled with asterisks. Al_2TiO_5 reflections are labelled with closed squares.

Table 1. Phase assemblage of zirconolite materials, as determined by Rietveld analysis of powder XRD data shown in Fig. 1.

Phase	$CaZr_{0.80}Ce_{0.20}Ti_{2.00}O_7$	$CaZr_{0.80}U_{0.20}Ti_{2.00}O_7$	$Ca_{0.80}Zr_{0.90}Ce_{0.30}Ti_{1.60}Al_{0.40}O_7$
Zirconolite-2M	81.06 ± 0.04	97.08 ± 0.02	–
Zirconolite-4M	9.6 ± 0.1	–	–
Zirconolite-3T	–	–	98.4 ± 0.6
Perovskite	8.7 ± 0.1	0.94 ± 0.61	–
ZrO_2	0.67 ± 0.04	–	–
UO_2	–	0.62 ± 0.12	–
$Zr_{1-x}U_xO_2$	–	1.34 ± 0.60	–
Al_2TiO_5	–	–	1.6 ± 0.6

The reported precision of phase fractions represents the uncertainty associated with parameter fitting in the Rietveld analysis.

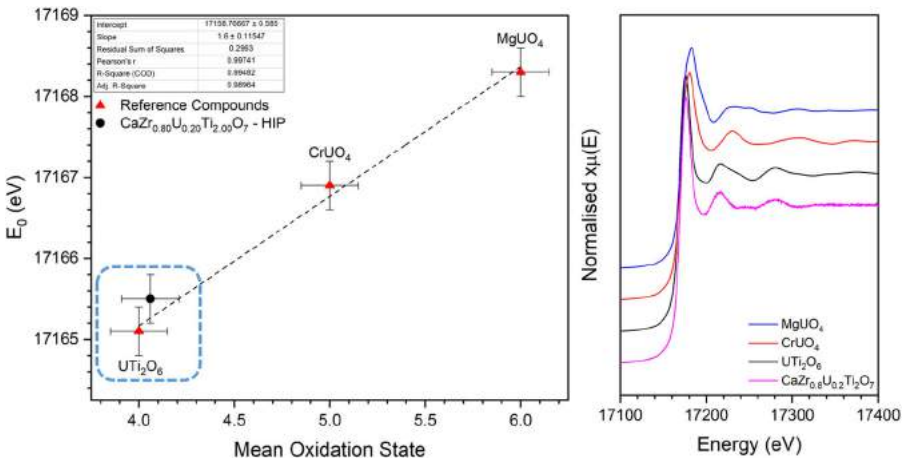

Fig. 2 U L_3 XANES data for $CaZr_{0.80}U_{0.20}Ti_{2.00}O_7$ alongside $U^{4+}Ti_2O_6$, $CrU^{5+}O_4$ and $MgU^{6+}O4$ reference compounds. Error bars represent the error on the linear regression of edge position of the samples to the edge position of known standards.

the target U^{4+} oxidation state (Fig. 2). Two key features of the data qualitatively indicated a U^{4+} valence: the white line features of the $CaZr_{0.80}U_{0.20}Ti_{2.00}O_7$ U L_3 absorption edge were similar to that of the $U^{4+}Ti_2O_6$ reference compound, while the edge positions of the $CrU^{5+}O_4$ and $MgU^{6+}O_4$ reference compounds were clearly shifted to higher energy when compared to $CaZr_{0.80}U_{0.20}Ti_{2.00}O_7$. The mean oxidation state of U in $CaZr_{0.80}U_{0.20}Ti_{2.00}O_7$ was determined by linear regression of the E_0 position, with respect to standards of known oxidation state, to be 4.06 ± 0.30. This confirms that the HIP environment was sufficiently reducing to maintain U as U^{4+}.

Inspection of the powder XRD data obtained for the reformulated $Ca_{0.80}Zr_{0.90}Ce_{0.30}Ti_{1.60}Al_{0.40}O_7$ composition (Fig. 1c) was consistent with the formation of single-phase zirconolite-3T, occupying the space group $P3_121$. It is important to note that this composition did not yield perovskite as a secondary phase, meaning the entire Ce inventory was contained wholly within the zirconolite-3T phase. This is attributed to the fact that the reformulated $Ca_{0.80}Zr_{0.90}Ce_{0.30}Ti_{1.60}Al_{0.40}O_7$ composition incorporated excess Zr and Ti as buffer phases and was synthesised by sintering under an air atmosphere, rather than by HIP. A satisfactory Le Bail fit was obtained using the structural model reported by Grey et al. for which single-crystal X-ray diffraction data of the synthetic $Ca_{0.80}Zr_{1.30}Th_{0.15}Ti_{1.35}Al_{0.40}O_7$ phase was published[20]. Although there are limited detailed structural analyses of the synthetic zirconolite-3T phase reported in the wider literature, the refinement statistics were satisfactory (R_p = 7.96%, R_{wp} = 10.29%). The output from this refinement produced cell parameters for the zirconolite-3T phase calculated to be a = 7.2377(2) Å, c = 16.6621(4) Å, and V = 755.90(4) Å^3. Close inspection of powder XRD data revealed minor reflections consistent with a pseudobrookite structured phase (nominally Al_2TiO_5), accounting for approximately 1.6 wt.% of the phase assemblage, presumably formed as a reaction product due to the excess 0.1 f.u. TiO_2. SEM-EDS analyses (Supplementary Fig. 4) confirmed the presence of an Al and Ti-containing phase present as an accessory phase within the zirconolite-3T matrix. EDS analysis established that the surrogate Ce fraction was not incorporated within this phase. The average composition of the zirconolite phase was calculated to be $Ca_{0.78(3)}Zr_{0.80(3)}Ce_{0.23(2)}Ti_{1.81(2)}Al_{0.39(2)}O_7$, normalised to seven oxygen atoms.

Perovskite influence on HIPed Ce-zirconolite leaching

Two successive static leaching experiments were performed on powdered material for each zirconolite composition, in a range of aggressive media at 90 °C, over a period of 7 d each (Fig. 3). Leaching data are reported and discussed, with reference to specific elements, as a function of the leaching efficiency from the ceramic wasteform material into the leaching solution. In this instance, a leaching efficiency of 100% Ce would represent the complete dissolution of the surrogate fissile inventory from the wasteform into solution. For $CaZr_{0.80}Ce_{0.20}Ti_{2.00}O_7$, in the first stage of leaching, the greatest level of Ce dissolution was achieved in 1M H_2SO_4; the elemental release of Ce in this medium was 14.7 ± 0.2% (Fig. 3a, Supplementary Table 1). Ca was preferentially dissolved into the leachate with respect to Ti, and Zr dissolution was considerably lower. The extent of elemental release in the first leaching step, under all leaching conditions, followed the same trend (Ce > Ca > Ti >> Zr), with the exception of 1M NaOH, which

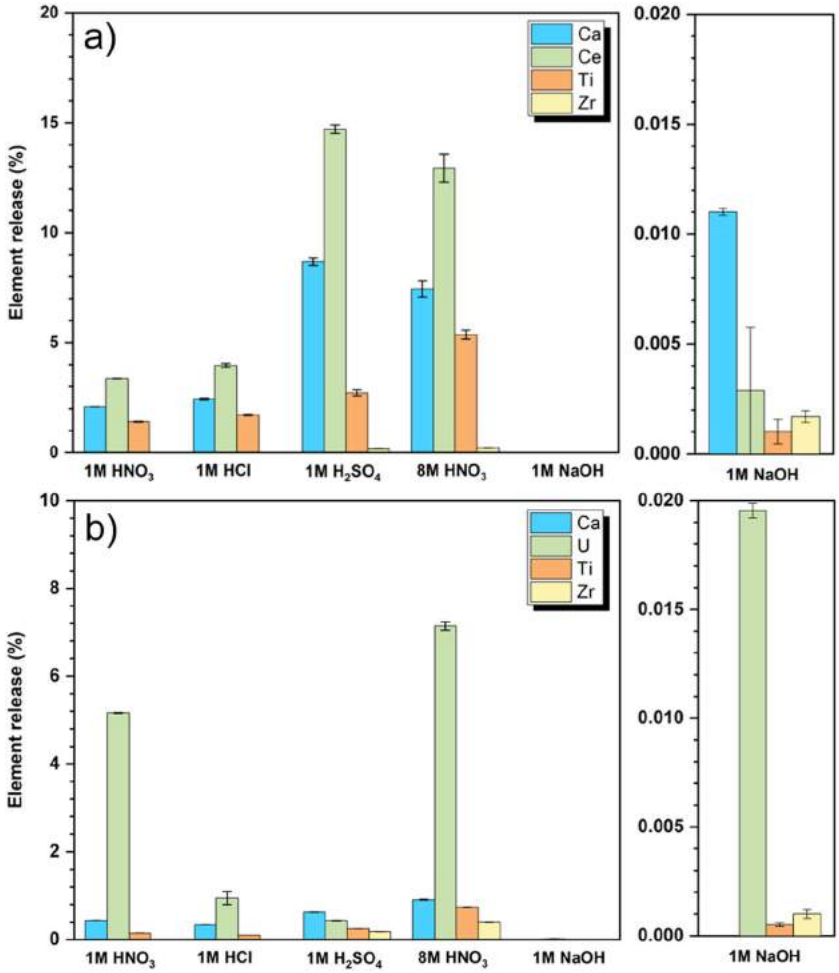

Fig. 3 Elemental release (%) of Ca, Ce, U, Zr and Ti from zirconolite samples into the aqueous leaching media. Showing results for **a** $CaZr_{0.80}Ce_{0.20}Ti_{2.00}O_7$ **b** $CaZr_{0.80}U_{0.20}Ti_{2.00}O_7$. Error bars represent the standard deviation of duplicate measurements.

exhibited extremely low elemental release. When exposed to 8M HNO_3, 12.9 ± 0.7% of the Ce inventory was dissolved into the leachate, indicating that the use of 8M HNO_3 or 1M H_2SO_4 resulted in the greatest extraction of the Ce surrogate. Similar behaviour was observed in the leaching of ThO_2, where sulphuric acid was more efficient at leaching Th than nitric and hydrochloric acid[21]. This was attributed to the higher strength of the metal–ligand complex for sulfate than for chloride or nitrate. The extent of elemental release was lower in the presence of 1M HNO_3 and 1M HCl, with the Ce release measured as 3.37 ± 0.01% and 4.0 ± 0.1%, respectively. A similar elemental release was observed for the other elements in these media and, in both cases, the leaching of Zr was negligible. The wasteform was most resistant to elemental extraction in the presence of 1M NaOH, with Ce extraction measured as 0.003 ± 0.003%.

After the termination of the first leaching experiment, the ceramic powders were recovered, washed with isopropanol, and the surface was examined by SEM, as shown in Fig. 4. The degree of visible surface damage, relative to the pristine material (Supplementary Fig. 5), was consistent with the extent of dissolution for each medium; for example, the specimens exposed to 1M H_2SO_4 and 8M HNO_3 presented the most visible surface degradation, in agreement with the higher percentage of elements released to these solutions. The presence of pitting may be an artefact of surface morphology or incongruent dissolution associated with the presence of multiple phases. No visible damage was observed for material recovered from 1M NaOH solution (data not shown).

High-magnification observations of specimens leached in 8M HNO_3 and 1M H_2SO_4 exposed the presence of small surface precipitates, approximately 1 μm in diameter (Figs. 4 and 5). EDS analysis revealed that they were enriched in Ti and O, and geochemical modelling indicated that TiO_2 (anatase and rutile) was saturated in solution; both suggest the precipitation of Ti from the leachate onto the ceramic surface. TiO_2 precipitation has previously been reported during perovskite dissolution[22,23], indicating that Ti may have been preferentially dissolved from the ceramic wasteform via the mechanism outlined by Pham et al.[24] in Eq. 1. It is inferred that the decomposition of $Ti(OH)_x^{(4-x)+}$ under hydrothermal conditions (i.e. T ≥ 90 °C) drives the nucleation and growth of TiO_2. The spherical morphology of these precipitates is consistent with those presented in similar work[25].

$$CaTiO_3 + (6-x)H^+_{(aq)} \rightarrow Ca^{2+}_{(aq)} + Ti(OH)_x^{(4-x)+} + (3-x)H_2O \quad (1)$$

To confirm whether the perovskite phase was preferentially leached, powder XRD data were collected on recovered specimens, to ascertain the amount of perovskite present after leaching relative to the pristine composition (Fig. 6). The relative intensity of the dominant perovskite reflection ($2\theta = 33.1^\circ$) was observed to decrease after leaching in all media, confirming that this phase was preferentially leached from the wasteform. In agreement with the elemental release results presented in Fig. 3, the 1M H_2SO_4 medium was most effective at leaching perovskite, with 2.6 ± 0.2

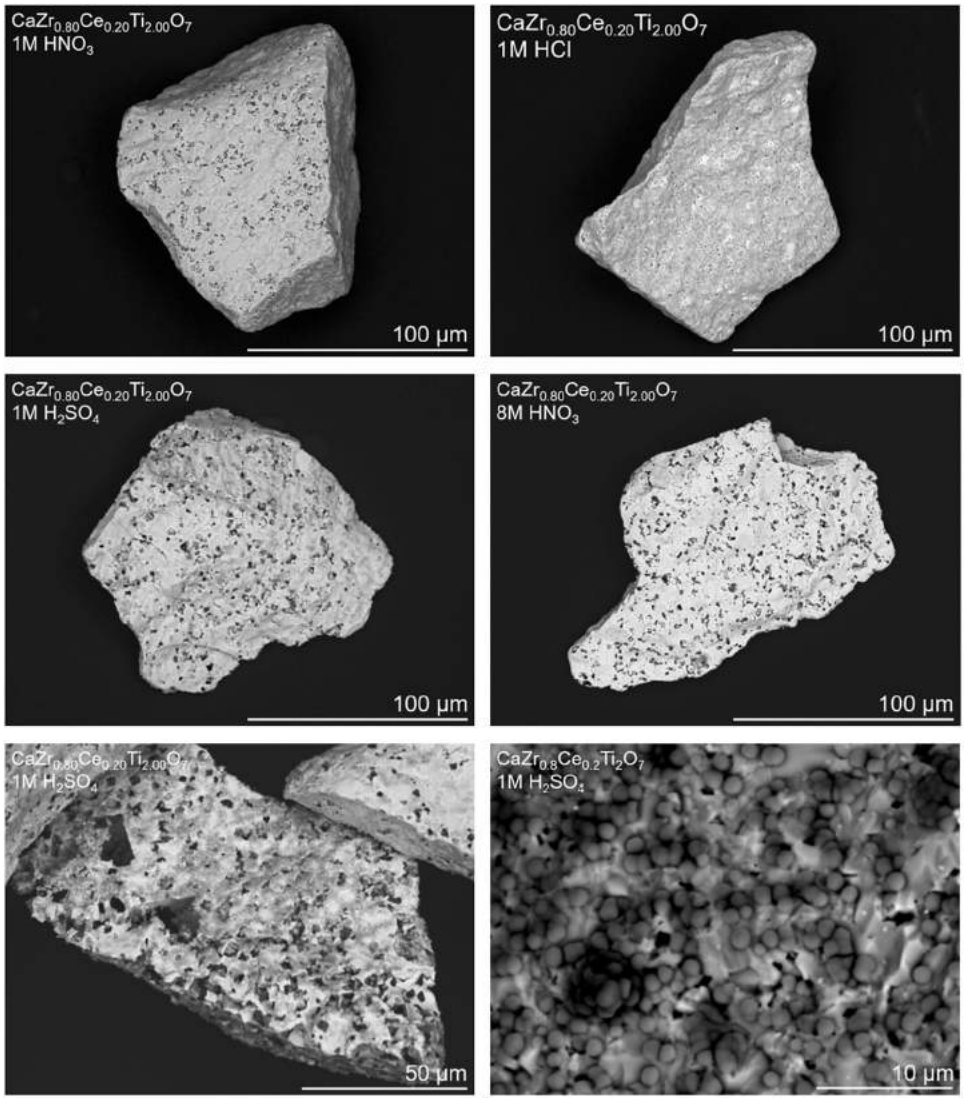

Fig. 4 SEM examination of $CaZr_{0.80}Ce_{0.20}Ti_{2.00}O_7$ ceramics exposed to 1M HCl, 1M HNO_3, 1M H_2SO_4, and 8M HNO_3 at 90 °C for 7 d. The scale bar on the upper 4 images is 100 µm, the bottom left is 50 µm and the bottom right, 10 µm.

wt.% remaining (corresponding to around two-thirds of the original perovskite fraction dissolved), as determined by Rietveld analysis of powder diffraction data collected on samples of the recovered material. Following dissolution in 8M HNO_3, an aqueous environment similar to that imposed during aqueous reprocessing of spent nuclear fuel, around one-third of the original perovskite fraction remained. It is important to note that the zirconolite-2M or zirconolite-4M reflections did not decrease relative to one another, indicating these phases may exhibit similar durability. Nevertheless, we acknowledge that the quantification of the phases based on powder XRD data is an artefact of the refinement output, and may not be entirely physically representative of the system.

XANES data were acquired at the Ce L_3 edge for specimens recovered after leaching (Table 2 and Supplementary Fig. 2). Comparison of the pristine and leached samples showed that the oxidation state of Ce in all cases was a combination of Ce^{3+} and Ce^{4+} however, subtle differences in the intensity of the doublet features for the leached samples were observed. Linear combination fitting (Table 2) revealed a small decrease in the Ce^{3+} content, from 59 ± 3 at.% Ce^{3+} in the pristine sample to 49 ± 3 at.% Ce^{3+} for zirconolite leached in 1M H_2SO_4 and 48 ± 3 at.% Ce^{3+} for 8M HNO_3. These values are consistent with preferential perovskite leaching. The relatively high fraction of Ce^{3+} present in the pristine sample was attributed to the reducing conditions imposed by the Cr/Fe-rich stainless steel containment using for HIP processing. While Ce^{3+} is preferentially accommodated in the Ca^{2+} site in perovskite, some of the Ce^{3+} inventory must also be located within the zirconolite phase. This is unsurprising, as we have previously demonstrated that considerable Ce^{3+} content may be present in single-phase zirconolite-2M[26]. Furthermore, Meng et al. confirmed that approximately 51% Ce^{3+} could be accommodated across a mixture of zirconolite-2M and -4M polytypes, in broad agreement with the Ce speciation presented here[10].

A second leaching experiment in fresh media was performed on the specimens that contained less than 4 wt.% perovskite after the first leaching (i.e. material leached in 1M H_2SO_4 and 8M HNO_3). The aim was to quantify the extent of Ce released after most of the accessible perovskite had been removed. After a further 7 d at 90 °C, the concentrations of Ca, Ce and Ti dissolved in the leachate were significantly reduced (Fig. 7 and Supplementary Table 2), from ~13% Ce in the first leaching step to 2.03 ± 0.01% and 3.46 ± 0.02% Ce release for 1M H_2SO_4 and 8M HNO_3, respectively, as a percentage of the remaining Ce inventory subsequent to the primary leaching trial. Therefore, it is evident that the accessory perovskite phase was the major contributor to Ce release in the first leaching step.

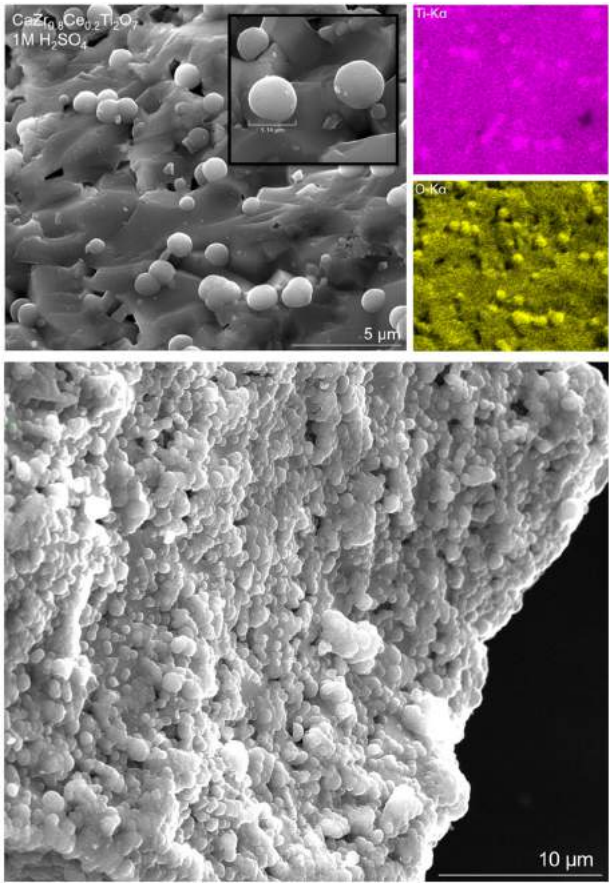

Fig. 5 SEM-EDS analysis of titanium-rich surface precipitates observed on $CaZr_{0.80}Ce_{0.20}Ti_{2.00}O_7$ particulates recovered from 1 M H_2SO_4 solution at 90 °C for 14 days (cumulative leaching time). The upper SEM image has a scale bar of 5 µm and the spherical precipitate is ~1 µm in size. The EDS images are Ti (pink) and O (yellow). The lower image has a scale bar of 10 µm.

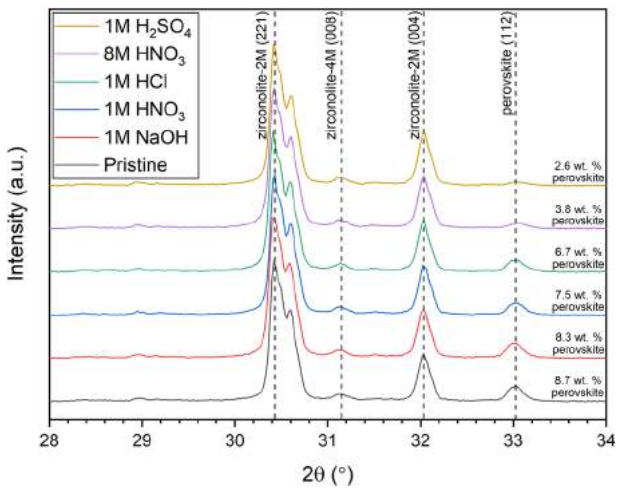

Fig. 6 Powder XRD data for $CaZr_{0.80}Ce_{0.20}Ti_{2.00}O_7$ following leaching at 90 °C for 7 days. The remaining amount of perovskite, relative to the pristine sample, was determined by Rietveld analysis of powder diffraction data for recovered material.

It should be noted that, despite thorough washing between leaching steps, spherical precipitates of TiO_2 were observed on the surface of specimens leached in 1M H_2SO_4 after the second leaching step in fresh media (Fig. 5). Geochemical modelling indicated that gypsum ($CaSO_4$) was saturated in solution for the H_2SO_4 medium in both leaching steps. Although there was no evidence for the formation of this phase, which is unlikely to precipitate in the strongly acidic medium, the modelling results suggest that calcium sulfate complexes are thermodynamically favourable under the conditions of the experiment. This may indicate the preferential leaching of Ca-containing phases and, when combined with the observation of TiO_2 precipitates, we hypothesise that even very low amounts of perovskite (~2 wt.%) can be dissolved, resulting in the formation of secondary phases. The Ce release within the 1M H_2SO_4 medium was somewhat lower than that in HNO_3 (Fig. 7), despite the fact that after leaching in HNO_3 the recovered product contained slightly more perovskite (3.8 wt.% and 2.6 wt.% for 8M HNO_3 and 1M H_2SO_4, respectively). Therefore, it is possible that the TiO_2 surface layer passivated the dissolution reaction to a certain extent, protecting the underlying ceramic from further corrosion. Further studies are required to investigate the passivating nature of this layer.

Table 2. Ce speciation (at.%) in $CaZr_{0.80}Ce_{0.20}Ti_{2.00}O_7$ determined by linear combination fitting of Ce L_3 XANES data with respect to Ce^{3+} and Ce^{4+} reference compounds.

Specimen	Ce speciation (at. %)		*R*-factor
	Ce^{3+}	Ce^{4+}	
$CaZr_{0.80}Ce_{0.20}Ti_{2.00}O_7$ — Pristine	59 ± 3	41 ± 3	0.0419
$CaZr_{0.80}Ce_{0.20}Ti_{2.00}O_7$ — 8 M HNO_3	48 ± 3	52 ± 3	0.0408
$CaZr_{0.80}Ce_{0.20}Ti_{2.00}O_7$ —1 M HNO_3	49 ± 3	51 ± 3	0.0503

Reported errors represent the error on the linear combination fit with reference to known standard data.

Plutonium surrogate leaching

To evaluate the influence of fissile surrogate choice on the leaching behavior, $CaZr_{0.80}U_{0.20}Ti_{2.00}O_7$ was subjected to the same accelerated leaching as $CaZr_{0.80}Ce_{0.20}Ti_{2.00}O_7$. Data for the first leaching step are shown in Fig. 3b and Supplementary Table 1, and the second step in Fig. 7 and Supplementary Table 2. In contrast to the first leaching of $CaZr_{0.80}Ce_{0.20}Ti_{2.00}O_7$ (Fig. 3a), the greatest release of U into the leaching medium was stimulated by 8M HNO_3, corresponding to a release of 7.1 ± 0.10%. Release fractions of the other constituents Ca, Ti and Zr were considerably lower than for U (Supplementary Table 1). As observed for the Ce-counterpart zirconolite, the element release generally followed the trend of surrogate (U) > Ca > Ti >> Zr under all conditions, with the exception of 1M H_2SO_4, in which a marginally greater amount of Ca was detected in the aqueous phase than U. As detailed previously, this is indicative of the preferential leaching of Ca from the minor accessory perovskite. The second highest degree of leaching was observed for 1M HNO_3 medium, resulting in 5.17 ± 0.01% U release. The zirconolite formulated with U was clearly more susceptible to leaching in HNO_3 media, whereas the Ce counterpart composition was preferentially leached in H_2SO_4. This is due to the oxidation of U^{4+} within the zirconolite structure (Fig. 2) to the highly soluble uranyl (U^{6+}) nitrate complex, a mechanism that is not available in the case of Ce^{4+} since it is already in its most oxidised form. While geochemical modelling indicated that polymorphs of TiO_2 were saturated in solution, SEM analysis of $CaZr_{0.80}U_{0.20}Ti_{2.00}O_7$ material recovered from solution did not evidence spherical TiO_2 precipitates. The lack of TiO_2 was attributed to the lower occupation of perovskite in the microstructure when compared with $CaZr_{0.80}Ce_{0.20}Ti_{2.00}O_7$.

Leaching in 1M HCl and 1M H_2SO_4 was less aggressive when compared to the HNO_3 solutions, with 0.9 ± 0.2% and ~0.4% of the

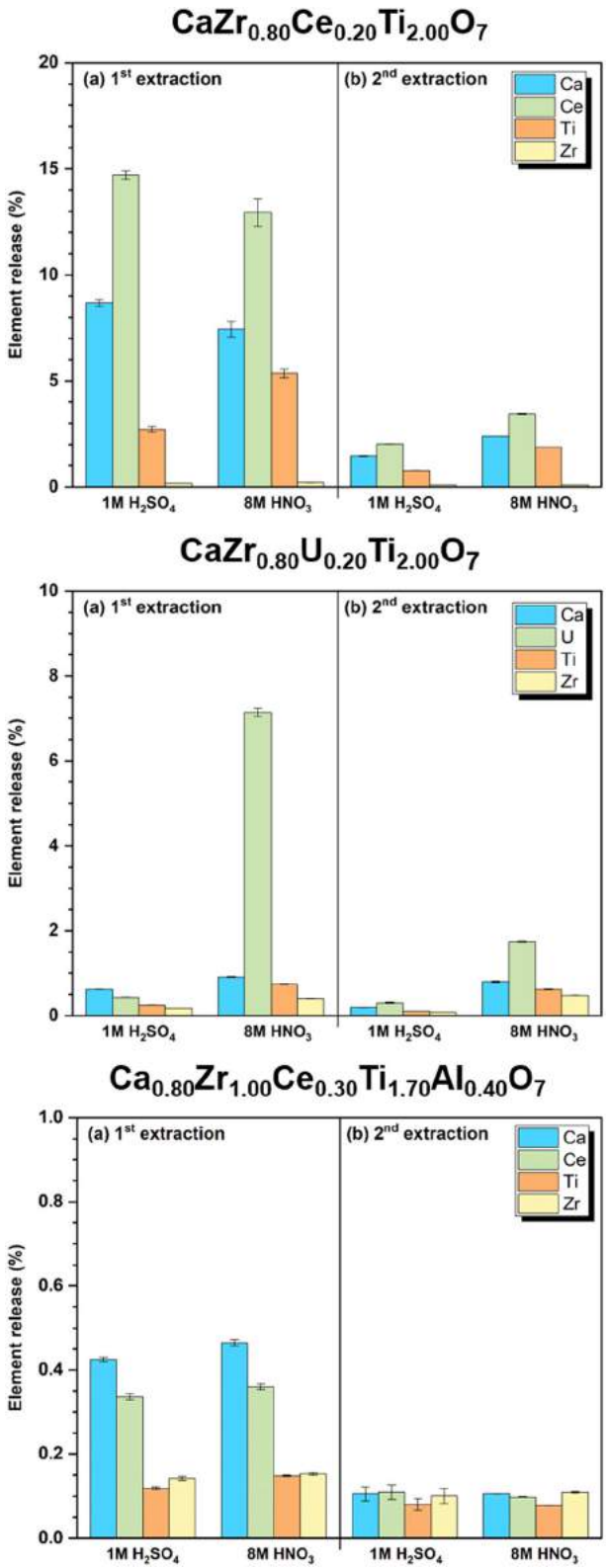

Fig. 7 Elemental release (%) for Ca, Ce, U, Ti and Zr measured for first and second leaching of $CaZr_{0.80}Ce_{0.20}Ti_{2.00}O_7$, $CaZr_{0.80}U_{0.20}Ti_{2.00}O_7$ and reformulated $Ca_{0.80}Zr_{0.90}Ce_{0.30}Ti_{1.60}Al_{0.40}O_7$ in 1M H_2SO_4 and 8M HNO_3, determined by ICP-OES analysis. Error bars represent the standard deviation of duplicate measurements.

initial U inventory dissolved from the ceramic, respectively. As with the corresponding Ce composition, a negligible release fraction was measured for each constituent element when exposed to 1M NaOH solution, as shown in the inset to Fig. 3 (b). Despite this, the concentration of U detected in the leachate amounted to a loss of 0.02 % U, with the remaining elements <0.001%.

In accordance with the procedure applied for the $CaZr_{0.80}Ce_{0.20}Ti_{2.00}O_7$ composition, the U-counterpart zirconolite specimens exposed to 8M HNO_3 and 1M H_2SO_4 were recovered and washed, prior to a second leaching step under identical conditions (Fig. 7). The amount of U released was significantly lower than in the first leaching step; in 8M HNO_3, only $1.7 \pm 0.01\%$ U was released into solution after the second leaching, compared to ~7% in the first. This decrease indicates that the first leaching step effectively removed accessory U-containing phases, which constituted less than 2 wt.% of the pristine phase assemblage (Table 1). The ceramic material remained largely resistant to leaching in 1M H_2SO_4 in the second leaching step, with only $0.30 \pm 0.01\%$ of the remaining U released into solution.

Given the fact that the Ce-containing counterpart still contained perovskite after the first leaching, which was particularly susceptible to leaching in 1M H_2SO_4, it is difficult to make a direct comparison between the leach rates of the two Pu surrogates, Ce and U, contained with the primary zirconolite phase. However, these results indicate that accessory phases in zirconolite materials, formulated using both surrogates, can strongly influence the dissolution of the Pu surrogate. Since $CaZr_{0.80}U_{0.20}Ti_{2.00}O_7$ contained less perovskite, the overall leach rates were lower, however, accessory U-containing phases were susceptible to oxidative leaching in HNO_3.

Accelerated leaching of reformulated Ce-zirconolite

Since the extent of dissolution in all media except 1 M H_2SO_4 and 8 M HNO_3 was negligible, the $Ca_{0.80}Zr_{0.90}Ce_{0.30}Ti_{1.60}Al_{0.40}O_7$ material was subjected to leaching in these media only. As previously noted this reformulated composition did not contain perovskite as an accessory phase. Results of the first leaching are shown in Fig. 7 and Supplementary Table 1; the Ce release was similar in both solutions, at $0.36 \pm 0.01\%$ and $0.34 \pm 0.01\%$ Ce, respectively. Recovery of material, washing, and subsequent introduction to fresh solution resulted in the lowest elemental release for all samples in the study (Supplementary Table 2). The Ce release was the same, within error, at $0.11 \pm 0.02\%$ and $0.098 \pm 0.001\%$, for 1M H_2SO_4 and 8M HNO_3, respectively. Clearly, the concentration of each element released from the $Ca_{0.80}Zr_{0.90}Ce_{0.30}Ti_{1.60}Al_{0.40}O_7$ ceramic formulation was significantly lower (on the order of tenfold in most instances) than the previous formulations containing accessory phases. Interestingly, the general trend in elemental release that was observed previously (Ce > Ca > Ti > Zr) was not observed after either leaching step; rather, each element was released congruently. These data confirm the high aqueous durability of single-phase zirconolite, even in extremely aggressive media. Geochemical modelling confirmed that TiO_2 polymorphs were saturated in solution for both 1M H_2SO_4 and 8M HNO_3 leaching media; nonetheless, SEM analysis of the recovered material failed to evidence surface precipitates.

Compositional design and surrogate choice

There was a marked improvement in the acid leaching resistance of all materials when accessory phases were eliminated. Accordingly, in the case of the reformulated $Ca_{0.80}Zr_{0.90}Ce_{0.30}Ti_{1.60}Al_{0.40}O_7$

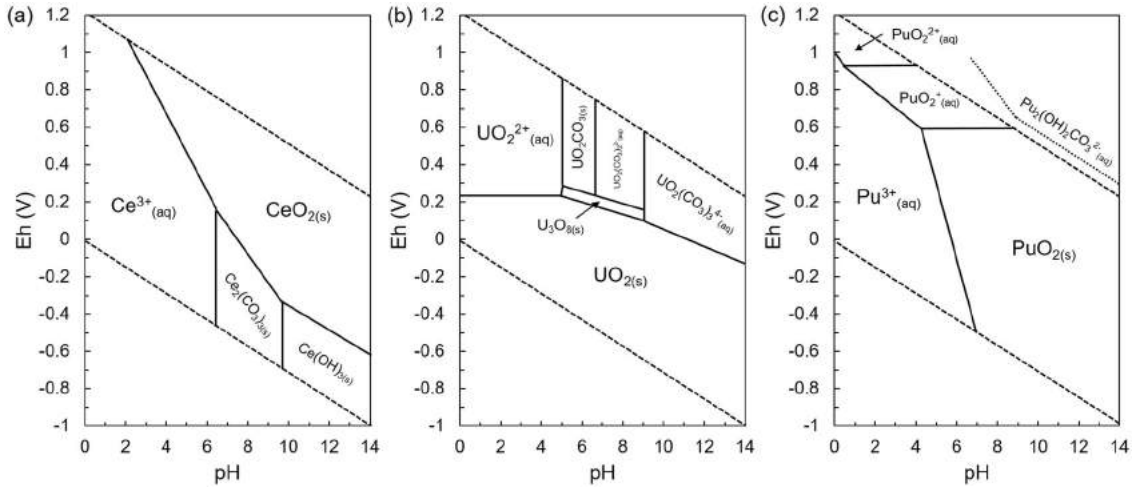

Fig. 8 Pourbaix diagrams for Ce, U and Pu. Showing **a** the Ce–C–O–H system; **b** the U–C–O–H system; and **c** the Pu–(C)–O–H system all at 25 °C and 1 bar, with 10^{-6} M Ce, U and Pu, and 10^{-3} M C. C is included since the experiments were performed in equilibrium with atmosphere CO_2. Adapted from Brookins[33].

composition, which was designed to preclude accessory phases, the resistance to leaching was extremely high. The presence of perovskite was particularly detrimental to leach resistance, with the effects most strongly evident in the Ce-containing $CaZr_{0.80}Ce_{0.20}Ti_{2.00}O_7$ composition.

Ce^{3+}-bearing perovskite formation during zirconolite synthesis is well documented. Clark et al. reported the stabilization of $Ca_{0.4}Ce_{0.4}TiO_3$ perovskite during the synthesis of zirconolite with stoichiometry $CaZr_{1-x}Ce_xTi_2O_7$ under reducing conditions[26]. Similarly, Blackburn et al. stabilised a Ce-bearing perovskite phase during synthesis of zirconolite using highly reducing spark plasma sintering[27]. The partial reduction of the Ce inventory to Ce^{3+} (1.34 Å in 12-fold coordination) presumably stabilises the perovskite phase due to greater compatibility with the 12-fold coordinated Ca^{2+} site (1.34 Å), with respect to the eightfold coordinated Ca^{2+} site in the zirconolite structure (1.12 Å). Since Ce^{3+} is more soluble than Ce^{4+}, especially under the acidic conditions of the experiments performed in the present study (Fig. 8), it is this Ce^{3+}-containing perovskite that preferentially dissolves in aqueous media.

This behaviour did not occur to the same extent in $CaZr_{0.80}U_{0.20}Ti_{2.00}O_7$, although the lower elemental release of all elements from this material during the second leaching step indicates that accessory U-containing phases may be less stable than zirconolite. These phases were identified as UO_2, $(Zr,U)O_2$ and perovskite, although it was not possible to confirm that perovskite contained U.

Since the reformulated composition contained no perovskite, there was no capacity for segregation of soluble Ce^{3+} from the main zirconolite-3T phase. The suppression of the accessory perovskite phase, into which Ce^{3+} preferentially partitions, was achieved through compositional reformulation whereby an excess of Zr and Ti were present. The application of such a wasteform design philosophy, in which ideal compositions are reformulated to account for potential variations in valence state, i.e. partial Ce^{3+} speciation, has clear implications for the fabrication of Pu-bearing ceramic phases related to the zirconolite system. Nevertheless, it is understood that the susceptibility of Pu^{4+} to reduce to the Pu^{3+} species, under the given conditions, is notably lower than for Ce^{3+} [9]. Hence, the capacity for Pu^{3+} segregation into a secondary perovskite phase, and thus premature release under acidic leaching conditions, is markedly reduced with respect to Ce^{3+}.

Comparison of the Pourbaix diagrams for Ce and U (Fig. 8a and b) shows that in aqueous media, these elements are expected to behave differently, largely on account of the propensity for oxidation of U^{4+} to aqueous U^{6+} species. According to these diagrams, provided Ce remains in its tetravalent state, it should be stable across a wide range of redox conditions. This explains the low level of Ce release exhibited in 1M NaOH, with pH 12. In accordance with Fig. 8a, if any Ce^{3+} is present within accessory mineral phases, as observed in the present study, exposure to acidic conditions will result in extensive leaching. In contrast, even in mildly oxidising conditions, U^{4+} will be readily oxidised to aqueous and soluble U^{6+} species across the whole pH range, including at high pH. This was exemplified in the current study by the oxidative dissolution of $CaZr_{0.80}U_{0.20}Ti_{2.00}O_7$ in HNO_3, which gave rise to greater U release than other less-oxidising acid solutions. At high pH, in 1M NaOH, the U release was an order of magnitude greater than the release of Ce in the counterpart sample.

The generic Pourbaix diagram (i.e. 25 °C, 1 bar) for Pu (Fig. 8c) most closely resembles that of Ce (Fig. 8a). The accessible oxidation states available to Pu within a zirconolite wasteform will be the same as those for Ce, i.e. Pu^{4+} and Pu^{3+}-stabilised perovskite (if present). Therefore, it is more likely that a Pu-containing zirconolite would behave like Ce than U under the leaching conditions applied here. Moreover, provided the perovskite content of a Pu-substituted zirconolite ceramic wasteform does not exceed trace levels, the leach resistance, even in aggressive acidic media, is expected to be very high and effectively preclude fissile material recovery. It should be noted, however, that Pu can exist in higher oxidation states, most notably PuO_2^{2+}, especially under highly oxidising, acidic conditions (Fig. 8c). For example, in nuclear fuel reprocessing performed in high-molarity HNO_3, Pu^{4+} is oxidised to the soluble plutonyl ion, $PuO_2^{2+}{}_{(aq)}$. Nevertheless, Pu is much less prone to oxidation into the more soluble +6 oxidation state than U and, therefore, less susceptible to the proposed oxidative dissolution mechanism. This is because the electrochemical cell potential of the U^{4+} to U^{6+} transition is lower than that of the corresponding reaction for Pu and thus occurs more readily. Therefore, even under highly oxidising acidic conditions, a single-phase Pu-zirconolite should be expected to exhibit a much lower Pu release than observed for U from a U-containing counterpart. In the present study, this equated to a release of ~1.7 % of the total U inventory.

In summary, we conclude that the susceptibility of zirconolite compositions to accelerated leaching is influenced by the leaching environment, the targeted zirconolite stoichiometry, and the choice of surrogate used. In particular, the potential for secondary phase ingrowth, which may segregate some portion of the fissile surrogate fraction, is considered to promote premature release for

Ce- and U-bearing zirconolite wasteforms. The accelerated leaching conditions imposed in these experiments do not pertain to disposal conditions, and hence these data cannot be considered representative of zirconolite wasteform leaching in groundwater. There is a clear need for further trials to underpin the dissolution behaviour of optimised zirconolite compositions under conditions representative of the geological disposal environment, to elucidate whether the effects observed in the present study also occur in multi-cation and -anion, near-neutral groundwater solutions, or whether other factors (e.g. complexation by carbonate ions, presence of colloids etc.) are likely to influence the overall dissolution mechanism.

METHODS

Materials synthesis

Zirconolite ceramics with nominal stoichiometry $CaZr_{0.80}Ce_{0.20}Ti_{2.00}O_7$ and $CaZr_{0.80}U_{0.20}Ti_{2.00}O_7$ were prepared from a mixture of component oxides: $CaTiO_3$ (Sigma Aldrich, 99.9% trace metals basis), ZrO_2 (Sigma Aldrich, 99.9% trace metals basis), TiO_2 (anatase, Sigma Aldrich, 99.9% trace metals basis), CeO_2 (Acros Organics, 99.9% trace metals basis) and UO_2 (ABSCO Ltd.). Materials were weighed according to target composition and placed into a 250 mL Y-stabilised ZrO_2 jar and milled at 500 rpm for approximately 40 min with ZrO_2 milling media, using a Fritsch P7 planetary mill. Isopropanol was added as a milling agent. The homogenised precursor slurries were then discharged and dried at 80 °C overnight to allow the evaporation of the excess solvent. Reclaimed batch materials were then calcined at 600 °C for 12 h (air atmosphere for $CaZr_{0.80}Ce_{0.20}Ti_{2.00}O_7$ and flowing Ar gas for $CaZr_{0.80}U_{0.20}Ti_{2.00}O_7$), before being packed into the walls of HIP canisters (grade 316 stainless steel) under uniaxial pressure to achieve maximum packing density. The can lids were then welded into place, before being placed under vacuum and evacuated until an internal can pressure of ~7 Pa was reached. The canisters were then heated under 300 °C until the vacuum recovered, before being crimped shut to ensure a hermetic seal. The cans were placed into the AIP-630 HIP unit and HIPed at 1300 °C, with a 100 MPa dwell pressure maintained for 4 h, using inert Ar gas as the densification medium. Processing of the radioactive ^{238}U containing $CaZr_{0.80}U_{0.20}Ti_{2.00}O_7$ sample was facilitated by the use of the active furnace isolation chamber (AFIC) plug-in component, protected under patent WO 2018/009782 A1[28,29]. The AFIC module is capable of processing U/Th-containing wasteform materials under hot isostatic conditions, preventing dispersal of radioactive material to the HIP pressure vessel in the event of a containment breach. The reformulated $Ca_{0.80}Zr_{0.90}Ce_{0.30}Ti_{1.60}Al_{0.40}O_7$ zirconolite composition was prepared by a conventional cold press and sinter method. Component oxides ($CaTiO_3$, ZrO_2, TiO_2, Al_2O_3 and CeO_2, as above) were weighed according to the desired composition and placed into a 125 mL ZrO_2-lined milling jar with 250 g of 3 mm ZrO_2 milling media, and 25 g isopropanol. The milling jar was placed into a Retsch PM100 Planetary Mill and homogenised at 500 rpm for 2 h. The powder slurry was recovered and dried to evaporate the excess solvent and pressed into the walls of a 25 mm stainless steel die under 100 MPa uniaxial pressure. Densified powder compacts were then placed into a tube furnace and sintered in air; the temperature was increased at a rate of 5 °C/min to 1250 °C, followed by 2 °C/min to 1350 °C with a dwell time of 4 h, before cooling to room temperature at a rate of 5 °C/min.

Materials characterisation

$CaZr_{0.80}Ce_{0.20}Ti_{2.00}O_7$ and $CaZr_{0.80}U_{0.20}Ti_{2.00}O_7$ compositions were sectioned from the HIP canister using a Buehler IsoMet 1000 low speed saw, with material from the bulk recovered for characterisation. All materials were crushed and sieved to recover material in the size fraction 75–150 µm. Powder X-ray diffraction (XRD) data were collected using a Bruker D2 Phaser (Cu Kα source: $\lambda = 1.5418$ Å) with a Ni filter, equipped with a Lynxeye position-sensitive detector. Data were acquired in the range $5^\circ \le 2\theta \le 80^\circ$ with a step size of $0.02^\circ\ s^{-1}$. Scanning electron microscopy (SEM) analyses were performed using either a Hitachi TM3030 (Figs. 4, Supplementary Fig. 1, 3 and 4) operating with a 15 kV accelerating voltage at a working distance of 8 mm or FEI Inspect 50 (Fig. 5) operating at 20 kV accelerating voltage and 10.6 mm working distance. Ce L_3 edge X-ray absorption near-edge structure (XANES) spectra were acquired in transmission mode at the Photon Factory Synchrotron beamline BL-27 (Tsukuba, Japan) using a conventional transmission configuration, with the ring operating at 2.5 GeV and 300 mA. Spectra were collected between 5590 eV and 5990 eV with the following energy steps (with a step rate $1\ s^{-1}$): 5 eV (5590–5690 eV), 0.5 eV (569 –5790), 1 eV (5790–5890 eV), 5 eV (5890–5990). U L_3 edge XANES was acquired at Diamond Light Source (Beamline B18 - Oxford, UK) using a fluorescence configuration. Incident radiation was scanned using a Si(111) monochromator and transmitted beam intensity was measuring using an ionisation chamber filled with a mixture of He and N_2 gas. Fluorescence emission was detected using a four-channel Si-drift detector. Ce L_3 and U L_3 edge XANES spectra were acquired alongside a selection of reference compounds: $CePO_4$, CeO_2, UTi_2O_6, $CrUO_4$ and $MgUO_4$, representing Ce and U in various oxidation states and coordination environment. XANES data reduction and analysis were performed using the Demeter suite[30]. A linear combination fit of Ce L_3 XANES was performed with respect to Ce reference compounds, to determine the relative speciation of Ce^{3+}/Ce^{4+}, using the Athena component of the Demeter package. The average oxidation state of U was calculated by linear regression of the U L_3 E_0 position (determined as the energy where the normalised edge step was equal to 0.5 i.e. $x\mu(E) = 0.5$), with respect to reference compounds of known oxidation state ($U^{4+}Ti_2O_6$, $CrU^{5+}O_4$, $MgU^{6+}O_4$). Compositions were prepared for XANES analysis by finely grinding reacted material with polyethylene glycol (PEG) and pressed in a 13 mm stainless steel die to a thickness equivalent to one absorption length.

Leaching methodology

Since the measured leaching efficiency could be strongly biased by the presence of an adherent fine fraction (<75 µm), prior to static leaching, particulates within the 75–150 µm size fraction were repeatedly washed in isopropanol solvent, as per the ASTM PCT-B protocol[31] and ultra-sonicated to suspend and remove fines. SEM analysis confirmed that the cleaning process had sufficiently removed any entrained fine particulates (Supplementary Fig. 5). Leach tests were performed using 0.5 g of material added to 10 mL of leachate within Teflon vessels. The surface area was determined geometrically and the resulting surface area to volume ratio was $600\ m^{-1}$. The leaching media investigated were 1M HNO_3 (Fisher, analytical reagent grade, 70%), 1M H_2SO_4 (Fluka, Puriss p.a. 95.0–97.0%), 1M HCl (Fisher, analytical reagent grade 37%), 1M NaOH (Merck, EMSURE pellets for analysis, 99–100%) and 8M HNO_3 (Fisher, analytical reagent grade, 70%). All experiments were performed in duplicate, with duplicate blanks (i.e. leaching media only), in a controlled temperature oven at 90 ± 2 °C for 7 days. At the termination of each experiment, an aliquot of each solution was removed from each vessel, filtered using a Whatman 0.22 µm nylon syringe filter, and diluted in 1% HNO_3. Elemental concentrations (mg L^{-1}) of constituent elements were analysed by Inductively Coupled Plasma Optical Emission Spectrometry (ICP-OES, Thermo Fisher 6000 iCAP Duo), using a six-point matrix-matched calibration with a 1% HNO_3 flush between samples. Concentrations measured in solution by ICP-OES were normalised to the nominal batch composition, thus allowing the batch leaching efficiency to be calculated as a percentage of the constituent element released from the pristine material into the leachate. The data were collated as such to compare the accelerated leaching properties of each zirconolite composition, with reference to the surrogate fissile fraction release to the aqueous phase in each instance. Accordingly, the normalised release of each element, reported as a percentage, was calculated from Eqs. 2 and 3.

$$m_{ij} = (C_{ij} \times V_{fj}) - \sum_{(k=1)}^{a} V_{bk} \times \frac{B_{ik}}{a} \quad (2)$$

where m_{ij} is equal to mass of element i released from the test sample j (in g); C_{ij} is equal to the concentration of element i measured in leaching solution from the test sample j (in g L^{-1}); V_{fj} is equal to the final volume of leachate in a test vessel containing the test sample j (in L); B_{ik} is equal to the concentration of element i measured in test blank k (in g); V_{bk} is equal to the final volume of solution in test blank k (in L); a is the number of blank solutions used for background solutions. This was then used to calculate the normalised elemental release as per Eq. 3:

$$NE_{\%} = \left(\frac{m_{ij}}{f_i \times m_j}\right) \times 100 \quad (3)$$

where $NE_{\%}$ is equal to normalised elemental release from sample j based on element i (in %); m_{ij} is as calculated from Eq. 2 (in g); f_i is the mass fraction of element i in test sample j; m_j is equal to the mass of test sample j (in g). The

reported values represent the average of duplicate samples. Geochemical modelling of the experimental data from the leaching solutions was performed with the geochemical speciation software PHREEQC, using the Lawrence Livermore National Laboratory thermodynamic database, LLNL-TDB[32]. These calculations are valid for temperatures in the range 0–300 °C. In order to quantify the degree of saturation of the solution in regards to the precipitation of some phases, the saturation index, SI, was calculated using Eq. 4.

$$SI = \log \frac{IAP}{K_S^0} \quad (4)$$

with *IAP* representing the ion activity product for the given phase dissolution reaction, and K_s^0 representing the standard solubility constant related to the phase.

DATA AVAILABILITY

The data that support these findings cannot be shared at this time, as the data also form part of an ongoing study.

Received: 12 January 2021; Accepted: 13 April 2021;
Published online: 20 May 2021

REFERENCES

1. Hyatt, N. C. Safe management of the UK separated plutonium inventory: a challenge of materials degradation. *npj Mater. Degrad.* **4**, 28 (2020).
2. Gatehouse, B. M., Grey, I. E., Hill, R. J. & Rossell, H. J. Zirconolite, $CaZr_xTi_{3-x}O_7$; Structure refinements for near-end-member compositions with x = 0.85 and 1.30. *Acta Cryst.* **B37**, 306–312 (1981).
3. Blackburn, L. R. et al. A systematic investigation of the phase assemblage and microstructure of the zirconolite $CaZr_{1-x}Ce_xTi_2O_7$ system. *J. Nucl. Mater.* **535**, 152137 (2020).
4. Gilbert, M. R. et al. Synthesis and characterisation of Pu-doped zirconolites - $(Ca_{1-x}Pu_x)Zr(Ti_{2-2x}Fe_{2x})O_7$. *IOP Conf. Ser. Mater. Sci. Eng.* **9**, 012007 (2010).
5. Ma, S. et al. Effects of ionic radius on phase evolution in Ln-Al co-doped $Ca_{1-x}Ln_xZrTi_{2-x}Al_xO_7$ (Ln = La, Nd, Gd, Ho, Yb) solid solutions. *Ceram. Int.* **44**, 15124–15132 (2018).
6. Begg, B. D., Day, R. A. & Brownscombe, A. Structural Effect of Pu Substitutions on the Zr-site in Zirconolite. in *Mat. Res. Soc. Symp. Proc.* **663**, 1–8 (2001).
7. Ewing, R. C., Weber, W. J. & Lian, J. nuclear waste disposal-pyrochlore ($A_2B_2O_7$): Nuclear waste form for the immobilization of plutonium and 'minor' actinides. *J. Appl. Phys.* **95**, 5949–5971 (2004).
8. Clinard, F. W. et al. Alpha decay self-irradiation damage in ^{238}Pu-substituted zirconolite. *J. Nucl. Mater.* **105**, 248–256 (1982).
9. Begg, B. D., Vance, E. R., Day, R. A., Hambley, M. & Conradson, S. D. Plutonium and neptunium incorporation in zirconolite. *Mater. Res. Soc. Symp. Proc.* **465**, 325–332 (1997).
10. Meng, C., Ding, X., Li, W., Zhao, J. & Yang, H. Phase structure evolution and chemical durability studies of Ce-doped zirconolite–pyrochlore synroc for radioactive waste storage. *J. Mater. Sci.* **51**, 5207–5215 (2016).
11. Cai, X., Teng, Y., Wu, L., Zhang, K. & Huang, Y. The synthesis and chemical durability of Nd-doped single-phase zirconolite solid solutions. *J. Nucl. Mater.* **479**, 455–460 (2016).
12. Strachan, D. M. et al. Radiation damage effects in candidate titanates for Pu disposition: Zirconolite. *J. Nucl. Mater.* **372**, 16–31 (2008).
13. Icenhower, J. P. et al. Dissolution kinetics of pyrochlore ceramics for the disposition of plutonium. *Am. Miner.* **91**, 39–53 (2006).
14. Smith, K. L., Lumpkin, G. R., Blackford, M. G., Day, R. A. & Hart, K. P. The durability of Synroc. *J. Nucl. Mater.* **190**, 287–294 (1992).
15. Vance, E. R. et al. Incorporation of uranium in Zirconolite ($CaZrTi_2O_7$). *J. Am. Ceram. Soc.* **85**, 1853–1859 (2002).
16. Zhang, Y. et al. Zirconolite-rich titanate ceramics for immobilisation of actinides - waste form/HIP can interactions and chemical durability. *J. Nucl. Mater.* **395**, 69–74 (2009).
17. Marples, J. A. C. The plutonium-zirconium phase diagram. *J. Less Common. Met.* **2**, 331–351 (1960).
18. Albiol, T., Serizawa, H. & Arai, Y. Studies in the PuO2-ZrO2 pseudo-binary phase diagram. *J. Nucl. Sci. Technol.* **3**, 834–837 (2002).
19. Vance, E. R. et al. In *Environmental Issues and Waste Management Technologies in the Ceramic and Nuclear Industries IX* .(eds. Vienna J. D. & Spearing D. R.) (Wiley, 2006).
20. Grey, I. E., Mumme, W. G., Ness, T. J., Roth, R. S. & Smith, K. L. Structural relations between weberite and zirconolite polytypes - Refinements of doped 3T and 4M $Ca_2Ta_2O_7$ and 3T $CaZrTi_2O_7$. *J. Solid State Chem.* **174**, 285–295 (2003).
21. Hubert, S., Heisbourg, G., Dacheux, N. & Moisy, P. Effect of inorganic ligands and hydrogen peroxide on ThO_2 dissolution. Behavour of $Th_{0.87}Pu_{0.13}O_2$ during leaching test. *Inorg. Chem.* **47**, 2064–2073 (2008).
22. Nesbitt, H. W. et al. Thermodynamic stability and kinetics of perovskite dissolution. *Nature* **289**, 358–362 (1981).
23. Myhra, S., Bishop, H. E., Rivière, J. C. & Stephenson, M. Hydrothermal dissolution of perovskite ($CaTiO_3$). *J. Mater. Sci.* **22**, 3217–3226 (1987).
24. Pham, D. K., Neall, F. B., Myhra, S., Smart, R. S. C. & Turner, P. S. Dissolution mechanisms of $CaTiO_3$ - solution analysis, surface analysis and electron microscope studies – Implications for Synroc. *Mat. Res. Soc. Symp. Proc.* **127**, 231–240 (1989).
25. Zhang, Z., Blackford, M. G., Lumpkin, G. R., Smith, K. L. & Vance, E. R. Aqueous dissolution of perovskite ($CaTiO_3$): effects of surface damage and [Ca^{2+}] in the leachant. *J. Mater. Res.* **20**, 2462–2473 (2005).
26. Clark, B. M., Sundaram, S. K. & Misture, S. T. Polymorphic transitions in cerium-substituted zirconolite ($CaZrTi_2O_7$). *Sci. Rep.* **7**, 2–10 (2017).
27. Blackburn, L. R., Walling, S. A. & Hyatt, N. C. et al. Synthesis and characterisation of $Ca_{1-x}Ce_xZrTi_{2-2x}Cr_{2x}O_7$: analogue zirconolite wasteform for the immobilisation of stockpiled UK plutonium. *J. Eur. Ceram. Soc.* **40**, 5909–5919 (2020).
28. Gardner, L. J., Walling, S. A. & Hyatt, N. C. Hot isostatic pressing: thermal treatment trials of inactive and radioactive simulant UK intermediate level waste. *IOP Conf. Ser. Mater. Sci. Eng.* **818**, 012009 (2020).
29. Hyatt, N. C. et al. The HADES Facility for High Activity Decommissioning Engineering & Science: part of the UK National Nuclear User Facility. *IOP Conf. Ser. Mater. Sci. Eng.* **818**, 012022 (2020).
30. Ravel, B. & Newville, M. ATHENA, ARTEMIS, HEPHAESTUS: Data analysis for X-ray absorption spectroscopy using IFEFFIT. *J. Synchrotron Radiat.* **12**, 537–541 (2021).
31. ASTM International. Standard test methods for determining chemical durability of nuclear, hazardous, and mixed waste glasses and multiphase glass ceramics: The Product Consistency Test (PCT). https://doi.org/10.1520/C1285-14.2.
32. Parkhurst, D. L. & Appelo, C. A. J. Description of input and examples for PHREEQC Version 3—A Computer Program for Speciation, Batch-Reaction, One-Dimensional Transport, and Inverse Geochemical Calculations. Chapter 43 of Section A, in Groundwater Book 6, Modeling Techniques, Techniques and Methods 6-A43 (1999). https://pubs.usgs.gov/tm/06/a43/pdf/tm6-A43.pdf.
33. Brookins, D. G. Eh-pH diagrams for geochemistry. *Geochim. Cosmochim. Acta* 53, (1989).

ACKNOWLEDGEMENTS

We acknowledge financial support from the Nuclear Decommissioning Authority (NDA) and EPSRC under grant numbers EP/S01019X/1, EP/N017870/1 and EP/R511754/1. CLC is grateful to EPSRC for the award of an Early Career Research Fellowship under grant number EP/N017374/1. This research utilised the HADES/MIDAS facility at the University of Sheffield established with financial support from EPSRC and BEIS, under grant EP/T011424/1. Collection of the Ce L_3 edge XAS data was performed under the approval of the Photon Factory Advisory Committee (Proposal No. 2019G586); the support of Yoshihiro Okamoto (Japanese Atomic Energy Agency) and Noriko Usami (The High Energy Accelerator Research Organisation - Kō Enerugī Kasokuki Kenkyū Kikō) during the experiment is gratefully acknowledged. We acknowledge Diamond Light Source for time on Beamline B18 under Proposal SP17243 and wish to thank G. Cibin for assistance with data acquisition.

AUTHOR CONTRIBUTIONS

Lewis Blackburn —conceptualisation, data collection, formal analysis, original draft preparation. Rachel Crawford— data collection, formal analysis, reviewing and editing. Samuel Walling — data collection, formal analysis, reviewing and editing. Laura Gardner — data collection, formal analysis, reviewing and editing. Max Cole — data collection, formal analysis, reviewing and editing. Shi-Kuan Sun— data collection, formal analysis, reviewing and editing. Clémence Gausse — data collection, formal analysis, reviewing and editing. Amber Mason — data collection, formal analysis, reviewing and editing. Martin Stennett —supervision, formal analysis, reviewing and editing. Ewan Maddrell— supervision, formal analysis, reviewing and editing. Neil Hyatt — funding acquisition, supervision, formal analysis, reviewing and editing. Claire Corkhill —funding acquisition, supervision, formal analysis, reviewing and editing.

COMPETING INTERESTS

The authors declare no competing financial or non-financial Interests.

ADDITIONAL INFORMATION

Supplementary information The online version contains supplementary material available at https://doi.org/10.1038/s41529-021-00171-8.

Correspondence and requests for materials should be addressed to C.L.C.

Reprints and permission information is available at http://www.nature.com/reprints

Publisher's note Springer Nature remains neutral with regard to jurisdictional claims in published maps and institutional affiliations.

Influence of Accessory Phases and Surrogate Type on Accelerated Leaching of Zirconolite Wasteforms. Supplementary Material

L. R. Blackburn[a], R. Crawford[a], S. A. Walling[a], L. J. Gardner[a], M. R. Cole[a], S. K. Sun[a], C. Gausse[a], A. R. Mason[a], E. R. Maddrell[b], M. C. Stennett[a], N. C. Hyatt[a] and C. L. Corkhill[a]

[a]*Immobilisation Science Laboratory, University of Sheffield, Department of Materials Science and Engineering, Sir Robert Hadfield Building, Mappin Street, S1 3JD, UK*

[b]*National Nuclear Laboratory, Workington, Cumbria, CA14 3YQ, UK*

Corresponding authors: c.corkhill@sheffield.ac.uk

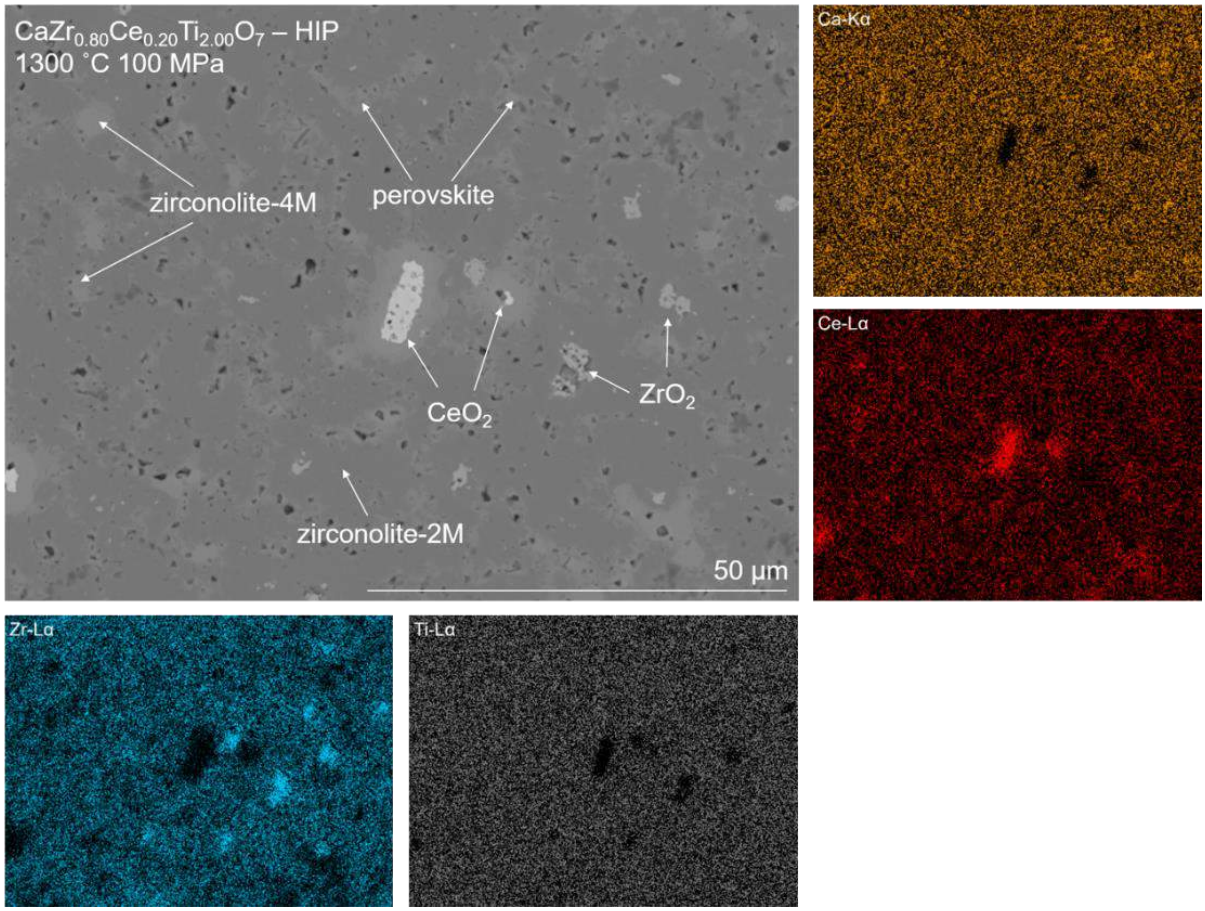

Supplementary Figure 1. SEM-EDS analysis of the bulk HIPed specimen with nominal composition $CaZr_{0.80}Ce_{0.20}Ti_{2.00}O_7$, HIPed at 1300 ˚C for 4 h at 100 MPa.

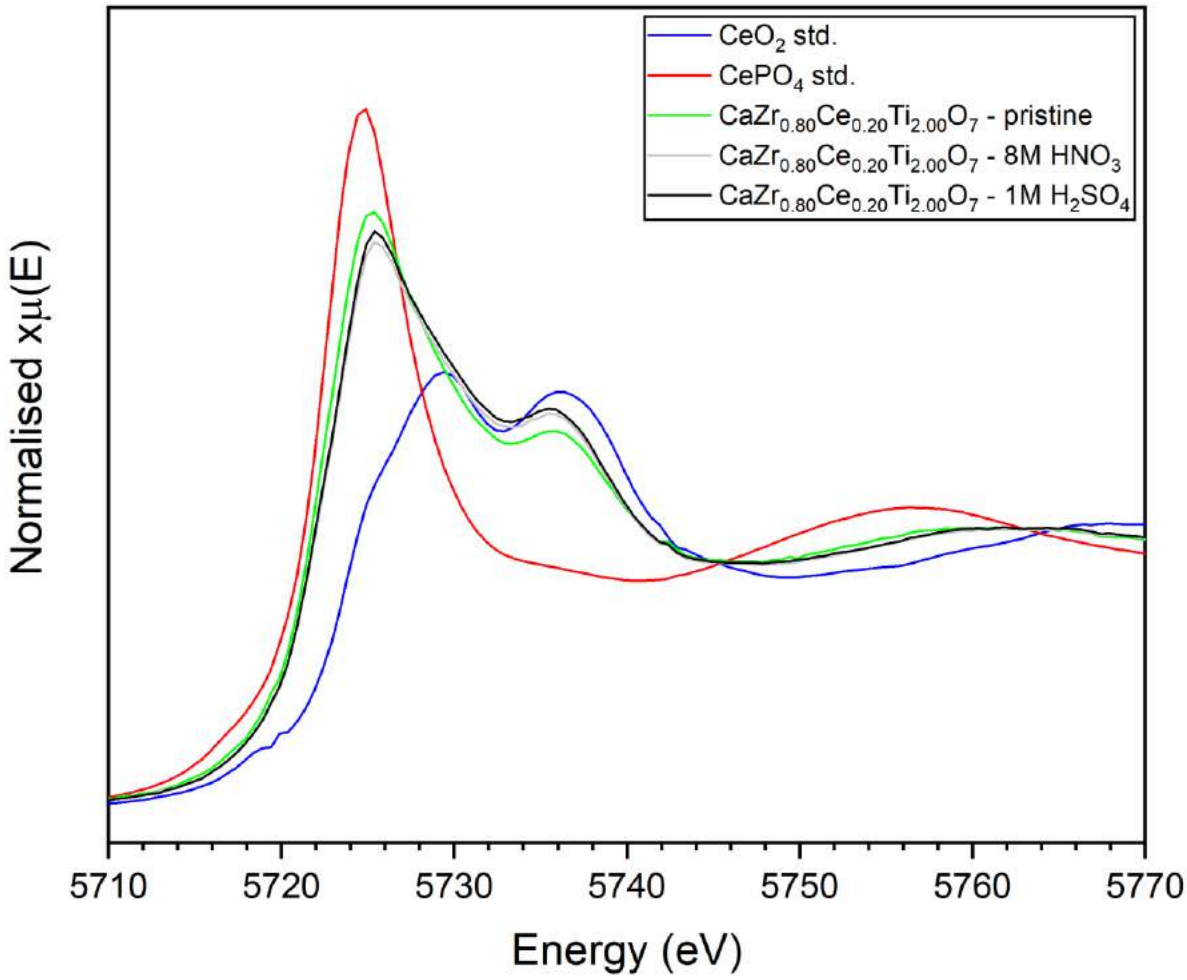

Supplementary Figure 2. Ce L_3 XANES data for HIPed $CaZr_{0.80}Ce_{0.20}Ti_{2.00}O_7$. Data shown correspond to pristine specimen, alongside material recovered from acid leaching in 8M HNO_3 and 1M H_2SO_4 at 90 ˚C for 14 d (cumulated extraction time). Data are presented alongside Ce^{3+} and Ce^{4+} reference compounds ($CePO_4$ and CeO_2, respectively).

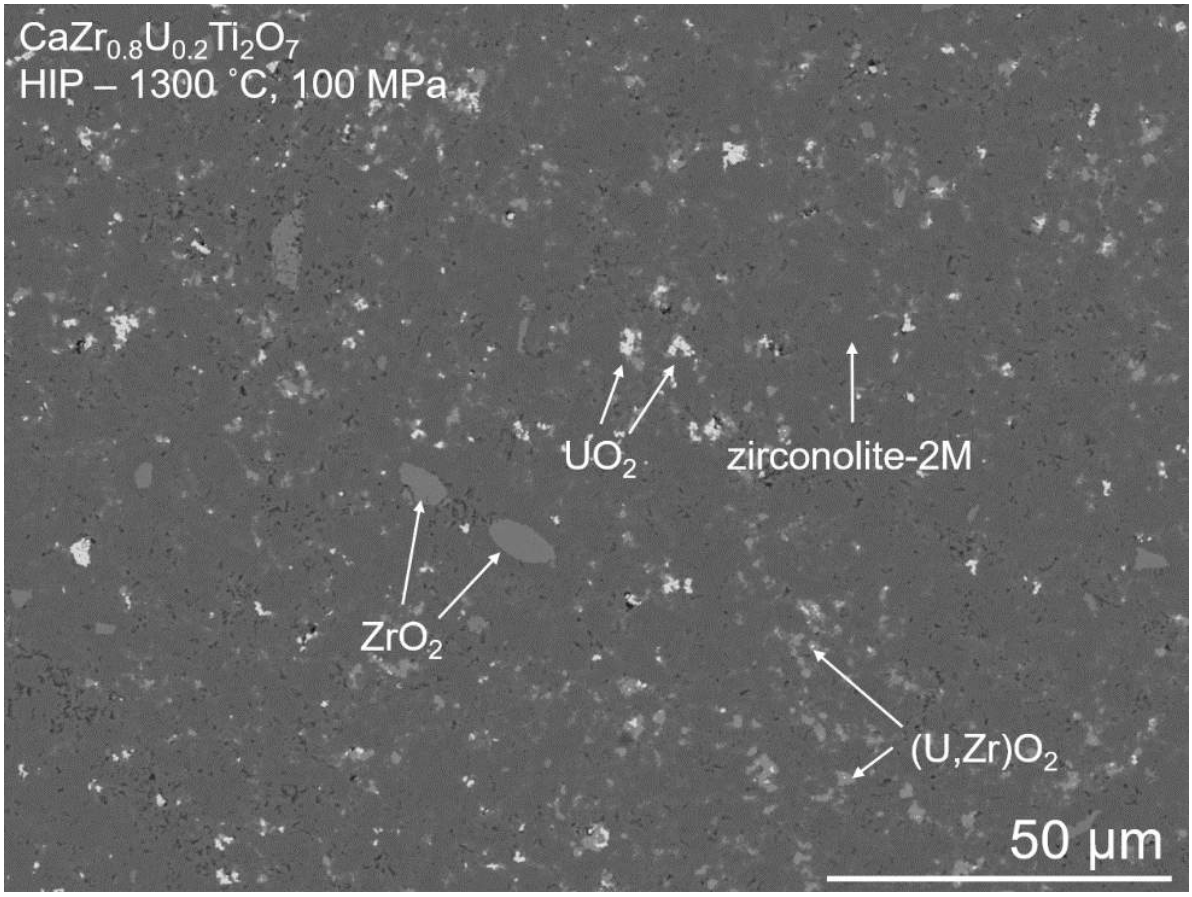

Supplementary Figure 3. Representative backscattered electron micrograph detailing the microstructure for $CaZr_{0.80}U_{0.20}Ti_{2.00}O_7$, HIPed at 1300 ˚C for 4 h at 100 MPa.

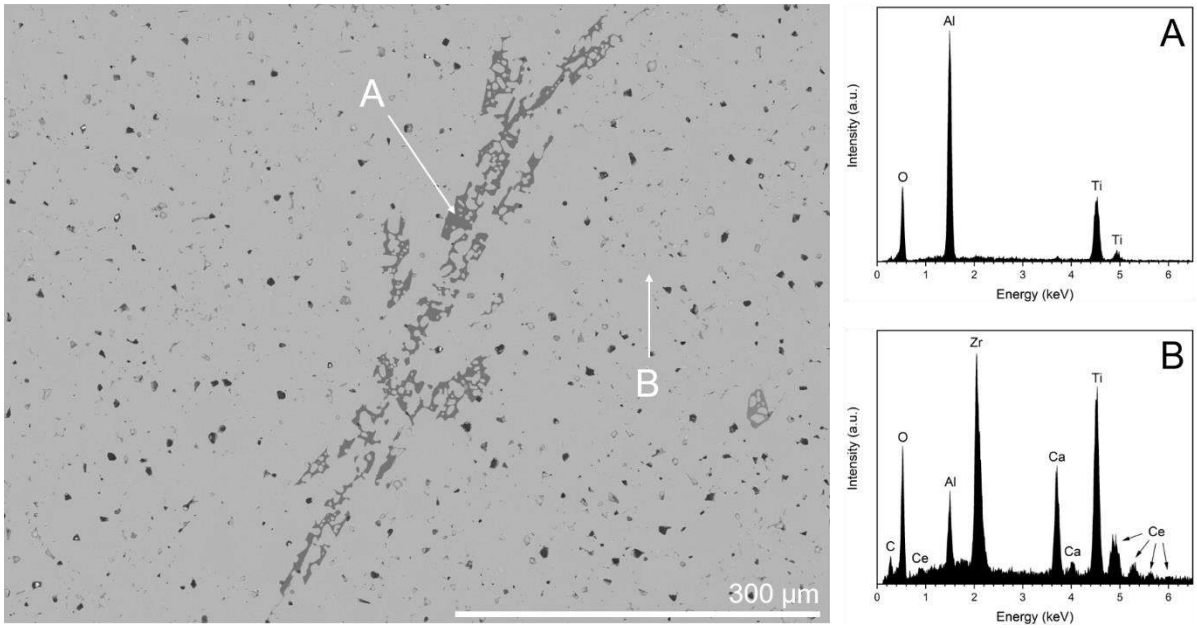

Supplementary Figure 4. SEM-EDS data collected for $Ca_{0.80}Zr_{1.00}Ce_{0.30}Ti_{1.70}Al_{0.40}O_7$. EDS spot data collected at point A (zirconolite-3T) phase and point B (Al_2TiO_5) confirm the phase assemblage identified by powder XRD.

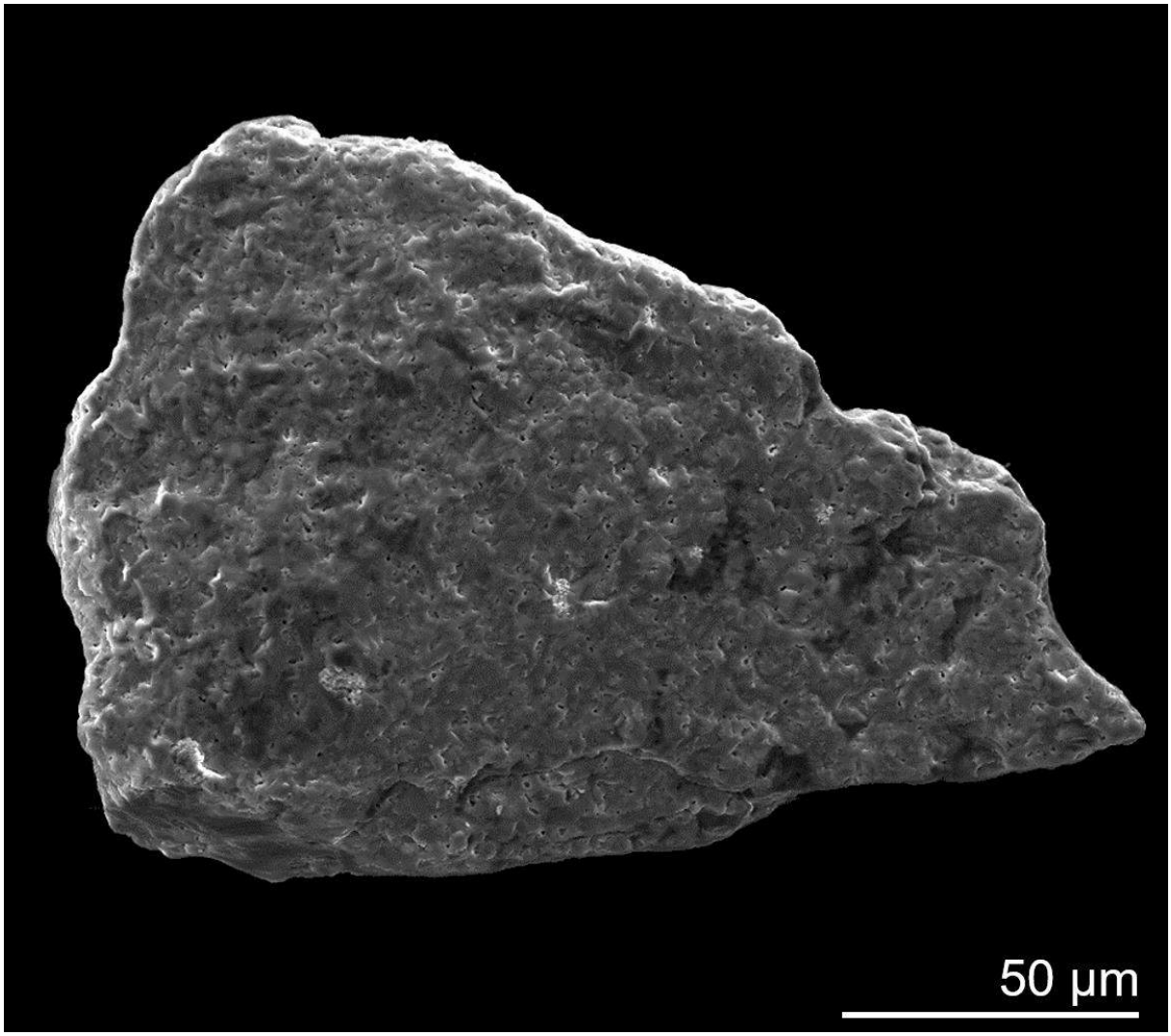

Supplementary Figure 5. SEM surface analysis of pristine $CaZr_{0.80}Ce_{0.20}Ti_{2.00}O_7$ material, prior to accelerated leaching.

Supplementary Table 1. Summary of all leaching data collected for Accelerated Leaching Stage 1 (600 m^{-1}, 90 °C, 7 d)

Composition	Leaching Medium	Accelerated Leaching Stage 1 - Elemental Release (%)									
		Ca	± s.d.	Ce	± s.d.	Ti	± s.d.	U	± s.d.	Zr	± s.d.
$CaZr_{0.80}Ce_{0.20}Ti_{2.00}O_7$	1M HNO_3	2.081	0.001	3.373	0.005	1.402	0.017	-	-	0.004	0.000
$CaZr_{0.80}Ce_{0.20}Ti_{2.00}O_7$	1M HCl	2.439	0.046	3.961	0.088	1.716	0.032	-	-	0.004	0.000
$CaZr_{0.80}Ce_{0.20}Ti_{2.00}O_7$	1M NaOH	0.011	0.000	0.003	0.003	0.001	0.001	-	-	0.002	0.000
$CaZr_{0.80}Ce_{0.20}Ti_{2.00}O_7$	1M H_2SO_4	8.679	0.159	14.712	0.202	2.723	0.135	-	-	0.167	0.004
$CaZr_{0.80}Ce_{0.20}Ti_{2.00}O_7$	8M HNO_3	7.443	0.367	12.938	0.638	5.364	0.209	-	-	0.207	0.008
$CaZr_{0.80}U_{0.20}Ti_{2.00}O_7$	1M HNO_3	0.439	0.002	-	-	0.149	0.003	5.166	0.007	0.009	0.000
$CaZr_{0.80}U_{0.20}Ti_{2.00}O_7$	1M HCl	0.337	0.002	-	-	0.103	0.001	0.948	0.146	0.004	0.000
$CaZr_{0.80}U_{0.20}Ti_{2.00}O_7$	1M NaOH	0.000	0.000	-	-	0.001	0.000	0.020	0.000	0.001	0.000
$CaZr_{0.80}U_{0.20}Ti_{2.00}O_7$	1M H_2SO_4	0.624	0.005	-	-	0.249	0.003	0.435	0.003	0.180	0.002
$CaZr_{0.80}U_{0.20}Ti_{2.00}O_7$	8M HNO_3	0.909	0.014	-	-	0.742	0.009	7.142	0.096	0.404	0.004
$Ca_{0.80}Zr_{1.00}Ce_{0.30}Ti_{1.70}Al_{0.40}O_7$	1M H_2SO_4	0.425	0.005	0.336	0.007	0.119	0.004	-	-	0.141	0.004
$Ca_{0.80}Zr_{1.00}Ce_{0.30}Ti_{1.70}Al_{0.40}O_7$	8M HNO_3	0.465	0.007	0.360	0.006	0.148	0.002	-	-	0.153	0.003

Supplementary Table 2. Summary of all leaching data collected for Accelerated Leaching Stage 2 (600 m^{-1}, 90 °C, 7 d)

Composition	Leaching Medium	Accelerated Leaching Stage 2 - Elemental Release (%)									
		Ca	± s.d.	Ce	± s.d.	Ti	± s.d.	U	± s.d.	Zr	± s.d.
$CaZr_{0.80}Ce_{0.20}Ti_{2.00}O_7$	1M H_2SO_4	1.464	0.021	2.031	0.007	0.768	0.005	-	-	0.097	0.001
$CaZr_{0.80}Ce_{0.20}Ti_{2.00}O_7$	8M HNO_3	2.394	0.001	3.462	0.019	1.873	0.002	-	-	0.099	0.000
$CaZr_{0.80}U_{0.20}Ti_{2.00}O_7$	1M H_2SO_4	0.194	0.002	-	-	0.107	0.000	0.301	0.013	0.082	0.000
$CaZr_{0.80}U_{0.20}Ti_{2.00}O_7$	8M HNO_3	0.802	0.015	-	-	0.624	0.009	1.741	0.013	0.482	0.001
$Ca_{0.80}Zr_{1.00}Ce_{0.30}Ti_{1.70}Al_{0.40}O_7$	1M H_2SO_4	0.105	0.017	0.110	0.018	0.080	0.013	-	-	0.101	0.018
$Ca_{0.80}Zr_{1.00}Ce_{0.30}Ti_{1.70}Al_{0.40}O_7$	8M HNO_3	0.105	0.000	0.098	0.001	0.078	0.000	-	-	0.109	0.001

9. SUMMARY, CONCLUDING REMARKS AND FUTURE WORK

9.1 Summary of Thesis Impact

Within this thesis, a novel study on the impact of surrogate choice in the development of zirconolite wasteforms was presented. A systematic experimental campaign, in which a solid state synthesis route was utilised to produce zirconolite ceramic materials, confirmed that surrogate oxidation states were controlled through the choice processing atmosphere. The substitution of tetravalent Pu surrogates within the Zr^{4+} site generally resulted in a transformation from the archetypical zirconolite-2M structure to the zirconolite-4M superstructure, resulting in an increase in unit cell volume due to a doubling of the c-axis, consistent with the limited studies that have been performed on the corresponding Pu solid solution. Imposing reducing conditions in the $CaZr_{1-x}Pu_xTi_2O_7$ system is known to result in the formation of the trigonal polytype zirconolite-3T, however this was only observed in the $CaZr_{1-x}Th_xTi_2O_7$ solid solution. Studies of the wider literature confirm that the zirconolite-3T polytype may also be stabilised through considerable substitution on the Ca^{2+} site, facilitated by an appropriate charge balancing mechanism, however this was not observed when synthesising the $Ca_{1-x}Ce_xZrTi_{2-2x}Cr_{2x}O_7$ solid solution. The data presented within this thesis indicate that, whilst larger trends in zirconolite polytype phase evolutions can be identified, surrogate choice and processing atmosphere can produce diversions from the expected phase fields.

9.2 Synthesis of $CaZr_{1-x}M_xTi_2O_7$ (M = Ce, U, Th)

A systematic comparison of Pu surrogate incorporation in the zirconolite phase was achieved in the $CaZr_{1-x}M_xTi_2O_7$ system (M = Ce/U/Th), with the effect of sintering atmosphere on Ce, U and Th substitution in the Zr^{4+} site determined by characterisation of the produced phase assemblage, microstructure and surrogate oxidation state. Ce accommodation in zirconolite was most readily achieved in air, whereby a transformation to the zirconolite-4M polytype was observed in the interval $0.10 \leq x \leq 0.20$. Imposing inert and reducing conditions were sufficient to reduce the Ce^{4+} inventory such that a secondary Ce-bearing perovskite phase was present, occupying 37.3 ± 0.4 and 47.6 ± 0.3 wt. % of the overall phase assemblage, respectively. Despite zirconolite-4M dominating the phase assemblage at high Ce concentration, when sintering in air, it was determined by Ce L_3 XANES data that around 28% of the available Ce inventory was reduced to Ce^{3+}. U was deployed as a Pu surrogate under identical processing conditions, however, the phase evolution and overall phase assemblages were varied, on account of variable oxidation states between U and Ce. Synthesis under inert conditions was sufficient to retain the majority of the U inventory as U^{4+}, allowing isovalent substitution for Zr^{4+}, promoting the formation of zirconolite-4M in the expected compositional interval. Imposing reducing conditions during the sintering stage promoted the formation of a U-substituted perovskite at all levels of targeted U concentration, alongside a $CaUTi_2O_7$ pyrochlore-structured phase above x = 0.30. These phase fields were confirmed by selected area electron diffraction of zirconolite-2M, zirconolite-4M and pyrochlore grains. The formation of higher oxidation states was achieved by synthesis in air, with the average valence state of U determined by U L_3 XANES to be > U^{5+}. Oxidative sintering significantly destabilised the phase assemblage, whereby a c-ZrO_2 structure with elevated U content was observed

in all compositions for which x ≥ 0.20. Analysis of the available validation studies that exist for Pu concluded that this behaviour is not replicated in air under the corresponding solid solution regime *i.e.* $CaZr_{1-x}Pu_xTi_2O_7$, hence this was considered to be a limiting factor in U-Pu surrogacy. The novel $CaZr_{1-x}Th_xTi_2O_7$ was synthesised under oxidising and reducing conditions, with the view to complement published Ce, U and Th solid solutions. Synthesis in air did not promote the formation of the intermediate zirconolite-4M phase, as would be expected. Rather, a binary mixture of zirconolite-2M and pyrochlore was observed in the compositional range 0.10 ≤ x ≤ 0.50, with the relative quantity of pyrochlore increasing from 6.8 ± 0.6 to 85.7 ± 0.1 wt. % in this interval. The formulation $CaZr_{0.40}Th_{0.60}Ti_2O_7$ was shown to form a single phase, with structural parameters refined by the Rietveld method. This novel pyrochlore phase may have applications for the immobilisation of Th-rich wastes and residues. Synthesis under 5% H_2/N_2 promoted Th^{4+} segregation in a secondary perovskite phase, alongside residual unincorporated ThO_2. The phase fields formed when targeting Ce^{4+}, U^{4+} and Th^{4+} as surrogates for Pu^{4+} are summarised in **Fig. 43**.

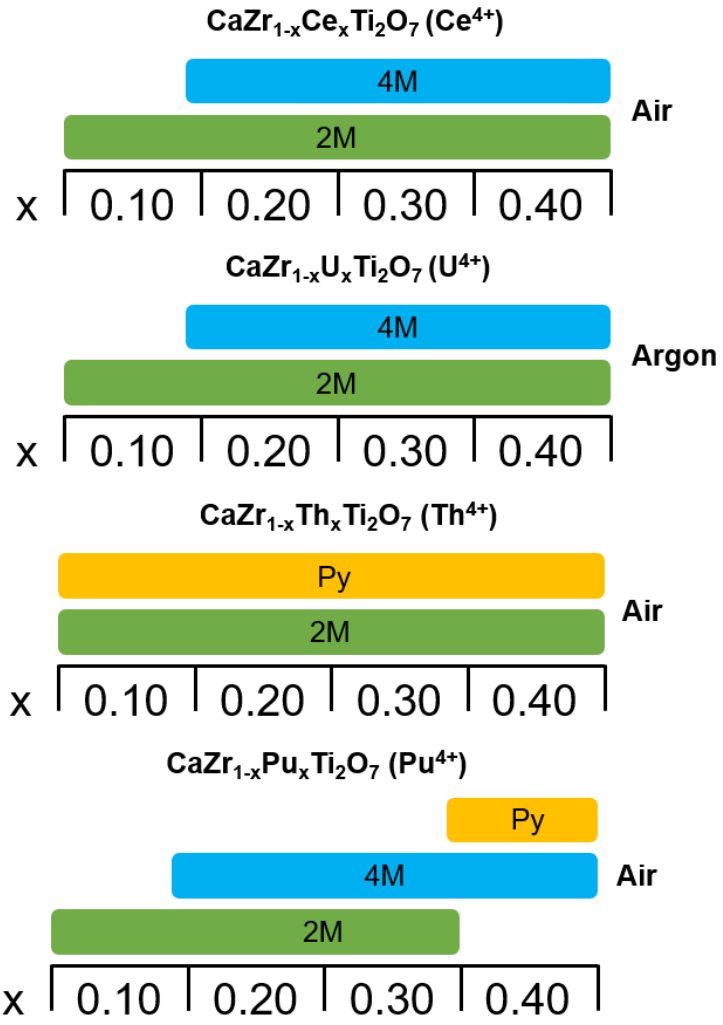

Fig. 43) Phase fields for $CaZr_{1-x}Ce_xTi_2O_7$, $CaZr_{1-x}U_xTi_2O_7$ and $CaZr_{1-x}Th_xTi_2O_7$ solid solutions produced in this thesis (targeting tetravalent Ce^{4+}, U^{4+} and Th^{4+}, respectively) alongside the reported $CaZr_{1-x}Pu_xTi_2O_7$ composition (targeting Pu^{4+}) from Begg *et al.* [1]

9.3 Synthesis of $Ca_{1-x}Ce_xZrTi_{2-2x}(Al,Fe,Cr)_{2x}O_7$

Survey of the available literature suggests that Pu^{4+} incorporation in the zirconolite phase may be most readily achieved *via* a charge coupled substitution, whereby Pu^{4+} is accommodated in the Ca^{2+} site, facilitated by the co-substitution of a lower valence charge balancing species across the available Ti^{4+} sites. The feasibility of Cr^{3+} as a charge balancing cation was systematically investigated, with Ce^{4+} deployed as a Pu^{4+} surrogate. A detailed characterisation of the phase evolution in the $0.05 \leq x \leq 0.35$ compositional interval was provided, confirming the formation of single phase zirconolite-2M in the range $0.05 \leq x \leq 0.15$. Above this threshold, ancillary phases Cr_2O_3, CeO_2, ZrO_2 and Ce-substituted perovskite were observed, although when targeting a Ce concentration corresponding to $x = 0.35$, the zirconolite phase remained present at ~ 94 wt. %. A polytype transformation to zirconolite-3T, as has been detailed for the analogous $Ca_{1-x}Pu_xZrTi_{2-2x}Fe_{2x}O_7$ solid solution, was not observed, as confirmed by selected area electron diffraction of $x = 0.05$ and $x = 0.35$ compositions. Ce L_3-edge XANES measurements were performed as to ascertain the dominant oxidation states of Ce across the bulk microstructure. Despite sintering under oxidising conditions, an ingrowth of between 16 – 27% Ce^{3+} was observed. Cr K-edge XANES data were consistent with uniform Cr^{3+} speciation; deconvolution of the Cr K pre-edge features for the single phase $Ca_{0.85}Ce_{0.15}ZrTi_{1.70}Cr_{0.30}O_7$ composition, alongside a suite of reference compounds, allowed the local coordination of Cr to be determined, by analogy, as consistent with substitution in the six-fold Ti^{4+} site. Evaluation of the microstructure by SEM and Archimedes density testing confirmed the suite of samples were poorly densified. Hence, a novel reactive spark plasma sintering technique was deployed for the sample with nominal composition $Ca_{0.80}Ce_{0.20}ZrTi_{1.60}Cr_{0.40}O_7$, with the view to observe the impact of the high densification technique on the phase assemblage relative to conventional sintering. Despite a marked increase to near theoretical density, the reducing conditions imposed by the graphite die were sufficient to completely reduce the available Ce^{4+} inventory to Ce^{3+}, determined by XANES analysis. Accordingly, the phase assemblage was significantly disrupted, with a secondary Ce-rich perovskite phase occupying 19.3 ± 0.4 wt. % of the microstructure.

9.4 Zirconolite Synthesis by Hot Isostatic Pressing

Immobilisation of the U.K. bulk PuO_2 inventory may be accomplished through a campaign of hot isostatic pressing (HIP), whereby a homogenised blend of PuO_2 and ceramic-forming precursor are discharged into stainless steel HIP cans, evacuated, and simultaneously heated and densified through the application of isostatic pressure under elevated temperature. Such a consolidation process would afford the greatest achievable density, producing waste packages of near-net shape that are compatible with placement alongside HLW inventories in the geological disposal environment. Accordingly, it is necessary to trial small scale inactive and active simulants of zirconolite wasteforms *via* HIP, to determine the feasibility of this process and the influence of the HIP environment on zirconolite phase formation relative to conventional sintering. Three zirconolite compositions corresponding to $CaZr_{0.80}Ce_{0.20}Ti_2O_7$, $CaZr_{0.80}U_{0.20}Ti_2O_7$ and $CaZr_{0.80}Th_{0.20}Ti_2O_7$ were prepared, pressed into the walls of stainless steel HIP canisters and processed at 1300 °C, with a dwell pressure of 100 MPa maintained for 4 h, with heating/cooling rates programmed to 10 °C/min. Samples were successfully densified and

consolidated in all instances with high yield of the zirconolite phase, demonstrating that the HIP process is feasible at the laboratory scale. The yield of secondary phases was dependent on the choice of surrogate deployed, with the Ce composition producing a minor zirconolite-4M phase and a considerable quantity of perovskite. Utilising U as a surrogate resulted in a near homogenous distribution of zirconolite-2M, alongside minor unincorporated UO_2 and a mixed $(U,Zr)O_2$ solid solution. These compositions were carried forward and characterised in detail in Chapter 9. Attempted synthesis of $CaZr_{0.80}Th_{0.20}Ti_2O_7$ yielded an undesirable phase assemblage comprised of unincorporated ThO_2 (3.6 ± 0.1 wt. %), $ThTi_2O_6$ (5.3 ± 0.3 wt. %) and $(Ca,Th)TiO_3$ (14.1 ± 0.6 wt. %) and therefore was not carried forward for accelerated leaching testing. With the view to compare zirconolite phase formation *via* conventional sintering, reactive spark plasma sintering and HIPing, a sample of $Ca_{0.80}Ce_{0.20}ZrTi_{1.60}Cr_{0.40}O_7$ batch material, as used in Chapter 6 studies, was processed by HIP, at 1320 °C, with a dwell pressure of 100 MPa maintained for 4 h. Despite a relatively high yield of zirconolite-2M (~ 92 wt. %), and a comparable fraction of secondary perovskite as achieved by sintering in air, approximately 4 wt. % of the wasteform was comprised of unincorporated CeO_2. Nevertheless, the high density achieved during the HIP process was advantageous to RSPS, insofar as Ce L_3 XANES confirmed that 93.2 ± 2% of the available Ce inventory remained as Ce^{4+}.

9.5 Effect of Surrogate and Secondary Phases on Zirconolite Durability

The primary mechanism by which radionuclides may migrate from the disposal environment into the biosphere is dissolution through contact with groundwater. Therefore, it is imperative during the design of wasteforms to undertake rigorous performance testing under controlled dissolution conditions, so as to ascertain the durability of the material, and allow extrapolation as to how long the immobilisation matrix will remain resistant to extensive leaching over timescales of 10^6 y. A hindrance to this approach is the high durability of titanate mineral species, with normalised release rates of actinide surrogates typically of the order 10^{-5} $gm^{-2}d^{-1}$. With such low release rates, that are often near the limit of detection for conventional solution analysis techniques (*e.g.* ICP-OES) it is, in some instances, advantageous to impose more aggressive leaching conditions, such that an accelerated measure of the dissolution behaviour may be elicited. In order to compare the influence of composition and surrogate choice on the dissolution of zirconolite, an accelerated leaching experiment was designed, loosely based on the PCT-B protocol, with acids such as H_2SO_4 and HNO_3 used as leaching media at 90 °C, over 7 d. Initially, samples of HIPed $CaZr_{0.80}Ce_{0.20}Ti_2O_7$ and $CaZr_{0.80}U_{0.20}Ti_2O_7$ were subjected to leaching in 1M HNO_3, 1M H_2SO_4, 1M HCl, 1M NaOH and 8M HNO_3, with the extent of dissolution characterised as a measure of the extraction efficiency of each element from the ceramic material into solution. The greatest Ce extraction was observed when exposed to 1M H_2SO_4, with 14.7 ± 0.2% of the original Ce inventory released into solution. The extent of dissolution was correlated with the quantity of Ce-rich perovskite present in the wasteform material, associated with the uptake and preferential release of Ce^{3+}. The HIPed $CaZr_{0.80}U_{0.20}Ti_2O_7$ material exhibited improved resistance to leaching in all environments, with the greatest quantity of the original U inventory leached in 8M HNO_3, corresponding to 7.1 ± 0.1% release. Reformulating the zirconolite composition to $Ca_{0.80}Zr_{0.90}Ce_{0.30}Ti_{1.60}Al_{0.40}O_7$, whereby an excess of approximately 0.1 f.u. excess Ti and Zr were added to preclude perovskite formation, was found to

yield near pure zirconolite-3T. Accordingly, the absence of any Ce-bearing secondary phases was shown to significantly increase the overall durability of the wasteform under all imposed conditions, with < 0.4% of the original Ce inventory released to solution in both 8M HNO_3 and 1M H_2SO_4. These data confirm that the choice of chemical surrogate, and in turn the relative yield secondary phases, has a notable influence on the durability of zirconolite wasteforms, with implications for the U.K. Pu disposal campaign.

9.6 Future Work

There are several further avenues of research that could complement the data published within this thesis. Primarily, this would involve an expanded systematic review of charge coupled solid solutions utilising U/Th in place of Ce, comparable to those examined in Chapters 6 and 7. For example, the synthesis and characterisation of $Ca_{1-x}U_xZrTi_{2-2x}Cr_{2x}O_7$, $Ca_{1-x}U_xZrTi_{2-2x}Al_{2x}O_7$, $Ca_{1-x}U_xZrTi_{2-2x}Fe_{2x}O_7$, $Ca_{1-x}Th_xZrTi_{2-2x}Cr_{2x}O_7$, $Ca_{1-x}Th_xZrTi_{2-2x}Fe_{2x}O_7$ and $Ca_{1-x}Th_xZrTi_{2-2x}Al_{2x}O_7$ solid solutions, in conjunction with existing Ce data sets, would provide a rigorous foundation to examine potential single-phase formulations that may be progressed to future Pu validation trials. Moreover, an extended examination of dual-site zirconolite compositions, whereby U/Th is partitioned between both Ca^{2+} and Zr^{4+} sites, with excess Ti and Zr included to preclude secondary phase formation, would greatly supplement the data presented in Chapter 8.

Zirconolite may also be a suitable wasteform for trivalent minor actinide species such as Am^{3+}. As such, there is an interest in the substitution behaviour of Ln^{3+} species (Sm^{3+}, Gd^{3+}, Ce^{3+}, Nd^{3+}) within zirconolite, and subsequent influence on polytype formation. There exist a number of systematic studies wherein Ln^{3+} cations were substituted across both Ca^{2+} and Zr^{4+} sites in zirconolite in equimolar proportions, *i.e.* $Ca_{1-x}Zr_{1-x}Ln_{2x}Ti_2O_7$ [2]–[6]. Dy has been previously utilised as a surrogate for Am in the development of actinide nitride alternative fuels, hence, it is feasible that Dy^{3+} incorporation within the zirconolite phase may simulate the solid solution behaviour of prevalent minor actinide species, such as Am^{3+} within a zirconolite polytype mixture.

It was demonstrated in Chapter 6 that reactive spark plasma sintering (RSPS) is a feasible processing route for the fabrication of high density zirconolite ceramics, with rapid processing times due to high heating/cooling rates achievable. However, the use of Ce as a Pu surrogate in such wasteform development trials proved detrimental, as the graphite die was capable of reducing the available Ce inventory entirely to Ce^{3+}, and as such the targeted zirconolite-rich wasteform was destabilised in favour of a Ce-rich perovskite phase. Therefore, an experimental campaign aiming to optimise the processing parameters (temperature, uniaxial pressure, heating/cooling gradient) of U/Th-doped zirconolite compositions, combined with spectroscopic data to elucidate prevalent surrogate oxidation states, would permit a greater understanding of the feasibility of the RSPS technique to immobilise Pu.

References

[1] B. D. Begg, R. A. Day, and A. Brownscombe, “Structural Effect of Pu Substitutions on the Zr-site in Zirconolite,” in *Mat. Res. Soc. Symp. Proc.*, 2001, vol. 663, pp. 1–8.

[2] M. Jafar, P. Sengupta, S. N. Achary, and A. K. Tyagi, “Phase evolution and microstructural studies in $CaZrTi_2O_7$-$Nd_2Ti_2O_7$ system,” *J. Am. Ceram. Soc.*, vol. 97, no. 2, pp. 609–616, 2014.

[3] M. Jafar, S. N. Achary, N. P. Salke, A. K. Sahu, R. Rao, and A. K. Tyagi, “X-ray diffraction and Raman spectroscopic investigations on $CaZrTi_2O_7$ - $Y_2Ti_2O_7$ system: Delineation of phase fields consisting of potential ceramic host materials,” *J. Nucl. Mater.*, vol. 475, pp. 192–199, 2016.

[4] M. Jafar, P. Sengupta, S. N. Achary, and A. K. Tyagi, “Phase evolution and microstructural studies in $CaZrTi_2O_7$ (zirconolite)-$Sm_2Ti_2O_7$ (pyrochlore) system,” *J. Eur. Ceram. Soc.*, vol. 34, no. 16, pp. 4373–4381, 2014.

[5] C. Meng, X. Ding, W. Li, J. Zhao, and H. Yang, “Phase structure evolution and chemical durability studies of Ce-doped zirconolite–pyrochlore synroc for radioactive waste storage,” *J. Mater. Sci.*, vol. 51, pp. 5207–5215, 2016.

[6] Y. B. Zhang *et al.*, “Phase evolution, microstructure and chemical stability of $Ca_{1-x}Zr_{1-x}Gd_{2x}Ti_2O_7$ ($0.0 \leq x \leq 1.0$) system for immobilizing nuclear waste,” *Ceram. Int.*, vol. 44, no. 12, pp. 13572–13579, 2018.